INTERPRETATION OF THE INFRARED EMISSION LINES FROM STARBURST GALAXIES AND ACTIVE GALACTIC NUCLEI BASED ON PHOTOIONIZATION MODELS

BORJA PÉREZ DÍAZ

UNIVERSIDAD
DE GRANADA

Supervised by
Dr. Enrique Pérez Montero
Dr. José Manuel Vílchez Medina

A dissertation submitted in partial fulfillment
of the requirements for the degree of
Doctor of Philosophy in Physics

Doctoral Programme in Physics and Mathematics
University of Granada

July 17, 2025

INSTITUTO DE
ASTROFÍSICA DE
ANDALUCÍA

EXCELENCIA
SEVERO
OCHOA

CSIC

Borja Pérez Díaz: *Interpretation of the infrared emission lines from starburst galaxies and active galactic nuclei based on photoionization models*

Cover designed by Paula Vizcaíno Valenzuela

SUPERVISOR:
Dr. Enrique Pérez Montero
Dr. José Manuel Vílchez Medina

To the Universe – ever simple, ever silent. The complexity lies not in its nature,
but in our need to understand it.

ACKNOWLEDGMENTS / AGRADECIMIENTOS

Es difícil condensar el agradecimiento de cuatro años de trabajo en unos pocos párrafos. Más aún cuando te das cuenta que no son solo cuatro años, sino toda una vida, académica y personal, que se condensa en esta tesis. Son tantas las personas que han tenido un papel protagonista en mi vida que es bastante probable que haya gente que quede sin mencionar. A esas personas, que por alguna razón del destino puedan estar leyendo esta tesis, les digo que lo que las palabras no expresan son las emociones que el cerebro aún no sabe analizar.

Creo justo y necesario empezar agradeciendo esta tésis a esas excelentes dos personas que me han guiado, mentorado, enseñado y cuidado en estos años de tesis. La suerte que he tenido de tener unos directores de tesis como Enrique y Pepe es difícil de entender si no les conoces en persona. Cuando conocí a Enrique en el año 2019, ya me quedé impresionado por el trabajo que hacía. No es una cuestión de tener más o menos recursos para hacer ciencia (que también ayudan), sino de tener ilusión y ganas. Eso es lo que he aprendido a nivel personal de trabajar con Enrique. A nivel académico, poco más que decir que dejo esta tesis como testigo de toda la paciencia que ha tenido Enrique para enseñarme cosas. A Pepe le conocí un poco más tarde, pero no por ello tiene menos impronta en todo esto. Desde las conversaciones de "marco de puerta" hasta los cafés donde "haya sitio", Pepe siempre ha estado ahí para aconsejarme en todo mi proceso académico. Y ya no hablo de la cantidad de temas de los que he aprendido gracias a él: modelos de evolución química, física al detalle del medio interestelar o procesos estelares. A ambos les agradezco que me hayan dado el espacio y la libertad para desarrollar ciencia a mi ritmo y a mi manera, respetando siempre mis opiniones, y con una paciencia infinita como la que hay que tener para tratar a un cabezota como yo. Y a ambos les echo en cara, pero con cariño, la cantidad de nuevas ideas que siempre saco cuando hablo con ellos, aunque muchas se hayan quedado en el tintero porque el tiempo es el que es. No quiero cerrar el párrafo sin mencionar a Rocko y toda su labor que ha hecho que este proceso sea mucho más fluído en todos los aspectos.

Si ya tuve suerte de tener a Enrique y Pepe como directores, contar con alguien como Juan Antonio es que toque la lotería. No solo es que sea una biblia andante del infrarrojo, no solo es que sepa prácticamente de todo lo que preguntes, es que además es una persona cercana y te alegra cualquier día, aunque te lo pases buscando una base de datos que resulta que no existe. Juan Antonio me acogió desde el primer día con cariño, me enseñó muchísimo del infrarrojo, me compartió sus herramientas y sus impresiones. Me invitó a Teruel, donde saqué provecho de una semana como si fuese una estancia de un mes. En resumen, Juan Antonio, puedes estar seguro de que esta tesis está moldeada por todo lo que me has ayudado.

El grupo de investigación no se reduce a Enrique y Pepe, ni mucho menos. Las conversaciones de ciencia (y de vida) con Antonio, las clases del master de detectores de Jorge, las conversaciones con Carolina sobre galaxias poco metálicas, las ideas de Ricardo para el alto redshift, el espíritu crítico (y muy aventurero) de Antonio Giménez, las cenas gourmet (y picantes) en casa de Saby, tantas charlas con Sergio acompañadas de una buena cerveza y la suerte de poder tutorar a Kostas. Muchas gracias a todos por darle un significado más humano y tierno a la palabra "grupo" sin perder nunca la etiqueta "de investigación".

Cuando me vine a Granada, para empezar el master y los primeros coletazos en ciencia, no estuve solo. Tuve la suerte de ser acogido en el Instituto de Astrofísica de Andalucía (IAA) por dos científicas que me ayudaron en los años más difíciles (pandemia) y más críticos en mi futuro académico. Tanto Pepa como Isabel me enseñaron muchísimas cosas, me apoyaron mucho en el máster y me mostraron la calidez de la que el IAA hace gala. Gracias de corazón por iniciarme en este apasionante mundo, por apostar por mí, y por ayudarme en todo momento a seguir en el mundo académico. También agradezco a Nimisha que me acogiese en Baltimore, en mi estancia en el Space Telescope Science Institute (STScI). Muchas gracias Nimisha por enseñarme los truquillos del James Webb, por presentarme a gente en el STScI, y, por las charlas científicas que tuvimos sobre galaxias a alto redshift.

Ya que he mencionado al IAA, me tocada entonces repasar a esas personas que le dan color a este centro de investigación de prestigio. Me encantaría ir uno a uno, pero entonces la gente va a pensar que esta tesis son sólo agradecimientos (aunque bien lo merecería). A Ana, Belén, Florín, Gerardo, Luis y Teresa, que empezamos juntos esta aventura sin precedentes. Sumo a Miguel, Roberto y Celia también, que aunque llegaron un poco después, en mi mente y en mi corazón siempre han estado ahí desde el principio. A los predocs que nos guiaron con su veteranía: Julio, Valentín, Anthony, Laura, Juan, Julio y Julia. A mis fieles compañeros de despacho Rohan y Marianna. A los predocs que les toca cubrir nuestra ausencia: Marta, Ixaka, Clara, Bet, Mendi, Antonio, Alberto, Oier, Lucía, Javi, Irene, Chema, David, Marina. A todas y todos, gracias de corazón por estos años inolvidables, por vuestra paciencia con mis verborreas, y por los ánimos en el día a día. No solo dais color al IAA, también a la gente que trabaja ahí. Creo que me puedo permitir deciros que, pase a lo que pase, os podéis sentir orgullosos de la impronta que dejáis a vuestro alrededor.

Voy a hacer mención especial a una persona del IAA con la que he compartido mucho más que ciencia. Hemos compartido piso, artículo, animes, videojuegos y experiencias vitales. Me has apoyado muchísimo en momentos donde no tenía claro cómo actuar. Hemos tenido tantas conversaciones en estos años, tantas discusiones sobre temas tan variados, que es difícil condensar todo en unas líneas. Simplemente decirte, Borja, que gracias por todo este tiempo y por todas las experiencias vividas.

En Granada he conocido a muchísima gente que ha hecho de esta experiencia inolvidable, como mis compañeros de Crossfit, con los que he peleado y sudado cada uno de los entrenamientos. La pandemia (sí, había que mencionarla) me brindó la oportunidad también de conocer a gente como Álex, Bárbara, Carlos, Carmen y Sara. Gracias por hacer tan amena una época tan difícil, por compartir inolvidables momentos a altas horas de la madrugada, por seguir ahí y demostrar que los lazos de amistad son tan fuertes que la distancia se convierte en algo anecdótico. Y como hay que decir, que la Fuerza os acompañe siempre.

Y qué decir de la gente de mi tierra asturiana. Gracias Andrés por las conversaciones filosóficas y por hacerme cuestionar tantos aspectos de la ciencia y de la vida. Gracias Pablo por las noches desconectando del trabajo y trabajando en equipo. Gracias Matías por tantas conversaciones y consejos y, especialmente, por la suerte de que te pudieses mudar a Granada. Gracias Mauro por escucharme, aconsejarme y decir las cosas como las piensas. Y cierro con una persona increíble, de una fortaleza inimaginable, y que considero mi familia extendida: Claudia, no sabes cuánto agradezco tenerte en mi vida. Pero especialmente, muchas gracias a todos por seguir ahí después de tanto tiempo y de tanta distancia.

Quiero dedicar este párrafo a una personal especial, una persona que me ha dado tanto cariño, apoyo y comprensión, que cualquier palabra que piense se queda corta para describirla. Muchas gracias por todo Nikola, por ser como eres, por aceptarme como soy, y por estar siempre ahí. A saber qué nos queda por vivir pero, pase lo que pase, tengo la certeza de que cada momento merecerá la pena.

Dejo para el final a esas personas que me han acompañado toda mi vida. A toda mi familia, por creer siempre en mi. A mis abuelos, con especial cariño para Aníbal y Monchu, por cuidarme siempre, por enseñarme todo lo que sabían y por apoyarme tanto. A mi hermano Iván, al que aprovecho para decir que no dudes nunca de ti mismo, que tengas claro que si te lo propones, lo conseguirás. Y, a mi padre y a mi madre, por apoyarme en mis sueños, por respetar todas mis decisiones, y por estar siempre ahí. No solo os doy las gracias, os digo que os llevo en el corazón y que soy lo que soy por vosotros.

No ha sido fácil escribir esto, en parte porque una vez el sentimiento domina la razón, las palabras brotan caóticas pero llenas de vida. No solo os doy las gracias por todo, también os pido disculpas por todos mis fallos. Os pido disculpas si no pude estar ahí en los momentos más duros. Os pido disculpas si no super elegir las palabras adecuadas. Pero como unos agradecimientos hay que acabarlos en positivo, simplemente os diré que de esta experiencia me llevo recuerdos preciosos e inolvidables. Gracias de corazón.

ABSTRACT

The evolution of galaxies is a wide field in astrophysics that can be studied through several approaches, being one of them the analysis of the chemical content of the interstellar medium (ISM). Big Bang Nucleosynthesis predicts a well constrained composition for the ISM, and any deviation from these initial conditions must be attributed to the different star formation processes that govern galaxy evolution and which are eventually shaped by hydrodynamical processes (inflows, outflows, ...) within galaxies.

The ionized gas offers a unique opportunity to analyze the chemical composition of the gas surrounding the most energetic events within galaxies such as star formation, Active Galactic Nuclei (AGN) or shocks, allowing us to understand the present-day composition of the gas that fuels and witnesses these events. Specifically, emission lines from the gas-phase ISM are key to constrain their physical and chemical properties, being collisionally excited lines (CELs) the best resource due to the their brightness in comparison to recombination lines (RLs).

Studies analyzing chemical properties, essentially traced by the oxygen content, of the ionized gas have been historically performed on galaxies whose activity is dominated by star formation (star-forming galaxies, SFGs) and by means of optical spectroscopic observations, which are easily retrieved from ground-based observatories for low-redshift galaxies. In the recent decades, these studies have been complemented with the analysis of AGNs, also relying on optical observations. High-redshift galaxies have been targeted as well, although in this case optical observatories (enhanced by space-based missions allowing deeper surveys) retrieved rest-frame ultraviolet (UV) spectra, using a similar approach to that developed for optical observations. With the advent of JWST and its potential for galaxies up to redshift ($z \sim 10$), we are now able to analyze chemical enrichment in the early Universe.

Optical and UV studies present several disadvantages. Both of them, specially the UV, are extremely affected by dust extinction and attenuation, and dusty regions might remain unobserved by optical and UV tracers. Optical and UV CELs are strongly dependent on the physical properties of the ISM, being the electron temperature a very important factor in their emissivity, and establishing a temperature threshold below which these emissions lines are too faint to be observed. Overall, optical $[3000\text{Å} - 9600\text{Å}]$ and UV $[900\text{Å} - 3000\text{Å}]$ studies are biased towards regions that match the proper conditions for a proper analysis. This incomplete picture of the chemical enrichment must be complemented with infrared (IR) observations $[9600\text{Å} - 700\mu\text{m}]$.

IR emission lines are almost insensitive to interstellar dust, given us a unique window for the analysis of dusty regions in galaxies. Due to the involved atomic transitions, temperature effects are mostly mitigated, allowing us to observe cold regions, and avoiding the problem of having a proper constrained for the temperature and density conditions within the ionized gas. The great variety of emission lines observable in the IR regime not only allows us to perform chemical diagnostics of the ISM; but also robust constraints on the dominant ionizing sources.

This thesis presents a detailed analysis on the use of IR emission lines to perform chemical evolution studies based on the composition of the gas-phase ISM. By means of the large amounts of archival data from past IR missions, we show the potential of IR emission line studies for ongoing (JWST, ALMA) and future (METIS) missions. We present our technique that we have developed based on photoionization models (HII-CHI-Mistry-IR), which follows a robust methodology whose validity has already been probed in other spectral regimes (optical and UV), and that can be applied for both SFGs and AGNs. We have structured the thesis as a transition from the optical to the infrared regime.

In the first chapters, we show the limitations of optical studies to assess the proper ionizing nature of the gas-phase ISM, using integral field spectroscopic data to analyze a sample of low-luminosity AGNs, whose ionizing nature is still puzzling. Our analysis of the nuclear regions reveals that even with the limitations of optical studies, an analysis of the chemical enrichment history of these galaxies can be performed if a robust methodology that analyzes the chemical composition as traced by a primary (oxygen) and secondary (nitrogen) elements is used. Moreover, the analysis of the chemical abundance radial gradients reinforces this conclusion.

In the remaining chapters, we show the use of our methodology for IR emission lines, showing that IR regime allows for a robust estimation not only of oxygen and nitrogen, but also of sulfur which is supposed to be less affected by dust depletion and, its relative abundance to oxygen is useful to assess the impact of dust depletion and whether nucleosynthesis of sulfur and oxygen follows the expected trend (i.e. a constant ratio). We also apply our methodology to a sample of (Ultra)-Luminous Infrared Galaxies [(U)LIRGs] which are characterized by large amounts of dust that shield their star formation processes. We obtain that, contrary to what it is inferred from optical studies, the majority of them do not deviate from the standard relations reported in the local Universe for SFGs and that the nitrogen content is essential to determine the chemical enrichment history in galaxies that suffer from strong hydrodynamical processes (as it is the case for the *deep-diving* phase).

Overall, these results highlight the importance of IR studies in the future years to complement our picture of chemical evolution in galaxies, understanding the possible differences among them depending on their dominant ionizing activity.

RESUMEN

La evolución de las galaxias es una amplia rama de la astrofísica que puede ser estudiada de varias maneras, siendo una de ellas el análisis de la composición química del medio interestelar. La nucleosíntesis del Big Bang predice una clara composición para el medio interestelar, y cualquier desviación de estas condiciones iniciales debe ser adscrita a los diferentes procesos de formación estelar que rigen la evolución de galaxias, y que son ocasionalmente alterados por procesos hidrodinámicos (entrada y/o salida de gas, ...) en las galaxias.

El gas ionizado ofrece una gran oportunidad para analizar el contenido químico del gas que rodea los eventos más energéticos de las galaxias, como formación estelar, Núcleos Activos o choques, permitiéndonos comprender la composición del gas en el momento actual, que sirve como combustible y testigo de dichos eventos. En concreto, las líneas de emisión que emite la fase gaseosa del medio interestelar son claves para restringir las propiedades físicas y químicas, siendo las líneas excitadas colisionalmente el mejor recurso debido a su brillo en comparación con las de recombinación.

Estudios analizando las propiedades químicas, principalmente por medio del contenido de oxígeno, del gas ionizado se han llevado a cabo, históricamente, en galaxias cuya actividad está dominada por formación estelar y por medio de observaciones espectroscópicas ópticas, que son realizadas de forma sencilla con observatorios en tierra para galaxias a bajo corrimiento al rojo. En las últimas décadas, estos estudios se han complementado con el análisis de galaxias que contienen Núcleos Activos, por medio también de observaciones ópticas. Galaxias con alto corrimiento al rojo han sido también estudiadas, aunque en estos casos los observatorios ópticos (con ayuda de misiones en el espacio que permiten observaciones más profundas) proporcionan el espectro en reposo del ultravioleta, usando ténicas similares a las desarrolladas para estudios ópticos. Con la llegada del JWST y su potencial para estudiar galaxias muy distantes, ahora podemos empezar a analizar el enriquicimiento químico en las primeras fases del Universo.

Estudios en los rangos óptico y ultravioleta presentan varios inconvenientes. Ambos, pero especialmente el ultravioleta, están afectados por extinción y atenuación por polvo, y por ese motivo algunas regiones caracterizadas por grandes cantidades de polvo pueden no ser observadas en estos rangos. Las líneas excitadas colisionalmente en los rangos óptico y ultravioleta sufren una fuerte dependencia de las condiciones físicas del medio interestelar, siendo la temperatura de los electrones un factor tan importante en su emisividad que establece un límite por debajo del cual dichas líneas son tan débiles que apenas se observan. En resumen, los estudios basados en los rangos óptico [$3000Å - 9600Å$] y ultravioleta [$900Å - 3000Å$] están sesgados a regiones que reúnen las condiciones necesarias para su análisis. Esta imagen incompleta del enriquecimiento químico debe ser complementado con observaciones infrarrojas [$9600Å - 700\mu$m].

Las líneas de emisión infrarrojas apenas se ven afectadas por el polvo interestelar, ofreciéndonos una oportunidad única para el análisis de las regiones con más polvo de las galaxias. Gracias a las transiciones atómicas involucradas, los efectos de la temperatura están esencialmente mitigados, permitiéndonos además observar regiones frías, y evitando el problema de tener una buena estimación de la temperatura y densidad de los electrones del gas ionizado. La gran variedad de líneas de emisión observables en el rango infrarrojo no solo nos permite realizar estudios de la composición química, también nos proporciona herramientas adicionales para determinar las fuentes de ionización dominantes.

Esta tesis presenta un análisis detallado del uso de las líneas de emisión infrarrojas para realizar estudios de evolución química basados en la composición de la fase gaseosa del medio interestelar. Por

medio de las bases de datos con información de misiones dedicadas al rango infrarrojo, mostramos el potencial de las líneas de emisión infrarrojas para misiones presentes (JWST, ALMA) y futuras (METIS). Presentamos la técnica que hemos desarrollado basada en modelos de fotoionización (HII-CHI-Mistry-IR), que sige una robusta metodología cuya válidez ya ha sido demostrada en otros rangos espectrales (óptico y ultravioleta), y que puede ser aplicada tanto a galaxias dominadas por formación estelar como por Núcleos Activos. Hemos estructurado la tesis como una transición desde el rango óptico hasta el infrarrojo.

En los primeros capítulos mostramos las limitaciones de los estudios ópticos para determinar la correcta fuente de ionización de la fase gaseosa del medio interestelar por medio de estudios de unidad integral de campo espectroscópico en galaxias que contienen Núcleos Activos de baja luminosidad (cuya naturaleza es aún incierta). Nuestro análisis de las regiones centrales muestra que incluso con las limitaciones de los estudios ópticos, se pueden realizar análisis de la historia de enriquecimiento químico de las galaxias si se utiliza una metodología consistent que permite estudiar la composición química por medio de elementos primarios (oxígeno) y secundarios (nitrógeno). Además, el análisis de los gradientes radiales de abundancias químicas refuerza esta idea.

En los siguientes capítulos, mostramos el uso de nuestro método para el estudio de líneas de emisión en el infrarrojo, demostrando que este rango espectral ofrece una robusta estimación no solo del contenido en oxígeno y nitrógeno, sino también de azufre que se supone está mucho menos afectado por depleción en polvo, y cuya abundancia relativa al oxígeno es útil para determinar el impacto de la depleción y si la nucleosíntesis de ambos elementos sigue la tendencia esperada (es decir, que es constante). También aplicamos nuestra metodología a una muestra de galaxias luminosas en el infrarrojo que están caracterizadas por grandes cantidades de polvo que enmascaran los procesos de formación estelar. Obtenemos que, a diferencia de lo que indicaban los estudios ópticos, la gran mayoría no se desvían de las relaciones obtenidas para galaxias en el Universo local, y que el contenido en nítrogeno es crucial para determinar el nivel de enriquecimiento químico en galaxias que sufren de fuertes procesos hidrodinámicos (como ocurre en la fase de *zambullido químico*).

En resumen, estos resultados destacan la importancia de los estudios basados en el rango infrarrojo en los próximos años para complementar nuestra perspectiva de la evolución química de las galaxias, entendiendo las posibles diferencias que pueden surgir como consecuencia de las diferentes fuentes de ionización que dominan la actividad de las mismas.

PUBLICATIONS

PUBLICATIONS FROM THIS THESIS

Pérez-Díaz, B., Pérez-Montero, E., Fernández-Ontiveros, J. A., & Vílchez, J. M. (2022). Measuring chemical abundances in AGN from infrared nebular lines: HII-CHI-MISTRY-IR for AGN. *A&A*, *666*, Article A115, A115. https://doi.org/10.1051/0004-6361/202243602

Pérez-Díaz, B., Pérez-Montero, E., Fernández-Ontiveros, J. A., Vílchez, J. M., & Amorín, R. (2024a). A departure from the mass-metallicity relation in merging galaxies due to an infall of metal-poor gas. *Nature Astronomy*, *8*, 368–376. https://doi.org/10.1038/s41550-023-02171-x

Pérez-Díaz, B., Pérez-Montero, E., Fernández-Ontiveros, J. A., Vílchez, J. M., Hernán-Caballero, A., & Amorín, R. (2024b). Chemical abundances and deviations from the solar S/O ratio in the gas-phase interstellar medium of galaxies based on infrared emission lines. *A&A*, *685*, Article A168, A168. https://doi.org/10.1051/0004-6361/202348318

Pérez-Díaz, B., Pérez-Montero, E., Zinchenko, I. A., & Vílchez, J. M. (2025). Chemical enrichment in LINERs from MaNGA: I. Tracing the nuclear abundances of oxygen and nitrogen in LINERs with varied ionizing sources. *A&A*, *694*, Article A18, A18. https://doi.org/10.1051/0004-6361/202452862

OTHER PUBLICATIONS

Arroyo-Polonio, A., Iglesias-Páramo, J., Kehrig, C., Vílchez, J. M., Amorín, R., Breda, I., Pérez-Montero, E., ... Hayes, M. (2023). A MUSE/VLT spatially resolved study of the emission structure of Green Pea galaxies. *A&A*, *677*, Article A114, A114. https://doi.org/10.1051/0004-6361/202346192

Goswami, S., Vilchez, J. M., Pérez-Díaz, B., Silva, L., Bressan, A., & Pérez-Montero, E. (2024). Contribution of very massive stars to the sulfur abundance in star-forming galaxies: Role of pair-instability supernovae. *A&A*, *685*, Article A81, A81. https://doi.org/10.1051/0004-6361/202348231

Montoro-Molina, B., Guerrero, M. A., Pérez-Díaz, B., Toalá, J. A., Cazzoli, S., Miller Bertolami, M. M., & Morisset, C. (2022). Chemistry and physical properties of the born-again planetary nebula HuBi 1. *MNRAS*, *512*(3), 4003–4020. https://doi.org/10.1093/mnras/stac336

Pérez-Díaz, B., Masegosa, J., Márquez, I., & Pérez-Montero, E. (2021). Chemical abundances in the nuclear region of nearby galaxies from the Palomar Survey. *MNRAS*, *505*(3), 4289–4309. https://doi.org/10.1093/mnras/stab1522

Pérez-Montero, E., Amorín, R., Pérez-Díaz, B., Vílchez, J. M., & García-Benito, R. (2023a). Assessing model-based carbon and oxygen abundance derivation from ultraviolet emission lines in AGNs. *MNRAS*, *521*(1), 1556–1569. https://doi.org/10.1093/mnras/stad621

Pérez-Montero, E., Fernández-Ontiveros, J. A., Pérez-Díaz, B., Vílchez, J. M., & Amorín, R. (2025). Exploring the hardness of the ionizing radiation with the infrared softness diagram. II. Bimodal distributions in both the ionizing continuum slope and the excitation in active galactic nuclei. *arXiv e-prints*, Article arXiv:2503.09267, arXiv:2503.09267. https://doi.org/10.48550/arXiv.2503.09267

Pérez-Montero, E., Fernández-Ontiveros, J. A., Pérez-Díaz, B., Vílchez, J. M., Kumari, N., & Amorín, R. (2024). Exploring the hardness of the ionising radiation with the infrared softness diagram.

I. Similar effective temperature scales for starbursts and (ultra)luminous infrared galaxies. *A&A*, *684*, Article A40, A40. https://doi.org/10.1051/0004-6361/202348089

Pérez-Montero, E., Zinchenko, I. A., Vílchez, J. M., Zurita, A., Florido, E., & Pérez-Díaz, B. (2023b). The softness diagram for MaNGA star-forming regions: diffuse ionized gas contamination or local HOLMES predominance? *A&A*, *669*, Article A88, A88. https://doi.org/10.1051/0004-6361/202244591

Spinoglio, L., Fernández-Ontiveros, J. A., Malkan, M. A., Kumar, S., Pereira-Santaella, M., Pérez-Díaz, B., Pérez-Montero, E., … Fischer, C. (2022). SOFIA Observations of Far-IR Fine-structure Lines in Galaxies to Measure Metallicity. *ApJ*, *926*(1), Article 55, 55. https://doi.org/10.3847/1538-4357/ac37b7

CONTENTS

I Prerequisites

II Results

III Appendix

LIST OF FIGURES

LIST OF TABLES

ACRONYMS

ADF	Abundance discrepancy factor
AGN	Active Galactic Nuclei
BBN	Big Bang Nucleosynthesis
BM	Baryonic matter
CEL	Collisionally excited lines
CR	Cosmic ray
DM	Dark matter
HCm	HII-CHI-Mistry
HLAGN	High-luminosity AGN
HOLMES	Hot low-mass evolved stars
IR	Infrared (spectroscopic range)
ICF	Ionization correction factor
IFS	Integral Field Spectroscopy
ISM	Interstellar medium
LLAGN	Low-luminosity AGN
LTE	Local thermodynamic equilibrium
MZR	Mass-metallicity relation
opt	Optical (spectroscopic range)
pAGB	Post-asymptotic giant branch
PAH	Polycyclic aromatic hydrocarbon
PG	Passive galaxy
PNe	Planetary nebulae
RG	Retired galaxy
RL	Recombination line
RS	Radiative shocks
S/N	Signal-to-noise ratio
sAGN	Strong AGN
SED	Spectral energy distribution

SFG	Star-forming galaxy
SNe	Supernovae
UV	Ultraviolet (spectroscopic range)
wAGN	Weak AGN

Part I

PREREQUISITES

1

INTRODUCTION

1.1 PHYSICS OF THE INTERSTELLAR MEDIUM

In the mid 2000s, Donald P. Cox wrote the following statement: *The interstellar medium (ISM) is a fascinating place to spend one's life* (D. P. Cox, 2005). Besides the poetry, this sentence actually evokes the importance of the ISM in the cosmological context. First of all, the ISM is a direct witness of all processes that shape galaxy evolution: star formation, quenching, aging, Active Galactic Nuclei (AGN), interactions between galaxies, ... Secondly, the ISM plays an active role on those processes, so understanding the main physical and chemical properties that characterize the ISM gives more insight in what makes the difference among galaxies. And, thirdly, the ISM provides a complex laboratory in which many physical processes (turbulence, radiation, ...) are important at different scales. Thus, we might conclude that if not spending one's life within the ISM, surely it is worthy spending one's life studying it.

1.1.1 *The multiphase ISM*

The ISM can be defined as the gas and dust, more or less mixed, that filled the space between stars in galaxies. This intuitive and short definition does not account for what observations tell us: that the ISM is complex, turbulent and multiphase. Indeed, observations of the ISM in our own Galaxy reveals that the ISM presents a complex structure even at small scales (see for instance the review by Frisch et al., 2011, on the ISM surrounding the Sun), it can be turbulent as demonstrated by observations of nearby star-forming regions (e.g. Ha et al., 2022) and it has different physical properties depending on its analyzed phase (e.g. D. P. Cox, 2005; Ferrière, 2001; Lequeux, 2005).

The idea of a *multiphase* ISM reflects that it can be separated in different components. Whereas all these components are mixed at some degree and affected by several physical properties, their differentiation comes from the observational constrain of using different spectral ranges. In terms of the composition of the ISM, the gas can be divided into molecular, neutral atomic and ionized atomic components (Lequeux, 2005). In terms of the characteristic temperature (T) of the gas, it can separated into cold, warm and coronal components (D. P. Cox, 2005).

- **Molecular gas**: This is the coolest component $\mathrm{T} \lesssim 100$ K (Lequeux, 2005; Madden et al., 2020; Togi & Smith, 2016) and is also characterized by high densities $\mathrm{n} \sim 10^3$ cm^{-3} (Lequeux, 2005). It is composed by different species of molecules, being the most abundant H_2 (up to four orders of magnitude, Togi & Smith, 2016), but direct observations mainly comes from other molecules such as CO (e.g. Leroy et al., 2011; Saintonge et al., 2017; Schruba et al., 2012) or even atomic transitions such as [C I] (e.g. Nesvadba et al., 2019; Valentino et al., 2020) or [C II] (e.g. Béthermin et al., 2020; Schaerer et al., 2020; Zhao et al., 2024), which are available in the radio, submillimeter and far-infrared regimes. The use of different molecule emission lines (such as HCN, HNC, CO,..) can also provide insights on different physical properties of the molecular gas (Aalto, 2007).

- **Neutral gas**: Also called atomic gas, this component presents two different phases: a *warm* component characterized by moderate temperatures $\mathrm{T} \sim 10^3 - 10^4$ K and low densities n ~ 0.1 cm^{-3}; and a *cold* component characterized by low temperatures $\mathrm{T} \sim 100$ K and relatively high densities n ~ 10 cm^{-3} (Dickey & Lockman, 1990; Kulkarni & Fich, 1985; Wolfire et al., 2003). These components are mainly traced by the HI 21cm line, originated by the hyperfine split related to the change in the electron's spin with respect to the proton's one (see Dutta, 2019, for a thorough review).

- **Ionized gas**: This is the hottest component of the gas and it might be divided into three categories. The *ionized gas* or *HII ionized gas* is characterized by moderately high $T \sim 10^4$ K and moderate densities $n \sim 1-100$ cm^{-3} (Kewley et al., 2019; Lequeux, 2005; Osterbrock & Ferland, 2006), and it is found surrounding sources of hard radiation, able to ionize the ISM (see later sections for more details). The *diffuse ionized gas* (DIG) is a little bit cooler $T \lesssim 10^4$ K and less dense $n \lesssim 0.1$ cm^{-3} (Berkhuijsen & Müller, 2008; Haffner et al., 2009; Zurita et al., 2000). Finally, there is also a very hot $T \gtrsim 10^5$ K and low density $n \lesssim 10^{-3}$ cm^{-3} component usually called *coronal gas* (Grimes et al., 2005; Owen & Warwick, 2009; Strickland et al., 2004). The hot coronal gas is clearly differentiated from the other two components, and it is observed by its X-ray emission (e.g. Mineo et al., 2012; Owen & Warwick, 2009; Strickland et al., 2004). The other two components (ionized and diffuse ionized) are mainly traced by their emission lines, observable in the ultraviolet (UV), optical (opt) and infrared (IR) regimes (e.g. Kewley et al., 2019; Maiolino & Mannucci, 2019; Osterbrock & Ferland, 2006), but the distinction between them is not as clear (see McClymont et al., 2024, and references therein).

These highlighted phases refer to the gas that composes the ISM, but there is an extra ingredient, the dust:

- **Interstellar dust**: Composed by solid particles of variable sizes between 0.3 nm and 0.3 μm (Draine, 2003; Galliano et al., 2018). They absorb the emission from the stars and the ISM, re-emitting it in the form of IR emission that can be modellized as modified black body emission for a temperature of $T \sim 10$ K, depending on the dust size, composition and location (e.g. Compiègne et al., 2011; Galametz et al., 2016; Hocuk et al., 2017; Relaño et al., 2016, 2020, 2022). There are many methods to trace dust properties such as direct IR spectroscopic or photometric observations to model the Spectral Energy Distribution (SED) of dust (e.g. Galliano et al., 2011), emission bands in the IR from aromatic compounds such as polycyclic aromatic hydrocarbons (PAHs; e.g. Smith et al., 2007), silicate emission useful to traced hot ($T>100$ K) dust (e.g. Hony et al., 2011) or ice absorption features (e.g. Yamagishi et al., 2015).

All components are equally important for the study of galaxy evolution. Molecular gas is essential for star formation, as their fractal (from clouds to clumps to cores) but also turbulent structure provides the conditions for the gas to gravitationally collapse and form stars as confirmed by theory (e.g. Falgarone & Puget, 1985; Larson, 2005) and observations (e.g. Falgarone et al., 1991; Schneider et al., 2011). Atomic gas acts as the reservoir from which molecular clouds can be formed (e.g. Dutta, 2019) and also traces the interactions between galaxies due to its extended morphology (e.g. Chung et al., 2009; Mihos et al., 2012). The ionized gas traces regions where recent star formation activity (among many others) is taking place due to their proximity to massive, young stars (e.g. Kehrig et al., 2008) and also to the later stages of their evolution such as planetary nebulae (PNe, e.g. Ali et al., 2012) or Supernovae (SNe; e.g. Li et al., 2024), as well as activity from the nuclear regions as in the case of Active Galactic Nuclei (e.g. Heckman & Best, 2014). Finally, dust is an essential ingredient as molecules form in the dust grain surface (see Wakelam et al., 2017, for a review), it prevents the overheating during the core-collapse that would lead to stars (e.g. Marchand et al., 2016; Vallucci-Goy et al., 2024), and it is present on many of the stellar evolution phases (e.g. Dell'Agli et al., 2023; Saikia et al., 2019).

In the present thesis we will focus on the ionized gas phase of the ISM, and, hereinafter any reference to the gas-phase ISM will refer exclusively to the ionized component. The ionized gas is easily detectable from its main cooling mechanism, emission lines (see Sec. 1.1.5 for more details), and it is ubiquitous around most of the energetic processes that are related to galaxy evolution (see Sec. 1.1.3). The great variety of emission lines detected in many spectral regimes, can be used to provide constraints to the physical and chemical properties of the gas (see Sec. 1.2). Thus, the ionized gas is a very valuable component of the ISM to efficiently study the present day rest-frame energetic processes and their interplay with the gas.

1.1.2 *Chemical enrichment in the ISM*

The ISM contains the chemical footprints of the different processes that enrich the ISM. Thus, if we know the primordial composition of the ISM from which galaxies and stars are formed, then we can track the chemical enrichment process by accounting for the differences. We will briefly review the main channels of element synthesis in the Universe, starting from the Big Bang Nucleosynthesis and then to stellar nucleosynthesis.

1.1.2.1 *Big Bang Nucleosynthesis*

In the cosmological framework of the Big Bang Theory, during the early phases of the Universe ($\sim$ 150 MeV-1MeV), the soup of light particles (quarks) that populate the Universe are bound into hadrons, mainly protons and neutrons. Due to the higher mass of neutrons, its decay and the temperature drop that favors the exothermic reaction of neutrons conversion into protons, the ratio after this phase is 1 neutron:7 protons. In other words, we would observe a Universe mainly composed by protons, i.e., ionized hydrogen H$^+$. This phase is called Baryogenesis (e.g. Affleck & Dine, 1985; Pereira et al., 2023).

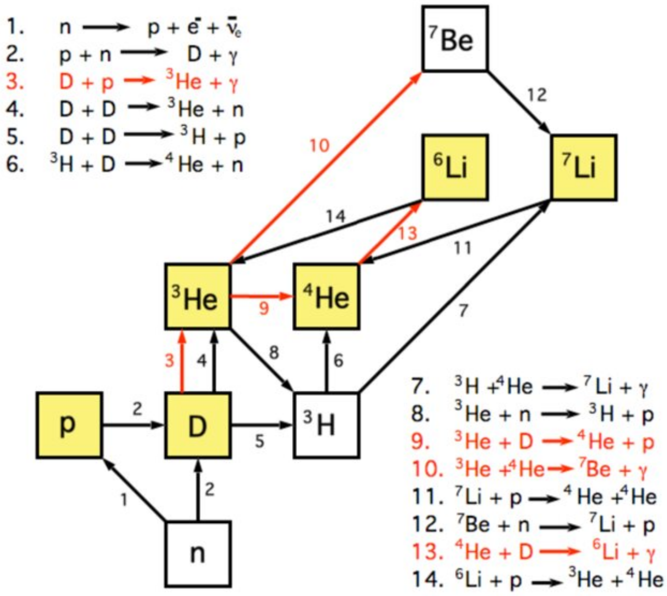

Figure 1.1: Big Bang Nucleosynthesis nuclear reactions. The only stable isotopes are: H, D, ^{3}He, ^{4}He, ^{6}Li and ^{7}Li (marked as yellow boxes). Figure taken from Gustavino (2014).

As energy drops, then the first nuclear reaction leading to the synthesis of an atom nuclei (besides H) happens ($\sim$ 1-0.1 MeV): deuterium (D) production. This is the first step in a chain of reactions that lead to the production of the very first light elements (Fields, 2023). Mainly hydrogen, helium (He), lithium (Li) and beryllium (Be) isotopes are produced. The reactions are shown in Fig. 1.1. The instability of atoms with mass of 5 and 8 particles, the Coulomb barriers and the cooldown of the Universe by its expansion limits to H, D, ^{3}He, ^{4}He, ^{6}Li and ^{7}Li the atoms nuclei produced during this phase (Cyburt et al., 2016). This phase is Big Bang Nucleosynthesis (BBN).

Among all the atoms produced in this phase, the most abundant is ^{4}He, as nearly all free neutrons end up in such state(e.g. Cyburt et al., 2016; Fields, 2023). The predicted value for this abundance is 12+log(H/He) $\sim$ 11.39 (e.g. Cyburt et al., 2016), mostly in agreement with observations[1] (e.g. Fernández et al., 2018; Izotov et al., 2013). Other elements such as D and ^{3}He are predicted to be 4 orders of magnitude less abundant than helium, and observations seem to confirm this prediction (e.g. Cooke et al., 2022; Guarneri et al., 2024; Riemer-Sørensen et al., 2017). Lithium, in addition to being the least abundant element by nine orders of magnitude, presents a clear disagreement between predictions and observations, leading to the so-called *primordial lithium problem* (see Fields, 2011; Makki et al., 2019, for reviews).

1.1.2.2 *Stellar nucleosynthesis*

Due to the BBN, first stars were formed from a material mainly composed by H and He, with a few amounts of D and Li. Those stars altered the chemical composition of their gas by means of nuclear fusion reactions (Iliadis, 2007). Here we will present a brief overview on these reactions and their outcomes.

The basic reaction that fuels stars, whose presence is used as criterion to determine whether a low-mass compact object is a star or a planet, is the H-burning, which occurs in stars with M>0.075 $M_{\odot}$ (Chabrier, 2003). By means of proton-proton chain reactions (pp-chains), protons are fused to give D, which later on is fused with another proton to give ^{3}He, which is fused later on with another ^{3}He to provide two protons and the stable ^{4}He[2].

Stars with sufficient mass ($M \gtrsim 0.33 M_{\odot}$; J. P. Cox & Salpeter, 1964; Hall & Jeffery, 2018) undergo another later burning phase, but in this case using as fuel the He produced before. These He nuclei are fused, by means of the triple-α process into carbon (^{12}C), which can fuse with another He nuclei into oxygen (^{16}O), and ^{16}O can also fuse into neon (^{20}Ne), although at a minor extent (e.g. deBoer et al., 2017). Depending on the initial mass of the star, if $M \lesssim 2.2\ M_{\odot}$, this He fusion is a runaway event in which a large amount of energy is released very quickly, leading to the so-called *He-flash* (e.g. Mocák et al., 2008).

Massive stars ($M \gtrsim 8 M_{\odot}$; Arcones & Thielemann, 2023; Strieder, 2010) match the conditions for stable C fusion. During this process, elements such as neon (^{20}Ne), sodium (^{23}Na), magnesium (^{24,25,26}Mg) and aluminum (^{27}Al). Neon burning also takes place in the same conditions, but it requires a higher temperature, implying that it is more concentrated and that photodisintegrations (Arcones & Thielemann, 2023; S. Jones et al., 2013) are important. Under this phase, elements such as oxygen (^{16}O) or silicon(^{28,29,30}Si) are produced (e.g. Arcones & Thielemann, 2023). At higher masses, oxygen burning can occur as well, leading to a great variety of elements: phosphorus (^{31,32}P), sulfur (^{31,32,33,34}S), chlorine (^{35,37}Cl), titanium (^{46}Ti), argon (^{36,37,38}Ar), potassium (^{39}K) and calcium (^{40}Ca) mainly (Arcones & Thielemann, 2023). In more massive stars ($M \gtrsim 11 M_{\odot}$; Arcones & Thielemann, 2023; Strieder, 2010), the silicon burning phase occurs, and the different products of previous burnings and photodisintegrations formed a wide variety of nuclei, up to iron (^{56}Fe), which is the element representing the turn-off point in the binding energy: heavier elements will consume more energy than release in their production.

The schematic overview of the different burning phases conducts to the classic onion structure of the burning shells, as each consecutive stage requires higher temperature and density (i.e. it is a deeper layer of the core). However, there are numerous effects that induces departures from this

---

[1] The primordial ^{4}He abundance is not directly observed, but rather estimated from the extrapolation of the trend between ^{4}He and a metal Z to the value Z= 0.

[2] Whereas this is the most probable reaction, there are other ways of producing He which are called branches of the pp-chain involving other atoms such as ^{7}Be and ^{7}Li.

Table 1.1: Stellar nucleosynthesis stable processes for different initial masses. * Denotes products from the CNO cycles.

Initial masses	H-burning	He-burning	C-burning	Ne-burning	O-burning
0.08 – 1.2 M⊙	pp-chain	No	No	No	No
1.2 – 2 M⊙	CNO*	No	No	No	No
2 – 8 M⊙	CNO	Yes	No	No	No
8 – 10 M⊙	CNO	Yes	Yes	Yes	No
$\gtrsim$ 10 M⊙	CNO	Yes	Yes	Yes	Yes
Main Products	He C,N,O,F*	C,O,Ne	Ne,Na,Mg,Al	O,Si	P,S,Cl Ar,Si,Ti

scheme and lead to changes in the production of some species. One of these aspects is rotation. Massive stars might also present rotational-driven mixing between layers, and can bring elements such as (^{12}C, ^{16}O) into the outer layers, in which CNO cycles (see Romano, 2022, for a review) will lead to the production of nitrogen (^{14,15}N; Limongi & Chieffi, 2018; Maeder et al., 2014; Meynet & Maeder, 2002; Przybilla et al., 2010). In the same way, if stars are born from a previously enriched material, then they already have C, N and O to undergo directly the CNO cycle during the H-burning phase, which is dominant in stars ($M \gtrsim 1.2\ M_\odot$; Arcones & Thielemann, 2023; Romano, 2022).

We present a summary of the main stages reviewed here in Tab. 1.1. We also highlight that other physical processes change and shape stellar nucleosynthesis. Stellar mass losses impact life-times and the cycle duration (e.g. Meynet et al., 2015). At low temperatures, some isotopes can liberate neutrons that help in the production of heavier nuclei by slow neutron capture (s-capture) processes (e.g. Reifarth et al., 2014). Explosive burning phases (when required mass or inner temperatures for stable fusion are not matched) can also happen accompanied by proton rich (p)-processes (e.g. Rauscher et al., 2002).

1.1.2.3 *Latest stages in stellar evolution*

We have presented above the main processes under which stars can synthesized elements during their lives. However, these elements do not enrich the surrounding ISM while these stars are in the main sequence. On the contrary, this enrichment process happens during the late stages of their lives as the outer parts of stars are driven away by stellar winds or energetic events.

For low- and intermediate mass stars ($M \lesssim 7 M_\odot$), only the H- and He-burning (only stable for $M \gtrsim 2\ M_\odot$) occurs, leaving a core constituted mainly by C and O (CO-dwarf), whereas the outer parts are expelled by stellar winds, leading to the PNe (Busso et al., 2001). This leads to an enrichment of C, N, F and elements from the s-capture process (e.g. Karakas & Lugaro, 2016; Kobayashi et al., 2020a).

Moderate mass stars ($7\ M_\odot \lesssim M \lesssim 10\ M_\odot$), depending on the efficiency of the stellar winds, might undergo the carbon fusion leaving a ONeMg core (Doherty et al., 2017) or even further burning phases (Leung & Nomoto, 2019). These stars undergo a phase called *electron capture supernovae* which is a favorable site for rapid neutron capture (r-capture) processes that produce heavy atoms (Kobayashi et al., 2020a).

Massive stars ($M \gtrsim 10\ M_\odot$) are the only ones that can undergo stable O and Si burning, characterized by the presence of an Fe-core. However, their fate is the most complex one, supernovae events (see Kobayashi et al., 2020a, for a thorough discussion on the model limitations). The core will eventually collapse due to the nuclear particle interactions, until nuclear forces stop the contraction, producing a shock wave which can enhance the production of the outer burning layers (Arcones & Thielemann, 2023; Curtis et al., 2019). The release of neutrinos as well as the outcome from the collapse of the star, leaving a neutron star or a black hole, are also important for the production of heavier elements (see Arcones & Thielemann, 2023; Kobayashi et al., 2020a, for thorough reviews).

As a remarkable note, most of the stars are supposed to be born in binary systems and this systems also contribute to the synthesis of elements. Type Ia supernovae are thought to be produced in systems characterized by a CO-dwarf and a main-sequence or red giant star (Kobayashi et al., 2020b). These systems are important contributors to the production of heavy metals such as manganese (Mn), copper (Cu) or zinc (Zn) among others (Kobayashi et al., 2020b, 2020a).

1.1.3 *Ionizing sources and their prevalence on galaxies*

The ionized gas receives its name because it is composed by ions from atoms that have lost electrons as a consequence of ionization, i.e. atoms gain enough energy which allows the release of electrons into the medium. Thus, an important aspect to understand the ionized gas is having a clear idea on the nature of the *ionizing sources* (see Fig. 1.2), distinguishing between photoionization (release of very energetic photons) or other mechanisms, such as shocks or cosmic rays. The ionizing front of each source limits the available photons and, consequently, the ions that will be expected in the surrounding ISM. All of them produce at least photons with energies $E_\lambda \geq 13.6$ eV, which is the required energy to ionize hydrogen. Ionizing sources can be segregated into two main categories: stellar and non-stellar. In this section we provide a quick overview on the main ionizing sources.

Starting with stellar sources, we can enumerate:

- **OB stars and associations**: Young clusters that contain massive, young stars such as O-type ($M \gtrsim 20\ M_\odot$, $T \gtrsim 3.5 \cdot 10^4$ K; Heap et al., 2006) and B-type stars ($8\ M_\odot \lesssim M \lesssim 20\ M_\odot$, $1.7 \cdot 10^4$ K $\lesssim T \lesssim 3.5 \cdot 10^4$ K; Nieva & Przybilla, 2014). As these massive stars have relatively short timescales ($\sim 3 - 40$ Myr), their presence implies recent star formation and, thus, these regions of gas surrounding the young clusters are called *star-forming regions* or *HII regions*. We also enclose in this category their corresponding massive evolved descendant stars (e.g. Supergiants, Wolf-Rayet, Luminous Blue Variables,...).

- **pAGB stars**: Post-asymptotic giant branch (pAGB) stars represent the late evolution of intermediate massive stars ($1.5\ M_\odot \lesssim M \lesssim 8\ M_\odot$; Ventura et al., 2017) and they are characterized by effective temperatures that can go beyond $T \gtrsim 3 \cdot 10^4$ K (Binette et al., 1994; Rauch, 2003). pAGB stars were proposed to explain the ionizing gas in retired galaxies, with residual star formation activity (e.g. Binette et al., 1994; Stasińska et al., 2008).

- **Supernova explosions**: Although there are several types of supernovae (SNe) events (see Gal-Yam, 2017, for a complete overview), all of them are characterized by being originated from stellar evolution and by the release of hot gas and considerable amounts of kinetic energy. This results in a surrounding ionized gas which can be extremely hot in the initial phases (thus detectable through X-ray emission; e.g. Dimitriadis et al., 2014; Nymark et al., 2006), which eventually cools down.

On the other hand, as non-stellar ionizing sources we have:

- **Radiative shock waves (RS)**: Shocks are ubiquitous in the ISM as they are produced by many sources: supernovae (previously detailed) and novae explosions, stellar winds, gas flows from secular evolution, feedback from extreme environments or even pure supersonic turbulence within the ISM. By means of compression and heating of the gas, shocks ionized the gas in two steps: first the front wave ionizes the pre-shocked material; and, then the wave passes leading to the post-shock phase, in which temperature and density of the gas increase as a result of the shock front (e.g. Allen et al., 2008; Dopita, 1976; Dopita, 1977; Sutherland & Dopita, 2017), as it is the case of supernovae remnants (e.g. Smirnova et al., 2025).

- **Active Galactic Nuclei (AGN)**: Almost all massive galaxies present a Supermassive Black Hole (SMBH) in their central part (e.g. Heckman & Best, 2014; Kormendy & Ho, 2013). Whereas in some cases the SMBH remains dormant (e.g. the Milky Way), in other cases the SMBH is fed by gas causing intense nuclear activity, which has been called AGNs. The emission from the inner parts (accretion disk and hot corona) leads to the production of ultraviolet and X-ray photons, that ionize the surrounding gas.

- **Cosmic Rays (CRs)**: They are highly energetic particles produced in extreme environments such as supernova remnants or AGNs (see Blasi, 2013, and references therein). The least energetic CRs can penetrate in molecular clouds, collide with atoms and molecules in the deepest parts, and release electrons that contribute to the excitation and ionization of gas (e.g. Dalgarno, 2006; Gabici, 2022; Gredel et al., 1989), inducing changes in the ISM (Ferland & Mushotzky, 1984; Koutsoumpou et al., 2025).

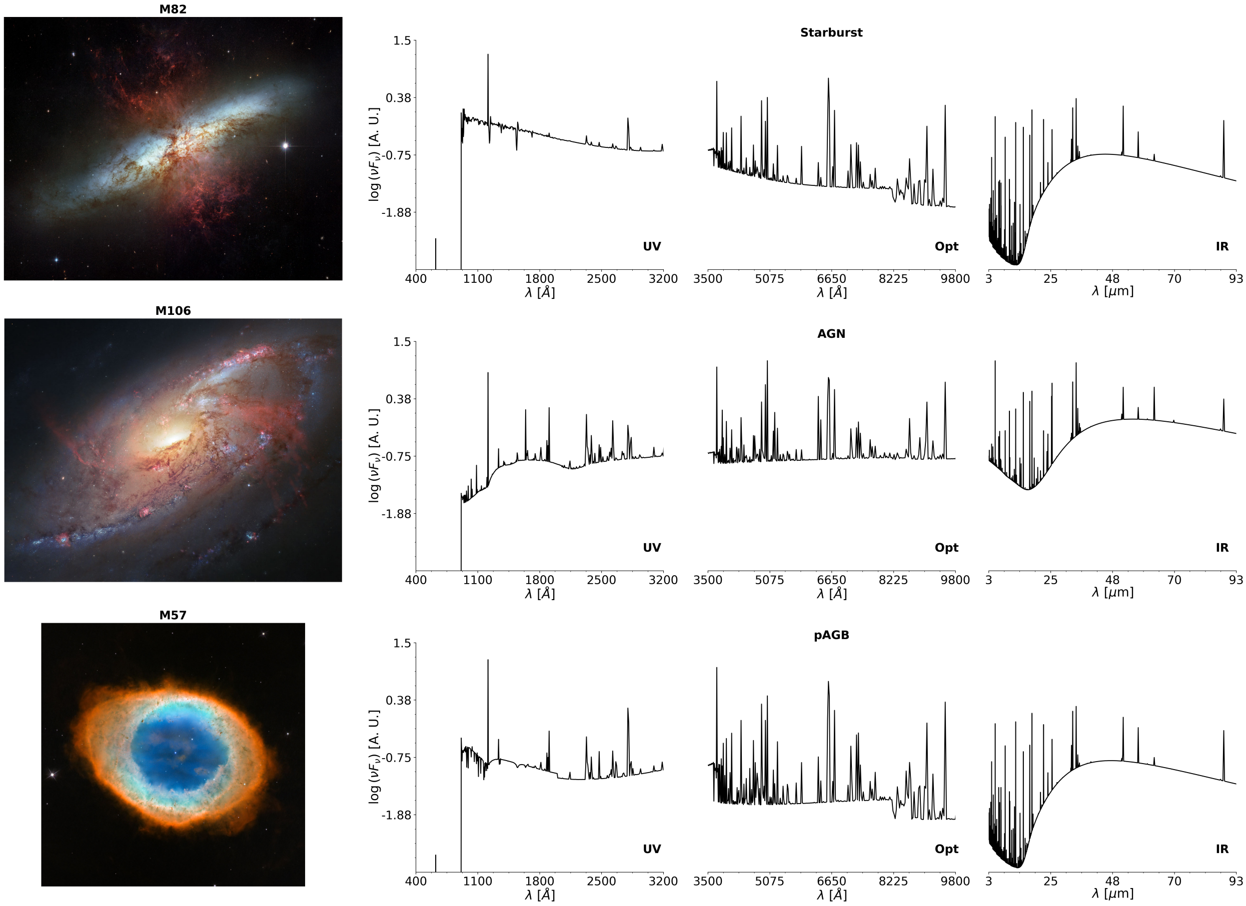

Figure 1.2: Composite figure of the most common ionizing scenarios and their expected spectra. Left column shows optical images retrieved from Hubble Space Telescope Legacy Archive. Right column shows the theoretical spectra across different regimes as computed from CLOUDY v17 (Ferland et al., 2017). HST images credits[3]: M82 [NASA, ESA and the Hubble Heritage Team (STScI/AURA). Acknowledgment: J. Gallagher (University of Wisconsin), M. Mountain (STScI) and P. Puxley (NSF)]; M106 [NASA, ESA, the Hubble Heritage Team (STScI/AURA), and R. Gendler (for the Hubble Heritage Team). Acknowledgment: J. GaBany]; M57 [NASA, ESA, and C. Robert O'Dell (Vanderbilt University)].

---

[3] Together with Fig. 1.1, these are the only figures in this work taken from the literature. The rest of figures shown throughout this work are original from this research. Sec. 2.5 provides a complete summary on all the samples used and their corresponding references.

Whereas most of these sources, if not all, might ionize the ISM of a galaxy, in many cases the lack of spatial resolution in large surveys of galaxies (e.g. Sloan Digital Sky Survey, Dark Energy Spectroscopic Instrument) as well as the lack of tools to disentangle them have favored that galaxies are classified by their dominant ionizing source. Whereas the tools for classifying galaxies will be a matter of discussion in a different section, we can name three main categories of galaxies: passive, star-forming and AGN host-galaxies.

1.1.3.1 *Passive galaxies*

Galaxies in this group are characterized by the lack of, or almost negligible detection, of emission lines that trace the ionized gas ISM (Cid Fernandes et al., 2011). Several mechanisms have been proposed and studied to assess how galaxies can become passive (or line-less) galaxies, among them the possibility of gas removal or the lack of either star-forming or AGN activity (Herpich et al., 2018; Michałowski et al., 2024; Nadolny et al., 2024; Ryzhov et al., 2025).

1.1.3.2 *Star-forming galaxies*

The ISM in this group of galaxies is mainly ionized by OB associations (clusters of young, massive stars), i.e., the main mechanism for ionizing is star formation. Most galaxies show that characteristic emission in the nuclear parts. As the main source of ionization are massive, young stars, photons that ionize the surrounding ISM are UV photons.

A very characteristic group of galaxies, which also are accounted here, are *starburst* galaxies, in which the star formation is either significantly higher than in previous epochs or it is both more spatially and temporary concentrated. However, as stated by Bergvall et al. (2016), the definition of starburst is something that must be carefully considered when analyzing different studies, as different criteria are used in the literature.

1.1.3.3 *AGN-host galaxies*

The ionized ISM in these galaxies is mainly due to their AGNs. For simplicity and historical reasons, we will refer to these groups of galaxies as AGNs. As the dominant mechanism for the other two groups of galaxies has been already explained, it is worthwhile to review the different parts of an AGN, based on the unified model (the reader can find more details on Heckman & Best, 2014; Kormendy & Ho, 2013; Netzer, 2015).

Surrounding the SMBH we find the accretion disk, whose accretion rate ($\dot{M}$) determines its geometry (e.g. Nemmen et al., 2014; Netzer, 2015). This accretion disk presents a radial temperature profile which is responsible for the emission of photons between the X-ray regime (inner parts) to the UV (outer parts). This structure is also surrounded by hot gas ($T > 10^7$ K), whose emission is partially intrinsic and partially due to the reflection the emission from the disk (e.g. Cao, 2009).

Table 1.2: Components of the AGN and their main properties. Distance (radial) has been approximated for a SMBH of $10^9 M_\odot$. References: Alloin et al. (2006), Bennert et al. (2006a, 2006b), Cao (2009), Mor et al. (2009), Mosquera et al. (2013), Netzer (2015), Reis and Miller (2013), and Ursini et al. (2020).

Component	Distance	Temperature	Emission
Accretion disk	$\sim 10^{-4}$ pc	$\sim 10^9$ K	X-ray - UV
Hot Corona	$\sim 10^{-4} - 10^{-3}$ pc	$\gtrsim 10^7$ K	X-ray
Broad Line Region (BLR)	$0.01 - 1$ pc	$\sim 10^4$ K	Broad recombination lines
Dusty Torus	$1 - 30$ pc	$\lesssim 1000$ K	IR
Narrow Line Region (NLR)	$0.1 - 1$ kpc	$\sim 10^4$ K	Narrow emission lines

The previous two components emit the photons responsible of the ionization in a dense ($n \sim 10^8$ cm^{-3}) and moderately hot ($T \sim 10^4$ K) gas that rotates at high velocity ($\sim 10^4$ km/s) due to its proximity to the SMBH (Alloin et al., 2006), this is the Broad Line Region (BLR). Beyond this region, the temperature conditions of proximity to the SMBH ensures that dust is not destroyed, and hence a dusty torus is formed, which absorbs partially the emission of the inner components and re-emits them in the infrared range. Finally, there is another region of ionized gas, much extended and much less dense ($n \sim 500 - 1000$ cm^{-3}) than the BLR, this is the Narrow Line Region. The gas in this zone moves at moderate velocities (~ 500 km/s) although the temperature is similar to that of the BLR (Alloin et al., 2006; Bennert et al., 2006a, 2006b).

Since the idea of AGN emerged as a consequence of Schmidt (1963) observations, due to the subsequent detections of AGNs with different properties, attempts on providing a taxonomy and unified scheme are numerous in the literature (e.g. Antonucci, 2012; Antonucci, 1993; Heckman & Best, 2014; Netzer, 2015; Padovani et al., 2017; Urry & Padovani, 1995). For the purposes of this work, we will consider two classifications. The first one is based on the detection (Type I) or lack (Type II) of broad permitted emission lines. The second one is based on the accretion efficiency[4] distinguishing between high-luminosity AGNs (HLAGNs, efficient) and low-luminosity AGNs (LLAGNs, inefficient).

1.1.4 *The structure of the ionized gas*

The gas-phase ISM is ionized by one or more of the previously discussed mechanisms. The contribution from CRs has been historically considered negligible, although it can be useful in some scenarios (e.g. Koutsoumpou et al., 2025). The shock contribution drastically affects the physical properties of the gas, but its treatment and implementation are complex (e.g. Allen et al., 2008; Contini & Aldrovandi, 1983; Contini & Viegas, 2001; Dopita, 1976; Dopita, 1977; Sutherland & Dopita, 2017). Hence, we will focus on the photoionization scenario, which can be applied to the analysis of HII regions, PNe and the NLR of AGNs.

1.1.4.1 *The ionization equilibrium*

When the ionization comes from the photons emitted by a source (e.g. young stars, pAGB stars or the accretion disk in AGNs), there is a balance between ionization and recombination. This is the so-called local ionization equilibrium (LIE).

Let us consider an element Y, which has an ionizing energy given by $E_Y = hc\lambda_Y^{-1}$. All photons released with enough energy might interact with the element, according to a specific cross section $\sigma(Y)$. Thus, the number of ions per unit of volume and per unit of time is given by (Osterbrock & Ferland, 2006):

$$n\left(Y^{+}\right)_{photo} = n\left(Y^{0}\right)\int_{\frac{hc}{\lambda}=E_I(Y^0)}^{\infty}\frac{\lambda L_\lambda}{hc}\sigma\left(Y^{0}\right) \approx n\left(Y^{0}\right)\left\langle\sigma\left(Y^{0}\right)\right\rangle\int_{\frac{hc}{\lambda}=E_I(Y^0)}^{\infty}\frac{\lambda L_\lambda}{hc} \tag{1.3}$$

---

[4] The efficiency is usually parametrized in terms of the Eddington ratio, defined as:

$$\lambda_{Edd} = \frac{L_{Bol}}{L_{Edd}} \tag{1.1}$$

where L_{Bol} is the bolometric luminosity of the AGN and Eddington luminosity can be estimated from the mass of the SMBH as (Netzer, 2015):

$$\lambda_{Edd} \approx 1.5 \cdot 10^{38}\frac{M_{SMBH}}{M_\odot} \tag{1.2}$$

Inefficient AGNs show typical values of $\lambda_{Edd} \sim 10^{-5} - 10^{-2}$ (Yuk et al., 2022).

where we have introduced an average cross section $\langle \sigma(Y) \rangle$, and L_λ is the luminosity per wavelength emitted by the source. As Y^+ is produced, recombinations might occur as ions might capture free electrons within the gas. Hence, the number of recombined ions per unit of volume and per unit of time is given by (Osterbrock & Ferland, 2006);

$$n\left(Y^0\right)_{recon} = n\left(Y^+\right) n_e \alpha\left(Y^+\right) \tag{1.4}$$

where $n\left(Y^+\right)$ is the ion density, n_e the electron density and $\alpha\left(Y^+\right)$ the recombination coefficient for the ion.

The LIE (or ionization-recombination equilibrium) implies that the photoionization and recombination processes are equal. Thus, we obtain that the equilibrium is governed by:

$$n\left(Y^+\right) n_e \alpha\left(Y^+\right) = n\left(Y^0\right) \left\langle \sigma\left(Y^0\right) \right\rangle \int_{\frac{hc}{\lambda}=E_I(Y^0)}^{\infty} \frac{\lambda L_\lambda}{hc} \tag{1.5}$$

Thus, the generalization can be easily extended as:

$$n\left(Y^{+(i+1)}\right) n_e \alpha\left(Y^{+(i+1)}\right) = n\left(Y^{+i}\right) \left\langle \sigma\left(Y^{+i}\right) \right\rangle \int_{\frac{hc}{\lambda}=E_I(Y^+)}^{\infty} \frac{\lambda L_\lambda}{hc} \tag{1.6}$$

With the additional constraint that there the fraction of ions must equal the total density of the element:

$$n\left(Y\right) = \sum_i n\left(Y^{+i}\right) \tag{1.7}$$

Overall, the physics of the ionization structure are governed not only by the ionizing source but also by the microphysical properties of the gas components (i.e. the recombination rates and cross sections). These properties do not only depend on the elements and their ions, but also on the temperature (T) of each species. Complexity arises from the fact that there is a competitive process among all elements and ions to capture the emitted photons, and hence, radiative transfer equations must be included as well.

This equilibrium defines an ionization structure that extends up to some point. In a first-order approximation, the structure is governed by the ionizing energy of each ion: ions with lower ionizing energies are present throughout large scales, whereas ions with high ionizing energies are located in a region very close to the ionizing source or even not present at all if there are no photons with enough energy. Complexity arises from the role of quantum effects governed by the cross section and the recombination rates. Additionally, this defines a volume of influence, i.e., the surrounding gas is mostly ionized until a narrow transition zone where gas is mainly neutral. The characteristics of this volume are mainly determined by the physical properties of the gas.

1.1.4.2 *Some useful definitions*

The ionization structure depends, as we have discussed above, on the composition of the gas. The simplest scenario is when we have a pure H gas surrounding the ionizing source. As H can be either neutral or ionized once (protons), the equilibrium equations are simplified although the dependence on quantum effects (cross section and recombination rates) does not erase. This simple scenario motivates the introduction of some useful definitions.

For a pure H gas, we have a zone which is mainly composed by protons (ionized H) and electrons. This zone expands from the closest part of the gas to the ionizing source up to a distance at which not enough photons either from the ionizing source or from the recombination photons (diffused emission) in the central region can ionize H, and hence an outer region of neutral H is expected. The region of the gas where H is essentially in the ionized form is called *HII region*.

It is important to provide a quantification of the interplay between the ionizing source and the surrounding ionized gas. Let us assume that the ionizing source is characterized by a luminosity at a wavelength (L_λ), that is, the total energy emitted per unit of time at a wavelength λ. As photons are carrying out that energy, and each photon is characterized by $E_\lambda = hc\lambda^{-1}$, then the total number of photons emitted at a given wavelength per unit of time would be:

$$Q_\lambda = \frac{\lambda L_\lambda}{hc} \tag{1.8}$$

Among all the emitted photons, the ionization is mainly driven by those with enough energy to at least ionize hydrogen. This is the number of ionizing photons emitted per unit of time, which can be calculated as:

$$Q_0 = \int_{\frac{hc}{\lambda}=13.6\ eV}^{\infty} Q_\lambda = \int_{\frac{hc}{\lambda}=13.6\ eV}^{\infty} \frac{\lambda L_\lambda}{hc} \tag{1.9}$$

These photons ionize the gas, which is mainly composed by hydrogen, thus we can define the ratio between the surface density, as defined by the inner face of the ionized gas located at a distance R_{in}, of ionizing photons and the density of ions by:

$$\hat{U} = \frac{Q_0}{4\pi R_{in}^2 n\left(H\right)} = \frac{\Phi_0}{n\left(H\right)} \tag{1.10}$$

A dimensional analysis of $\hat{U}$ reveals that has units of velocity, and we refer to it as *dimensional ionization parameter*. By normalizing $\hat{U}$ to the speed of light (universal constant), we obtain the *dimensionless ionization parameter* (hereinafter ionization parameter) as:

$$U = \frac{Q_0}{4\pi R_{in}^2 n\left(H\right) c} = \frac{\Phi_0}{n\left(H\right) c} \tag{1.11}$$

A direct interpretation of this quantity is that, for a cloud of specific density, the ionization parameter U is governed by the intensity (flux or luminosity) of the ionizing source.

We can also provide a characteristic value for the size of the HII region, i.e., at which distance (R_s) the transition from pure ionized to neutral (although smooth) occurs. The pure ionized H region is given by the number of emitted ionizing photons (Q_0), which is essentially equal to the total number of recombinations, i.e., for each recombination of H^+ there is a photon with enough energy to excite it again. Thus, the total number of recombinations per unit of time (N_{rec}) is given by:

$$N_{rec} = V\left(R_s\right) n\left(H^+\right) n_e \alpha\left(H^+\right) = V\left(R_s\right) n\left(H^+\right)^2 \alpha\left(H^+\right) \approx V\left(R_s\right) n\left(H\right)^2 \alpha\left(H^+\right) \tag{1.12}$$

Notice that: i) the electron density equal the density of H^+ as this is the only element present in the gas, and ii) the density of H^+ can be approximated by the total density of H as we can assume that beyond the ionized region, electron density drops to zero. For a spherical approximation, the volume ($V\left(R_s\right)$) is given by $(4/3)\pi R_s^3$. From the balance we have:

$$Q_0 = \frac{4}{3}\pi R_s^3 n\left(H\right)^2 \alpha\left(H^+\right) \tag{1.13}$$

Hence, the radius is expressed as:

$$R_S = \left[\frac{3Q_0}{4\pi n\left(H\right)^2 \alpha\left(H^+\right)}\right]^{1/3} \tag{1.14}$$

This is the so-called *Strömgren radius*, and it is usually in the order of parsecs for most of the stellar sources.

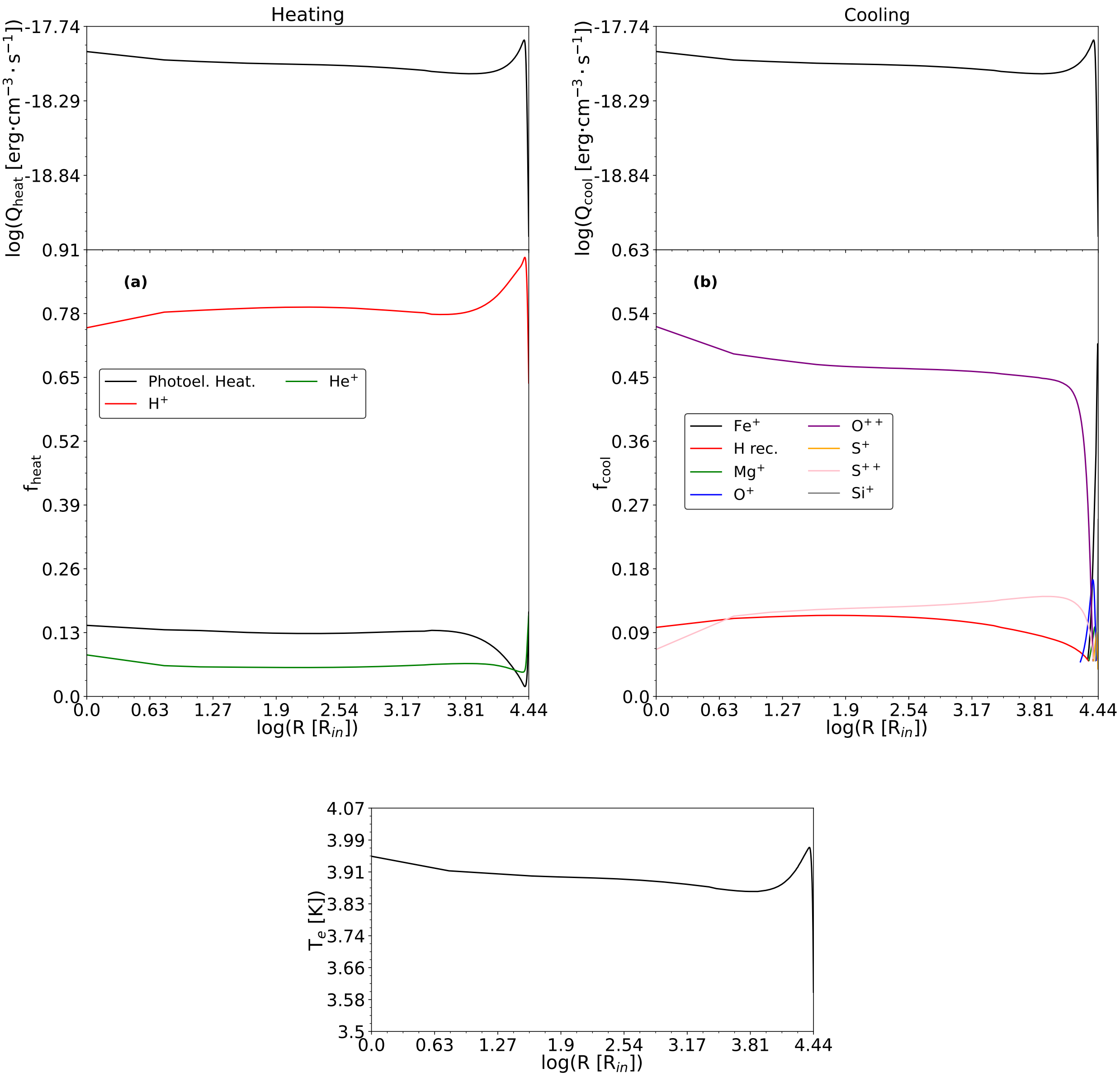

Figure 1.3: Heating (left column) and cooling (right column) mechanisms in a simulated (CLOUDY v23, Chatzikos et al. 2023; Gunasekera et al. 2023) HII region surrounding a recent burst of star formation as function of the distance from the inner face (R_{in}). The ionizing source has been computed with POPSTAR (Mollá et al., 2009), after 1 Myr. The gas is supposed to have an electron density of n_e = 500 cm^{-3} and solar composition (Asplund et al., 2009). Top panels show the total sum of heating/cooling rates, whereas bottom panels show the proportion of the main agents. Bottom final panel shows the temperature profile. Model calculated for $\log(U) = -2.5$.

1.1.4.3 *The thermal equilibrium*

The density of the ionized gas, in terms of ions and neutrals atoms, is so low ($n \sim 1\,\mathrm{cm}^{-3}$) that a Local Thermodynamic Equilibrium (LTE) should not be applied. However, as the ISM is characterized by heavier ions, thus the electron density is higher. As electron collisions are more frequent, we can assume that the electron distributions are in LTE, and hence, their properties, density (n$_e$) and

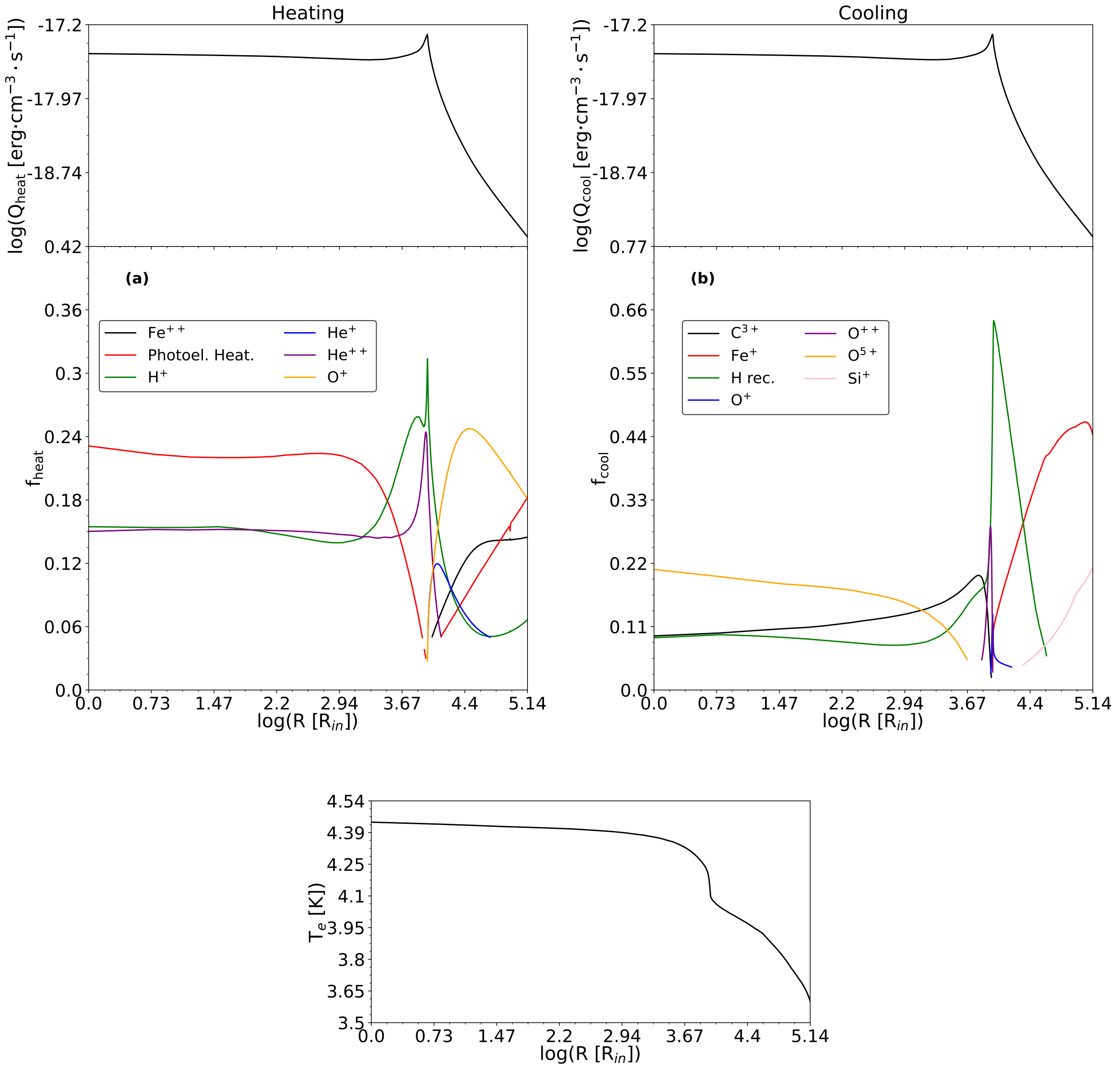

Figure 1.4: Same as Fig. 1.3 but assuming that the ionizing source is an AGN, with slopes $\alpha_{OX} = -0.8$ and $\alpha_X = -1$ (this is a parametrization of the expected SED from an AGN, and specific details can be found in Sec. 2.3 and 2.4). Model calculated for $\log(U) = -1.5$.

temperature (T_e), are given as characteristics of the ionized gas. In other words, the electrons are assumed to have a maxwellian statistical distribution governed by their temperature (T_e).

Whereas density is assumed to not significantly change from the initial conditions, temperature can be determined by the balance between heating and cooling mechanisms. We show in Fig. 1.3 and 1.4, different agents act in the heating/cooling process, but an equilibrium is achieved at all distances. This equilibrium determines the overall temperature profile.

As hydrogen is the most abundant element, there is a clear source of heating due to the photoionizing photons that exceed the energy threshold of H. Secondly, we should expect a similar scenario for the He ionization, but in this case the contribution should be much lower as He is less abundant. Finally, we must account for the heating as a consequence of dust grains can capture far-UV photons and emit electrons due to the photoelectric effect. Whereas this last effect is not dominant in the case of HII regions (stars do not produce such amount of FUV photons), it is quite significant in the case of the AGNs, as the emission of the accretion disk provides enough FUV photons. Moreover, in the case of AGNs we also observe more sources of ionization of different species as they produce more energetic photons (see Fig. 1.4).

On the cooling side, we observe that cooling via recombination is not dominant in most of the gas. On the contrary, we observe that gas cools down by emitting photons in the form of a weak continuum but with strong emission lines.

1.1.5 *The emission line spectrum*

These emission lines that are the main drivers of cooling, depending on their nature, can be classified as recombination lines (RLs) or collisionally excited lines (CELs)[5]. In both cases, these emission lines are the result of the de-excitation within atoms of electrons in upper energetic levels to lower levels.

For a given ion (Y^+), the total de-excitation of ions releasing photons of wavelength ($\lambda = hcE^{-1}$) produces an emission line whose flux is given by:

$$F_\lambda = n\left(Y^+\right) n_e j_\lambda \tag{1.15}$$

where $n\left(Y^+\right)$ is the density of the ions, n_e is the electron density and j_λ is the emissivity of the transition. The emissivity depends on many factors, but specifically it changes due to the nature of the emission line, i.e., it can show different behaviors depending on it being associated to a RL or CEL. Below, We shortly review the expected form for each case.

1.1.5.1 *Recombination lines*

RLs result from ions that capture free electrons within the ionized nebula, and the de-excitation of these electrons into the lower levels result in photon emission whose wavelengths correspond to the energy difference between the levels. Let us consider a particular element in the gas (Y), whose ions Y^+ are capturing electrons into the level m. If electrons de-excite to the level ℓ, the emissivity of the expected line is given by (Osterbrock & Ferland, 2006; M. Peimbert et al., 2017):

$$j_\lambda = \frac{E_{m\ell}}{4\pi} \alpha_{m\ell}^{eff} \tag{1.16}$$

where $E_{m\ell}$ is the energy separation between the levels (i.e. the wavelength of the corresponding emission line will be given by $\lambda = hcE_{m\ell}^{-1}$) and $\alpha_{m\ell}^{eff}$ is the effective recombination coefficient.

The effective recombination coefficient is the critical part that changes the expected emission from different emission lines produced by the same ion. This value represents the probability of the de-excitation for the electron by the specific transition, showing a strong dependence on the electron temperature (T_e), but also on the electron density. Values are generally computed from already available data tables for different specific conditions and interpolated.

Apart from the recombination coefficient (which encloses the temperature dependence) and the electron density (which is a measurable value for the whole gas), the flux depends on the density of the ion. This is the main reason why the brighter recombination lines are those of hydrogen, followed up by helium. Both elements are the most abundant elements in the ISM. However, due to the low abundances of heavier elements, these recombination lines are much fainter.

---

[5] Another important category of emission lines are the so-called *flourescence* lines, which are basically RLs much more brighter due to the excitation from other lines or ionizing sources.

1.1.5.2 *Collissionaly excited lines*

Due to the density conditions observed in the ionized gas, specifically for electron densities in the orders of $n_e \sim 10^2 - 10^3$ cm^{-3}, there is also the possibility of electrons exciting atoms and ions due to collisions. The complexity of these transitions (in comparison to the RLs) arises in the fact that the balance between collisional and spontaneous excitations and collisional and spontaneous de-excitations to the different atomic levels must be solved, by means of numerical approximations (e.g. Kewley et al., 2019; Osterbrock & Ferland, 2006; M. Peimbert et al., 2017) accounting for the electron density (n_e), the fraction of ions in each state, and the collisional (de)-excitation rates.

The collisional rates are important quantities to determine the fraction of ions on a particular level. Both of them depend on the electron temperature (T_e) and density (n_e), but in different ways. The collisional excitation rates go as (Kewley et al., 2019; Osterbrock & Ferland, 2006):

$$R_{coll,ex} \propto n_e T_e^{-\frac{1}{2}} \exp\left(-\frac{E}{k_B T_e}\right) \tag{1.17}$$

whereas the collisional de-excitation rates depend as (Kewley et al., 2019; Osterbrock & Ferland, 2006):

$$R_{coll,de-ex} \propto n_e T_e^{-\frac{1}{2}} \tag{1.18}$$

This is why, for the same temperature, density can make radiative de-excitations much less inefficient. The limit is marked by the critical density n_c which is the exact value of density at which, radiative de-excitations equals collisional de-excitations.

The emissivity of an ion $n\left(Y^+\right)$, which has been excited by collisions to the atomic level m and radiatively decays into level ℓ is given by (Osterbrock & Ferland, 2006):

$$j_\lambda = \frac{E_{m\ell}}{4\pi n_e} f_m A_{m\ell} \tag{1.19}$$

where, again, $E_{m\ell}$ is the energy separation between the levels (or equivalently the wavelength), f_m is the fraction of ions on the state m (which depends on electron temperature and density as seen above) and $A_{m\ell}$ is the spontaneous probability transition (which is tabulated in atomic data files). It must be noted that f_m for each ion is determined by the excitations to the desired level (from collisions) and the de-excitations (from colissions and radiation), which in equilibrium should be equal.

First of all, the average energy that can characterize the ISM is of the order of few eV (for a temperature of $T_e \sim 10^4$ K), which implies that electrons are only able to excite ions whose upper levels are separated by few eV. This is the main reason why these emission lines mainly come from heavy (metal) ions, and not from hydrogen or helium ions. Secondly, the excited ions must decay emitting photons (radiative decay), and this is extremely affected by the electron density of the gas. And thirdly, there is a stronger dependence (with respect to the RLs) on temperature (T_e) as not only spontaneous transitions are accounted for, but also the collisional (de)-excitation rates.

Fig. 1.5 is quite illustrative to asses the differences between CELs and RLs. First of all, we can observe that emissivities for RLs are low when compared to the ones of CELs, highlighting again why metal RLs are not detected in most cases while we detect bright metal CELs. On the other hand, there is little change (< 1 dex) on the emissivity of RLs whereas the change in CELs goes beyond 1.5 dex, and in most cases up to 4 dex. These lines that drastically change their emissivity with temperature are called *auroral lines*.

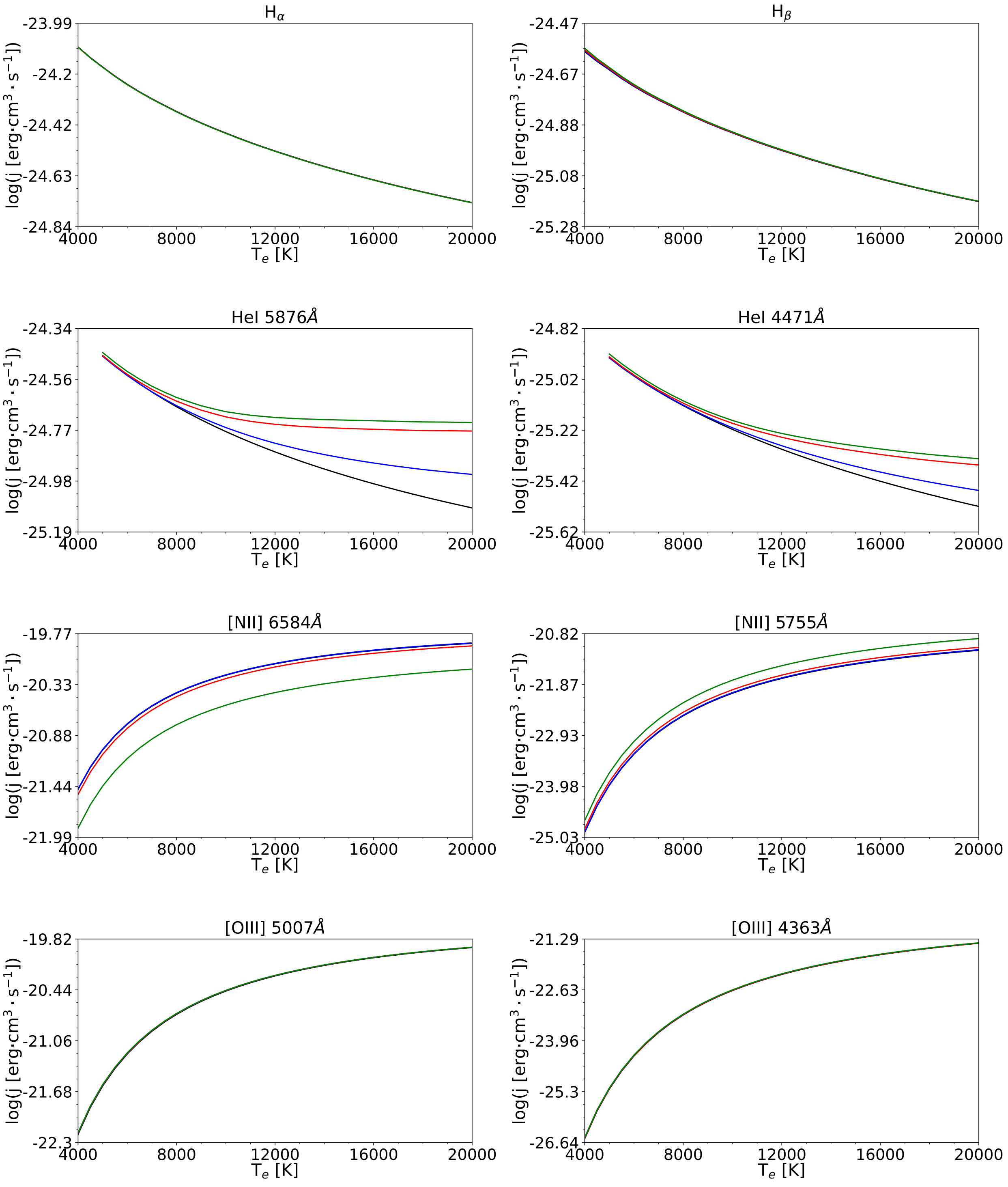

Figure 1.5: Emissivity of emission lines as a function of the electron temperature computed from PYNEB (Luridiana et al., 2015). Top panels show the emissivity from RLs (H and He), and bottom panels for CELs (N and O). Different values of the electron density are used: $n_e = 100$ cm^{-3} (black), $n_e = 10^3$ cm^{-3} (blue), $n_e = 10^4$ cm^{-3} (red) and $n_e = 10^5$ cm^{-3} (green).

1.2 PLASMA DIAGNOSTICS FROM EMISSION LINES

In their review, Lisa J. Kewley and collaborators quoted the following statement from an anonymous source: *To try to make a model of an atom by studying its spectrum is like trying to make a model of a grand piano by listening to the noise it makes when thrown downstairs* (Kewley et al., 2019). The ISM is mainly

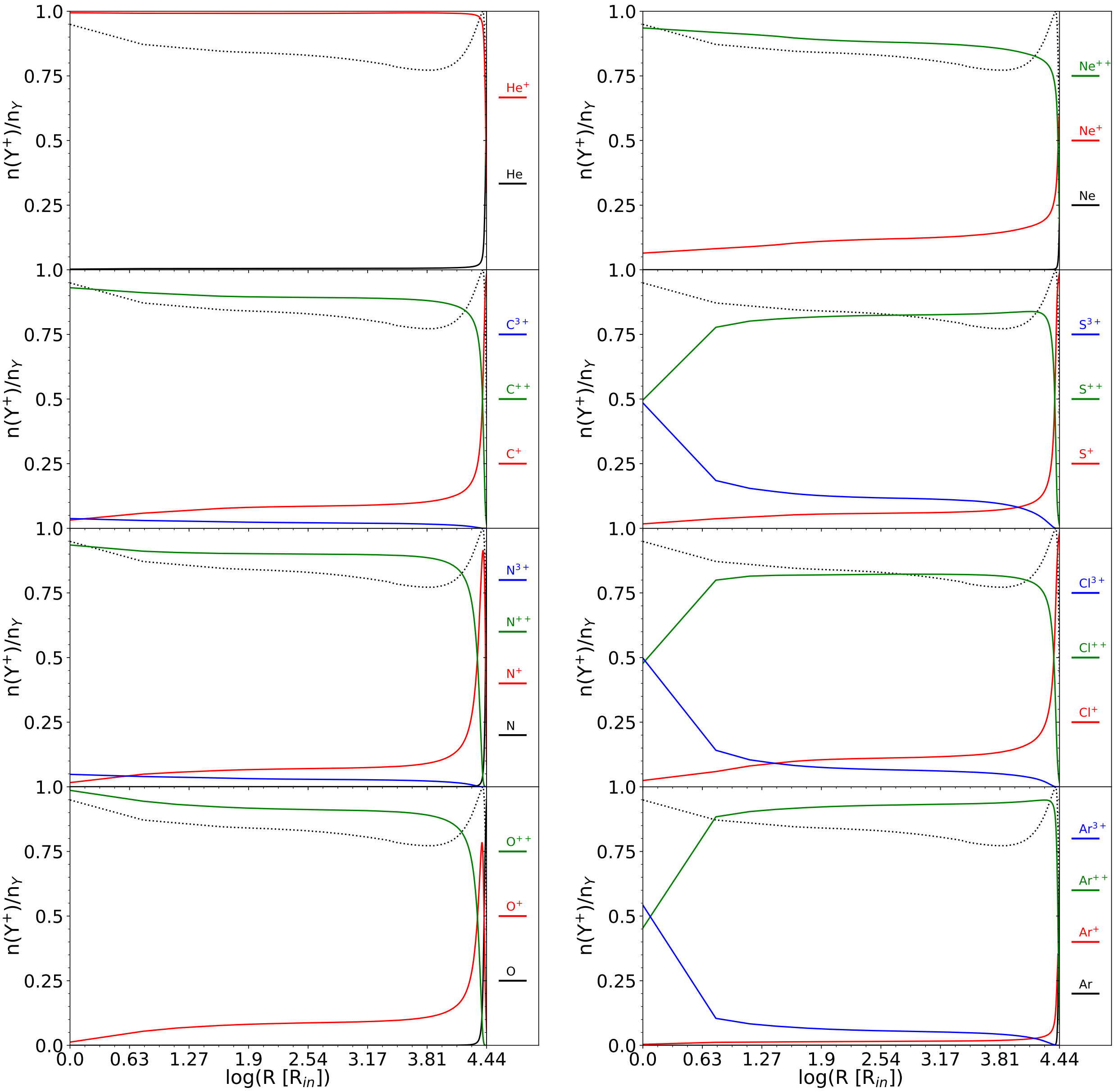

Figure 1.6: Ion fractions, obtained with CLOUDY V23, in a HII region surrounding a recent burst of star formation as function of the distance from the inner face (R_{in}). The ionizing source has been computed with POPSTAR (Mollá et al., 2009), after 1 Myr. For the gas it is assumed an electron density of $n_e = 500$ cm^{-3} and solar composition (Asplund et al., 2009). Black dashed line represents te normalized temperature profile. Model calculated for $\log(U) = -2.5$.

composed by H and He, but as we have discussed above, there are heavier atoms that significantly contribute to the cooling of the gas-phase ISM. Thus, accurate models for specific atoms and their ions are needed to understand their excitations and de-excitations. Therefore, we rely on atomic databases for the different parameters (e.g. Dere et al., 2019; Fang et al., 2011; Kisielius et al., 1998; Pequignot et al., 1991), which can be managed with specific software such as PYNEB (Luridiana et al., 2015; Morisset et al., 2020) or within photoionization models such as CLOUDY (Chatzikos et al., 2023; Ferland et al., 2017; Gunasekera et al., 2023) or MAPPINGS (Sutherland & Dopita, 2017). However, as they are the main cooling agents, the spectrum from ions are accessible for different observational ranges, making them an invaluable source of information of the ISM.

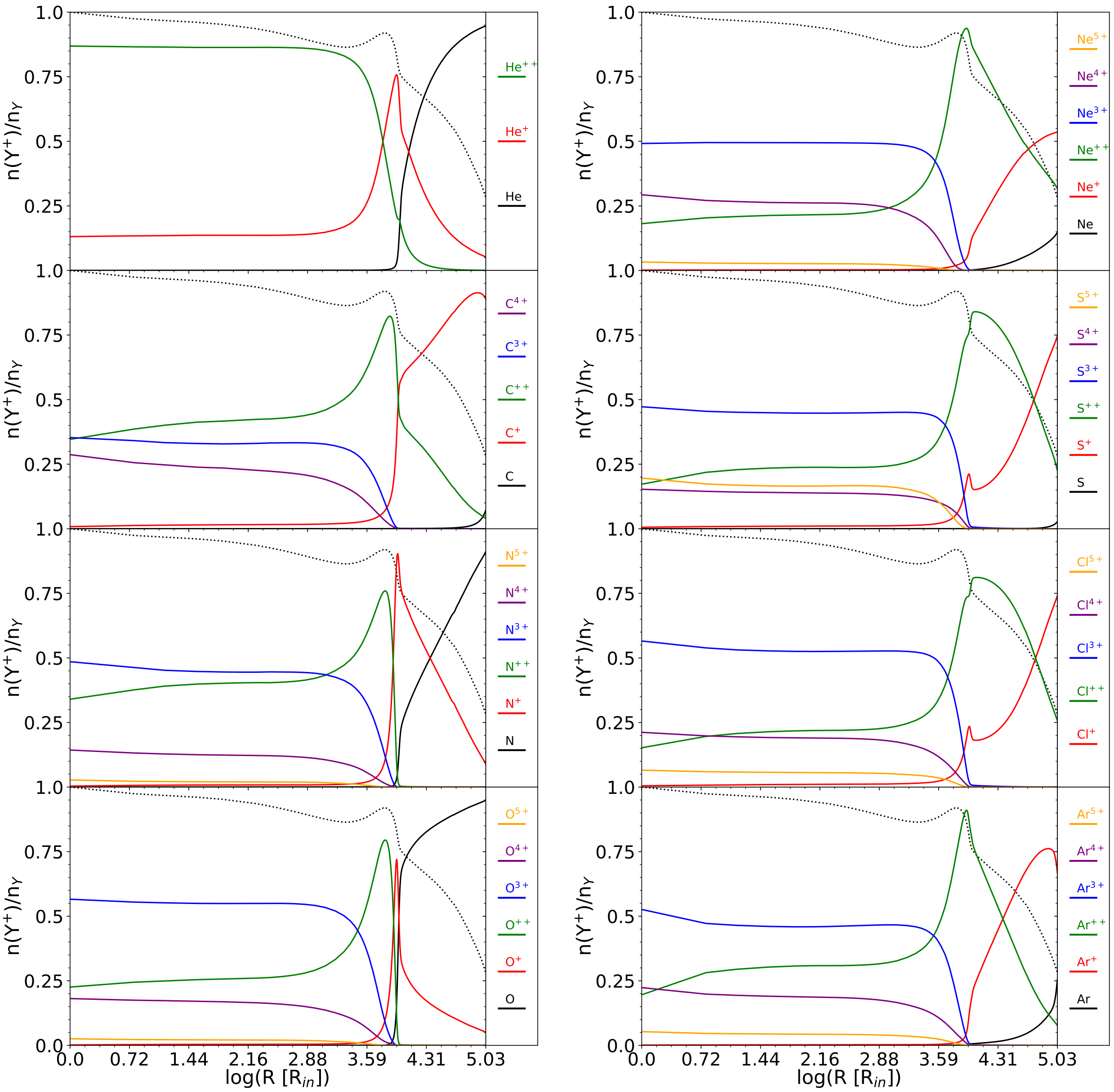

Figure 1.7: Same as Fig. 1.6 but assuming that the ionizing source is an AGN, with slopes $\alpha_{OX} = -0.8$ and $\alpha_X = -1$. Model calculated for $\log(U) = -2.5$.

1.2.1 *Emission lines tracing the ISM*

Emission lines from the gas-phase ISM are easily observed in the UV [900Å – 3000Å], optical [3000Å – 9600Å] and IR [9600Å – 700μm] ranges. As they are emitted by ions and atoms, their origin within the gas is set by how ions are distributed. These distribution will be marked by the photoionization and the equilibrium reached between heating and cooling, as well as the physical and chemical properties of the gas.

By means of photoionization models (see Sec. 2.3), we can have a very good estimation of the distribution of the ions, which is the result not only from the balance between heating and cooling processes, but also from their ionizing energies. Fig. 1.6 and Fig. 1.7 show how ions are distributed assuming different ionizing sources across the gas-phase ISM. First of all, we observe notable differences just by assuming different ionizing source. Specifically, we observe that higher ionized species (e.g. O^{3+}, He^{++}, Ne^{4+}) are present when the gas is ionized by an AGN (see Fig. 1.7). On the other hand, when analyzing an HII region, we observe that while some ionic species are dominant through the whole gas, at distances closer to the source we observe a non-negligible contribution of higher ionized species (as it is the case for S or Ar). This motivates a scheme of the ionized gas based on the existence of an ionizing structure.

In the case of HII regions, their structure can be defined by three ions, due to their ionization energies (or, equivalently, ionization potentials). The ion O^{++} with an ionization energy of 35.1 eV defines the high-excitation zone. The ion S^{++}, with an ionization potential of 23.3 eV, defines the intermediate-excitation zone. And finally, ions such as N^+, O^+ or S^+ (with ionizing energies of 14.5 eV, 13.6 eV and 10.4eV respectively) define the low-excitation zone. These three zones corresponds respectively to the inner most, intermediate and outer zones (see Fig. 1.6). In the case of AGNs it is also important to define an extremely high-excitation zone, which can be traced by ions such as Ne^{4+} or O^{3+}, that are characterized by high ionization potentials (97.1 eV and 54.9 eV respectively), not observed in HII regions (see Fig. 1.7).

These ionic species can be detected from their emission lines. For example, by looking at the sulfur emission line [S IV], we are retrieving information from the parts closer to the ionizing source of an HII region, whereas lines such as [O III] or [Ne III] are useful to study the extent of the ionized gas. Low ionized species emit emission lines such as [Ne II] or [S II] which become brighter in the outermost parts, allowing us to define a boundary or limit between ionized gas and diffuse ionized gas within the same cloud. On the other hand, the detection of particular emission lines such as [Ne V] or [O IV] can be use to discriminate certain ionizing sources as those ions are only observed when objects with a very hard field of radiation ionize the gas.

1.2.2 *Dust extinction*

Dust and ionized gas are two components of the ISM that are often mixed. Within the ionized gas, dust grains scatter and/or absorb part of the emitted photons, being both processes governed by the size of the dust grains. For photons with blue ($\lambda \lesssim 6000$Å) wavelengths, the joint effects of absorption and scattering are more pronounced that for redder photons. In the case of a continuum emission, this would imply a continuous excess in the redder with respect to the bluer parts of the spectrum. In the case of emission lines, this implies that those at bluer wavelengths are much more affected (the observed flux is significantly lower) than those at longer wavelengths. This is the attenuation effect, and it can be parametrized on several ways.

When studying emission lines, the dust attenuation of the flux of an emission line at wavelength λ can be expressed as (e.g. Howarth, 1983; Osterbrock & Ferland, 2006; Pérez-Montero, 2017):

$$F_{\lambda,obs} = F_{\lambda,th} \exp\left(-\tau_{\lambda}\right) = F_{\lambda,th} \cdot 10^{-Cf(\lambda)} \tag{1.20}$$

where $F_{\lambda,obs}$ and $F_{\lambda,th}$ are the observed (dust affected) and emitted fluxes of the emission lines, $f(\lambda)$ represents the *extinction law*, that gives the dust absorption as a function of the wavelength and C is the amplitude of the function (i.e. a measure of how much dust is producing the extinction).

When studying objects, such as stars, it is better to use colors, i.e., the difference between the total flux retrieved from two filters, also known as *color*. Let us assume that we have two filters, with effective wavelengths λ_1 and λ_2. Due to dust attenuation, the color changes (usually called *color excess*) as (e.g. Cardelli et al., 1989):

$$\begin{aligned} E\left(F_1 - F_2\right) &= \left[m_{\lambda_1} - m_{\lambda_2}\right]_{obs} - \left[m_{\lambda_1} - m_{\lambda_2}\right]_{th} = \left[m_{\lambda_1,obs} - m_{\lambda_1,th}\right] - \left[m_{\lambda_2,obs} - m_{\lambda_2,th}\right] \\ &= -2.5\log\left(\frac{F_{\lambda_1,obs}}{F_{\lambda_1,th}}\right) + 2.5\log\left(\frac{F_{\lambda_2,obs}}{F_{\lambda_2,th}}\right) \equiv A_{\lambda 1} - A_{\lambda_2} \end{aligned} \tag{1.21}$$

where we have introduced the definition of magnitude (m_λ). The parameter A_λ is called the *number of magnitudes of extinction* at a wavelength λ, and it has a direct relation with the extinction parametrization in emission lines by:

$$A_\lambda = -2.5\log\left(\frac{F_{\lambda,obs}}{F_{\lambda,th}}\right) = 2.5Cf(\lambda) \tag{1.22}$$

The amount of extinction in terms of color excess is generally provided by means of the filters B ($\lambda_{eff} \approx 4450$Å) and V ($\lambda_{eff} \approx 5510$Å) from the Johnson's system (e.g. Cardelli et al., 1989; Howarth, 1983).

Numerous works have been published on how to parametrize the extinction (e.g. Blagrave et al., 2007; Calzetti et al., 2000; Cardelli et al., 1989; Gordon et al., 2003; Howarth, 1983), and all of them provide the extinction curve in terms of $A_\lambda/A_V = f(\lambda)/f(V)$ and in terms of the ratio of total-to-selective extinction $R_V \equiv A_V/E(B-V)$, who plays the role of scale for the curve in the UV. We show in Fig. 1.8 examples of different extinction curves for three values of R_V (notice that the most accepted one is $R_V = 3.1$). Although the parametrization curves differ in the UV regime, where dust effects are more important and R_V plays a significant role, for the optical regime little difference is found among the proposed curves or the values of R_V, so the dust extinction correction is fairly robust. Dust extinction effects in the IR regime are essentially mitigated.

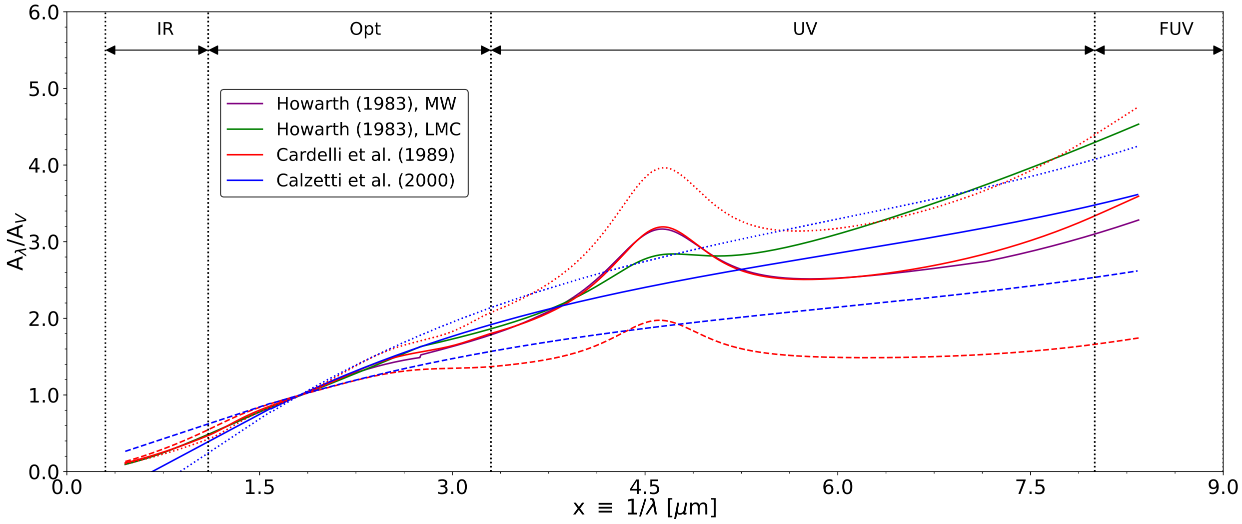

Figure 1.8: Extinction curves across different spectral regimes. Solid lines represent $R_V = 3.1$, dotted lines $R_V = 2.5$ and dashed lines $R_V = 5.0$

Without knowing all the physical and chemical parameters that govern the emissivity of a line (see Sec. 1.1.5), it is not possible to have an estimation of the expected flux for an emission line. As its flux depends on a first order approximation on the ion density and emissivity (see Eq. (1.15)), a ratio between emission lines of the same ion will cancel the uncertainty due to the ion abundance. On the other hand, as hydrogen is the most abundant element, the use of H I recombination lines, specifically Balmer lines that are bright in the optical regime[6], are generally used for this purpose.

---

[6] The largest wavelength in the Balmer series corresponds to H_α ($\lambda = 6563$Å), and in some cases due to the limitations of the spectroscopic observations, only this Balmer line is available. Whereas the next series, Paschen, can be observed in the NIR, the emissivity of these lines is typically $\sim 0.5\%$ of the Balmer ones. In this case, Zamora et al. (2022) propose to use helium (He I) emission lines to measure dust extinction.

As the brightest Balmer lines are H_α and H_β, they are the most used. The observed flux after dust attenuation is given by:

$$\left(\frac{F_{H_\alpha}}{F_{H_\beta}}\right)_{obs} = \left(\frac{F_{H_\alpha}}{F_{H_\beta}}\right)_{th} 10^{-C\left[f(H_\alpha)-f(H_\beta)\right]} \equiv \left(\frac{F_{H_\alpha}}{F_{H_\beta}}\right)_{th} 10^{-c\left(H_\beta\right)\left[\frac{f(H_\alpha)}{f(H_\beta)}-1\right]} \tag{1.23}$$

where $c\left(H_\beta\right) = Cf\left(H_\beta\right)$. By assuming this form, we minimize uncertainties in the extinction curve, as they are accounted within the extinction parameter $c\left(H_\beta\right)$. Thus, if we know the theoretical ratio between these two recombination lines, then the extinction parameter can be obtained as:

$$c\left(H_\beta\right) = \frac{\left(\frac{F_{H_\alpha}}{F_{H_\beta}}\right)_{obs} / \left(\frac{F_{H_\alpha}}{F_{H_\beta}}\right)_{th}}{1 - \frac{f(H_\alpha)}{f(H_\beta)}} \tag{1.24}$$

which is always a positive value. In order to directly use $c\left(H_\beta\right)$, then the rest of emission lines can be corrected by expressing them in relation to H_β:

$$\left(\frac{F_\lambda}{F_{H_\beta}}\right)_{obs} = \left(\frac{F_\lambda}{F_{H_\beta}}\right)_{th} 10^{-c\left(H_\beta\right)\left[\frac{f(\lambda)}{f(H_\beta)}-1\right]} \tag{1.25}$$

The theoretical ratio between H_α and H_β depends on the recombination case: *case A* when the gas is optically thin and all recombination photons escape; or *case B* (physical conditions of the majority of studied ionized gas corresponds to this case) when all emitted recombination photons from Lyman-α ($\lambda = 1215.7$Å) are absorbed by the immediate gas[7]. An additional dependence arises from the fact that electron temperature and density conditions also change the expected ratio (e.g. Luridiana et al., 2015; Pérez-Montero, 2017). For HII regions, under Case B recombination and for the generic physical properties of $n_e = 100$ cm^{-3} and $T_e = 10^4$ K, the ratio between H_α and H_β is expected to be 2.86. In the case of AGNs, for Case B recombination it has been proposed the value of 3.1 (Gaskell & Ferland, 1984), which has been observationally confirmed by other studies (Barquín-González et al., 2024). For PNe, as the physical conditions are more varied, the most typical values are located in the range $[2.7, 3.1]$ (Montoro-Molina et al., 2022; Ueta & Otsuka, 2021).

As a final remark, the extinction parameter is often expressed in other terms such as the color excess $E(B-V)$ or as the extinction magnitude A_V (photometric measurement), which are related to $c\left(H_\beta\right)$ (spectroscopic measurement) as:

$$E\left(B-V\right) = \frac{A_V}{R_V} = \frac{2.5c\left(H_\beta\right)f\left(V\right)}{R_V f\left(H_\beta\right)} \tag{1.26}$$

In other words, the conversion depends on the extinction curve and R_V values assumed.

---

[7] We note that the contribution from fluorescence can also affect the photon emission in H I and He I, allowing us to define Case C when fluorescence are significant within case A or case D when fluorescence are significant within case B. Generally, these effects are small and the general assumption of Case B is overall a good approximation (e.g. M. Peimbert et al., 2017).

1.2.3 *Physical properties of the ISM*

Emission lines do not only provide us with tools for observing directly the ionized gas, but also for estimating the physical properties that characterize it. As we have pointed out, the emissivity of emission lines depends not only on the density of ions that emit them, but also on the physical properties such as electron density (n_e) and temperature (T_e). Therefore, a careful selection of emission lines can provide diagnostics to improve our understanding of the ISM.

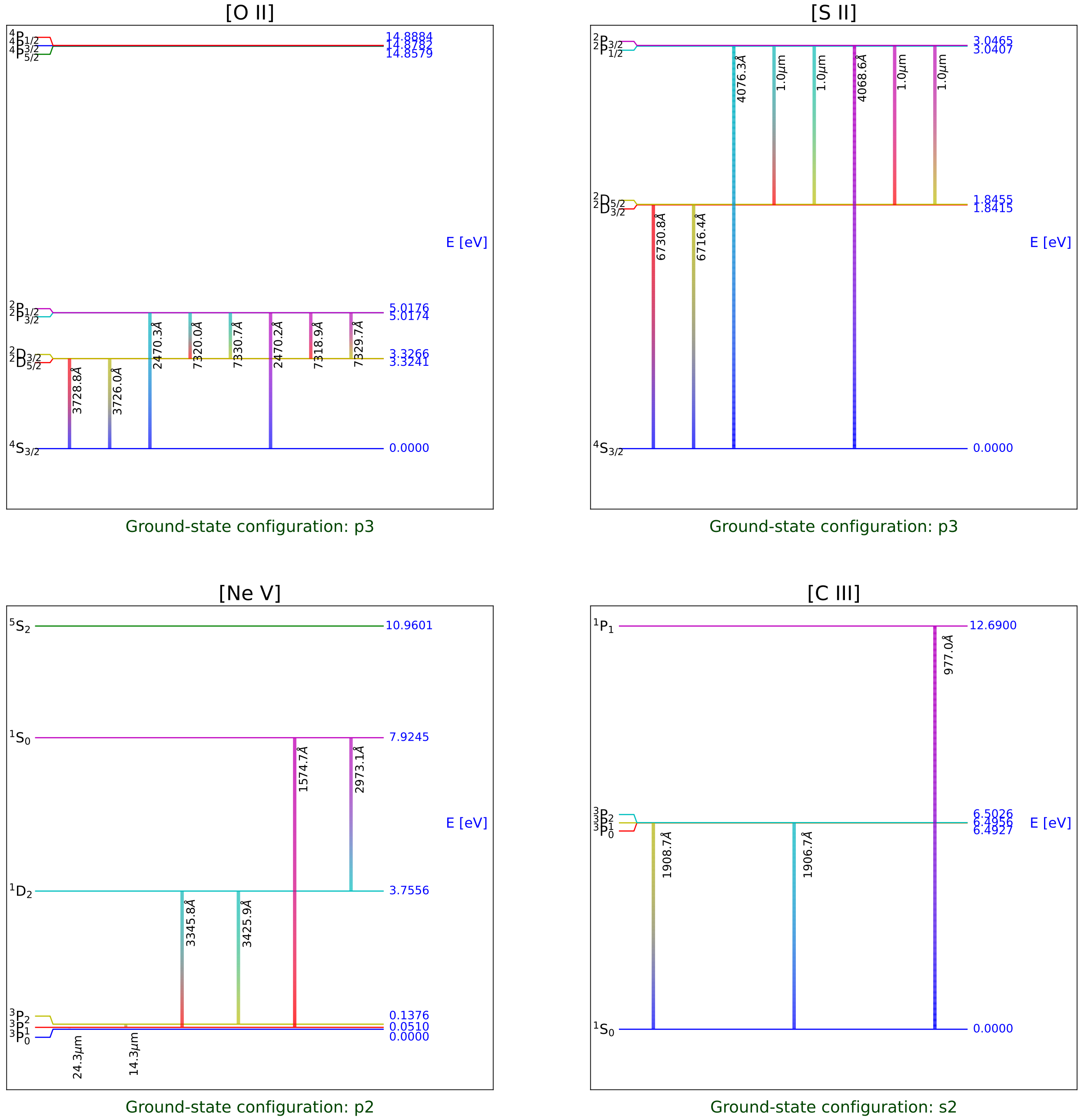

Figure 1.9: Grotrian diagrams[8] for different ionized atoms. Grotrian diagrams have been obtained with PYNEB assuming $T_e = 10^4$ K and $n_e = 100$ cm^{-3}.

Let us start with measurements of the electron density. Some ions present energy levels that are very close in terms of energy, as they only differ in the spin coupling of electrons in the outer levels.

---

[8] Hereinafter, Grotrian diagrams for each ion present the energy levels tagged with their spectroscopic notation, i.e., a level is defined by the spin (S), orbital (L) and total angular momentum (J) quantum numbers as: $^{2S+1}L_J$.

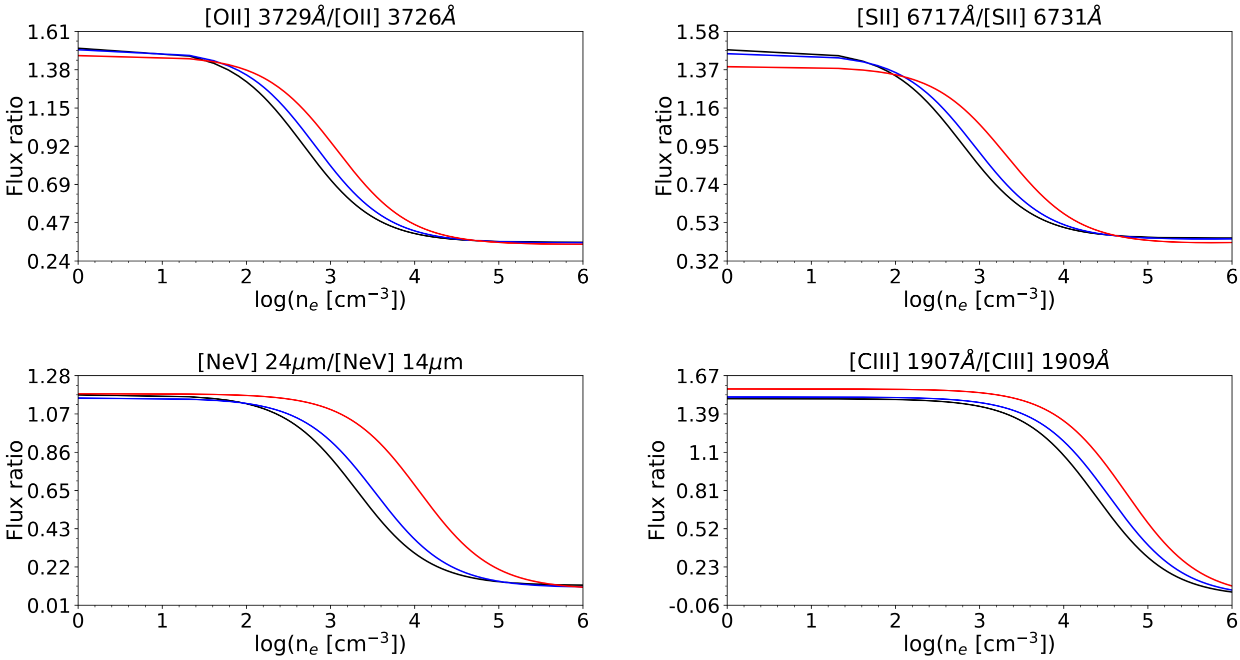

Figure 1.10: Emission line ratios sensitive to the electron density, computed with pyneb. Different values of the electron temperature are used: $T_e = 5 \cdot 10^3$ K (black), $T_e = 10^4$ K (blue) and $T_e = 5 \cdot 10^4$ K (red).

Some examples are shown for O^+, S^+, Ne^{4+} and C^{2+} (see Fig. 1.9). Let us consider these two states p and m, with corresponding energies $E_p \approx E_m$. According to Eq. (1.15) and (1.19), the flux ratio is given by:

$$\frac{F_{\lambda(p)}}{F_{\lambda(m)}} \approx \frac{f_p A_{p\ell}}{f_p A_{m\ell}} \tag{1.27}$$

As the excitation rate (Eq (1.17)) should be mostly similar (without taking into account departures due to minor quantum effects), the fraction in each energetic state is governed by the balance between those excitations and collisional de-excitations together with spontaneous decays. Those rates show an slight dependence on temperature as well (due to the nature of A and $R_{coll,de-ex}$), but a strong dependence on electron density. Thus the ratio of such emission lines (called doublets) can be used as tracer of density.

We show in Fig. 1.10 some examples of emission line ratios between doublets. We observe that there is a mild dependence on temperature, but overall they are excellent tracers of the electron density (n_e) in certain ranges. Moreover, we explicitly show examples of tracers that can be used in different spectroscopic regimes: optical ([O ii], [S ii]), UV ([C iii]) or IR ([Ne v]). However, the range of validity for the estimation must be considered as well. As IR emission lines are characterized by been emitted from energetic levels which are close, collisional de-excitations can become significant if density is high enough, and hence, the validity of the [Ne v] doublet is constrained to $n_e \lesssim 5 \cdot 10^3$ cm^{-3}. On the contrary, due to the high separation of the energetic levels which originates UV lines, their critical densities are much higher and hence they can be used to trace density in denser regimes (up to $n_e \lesssim 10^6$ cm^{-3}). Complementary, there is a lower limit as well. If density becomes significantly low, only collisional excitations and radiative de-excitations will occur, so the ratio in Eq. (1.27) becomes constant[9]. Following the previous argument, UV line ratios have a higher lower-limit than IR line ratios.

---

[9] The number of excited ions by collisions will equal the number of de.excited ions by radiation, and hence, each part of the fraction exclusively depends on the collisional strength of each level.

As we have already discussed in Sec. 1.1.5, there are some emission lines whose emissivity strongly depends on temperature, the auroral lines. These CELs (auroral lines) are emitted when the energetic state goes from the second lowest to the lowest excited states (which also emits its own CELs when de-exciting to the ground level). As the difference on energy is non-negligible, the ratio between both emission lines is driven mainly by temperature, as it changes the rate of collisional excitations (Eq. (1.17)). Example of such emission lines are [O III] λ4363Å, [S III] λ6312Å, [Ne III] λ3342Å and [N II] λ5755Å. We show in Fig. 1.11 the corresponding Grotrian diagrams.

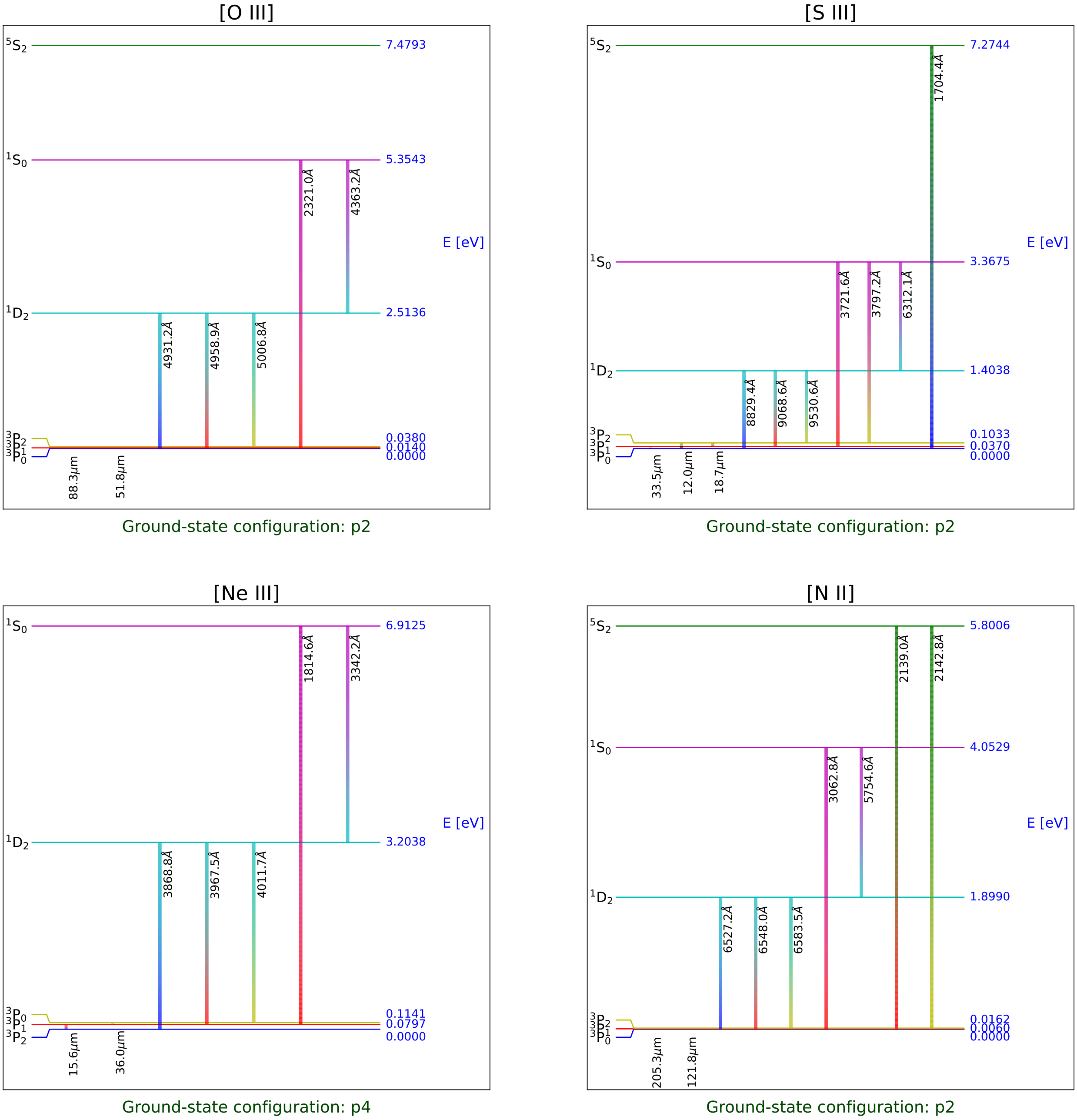

Figure 1.11: Grotrian diagrams for different ionized atoms that emit auroral lines. Grotrian diagrams have been obtained with PYNEB assuming $T_e = 10^4$ K and $n_e = 100$ cm^{-3}.

Another important aspect from auroral lines is that, as the difference in energy between the two first ionized levels and between the first and ground levels are quite similar, for the same observable range there is available a CEL which traces the de-excitations from the first to the ground level (see

Fig. 1.11). Thus, the ratio between these two emission lines can be used to trace temperature. We show an example of those ratios in Fig. 1.12.

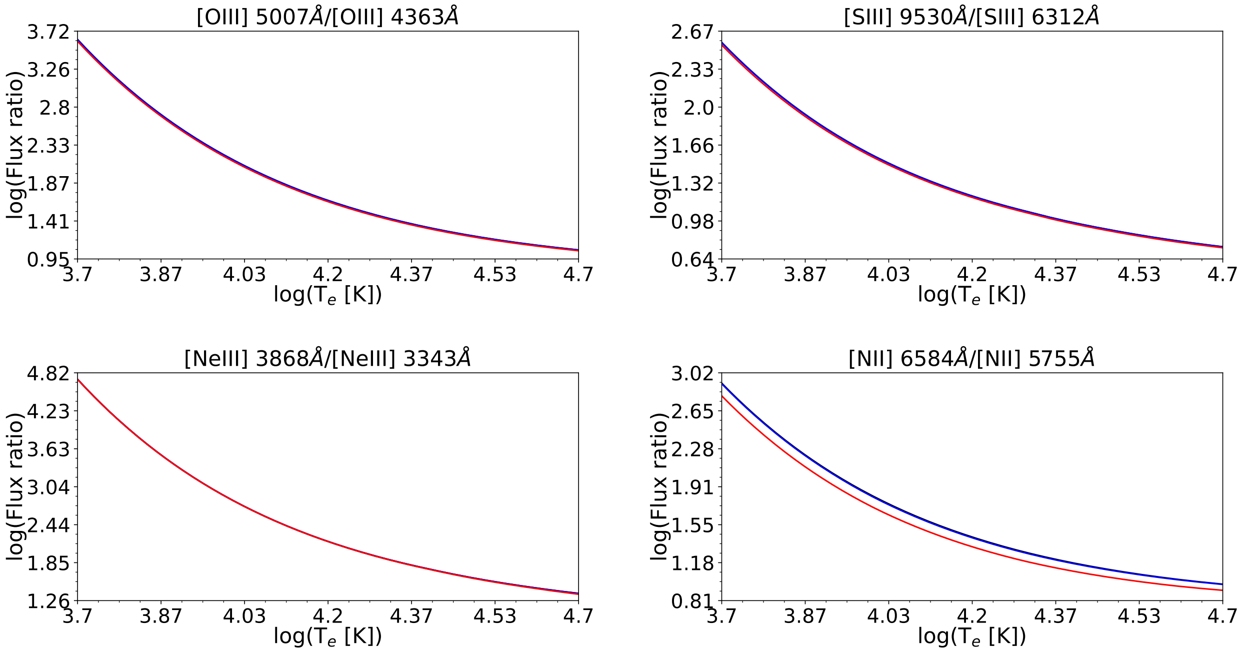

Figure 1.12: Emission line ratios sensitive to the electron temperature, computed with PYNEB. Different values of the electron density are used: $n_e = 100\ \mathrm{cm}^{-3}$ (black), $n_e = 10^3\ \mathrm{cm}^{-3}$ (blue) and $n_e = 10^4\ \mathrm{cm}^{-3}$ (red).

Again, there is mild dependence on electron density, but by assuming a particular value of the density, we can obtain a good estimate of the temperature. As a matter of fact, this can be done in an iterative process. By assuming a particular value of the temperature (initial guess), a value of the density can be estimated. With that value, then an estimation of the temperature can be provided as well. The process can be stopped when there is little variation on the estimated values. For this purposes, either direct use atomic databases (e.g. Luridiana et al., 2015) or calibrations proposed in the literature (e.g. Pérez-Montero, 2017).

It is important to note that temperatures (and densities) derived from different emission line ratios might not match. This is due to the fact that both, density and temperature, are not characterized through the gas by a single value rather than by a profile. As we already pointed out, ions also show characteristic profiles across the gas. Hence, depending on the observed ion, we are getting information from different parts of the nebula. For a given element, its ions will be distributed according to the excitation zones previously defined, and hence will be mainly tracing the physical properties on such zones. This is illustrated in Fig. 1.13, where we observe that we can obtain different values depending on the used set of emission lines.

1.2.4 *Chemical properties of the ISM*

The emission line spectrum that we observe from the gas-phase ISM does not only depend on the physical properties of the ISM, but also on its chemical composition. Therefore, once we have an estimation of the physical properties of the ISM, we can use the emission line fluxes to estimate its chemical composition.

The major component of the gas-phase ISM is hydrogen, and thus, chemical abundances are usually referred as fractions in relation to the amount of H, i.e., as $n\left(Y\right)/n\left(H\right)$, being Y a generic element. Since heavy elements present really small proportions, it is more useful to express them in

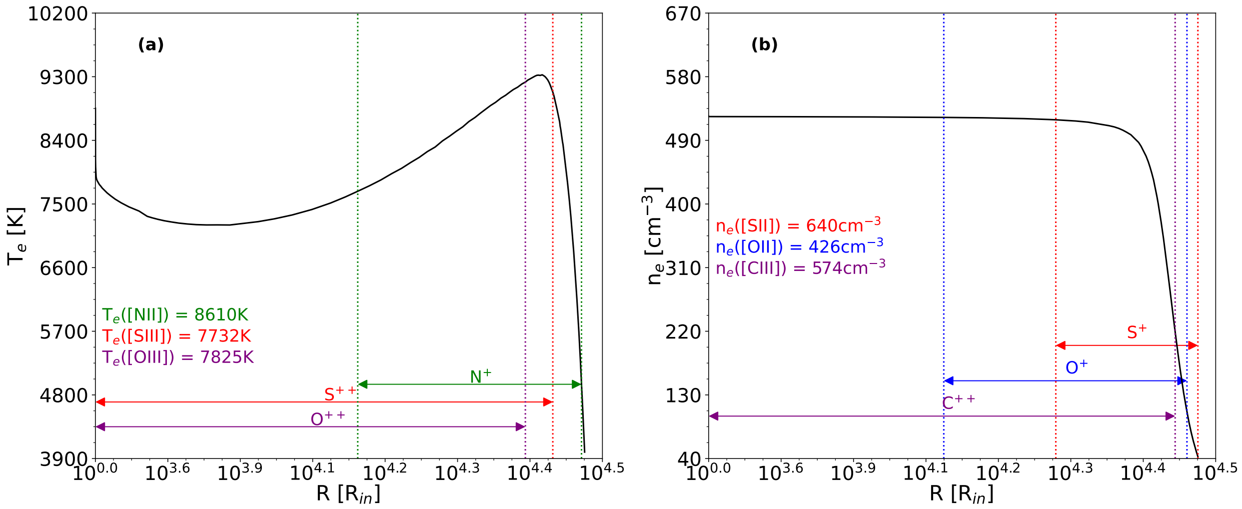

Figure 1.13: Electron temperature and density profiles obtained with CLOUDY V23, in a HII region surrounding a recent burst of star formation as function of the distance from the inner face (R_{in}). The ionizing source has been computed with POPSTAR after 1 Myr. An electron density of $n_e = 500\ \mathrm{cm}^{-3}$ and solar composition (Asplund et al., 2009) has been assumed for the gas. Model calculated for $\log(U) = -2.5$. Vertical dashed lines mark the limits of each ion element being at least 15% of the total density of the element. Temperature and density estimations have been computed with PYNEB.

the logarithmic form $\log(n\,(Y)\,/n\,(H))$ or, using the form $12 + \log(n\,(Y)\,/n\,(H)) \equiv 12 + \log(Y/H)$, so that all element abundances show positive values.

The ionized gas is mainly defined by the ionization of H, we can assume that $n\,(H^+) \approx n\,(H)$. If we have a good estimation on the physical properties of the ISM, we can estimate the abundance of an ion relative to H by means of the emission line ratios between an emitted line from that ion and a hydrogen recombination line. From Eq. (1.15), we obtain that:

$$\frac{F\,(Y)_{\lambda_1}}{F\,(H)_{\lambda_H}} = D\,(n_e, T_e, \lambda_1, \lambda_H)\,\frac{n\,(Y^+)}{n\,(H^+)} \tag{1.28}$$

the factor D encompasses the dependence of emissivity not only on the physical properties of the gas, but also on the observed transitions and the nature of the emission line (RL or CEL).

As described in Sec. 1.2.1 (see also Fig. 1.6 and 1.7), the total abundance of an element Y is given by the sum of the abundances of all its ions. For each ion Y^{i+}, there must be at least an emission line at a wavelength λ_i. Hence, the total abundance can be expressed as:

$$\frac{n\,(Y)}{n\,(H)} = \sum_{i=0}^{n} \frac{n\,(Y^{i+})}{n\,(H^+)} = \sum_{i=0}^{n} \left[\frac{1}{D\,(n_e, T_e, \lambda_i, \lambda_H)}\,\frac{F\,(Y^{i+})_{\lambda_i}}{F\,(H)_{\lambda_H}} \right] \tag{1.29}$$

This is the so-called *direct*- or T_e-method.

As in the case of dust extinction, the majority of these studies have been performed using optical data, and the hydrogen recombination line used is generally H_β. In the optical regime, the oxygen abundance might be constrained[10] with [O II]λ3729Å for O^+ and [O III]λ5007Å for O^{++}. Once we have an estimation of the physical properties, which preferentially should be obtained with emission lines from the same ions, to avoid uncertainties within the gas profiles, then the coefficients A can be estimated either by means of formula approximations (Pérez-Montero, 2017) or by directly

---

[10] As shown in Fig. 1.6, the contribution from neutral O can be mainly neglected.

computing them from atomic databases (Luridiana et al., 2015). We show in Tab. A.1 an example of values for certain physical properties.

Physical properties of gaseous nebulae are, empirically, constrained by means of optical emission lines, as auroral lines (necessary for the estimation of the electron temperature) are detected in that range. Hence, the available set of emission lines to constrain the chemical abundance mainly comes from the optical regime (unless a multiwavelength study is performed). For some elements, such as O, this is not a problem since it is distributed mainly as O^+ and O^{++}. For other elements, such as S, it is necessary to account for ions whose emission lines are not detected in the optical regime (e.g. [S IV]$\lambda 10 \mu$m). In these cases, the total abundance derived from the observed ions is corrected by a function called ionization correction factor (ICF), as:

$$\frac{n\left(Y\right)}{n\left(H\right)} = \mathrm{ICF}\left(\sum_{i=n_{0,obs}}^{n_{obs}} \frac{n\left(Y^{i+}\right)}{n\left(H^{+}\right)} \right) \sum_{i=n_{0,obs}}^{n_{obs}} \frac{n\left(Y^{i+}\right)}{n\left(H^{+}\right)} \tag{1.30}$$

which is mainly a function of the abundances already estimated using their corresponding emission lines. These ICFs are essentially calculated from photoionization models, as the total abundance as well as all physical parameters of the ISM are controlled (see Amayo et al., 2021, for a recent update on the proposed ICFs).

Not only is useful to estimate the relative abundances of heavy elements with respect to H, but also in relation to other metals. As discussed in Sec. 1.1.2, elements are produced by different stars, and hence, the analysis of ratios of different elements gives clues on the star formation processes. As oxygen is the most abundant heavy element (e.g. M. Peimbert et al., 2007), it is used as common denominator. Thus, the relative abundance of an element Y with respect to O, can be expressed as:

$$\frac{n\left(Y\right)}{n\left(O\right)} = \frac{\sum_{i=0}^{n} n\left(Y^{i+}\right)}{\sum_{j=0}^{n} n\left(O^{j+}\right)} = \frac{\sum_{i=0}^{n} D^{-1}\left(n_e, T_e, \lambda_i, \lambda_H\right) F\left(Y^{i+}\right)_{\lambda_i} / F\left(H\right)_{\lambda_H}}{\sum_{j=0}^{n} D^{-1}\left(n_e, T_e, \lambda_j, \lambda_H\right) F\left(O^{j+}\right)_{\lambda_j} / F\left(H\right)_{\lambda_H}} \tag{1.31}$$

Again, in most cases due to observational limitations, ICFs must be used to convert the observed ionic abundances into total abundances. For example, in the case of N/O, optical observations only provide information for N^+, whereas it is clear that N^{++} shows an important contribution. In the same way, total abundances might be obtained by:

$$\frac{n\left(Y\right)}{n\left(H\right)} = \mathrm{ICF}\left(\frac{\sum_{i=0,obs}^{n,obs} n\left(Y^{i+}\right)}{\sum_{j=0,obs}^{n,obs} n\left(O^{j+}\right)} \right) \frac{\sum_{i=0,obs}^{n,obs} n\left(Y^{i+}\right)}{\sum_{j=0,obs}^{n,obs} n\left(O^{j+}\right)} \tag{1.32}$$

1.2.5 *Nature of the ionizing sources*

Emission lines can also provide good diagnostics to constrain the ionizing sources. These studies highly depend on the observing range, as the emission lines of particular ions are only observable in certain spectroscopic regimes. In addition, there is a strong absorption of the UV emission, so indirect analysis such as those provided by emission lines are required for a proper distinction. Nevertheless, it is important to have a good constraint as the methods used or even the necessity of incorporating ICFs to the measured abundances are highly dependent on the ionization structure of the gas-phase ISM.

In a first-order approximation, the simple detection of particular emission lines already provides a discrimination of the ionizing source. For example, the detection of He II emission lines (at $\lambda = 4686$Å in the optical or $\lambda = 1642$Å in the UV) is already a good tracer of hard ionizing radiation, since its ionizing energy (54.4 eV) implies that photons can only be produced by very massive stars, such as those formed in low-metallicity galaxies (e.g. Kehrig et al., 2015, 2018) or first generation (Population III) of stars (e.g. Venditti et al., 2024). Other energetic scenarios such as AGNs and fast RS can also produce these photons (e.g. Allen et al., 2008; Pérez-Montero et al., 2023b). The kinematical profile of the detected He II line, either broad (stellar) or narrow (nebular) can also be used as a constraint for the ionizing source (e.g. Kehrig et al., 2018). In the IR regime, the detection of [Ne V] emission lines (either at $\lambda = 14.3\mu$m or $\lambda = 24.3\mu$m) has been proposed to be a signature of AGN emission (Armus et al., 2007; Genzel et al., 1998; Mingozzi et al., 2025; Pérez-Torres et al., 2021), as only[11] AGN SEDs are able to produce enough photons with energies $\gtrsim 97.1$ eV.

The ionization parameter (U, Eq. (1.11)) also offers embedded information from the ionization source, but it has a strong dependence on the geometry of the gas. If the ionization parameter is high, for a fixed density and geometry, it implies that more ionizing photons are produced (Q_0, Eq. (1.9)). Although it also depends on bot the radius of the gas envelope and on density, given that density is usually well constrained in the range [100 cm^{-3}, 500 cm^{-3}], variations on U are mainly driven by changes in the luminosity of the ionizing source.

The ratio between two emission lines of two ions from the same element is also a useful tool to quantify the ionization parameter. Let us assume that we observe two emission lines at wavelengths λ_1 and λ_2, emitted by ions Y$^{(i+1)+}$ and Y^{i+}. From Eq. (1.15), the ratio can be expressed as:

$$\frac{F_{\lambda_1}}{F_{\lambda_2}} = \frac{n\left(Y^{(i+1)+}\right) j_{\lambda_1}}{n\left(Y^{i+}\right) j_{\lambda_2}} \tag{1.33}$$

The density of an ion can be expressed in terms of the total density of the element, such as $n\left(Y^{i+}\right) = f_{i+} n\left(Y\right)$, thus we can remove any dependence on the absolute density:

$$\frac{F_{\lambda_1}}{F_{\lambda_2}} = \frac{f_{(i+1)+} j_{\lambda_1}}{f_{i+} j_{\lambda_2}} = \frac{f_{(i+1)+}}{f_{i+}} G\left(n_e, T_e\right) \tag{1.34}$$

where G is the ratio between the emissivities of the lines, which depends on the physical conditions of the emitting gas.

Let us now consider the ratio between the two consecutive ions. For a given ion Y^{i+}, we have that some photons will ionize it to $Y^{(i+1)+}$, particularly those with enough energy ($E_\lambda = E_I\left(Y^{i+}\right)$), which do not depend only on the available photons but also on the cross section between them and the ions $\sigma\left(Y^{+}\right)$. On the other hand, some of those ions recombine, going again as Y^{i+}, which can be determined by the total recombination coefficient $\alpha\left(Y^{i+}\right)$. Thus, the ionization balance implies that (Osterbrock & Ferland, 2006; Vilchez & Pagel, 1988):

$$\frac{n\left(Y^{(i+1)+}\right)}{n\left(Y^{i+}\right)} = \frac{f_{(i+1)+}}{f_{i+}} \approx \frac{Uc\langle\sigma\left(Y^{i+}\right)\rangle}{\alpha\left(Y^{i+1}\right)} \frac{\int_{\frac{hc}{\lambda}=E_I(Y^{i+})}^{\infty} \frac{\lambda L_\lambda}{hc}}{\int_{\frac{hc}{\lambda}=13.6\ eV}^{\infty} \frac{\lambda L_\lambda}{hc}} \tag{1.35}$$

Thus, the ratio between the ions can also depend on the shape of the SED of the ionizing source, in addition to the ionization parameter. Indeed, if the ionizing source is hard, we expect much more photons able to ionize further the element and, thus, the ratio $\frac{f_{(i+1)+}}{f_{i+}}$ increases. In some cases, it is not possible to find two consecutive ions, so the best approach is to use the highest-ionized ion and the second highest, as the first one is the most affected by the ionization degree of the nebula.

---

[11] The detection of [Ne V] emission in galaxies with no previous evidence of AGN activity (e.g. Hernandez et al., 2025; Izotov et al., 2021; Mingozzi et al., 2025) has challenged this general conception, but there is still caveats in whether non-AGN sources, such as fast radiative shocks (e.g. Izotov et al., 2021) or X-ray binaries (e.g. Hernandez et al., 2025), can reproduce the observed ratios.

Another interesting parameter that can be used to constrain the SED of the ionizing source is the so-called *softness parameter* (η), defined as (Vilchez & Pagel, 1988):

$$\eta \equiv \frac{n\left(O^{+}\right)/n\left(O^{++}\right)}{n\left(S^{+}\right)/n\left(S^{++}\right)} = \frac{\alpha\left(O^{+}\right)\langle\sigma\left(S^{+}\right)\rangle}{\alpha\left(S^{+}\right)\langle\sigma\left(O^{+}\right)\rangle} \frac{\int_{\frac{hc}{\lambda}=23.3eV}^{\infty} \frac{\lambda L_{\lambda}}{hc}}{\int_{\frac{hc}{\lambda}=35.1eV}^{\infty} \frac{\lambda L_{\lambda}}{hc}} \tag{1.36}$$

Besides the implied atomic coefficients, the definition of η as presented above clearly highlights a dependence on the SED. If the ionizing source can be approximated to a blackbody of temperature (T), then the eta parameter behaves as:

$$\eta \propto A \exp\left(\frac{B}{T}\right) + C \tag{1.37}$$

being A, B and C constants. As stars can roughly be interpreted as blackbodies with $T = T_{eff}$ (effective temperature), η can be used as a proxy for the effective temperature of the ionizing stars (e.g. Pérez-Montero & Vílchez, 2009; Pérez-Montero et al., 2019b; Vilchez et al., 1988). Although η is purely defined based on abundances, it can be directly translated into a ratio between emission lines multiplying by the corresponding emissivities (this is η'), although it presents an additional dependence on electron temperature and density, the ionization parameter and metallicity, leading to the creation of the so-called *softness diagram* (Pérez-Montero & Vílchez, 2009; Pérez-Montero et al., 2023b).

The above mentioned diagnostics have a theoretical explanation, but there other diagnostics that have been extensively used in the literature to discriminate the dominant ionizing source. This is the case of the classical BPT diagrams (Baldwin et al., 1981; Kauffmann et al., 2003; Kewley et al., 2006) and the WHAN diagram (Cid Fernandes et al., 2010, 2011). (Baldwin et al., 1981) proposed a series of diagrams based on optical emission lines to differentiate between extragalactic objects and HII regions and PNe. The emission lines used for such classification were [Ne v]λ3426Å, [O ii]λ3727Å, He iiλ3426Å, H$_{\beta}$, [O iii]λ5007Å, [O i]λ6300Å, H$_{\alpha}$ and [N ii]λ6584Å. They found out not only that local and extragalactic data are clearly differentiated, but also that those diagrams are helpful in distinguishing objects ionized by massive stars such as HII regions or star-forming galaxies (SFGs), ionized by power-law like sources such as AGNs or ionized by shocks. These are the *BPT diagrams* or *diagnostic diagrams*.

Some revisions were made to that preliminary scheme, among them the work by Veilleux and Osterbrock (1987), who reduced the number of diagnostics and proposed a smaller set of emission line ratios to be used. These ratios were: [O iii]λ5007Å/Hβ, [N ii]λ6584Å/Hα, [S ii]λ, λ6717, 6731Å/Hα and [O i]λ6300Å/Hα. The advantage of using these ratios is that: i) it only involves strong optical emission lines which are easily detected; ii) lines are in a region of the spectrum which is usually covered; and, iii) the ratios are made minimizing dust extinction effects. Based on that work, Kewley et al. (2001) provided a clear demarcation where SFGs (and starburst galaxies) are located by means of photoionization models.

With the advent of large spectroscopic surveys, such as Sloan Digital Sky Survey (SDSS; Blanton et al., 2003; Stoughton et al., 2002; York et al., 2000), the number of available spectra for extragalactic objects increased several orders of magnitude, allowing for empirical constrains on the BPT diagrams. The works by Cid Fernandes et al. (2010), Kauffmann et al. (2003), and Kewley et al. (2006) allow us to define different regions in each diagram, where star-forming galaxies, AGNs and LLAGNs are mainly found. This is illustrated in Fig. 1.14.

Later on, an additional diagnostic was proposed by Cid Fernandes et al. (2010, 2011) based on the [N ii]λ6584Å/Hα and the equivalent width of Hα ($W_{H_{\alpha}}$). This is the so-called *WHAN diagram*. Motivated by the work from Stasińska et al. (2008), showing that passive galaxies whose emission

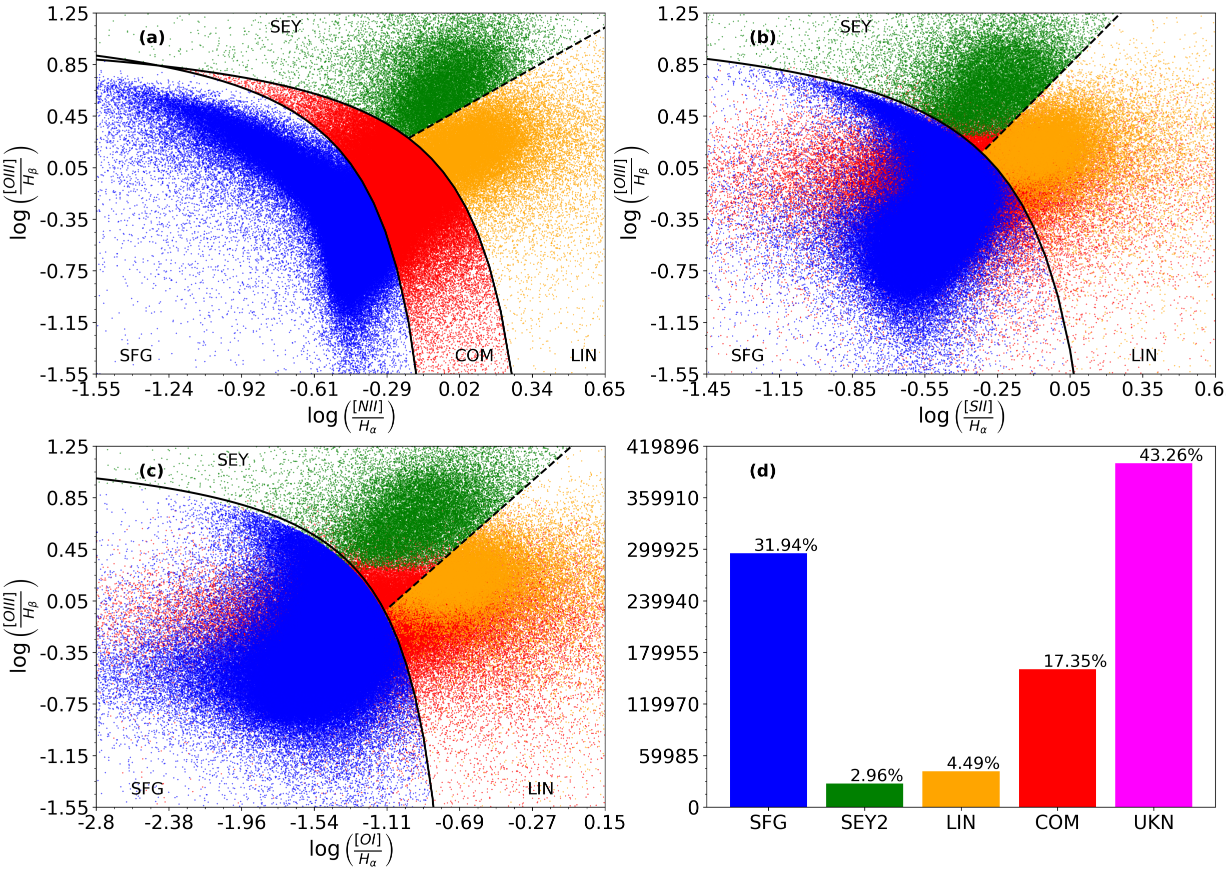

Figure 1.14: Diagnostic diagrams for the SDSS DR9 GalSpec catalog of galaxies. Colors identify different spectroscopic classes: blue for star-forming galaxies (SFGs), green for Seyferts (SEY), red for composite galaxies (COM) and orange for LINER-like galaxies (LIN). Only galaxies unambiguously classified in the three diagrams are shown. Panels a), b) and c) show each diagnostic whereas panel d) shows the statistics. Unknown sources (magenta) are those objects that change their classification from one diagnostic to the other.

was attributed to hot low-mass evolved stars (HOLMES) were classified as LINERs in the BPT diagrams, Cid Fernandes et al. (2010) proposed also a distinction based on the strength of W_{H_α}. This diagram allows for a differentiation between star-forming galaxies, strong AGNs (sAGNs), weak AGNs (wAGNs), retired galaxies (RGs) and passive galaxies (PGs). We show an example of such classification in Fig. 1.15, for the same galaxy sample classified in Fig. 1.14.

1.3 CHEMICAL EVOLUTION OF GALAXIES

In the preface to the second edition of their *Galaxies in the Universe* textbook, Lisa S. Sparke and John S. Gallagher wrote: *We must take the Universe as we find it, and deduce how the basic properties of matter have constrained the galaxies that happened to form* (Sparke & Gallagher, 2006). Indeed, our current understanding (and uncertainties) from how galaxies form and evolve mainly come from observations, either from large surveys in which statistics helps us getting a wide picture or by targeting particular types of objects which allow us to test the boundaries of our theories and models. Observations are also complemented by predictions made either by hydrodynamical simulations (e.g. Davis et al., 1985; Schaye et al., 2015; Springel et al., 2018) or semi-analytic models (e.g. Bower et al., 2006; Cole et al., 2000; Nadler et al., 2023).

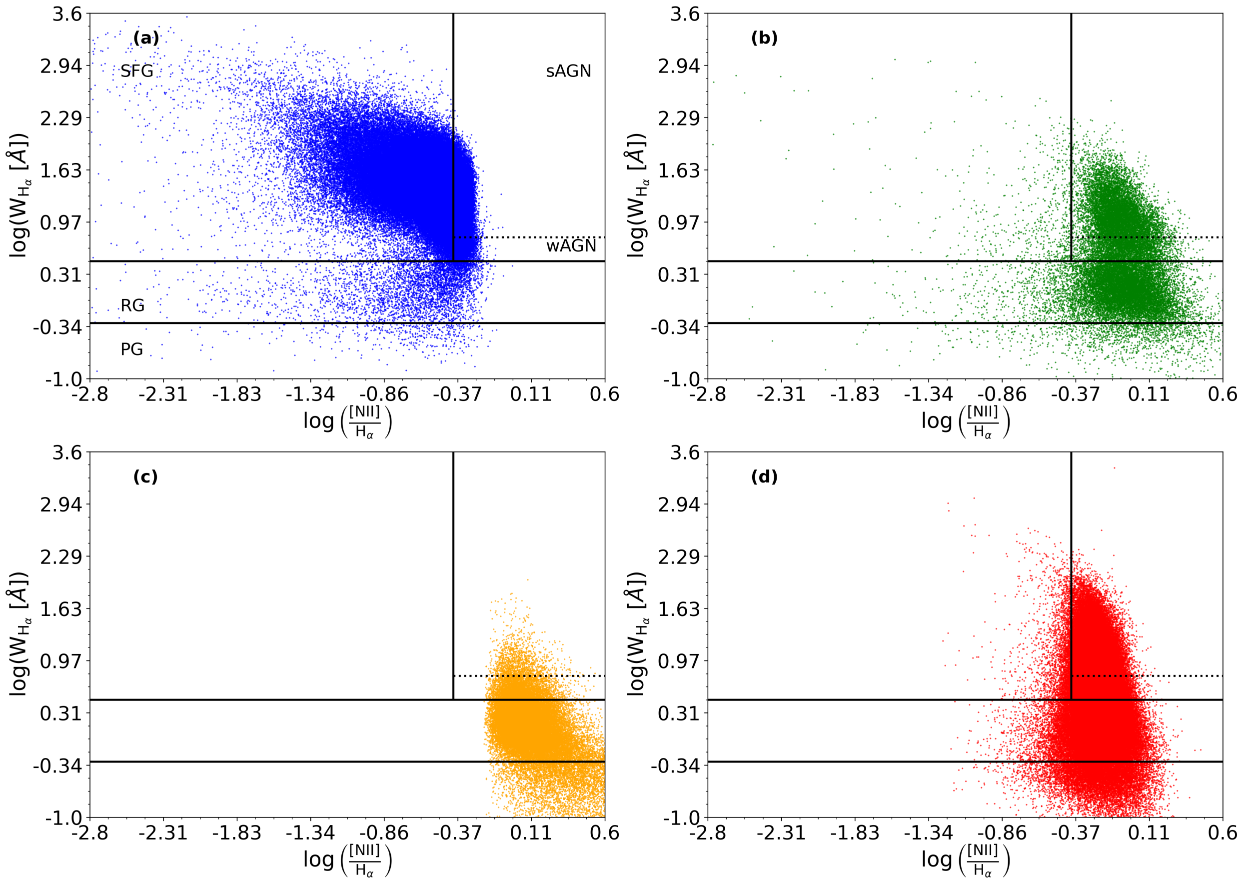

Figure 1.15: WHAN diagram for the SDSS DR9 GalSpec catalog of galaxies. Only galaxies unambiguously classified in the three diagnostic diagrams are shown. Colors follow the same code as Fig. 1.14. Each panel shows the classification for each spectral class: a) SFGs, b) Seyferts, c) LINER-like, and d) composite.

Our current understanding of galaxy formation and evolution requires two ingredients: dark (DM) and baryonic (BM) matter. As DM only interacts by gravity, we have a good understanding on how DM evolved. Complexity increases drastically when we study the evolution of BM (stars, gas, dust), as not only gravity but many other physical processes at different spatial and temporal scales take place. A proper knowledge on the chemical composition of the baryonic matter, which is governed by the star formation history of a galaxy, provides clues on how galaxies evolved, and give constraints for theory and models aiming to provide a framework to understand galaxy evolution.

The chemical evolution of galaxies can be studied through many ways. The first way is to analyze the chemical composition of stars (in our own Galaxy) or stellar populations (extragalactic sources), by means of fitting the observed spectrophotometric continuum data to stellar synthesis models that control all synthesis parameters, among them stellar metallicity (e.g. Cappellari, 2017; Conroy, 2013; Leitherer et al., 2011). Another way is to estimate the chemical composition of the gas-phase ISM, by means of the analysis of its emission lines (see Sec. 1.2.4). Finally, the chemical evolution of galaxies can also be studied through models, either from numerical simulations (e.g. Dubois et al., 2016; Schaye et al., 2015; Springel et al., 2018), analytical models (e.g. Kobayashi et al., 2000, 2020a; Vincenzo et al., 2016) or semi-analytical models (e.g. Tissera et al., 2025; Yates & Kauffmann, 2014; Zoldan et al., 2017).

The ratio between different elements observed in the ionized gas tells us the present chemical enrichment of the ionized gas, and, hence, it allows us to trace the impact of the different enrichment processes that galaxies have undergone. Therefore, in this section, we will constrain ourselves to the observations and predictions for the chemical evolution of galaxies as traced by their gas-phase ISM.

1.3.1 *Galaxy formation: leading theory and caveats*

Before directly addressing observational results and models for galaxy chemical evolution, it is important to review the formation of galaxies. Under the general assumed ΛCDM cosmological model, primordial dark matter density fluctuations led to the formation of DM halos (e.g. Davis et al., 1985; Springel et al., 2018), which had a hierarchal growth, where big halos became bigger by means of mergers and/or accretion from the Cosmic Web (e.g. Cole et al., 2000; Martizzi et al., 2019). Galaxies formed from the pristine gas that was trapped with those DM halos (Cole et al., 2000; Davis et al., 1985; Schaye et al., 2015; Springel et al., 2018).

Whereas this is the most accepted theory, we must bear in mind caveats arising from two different branches: either related to the cosmological model or to the hierarchical growth. In the first group, we have problems such as the Hubble constant tension (see Verde et al., 2024, for a review) or the amplitude of the matter fluctuations (e.g. Adil et al., 2024; Planck Collaboration et al., 2020, e.g.), among many others (see Efstathiou, 2025, for a recent review on the challenges to the cosmological model). In the second group, we still have caveats such as the missing satellite problem (e.g. Nashimoto et al., 2022; Strigari et al., 2007) or the fact that most massive DM halos fail to form galaxies (too-big-to-fail problem; e.g. Garrison-Kimmel et al., 2013; Ogiya & Burkert, 2015), among other problems that are detailed in the review by Bullock and Boylan-Kolchin (2017).

1.3.2 *Observational trends*

The primordial composition of the ISM gives the starting point for the chemical evolution of galaxies, but it settles mainly a zero starting point for the heavier elements (i.e. metals). In order to provide a reference standard frame, chemical evolution studies have been anchored their results to the chemical composition of the Sun. The analysis of the chemical composition of the gas-phase ISM is a field of study that has spread over many decades. The very first works dated from the late 60s/early 70s (e.g. McClure & van den Bergh, 1968; M. Peimbert & Costero, 1969; M. Peimbert, 1967; Searle, 1971), but our understanding of the chemical composition of the Sun has changed over decades. Hence, when comparing studies across different years, it is important to have in mind how Solar abundances have been revisited over the years. We provide in Tab. 1.3 an overview of the evolution of the solar abundance determination for some of the most studied elements.

As a general remark, the words chemical abundances and metallicities are frequently used in the literature indistinctly. For the present thesis, we use *metallicity* to refer to the oxygen (12+log(O/H)) abundance, since it is generally used as a tracer for the global metallicity. On the other hand, we use the term *chemical abundances* when we refer to other elements or ratios of different elements that might also include O. These ratios are essential to constrain the different stellar chemical enrichment processes, as they can only be altered by how stars have been formed throughout galaxy evolution, proving us with a glimpse on product from the star formation history of the galaxy, in other words, on its evolution.

1.3.2.1 *Relationship between N and O abundances*

Early studies of the nitrogen and oxygen abundances in HII regions showed that nitrogen could not only have a secondary production (i.e. once the ISM was already enriched with O). The results from M. Peimbert et al. (1978), Rayo et al. (1982), Shaver et al. (1983) and Vilchez et al. (1988) showed in some cases mainly constant (or with very little variation) log(N/O) across galactic disks. If

Table 1.3: Results for the chemical composition of the solar photosphere over decades (Y/H = 12+log(Y/H)). Code references: GMA60 (Goldberg et al., 1960); RA76 (Ross & Aller, 1976); AG88 (Anders & Grevesse, 1989); GS98 (Grevesse & Sauval, 1998); AS+09 (Asplund et al., 2009); LO+21 (Lodders, 2021).

	GMA60	RA76	AG89	GS98	AS+09	LO+21
He/H	-	10.8 ± 0.2	10.99 ± 0.04	10.93 ± 0.004	10.93 ± 0.01	10.924 ± 0.02
Li/H	0.96	1.0 ± 0.1	1.16 ± 0.1	1.1 ± 0.1	1.05 ± 0.10	1.04 ± 0.10
C/H	8.72	8.62 ± 0.12	8.56 ± 0.04	8.52 ± 0.06	8.43 ± 0.05	8.47 ± 0.06
N/H	7.98	7.95 ± 0.15	8.05 ± 0.04	7.92 ± 0.06	7.83 ± 0.05	7.85 ± 0.12
O/H	8.96	8.84 ± 0.07	8.93 ± 0.04	8.83 ± 0.06	8.69 ± 0.05	8.71 ± 0.04
Ne/H	-	7.57 ± 0.12	8.09 ± 0.10	8.08 ± 0.06	7.93 ± 0.10	8.15 ± 0.10
Na/H	6.30	6.28 ± 0.05	6.33 ± 0.03	6.33 ± 0.03	6.24 ± 0.04	6.21 ± 0.04
Mg/H	7.40	7.60 ± 0.15	7.58 ± 0.05	7.58 ± 0.05	7.60 ± 0.04	7.56 ± 0.05
S/H	7.30	7.2 ± 0.15	7.21 ± 0.06	7.33 ± 0.11	7.12 ± 0.03	7.15 ± 0.05
Ar/H	-	6.0 ± 0.2	6.56 ± 0.10	6.40 ± 0.06	6.40 ± 0.13	6.50 ± 0.10
Ca/H	6.15	6.35 ± 0.10	6.36 ± 0.02	6.36 ± 0.02	6.34 ± 0.04	6.31 ± 0.03
Fe/H	6.57	7.50 ± 0.08	7.67 ± 0.03	7.50 ± 0.05	7.50 ± 0.04	7.48 ± 0.04

nitrogen is only produced via CNO cycles from stars born from O-enriched gas, then the log(N/O) should always be increasing as O increases. This was the first evidence for a primary production of N (Edmunds & Pagel, 1978).

Nowadays, we have a better understanding of the relation between nitrogen and oxygen, usually traced in the log(N/O) vs 12+log(O/H) (or in short N/O vs O/H) diagram. There is an oxygen threshold (O/H_{Thres}) that limits the main production of nitrogen. For lower O abundances, N and O mainly come from the same massive stars (due to rotational effects in the stellar nucleosynthesis; e.g. Limongi & Chieffi, 2018), thus a log(N/O) constant value is expected. For higher O abundances, N now is also produced by intermediate-massive stars via CNO cycles, so it is expected that the log(N/O) ratio increases as O increases. Indeed, this behavior has been extensively reported in the literature both for HII regions (e.g. Alloin et al., 1979; Belfiore et al., 2015; Bresolin et al., 2009; van Zee & Haynes, 2006; van Zee et al., 1998; Vila-Costas & Edmunds, 1993) and for star-forming dominated galaxies (e.g. Andrews & Martini, 2013; Coziol et al., 1999; Curti et al., 2017; Lara-López et al., 2009; Larsen et al., 2001; Vincenzo et al., 2016). We show in Fig. 1.16 examples of the N/O vs O/H relation for star-forming galaxies from SDSS (panel (a)) and from HII regions in sample of galaxies from MaNGA (panel (b)).

Although well studied, the N/O vs O/H relation still present some uncertainties. In terms of the parametrization of the relation, there is no clear demarcation from where the secondary production dominates over the primary. Some authors proposed O/H_{Thres} = 8.4 (e.g. Vincenzo et al., 2016), others slightly higher values such as 8.5 (e.g. Andrews & Martini, 2013) or 8.6 (e.g. Pérez-Díaz et al., 2021). Nevertheless, given the uncertainties in the estimation of chemical abundances, these results are compatible. Another source of uncertainty is the fact that hydrodynamical processes within galaxies (such as inflows or outflows) might affect the composition of the gas (e.g. Amorín et al., 2010; Kobulnicky & Skillman, 1996; Kumari et al., 2018; Villar Martín, M. et al., 2024).

Even taking into account inflows and/or outflows, there are still examples of galaxies that do not follow at all the log(N/O) vs 12+log(O/H) relation. This is the case at high redshifts, as the detection of the so-called *extreme N-emitters*, high-redshift galaxies with prominent N emission lines, low O/H abundances and high N/O ratios (e.g. Cameron et al., 2023; Castellano et al., 2024; Isobe et al., 2023; Schaerer et al., 2024), clearly highlights the need for revisiting this relation. Several theories have been proposed to explain these observations (Wolf-Rayet stars, supermassive stars, pAGb stars, globular clusters footprints, ...) but there is still no consensus on the main mechanism(s). Another

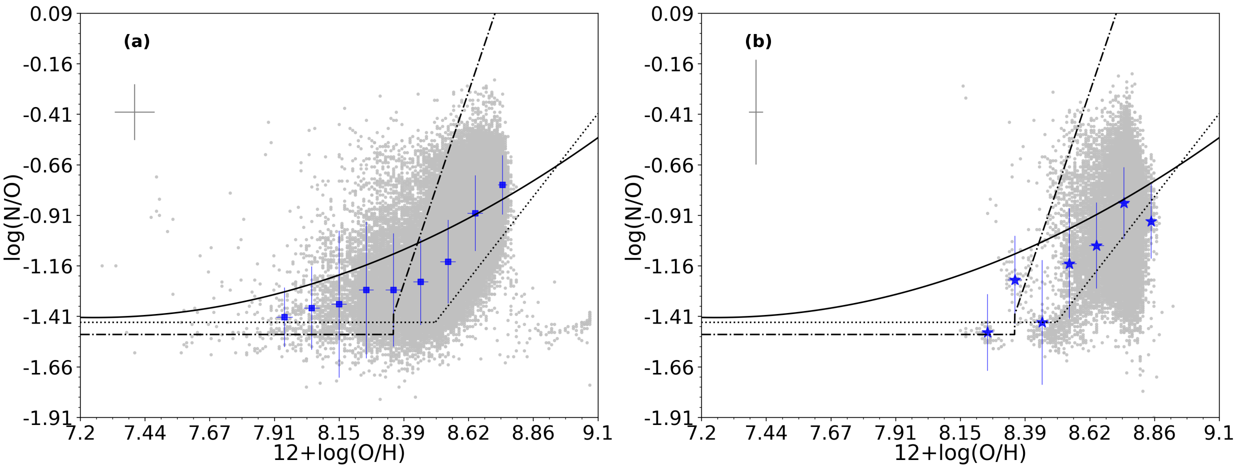

Figure 1.16: N/O vs O/H diagram for a sample of SFGs from SDSS DR9 GalSpec catalog of galaxies (a) and for HII regions from a sample of galaxies from MaNGA. Typical error bars (gray) as well as the median values for binned data (blue) are shown in each plot. Lines show reported relations in the literature: black solid (Coziol et al., 1999), dotted (Andrews & Martini, 2013) and dash-dotted (Belfiore et al., 2015).

puzzling group of galaxies are the ones whose activity is dominated by AGNs. Some authors report that they follow the same trend (e.g. Flury & Moran, 2020), others that there is no trend at all (e.g. Pérez-Díaz et al., 2021) and others that they follow a different trend (e.g. Oliveira et al., 2024a). It is important to keep in mind that the previous results depend mostly on the methodology and types of analyzed AGNs.

1.3.2.2 *Relationships between O and C, S, Ne, Ar abundances*

As carbon is produced in a similar (but not identical) way as nitrogen, then a similar relation is expected between log(C/O) and 12+log(O/H). Indeed, this relation has been reported by many authors (e.g. Berg et al., 2016; Erb et al., 2010; Henry et al., 2000; Llerena et al., 2022; Pérez-Montero & Amorín, 2017). As in the case of the N/O vs O/H relation, a scatter is expected by the same physical processes, which is even increased by the depletion effect (e.g. Pérez-Montero & Amorín, 2017). Whereas there is no clear picture on how C/O behaves in AGN-dominated galaxies, there is a hint that they might show the same deviations as reported in N/O (Pérez-Montero et al., 2023b). Interestingly, C/O ratios in extreme N-emitters at high redshift galaxies do not deviate much from the expected trend (e.g. Schaerer et al., 2024).

Sulfur, neon and argon (α-elements) are produced by the same stellar nucleosynthesis processes than oxygen, so it is expected that log(S/O), log(Ar/O) and log(Ne/O) show an almost constant behavior. Whereas for Ne and Ar studies show that they mainly[12] follow the expected trend (e.g. Arellano-Córdova et al., 2024; Berg et al., 2020; Croxall et al., 2016; Thuan et al., 1995), a different picture arises when analyzing the log(S/O) abundance ratio. Whereas some authors claim that S/O shows the expected constant behavior (e.g. Arellano-Córdova et al., 2024; Berg et al., 2020), others find clear deviations (Díaz & Zamora, 2022; Dors et al., 2023).

1.3.2.3 *Radial gradients in disk galaxies*

The analysis of HII regions within the disk of galaxies does not only provide information on the relations between different chemical species, but also on how these abundances vary across

---

[12] Most of these studies report some deviations at high abundances, but given the uncertainties in the used ICFs and the impact of dust depletion, they must be revisited.

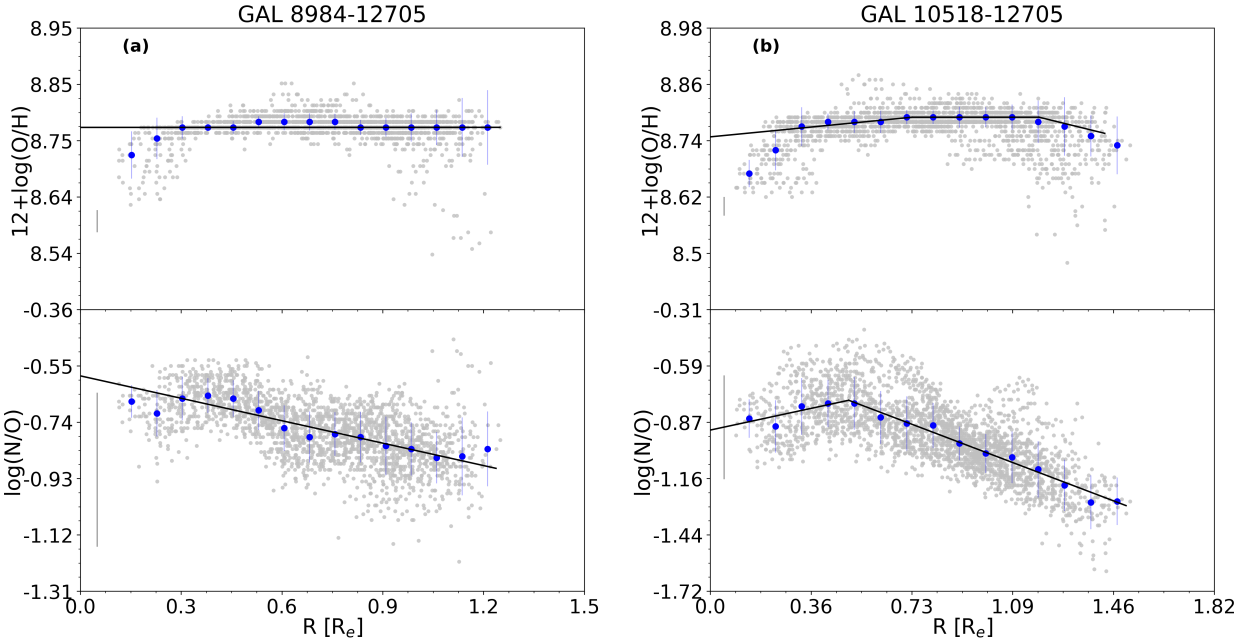

Figure 1.17: Gas-phase abundance radial gradients for O/H (top panels) and N/O (bottom panels) for two galaxies from MaNGA. Typical error bars (gray) as well as the median values for binned data (blue), ensuring at least 10 HII regions, are shown in each plot.

different distances within the same galaxy. The very first analysis of such gradients already lead to the conclusion that there is a negative radial metallicity gradient: HII regions located closer to the galaxy center are characterized by higher 12+log(O/H) abundances than those located in the outer parts (e.g. Garnett & Shields, 1987; Pagel & Edmunds, 1981; Vila-Costas & Edmunds, 1992; Vilchez et al., 1988). Likewise, a similar behavior for the radial gradient of the log(N/O) ratio has been reported (e.g. Pilyugin et al., 2004; Vila-Costas & Edmunds, 1993). We show in Fig. 1.17 (a) an example of such gradients.

Thanks to the advent of the Integral Field Spectroscopy (IFS, e.g. CALIFA, MaNGA, SAMY), the statistical number of galaxies for which metallicity gradients can be estimated has substantially increased. In the majority of cases, the idea of a negative metallicity gradient (either traced by O/H or N/O) for the disc of galaxies seems to be confirmed (e.g. Belfiore et al., 2017; Pérez-Montero et al., 2016; Sánchez et al., 2014; Sánchez-Menguiano et al., 2016; Zinchenko et al., 2021). However, there is also evidence for galaxies that do not follow such trend. At high redshifts, some galaxies might show flat or even positive gradients (e.g. Carton et al., 2018). Interacting galaxies also show deviations from the negative metallicity gradient (e.g. Rupke et al., 2010). Moreover, Sánchez-Menguiano et al. (2018) found that a single metallicity gradient cannot reproduce the observed metallicity gradients in nearby spiral galaxies. We show in Fig. 1.17 (b) an example of a deviation from the single, negative slope metallicity gradients.

1.3.2.4 *Mass-metallicity, mass-NO and fundamental metallicity relations*

The first works on chemical abundances of the gas-phase ISM also reported a relation between the galaxy stellar mass (M_*) and metallicity (traced by O/H) of the galaxy (e.g. Garnett & Shields, 1987; Lequeux et al., 1979; Skillman et al., 1989). These results were later confirmed with the analysis of large spectroscopic surveys (e.g. Curti et al., 2020; Duarte Puertas et al., 2022; Lamareille et al., 2004; Mannucci et al., 2010; Tremonti et al., 2004). This is te so-called *mass-metallicity relation* (MZR). Given the relation between N/O and O/H, a similar result (mass-NO relation, MNOR) was expected and found between the stellar mass and the N/O ratio (e.g. Andrews & Martini, 2013; Pérez-Montero &

Contini, 2009; Pérez-Montero et al., 2016; Schaefer et al., 2022). We show examples of both relations in Fig. 1.18.

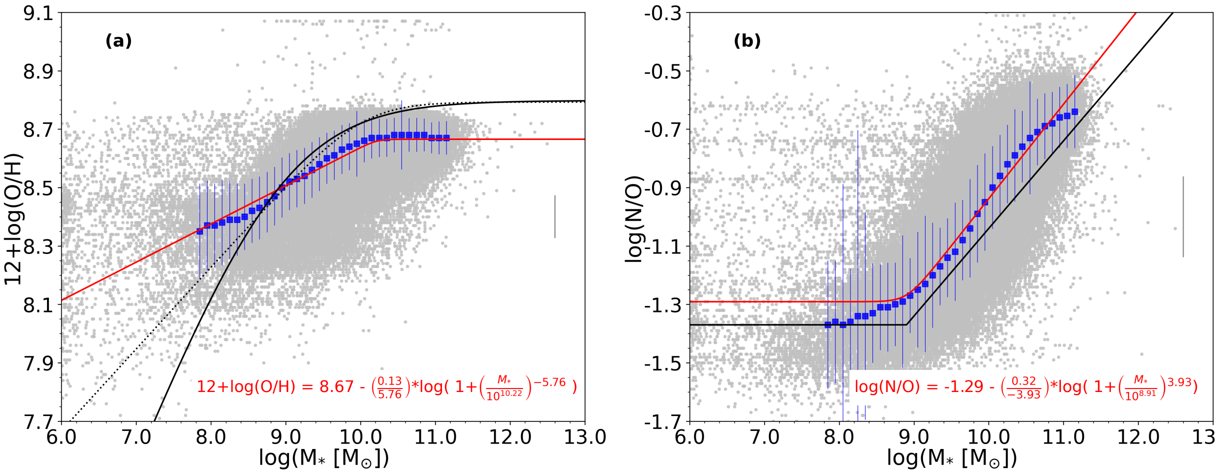

Figure 1.18: Mass-metallicity (a) and mass-NO relations (b) for the whole sample of SFGs from SDSS DR9 GalSpec catalog of galaxies. Typical error bars (gray) as well as the median values for binned data with at least 250 galaxies (blue) are shown in each plot. Black lines show the reported relations in the literature: solid from Andrews and Martini (2013) and dotted from Curti et al. (2020). Red lines show our best fit.

For both cases, a considerable scatter in the relation is found. Before addressing physical drivers of the scatter it is important to note two numerical caveats. First of all, the dynamical range of variation for the chemical abundance tracers is ~ 1.5 dex, but stellar mass varies in a considerable longer range $\sim 5-6$ dex. Secondly, the uncertainty in the chemical abundance estimation is also an important driver of the scatter. Nevertheless, the increase in statistics might considerably reduce the two previous effects, and hence the scatter reported in relations with at least $100,000$ galaxies can be analyzed in a statistical way. Indeed, several works have been devoted to the analysis of what physical properties might explain the scatter: star-formation rate (SFR; e.g. Curti et al., 2020; Lara-López et al., 2010; Mannucci et al., 2010), feedback from star formation (e.g. Blanc et al., 2019) and/or AGN activity (e.g. Thomas et al., 2019), secular evolution (e.g. Somerville & Davé, 2015), stellar age (e.g. Duarte Puertas et al., 2022), galactic environment (e.g. Y.-j. Peng & Maiolino, 2014) or redshift (e.g. Mannucci et al., 2009). We show in Fig. 1.19 the effects of the SFR and stellar age on the MZR and MNOR relations.

The effect of SFR in the MZR arises not only because it correlates with stellar mass (see Kennicutt & Evans, 2012, for a review), but also due to its probable correlation with the metallicity (e.g. Curti et al., 2020; López-Sánchez & Esteban, 2010; Mannucci et al., 2010). Hence, Mannucci et al. (2010) proposed to analyze the MZR in terms of a new quantity, a corrected stellar mass accounting for the SFR ($\log(M_*) - \mu \log(SFR)$). Although several values of μ have been proposed, it must be noted that this is a way of projecting a 3D relation onto a plane, implying that the value of μ will depend on the underlying 3D relation. This is the so-called *fundamental metallicity relation* (FMR). Likewise, the work from Duarte Puertas et al. (2022) also highlights that stellar age (usually traced by means of the $D(4000)$ index[13]) shapes de MZR and MNOR. Hence, a similar approach can be performed and project the relation onto a plane, driven by $\log(M_*) - \tilde{\mu} D(4000))$. We show such projections in

---

[13] Initially proposed by Bruzual A. (1983) as the ratio between the mean flux density in the range 4050-4250Å (red part) and that in the range 3750-3950Å (blue part), $D(4000)$ index traces stellar age since the lack of massive blue stars increases this index as well as evolved stars produce more metal absorption reducing as well the contribution of stellar populations to the blue part(Balogh et al., 1999; Bruzual A., 1983; Hamilton, 1985; Poggianti & Barbaro, 1997).

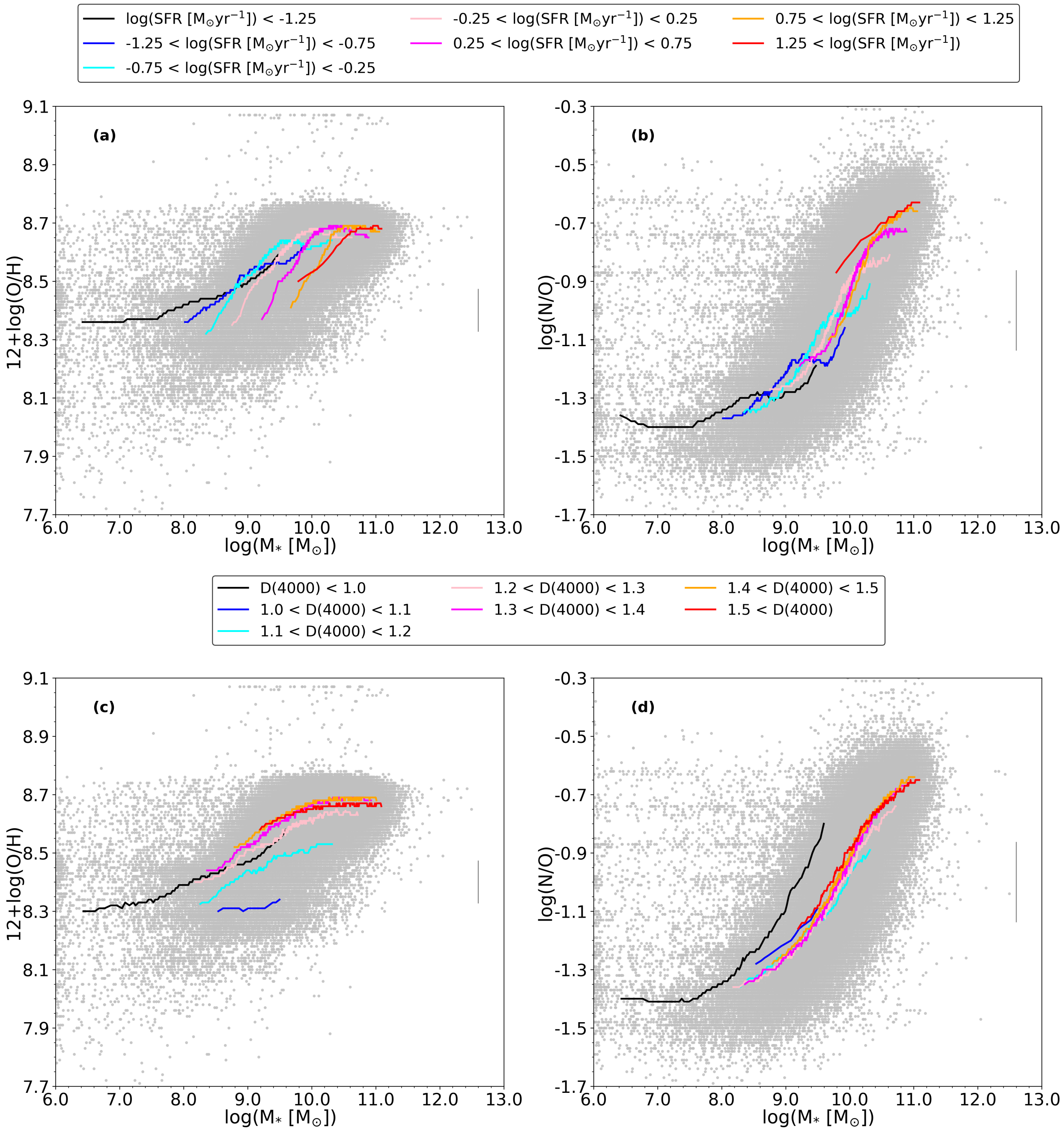

Figure 1.19: Mass-metallicity and mass-NO relations from Fig. 1.18. Panels (a) and (b) show the running medians (at least 1000 data points) for galaxies with SFR in specific ranges. Panels (c) and (d) show the running medians (at least 1000 data points) for galaxies with $D(4000)$ in specific ranges.

Fig. 1.20. The value of μ and $\hat{\mu}$ can be interpreted as a quantification of the effect on the corrected property: larger values imply a large correction, i.e., a strong dependence.

It is also important to note the limitations of these relations. First of all, there is still a debate on whether the relation exists (e.g. Baker et al., 2023), or it should be tracked with other properties such as the stellar mass corrected from SFR (e.g. Mannucci et al., 2010) or even other properties such as the gravitational potential (e.g. Sánchez-Menguiano et al., 2024a). Second, they have been extensively studied for SFGs, but there is not yet a clear picture on whether AGN-dominated galaxies follow or not the same trend (e.g. Pérez-Díaz et al., 2021; Thomas et al., 2019). Third, there is an intrinsic lower mass limit to these studies due to the sample selection criteria, thus the low-mass

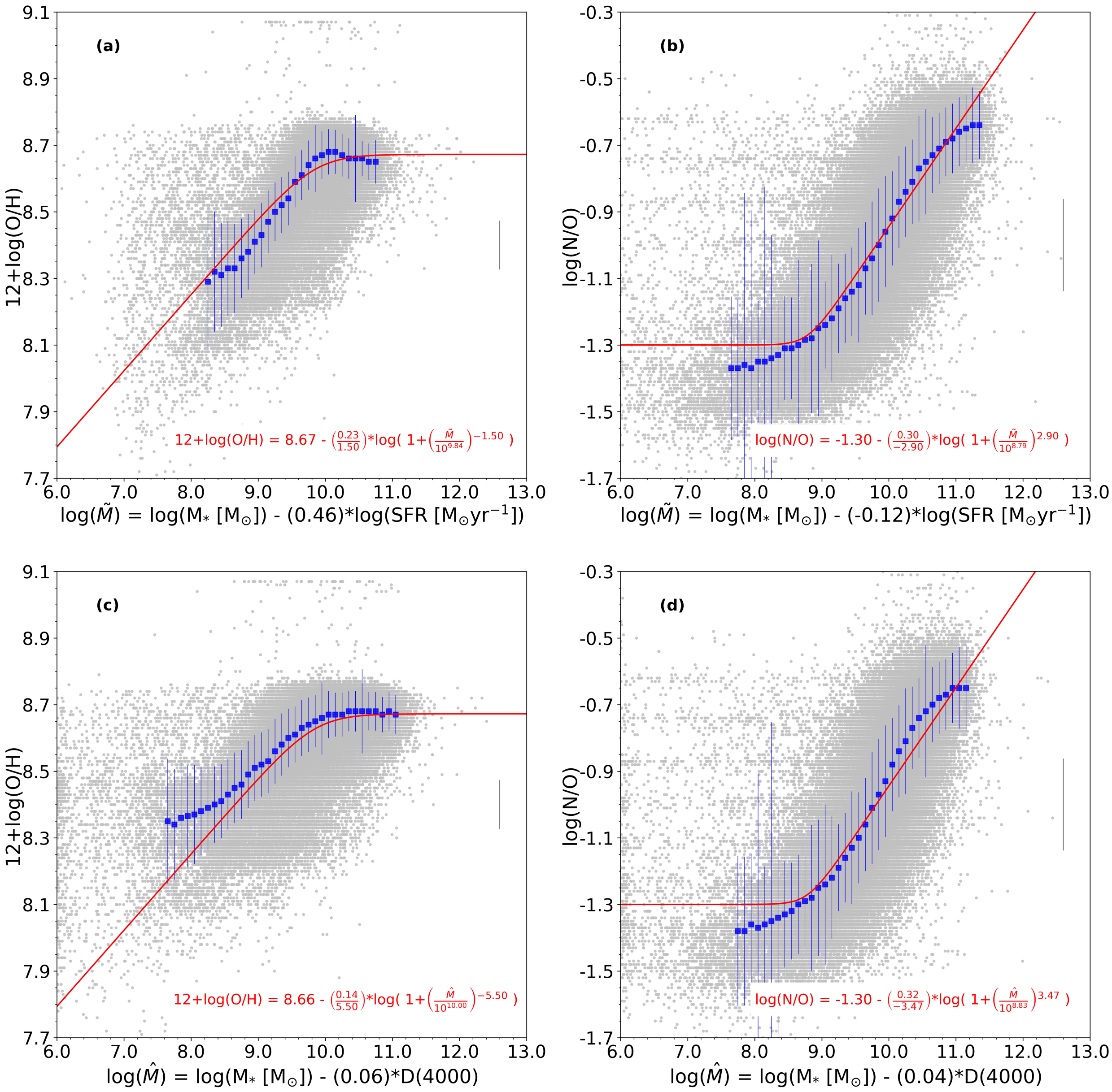

Figure 1.20: Fundamental metallicity relations for the whole sample of SFGs from SDSS DR9 GalSpec catalog of galaxies. Panels (a) and (b) show the projection onto the SFR axis. Panels (c) and (d) onto the $D(4000)$ axis. Typical error bars (gray) as well as the median values for binned data with at least 250 galaxies (blue) are shown in each plot. Red lines show our best fit.

end of these relations must be carefully studied either targeting local analogs (e.g. Amorín et al., 2010; Calabrò et al., 2017; Yang et al., 2017a, 2017b) or galaxies at high redshifts (e.g. Chemerynska et al., 2024; Curti et al., 2024; Simmonds et al., 2024).

1.3.3 *Theoretical framework: models and simulations*

We have summarized the most important relations observed in the study of chemical enrichment in galaxies through the analysis of their ISM. Having a clear picture of the observed relations is as important as providing a theory that is able to reproduce them in order to figure out their main physical drivers. We will briefly review the ongoing theories that have been proposed to reproduce chemical evolution of galaxies.

1.3.3.1 *Fundamental ingredients*

It is beyond the scope of this work to deeply analyze all the aspects, caveats and used methods for the build-up of chemical evolution models either by analytical, semi-analytical or simulation methods. A good picture on galaxy chemical evolution modeling can be found in Matteucci (2012, 2021), Somerville and Davé (2015), Mitchell et al. (2018) and Kobayashi et al. (2020a), among many others. In this section, we briefly describe the most important parameters that govern chemical evolution according to models.

- The total baryonic mass of the system (M_{tot}). This parameter is usually separated into components. On one hand, we can separate it into the gas mass (G) and stellar mass (M_*). In terms of the composition, we can separate the mass into the mass that is present in each element Z (M_Y).

- The shape and amplitude of the function that represents star formation. Due to the fragmentation during the collapse of molecular clouds, stars of different masses form according to an empirical law, the initial mass function (IMF). Many studies are available on the literature devoted to the determination of the shape of the IMF (see Hennebelle & Grudić, 2024, for a recent review). Once the shape of the IMF ($\Phi(M)$) is fixed, then the produced stellar mass is needed. This is parametrized by means of the SFR, which fixes the amplitude. A useful parameter that relates SFR and the mass of gas (reservoir) is the star-formation efficiency (SFE):

$$SFE = \frac{SFR}{G} \tag{1.38}$$

- The fraction of ejected mass for each star of mass m. For a given star, there is fraction of its mass that is ejected into the ISM ($e(m)$) and another fraction that remains as *star* i.e. the remaining product of the stellar evolution ($s\,(m)$). Although stars progressively loss mass, a good approximation is to trace the total mass ejected after their expected lifetime ($\tau\,(m)$):

$$e\,(m) = m - s\,(m) \tag{1.39}$$

  In some cases, specifically for very low mass stars, a good approximation is to assume $m \approx s\,(m)$. For the rest, stellar evolution models provide good estimates for the expected $s\,(m)$. At any given time, the total mass ejected is given by:

$$E\,(t) = \int_{m_{low}}^{m_{up}} e\,(m)\,\mathrm{SFR}\,(t)\,\Phi\,(m)\,dm = \int_{m_{low}}^{m_{up}} [m - s\,(m)]\,\mathrm{SFR}\,(t)\,\Phi\,(m)\,dm \tag{1.40}$$

  being m_{low} and m_{up} the limits from the IMF.

- The stellar yields (p) for each element. For a given star of mass m, its chemical composition changes due to stellar nucleosynthesis. The total mass ejected from that star has a particular composition p_y, so the total mass of an element Y ejected from a star of mass m is given by (Meynet & Maeder, 2002):

$$e_y\,(m) = p_y m = \int_{s(m)}^{m} \left[Y\,(\tilde{m}) - Y^0\right] d\tilde{m} \tag{1.41}$$

where Y^0 is the initial fraction and $Y\left(\tilde{m}\right)$ the fraction at a distance that comprehends a mass $\tilde{m}$. The *yield* is defined as the fraction between the mass of element Y ejected into the ISM $\left(E_Y\left(t\right)\right)$ and the mass retained in the stellar remnants $\left(S\left(t\right)\right)$:

$$P = \frac{E_y\left(t\right)}{S\left(t\right)} = \frac{\int_{m_{low}}^{m_{up}} p_y m \mathrm{SFR}\left(t\right) \Phi\left(m\right) dm}{\int_{m_{low}}^{m_{up}} s\left(m\right) \mathrm{SFR}\left(t\right) \Phi\left(m\right) dm} = \frac{1}{1-R} \int_{m_{low}}^{m_{up}} p_y m \Phi\left(m\right) dm \tag{1.42}$$

being $R \equiv E\left(t\right) \cdot \mathrm{SFR}^{-1}\left(t\right)$, which is considered as the return fraction. Yields are usually taken from studies of stellar models, in which numerous effects such as rotational mixing are included (e.g. Hirschi et al., 2005, and references therein).

- The inflow and outflow rates. The system might be fed with gas from outside the galaxy and might also lose gas as a consequence of strong winds that drive away certain amounts of gas. The rates of mass inflow $\left(\dot{M}_{in}\right)$ and outflow $\left(\dot{M}_{out}\right)$ determine the integrated flow rate $A\left(t\right)$ for the system:

$$\frac{dG}{dt} = A\left(t\right) \tag{1.43}$$

With all these ingredients, and the initial conditions from which we want to consider the galaxy system evolution, we can have a track of the chemical enrichment of the gas-phase ISM. In order to analytically solve the equations, certain relations and forms need to be assumed so the integrals can be computed, otherwise it is necessary to use numerical methods. Additionally, we can track the evolution at spatial scales by adding radial dependence on the corresponding ingredients.

1.3.3.2 *The relation among chemical abundances*

Starting from an almost identical chemical composition, the relations between different elements are mostly governed by the yields P. As α-elements are produced by the same stellar processes as O, it is expected a constant behavior between them driven by the yields. However, it is important to note the effects of dust depletion which might have an important role at high metallicities (e.g. Calura et al., 2008).

The relation between N/O vs O/H is not only governed by the stellar yields (P), but also by flow rates and the star formation efficiency. Accounting for both, primary and secondary production, Köppen and Edmunds (1999) and Köppen and Hensler (2005) show that the position of a galaxy (or HII region) in the N/O vs O/H might be altered. On the other hand, Mollá et al. (2006) show that SFE also plays a role in shaping the relation. Local contamination from Wolf-Rayet stars (e.g. López-Sánchez & Esteban, 2010) and the time delay between primary O ($\sim$ Myr) and secondary N production ($\sim$ Gyr) also introduces scatter in the relation. The same scenario applies to the C/O vs O/H relation.

Very recently, it has been proposed that N production can be extremely affected in dense star clusters: massive stars quickly sink into the centers by means of mass segregation, and there they collide and merge, reducing the production of O and C (Cameron et al., 2023). However, it must be noted that this theory arises from the need to explain the high N/O ratios at high redshifts, and it is still under debate (e.g. Schaerer et al., 2024).

1.3.3.3 *The inside-out growth of galaxies*

The pioneering works from Chiosi (1980) and Matteucci and Francois (1989) provided the theoretical framework to reproduce the metallicity gradients observed in the disks of the Milky Way and nearby galaxies. Considering chemical evolution models with radial resolution (i.e. dependence on the distance to the galactic center), they proposed that the infall rate follows an exponential like:

$$A\left(r,t\right) = A_0\left(r\right)\exp\left(-\frac{t}{\alpha r+\beta}\right) \tag{1.44}$$

where α and β are constants that parametrize the infall time-scale dependence on the radii. If α is positive, then at higher distances from the galactic center the time-scale is considerable longer than at the inner parts. Gas concentrates more efficiently in the inner parts, and thus, star-formation is enhanced. Thus the chemical enrichment in the inner parts is faster than in the outer parts, leading to the negative metallicity gradient. This is the *inside-out growth*[14] of galaxies (Belfiore et al., 2019; Chiappini et al., 2001; Matteucci & Francois, 1989).

As important as the inflow rate is the outflow rate, related to the feedback from star formation (e.g. Lian et al., 2018). It has been demonstrated by means of galaxy simulations and chemical evolution models that out-of-balanced effects of inflows and/or outflows can drastically change the shape of the metallicity gradient (Tapia-Contreras et al., 2025).

1.3.3.4 *The bathtub model*

In order to reproduce the mass-metallicity relation, simple analytical models were developed (e.g. Bouché et al., 2010; Dayal et al., 2013; Lilly et al., 2013). These models treat the galaxy as a system of two integrated components: the galaxy system whose variations in gas, stars and chemical enrichment are traced; and the halo. These models assumed the halo as a sinking source: a fraction of the gas inflows goes to the halo, and the other to the gas reservoir in the galaxy system; likewise, outflows expel gas, a fraction of which is trapped within the halo, while the other manages to escape.

The simplicity of these models comes from the fact that gas drives all the major physical processes. The SFR is assumed to be of the form $\text{SFR}\left(t\right) = \epsilon_{SFR}G\left(t\right)$, being ϵ_{SFR} the inverse of the star-formation time scale. In the same way, the outflow rate is assumed to be a scaling relation of the SFR ($\dot{M}_{out} = \xi\left(M\right)\text{SFR}\left(t\right)$), where the proportional factor might depend on mass (reflecting the gravitational potential barrier that the outflow might overcome). Due to mass conservation of the system, it can be demonstrated (e.g. Lilly et al., 2013), that the infall rate is also proportional to the star formation rate ($\dot{M}_{in} = \gamma\left(M\right)\text{SFR}\left(t\right)$).

With all these ingredients, the evolution of stellar mass over time is simply governed by the SFR:

$$\frac{dM_*}{dt} = \text{SFR}\left(t\right) = \epsilon_{SFR}G\left(t\right) \tag{1.45}$$

whereas the evolution of the gas mass is the increase due to the inflow rate, the gas lost in stellar remnants, and the loss of mass as outflows:

$$\frac{dG}{dt} = \dot{M}_{in}\left(t\right) - \dot{M}_{out}\left(t\right) - \left(1-R\right)\text{SFR}\left(t\right) = \left[\gamma\left(M\right) - \xi\left(M\right) + R - 1\right]\epsilon_{SFR}G\left(t\right) \tag{1.46}$$

Finally, the mass of an element Y within the gas-phase ISM evolves according to: 1) the contribution expelled from stars (which can be express in terms of the yield P); 2) the contribution from the

---

[14] Whereas these models based on radial symmetry provide a simple solution, they are the ground base to explore and fit other scenarios. For example, introducing the perpendicular axis to he radial plane, models are able to reproduce episodes in which gas accreted from te disk to the halo can be recaptured by the disc at different scales (galactic fountains; e.g. Spitoni et al., 2013). More sophisticated attempts based on 2D models that have been able to reproduce azimuthal inhomogeneities, explaining the scatter observed in the literature (Spitoni et al., 2019, 2023).

infalling gas with composition Y^0; 3) the mass of Y captured in the stars remnants; and 4) the mass lost due to the outflow effect. Hence, we have:

$$\begin{aligned}\frac{dM_Y}{dt} &= P\,(1-R)\,\mathrm{SFR}\,(t) + Y^0\dot{M}_{in}\,(t) - Y\,(1-R)\,\mathrm{SFR}\,(t) - Y\dot{M}_{out}\,(t) \\ &= \left[P\,(1-R) + Y^0\gamma\,(M) - Y\,(1-R) - Y\xi\,(M)\right]\epsilon_{SFR}G\,(t)\end{aligned} \tag{1.47}$$

Although further simplifications and operations can be made, the physics of the system is governed by Eq. (1.45)-(1.47), i.e., the total amount of gas regulates the system. This is the main reason why these models are called *gas regulation* or *bathtub* models. Whereas they rely on many assumptions, they are able to reproduced the MZR and FMR observed in galaxies (e.g. Dayal et al., 2013; Lilly et al., 2013) and their formalism can also be implemented to reproduce metallicity gradients (e.g. Belfiore et al., 2019). The major caveat from these models is that their implicit relations are based on the idea that there is an equilibrium between inflows, outflows and star-formation governed by the gas (Dayal et al., 2013; Lilly et al., 2013), which might not be accurate for certain critical moments of galaxy evolution (e.g. Faisst et al., 2025; Förster Schreiber & Wuyts, 2020).

1.4 CONTEXT AND OUTLINE OF THE THESIS

Throughout this introduction we have outlined and reviewed three major research areas: the physics of the ISM, the diagnostics from emission lines and the chemical evolution of galaxies. Although each area is complex enough, the three of them are essential for the work we present in this thesis. From a theoretical point of view, the chemical enrichment of the ISM explains the expected composition of the ionized gas which affects its ionization structure. From an observational point of view, a similar picture emerged. Present day activity in galaxies is traced by their ionized gas, e.g., by their emission lines. Thus, knowledge on the physical processes behind those emission lines is key in understanding their nature and to provide proper knowledge. The information from those emission lines allows us to constrain the chemical composition of the gas, and having a clear picture on how different elements are synthesized and ejected into the ISM is essential to understand the estimations. Finally, chemical evolution models for galaxies are a powerful tool not only to check which physical drivers might explain the estimations, but also to perform additional tests that might complement the picture arising from observations.

The analysis of the chemical abundance ratios of the gas-phase ISM is a key component for our understanding of galaxy evolution, as it provides us with information on the recent and far past chemical enrichment history of the galaxy, which is governed by stellar processes and gas dynamics. The vast majority of works rely on the use of optical emission lines to perform the chemical and physical diagnostics of the ISM. However, other regimes can provide a different perspective and minimize caveats from the optical studies. This thesis aims at emphasizing the importance of the IR regime, and to provide the tools required to perform chemical and physical diagnostics of the gas-phase ISM.

In addition, the majority of studies have targeted galaxies whose activity is mainly dominated by star formation, but there is an important fraction of galaxies that have undergone an AGN-dominated phase in the past or that still holds nowadays. Thus, the chemical evolution of galaxies needs to be complemented with the picture of the AGN. Additionally, to compare both cases, the same methodology must be applied to minimize the uncertainties. Thus, this thesis does not only provide a new methodology for the IR regime, but also ensures to provide a versatile tool that can be applied for both, SFGs and AGNs.

The structure of this work is as follows[15]:

- Chapter 2 reviews the limitations of optical observations and highlights the importance of the IR regime in the study of the chemical enrichment history of galaxies. In this chapter we also present a physically motivated and detailed outline of the methodology developed for the determination of chemical abundances from IR emission lines. We also outline the different galaxy samples used for this research.

- Chapters 3 and 4 show results obtained for a sample of LLAGNs, using optical-IFS data. Chapter 3 is focused on their chemical treatment, focusing on the fact that optical regime cannot rule out some ionizing scenarios and, hence, the uncertainty forces to consider all of them. Chapter 4 comes naturally as a follow-up analysis from the data used in Chapter 3, and allows us to test, for the first time, the metallicity gradients in galaxies whose central activity is not dominated by star-formation.

- Chapters 5 and 6 correspond to the analysis, test and results of our methodology to estimate chemical abundances from IR emission lines. In these two chapters, we focus on the determination of N/O, O/H and S/H for both, SFGs and AGNs. Chapter 5 serves as a transition, showing the potential of IR diagnostics and comparing the results to those obtained from optical studies. Chapter 6 provides an additional improvement to the methodology, focusing on the advantage of IR emission lines for the estimation of sulfur abundances.

- Chapter 7 highlights and exemplifies the importance of the IR regime, and uses a sample of ultra-luminous infrared galaxies (ULIRGs) as reference sample. In this work, thanks to the use of IR emission lines, we were able to shed light on whether these galaxies behave, chemically speaking, in the same way as other active galaxies, as well as to get a picture on how they might have evolved and its implications for chemical evolution models.

- Chapter 8 provides a summary and evaluation of the major conclusions from this work. Additionally, a brief summary on the future lines of research covering some aspects not reviewed in this work and others that naturally arise from our results is also included.

---

[15] The reader might be curious on why the chapters do not follow the date order of publications. We have decided to sort the chapters according to the logical flow of how the IR regime arises as a fundamental part of the chemical evolution of galaxies.

2

A NEW METHODOLOGY FOR THE INFRARED EMISSION LINES

We present in this chapter a detailed analysis on the methodology developed for the study of IR emission lines. Starting from a review of the limitations of optical spectroscopic observations (Sec. 2.1), we analyze the potential of IR emission lines to perform similar studies (Sec. 2.2). In Sec. 2.3 and 2.4 we explain the tools and how our methodology is built upon them. Finally, we summarize in Sec. 2.5 the samples of galaxies which are analyzed in this research.

2.1 LIMITATIONS OF THE OPTICAL REGIME

The vast majority of studies of chemical abundances based on emission lines from the ionized gas-phase of the ISM rely on $[3000\text{Å} - 9600\text{Å}]$ observations. This is mainly cause due to the fact that optical emission is accessible from ground-based observatories. Moreover, large spectroscopic surveys have been performed with optical observations. In this section, we review the caveats from optical analysis, explaining some of the workarounds proposed and the limitations that cannot be overcome.

2.1.1 *Physical and chemical diagnostics from optical emission lines*

The use of optical emission lines for chemical abundance determinations present three major caveats that limit the applicability and accurateness of the methods based on this regime, including: the necessity of reliable measurements of emission lines; the need for ionization correction factors due to the unseen ions in this regime and, finally, a larger dust extinction. Thereafter, we examine below in more detail these problems.

2.1.1.1 *Missing auroral lines*

As we have explained in Sec. 1.2.4, the direct method relies on the measurement of auroral lines that are observable in the optical regime, such as [O III] λ4363Å, [S III] λ6312Å, [Ne III] λ3342Å or [N II] λ5755Å. Given the high dependence of the emissivity of CELs on temperature, the measurement of these emission lines is crucial. However, applying this methodology is restricted to particular objects, due to the challenges regarding their detection:

- There are at least three ionizing zones (low-, intermediate and high-excitation zones), traced by different ions. As temperature does not follow a constant profile, then having accurate measurements of the temperature of at least one auroral line from an ion in each zone should be indispensable. In practice, this kind of analyses is limited to very few objects, and it is more convenient to use reported relations, either empirical or from photoionization models to convert temperatures for different excitation zones from just one measured temperature (e.g. Pérez-Montero, 2017).
- When electron temperature is low ($\lesssim 8500$ K), then their emissivity its more than 100 times fainter than other CELs from the same ion. As metals are efficient coolants, the more metals present in the ISM, the lower the temperature would be and, hence, detecting and measuring auroral lines in spectroscopic observations is no longer an option. This is exemplified in Fig. 2.1, both for SFGs and AGNs.

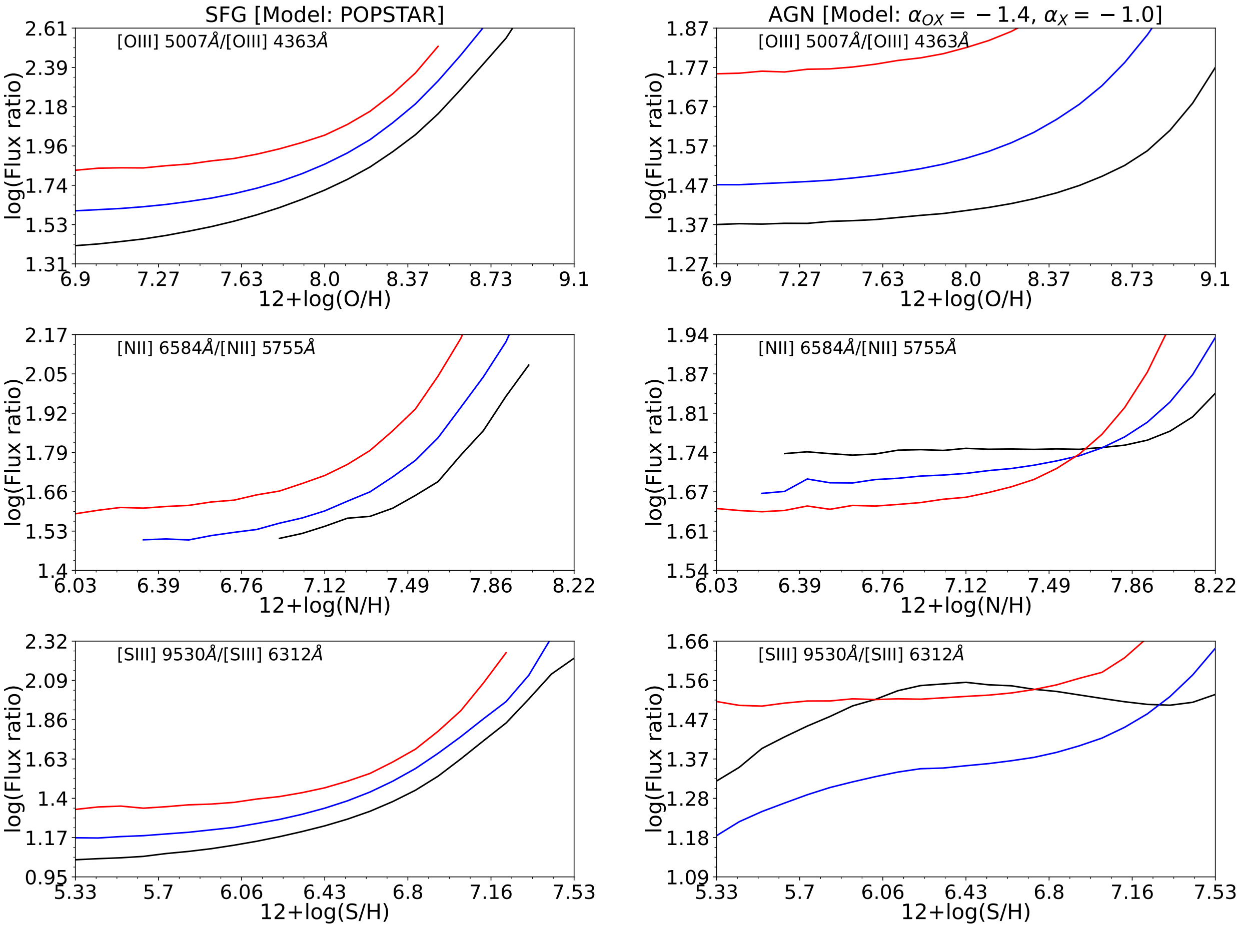

Figure 2.1: Emission line ratios involving auroral lines as a function of the chemical composition of the gas-phase ISM from models computed with CLOUDY v17. Left column shows the results assuming an ionizing source computed with POPSTAR (Mollá et al., 2009), after 1 Myr burst while the gas has an electron density of $n_e = 100$ cm^{-3}. Right column shows the results assuming an AGN, with slopes $\alpha_{OX} = -0.8$ and $\alpha_X = -1$ and the electron density is set to $n_e = 500$ cm^{-3}. For each model, we consider different ionization parameters: $\log(U) = -3.5$ (red), $\log(U) = -2.5$ (blue), $\log(U) = -1.5$ (black).

The major problems of the detection of auroral lines rely in the need to reduce the continuum noise so that the signal-to-noise (S/N) ratio would be high enough for a reliable measurement. As the S/N is limited by the technical capabilities of the observing instruments and telescopes as well as the exposure time, an alternative in large spectroscopic surveys is to stack spectra from groups of galaxies so the noise continuum is minimized (e.g. Andrews & Martini, 2013). Several caveats arise from the stacking procedure. First of all, galaxy groups must be chosen in a way that at least most if not all galaxies are characterized by similar values of the property to be studied. In the case of estimation of chemical abundances (O/H), due to the MZR, selecting galaxies with similar stellar masses would ensure that oxygen abundances would at least be in a similar range and, hence, the value would be representative of the sample. However, as the stacked spectra is taking as representative of a group of galaxies, the scatter is going to disappear as there is only one value per property value. For example, in Fig. 1.19 we show how stellar age drives part of the scatter, and the stacked procedure does not reproduce such scatter as galaxies with different stellar ages are stacked in the same group. In other words, the stacking procedure would only help in analyze whether the property used for the group selection correlates with the derived properties from the stacked spectra.

To provide a chemical estimation of the gas-phase ISM avoiding the problems from stacking, strong emission line calibrators have been proposed (e.g. Curti et al., 2017; Pilyugin & Grebel, 2016). Either using samples of galaxies whose chemical abundances can be estimated by means of the direct method (empirical calibrations) or photoionization models, authors have proposed relations between strong optical emission lines that are easily observed, such as [O II] $\lambda3727$Å, H_β, [O III] $\lambda5007$Å, H_α [N II] $\lambda6584$Å or [S II] $\lambda6717,6731$Å and the derived abundances. This method has the advantage that can be easily applied in large samples of galaxies, but the greatest caveat is that they are not valid for all cases, as their applicability is limited by the sample used for calibration. Moreover, results obtained from calibrators can drastically affect some results such as the shape of the MZR (Kewley & Ellison, 2008). We show in Tab. 2.1 and 2.2 a summary of the most widely used optical calibrators and the most recent calibration available.

Table 2.1: Optical emission line calibrators for the determination of 12+log(O/H) abundances. Reference codes: Ji+19 (Jiang et al., 2019); Do+21 (Dors, 2021); Cu+17 (Curti et al., 2017); Ca+20 (Carvalho et al., 2020); Pi+16 (Pilyugin & Grebel, 2016); FM20 (Flury & Moran, 2020); Jo+15 (T. Jones et al., 2015); Sta+06 (Stasińska, 2006); PM+05 (Pérez-Montero & Díaz, 2005)

Name	Lines	Applicability	Calibration	Range	Method
R23	[O II]$\lambda3726,3729$Å,H_β, [O III]$\lambda4959,5007$Å	SFGs	Ji+19	[7.3, 8.6]	T_e-method
		AGNs	Do+21	[8.2, 8.8]	T_e-method
N2	[N II] $\lambda6584$Å,H_α	SFGs	Cu+17	[7.7, 8.8]	T_e-method
		AGNs	Ca+20	[8.2, 9.0]	Models
O3N2	H_β, [O III]$\lambda5007$Å, [N II]$\lambda6584$Å,H_α	SFGs	Cu+17	[7.7, 8.8]	T_e-method
R-cal	[O II]$\lambda3727,3729$Å,H_β, [O III]$\lambda5007$Å,[N II]$\lambda6584$Å	HII reg.	Pi+16	[7.1, 8.7]	T_e-method
S-cal	,H_β,[O III]$\lambda5007$Å [S II]$\lambda6717,6731$Å,[N II]$\lambda6584$Å	HII reg.	Pi+16	[7.1, 8.7]	T_e-method
O3+N2	H_β, [O III]$\lambda5007$Å, [N II]$\lambda6584$Å,H_α	AGNs	FM+17	[7.5, 9.0]	T_e-method
O2Ne3	[O II]$\lambda3726,3729$Å, [Ne III]$\lambda3868$Å,H_δ	SFGs	Jo+15	[7.8, 8.6]	T_e-method
Ar3O3	[O III]$\lambda5007$Å, [Ar III]$\lambda7135$Å	SFGs	Sta+06	[7.2, 8.8]	T_e-method
S3O3	[O III]$\lambda5007$Å, [S III]$\lambda9069$Å	SFGs	Sta+06	[7.5, 8.8]	T_e-method
S23	H_β,[S II]$\lambda6717,6731$Å, [S III]$\lambda9069,9531$Å	SFGs	PM+05	[7.1, 8.9]	T_e-method
S23O23	[O II]$\lambda3726,3729$Å,H_β, [O III]$\lambda4959,5007$Å, [S II]$\lambda6717,6731$Å, [S III]$\lambda9069,9531$Å	SFGs	PM+05	[7.1, 9.]	T_e-method

Another way to estimate chemical abundances without the detection of auroral emission is to use photoionization models (see Sec. 2.3 for more details). The balance between heating and cooling processes happens at a given temperature, thus we must model them. The ionizing source, the dust content, the geometry, density and the chemical abundance ratios of the gas are parameters that are introduced as inputs. Optical emission lines can be used (see Sec. 1.1.3 for the caveats) to provide a diagnostic on the ionizing source and the rest of parameters are either assumed or estimated from observations. The last ingredients, chemical abundances and ionization parameters are varied in order to reproduce the observed emission lines. This is the *tailored photoionization model* method (e.g. Oliveira et al., 2022, 2024a; Pérez-Montero & Díaz, 2007). Another advantage of photoionization

Table 2.2: Optical emission line calibrators for the determination of log(N/O) abundances. Reference codes: Flo+22 (Florido et al., 2022); PM+19 (Pérez-Montero et al., 2019a).

Name	Lines	Applicability	Calibration	Range	Method
N2O2	[N II]λ6584Å,[O II]λ3726, 2729Å	SFGs AGNs	Flo+22 PM+19	$[-1.6, -0.5]$ $[-2.0, 0.0]$	T_e-method Models
N2S2	[N II]λ6584Å,[S II]λ6717, 6731Å	SFGs AGNs	Flo+22 PM+19	$[-1.6, -0.5]$ $[-2.0, 0.0]$	T_e-method Models
N2	[N II]λ6584Å,H_α	SFGs	Flo+22	$[-1.6, -0.5]$	T_e-method
O3N2	H_β, [O III]λ5007Å, [N II]λ6584Å,H_α	SFGs	Flo+22	$[-1.6, -0.5]$	T_e-method

models is that they can be used to provide calibrations for strong emission line calibrators based on the predicted ratios of emission lines. However, this tailored method is much more inefficient than the application of a calibration, and thus it is more used when dealing with few objects.

2.1.1.2 *Recombination lines for abundance estimations*

The theory that we have outlined in Sec. 1.2.4 for the estimation of chemical abundances from emission lines can be applied as well to metal RLs, although we have already explained that these emission lines are extremely faint and only accessible from high signal-to-noise (S/N) ratio observations of bright HII regions (e.g. García-Rojas et al., 2007), SNe remnants (e.g. Docenko & Sunyaev, 2008) and PNe (e.g. M. Peimbert et al., 2004). In the case that enough metal RLs are observed, then the derivation of chemical abundances from them offers the advantage that their emissivities, governed mainly by the effective recombination coefficient (α_{eff}), are less affected by temperature than optical CELs.

When comparing the abundance derivations from metal CELs and those from RLs, some authors have reported systematic higher abundances when they are derived from RLs as compared to those derived from CELs (e.g. Corradi et al., 2015; García-Rojas et al., 2009; García-Rojas & Esteban, 2007; Tsamis et al., 2003). This difference, known as *abundance discrepancy factor* (ADF), can be defined as:

$$\log\left(\mathrm{ADF}\left[X^{i+}\right]\right) \equiv \log\left(X^{i+}/H^{+}\right)_{\mathrm{RLs}} - \log\left(X^{i+}/H^{+}\right)_{\mathrm{CELs}} \tag{2.1}$$

which can go up to 0.5 in HII regions and 0.7 for SNe, although chemical inhomogeneities within the gas can provide even higher values (e.g. Corradi et al., 2015; M. Peimbert et al., 2017).

There is still a debate on the origin of this discrepancy. On the one hand, some authors proposed that temperature fluctuations within the ionized gas (e.g. García-Rojas et al., 2007; Méndez-Delgado et al., 2023) might be responsible as these fluctuations would induce wrong determinations from CELs, which are much more affected by temperature. On the other hand, some authors proposed that metal RLs might be affected by flourescence excitations and/or resonance lines (e.g. Tsamis et al., 2003), thus abundances from RLs might be affected by these effects. Other scenarios explored proposed that either electrons might not be well reproduced by a maxwellian statistical distribution (e.g. Nicholls et al., 2012) or chemical inhomogeneities (e.g. Stasińska et al., 2007) to explain ADFs. Nevertheless, IR CELs might provide more insights as their emissivity is much less affected by temperature, and, hence, their abundance estimations in comparison to those from RLs may rule out or reinforce the proposed scenarios (e.g. Chen et al., 2023, 2024; Tsamis et al., 2003).

2.1.1.3 *Application of ICFs*

Even in the best scenario for the application of the direct method to derive abundances, where we have a spectrum with reliable measurements of auroral lines to derive temperatures for all excitation zone, an additional problem arises when not all the ionization stages of an element are observed. Let us consider oxygen, with ionization potentials (O^{+} 13.62 eV; O^{++} 35.11 eV; O^{3+} 59.94 eV), as it is the target of most studies. For the vast majority of SFGs and HII regions, given the ionizing sources (massive stars), O^{+} and O^{++} (whose emission lines can be easily observed in the optical regime) are enough to provide an estimate of the O/H abundance ratio, since the amounts of higher ionized atoms are either negligible or null. This is not the case of AGNs, where a significant fraction of O^{3+} is observed (see Fig. 1.7). More drastically, there are other important elements such as nitrogen (N^{+} 14.53 eV; N^{++} 29.60 eV; N^{3+} 47.44 eV) or sulfur (S^{+} 10.36 eV; S^{++} 23.34 eV; S^{3+} 34.79 eV) for which high ionized species (N^{++} and S^{3+}) are not negligible in all cases but they cannot be observed by means of optical emission lines.

To provide accurate measurements in these conditions, ICFs (see Eq. (1.30)) are used (e.g. Amayo et al., 2021). As these ICFs are mainly calibrated using photoionization models that allow us to control the distribution and fraction of each ion, the caveats arise from how models are computed. For example, Amayo et al. (2021) proposed a series of ICFs calibrated with photoionization models that mimic the conditions of giant HII regions, but they are inadequate for AGNs. Although there are some proposed ICFs in the literature for AGNs as well (e.g. Dors et al., 2022; Dors et al., 2023; Flury & Moran, 2020) they are still sensitive to the input conditions of the used photoionization models.

The use of tailored photoionization models, also proposed for the lack of auroral lines, are a good alternative as well to the use of ICFs. Since photoionization models are computed for the total element abundance, and they account for the different ion fractions, once emission lines are fitted, we directly have an estimation of the total abundance. Together with the problem of its applicability to large spectroscopic surveys, the use of tailored photoionization models have a strong caveat due to the fact that if there is no constrain on the ionization degree of the nebula, the proportion of highly excited ions might not be constrained, hence, a model with low-ionization degree and low abundances can predict similar lines as those with high-ionization degree and high abundances. A workaround to this problem is to use lines from other ionic species but that have similar ionization potentials.

2.1.1.4 *Correcting from dust extinction and depletion*

The optical regime is affected by dust extinction, although at a lower extent in comparison to the UV regime (see Fig. 1.8). Moreover, dust extinction (which can be used as a proxy for the amount of dust in a galaxy) correlates with galaxy properties such as stellar mass, SFR and metallicity (e.g. Asari et al., 2007; Garn & Best, 2010; Iglesias-Páramo et al., 2007; Pannella et al., 2009; Sobral et al., 2012; Zahid et al., 2012). We show in Fig. 2.2 the dependence of the color excess (E(B-V)) as a function of different galaxy properties for a sample of SFGs from SDSS. The fact that the three actors are also related by means of the MZR and FMR relations implies that this relation is expected from galaxy evolution. Massive galaxies have had longer time to form dust, their strong gravitational well is more efficient in retaining them due to their gravitational potentials and they also show higher star formation rates (e.g. Garn & Best, 2010). In this scenario, metallicity can only increase due to galaxy evolution, helping cooling down the gas and alleviating dust destruction from thermal sputtering in shock waves (e.g. Priestley et al., 2022; Yamasawa et al., 2011).

An additional problem is the non-uniform distribution of dust within galaxies and that the dust-to-gas ratios has been reported to vary with metallicity and across galaxy disks (e.g. Vílchez

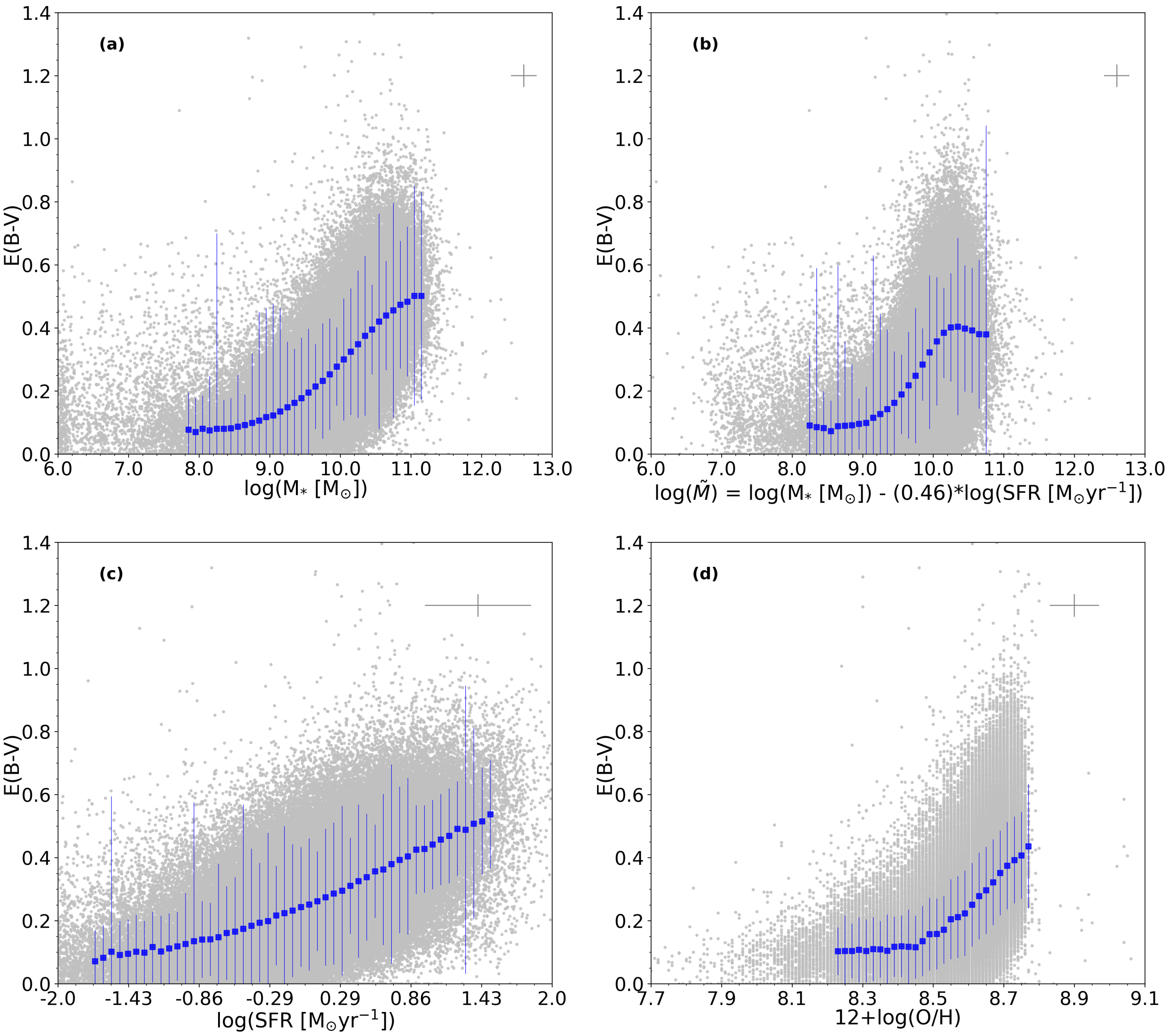

Figure 2.2: Color excess E(B-V) for the whole sample of SFGs from SDSS DR9 GalSpec catalog of galaxies as a function of stellar mass (a), stellar mass corrected from SFR (b), SFR (c) and metallicity (d). Typical error bars (gray) as well as the median values for binned data with at least 250 galaxies (blue) are shown in each plot.

et al., 2019). It has been observed and proposed that dust is associated to star formation, as it acts as both catalyst and shield helping the cooldown and subsequent collapse of the gas into stars (e.g. Byrne et al., 2019; Chastenet et al., 2025; Glover & Clark, 2012; Relaño et al., 2016). This is also crucial when analyzing starburst galaxies at high-redshift, as it has been shown that more than 20% of star-formation at high redshifts occur within dusty galaxies luminous in the IR (e.g. Algera et al., 2023; Bouwens et al., 2022; Colina et al., 2023). Dusty embedded regions are not only optically obscured due to dust extinction, but also because they intrinsically show lower temperatures and, hence, emissivity from optical emission lines drops.

Another problem is the composition of dust. Although we do not have a clear picture on its composition, we have observational evidences that dust amounts might grow by means of gas-phase metal incorporation (e.g. Relaño et al., 2016). Particularly, it has been reported that there is a factor of ~ 0.1 dex of the O/H content that goes into dust (e.g. A. Peimbert & Peimbert, 2010; Przybilla et al., 2008) at solar abundances. This effect is called *dust depletion*. Our understanding of gas depletion is limited. The most embedded regions are optically obscured, and hence only the brightest emission lines (or even none), which are H RLs and O CELs, can be seen. Hence, we have some hints on the depletion of O, but for many other elements these remains unclear. Thus, dust depletion is an important factor to be taken into account when comparing relative chemical abundance ratios (e.g. N/O, S/O, Ne/O).

2.1.2 *Constraining the nature of the ionizing source*

With independence on the methodology followed to estimate chemical abundances, having a good guess on the ionizing source is crucial. When applied the direct method, the temperature relations drastically change from SFGs (or HII regions) to AGNs (e.g. Dors et al., 2020; Flury & Moran, 2020). The calibrations, even for the same emission line ratio, change between AGNs and SFGs (see references in Tab. 2.1 and 2.2). If tailored photoionization models are used, then the ionizing source is a necessary ingredient that can drastically change the structure of the ionized gas (see the comparison between Fig. 1.3 and 1.4 or between Fig. 1.6 and 1.7).

As we have discussed in Sec. 1.2.5, the most used diagnostics to segregate ionizing sources are the BPT diagrams, which are empirically calibrated. As the optical regime does not trace high-ionized metal species, the same set of emission lines (but not at the same intensity) is observed in SFGs or AGNs. Thus, the relative ratios between these lines can help in providing a diagnostic on the ionizing source. The problem from these diagnostics is that show dependence on many other properties from the ISM rather than the ionized source.

We show in Fig. 2.3 and 2.4 results from grids of our computed photoionization models accounting for the dominant ionizing source in SFGs and AGNs respectively on the BPT diagrams[1]. Whereas SFGs models seems to be well constrained in these diagrams[2], this is not the case for AGNs. In the [O III]$\lambda 5007$Å/H$_\beta$ vs [N II]$\lambda 6584$Å/H$_\alpha$ diagram, it is clear that both 12+log(O/H) and log(N/O) can drive an AGN from the Seyfert to the SFG region. In the case of [O III]$\lambda 5007$Å/H$_\beta$ vs [S II]$\lambda 6717, 6731$Å/H$_\alpha$, the major driver is 12+log(O/H). Therefore, in the case that no other complementary information (e.g. X-ray emission, broad emission lines, ...) is available, there is a bias on the selection of AGNs.

2.2 THE INFRARED PERSPECTIVE: BEYOND OPTICAL BOUNDARIES

The outlined caveats from the optical regime do not imply that we must abandon it, but rather we must complement our studies with other regimes. There is no such a thing as an optimal regime, as all of them have their advantages and disadvantages, but the IR [1μm-300μm] stands as an excellent tool to perform similar studies as those with optical observations. In this section we review the performance of IR emission lines for chemical and physical studies of the ISM.

2.2.1 *Advantages of the IR regime*

Dust attenuation has an almost negligible effect on IR emission lines. In fact, the extinction curves for the IR regime (e.g. Gordon et al., 2021) predict that infrared emission lines lose on average $\sim 8\%$ of their emission in dusty environments ($E(B-V) \approx 1.2$), whereas optical lines such as [O III]$\lambda 5007$Å loses no less than $\sim 97\%$. Therefore, IR emission lines allow us to peer through dusty environments which remain almost blind to optical observations.

---

[1] In the case of WHAN diagram, a similar result is obtained (see Sec. 3.6.3 for more details).

[2] This result is confirmed observationally even for extreme conditions as those reported in Extreme Emission Line Galaxies (EELGs) and local analogues of high-redshift star-forming galaxies (e.g. Arroyo-Polonio et al., 2023; Jaskot & Oey, 2013; Mingozzi et al., 2024; Pérez-Montero et al., 2021).

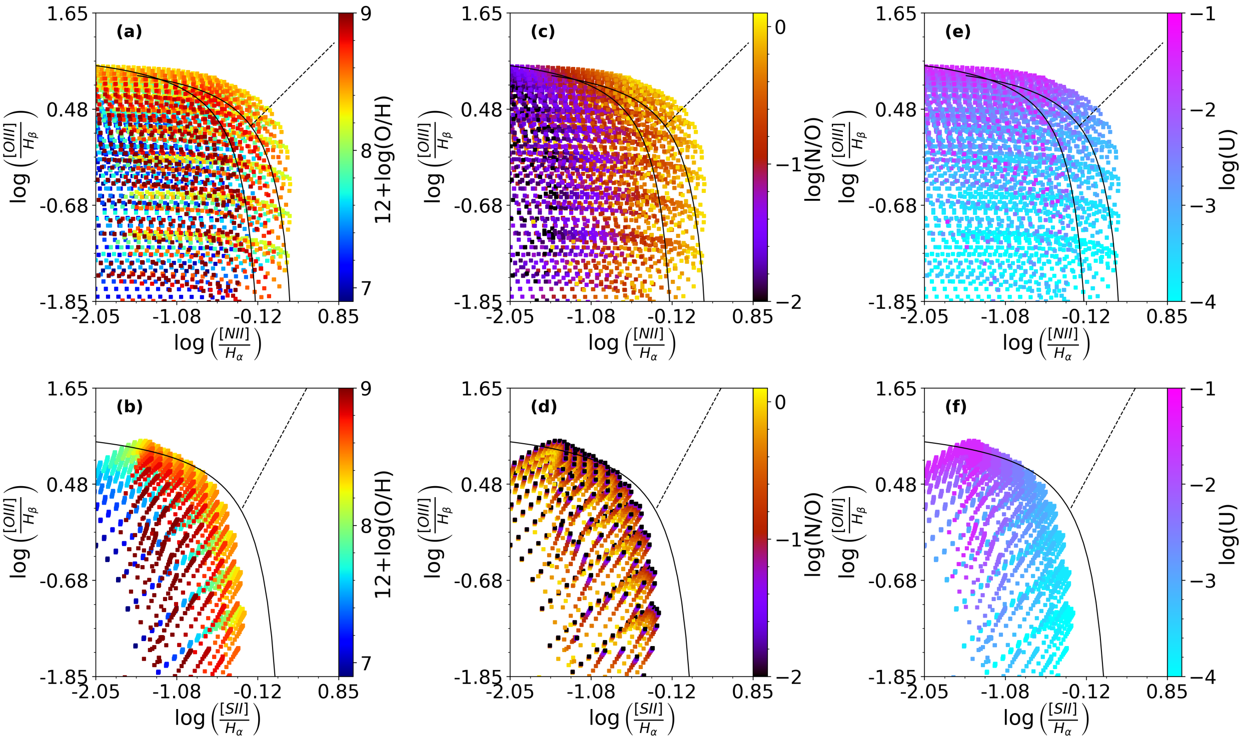

Figure 2.3: Diagnostic diagrams based on N (top row) and S (bottom row) lines for a grid of photoionization models from CLOUDY v17 reproducing the conditions of SFGs. The ionizing source is computed with POPSTAR (Mollá et al., 2009), after 1 Myr burst while the gas has an electron density of $n_e = 100$ cm^{-3}. Free parameters are: 12+log(O/H) (a and b), log(N/O) (c and d) and log(U) (e and f).

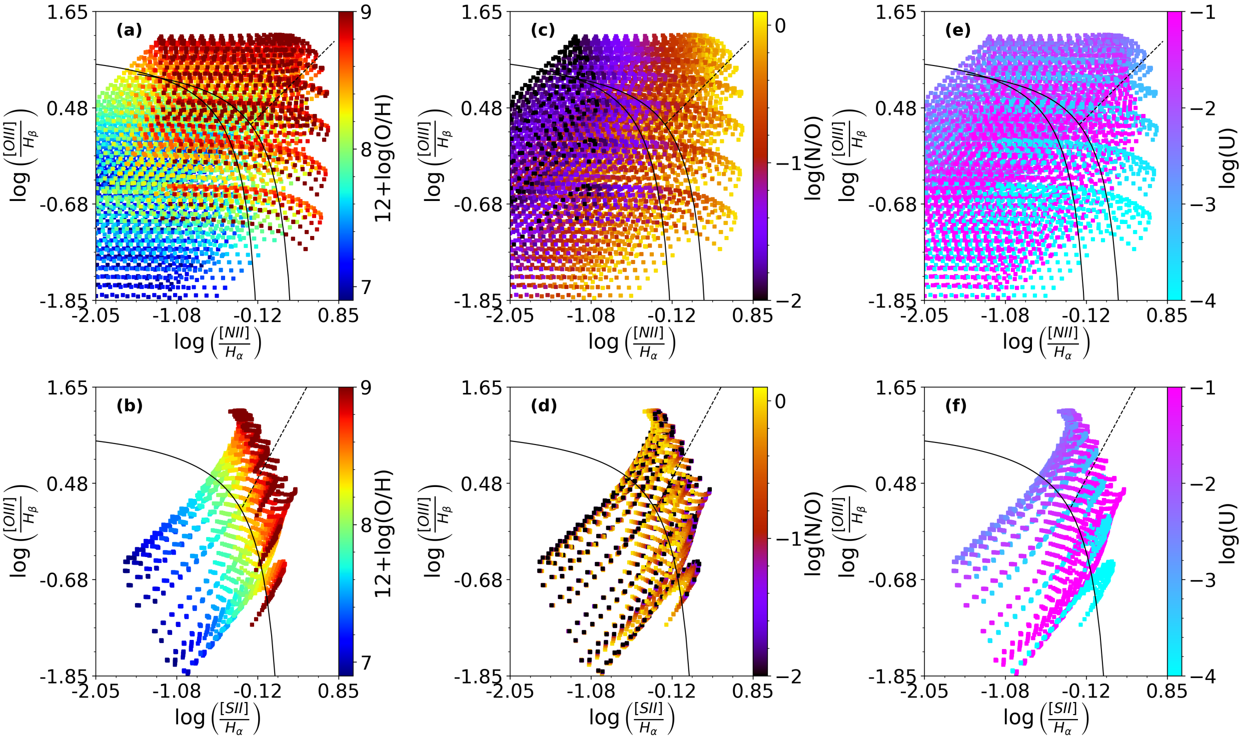

Figure 2.4: Same as Fig. 2.3 but in this case the ionizing source is an AGN, with slopes $\alpha_{OX} = -0.8$ and $\alpha_X = -1$ and the electron density is set to $n_e = 500\text{cm}^{-3}$.

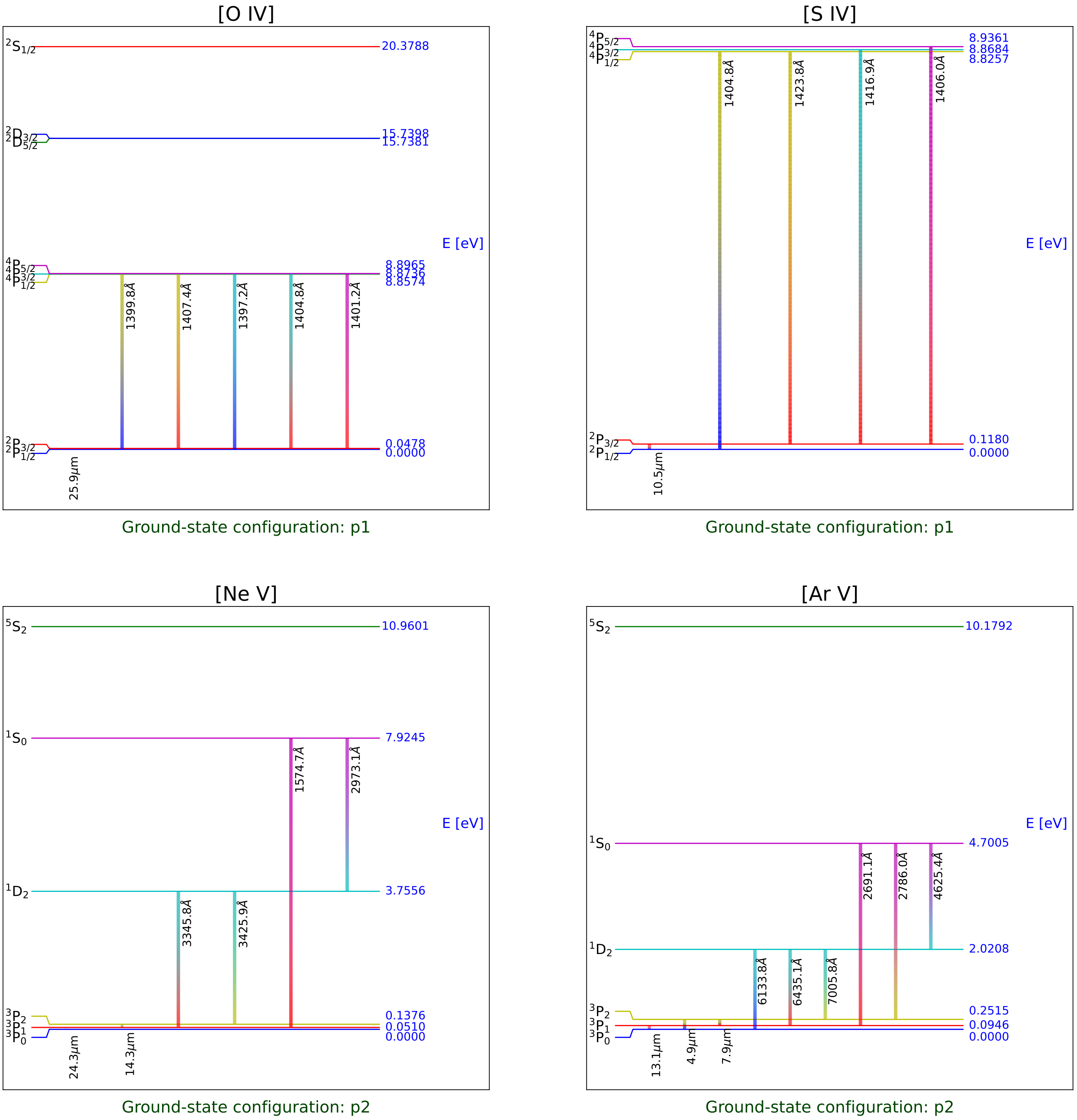

Figure 2.5: Grotrian diagrams for different highly-ionized elements. Grotrian diagrams have been obtained with PYNEB assuming $T_e = 10^4$ K and $n_e = 100\ \text{cm}^{-3}$.

The IR regime also provides an unique window to observe highly-ionized elements. We have already shown that ions such as S^{+3} are present in the gas-phase ISM of HII regions and SFGs (see Fig. 1.6), whereas ions such as O^{+3}, Ne^{+4} or Ar^{+4} are ubiquitous to the NLR of AGNs (see Fig. 1.7). The transitions observed in these ions, due to the separation energies, are mainly traced in the UV and IR regimes. However, as UV is greatly affected by dust, the observed emission of [O IV]λ1407Å from a dusty region ($E(B-V) \approx 1.2$) is reduced by more than 99.9%, whereas the emission from [O IV]$\lambda 25.9\mu$m is reduced by 8%. Therefore, these ions can be easily traced in the IR regime.

Another advantage of the IR emission lines is their little dependence on electron temperature (T_e). Indeed, as these transitions are associated to energy levels close to the ground state and with little separation among them, the relative population is mainly driven by electron density, follow up by little dependence on temperature. Whereas IR RLs show essentially the same trend as their optical

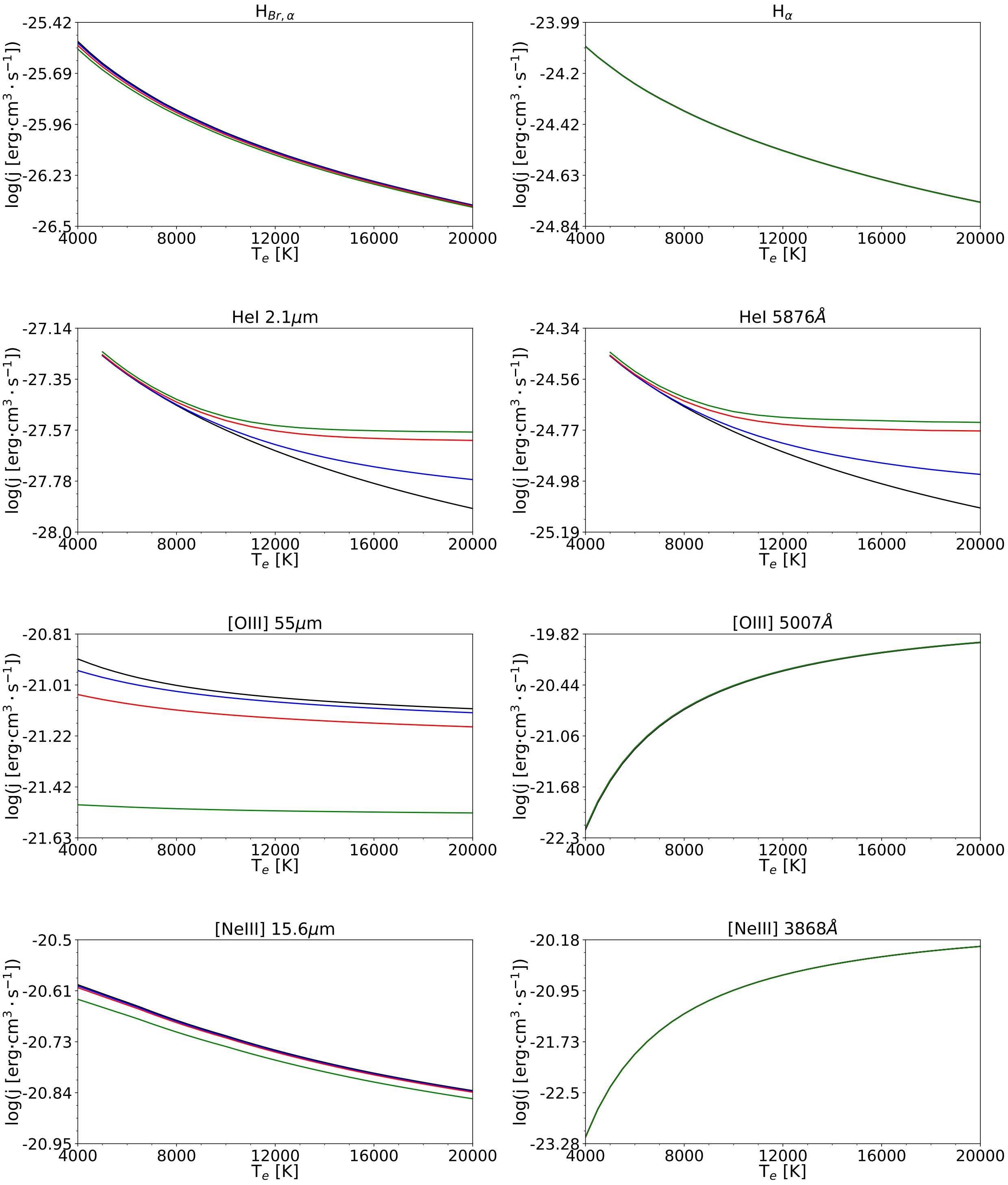

Figure 2.6: Comparison of the emissivity of IR and optical emission lines from the same ions as a function of the electron temperature computed from PYNEB. Top panels show the emissivity from RLs (H and He), and bottom panels for CELs (O and Ne). Different values of the electron density are used: $n_e = 100$ cm^{-3} (black), $n_e = 10^3$ cm^{-3} (blue), $n_e = 10^4$ cm^{-3} (red) and $n_e = 10^5$ cm^{-3} (green).

counterparts, IR CELs show very little dependence in comparison to the optical ones. Moreover, optical CELs drastically drop their emissivity when electron temperature is low, but in the case of IR CELs they are still as bright as at high temperatures (see Fig. 2.6). This is extremely useful as we do not need to accurately constrain the temperature structure for each ion, given the fact these corrections will play a negligible role. Additionally, IR lines allow us to trace cold ionized gas ($\lesssim 6000$ K), that emits extremely faint optical CELs.

2.2.2 *General caveats for the IR*

Although we have enumerate a serious of strong advantages of the IR observations in comparison to the optical, there is also an important number of challenges to the IR observations. We will shortly review all these problems and list the workarounds.

2.2.2.1 *Challenging IR observations*

IR observations are challenging themselves as *warm* objects ($T \sim 200 - 300$ K) emit the bulk of their emission in this regime. For ground-based observations, the emission from molecules in the lower Earth atmosphere ($T_{eff} \sim 250$ K; Harries et al., 2008) as well as the emission of the telescope itself (given it is at the ground temperature) introduces a significant background noise in the observations. For comparison, the background noise from ground-based observations can be up to $6-7$ orders of magnitude stronger than the one retrieved from space-based observations (e.g. Elliott et al., 2013). For the far-IR (FIR), the molecules of water vapor present in the Earth atmosphere absorb a great amount of the emission coming to ground-based observatories (e.g. van Vleck, 1947; Young et al., 2012).

The technical development over the last half-century has allowed us to send space missions with telescopes that help us retrieve more efficiently IR emission from galactic and extragalactic sources (see Elliott et al., 2013, for a technical review). We present in Appendix B an overview of such missions.

2.2.2.2 *Measuring hydrogen RLs*

Another important challenge with IR observations is the detection of H RLs. In the IR regime, we can detect transitions according to the Brackett ($n \rightarrow 4$), Pfund ($n \rightarrow 5$) and Humphreys ($n \rightarrow 6$) series. Due to the involved transitions, these emission lines have a lower emissivity than the optical ones and, among them, the brightest are the ones corresponding to the closest levels, i.e., α-lines. Namely, these are Brackett-α (H I $\lambda 4.05 \mu$m), Pfund-α (H I $\lambda 7.46 \mu$m) and Humphreys-α (H I $\lambda 12.35 \mu$m).

Hydrogen RLs are necessary in order to provide *absolute* (i.e. relative to H) values of the chemical abundances, otherwise we could only constrain chemical abundance ratios between metals. These RLs can be much fainter than other CELs in the IR regime (see Fig. 2.7) and, in some cases, they are not retrieved in certain observations. Nevertheless, as we discuss in Sec. 2.2.3, there are workarounds to estimate chemical abundances in certain scenarios.

2.2.2.3 *Critical density of IR lines*

Although IR emission lines are not affected by temperature, they show a strong dependence on density. We have already defined critical density (n_c) as the threshold density at which the number of collisional de-excitations surpasses that of radiative de-excitations. The value of n_c will depend mainly on three factors: the ion, the temperature and the transition.

For a given ion Y^+, we have a set of emission lines that represent the different transitions. The longer the wavelength, the smaller the energetic gap between the initial and final levels. As the energy gap between levels is smaller, collisional de-excitations are more likely to occur, as electrons are more capable of abandoning the levels. This is what happens with IR emission lines: [O III]λ5007Å

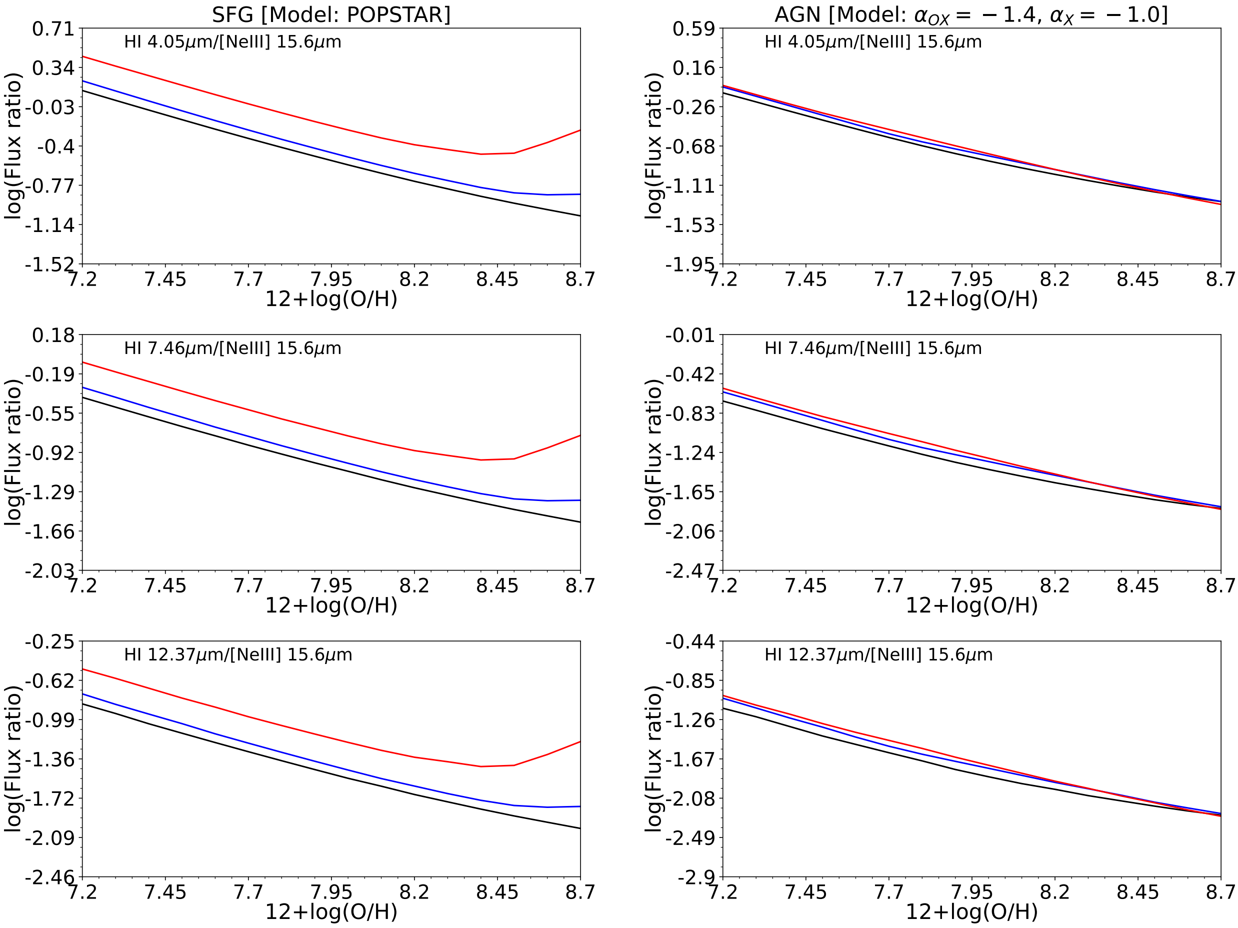

Figure 2.7: Hydrogen recombination lines in the IR regime relative to [Ne III] emission as a function of the gas-phase ISM oxygen abundance from models computed with CLOUDY V17. Left column shows the results assuming an ionizing source computed with POPSTAR (Mollá et al., 2009), after 1 Myr burst while the gas has an electron density of $n_e = 100$ cm^{-3}. Right column shows the results assuming an AGN, with slopes $\alpha_{OX} = -0.8$ and $\alpha_X = -1$ and the electron density is set to $n_e = 500$ cm^{-3}. For each model, we consider different ionization parameters: $\log(U) = -3.5$ (red), $\log(U) = -2.5$ (blue), $\log(U) = -1.5$ (black).

has a critical density of $n_c \sim 7 \cdot 10^5$ cm^{-3} whereas for [O III]$\lambda 88\mu$m is $n_c \sim 500$ cm^{-3}. A list of the critical densities of the most bright IR CELs is provided in Tab. 5.1.

Therefore, IR emission lines are inefficient in tracing high-density regions ($n \sim 10^4$ cm^{-3}), as their emissivity drastically drops as a consequence of the decrease in the radiative de-excitations rate. As density might not be uniform across the gas, the densest regions will be opaque to far-IR lines, and hence this effect must be considered when combining information from mid-IR and far-IR observations.

2.2.3 *Diagnostics from IR emission lines*

2.2.3.1 *Physical and chemical properties of the ISM*

As IR emission lines show low critical densities, it is important to have a good constrain for it. There are numerous doublets in the IR that can be used to estimate density, such as [S III]$\lambda 18.7\mu$m and [S III]$\lambda 33.5\mu$m, [O III]$\lambda 52\mu$m and [O III]$\lambda 88\mu$m or [Ne III]$\lambda 15.6\mu$m and [Ne III]$\lambda 36\mu$m (valid for both SFGs and AGNs) and the doublet [Ne V]$\lambda 14.3\mu$m and [Ne V]$\lambda 24.3\mu$m. As the involved energy is much lower, the energetic transitions associated to the doublets imply a higher separation in the wavelengths, making them much easier to be measured than in the optical regime. We show in Fig. 2.8 the behavior of these doublets as a function of density.

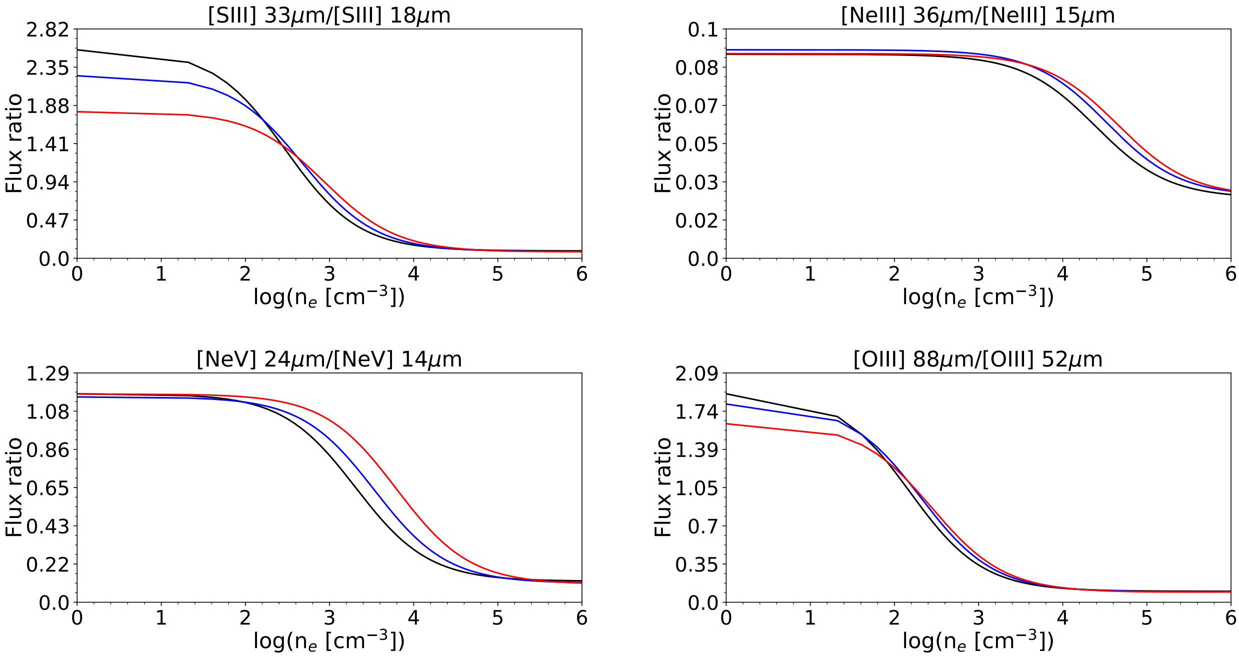

Figure 2.8: IR emission line ratios sensitive to the electron density, computed with PYNEB. Different values of the electron temperature are used: $T_e = 5 \cdot 10^3$ K (black), $T_e = 10^4$ K (blue) and $T_e = 2 \cdot 10^4$ K (red).

Due to the impossibility of providing a constrain on the electron temperature from IR emission lines, the alternatives to provide estimations of chemical abundances rely on photoionization models, which are necessary to calibrate strong emission line ratios (e.g. Fernández-Ontiveros et al., 2021; Kewley et al., 2019; Nagao et al., 2011). Most of the ratios proposed only involve metal CELs, as H RLs are not usually observed (e.g. Fernández-Ontiveros et al., 2016; Nagao et al., 2011) for testing ratios involving H lines. Kewley et al. (2019) proposed a series of ratios (see Tab. 3 from that work) using H I Humphreys-α and H I Pfund-α, but they were not tested on a sample. Later on, Fernández-Ontiveros et al. (2021) explored the use of those ratios in a sample of star-forming dominated galaxies. We show in Tab. 2.3 and Tab. 2.4 strong emission line ratios proposed to estimate 12+log(O/H) and log(N/O).

Table 2.3: IR emission line calibrators for the determination of 12+log(O/H) abundances. Reference codes: FO+21 (Fernández-Ontiveros et al., 2021), Kew+19 (Kewley et al., 2019), TW (this work).

Name	Lines	Applicability	Calibration	Range	Method
Ne23	[Ne II] $\lambda 12\mu$m,$H_{Hu-\alpha}$, [Ne III] $\lambda 15\mu$m	SFGs	FO+21	[7.0, 8.9]	Models
S34	[S IV] $\lambda 10\mu$m, $H_{Hu-\alpha}$, [S III] $\lambda 18\mu$m	SFGs AGNs	FO+21 TW	[7.0, 8.9] [7.0, 8.9]	Models Models
O3N2	[O III] $\lambda 88\mu$m, [N II] $\lambda 122\mu$m	SFGs	FO+21	[8.4, 8.9]	Models
O3N3	[O III] $\lambda 88\mu$m, [N III] $\lambda 57\mu$m	SFGs	Kew+19	[7.63, 9.3]	Models

Paradoxically, while the IR regime offers the opportunity of measuring CELs from highly-ionized species such as O^{+3}, Ar^{+4} or Ne^{+4}, which are associated to the AGN-dominated galaxies (e.g. Armus et al., 2007; Genzel et al., 1998; Tommasin et al., 2010), the calibrations proposed and explored were

Table 2.4: IR emission line calibrators for the determination of log(N/O) abundances. Reference codes: Pe+21 (B. Peng et al., 2021); TW (this work).

Name	Lines	Applicability	Calibration	Range	Method
N3O3	[O III] $\lambda 52\mu m$, [N III] $\lambda 57\mu m$	SFGs	Pe+21	$[-2.0, 0.0]$	Models
		AGNs	TW	$[-2.0, 0.0]$	Models
N3S34	[S IV] $\lambda 18\mu m$, [S III] $\lambda 18\mu m$, [N III] $\lambda 57\mu m$	SFGs	TW	$[-2.0, 0.0]$	Models
		AGNs	TW	$[-2.0, 0.0]$	Models

never adapted or tested in AGNs. This natural extension of the chemical diagnostics based on IR lines to AGNs constitutes the work that we present in Chapter 5.

2.2.3.2 *Ionizing source*

The detection of lines such as [O IV]$\lambda 26\mu$m, [Ne V]$\lambda 14\mu$m or [Ne V]$\lambda 24\mu$m, ideally, would be enough criteria to asses the AGN nature of a source. However, it has been observed that several sources which were confirmed to be star-forming dominated present some emission of these CELs (e.g. Armus et al., 2007; Fernández-Ontiveros et al., 2016; Sturm et al., 2002; Tommasin et al., 2010). This is due to the fact that most of the observations from *Spitzer* and *Hershel*, which have provided the largest data archives until the advent of James Webb Space Telescope[3] (JWST), were done with the integrated spectra of galaxies in which star-formation and AGN activity can simultaneously occur. Therefore, as in the case of optical spectroscopic observations, diagnostics diagrams are needed to quantify these combination.

The first diagnostic based on purely IR spectroscopic features (not only emission lines) was explored by Genzel et al. (1998). They obtained that not only AGNs typically show high [O IV]$\lambda 26\mu$m/[Ne II]$\lambda 12\mu$m and [Ne V]$\lambda 14\mu$m/[Ne II]$\lambda 12\mu$m ratios, but also lower equivalent widths of the PAH bands. These was attributed to the hard radiation field of AGNs, which are able to destroy a great amount of the PAH grains in their surroundings. This idea motivates the use of diagnostic diagrams based on the strength of the PAH emission and the ratio between the CELs from highly- and moderately-ionized excitation regions (Armus et al., 2007; Sturm et al., 2002; Tommasin et al., 2010).

Initially, the distinction between SFGs and AGNs was empirically done (Armus et al., 2007; Tommasin et al., 2010). The regions marked in the diagram were obtained assuming that PAH emission only comes from SFGs, and [Ne V] (or [O IV]) only comes from AGNs. Considering observational limits for each sample, they provide regions by empirically mixing the emission from observations (Tommasin et al., 2010). This can also be done, as we show in Fig. 2.9, using photoionization models. We consider intermediate cases of AGN and SFG emission by assuming a linear combination of the spectroscopic properties and the continuum. Although not entirely accurate, it is a good approximation for the mixing scenario, and we obtain similar results. We define the following regions:

$$\text{AGN dominated} = \begin{cases} W_{PAH\ 6.2\mu m} \leq 0.06\mu\text{m} \\ [\text{Ne V}]\lambda 14\mu\text{m}/[\text{Ne II}]\lambda 12\mu\text{m} \geq 0.15 \ \text{ or} \\ [\text{O IV}]\lambda 26\mu\text{m}/[\text{Ne II}]\lambda 12\mu\text{m} \geq 0.4 \end{cases} \tag{2.2}$$

---

[3] It should be noted the detection of [Ne V] emission from JWST data in galaxies with no previous evidence of AGN activity (e.g. Hernandez et al., 2025; Mingozzi et al., 2025), although there is still a debate on the origin of such emission.

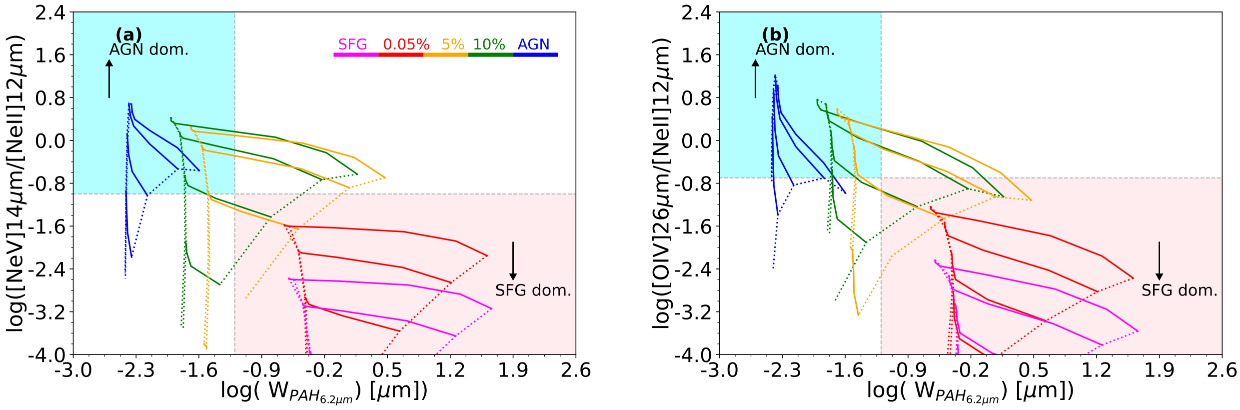

Figure 2.9: Diagnostic diagrams, computed for this research, based on ratios of IR high-excitation lines and the equivalent width of the PAH feature at 6.2μm. The blue area represents the AGN dominated region (Eq. (2.2)) and the red one the SFG dominated (Eq. (2.3)). A grid of photoionization models varying density and the ionization parameter, for both an AGN ($\alpha_{OX} = -1.2$) and for SFG (using a 1 Myr burst from POPSTAR, as ionizing source), are combined linearly and plotted following the color proportions.

$$\text{SFG dominated} = \begin{cases} W_{PAH\ 6.2\mu m} > 0.06\mu\text{m} \\ [\text{Ne}\,\textsc{v}]\lambda 14\mu\text{m}/[\text{Ne}\,\textsc{ii}]\lambda 12\mu\text{m} < 0.15 \ \text{ or} \\ [\text{O}\,\textsc{iv}]\lambda 26\mu\text{m}/[\text{Ne}\,\textsc{ii}]\lambda 12\mu\text{m} < 0.4 \end{cases} \tag{2.3}$$

Similarly, Spoon et al. (2007) proposed to replace the ratio between CELs by the strenght of the silicate feature at 9.8μm. This modification was introduced to account for a diagnostic of strong obscured systems. This diagram offers a clear demarcation between ULIRGs and AGNs, complementing the information from the other diagnostics (Spoon et al., 2007, 2022).

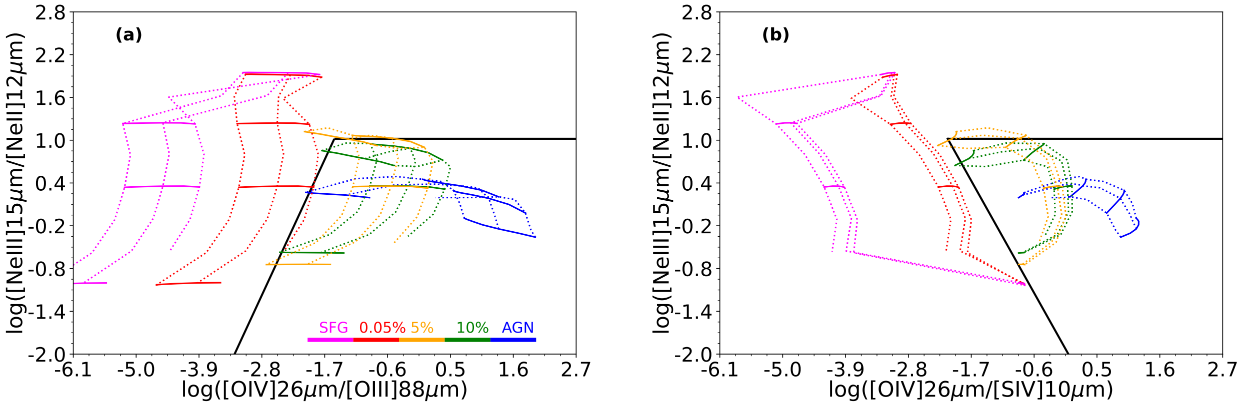

Figure 2.10: Diagnostic diagrams, computed for this research, based on ratios of IR high-excitation lines. The AGN dominated area is delimited by solid black lines following Eq. (2.4) (a) and (2.4) (b). Photoionization models are shown following the same convention as in Fig. 2.9

Diagnostic diagrams based purely on emission lines have also been explored (e.g. Fernández-Ontiveros et al., 2016; Sturm et al., 2002). Among all of them, the diagnostic based on the [Ne III]$\lambda 15\mu$m/[Ne II]$\lambda 12\mu$m and [O IV]$\lambda 26\mu$m/[O III]$\lambda 88\mu$m offers the best results (e.g. Fernández-Ontiveros et al., 2016). Contrary to the dependence on metallicity of optical diagnostics, the involved ratios only depend on the ionizing source and density as the proposed emission lines ratios cancel the abundance dependence. For AGN dominated sources, we expect a high [O IV]$\lambda 26\mu$m/[O III]$\lambda 88\mu$m, whereas the ratio [Ne III]$\lambda 15\mu$m/[Ne II]$\lambda 12\mu$m can only be high for SFGs dominated objects, as they cannot produced photons with enough energy to further ionize Ne. This is show in Fig. 2.10 (a) along with the sequences of photoionization model grids previously described. Alternatively, $[\mathrm{O\,III}]\lambda 88\mu\mathrm{m}$ can be replaced with[4] $[\mathrm{S\,IV}]\lambda 10\mu\mathrm{m}$ (e.g. Fernández-Ontiveros et al., 2016; Martínez-Paredes et al., 2023; Richardson et al., 2022), since the ions have similar ionizing potentials (see Fig. 2.10 (b)). We define the following regions:

$$\text{AGN dominated} = \begin{cases} \log\left([\mathrm{Ne\,III}]/[\mathrm{Ne\,II}]\right) \leq -1.02 \\ \log\left([\mathrm{Ne\,III}]/[\mathrm{Ne\,II}]\right) \leq 1.73 \log\left([\mathrm{O\,IV}]/[\mathrm{O\,III}]\right) + 3.67 \end{cases} \tag{2.4}$$

$$\text{AGN dominated} = \begin{cases} \log\left([\mathrm{Ne\,III}]/[\mathrm{Ne\,II}]\right) \leq -1.02 \\ \log\left([\mathrm{Ne\,III}]/[\mathrm{Ne\,II}]\right) \geq -1.43 \log\left([\mathrm{O\,IV}]/[\mathrm{S\,IV}]\right) - 2.0 \end{cases} \tag{2.5}$$

Lastly, it is important to mention that, once the general nature of the source is constrained, the shape can also be estimated. Pérez-Montero and Vílchez (2009) showed that mid-IR lines can be used for the estimation of the effective temperature of young stars in HII regions, following a similar prescription of the softness diagram (Eq. (1.36)), a result that can also be applied to the integrated spectra of SFGs (Pérez-Montero et al., 2024). Moreover, thanks to the high excitation emission lines, it is also possible to provide a quantification on the hardness of the AGN SED (Pérez-Montero et al., 2025).

2.3 PHOTOIONIZATION MODELS

Until now, we have made use of *photoionization models* with the only explanation that they allow us to understand the non-equilibrium gas physical and chemical composition. Hence, we have used them to model and reproduce the expected spectrum and structure of the ionized gas in some of the most common extragalactic scenarios. Although this is an accurate definition, it is important to have a clear idea of what they can and cannot do, especially since they are the core of the methodology used in this work.

There is a limited offer of photoionization codes available, mainly due to the complexity in the physical modeling as well as in the atomic/molecular data compilation. Whereas this might be a limitation, the first codes were developed in the late 1970s, and since many people have been contributing and improving them. Namely, three codes outstand in the literature: CLOUDY[5] (Chatzikos et al., 2023; Ferland et al., 2017), MAPPINGS[6] (Sutherland & Dopita, 2017) and 3D-MOCASSIN[7] (Hubber et al., 2016).

2.3.1 *Assumptions and limitations*

Photoionization models are built upon microphysics codes that determine the non-equilibrium ionization, thermal and chemical state of gas clouds (ionized or not by a source) through solutions to the equations of statistical and thermal equilibrium, equations of balance between ionization-neutralization and between heating-cooling. A full explanation on the derivation and explicit form of these equations is provided in Osterbrock and Ferland (2006). These equations are solved starting from specific initial conditions and using atomic and molecular databases up-to-date.

---

[4] Notice that this replacement is helpful for JWST observations as they can cover all these lines in nearby systems.

[5] All versions of the code are available through https://gitlab.nublado.org/cloudy/cloudy.

[6] The latest version is available at https://mappings.anu.edu.au/.

[7] Details on installation and updates are provided in https://mocassin.nebulousresearch.org/.

The majority of the photoionization codes assumes spherical geometry, dealing with 1D equations. The spherical geometry might be changed into plane-parallel geometry as long as the inner radius of the gas (illuminated face of the gas) and the outer radius (boundary or shield face) have a certain proportion. In both cases, the gas is divided into concentric shells (zones) ensuring that: i) physical (e.g. density, cooling, heating,...) conditions are nearly constant; and, ii) all microphysical processes occur at a shorter timescale[8] than the recombination of H. On the other hand, the gas can be treated as a dynamical structure (i.e. it is expanding) or as a steady one.

The spherical symmetries imposed allow faster calculations, but it might no be representative of the observing scenarios. 3D-photoionization codes such as 3D-MOCASSIN require greater computational resources, so elaboration of grids of models is feasible for a limited number. In the recent years, pseudo-3D codes have been developed, in which 3D-structures of ionized gas are computed from a cubic grid of 1D-photoionization codes in which the inputs are generated from the radial and polar coordinates of the different profiles within the gas and the solid angle from each beam in the distribution (in case of clumpy distributions) is used to weight the integrated (sum) output (e.g. Moraes & Diaz, 2009; Morisset et al., 2005). Examples of these implementations are CLOUDY3D (Morisset & Stasinska, 2008; Morisset, 2006) and RAINY3D (Moraes & Diaz, 2009). Although the computational time also increases as a grid of 1D-models are generated per each 3D-model, it is still faster than pure 3D-photoionization codes (Morisset et al., 2005).

In some cases, the dynamics of the gas surrounding an ionizing object might be on the scale of supersonic motions. In this scenario, the kinetic energy generates radiative shocks that not only introduce changes in the physical (increase on density and temperature) and chemical (dust grain destruction), but also in the radiative cooling (e.g. Aldrovandi & Contini, 1985; Contini & Aldrovandi, 1983; Dopita, 1976; Dopita et al., 1977; Dopita, 1977). The treatment of these conditions adds more complexity to the equations and solutions, and photoionization codes usually do not implement them. Only MAPPINGS provides a self-consistent treatment of fast radiative shocks and photoionized gas (Allen et al., 2008; Sutherland & Dopita, 2017), although the chemistry traced by the code (atoms, molecular species) is more limited than others (e.g. CLOUDY). As in previous cases, shock models also assume a geometry since a proper multidimensional treatment increases significantly the use of computational resources to provide just one model (Sutherland et al., 2003b, 2003a).

2.3.2 *Basic ingredients*

Photoionization codes have the great advantage of being capable of predicting the thermal and ionization structure of an ionized gas from a small reduced set of parameters (inputs) that govern the initial conditions from which equations are solved. The input set of parameters is hence the most critical part when modeling the ionized gas. These basic ingredients are: i) the geometry and density of the gas; ii) the chemical composition (atomic and molecular) of the gas; and iii) the incident radiation field. For the purposes of this work, we only discuss hereinafter 1D models.

2.3.2.1 *Geometry and density*

As geometry is usually assumed to be spherical (or plane-parallel at most), the critical parts for the calculation are how gas is distributed. The basic scenario is one in which gas only fills a small portion of the geometry (*open geometry*). The contrary scenario happens when gas fills the whole geometry, which is called *closed geometry*. To provide a quantification of these situations (and the intermediate ones), we use the *covering factor* ($\Omega\,(4\pi)^{-1}$), which represents the fraction of the solid

---

[8] The recombination timescale is given by $\tau = \alpha^{-1}\,(H, T_e)\, n_e^{-1}$, where α is the sum of all recombination combinations (which depends on temperature and the recombination case) and n_e is the electron density.

angle from the ionizing source (4π) covered by gas with enough density to absorb the ionizing radiation. If the covering factor is low (open geometry), then the light from the ionizing radiation field that is not absorbed in the illuminated face of the gas escapes without much (if any) interaction. On the contrary, when the covering factor is high (closed geometry), then any radiation that might escape the illuminated face in the direction of the central source will interact with the other side of the gas.

Another important aspect regarding geometry is whether it is static (i.e. the radius is initially defined and does not change over time) or dynamic (i.e. the radius changes over time as a consequence of the expansion of the outer shells). If the ionized gas is expanding, then while photons from the ionizing source are absorbed by the gas, the diffuse ones emitted by the gas towards the opposite direction are considered to never reach the gas, due to the expansion.

Once we have defined the geometrical space that contains the gas, density must be set. Density needs to be parametrized as a radial function so that shells can be defined. As it is well-known that the ISM is not uniformly distributed but rather have a clumpy structure (e.g. Crovisier & Dickey, 1983; Elmegreen, 1997; Kalberla & Haud, 2019), it is important to quantify it. This is done by means of the *filling factor*, which is the fraction of the volume occupied by condensations in density of the gas, and it is assumed that the space between those condensations is empty.

The outer radius is the last parameter that needs to be addressed to fully understand the geometry of the gas and its predictions. Depending on the obtained value, models are not only able to determine if the plane-parallel approximation is feasible, but also the hydrogen-ionization structure. If the outer radius is low enough, then the boundary face of the cloud is the limit of the ionized hydrogen structure. This is the *matter-bounded* scenario. On the other hand, the outer radius can be far beyond the limit where ionized hydrogen drops, and hence both ionized and neutral regions coexist. This is the *radiation-bounded* scenario.

2.3.2.2 *Chemical composition*

The chemical composition of the gas, i.e., the abundance of elements, molecules and dust grains plays a fundamental role in the cooling and heating processes and, hence, in the resulting structure of the ionized gas. This is fully controlled in the input parameters. The main limitation to what species can be traced is given by the available databases used by the codes. For example, the latest version of *cloudy* follows the 30 lightest elements (from H to Zn), including all ionizing stages and different energetic levels (up to 100 for Fe) as well as 38 different molecules (Chatzikos et al., 2023; Gunasekera et al., 2023). MAPPINGS also has the same number of elements, but only dust is accounted for.

2.3.2.3 *Ionizing radiation field*

The ionizing radiation field accounts for the incident spectra of energetic photons that impact in the surrounding gas. This is controlled by the nature of the ionizing source (see Sec. 1.2.5 for more details). The ionizing radiation field has two main properties: the shape (i.e. the relative number of photons emitted at specific energies) and the luminosity (the absolute number of emitted photons).

The shape of the ionizing radiation field is assumed by the type of source: stellar (e.g. young stellar clusters) or non-stellar (e.g. AGNs). We show in Fig. 2.11 examples of the SED for different ionizing sources. Although the brightness of the SED can be given in terms of the absolute luminosity (L [$\mathrm{erg \cdot s^{-1}}$]), it is usually provided in terms of intensity (F [$\mathrm{erg \cdot s^{-1} \cdot cm^{-2}}$]). Alternatively, as the density is provided in the inner face of the gas, the ionization parameter U (Eq. (1.11)) can also be used to quantify the brightness of the source.

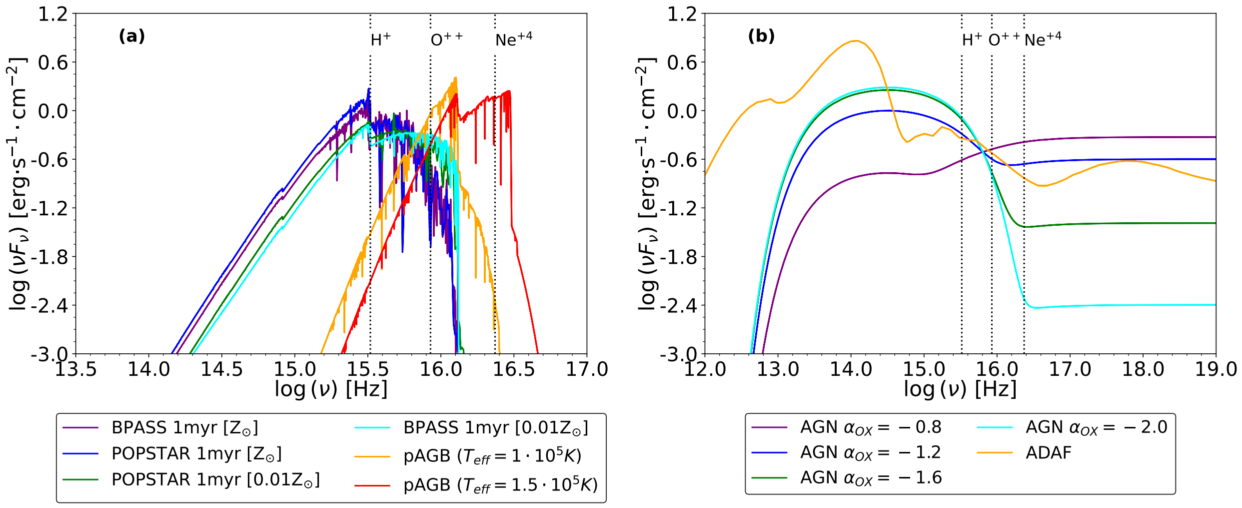

Figure 2.11: Comparison of spectral energy distributions (SEDs) modelling stellar (a) and non-stellar (b) sources. Details on the generation of these SEDs are provided in Sec. 2.4.2. Vertical lines show the ionization energies of some ions.

2.3.3 *Applicability to large surveys*

As photoionization models predict a large number of spectroscopic features (mainly emission lines), they can be used to constrain input parameters. This is the tailored models technique, which can be used not only for constraining chemical abundances but also to provide predictions for other observations. As this technique involves the generation of a grid of photoionization models, where the grid dimension is given by the uncertainty assumed for the studied properties, this is not applied to large samples of galaxies.

Instead, fixed grids of photoionization models are reproduced in which some properties are left as free parameters, and others are fixed assuming average properties representative of the type of analyzed galaxies (e.g. Blanc et al., 2015; Mingozzi et al., 2020; Pérez-Montero, 2014; Pérez-Montero et al., 2019a; Thomas et al., 2019). This is the underlying idea of many codes such as HII-CHI-Mistry (Pérez-Montero, 2014), IZI (Blanc et al., 2015), NebulaBayes (Thomas et al., 2018) or homerun (Marconi et al., 2024). All these codes do not produce photoionization models, but they rely on an already computed grid of photoionization models. The main differences among the codes are: i) which and how many free parameters are fitted; ii) which fitting or weight technique is used; and, iii) how the grids were computed.

2.4 HII-CHI-MISTRY

HII-CHI-Mistry (hereinafter, HCm) is a collection of Python open-source codes[9] developed to analyze spectroscopic observations of bright emission lines from the ionized gas either in the optical (Pérez-Montero, 2014), ultraviolet (Pérez-Montero & Amorín, 2017) or infrared (Fernández-Ontiveros et al., 2021) ranges. HCm compares observational values of certain emission lines with the predictions from photoionization models in already-computed extensive grids for different ionizing scenarios.

HCm can be used for the estimation of chemical abundances in the gas-phase ISM and/or to infer physical properties of both the gas (photon escape fraction, ionization parameter; e.g. Pérez-Montero et al., 2019b, 2020) and ionizing source (effective temperature). In this section, we focus on

---

[9] All code versions and flavors are accessible at https://home.iaa.csic.es/~epm/HII-CHI-mistry.html or at the git repository https://github.com/Estallidos/HII-CHI-Mistry.

describing the capabilities of HCm to estimate chemical abundances, which has been demonstrated to provide similar solutions to the direct method in the optical (see Fig. C.1 and C.2), making it a reliable tool to estimate chemical abundances in the absence of auroral lines.

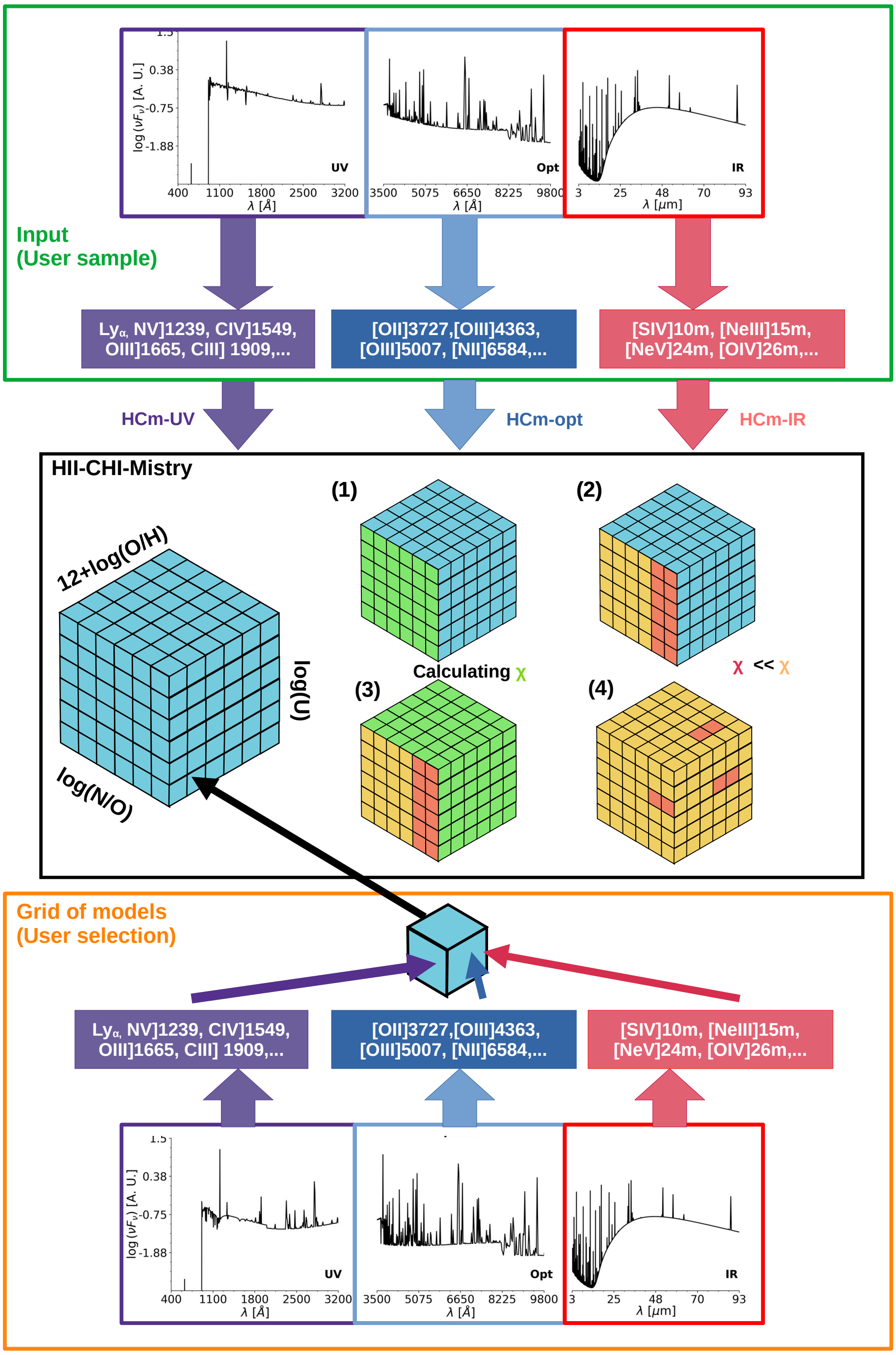

Figure 2.12: Schematic overview on how HII-CHI-Mistry works.

2.4.1 *General description*

2.4.1.1 *A bayesian-like approach*

Let us assume that we want to constrain a property of the gas-phase ISM (Y), and we have the observed spectrum of the source. By means of photoionization models, we can generate a grid in which the property is a free parameter in the range $[Y_1, Y_2]$, with a step (fixed or variable) ΔY. For each model, we would have the prediction of the spectrum in the same observing range. For example, we can use the observed $[F_1, F_2, ..., F_N]$ fluxes of the N-brightest emission lines. The grid of photoionization models, based on each value of the free parameter Y_i, provides the predictions $[T_1\,(Y_i), T_2\,(Y_i), ..., T_N\,(Y_i)]$. For an N-dimensional set of observed emission lines, we then have a NxM matrix of predictions, being M the number of values (related to the uncertainty in constraining the explored property). The above scenario can easily be generalized into multidimensional problem: to constrain a set of $\tilde{M}$ physical properties $(Y_1, Y_2, ..., Y_{\tilde{M}})$ from N emission lines, we need to use a grid of photoionization models with $\tilde{M}$ free parameters to have a matrix of predictions of the size $\mathrm{NxM_1x...xM_{\tilde{M}}}$.

As observations and predictions are compared, we must define a metric, which accounts for the differences among them. In the case of HCm, we define the metric between the observation (F_i) and the prediction $\left(T_i\left(Y_{j_1}, Y_{j_2}, ...Y_{j_M}\right)\right)$ as:

$$\chi_{i,j_1,j_2,...,j_M} = \frac{\left(F_i - T_i\left(Y_{j_1}, Y_{j_2}, ...Y_{j_M}\right)\right)^2}{T_i\left(Y_{j_1}, Y_{j_2}, ...Y_{j_M}\right)} \equiv \frac{\left(F_i - T_{i,j_1,j_2,...,j_M}\right)^2}{T_{i,j_1,j_2,...,j_M}} \tag{2.6}$$

Let us assume that we want to estimate the property Y_L. Then, the metric distance associated to each value of Y_L explored in the grid is given by:

$$\chi_{i,j_L} = \sum_{j_1}\sum_{j_2}....\sum_{j_M}\chi_{i,j_1,j_2,...j_L,...,j_M} = \sum_{j_1}\sum_{j_2}....\sum_{j_M}\frac{\left(F_i - T_{i,j_1,j_2,...j_L,...,j_M}\right)^2}{T_{i,j_1,j_2,...j_L,...,j_M}} \tag{2.7}$$

And, considering all the N-observed emission lines, that distance is given by:

$$\chi_{j_L} = \left[\sum_{i}^{N}\chi^2_{i,j_L}\right]^{1/2} \tag{2.8}$$

Therefore, we can obtain an estimation of the property Y_L, from a set of N emission lines, by weighting the value of the property in each model with the distance given by the weight sum:

$$\hat{Y}_L = \left[\sum_{j_L}^{M}\frac{Y_{j_L}}{\chi^2_{j_L}}\right]\cdot\left[\sum_{j_L}^{M}\frac{1}{\chi^2_{j_L}}\right]^{-1} \tag{2.9}$$

The uncertainty in the estimation is calculated considering: i) the uncertainty in the measured emission line; and, ii) the step in the grid for the desired property. In a Monte Carlo procedure of N iterations, the nominal value of the observed emission line F_k is randomly drawn from the range $[F_k - \delta F_k, F_k + \delta F_k]$, the estimation of the property is performed again with that random value, and the error is given by the quadratic weight sum of the dispersion:

$$\left(\Delta\hat{Y}_L\right)^2 = \left[\sum_{g}^{N_{monte}}\frac{\left(\hat{Y}_L - \left(\hat{Y}_L\right)_g\right)^2}{\chi^2_g}\right]\cdot\left[\sum_{g}^{N_{monte}}\frac{1}{\chi^2_g}\right]^{-1} \tag{2.10}$$

As compared to the pure Bayesian method, in which a loss function is defined and then minimized to provide the best fitting model, the bayesian-like approach offers a different solution. First of all, as all models are weighted and considered, even if the observations are not reproduced by any individual model, the combination of some models might reproduce it (increasing also the uncertainty). Second, in the case where two models might show the lowest χ (i.e. are the most favorable), this methodology accounts for both of them whereas in the minimization method only one is forced to be selected. And, third, in the case that a free parameter is redundant (i.e. it shows a strong dependence on other free parameter), then models will be equally weight not affecting the solution for the parameter, whereas in the pure Bayesian method this would lead to a strong degeneracy.

2.4.1.2 *Implementation in the code*

The code estimates chemical abundances O/H and N/O as well as U from a selected (see Sec. 2.4.2 for more details) grid of models that have these three properties as free parameters. HCm optimizes the Bayesian-like approach in two ways. First of all, rather than considering single emission line fluxes, the code uses emission line ratios (e.g. N2O2, R23, S34, see Sec. 2.4.3 for more details) that are sensitive to the free parameters. This reduces degeneracy and synthesized the information. Secondly, the code estimates the three quantities in two steps: i) an estimation of N/O (alternatively C/O for UV emission lines) which is assumed to be mostly independent from the other two free parameters (O/H and U); and, ii) a simultaneous estimation of O/H and U from an N/O-constrained grid of models based on that preliminar estimation (Pérez-Montero, 2014).

Emission line ratios tracing N/O are expected to show little to none dependence on O/H or U (e.g. Florido et al., 2022; Pérez-Montero & Contini, 2009; Spinoglio et al., 2021), so the weight χ derived from Eq. (2.7) reflects the same negligible dependence, ensuring a robust independent estimation. Once N/O is constrained, the grid of models (3D) can be collapsed into a smaller grid (almost 2D) accounting for those models whose N/O are compatible with the estimation. Hence, the weights χ estimated in this second iteration will only depend on O/H and U, avoiding any possible additional dependence on N/O if the whole grid were considered. Moreover, this second iteration with constrained N/O allows the usage of N emission lines to perform the estimation.

Once all parameters are estimated, the code performs the Monte Carlo iteration process to calculate the uncertainty of each estimation. This uncertainty mostly depends on: i) the accuracy of the emission line measurements; ii) the number of input emission line ratios measured in the observed spectrum; and, iii) the step in the grid of photoionization models. We show in Fig. 2.12 a scheme on how HCm works.

2.4.2 *Grids of models*

The core of the HCm is the grid of models that are used for the estimation (which is the same for all cases). This grid of models must take into account all the ingredients reviewed in Sec. 2.3.2: i) the dominant source of the ionization (e.g. starbursts, AGNs, pAGBs); ii) the expected geometry of the gas; and, iii) the chemical composition of the gas. Therefore, before applying HCm it is mandatory that the user makes a choice on the grid to be used, preferentially based on observational constraints such as diagnostic diagrams or multiwavelength studies.

2.4.2.1 *Default grids*

Over the years, we have built a series of photoionization models that reflect the most common ionizing scenarios. In this section we review the grids of photoionization models that we have built and analyze for which ionizing scenario is more suitable. All grids of models have been calculated with CLOUDY v17 (Ferland et al., 2017).

- **POPSTAR**: This grid of models was calculated from an ionizing cluster SED from the synthesis evolutionary model POPSTAR (Mollá et al., 2009), with a burst of 1 Myr[10] and the IMF from Chabrier (2003). The metallicity of the stellar population is assumed to be the same one as the gas. The geometry of the gas is assumed to be plane-parallel and a constant density value of 100 cm^{-3} and filling factor of 0.1 are assumed. The amplitude of the SED is given by the ionization parameter $\log(U)$ (Eq. (1.11)) which is a free parameter in the range $[-4.0, -1.5]$ with steps of 0.25 dex. This is the expected scenario in SFGs (Pérez-Montero, 2014).

- **BPASS**: This grid of models was calculated assuming an ionizing cluster SED from BPASS v2.1 (Eldridge et al., 2017), assuming a 1 Myr burst with the Salpeter (1955) IMF for $x = -1.35$ and a top-heavy limit of $M_{up} = 300 M_{\odot}$. The metallicity of the stellar population is assumed to be the same as that of the gas. The geometry and density parameters for the gas are the same ones as those assumed for the POPSTAR grid. The ionization parameter is again free in the range $[-4.0, -1.5]$ with steps of 0.25 dex. This assumptions mimic the expected conditions of the ISM in extreme emission line galaxies (Pérez-Montero et al., 2021).

- **pAGB**: These grids of models were calculated assuming non-local thermodynamic equilibrium (NLTE) stellar atmospheres from Rauch (2003), assuming $\log(g) = 6$ nd normalized fractions of: He $= 0.33$, C $= 0.50$, N $= 0.02$ and O $= 0.15$. Three different effective temperatures are considered: $5 \cdot 10^4$, $1 \cdot 10^5$ and $1.5 \cdot 10^5$ K. The ionized gas is assumed to follow as well a plane-parallel geometry, with a constant density of 500 cm^{-3} and a filling factor of 0.1. The ionization parameter varies in the range $[-4.0, -0.5]$, in steps of 0.25 dex. This is the proposed scenario for retired galaxies and some LINER-like galaxies (Oliveira et al., 2024a; Pérez-Díaz et al., 2025).

- **AGN power laws**. These grids of models were calculated assuming that the AGN SED is given by two components: a Big Blue Bump whose peak is at 13.6 eV, and a power law given by $\alpha_X = -1$. To model different AGNs, we used different values of the spectral index α_{OX} $[-0.8, -1.0, -1.2, -1.4, -1.6, -1.8, -2.0]$, i.e., the power law fitting the continuum between 2 keV and 2500 Å. The geometry is again plane-parallel, with a constant density of 500 cm^{-3} and a filling factor of 0.1. The ionization parameter is again in the range $[-4.0, -0.5]$, in steps of 0.25 dex. These conditions mimic the expected ones for the NLR of AGNs (Dors et al., 2014; Pérez-Díaz et al., 2021; Pérez-Montero et al., 2019a).

- **Advection-dominated accretion flow (ADAF)**. This grid of models was calculated from the RIAD-SED code (Nemmen et al., 2014; Yuan et al., 2005, 2007), assuming the average conditions for reproducing LLAGN SEDs (Nemmen et al., 2014). This SED represents the departure from the power law SED due to the truncation of the accretion disk as a consequence of inefficient accretion. The rest of the conditions (geometry, density and ionization parameter) are identical to the ones used in the power law grids. This is the expected scenario for galaxies whose main ionizing source are LLAGNs (Nemmen et al., 2014; Pérez-Díaz et al., 2025).

For all the above mentioned grids of models, the initial grain conditions are governed by the dust-to-gas ratio which is assumed to be $7.5 \cdot 10^{-3}$ and the size distribution which follows the reported behavior by Mathis et al. (1977). The metal composition of the ISM is set by two values:

---

[10] Different cluster ages have been tested to check the effects in the estimation of chemical abundances, concluding that grid of models with different cluster ages introduce changes that are below the observational uncertainties. Overall, this age would be representative of young, nearly zero age main sequence, star-forming regions like the case of most giant HII regions studied.

the O abundance in the range [6.9, 9.1] with steps of 0.1 dex and the N/O ratio in the range [−2.0, 0.0] with steps of 0.125 dex. With the exception of C (which is assumed to have a fixed ratio given by the solar log(C/N) = 0.6, Asplund et al. 2009), the rest of elements scale with O from the solar abundance composition reported by Asplund et al. (2009).

Two stopping criteria for each model computation in each grid have been considered: when the ratio of H^+ drops below 98% or 2%. In the case of SFG and EELGs, it has been demonstrated that both assumptions predict similar emission line ratios (Pérez-Montero, 2014; Pérez-Montero et al., 2021), but in the case of AGN models, this selection might introduce changes in the estimation of the ionization parameter (Pérez-Díaz et al., 2021, 2022).

2.4.2.2 *Constraints on the grids*

In some cases, due to degeneracies in the emission line ratios involved or due to the lack of measurements, it is necessary to provide a reduced number of models in the used grids to perform the calculation. These are called *constraint laws*, and they are based on empirical observations, although all of them have a theoretical motivation. We show them in Fig. 2.13.

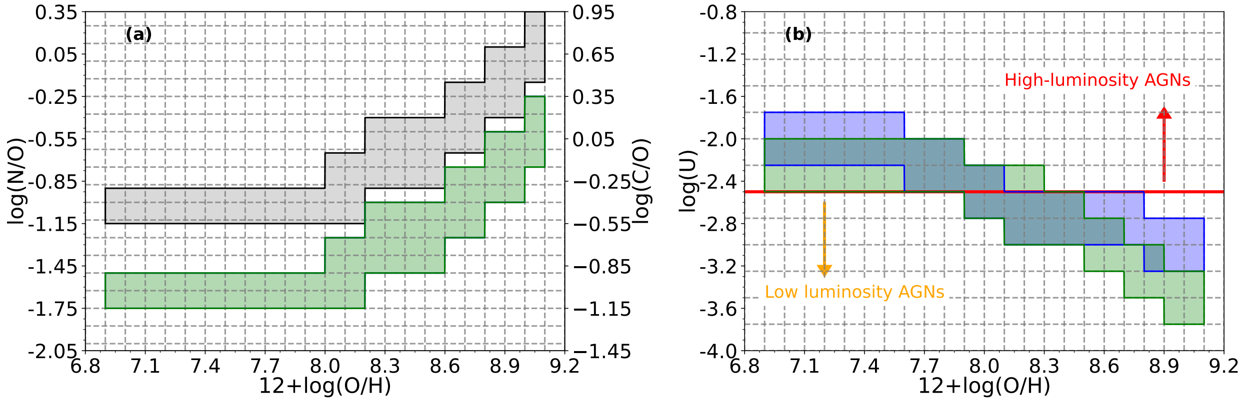

Figure 2.13: Graphical representation on the grid constraints assumed by HCm between N/O and O/H (a), and between U and O/H (b). In panel (a), green lines marked the limits for SFG models (EELGs use the same ones) and black lines for AGN models. In panel (b), green lines marked the limits for SFG models and blue lines for EELG models. AGN models are only constrained by setting and upper limit or lower limit to the ionization parameter.

In the case that no nitrogen or carbon lines are measured, then it is impossible to provide an estimation of the log(N/O) or log(C/O) ratio. In this case, HCm can assume the relations show in Fig. 2.13 (a), which represent the trend found in the majority of observed galaxies (Pérez-Montero, 2014; Pérez-Montero & Amorín, 2017; Pérez-Montero et al., 2019a). Notice that, by assuming these relations, then the log(C/O) and log(N/O) are no representative for the object, but rather the expected value in case the observed galaxy would follow the expected trend (see Sec. 1.3.2).

In the optical regime, all strong line ratios (not based on auroral lines) for SFGs show a dependence on the ionization parameter log(U). Hence, in order to break the degeneracy it is necessary to assume a relation between U and O/H. The code uses the standard relation reported in the literature (Dopita et al., 2006; Massey et al., 2005; Pérez-Díaz et al., 2021; Pérez-Montero, 2014; Pérez-Montero et al., 2021). Although there is not yet a clear picture on what drives these dependence (Dopita et al., 2006; Massey et al., 2005), it is more likely associated to the fact that ratios between different O ion emission lines are sensitive not only to the ionization parameter, but also to the effective temperature of the star (e.g. Pérez-Montero et al., 2023b; Vilchez et al., 1988), which is expected to decrease as more stars with higher abundances are coolers. Nevertheless, this result can only be applied to ionized gas surrounding a stellar source.

In the case of AGNs, some of the emission line ratios tracing the ionization parameter show a degeneracy due to the presence of higher ionized elements which are not traced. In that case, to break the degeneracy the code can constrain the ionization parameter in two regimes: low ionization ($\log(U) < -2.5$) and high ionization ($\log(U) > -2.5$). The choice is made essentially by the empirical fact the models have a turnover point around that limit (e.g. Pérez-Díaz et al., 2021).

2.4.2.3 *Customized grids*

Complementary to the large number of photoionization models already provided with the code, it is possible to implement a grid customized by the user. The key part of the code is that observations are compared to predictions following a χ^2-methodology, but the matrix of expected values can be obtained by different procedures (e.g. building empirical libraries from galaxy observations) and with different codes (e.g. MAPPINGS). In a similar fashion, the constraints on the grid of models to break degeneracies when not all emission lines are provided can be modified or removed.

Table 2.5: HII-CHI-Mistry flavors and their inputs. Last three columns show the emission line ratios used to calculate the χ^2 of the final estimation. *In the case of the UV version, this is replaced by log(C/O). †The temperature sensitive ratio $R_{O3} \equiv$ [O III]λ5007Å/O III]λ1665Å. ‡The temperature sensitive ratios $R_{O3} \equiv$ [O III]λ5007Å/[O III]λ4363Å, $R_{O2} \equiv$ [O II]λ3726, 3729Å/[O II]λ7319, 730Å, $R_{N2} \equiv$ [N II]λ6584Å/[N II]λ5755Å and $R_{S3} \equiv$ [S III]λ9069Å/[S III]λ6312Å. References: Pérez-Montero (2014), Pérez-Montero and Amorín (2017), Pérez-Montero et al. (2019a), Pérez-Díaz et al. (2021), Fernández-Ontiveros et al. (2021), Pérez-Díaz et al. (2022), Pérez-Montero et al. (2023a).

Flavor	Input lines	Type	N/O*	O/H	U
HCm-UV	Lyα, [N V] λ1239Å, C IV λ1549Å, He II λ1640Å, O III]λ1665Å, C III]λ1909Å, H$_\beta$, [O III]λ5007Å	SFG	$R^{\dagger}_{O3}$, C3O3	$R^{\dagger}_{O3}$, N5, N5He2, C34, C34He2, C34Hb	C3C4, N5He2, C34He2
		AGN	$R^{\dagger}_{O3}$, C3O3	$R^{\dagger}_{O3}$, N5, N5He2, C34, C34He2, C34Hb	C3C4, N5He2, C34He2
HCm	[O II] λ3726, 3729Å, [Ne III]λ3868Å,[O III]λ4363Å, [O III]λ4959Å, [O III]λ5007Å, [N II]λ5755Å, [S III]λ6312Å, [S II]λ6717, 6731Å, [O II]λ7319, 7330Å, [S III]λ9069Å, [S III]λ9532Å	SFG	$R^{\ddagger}_{O3}$,$R^{\ddagger}_{O2}$, $R^{\ddagger}_{N2}$, $R^{\ddagger}_{S3}$, N2O2 N2S2, O3N2	$R^{\ddagger}_{O3}$,$R^{\ddagger}_{O2}$, $R^{\ddagger}_{N2}$, $R^{\ddagger}_{S3}$, R23, S23, R2Ne3	O2O3, O2Ne3, O3S2, S2S3 N2S3
		AGN	$R^{\ddagger}_{O3}$,$R^{\ddagger}_{O2}$, $R^{\ddagger}_{N2}$, $R^{\ddagger}_{S3}$, N2O2 N2S2, O3N2	$R^{\ddagger}_{O3}$,$R^{\ddagger}_{O2}$, $R^{\ddagger}_{N2}$, $R^{\ddagger}_{S3}$, R23, S23, R2Ne3	O2O3, O2Ne3, O3S2, S2S3 N2S3
HCm-IR	H I λ4.05μm, [Ar II] λ6.98μm, H I λ7.46μm, [Ar V] λ7.90μm, [Ar III] λ8.99μm, [S IV] λ10.5μm, H I λ12.4μm, [Ne II] λ12.8μm, [Ar V] λ13.1μm, [Ne V] λ14.3μm, [Ne III] λ15.5μm, [S III] λ18.7μm, [Ne V] λ24.3μm, [O IV] λ26μm, [S III] λ33μm, [O III] λ52μm, [N III] λ57μm, [O III] λ88μm, [N II] λ122μm, [N II] λ205μm	SFG	N3O3, N3S34	Ne23, Ar23 O34, S34, N23	Ne2Ne3, Ar2Ar3, O3O4, S3S4, N2N3, O3N2
		AGN	N3O3, N3S34	Ne235, Ar235, O34, S34, N3	Ne23Ne5, Ar23Ar5, O3O4, S3S4

In this case, it is important to note that the accuracy and reliability of the estimations are directly tied to the models and assumptions introduced in the customized grid. The default grids provided with the code have been tested over numerous samples of galaxies (e.g. Pérez-Díaz et al., 2021, 2025; Pérez-Montero, 2014; Pérez-Montero et al., 2019a, 2021), but any personalized grid should be tested in a control sample to have a clear picture of its performance.

2.4.3 *Flavors of the code*

As photoionization models predict the whole emission line spectrum, from X-rays to radio, HCm has been developed to take advantage of the grids of models at different ranges. Particularly, HCm has been designed to operate with UV, optical or IR emission lines, each regime has its own version of the code which we call *flavor*. Whereas the overall methodology remains unchanged, the lines and calculated ratios used differ depending not only on the grid of models, but also on the spectroscopic regime (i.e. on the emission line input).

We provide in Tab. 2.5 an overview on the input emission lines adopted and the ratios that are calculated and used for the estimation[11]. The code only makes a preference when auroral emission lines are introduced as inputs (UV and opt flavors), but it must be noticed that the code does not make a selection based on the quality of the emission line measurements.

2.5 GALAXY SAMPLES

Through this work, we have used several galaxy samples to both test the performance of our methodology and to perform studies on chemical enrichment of the ISM. We briefly review these samples.

2.5.1 *Samples based on optical spectroscopic observations*

2.5.1.1 *SDSS DR9 Galspec*

For Chapters 1 and 2, we used the Sloan Digital Sky Survey Data Release 9 GalSpec Catalogue (SDSS DR9 GalSpec; Ahn et al., 2012), which provides the already reduced, continuum-subtracted, and fitted optical spectroscopic data for more than $1,400,000$ galaxies. Particularly, from the GalSpec database[12] we selected all objects classified as galaxies. This sample was used to generate Fig. 1.14 and 1.15.

Later on, we constrained the sample to those galaxies classified as bona fide SFGs and whose spectral lines were measured with less than a 20% uncertainty (relative error), to perform the chemical diagnostic with HCm, assuming POPSTAR grid of models and the following reddening-corrected emission lines: [O II]$\lambda 3727$Å, [Ne III]$\lambda 3868$Å, [O III]$\lambda 5007$Å, [N II]$\lambda 6584$Å, and [S II]$\lambda 6717$Å+[S II]$\lambda 6731$Å. Reddening correction was performed assuming Howarth (1983) extinction law and $R_V = 3.1$. We also retrieved ancillary data of their stellar masses, star formation rates and stellar ages. This sample was used to generate Fig. 1.16 (a), 1.18, 1.19, 1.20 and 2.2.

2.5.1.2 *SDSS-IV MaNGA LINER-like sample*

SDSS-IV MaNGA survey[13] is an integral field spectroscopic survey with over $10,000$ local galaxies (Blanton et al., 2017; Bundy et al., 2015). From that sample, we selected those galaxies whose central region shows LINER-like emission, obtaining a sample of 105 LINERs. Details[14] on the selection, treatment and analysis of this sample are found in Chapters 3 and 4. Additionally, Fig. 1.16 (b) and 1.17 have been generated as well from that sample.

---

[11] In this work we focus on the optical and infrared flavors of the code, but the reader is encouraged to look up at the references for the UV version (Pérez-Montero & Amorín, 2017; Pérez-Montero et al., 2023a), as well as its use for the softness and hardness diagnostics of the ionizing sources (Pérez-Montero et al., 2019b, 2020, 2023b, 2024, 2025).

[12] Accessible through https://www.sdss3.org/dr9/algorithms/galaxy_mpa_jhu.php.

[13] Accessible through https://www.sdss4.org/dr17/manga/.

[14] Emission lines were retrieved using ELF3D code (Zinchenko private communication), following the same prescriptions as in Zinchenko et al. (2016).

2.5.2 *Samples based on IR spectroscopic observations*

2.5.2.1 *IDEOS galaxy sample*

The Infrared Database of Extragalactic Observables from Spitzer[15] (Hernán-Caballero et al., 2016; Spoon et al., 2022) is a public catalog of 77 fitted observables of 3335 galaxies in the range [5.4μm, 36μm] observed with *Spitzer*/ICS. From this initial sample, we selected those galaxies classified as SFG and AGN based on their PAH features and the relative emission of neon emission lines. A detailed explanation, analysis and discussion is found in Chapter 6.

2.5.2.2 *The combined AKARI - Spitzer - Herschel - SOFIA sample*

Three different samples were created merging the available spectroscopic observations from the near- to far-IR from different observatories:

- SFG dominated sample composed by 28 dwarf galaxies, 19 active star-forming galaxies and nine low-redshift (U)LIRGs. This sample, compiled by Fernández-Ontiveros et al. (2021), has the spectroscopic measurements of emission lines from the near- (*AKARI*/IRC), mid- (*Spitzer*/IRS) and far-IR (*Herschel*/PACS and *SOFIA*/FIFI-LS). Optical counterpart observations were also retrieved from the literature (see Fernández-Ontiveros et al., 2021, for more details).

- AGN dominated sample composed by 58 active galaxies with [Ne v] emission. As in the previous case, the sample combines IR spectroscopic observations from the near- to far-IR regime. Details on the sample are found in Chapter 5.

- (U)LIRG sample from IDEOS with *AKARI*/IRC observations of the H recombination line Brackett-α and, in some cases, *SOFIA*/FIFI-LS of far-IR emission lines. This sample is used for the analysis presented in Chapter 7.

---

[15] Accessible through http://ideos.astro.cornell.edu/.

Part II

RESULTS

3

TRACING THE NUCLEAR ABUNDANCES OF OXYGEN AND NITROGEN IN LINERS WITH VARIED IONIZING SOURCES

Chapter based on the publication: B. Pérez-Díaz, E. Pérez-Montero, I. A. Zinchenko and J. M. Vílchez (2025) *"Chemical enrichment in LINERs from MaNGA: I. Tracing the nuclear abundances of oxygen and nitrogen in LINERs with varied ionizing sources", published in Astonomy & Astrophysics, volume* 694, *A*18, *doi:*10.1051/0004-6361/202452862.

3.1 ABSTRACT

The chemical enrichment in low-ionization nuclear emission-line regions (LINERs) is still an issue with spatial resolution spectroscopic data because we lack studies and because the nature of their ionizing source is uncertain, although they are the most abundant type of active galaxies in the nearby Universe. Considering different scenarios for the ionizing source (hot old stellar populations, active galactic nuclei, or inefficient accretion disks), we analyze the implications of these assumptions to constrain the chemical content of the gas-phase interstellar medium. We used a sample of 105 galaxies from the survey called Mapping Nearby Galaxies at Apache Point Observatory (MaNGA), whose nuclear central spaxels show LINER-like emission. For each scenario we considered, we built a grid of photoionization models (4928 models for each considered ionizing source) that were later used in the open-source code HII-CHI-Mistry. This allowed us to estimate chemical abundance ratios such as 12+log(O/H) or log(N/O) and to constrain the ionization parameters that characterize the ionized interstellar medium in these galaxies. The oxygen abundances in the nuclear region of LINER-like galaxies are spread over a wide range $8.08 < 12+\log(O/H) < 8.89$, with a median solar value (in agreement with previous studies) when models for active galactic nuclei are considered. Nevertheless, the nitrogen-to-oxygen ratio we derived is much less affected by the assumptions on the ionizing source and indicates suprasolar values ($\log(N/O) = -0.69$). By comparing the different scenarios, we show that if hot old stellar populations caused the ionization of the interstellar medium, a complex picture (e.g., outflows and/or inflows that scale with the galaxy chemical abundance) would be needed to explain the chemical enrichment history, whereas the assumption of active galactic nucleus activity is compatible with the standard scenario that is found in most galaxies.

3.2 INTRODUCTION

Among the different approaches for analyzing the evolution of galaxies, the metal content of the interstellar medium (ISM) is a very important constraint. While Big Bang nucleosynthesis allows us to explain the majority of hydrogen (H), helium (He), lithium (Li), and deuterium (D) in the ISM (Cyburt et al., 2016), nearly all the remaining elements are produced by means of the different star formation processes that govern the evolution of galaxies (e.g. Duarte Puertas et al., 2022; Kobayashi et al., 2020a), which are ultimately shaped by other processes such as inflows, outflows, or merger events that affect the hydrostatic equilibrium within galaxies (e.g. Pérez-Díaz et al., 2024a; Sharda et al., 2024).

Since the pioneering works from M. Peimbert and Costero (1969), M. Peimbert (1967), Searle (1971), and Searle and Sargent (1972), the chemical content of the gas-phase ISM is generally traced by the oxygen abundance since it is the most abundant element in mass (∼ 55%; M. Peimbert et al., 2007), and its presence helps to cool the nebula through emission lines that are detected in the ultraviolet (UV), optical (Opt), and infrared (IR) regimes. The brightest of these lines arise from collisional excitation. The oxygen abundance, expressed relative to hydrogen [12+log(O/H)], is affected by flow dynamics that can alter one or both quantities. Hence, complementary information is required to constrain the chemical enrichment stage of the ISM. In a simplified picture of the complex nucleosynthesis of elements such as nitrogen (N) and carbon (C), they are produced by massive stars (primary), but an additional channel of production arises when oxygen is already present in the ISM from which intermediate-mass stars were born, allowing them to produce N and C via CNO cycles (secondary; e.g. Henry et al., 2000). Complexity arises from other important aspects in chemical evolution models such as the time delay of ISM pollution from intermediate-mass stars (e.g. Vincenzo et al., 2016), the role of fast-rotator stars (e.g. Grisoni et al., 2021), or variations in the star formation histories (e.g. Mollá et al., 2006). Thus, by analyzing the log(N/O) and/or log(C/O) ratios, we gain additional information to constrain the chemical enrichment history in galaxies.

The presence of these elements in the gas-phase ISM helps to cool it by emission lines, which are used to estimate the chemical content. Recipes for estimating chemical abundances in the gas-phase ISM have been proposed, exploited, and perfected over the past decades. All of them can be summarized into three main groups. The first group relies on using auroral emission lines, such as [O III]λ4363Å, [N II]λ5755Å and/or [S III]λ6312Å as well as other collisionally excited lines (CEls) to constrain the physical properties of the gas-phase ionized ISM such as the electron temperature (T_e) and density (n_e). This is called the direct method or T_e-method (e.g. Pérez-Montero & Amorín, 2017). Some problems that arise from this method are i) the faint nature of these auroral emission lines, ii) the lack of emission lines from high-ionized species (e.g., [OIV], [SIV], and [NeV]) in the optical range imposes an assumption on the ionization correction factors (ICFs), and iii) the fluctuations of the physical properties required, such as the temperature, might induce systematic uncertainties in their determination (Méndez-Delgado et al., 2023), although some ratios such as log(N/O) are not affected by these fluctuations. The second technique relies on the use of photoionization models such as CLOUDY (Ferland et al., 2017), MAPPINGS (Sutherland & Dopita, 2017) , or SUMA (Contini & Aldrovandi, 1983), in which the physical and chemical conditions in the gas-phase ISM as well as the source of ionization are given and are then constrained either to directly match the observations with customized models (e.g. Pérez-Montero et al., 2010) or by Bayesian approaches such as HII-CHI-MISTRY (HCM; Pérez-Montero, 2014), NEBULABAYES (Thomas et al., 2018), or HOMERUN (Marconi et al., 2024). Finally, a different technique that is more widely used because it is easy to apply is the use of strong emission-line ratios or combinations that correlate with the chemical abundances, which are calibrated by using one of the other two previous techniques. A summary of these calibrators can be found in Tab. 1 from Maiolino and Mannucci (2019).

These techniques have been used over decades (Andrews & Martini, 2013; Fernández-Ontiveros et al., 2021; Lequeux et al., 1979; McClure & van den Bergh, 1968; Pérez-Montero & Díaz, 2005; Thuan et al., 1995; Vilchez et al., 1988), especially for analyzing the chemical composition of the gas-phase ISM in star formation dominated galaxies (SFGs) over different cosmic times from either slit spectroscopy or integral field spectroscopy. However, to properly constrain the galaxy chemical evolution, the studies cannot focus on SFGs alone, but also need to study galaxies hosting active galactic nuclei (AGNs), which have an important role not only in galaxy evolution (e.g. de Nicola et al., 2019; Page et al., 2004) because AGN feedback affects the gas cooling, and consequently, the star formation (Capelo et al., 2023; Morganti, 2017), but also in cosmological structures (e.g. Eckert et al., 2021; Gitti et al., 2012; Nobels et al., 2022). However, studies of the chemical content of the gas-phase ISM within galaxies hosting AGNs are rather rare. The gas-phase ISM surrounding the supermassive black hole (SMBH) in AGNs is divided into two different regions: the broad-line region (BLR), which is located close ($r \sim 0.01$ pc; Mandal et al., 2021) to the SMBH and is characterized by high densities ($n_e > 10^9$ cm^{-3}) and broad emission-line components (> 1000 km/s) (Peterson, 2006); and the narrow-line region, which is located at greater distances (r $\gtrsim 1$ pc; Peterson et al., 2013) and has lower densities ($n_e \sim 10^3$ cm^{-3}), and narrower emission-line components (~ 500 km/s) (Peterson, 2006). The BLR presents several problems for the estimation of its abundance composition both observationally due to the high covering factors (Gaskell, 2009) and theoretically due to the complex gas dynamics governing its motion (Gaskell, 2009) or even the high variability in the broad emission lines that trace the BLR (Ilić et al., 2017). These problems disappear for the NLR because the physical properties are very similar to those of HII regions.

Nevertheless, the determination of chemical abundances in the NLR presents some caveats. It was shown by Dors et al. (2015) that when the direct method is used to constrain the chemical abundances, unexpectedly low chemical abundances are obtained that are not found with other techniques. Moreover, the lack of a detection in the optical of emission lines from highly ionized species, which are expected because the ionizing front from the AGN is harder (Pérez-Díaz et al., 2022, 2024a), adds more uncertainty to its estimates. Hence, most of the techniques for studying chemical abundances in the NLR of AGNs rely on either using photoionization models to directly estimate their abundances or on providing calibrations to estimate them in larger samples (e.g. Carvalho et al., 2020; Dors et al., 2023; Pérez-Díaz et al., 2021, 2022; Pérez-Montero et al., 2019a).

An additional bias in the studies of chemical abundances in AGNs is that they mainly target Seyferts 2, that is, highly ionized AGNs, whereas low-luminosity AGNs (LLAGNs), such as LINERs, are the most common type of AGN in the local Universe (Ho et al., 1997). Studies of chemical abundances in LLAGNs are even rarer. One of the main reasons for this rarity is the fact that there is no consensus in the literature about the source of ionization of LINERs. Possible sources include i) sub-Eddington accretion (Ho, 2009; Kewley et al., 2006) onto SMBHs, which can later affect the flow of gas by even truncating the disk through advected-dominated flows (ADAFs; Nemmen et al., 2014); ii) hot old stellar populations that are dominated by post-asymptotic giant branch (pAGB) stars (Binette et al., 1994; Stasińska et al., 2008); and iii) fast radiative shocks (Allen et al., 2008; Dopita & Sutherland, 1995).

Annibali et al. (2010) targeted 67 early-type galaxies in the local Universe in one of the first works that estimated the oxygen abundances in a statistically significant sample of LLAGNs, since of these galaxies ($\sim 72\%$) hosted LINERs. However, the authors relied on calibrations that were obtained from photoionization models assuming AGNs (Storchi-Bergmann et al., 1998) as the source of ionization, or on empirical calibrations taken from the analysis of early-type galaxies, which would mimic the conditions in their sample (Kobulnicky et al., 1999). Their resulting oxygen abundances were in the range $8.49 < 12+\log(\mathrm{O/H}) < 9.01$, and most of them were slightly suprasolar[1].

More recently, (Pérez-Díaz et al., 2021) systematically analyzed 16 Seyferts 2 and 40 LINERs from the Palomar Spectroscopic Survey (Ho et al., 1997), complemented by an additional sample of 25 LINERs from (Pović et al., 2016). To estimate the oxygen abundances, the authors employed HII-CHI-Mistry (hereinafter HCm; Pérez-Montero, 2014; Pérez-Montero et al., 2019a), a Bayesian-like code that relies on a large grid of photoionization models, assuming AGNs as the source of ionization, because they found that multiwavelength studies indicated AGN feature emissions in X-rays and radio wavelengths. The authors reported that some ($\sim 15\%$) LINERs were characterized by unexpectedly low oxygen abundances ($12+\log(\mathrm{O/H}) < 8.3$). Later on, Oliveira et al. (2022) presented an analysis of the nuclear region of 43 LINERs from the SDSS IV - MaNGA survey (Blanton et al., 2017; Bundy et al., 2015) from photoionization models assuming pAGB stars as the source of ionization. They concluded that their sample of LINERs was characterized by solar-like oxygen abundances of $8.54 < 12+\log(\mathrm{O/H}) < 8.84$. A similar result was found in a recent study by Oliveira et al. (2024b), who reported that weak AGNs present oxygen abundances in the range

---

[1] Hereinafter, we assume the solar abundances reported by Asplund et al. (2009), that is, $12+\log(\mathrm{O/H})_\odot = 8.69$, $12+\log(\mathrm{N/H})_\odot = 7.83$, and $\log(\mathrm{N/O})_\odot = -0.86$.

$8.50 < 12+\log(O/H) < 8.90$. Only the study by (Krabbe et al., 2021), who only analyzed one LINER galaxy (UGC 4805) based on MaNGA data and photoionization models, simultaneously explored the AGN and the pAGBs ionizing scenarios. While their finding of metallicity trends did not provide a conclusive clue, they suggested that the pAGB scenario is the most favorable based on the position of this nucleus on some specific diagnostic diagrams for the observed emission lines, as well as on the observed high degree of ionization.

Nitrogen abundances in LLAGNs have been analyzed even more infrequently. Except for the pioneering work of Pérez-Díaz et al. (2021), only the recent work by Oliveira et al. (2024a) analyzed the $\log(N/O)$ abundance ratio and its relation with the $12+\log(O/H)$ abundance in order to constrain the chemical enrichment of these objects. Although both studies employed photoionization models and assumed different ionizing sources (AGNs and pAGBs, respectively), the results were consistent. This shows that LINERs tend to have slightly higher $\log(N/O)$ than is reported in SFGs.

Exploiting the capabilities of integral field spectroscopic (IFS) data from the SDSS IV - MaNGA survey (Blanton et al., 2017; Bundy et al., 2015), we present a series of papers that analyze the spatially resolved chemical enrichment of the gas-phase ISM in galaxies hosting LINER-like nuclear emission. We consider for the first time different scenarios that might explain the observed emission in a statistically significant sample of galaxies. This first paper of the series focuses on the determination of nuclear chemical abundances in this sample, and it is organized as follows. In section 3.3 we explain the selection of the sample of galaxies hosting LINER-like emission. We also introduce other different criteria we used in this study. In section 3.4 we discuss the method we employed to estimate the chemical abundances in our sample. In section 3.5 we present the main results of this study, and we discuss them in section 3.6. In section 3.7 we summarize the main conclusions. We assumed the cosmological parameters given by $\Omega_m = 0.3$, $\Omega_\Lambda = 0.7$, and $H_0 = 67$ km/s/Mpc.

3.3 SAMPLE SELECTION

3.3.1 *MaNGA data and emission-line measurements*

The Mapping Nearby Galaxies at Apache Point Observatory (MaNGA; Bundy et al., 2015) is part of the Sloan Digital Sky Survey IV (SDSS IV; Blanton et al., 2017). For this work, we used data release 17 (DR17; Abdurro'uf et al., 2022). We used individual spaxels whose size was significantly smaller than that of the point spread function (PSF) in the MaNGA datacubes. The spatial resolution of these cubes has a median full width at half maximum (FWHM) of 2.54 arcsec (Law et al., 2016).

We examined the MaNGA spectra as outlined in Zinchenko et al. (2016, 2021). Briefly, we used the code STARLIGHT (Asari et al., 2007; Cid Fernandes et al., 2005; Mateus et al., 2006) to fit the stellar background across all spaxels, adapting it for parallel datacube processing. Simple stellar population (SSP) spectra from Bruzual and Charlot (2003) evolutionary synthesis models were used for stellar fitting, and we subtracted them from the observed spectrum for a pure gas spectrum. Then, we fit emission lines using our ELF3D code. Each emission line was fit with a single-Gaussian profile. For each spectrum, we measured the fluxes of the [O II]$\lambda,\lambda3726,3729$Å (hereinafter [O II]$\lambda3727$Å), [Ne III]$\lambda3868$Å, H_β, [O III]$\lambda4959$Å, [O III]$\lambda5007$Å, [N II]$\lambda6548$Å, H_α, [N II]$\lambda6584$Å, and [S II]$\lambda,\lambda6717,6731$Å lines with a signal-to-noise ratio (S/N) above 3.

3.3.2 *Sample classification*

From the original sample of galaxies presented in the SDSS IV - MaNGA survey, we initially selected the galaxies that were classified as LINERs in at least one of the three diagnostic (BPT) diagrams (Baldwin et al., 1981; Veilleux & Osterbrock, 1987) with the semi-empirical constraints proposed by Kauffmann et al. (2003) and Kewley et al. (2006). For this purpose, we used the emission lines H_β, [O III]λ5007Å, [O I]λ6300Å, [N II]λ6584Å, [S II]λ6717Å, and [S II]λ6731Å. Additionally, we complemented the diagrams with information on the equivalent width (EW) for H_α, as proposed by Cid Fernandes et al. (2011), since the strength of these feature allowed us to better distinguish between galaxies whose activity is dominated by strong AGNs (sAGN; $W_{H_\alpha} > 6$Å), weak AGNs (wAGN; Å $< W_{H_\alpha} <$ 6Å), and retired galaxies (RG; 0.5Å $< W_{H_\alpha} <$ 3Å). Below this limit lies the region that is dominated by passive galaxies (PG; $W_{H_\alpha} <$ 3Å), which are mainly line-less galaxies (Cid Fernandes et al., 2011).

To perform the classification, we focused our attention on the central spaxel for each galaxy. The median distance for our sample of galaxies is 150.56 Mpc within the range of [35.24 Mpc, 560.09 Mpc]. This implies that the angular sampling is 1.460 kpc on average within the range of [0.342 kpc, 5.4 kpc] for the 2″ fiber coverage in the sky (Bundy et al., 2015). This allowed us to capture most of the emission when an AGN is the source of ionization, considering the average sizes of the narrow- line region ($\sim 1-5$ kpc; Bennert et al., 2006a, 2006b). This range can also accommodate the case in which pAGB stars ionize the gas-phase ISM (e.g. Binette et al., 1994). While other authors integrated the flux in a circular aperture with a radius of 1 kpc (Oliveira et al., 2024a), we obtained that the average change in the emission-line flux ratios is smaller than 5%, and the classification and later results are therefore not affected by selecting either the central spaxel or an aperture of 1 kpc.

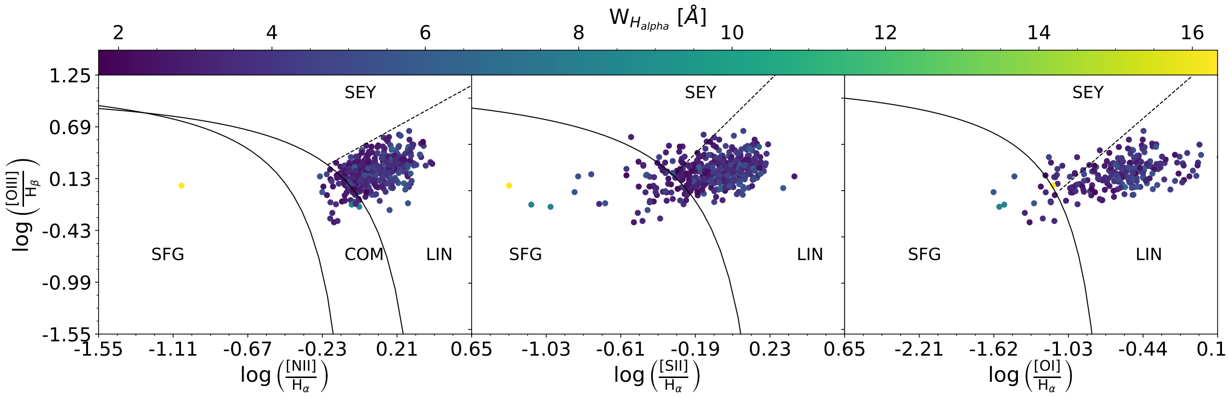

Figure 3.1: Diagnostic diagrams of the central spaxels in our sample of galaxies. The color bar shows the equivalent width for H_α (W_{H_α}). The solid and dashed lines represent the region limits as defined by Kewley et al. (2006), with the exception of the separation between Seyfert 2 and LINERs in the [N II]/H_α diagram, which was taken from Cid Fernandes et al. (2010). Each region is labeled as follows: SFG for star-forming galaxies, SEY for Seyferts, LIN for LINERs, and COM for composites.

We show in Fig. 3.1 the diagnostic diagrams for the central spaxels in our sample of galaxies from MaNGA. When we only consider the galaxies that are classified by at least one of the diagrams as LINERs, the sample contains 429 galaxies. Considering that problems of contamination from diffuse ionized gas (DIG) in [S II] are higher than in [N II] lines (Pérez-Montero et al., 2023b), we imposed the condition that galaxies are simultaneously classified as LINERs in all three diagrams. This reduced the sample to 329 galaxies, with values of W_{H_α} in the range [1.74Å, 9.25Å]. We cannot rule out the possibility of contamination from different ionizing sources (e.g. the combination of star formation and AGN activity; Davies et al., 2016), and we therefore complemented our classification with information from the WHAN diagram (Cid Fernandes et al., 2011). As shown in Fig. 3.2, the majority of our galaxies fall in the wAGN region, and some galaxies present slightly higher or lower values. Only one galaxy is classified as SFG due to the weak ratio of H_α and [N II]λ6584Å. Tab. 3.1 shows that the majority of the sample falls in the wAGN region (300; $\sim$ 70%). When we focus our

Table 3.1: Classification of the central spaxels from the preliminary sample of 429 galaxies selected from MaNGA. The headline row shows the classifications based on the WHAN diagram (Cid Fernandes et al., 2010, 2011). The first column shows the classification based on the BPT diagrams (Kauffmann et al., 2003; Kewley et al., 2006). In parentheses, we provide the relative percentage per group.

Classification	SFG	sAGN	wAGN	RG	PG	Total
LINERs	0 (0.00)	7 (2.13)	239 (72.64)	83 (25.23)	0 (0.00)	329 (76.87)
Composites	0 (0.00)	2 (4.17)	26 (54.17)	20 (41.67)	0 (0.00)	48 (11.21)
Ambiguous	1 (1.96)	0 (0.00)	35 (68.63)	15 (29.41)	0 (0.00)	51 (11.92)
Total	1 (0.23)	9 (2.10)	300 (70.09)	118 (27.57)	0 (0.00)	429 (100.00)

attention only on the galaxies that are classified as LINERs based on the BPT diagram (329; ∼ 77%), the percentage of wAGN-like galaxies is even higher than in the overall sample (∼ 73%).

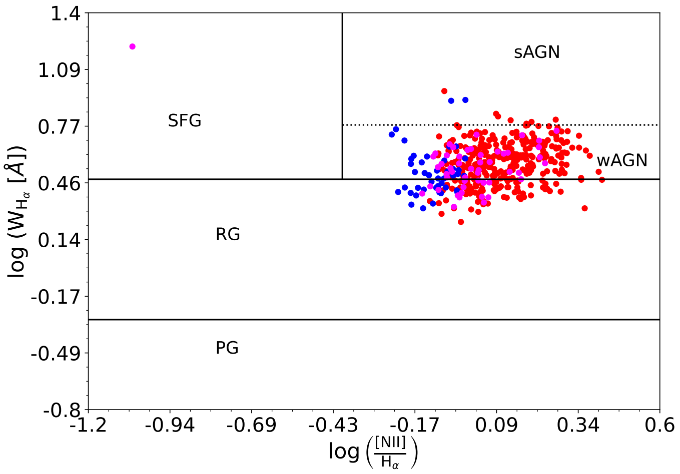

Figure 3.2: WHAN diagram, showing the region demarcations as provided by Cid Fernandes et al. (2010, 2011). The color code represents the classification as given by the BPT diagrams (see Figure 3.1): Red dots represent galaxies classified as LINERs, blue dots represent galaxies falling in the composite region, and magenta dots show galaxies without a clear classification. Each region is labeled as follows: SFG for star-forming galaxies, sAGN for strong AGNs, wAGN for weak AGNs, RG for retired galaxies, and PG for passive galaxies.

Another constraint we added to the sample selection is that the detected LINER-like emission mainly comes from the central spaxel. By restricting our sample with this criterion, we ensured i) that there are enough HII regions to analyze spatially resolved properties in all galaxies, such as metallicity gradients (second paper of these series), ii) that the origin of the LINER-like emission cannot be automatically excluded to be an AGN, and iii) that we can test for the same galaxy what occurs in their SF-dominated regions as opposed to the nuclear region. By adding this constraint, we obtained a sample of 105 galaxies, all of which show LINER-like emission according to all BPT diagrams for the central spaxels. Of these, 57 are classified as wAGN and 48 as retired galaxies according to the WHAN diagram (Cid Fernandes et al., 2010, 2011).

3.4 DETERMINING THE CHEMICAL ABUNDANCE

In this section, we present a detailed explanation of the method we used to estimate the chemical abundances as well as other physical parameters from the nebular emission that we retrieved from the MaNGA data. Because we accounted for possible different natures of the ionizing source in the nuclear regions of our sample of galaxies, we simultaneously analyzed all these scenarios by means of photoionization models.

3.4.1 *HII-CHI-Mistry*

To estimate the chemical abundances, we relied on the Bayesian-like Python code HII-CHI-MISTRY[2] (or HCM), which was originally developed by Pérez-Montero (2014) for HII regions, but was later extended to AGN sources (Pérez-Díaz et al., 2021; Pérez-Montero et al., 2019a) and extreme emission-line galaxies (Pérez-Montero et al., 2021) for the optical version. We made use of the optical version 5.5 of the code. HCM uses a grid of photoionization models with three free parameters: the chemical properties of the gas-phase ISM 12+log(O/H) and log(N/O), and the ionization parameter log(U), estimated by comparing emission line ratios that are sensitive to these parameters. Other important properties for the computation of photoionization models such as the geometry, the density, the dust-to-gas ratio, and the stopping criteria were explored for each grid of models. In a first iteration, the code estimates log(N/O) and uses this estimate to constrain the grid of models. This first estimation was always done because we have all necessary emission lines for this determination (e.g., [O II]λ3727Å, and [N II]λ6584). In a second iteration, the code performs an estimation of 12+log(O/H) and log(U). Since all these parameters are free in the grid of models, all quantities were estimated independently of each other, and no relation was assumed between them.

As input for HCM, we used the emission-line ratios [O II]λ3727Å, [Ne III]λ3868Å, [O III]λ5007Å, [N II]λ6584Å, and [S II]λ6717Å+[S II]λ6731Å, referred to H_β emission. All emission-line ratios were corrected for reddening assuming case B photoionization and an expected ratio of H_α and H_β of 3.1 for standard conditions in the NLR, that is, an electron density $n_e \sim 500$ cm^{-3} and an electron temperature $T_e \sim 10^4$ K (Osterbrock & Ferland, 2006), and the extinction curve from Howarth (1983) for $R_V = 3.1$.

3.4.2 *Grids of photoionization models*

Whereas HCM allowed us to perform the same method regardless of the source of ionization, the user must select the grid of photoionization models to be used in the estimation. The differences therefore emerge based on the assumed spectral energy distribution (SED). All models were computed using CLOUDY[3] v17 (Ferland et al., 2017)

In the case of HII regions, we chose a star formation cluster with an age of 1 Myr as the ionization source. We used the POPSTAR (Mollá et al., 2009) synthesis code for an initial mass function (IMF) that followed the trend reported by Chabrier (2003). The gas density was assumed to be 100 cm^{-3}. By allowing variation in the ionization parameter and metallicity, Pérez-Montero (2014) demonstrated that these models are able to reproduce the emission-line ratios observed in HII regions.

For the nuclear emission, we built different grids of photoionization models that accounted for all proposed scenarios to reproduce the LINER-like emission. We list them below.

- Active galactic nucleus SEDs composed of two components: The first component represents the big blue bump, which peaks at 1 Ryd, and the other component represents a power law with a spectral index $\alpha_X = -1$ that represents the nonthermal X-rays radiation. To test different regimes in the hardness of the ionization, we selected several values for the slope in the power law that traced the continuum between 2.5 keV and 2500 Å (α_{OX}) given by $\alpha_{OX} = [-0.8, -1.0, -1.2, -1.4, -1.6, -1.8, -2.0]$. Although it was reported that slopes below $\alpha_{OX} = -1.4$ do not

---

[2] The code is publicly available at http://home.iaa.csic.es/~epm/HII-CHI-mistry.html.

[3] The code is publicly available at https://gitlab.nublado.org/cloudy/cloudy.

reproduce the observed emission-line ratios well (Carvalho et al., 2020; Oliveira et al., 2024b), we explored all these scenarios to search for significant differences caused by the choice of this parameter.

- Post-AGB SEDs obtained from the grid of nonlocal thermodynamic equilibrium (NLTE) model atmospheres[4] provided by (Rauch, 2003) for three different effective temperatures: $5 \cdot 10^4$ K, $1 \cdot 10^5$ K and $1.5 \cdot 10^5$ K. These SEDs were computed assuming $\log g = 6$, and we assumed normalized fractions of 0.33 for helium, 0.50 for carbon, 0.02 for nitrogen, and 0.15 for oxygen.

- An advection-dominated accretion flow (ADAF) model for the AGN, which represents the truncation of the accretion disk due to inefficiency in the accretion process. In particular, we made use of the code RIAF-SED[5] (Nemmen et al., 2014; Yuan et al., 2005, 2007). Considering the large number of free parameters for the computation, we used the average SED that characterized ADAF emission in LLAGN (see Nemmen et al., 2014, for more details).

For each considered SED, we modeled the ISM by allowing the oxygen abundance to vary in the range $6.9 \leq 12+\log(\mathrm{O/H}) \leq 9.1$ in steps of 0.1 dex, the nitrogen-to-oxygen ratio varied in the range $-2.0 \leq \log(\mathrm{N/O}) \leq 0.0$ in steps of 0.125 dex, and the ionization parameter varied in the range $-4.0 \leq \log(U) \leq -0.5$ in steps of 0.25 dex. This last parameter was preliminarily constrained in the range $-4.0 \leq \log(U) \leq -2.5$ based on previous findings (e.g. Oliveira et al., 2022, 2024a; Pérez-Díaz et al., 2021) because it was needed to break the degeneracy reported in some emission line ratios (Pérez-Díaz et al., 2021; Pérez-Montero et al., 2019a). For all models, a density of 500 cm^{-3} was assumed. In total, we computed 4928 models per ionizing source, which yields a total of 54208 models. We also explored the effects of the stopping criteria by considering two different scenarios: for a ratio of ionized hydrogen atoms of 0.98 and of 0.02. As already reported in other studies (e.g. Pérez-Díaz et al., 2021, 2022), these two scenarios do not introduce significant differences (they are lower (~ 0.05 dex) than the steps in the grid of models) in the chemical abundance estimations.

3.5 RESULTS

3.5.1 *Oxygen and nitrogen abundances*

In Tab. 3.2 and 3.3 we provide the overall statistics for the derived oxygen abundance and nitrogen-to-oxygen abundance ratio, respectively, in our selected sample of LINERs. We give the results for each ionizing source in the models we used to calculate the abundances for the whole sample, and we also list them according to their classification as wAGN or as retired galaxies (RG).

For 12+log(O/H), there is no difference between the median values derived for wAGN and RGs, (~ 0.05 dex; this is lower than the grid step and compatible within the errors). It is always close to the solar value ($12+\log(\mathrm{O/H}) \sim 8.69$; Asplund et al., 2009). Only for the ADAF models did we obtain subsolar median values, but still no significant difference was found between the two families. The case of pAGB models is particularly interesting ($T_{eff} = 1 \cdot 10^5$ K and $T_{eff} = 1.5 \cdot 10^5$ K) because the difference between the resulting median values in each family increases (~ 0.1 dex), although they are still compatible within the errors. Overall, the lower values of the oxygen abundance are found in galaxies that are classified as RG, with values ~ 0.3 dex below the solar abundance. For pAGB models, both distributions reach subsolar values, below ~ 0.4 dex for wAGN and ~ 0.6 dex for RGs. This differentiation between AGN (and ADAF) models and pAGB models is highlighted in Fig. 3.3.

---

[4] They can be downloaded from http://astro.uni-tuebingen.de/~rauch/TMAF/flux_H-Ca.html.
[5] The code is publicly available at https://github.com/rsnemmen/riaf-sed.

Table 3.2: Properties of the resulting distribution of the derived oxygen abundances. For each photoionization model (1) and each group of LINERs (2) the median value (3), standard deviation (4), minimum (5) and maximum values (6) are provided.

Model (1)	Class. (2)	12+log(O/H)$_{med}$ (3)	12+log(O/H)$_{sd}$ (4)	12+log(O/H)$_{min}$ (5)	12+log(O/H)$_{max}$ (6)
AGN $\alpha_{OX} = -0.8$	wAGN	8.72	0.05	8.59	8.84
	RG	8.71	0.08	8.36	8.82
	All	8.72	0.06	8.36	8.84
7 AGN $\alpha_{OX} = -1.0$	wAGN	8.66	0.04	8.54	8.77
	RG	8.64	0.07	8.36	8.76
	All	8.65	0.06	8.36	8.77
AGN $\alpha_{OX} = -1.2$	wAGN	8.57	0.05	8.47	8.68
	RG	8.59	0.04	8.46	8.64
	All	8.58	0.04	8.46	8.68
AGN $\alpha_{OX} = -1.4$	wAGN	8.70	0.05	8.57	8.79
	RG	8.66	0.07	8.37	8.75
	All	8.68	0.07	8.37	8.79
AGN $\alpha_{OX} = -1.6$	wAGN	8.70	0.05	8.59	8.78
	RG	8.64	0.08	8.32	8.78
	All	8.69	0.07	8.32	8.78
AGN $\alpha_{OX} = -1.8$	wAGN	8.70	0.05	8.55	8.78
	RG	8.64	0.08	8.31	8.76
	All	8.68	0.07	8.31	8.78
AGN $\alpha_{OX} = -2.0$	wAGN	8.70	0.05	8.54	8.79
	RG	8.64	0.08	8.30	8.76
	All	8.69	0.08	8.30	8.79
pAGB $T_{eff} = 5 \cdot 10^4$ K	wAGN	8.47	0.02	8.41	8.55
	RG	8.47	0.02	8.44	8.53
	All	8.47	0.02	8.41	8.55
pAGB $T_{eff} = 1 \cdot 10^5$ K	wAGN	8.64	0.11	8.28	8.74
	RG	8.50	0.14	8.07	8.74
	All	8.57	0.13	8.07	8.74
pAGB $T_{eff} = 1.5 \cdot 10^5$ K	wAGN	8.56	0.16	8.25	8.82
	RG	8.41	0.16	8.08	8.72
	All	8.50	0.17	8.08	8.82
ADAF	wAGN	8.51	0.04	8.43	8.60
	RG	8.50	0.04	8.42	8.62
	All	8.51	0.04	8.42	8.62

Examining the log(N/O) ratio, we find a completely different picture to that depicted for oxygen. For a given particular model, log(N/O) behaves in a statistically similar way for both groups of galaxies (differences below 0.06 dex). For a given group, there is little difference between the N/O ratios obtained assuming distinct AGN models. For either pAGB or ADAF models, the median value increases with respect to AGN models (~ 0.15 dex). Nevertheless, they are still compatible considering the standard deviations of the distributions. Overall, we found that median values cluster around the solar abundance ratio (log(N/O)~ -0.86; Asplund et al., 2009), but there is a wider range of values (~ 0.9 dex) than is observed for 12+log(O/H) (~ 0.4 dex). In Fig. 3.4 we show the distributions of the log(N/O) estimations for each group and for the whole sample. There is little difference among them and for each photoionization grid of models.

As shown in Fig. 3.3 (see also Tab. 3.2), the oxygen abundances estimated from pAGB models with temperatures as low as $T_{eff} = 5 \cdot 10^4$ K spread over a very narrow range of values [8.4, 8.6], which

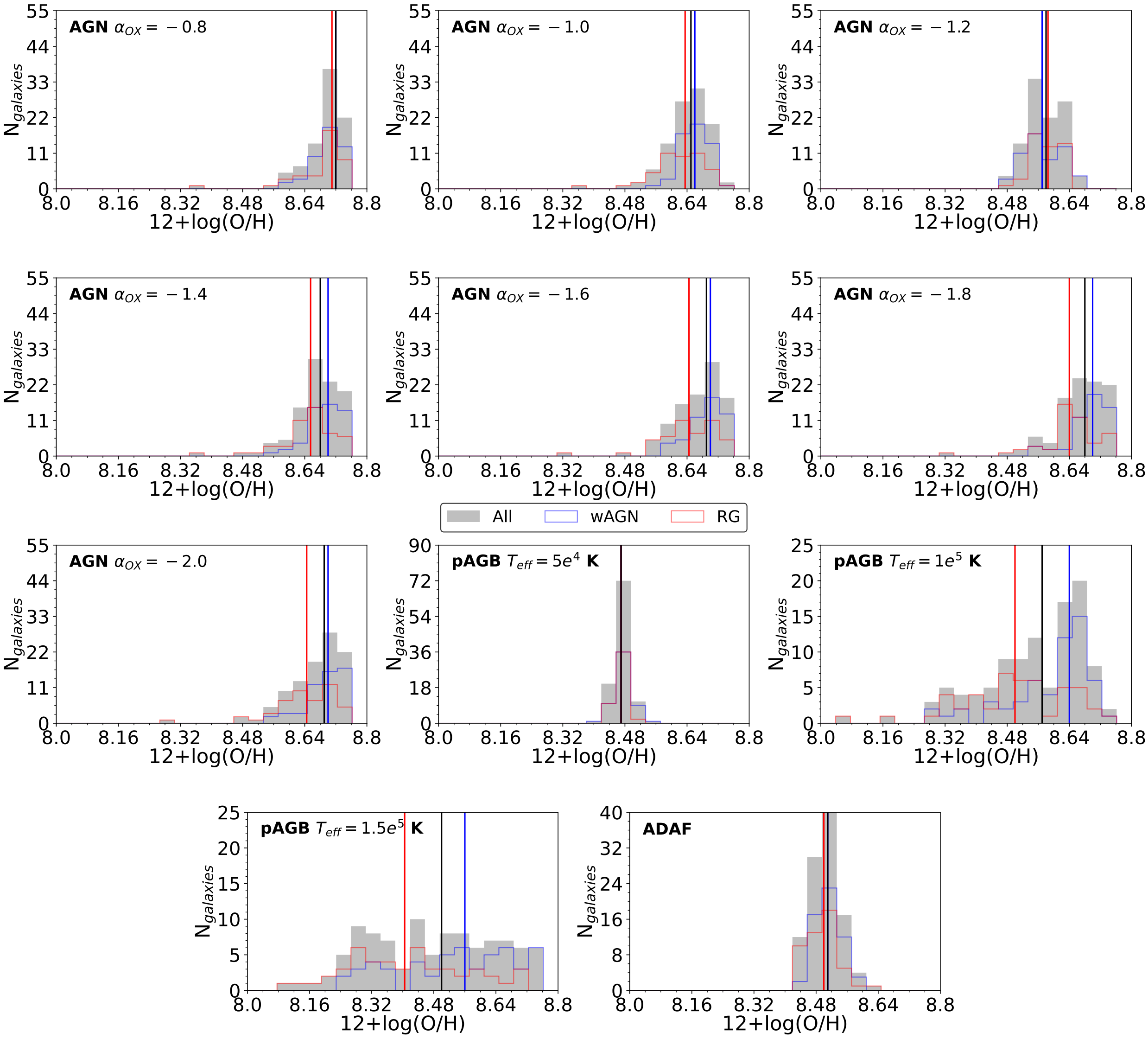

Figure 3.3: Histograms for 12+log(O/H) nuclear abundance ratios for LINERs for each photoionization grid of models. The step-filled gray histogram corresponds to all LINERs in our sample. The step blue and red histograms correspond to wAGNs and RGs, respectively. The vertical solid lines represent the median values for each distribution.

is even shorter than the range observed from the ADAF models. The photoionization models reveal that no O^{3+} is predicted by these models in the nebulae because their ionizing incident radiation field is comparatively softer. Hence, in order to properly provide a simultaneous estimation of the oxygen abundance (mainly traced through the sum of O^{++} and O^{+} emission lines) and the ionization parameter (mainly traced through the ratio of O^{++} and O^{+} emission lines), these models with a lower effective temperatures constrain the obtained oxygen abundance in a more restricted range than other models with higher T_*, which allow a larger variation in the same involved lines, as these same models predict a higher abundance of other more highly ionized species such as O^{3+}.

3.5.2 *N/O versus O/H relation*

The log(N/O) versus 12+log(O/H) relation allows us to check whether the ISM follows a standard chemical enrichment history that is characterized by constant log(N/O) values at low metallicities (12+log(O/H) < 8.6, e.g. Belfiore et al. 2015) due to the primary production of N and a positive

Table 3.3: Same as Tab. 3.2, but for the nitrogen-to-oxygen abundance ratios log(N/O).

Model (1)	Class. (2)	$\log(N/O)_{med}$ (3)	$\log(N/O)_{sd}$ (4)	$\log(N/O)_{min}$ (5)	$\log(N/O)_{max}$ (6)
AGN $\alpha_{OX} = -0.8$	wAGN	−0.88	0.16	−1.20	−0.39
	RG	−0.79	0.14	−1.15	−0.47
	All	−0.84	0.15	−1.20	−0.39
AGN $\alpha_{OX} = -1.0$	wAGN	−0.81	0.15	−1.14	−0.42
	RG	−0.74	0.14	−1.12	−0.43
	All	−0.78	0.15	−1.14	−0.42
AGN $\alpha_{OX} = -1.2$	wAGN	−0.82	0.15	−1.17	−0.39
	RG	−0.73	0.14	−1.08	−0.44
	All	−0.79	0.15	−1.17	−0.39
AGN $\alpha_{OX} = -1.4$	wAGN	−0.83	0.15	−1.19	−0.40
	RG	−0.75	0.14	−1.11	−0.50
	All	−0.79	0.15	−1.19	−0.40
AGN $\alpha_{OX} = -1.6$	wAGN	−0.84	0.16	−1.22	−0.38
	RG	−0.74	0.13	−1.11	−0.48
	All	−0.79	0.15	−1.22	−0.38
AGN $\alpha_{OX} = -1.8$	wAGN	−0.83	0.15	−1.18	−0.38
	RG	−0.75	0.14	−1.12	−0.47
	All	−0.81	0.15	−1.18	−0.38
AGN $\alpha_{OX} = -2.0$	wAGN	−0.83	0.15	−1.19	−0.38
	RG	−0.75	0.14	−1.11	−0.47
	All	−0.80	0.15	−1.19	−0.38
pAGB $T_{eff} = 5 \cdot 10^4$ K	wAGN	−0.63	0.13	−0.93	−0.33
	RG	−0.56	0.12	−0.88	−0.33
	All	−0.58	0.13	−0.93	−0.33
pAGB $T_{eff} = 1 \cdot 10^5$ K	wAGN	−0.71	0.15	−1.05	−0.24
	RG	−0.62	0.13	−1.00	−0.34
	All	−0.67	0.15	−1.05	−0.24
pAGB $T_{eff} = 1.5 \cdot 10^5$ K	wAGN	−0.71	0.15	−1.06	−0.27
	RG	−0.64	0.14	−1.00	−0.37
	All	−0.70	0.15	−1.06	−0.27
ADAF	wAGN	−0.74	0.15	−1.07	−0.27
	RG	−0.65	0.13	−0.99	−0.36
	All	−0.70	0.15	−1.07	−0.27

increasing correlation at higher metallicities caused by the contribution of the secondary production in intermediate-mass stars (e.g. Andrews & Martini, 2013; Belfiore et al., 2015; Coziol et al., 1999; Vila-Costas & Edmunds, 1993; Vincenzo et al., 2016).

We show in Fig. 3.5 the observed behavior in the N/O versus O/H diagram for our estimations of nuclear abundances in our sample of LINERs. Generally, no distinction is found between galaxies classified as wAGN or RG. While our galaxies fall in the region delimited by the scatter in the literature, there seems to be an anticorrelation for AGN models, with the exception of the estimations provided by AGN models with $\alpha_{OX} = -1.2$. The Pearson coefficient correlations for these models are in the range of [−0.57 to −0.11] while the p-values are lower than 0.05in most of the cases (with the exception of AGN models with $\alpha_{OX} = -0.8$). This indicates that there is indeed such an anticorrelation. When pAGB models are considered (excluding those with a low effective temperature), these coefficients are even higher, ~ -0.62 with pAGB models of $T_{eff} = 1 \cdot 10^5$ K and ~ -0.70 with pAGB models of $T_{eff} = 1.5 \cdot 10^5$ K, and the p-values are even lower than 0.0005.

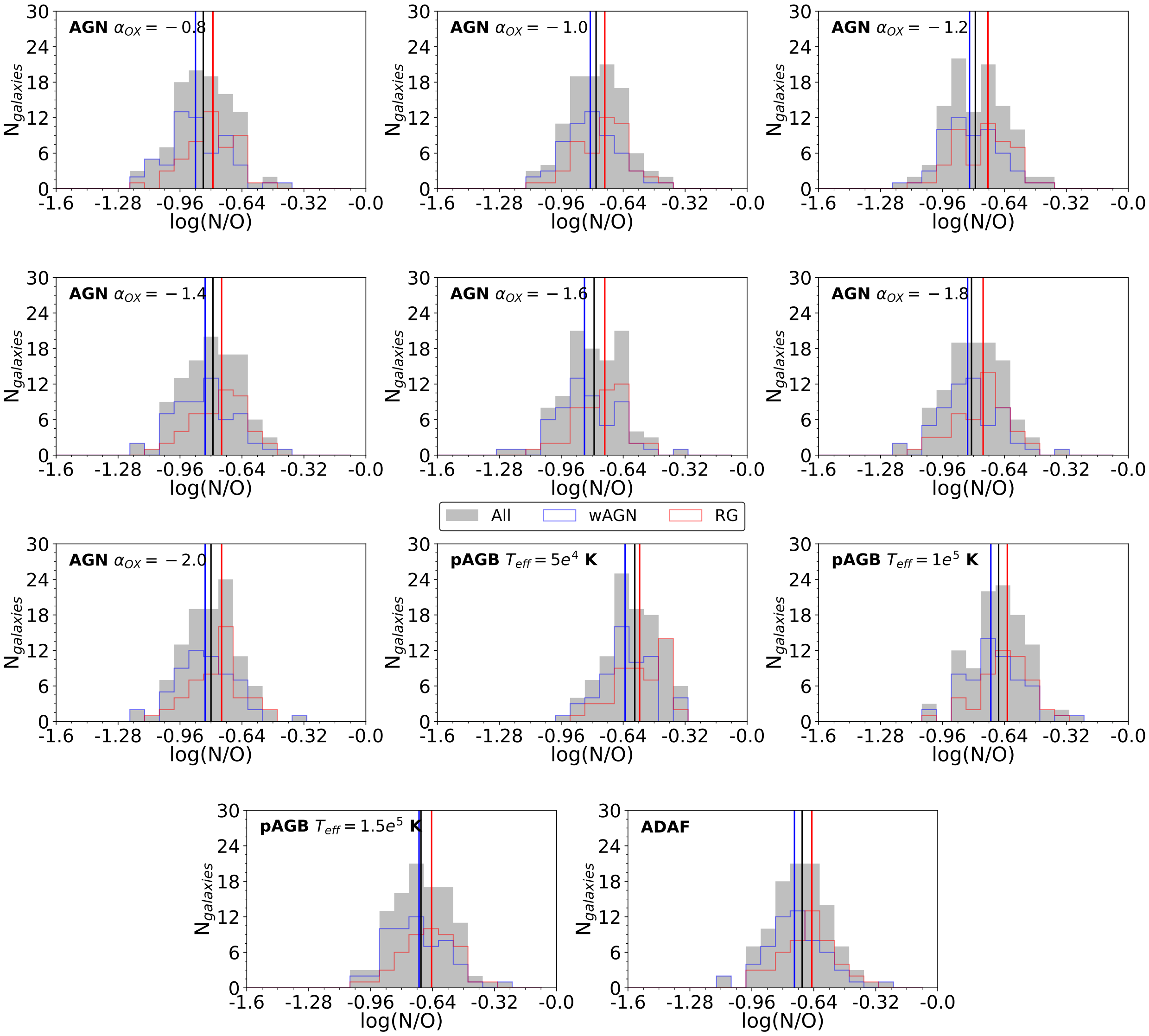

Figure 3.4: Same as Fig. 3.3, but for log(N/O) nuclear abundance ratios.

The ADAF models and AGN models with $\alpha_{OX} = -0.8$ and $\alpha_{OX} = -1.2$ seem to follow the reported relation for SFGs, but their Pearson coefficient correlations reveal that we cannot exclude the possibility that there is no correlation at all.

3.5.3 *Mass-metallicity relation*

The galaxy mass assembly is tied to the enrichment of the gas-phase ISM as star formation leads to the production of metals, a fraction of which can be ejected later into the surrounding ISM in their late stages of life. The well-known mass-metallicity relation (MZR; Andrews & Martini, 2013; Lequeux et al., 1979; Pérez-Montero et al., 2016; Tremonti et al., 2004) is a natural result that arises from this galaxy evolution scheme. While the use of the oxygen abundance as tracer of the metallicity might lead to incorrect conclusions, as is the case when masses of inflowing and/or outflowing gas alter the ratio of oxygen and hydrogen (Amorín et al., 2010; Köppen & Hensler, 2005; Pérez-Díaz et al., 2024a), the same analysis can be made using the nitrogen-to-oxygen abundance ratio as a tracer of this metallicity (MNOR; Pérez-Montero & Contini, 2009; Pérez-Montero et al.,

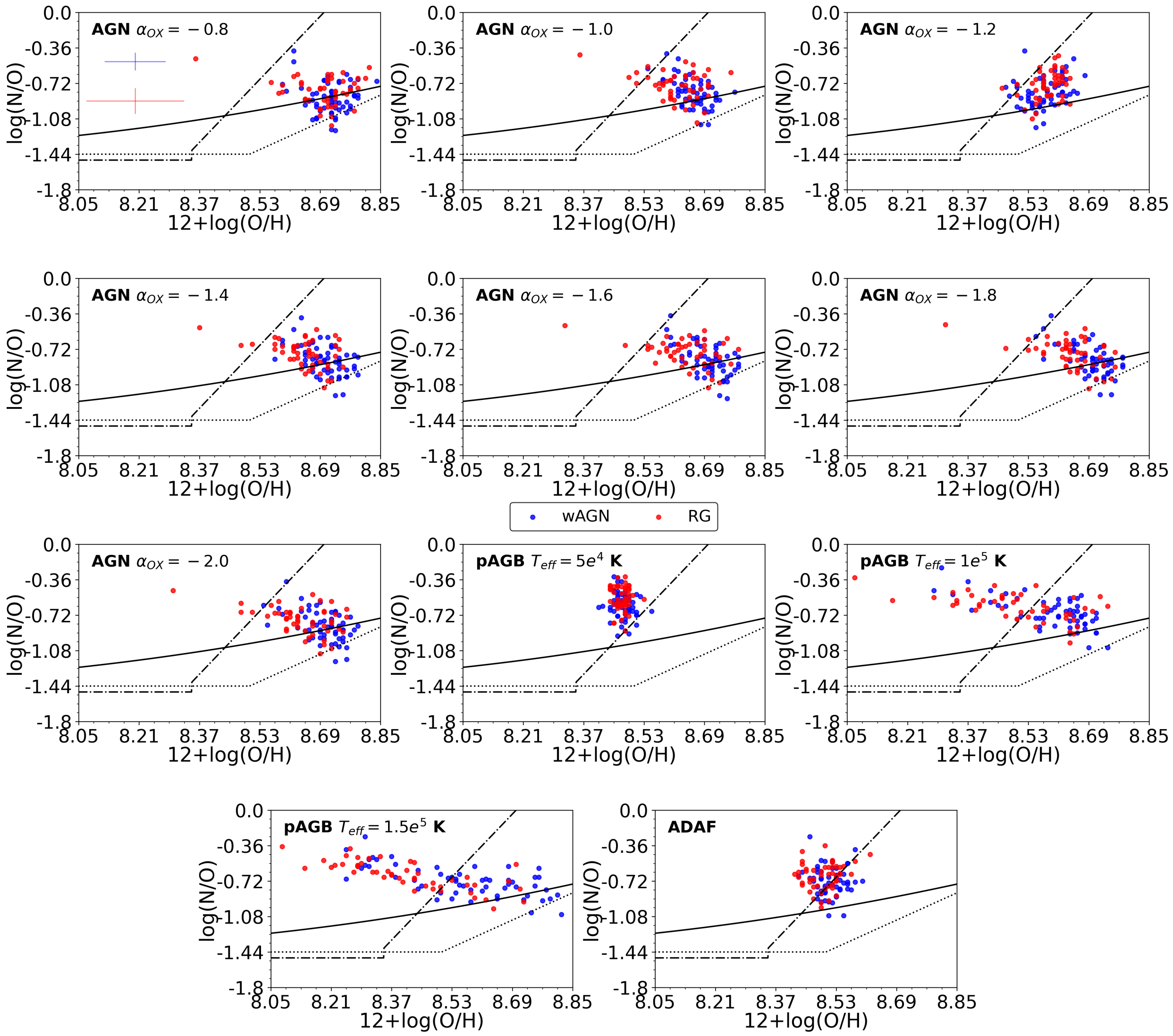

Figure 3.5: Relation of the nuclear estimations of log(N/O) and 12+log(O/H) in our sample of LINERs for each grid of photoionization models. The first plot shows the typical errors for the data. The solid back line represents the fit provided by Coziol et al. (1999), the dotted line shows the fit by Andrews and Martini (2013), and the dash-dotted line shows the fit by Belfiore et al. (2015).

2016), with the advantage that the hydrodynamical processes that alter the MZR do not affect the MNOR.

In order to study these fundamental relations in our sample of galaxies, we retrieved the stellar mass data from the NASA-Sloan Atlas (NSA) catalog[6]. These values were estimated from a K-correction fit to the elliptical Petrosian fluxes assuming the initial mass function (IMF) from Chabrier (2003) and the stellar population models from Bruzual and Charlot (2003).

As a general caveat, we used the abundance estimation from the nuclear region, whereas the reported relations were found in the chemical abundance estimation for the whole galaxy, which is more representative of the metallicity at the effective radius (e.g. Sánchez-Menguiano et al., 2024b) than in the nuclear region. Nevertheless, this study gives insights into whether our derived chemical abundances and the relations between them in the nuclear region can be driven by the physical galaxy parameters, which are known to play a major role in their evolution.

---

[6] https://www.sdss4.org/dr17/manga/manga-target-selection/nsa/.

Table 3.4: Results for the Pearson coefficient correlation test between log(N/O) and 12+log(O/H) (assuming that there is no correlation as the null hypothesis. For each photoionization model (1) and each group of LINERs (2), we provide the Pearson statistic (3) and the p value (4).

Model (1)	Class. (2)	ρ_{Pear} (3)	p-value (4)
AGN $\alpha_{OX} = -0.8$	wAGN	−0.111572	0.408650
	RG	−0.196387	0.180956
	All	−0.175399	0.073503
AGN $\alpha_{OX} = -1.0$	wAGN	−0.526893	0.000025
	RG	−0.294983	0.041814
	All	−0.427234	0.000005
AGN $\alpha_{OX} = -1.2$	wAGN	0.294352	0.026245
	RG	0.321981	0.025631
	All	0.313398	0.001133
AGN $\alpha_{OX} = -1.4$	wAGN	−0.487242	0.000121
	RG	−0.419451	0.003001
	All	−0.482328	0.000000
AGN $\alpha_{OX} = -1.6$	wAGN	−0.568648	0.000004
	RG	−0.377912	0.008091
	All	−0.486132	0.000000
AGN $\alpha_{OX} = -1.8$	wAGN	−0.572961	0.000003
	RG	−0.474195	0.000662
	All	−0.535446	0.000000
AGN $\alpha_{OX} = -2.0$	wAGN	−0.479811	0.000159
	RG	−0.437627	0.001867
	All	−0.477085	0.000000
pAGB $T_{eff} = 5e^4$ K	wAGN	−0.176009	0.190313
	RG	−0.047178	0.750168
	All	−0.139873	0.154701
pAGB $T_{eff} = 1e^5$ K	wAGN	−0.669445	0.000000
	RG	−0.548444	0.000054
	All	−0.620041	0.000000
pAGB $T_{eff} = 1.5e^5$ K	wAGN	−0.656832	0.000000
	RG	−0.757362	0.000000
	All	−0.707616	0.000000
ADAF	wAGN	−0.066046	0.625464
	RG	0.156851	0.287032
	All	−0.006464	0.947821

We show in Fig. 3.6 the MZR in our sample of LINERs. First of all, we note that some galaxies lie on the reported relation (Curti et al., 2020) for SFGs. This is especially true for AGN models, which cluster around the relation, although they show systematically lower metallicities (~ -0.15 dex). Analyzing the different subtypes of galaxies, we observe that although their host galaxies are characterized by stellar masses in the same range $[10^{9.8} M_\odot, 10^{11} M_\odot]$, the median value for RGs is lower ($10^{10.33} M_\odot$) than for wAGNs ($10^{10.63} M_\odot$). For pAGB with $T_{eff} = 5 \cdot 10^4$ K, the retrieved relation seems to lie far below the reported relation and varies little in metallicity, which again highlights the problem of assuming low effective temperatures for the ionizing source. When we considered other pAGB models, we retrieved no relation at all between mass and metallicity.

The picture that arises from the MNOR (Fig. 3.7) complements our result form the log(N/O) versus 12+log(O/H) relation. First of all, there is very little difference in the obtained relations as a function of the assumed models. Second, most of our sample lies above the reported relation

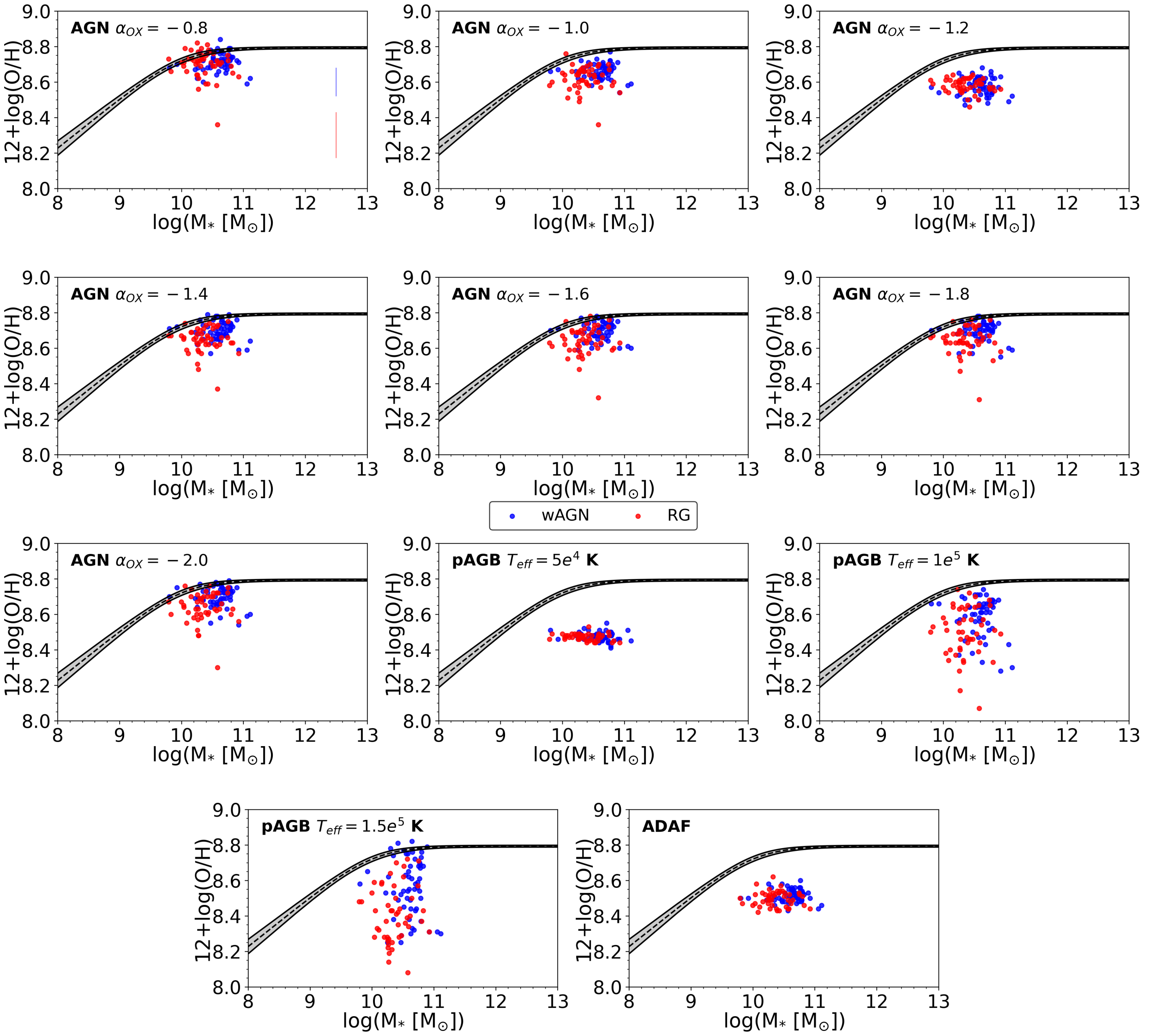

Figure 3.6: Mass-metallicity relation determinations in the nuclear regions of our sample of LINERs for different grids of photoionization models. The first plot shows the typical errors for the data. The dashed line represents the fit from Curti et al. (2020), and the gray shaded area shows the corresponding uncertainty on the relation.

(Andrews & Martini, 2013). This is consistent with the anomalous relation observed in Fig. 3.5: While the oxygen abundances might be consistent (or slightly lower) with their corresponding mass, the nitrogen-to-oxygen abundance ratio increases with respect to the expected ratio, which indicates that the scenario for the N evolution is more complex.

3.5.4 *Comparison with the extrapolation from galaxy gradients*

Although this procedure and all its associated results will be discussed in a forthcoming paper of this series, we briefly explain the procedure for estimating metallicity gradients in the same galaxies which are hosting the nuclear regions classified as LINERs. First of all, we selected the spaxels classified as HII regions in each galaxy according to the three diagnostic diagrams (Baldwin et al., 1981; Kewley et al., 2006). Second, we used HCm to consistently derive the metallicities for each HII region using POPSTAR as ionizing source in the models (see Sec. 3.4 for more details). Finally, for both 12+log(O/H) and log(N/O), we used a piecewise method (Tapia; Tissera private

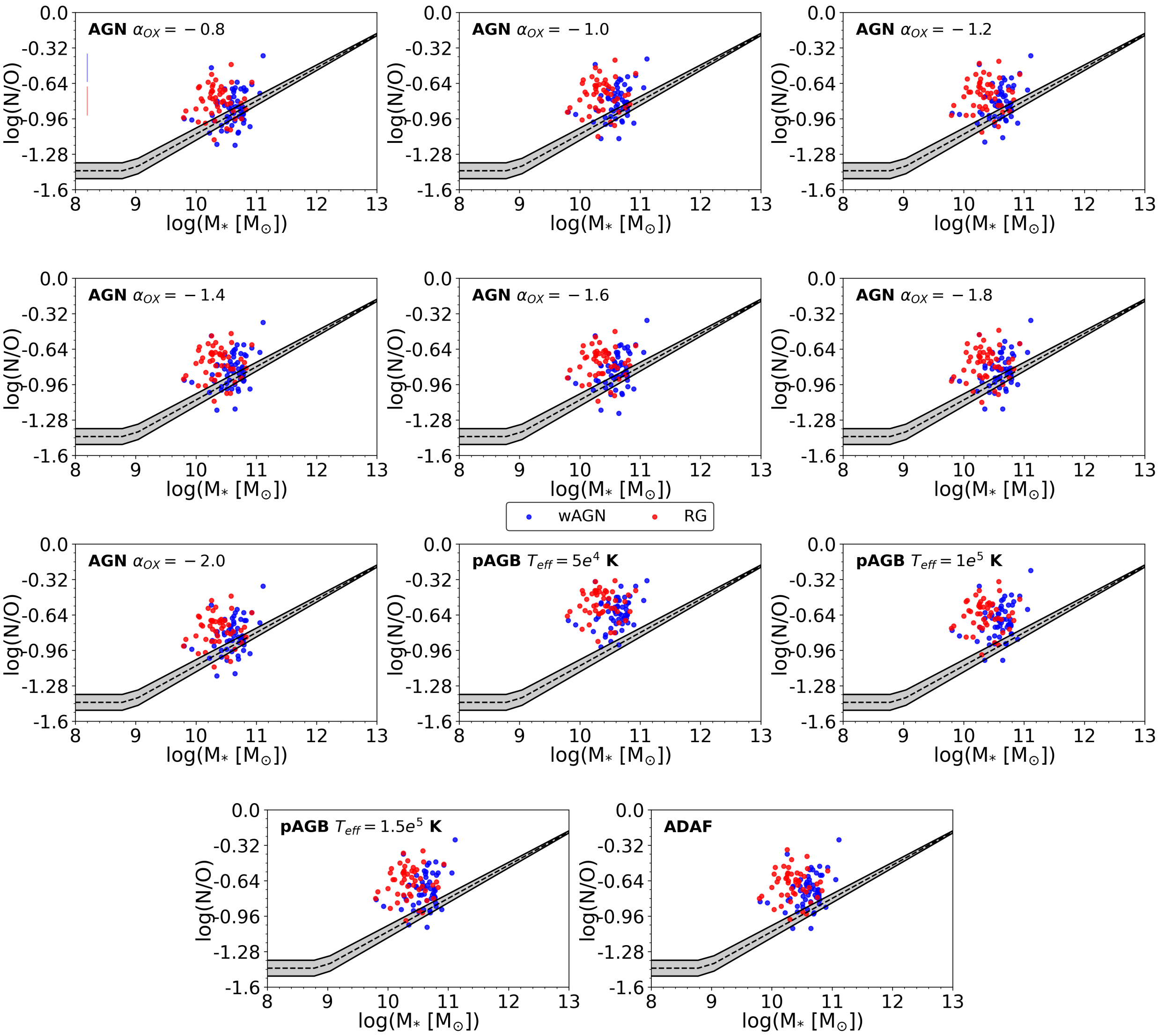

Figure 3.7: Mass-NO relation based on the metallicity determinations in the nuclear regions of our sample of LINERs for different grids of photoionization models. The first plot shows the typical errors for the data. The dashed line represents the fit from Andrews and Martini (2013), and the gray shaded area shows the corresponding uncertainty on the relation.

communication) to estimate the metallicity gradient for the HII regions alone, and we allowed the profile to present breaks. The gradients were calculated by normalizing distances to the R_{50} radius, defined as the azimuthally averaged SDSS-style Petrosian containing 50% light radius from the r-band.

From Fig. 3.8 we conclude that in the case of 12+log(O/H), the extrapolations from the gradients within galaxies and the estimations from the nuclear emission do not match because the distribution of the differences is wide (over 0.6 dex), even though the median difference is close to zero. We also obtained the highest offset and dispersion when the chemical abundances from the nuclear regions were estimated using pAGB models. This result holds true for both groups of galaxies we considered in this analysis (wAGNs and RGs) . A completely different idea emerges from Fig. 3.9, where the extrapolations from the gradients and the nuclear estimations match for the log(N/O) abundance ratio. This leads to narrower distributions of the differences ($\sim$ 0.4 dex) and to median differences much closer to zero.

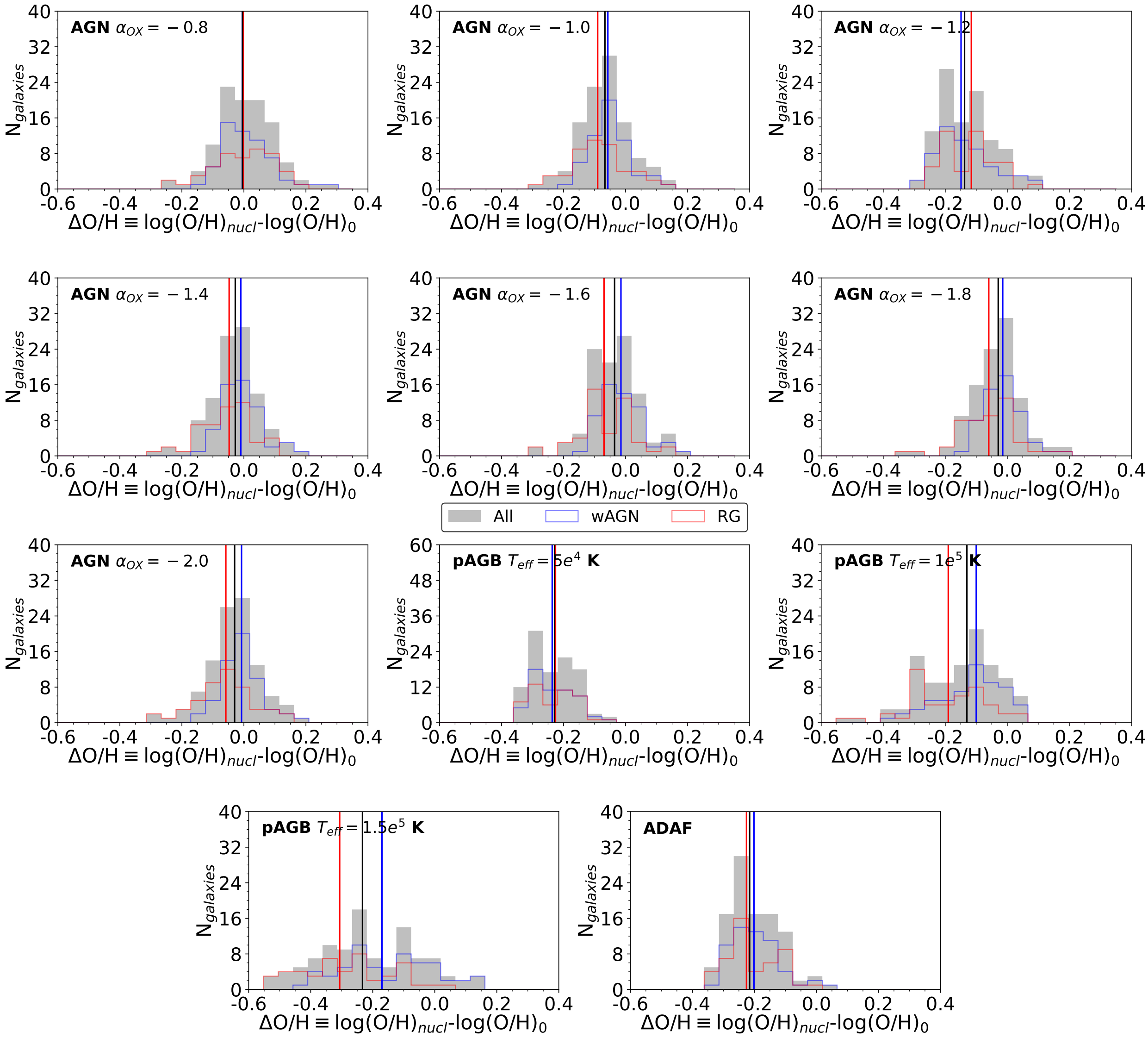

Figure 3.8: Histograms of the difference between 12+log(O/H)$_{Nucl}$ as estimated in the central regions using different photoionization models and 12+log(O/H)$_0$, as extrapolated from metallicity gradients. The step-filled gray histogram corresponds to all LINERs in our sample. The step blue and red histograms correspond to wAGNs and RGs, respectively. The vertical solid lines represent the median values for each distribution.

3.6 DISCUSSION

In the following section, we omit the analysis of pAGB models with $T_{eff} = 5 \cdot 10^4$ K because we determined in Sec. 3.5 in agreement with previous works (e.g. Krabbe et al., 2021; Oliveira et al., 2022) that they are inefficient in reproducing the observed emission-line ratios. Hence, throughout this discussion, we only refer to the pAGBs that are characterized by $T_{eff} = 1{\cdot}10^5$ K and $T_{eff} = 1.5{\cdot}10^5$ K.

3.6.1 *Comparison of the abundance estimations with the literature*

Although only a few studies analyzed the chemical abundances in LINERs (fewer than for SFGs or Seyferts 2), we can compare our results with them. We considered the works from Annibali

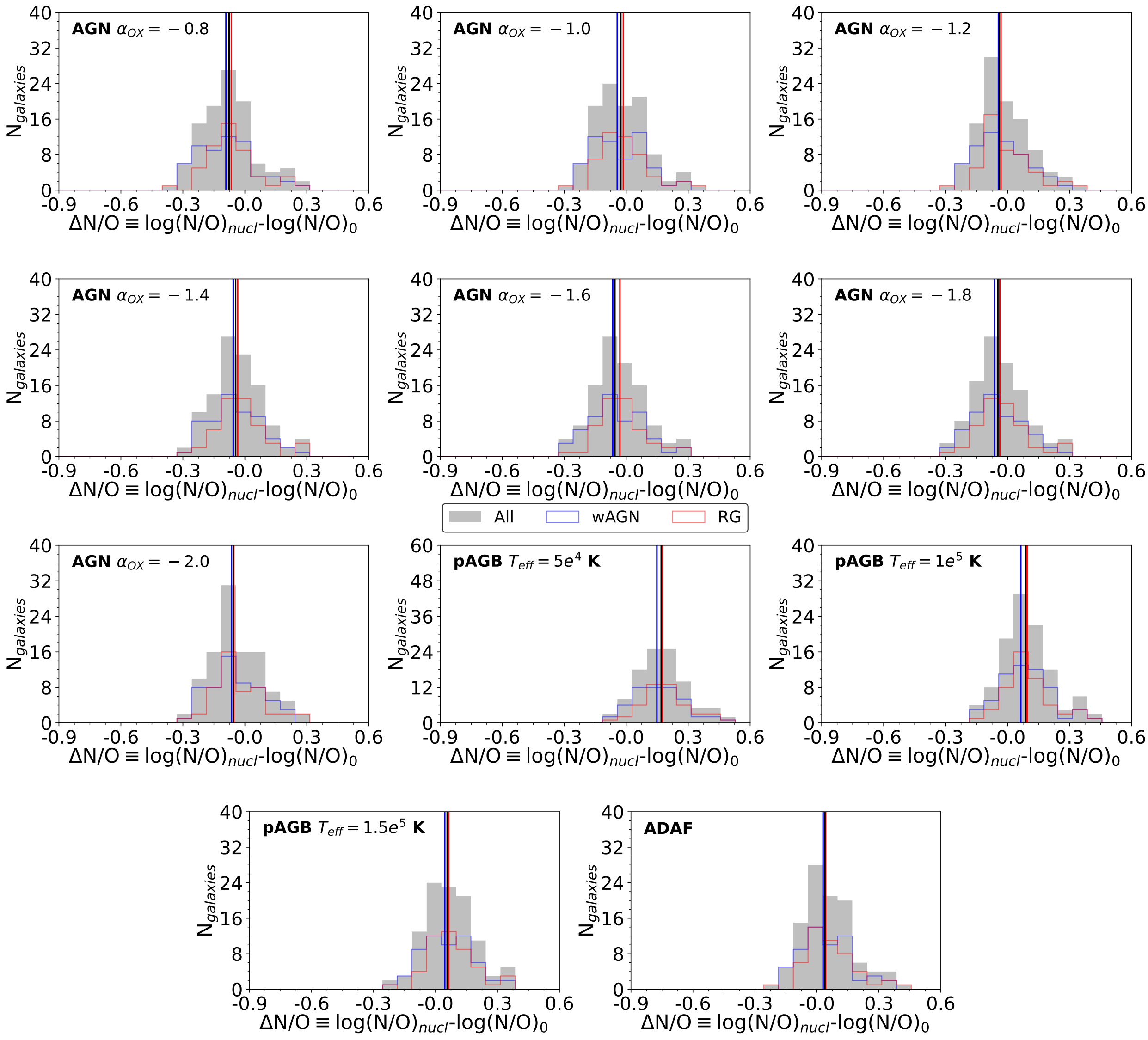

Figure 3.9: Same as Fig. 3.8, but for the difference log(N/O) as estimated in the central regions using different photoionization models and log(N/O)$_0$ as extrapolated from metallicity gradients.

et al. (2010), Oliveira et al. (2022, 2024a) and Pérez-Díaz et al. (2021), as these studies analyzed statistical significant samples of LINERs.

Annibali et al. (2010) obtained that when they used the results of Kobulnicky et al. (1999) (which accounts for pAGN ionization) to estimate 12+log(O/H) for their sample of early-type galaxies, the abundances reported in the nuclear region lay in the range [8.20, 9.01], which agrees with the results obtained for our sample of LINERs for all models. Conversely, when they used the calibration of Storchi-Bergmann et al. (1998) (which accounts for AGN activity), the range was constrained to [8.54, 8.94] because the validity range for this calibration is above 12+log(O/H) > 8.4. This range also agrees with our findings when we used AGN models as the ionizing source, although we were able to retrieve lower values than are traced by this calibration.

Oliveira et al. (2022) analyzed a sample of 43 LINERs from MaNGA that were classified as RGs in the WHAN diagram (Cid Fernandes et al., 2010, 2011). Assuming pAGB ionization, and by means of photoionization models, they used calibrations based on N2 ($\equiv$ [N II]λ6584Å/H$_{\alpha}$) and O3N2 ($\equiv$ [O III]λ5007Å/[N II]λ6584Å) line ratios and obtained oxygen abundances in the range [8.4, 8.84]. In contrast to our results, they did not obtain any LINER with 12+log(O/H) < 8.4 as we did. In particular, in the case of RGs, we obtained that 10 RGs (21%) show metallicities below that limit. In their nitrogen-to-oxygen abundance ratio, we found that this group of low-metallicity LINERs is also characterized by suprasolar log(N/O) ratios [−0.67, −0.34]. Since the photoionization models built by Oliveira et al. (2022) assumed a relation of log(N/O) and 12+log(O/H), their higher abundances might be interpreted as a consequence of using nitrogen emission lines as tracers of the oxygen abundance without an independent estimation of the log(N/O) ratio. This might explain the discrepancy.

Oliveira et al. (2024a) more recently shed more light on the oxygen abundances in LINERs. In contrast to the previous work by Oliveira et al. (2022), they used customized photoionization models to simultaneously constrain the N and O abundances, without assuming any relation between them, similar to our work. Their results for 40 out of the 43 previous RG LINERs on their oxygen content are in the range $8.0 \leq$ 12+log(O/H) ≤ 9.0, which is similar to our findings, especially when pAGB models are considered for RGs ($8.07 \leq$ 12+log(O/H) ≤ 8.82). However, there is a slight discrepancy between their mean value 12+log(O/H) = 8.74 and ours for RGs 8.57 (8.50) for pAGB models with $T_{eff} = 1 \cdot 10^5$ K ($T_{eff} = 1.5 \cdot 10^5$ K). Even though they are still compatible within the errors, this discrepancy might be interpreted as a consequence of the fact that Oliveira et al. (2024a) considered dust-free photoionization models, whereas our grid of models accounted for a standard dust-to-gas ratio. For the nitrogen-to-oxygen abundance ratios, Oliveira et al. (2024a) reported a mean value of log(N/O) = -0.69 ± 0.16 with a range [−1.05, −0.42], which agrees very well with the results we reported, although we detected only a few (three) LINERs with higher ratios.

Finally, we also compared our results to those provided by Pérez-Díaz et al. (2021), who analyzed 40 LINERs from the Palomar Spectroscopic Survey (Ho et al., 1993, 1997) with the same method as we used, but only considered AGN models with $\alpha_{OX} = -0.8$. They estimated a median 12+log(O/H) = 8.63 ± 0.26 and a range of metallicities given by [8.04, 8.85] for their sample of LINERs. Their median value is consistent with the values we report in this work for the different grids of photoionization models for AGN or pAGB sources and for both types of LINERs (wAGNs and RGs). However, we were not able to retrieve oxygen abundances below 12+log(O/H) < 8.2 with AGN models, which might be explained by the higher spatial resolution in the Palomar Spectroscopic Survey. For log(N/O), their findings also agree with those provided by Oliveira et al. (2024a) and with ours, although the median value that we obtained for AGN models is slightly lower (log(N/O)~ -0.80).

3.6.2 *Relation between the nuclear chemical abundances and the host galaxy properties*

The relation between 12+log(O/H) and log(N/O) we obtained for our sample of LINERs in MaNGA is a result that merits a thorough examination because of its connotations for the evolution of galaxies and the processes driving their chemical enrichment. Our findings are well illustrated in Fig. 3.5 for different scenarios as a function of the SED considered in the models to calculate the abundances.

- **Strong negative trend**: When pAGB models were accounted for, we obtained a strong anticorrelation between log(N/O) and 12+log(O/H). When pAGB models with effective temperature $T_{eff} = 1 \cdot 10^5$ K were considered, the Pearson correlation coefficients were −0.54 for RGs and −0.67 for wAGNs. For $T_{eff} = 1.5 \cdot 10^5$ K, the coefficients changed to −0.75 and −0.65, respectively. In both cases, the anticorrelation reaches beyond the limits of the scatter found in the literature.

- **Positive trend**: A positive trend was only retrieved for an AGN model with a slope $\alpha_{OX} = -1.2$ (Pearson correlation coefficients of 0.32 and 0.29 for RGs and wAGNs, respectively).

- **Slightly negative trend compatible with the scatter**: For the remaining AGN models, we found negative Pearson correlation coefficients in the range [−0.42, −0.19] for RGs and [−0.53, −0.17] for wAGNs. In all these scenarios, the position in the N/O versus O/H diagram is still compatible with the different relations reported in the literature to account for the scatter.
- **Nonexistent trend**: Pearson correlation coefficients very close to zero (0.105 and −0.06 for RGs and wAGNs, respectively) were found when we considered the ADAF model for inefficient accretion.

In a first-order approximation, omitting dynamical processes that affect the gas-phase ISM (inflows and/or outflows), the N/O versus O/H relation should represent the two scenarios of N production: i) The production of N and O mainly from massive stars, which yields a constant log(N/O) over 12+log(O/H) < 8.5 (Andrews & Martini, 2013; Vincenzo et al., 2016), and ii) an increasing log(N/O) ratio over 12+log(O/H) > 8.5 (Andrews & Martini, 2013; Vincenzo et al., 2016) as a consequence of the non-negligible contribution of N via intermediate-mass stars ($4-7$ $M_\odot$; Kobayashi et al., 2020a) from the CNO cycles to which the oxygen already present in the stars contributes. In this scenario, the delay between nitrogen production and ejection, the N enrichment through Wolf-Rayet stars (e.g. Kobulnicky et al., 1997; López-Sánchez & Esteban, 2010) (although it might be negligible at kiloparsec scales e.g. Pérez-Montero et al. 2011) together with the differences in the star formation efficiency (e.g. Mollá et al., 2006) explain the scatter in the relation reported in the literature. We exemplified this here with the relations from Andrews and Martini (2013) and Belfiore et al. (2015). This scenario allowed us to explain not only the observed relation for AGN models in the N/O versus O/H diagram, but also the slight deviation by −0.15 dex for our sample of LINERs compared to other reported fits of the MZR, as shown in Fig. 3.6, whereas the deviation in the MNOR diagram (see Fig. 3.7) is stronger.

Nevertheless, the expected scatter in the O/H versus N/O relation can be even higher when the galaxy (or the central region) is not considered as a closed-box model and gas inflows and outflows as a consequence of stellar evolution or AGN activity are accounted for. As shown by inflow/outflow chemical evolution models (e.g. Köppen & Edmunds, 1999) and supported by observations of interacting systems such as (ultra-) luminous infrared galaxies (Pérez-Díaz et al., 2024a), the chemical enrichment of green-pea galaxies (e.g. Amorín et al., 2012; Amorín et al., 2010) and specific cases of spatially resolved galaxies such as NGC 4214 (Kobulnicky & Skillman, 1996) or NGC 4670 (Kumari et al., 2018). In this case, not only effects on the N production must be taken into account, but also those on the mixing and gas removal/supply, which affect the 12+log(O/H) abundance ratio. As shown by Pérez-Díaz et al. (2024a), massive infalls of metal-poor gas can drastically dilute 12+log(O/H), but log(N/O) remains mostly unaffected by the process, which might explain the high nitrogen-to-oxygen ratios (log(N/O) > -0.70) at low oxygen abundances (12+log(O/H) < 8.4) observed for pAGB models. For the Teacup nebula, (Villar Martín, M. et al., 2024) showed that outflows might cause a pollution from the central region toward the outer parts, which would lower the oxygen abundances but maintain high N/O ratios. This result was also found by Oliveira et al. (2024a) for customized photoionization models based on pAGB SEDs in their sample of RGs. If this is the scenario, then we should expect a significant scatter in the MZR diagram, and the MNOR diagram should mimic the behavior for the remaining models. This is what we obtained for pAGB models.

In order to assess the origin of the observed anticorrelation between O/H and N/O under certain model assumptions, we explored the influence of different galaxy and gas properties, as shown in Fig. 3.10. For this plot, we took estimates for wAGN galaxies assuming AGN models into account and pAGB models ($T_{eff} = 1 \cdot 10^5$ K) for RG galaxies. First of all, it is clearly shown that whereas wAGNs follow the N/O versus O/H relation within the scatter, this is not the case for RGs because they show an anticorrelation that exceeds the scatter. In panels a) and b) we analyze whether this relation is

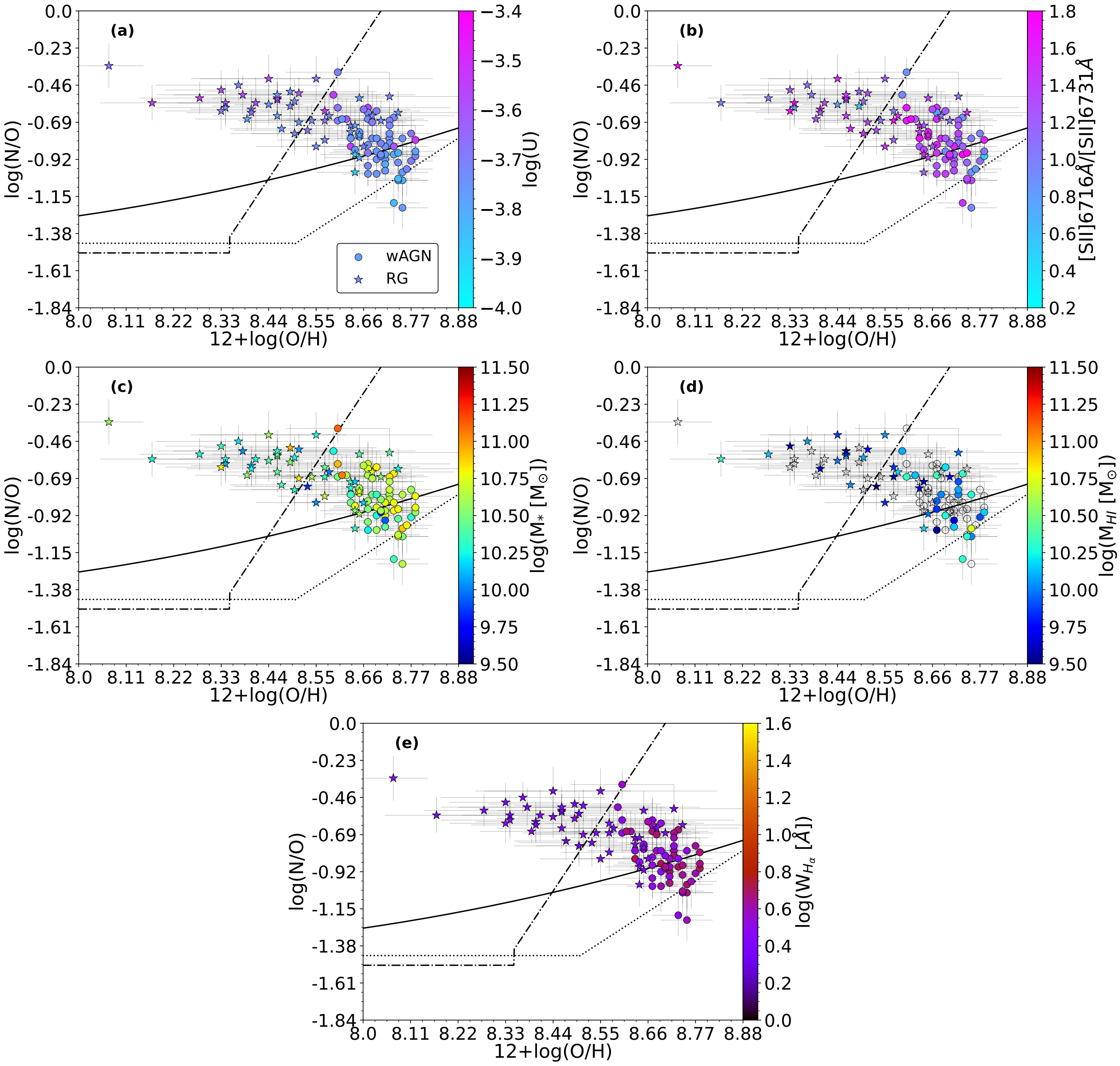

Figure 3.10: log(N/O) vs. 12+log(O/H) diagram for our sample of LINERs. The dots represent galaxies classified as wAGN, and the chemical abundances correspond to AGN models with $\alpha_{OX} = -1.6$. The stars correspond to galaxies classified as RG whose chemical abundances were estimated assuming pAGB models with $T_{eff} = 1 \cdot 10^5$ K. The color bar shows different properties: a) The ionization parameter as estimated from emission lines. b) The sulfur ratio tracer of the electron density. c) The stellar mass as retrieved from the NSA catalog. d) The HI mass as retrieved from the NSA catalog. e) The equivalent width of H_α. The empty symbols correspond to galaxies without a measurement of the represented property.

driven by physical properties of the gas-phase ISM, such as the electron density or the ionization parameter. None of them are correlated. In panel c) we show the anticorrelation as a function of the stellar mass. There is again no relation at all. In panel d) we show the HI mass reported for each galaxy. This panel allows us two conclusions: i) neither the scatter within the reported relation nor the anticorrelation are driven by the amount of gas, as is observed for the sample of wAGNs and, ii) only one of the LINERs classified as RG and with high log(N/O) (> -0.6) and low 12+log(O/H) (< 8.25) has a slightly higher gas content than the rest of the sample. However, because we lack measurements for most of them, it is not possible to asses whether this object is an outlier. Finally, we present in panel e) the equivalent width of H_α. Based on these results, we can explore the inflow and/or outflow scenarios for the anticorrelation.

For the inflow of gas as the major driver of the observed relation, we found several caveats. The first caveat is the origin of the gas. In the case of green-pea galaxies, the impact of metal-poor high-velocity clouds (HVCs; e.g. Köppen & Hensler, 2005) or gas accretion from the cosmic web (Sánchez Almeida et al., 2015) was proposed. In the case reported by Pérez-Díaz et al. (2024a), gas is driven by merger interaction, and the amount of gas that dilutes the metallicity from 12+log(O/H) = 8.7 (solar) to 12+log(O/H) = 8.1 can be expected to arise from the reservoirs of gas from the galaxy itself as well as tidal gas taken from the companion (e.g. Montuori et al., 2010; Rupke et al., 2010; Sparre et al., 2022). Considering that the anticorrelation holds in RGs, which are assumed to be populated by pAGB, it is necessary to justify not only the presence of this gas (which is not found in the mass of HI), but also the physical driver toward the nuclear region of these galaxies. The second caveat is also related to the first, and it is the chemical composition of the inflowing gas. To dilute the oxygen content by more than 0.5 dex, metal-poor gas is required, and because gas flows from the outer to the inner parts, an almost flattened gradient is expected. When the timescale of the gas dynamics is long enough, a positive gradient from the center to the outer parts is expected. This scenario and its implications are explored in the second paper of this series. The third caveat is the consequences of this inflowing gas. Due to the amount of gas required, and as reported by Pérez-Díaz et al. (2024a) in (U)LIRGs as well as in simulations (Montuori et al., 2010), an increase in the star formation rate is expected, and the equivalent width of H_α should be higher (Cid Fernandes et al., 2010) for the most extreme cases. This implies that they would have never been classified as RGs. Moreover, there is no trend of an increasing equivalent width of H_α, as shown in Fig. 3.10 (panel e).

On the other hand, when we consider the outflow scenario as the major driver of this relation, some caveats arise. The first caveat is that the observational results for a sample of LINERs classified as RGs presented by Oliveira et al. (2024a) show no evidence of disturbed kinematics in the gas, as would be expected from the outflow scenario. Another caveat arises from the metallicity gradient: An outflow would carry gas for some distance, depending on its power. A change in the metallicity gradient for both 12+log(O/H) and log(N/O) is therefore expected, with a change in the slope of the gradient at some point as a consequence of the additional enrichment, as is the case in AGN-powered outflows (e.g. Villar Martín, M. et al., 2024). Although we will explore this scenario in the next paper, we already have some hints. If outflows pollute the ISM at galactic scales, then the increase in log(N/O) would translate into an overestimation of the log(N/O) extrapolated to the nuclear region. In contrast to this idea, we find in Fig. 3.9 that the nuclear estimation and nuclear extrapolation agree very well. Finally, if outflows are indeed present in sources that are assumed to be ionized by pAGB, the most likely scenario is that these systems of pAGB stars drive the outflows. Because they are required to ionize the whole nuclear region, the gas would account for an additional contribution of shock emission. We therefore assume that purely pAGB models are not suitable for modeling the ionizing structure.

Although we cannot entirely exclude an inflowing and/or outflowing scenario that would explain the observed anticorrelation between 12+log(O/H) and log(N/O) when pAGB stars are assumed to cause the emission on some LINERs, we must bear in mind the numerous caveats that these scenarios imply and that should be revised in future works. We also highlight that this is not a problem when all LINERs are considered to host AGNs because the anticorrelation is much weaker and compatible with the scatter in the relation, as reported in the literature.

3.6.3 *Source of ionization*

The nature of the source of the gas ionization in LINER-like galaxies is still an open question (e.g. Binette et al., 1994; Kewley et al., 2006; Nemmen et al., 2014). Of the different scenarios that were proposed to explore the origin of ionization of the nuclear gas-phase ISM in LINERs, we explored three scenarios: i) Standard AGN models with different SEDs shapes, ii) pAGB stars, and iii) inefficient accretion leading to an ADAF regime. With the exception of shocks, which were omitted from this study due to the large number of free parameters required to model this emission (e.g. Sutherland & Dopita, 2017), all of them represent the scenarios proposed in the literature to explain this emission.

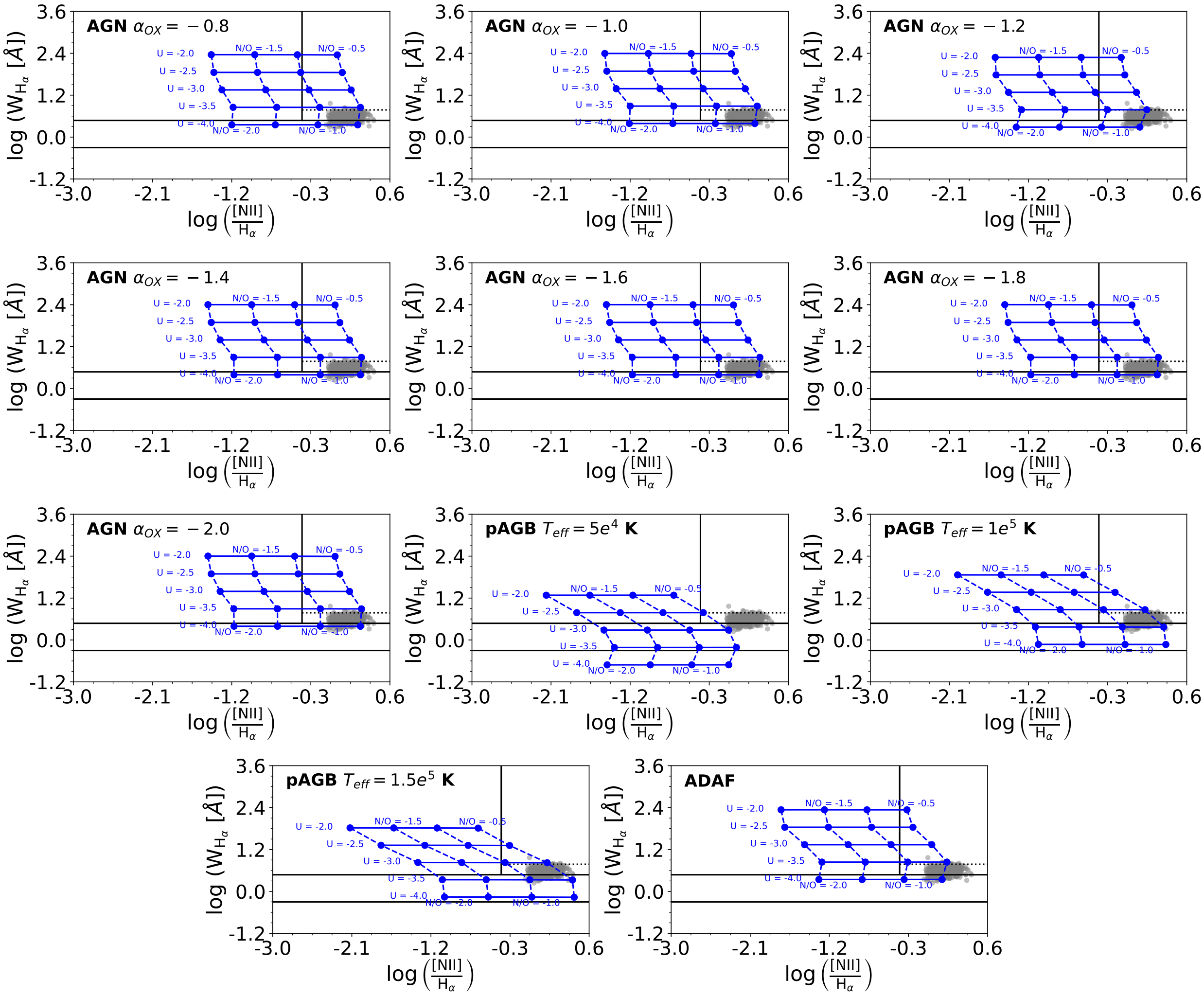

Figure 3.11: WHAN diagram for the LINER-like nuclear regions in our sample (gray dots) showing the coverage of the different grids of photoionization models. The grid of models was obtained by limiting the oxygen abundance to 12+log(O/H)=8.6 and employing different values of the ionization parameter log(U) as well as the nitrogen-to-oxygen abundance ratios log(N/O).

One of the major caveats of the identification of LINERs based on their optical emission lines arises from its possible classification from the diagnostic diagrams. Due to the uncertainty in the classification through the BPT diagrams (Baldwin et al., 1981; Kauffmann et al., 2003; Kewley et al., 2006), Cid Fernandes et al. (2010) proposed an alternative version using the information from the equivalent width of H_α to distinguish between AGNs and retired galaxies. To demonstrate the caveats of distinguishing wAGNs and RGs, we built a semi-empirical galaxy grid by rescaling the W_{H_α} predictions from our grids of photoionization models to the observed Balmer lines and continua in the central spaxels. We then consistently retrieved the expected position on the WHAN diagram for our semi-empirical modeled galaxies based on different properties of the gas-phase ISM (log(N/O) and log(U)). Fig. 3.11 shows that the position of a galaxy in the WHAN diagram is better provided by a particular combination of log(N/O) (which allows movement in the X-axis) and log(U) (which allows changes in the equivalent width) rather than by the ionizing source, although there are differences between the different ionizing sources, but they are not so extreme as to provide a clear classification.

Our study of the chemical abundances in the gas-phase ISM in our selected sample revealed some interesting constraints when different SEDs based on these assumptions were considered in the models. First of all, pAGB models are required to have high effective temperatures ($T_{eff} \geq 1 \cdot 10^5$ K) to reproduce the observed properties (Krabbe et al., 2021) and to obtain reasonable estimations of the oxygen abundance that are consistent with other galactic properties, as found in this work. ADAF models simulate an ionizing SED that is produced by inefficient accretion (e.g. Nemmen et al., 2014) and are not valid for determining LINERs out of the range of $8.4 < 12+\log(O/H) < 8.6$, in contrast to the rest of models explored in our work and in previous studies (Oliveira et al., 2022, 2024a; Pérez-Díaz et al., 2021).

The remaining two scenarios, pAGB stars or AGN standard activity, show slight differences in the estimated oxygen content. The first scenario provides wider ranges and a lower median value ($12+\log(O/H) = 8.50 - 8.57$) than the second ($12+\log(O/H) = 8.68 - 8.72$), although the differences are still compatible within the dispersion observed in our sample. As our sample is according to the WHAN diagram composed of wAGNs and RGs in a similar proportion (54.3% and 45.7%, respectively), it might be expected that the pAGB scenario is favored in RGs and the AGN is more accurate for wAGNs. However, we found no such evidence. Conversely, based on the position of RGs in the MZR (see Fig. 3.6), when pAGB stars are the source of ionization, then there is an offset of more than 0.5 dex from the expected value of 12+log(O/H) according to their stellar mass. Moreover, when we account for the secular evolution within the galaxy, we obtain a higher offset between the oxygen abundance as calculated assuming pAGB models and the values extrapolated from the gradient, even in the case of LINERs classified as RGs.

For the pAGB scenario, an additional problem arose. When we considered that pAGB stars emit $5 \cdot 10^{46}$ ionizing photons per second on average (Valluri & Anupama, 1996), and the average H_α luminosity in the integrated nuclear (r = 1 kpc) region is $\log(L(H_\alpha)\ [erg/s]) = 39.35$ (e.g. Krabbe et al., 2021), we can make use of the relation between the number of ionizing photons and the expected Hα luminosity (Osterbrock & Ferland, 2006), which is given by

$$N_{ion.\ ph}[s^{-1}] \approx 7.31 \cdot 10^{11} L\left(H_\alpha\right)[erg \cdot s^{-1}]. \tag{3.1}$$

to estimate the number of pAGB stars needed to reproduced that central emission assuming ionization-bounded conditions,

$$N_{pAGB} = \frac{N_{ion.\ ph,tot}}{N_{ion.\ ph,pAGB}} \approx 1.463 \cdot 10^{-35} L\left(H_\alpha\right)[erg \cdot s^{-1}], \tag{3.2}$$

which in this particular case yields $3.2 \cdot 10^4$ stars within a radius of 1 kpc. Since all these stars ionize the gas nowadays today, we can assume that they were formed roughly at the same time. Assuming the initial mass function (IMF) form from Salpeter (1955), we can then obtain the expected number of stars in a range of mass as

$$N = \int_{M_{min}}^{M_{max}} \xi\left(M\right) dM = \int_{M_{min}}^{M_{max}} \xi_0 M^{-2.35} dM. \tag{3.3}$$

We consider that the expected mass of the progenitors of pAGB stars ranges in $[1.5\ \mathrm{M}_\odot, 8\ \mathrm{M}_\odot]$ (e.g. Ventura et al., 2017). Given that the validity of the Salpeter IMF has a minimum value of $0.5\ \mathrm{M}_\odot$ and that we only consider an upper limit of $20\ \mathrm{M}_\odot$ (quite conservative), the probability of finding one pAGB star can then be calculated as

$$p = \frac{\int_{1.5M_\odot}^{8M_\odot} \xi_0 M^{-2.35} dM}{\int_{0.5M_\odot}^{20M_\odot} \xi_0 M^{-2.35} dM}, \tag{3.4}$$

which gives 20.46%, which is consistent with the idea that per globular cluster ($\sim 10^5$ L⊙) one pAGB star is expected (Renzini & Buzzoni, 1986; Valluri & Anupama, 1996). This is an upper limit to the probability of finding one pAGB star. Thus, the minimum number of globular clusters expected within a radius of 1 kpc should be around $\sim 3.2 \cdot 10^4$. For comparison, the number of globular clusters reported in the inner part of the Milky Way ($r < 3.5$ kpc) is lower than 100 (Bica et al., 2024). Thus, a pAGB nature of the ionizing source is less favored.

Overall, we cannot conclude on the source of ionization without other spectral regimes. For the AGN scenario, X-ray counterparts from the accretion disk surrounding the SMBH must be expected. This approach was followed by Pérez-Díaz et al. (2021) to justify the assumption of AGN activity when they analyzed their sample of LINERs from the Palomar Spectroscopic Survey. Additional constrains can be obtained with X-ray data, such as, the shape (α_{OX}) of the SED. Another important constraint can be found in the use of infrared (IR) emission lines, which trace highly ionic species such as O^{++}, O^{3+}, Ne^{++}, Ne^{4+}, Ne^{5+}, Ar^{++}, Ar^{4+}, or Ar^{5+} (Pérez-Díaz et al., 2022, 2024b). They might provide SED constraints by means of diagnostic diagrams such as the softness diagram (e.g. Pérez-Montero et al., 2024). We cannot exclude the possibility that pAGB stars ($T_{eff} \geq 1 \cdot 10^5$ K) contribute to the ionization of the gas-phase ISM together with central AGN emission, although the exact combination of these two ionizing sources is a much more complex issue for which better constraints are needed.

3.6.4 *N/O as an unbiased tracer of chemical enrichment*

Throughout this study, we distinguished between LINERs classified as wAGNs and RGs as a consequence of the uncertainty in the nature of the ionizing source in these objects (e.g. Márquez et al., 2017). For this reason, we explored different ionizing scenarios. On the one hand, we obtained different 12+log(O/H) estimations when we accounted for the AGN or the pAGB scenario (see Tab. 3.2 and Fig. 3.8). In contrast, an almost negligible change (considering the uncertainties) was found for the estimation of log(N/O) for all the assumed SEDs.

The importance of estimating log(N/O) was already highlighted by several authors (e.g. Pérez-Díaz et al., 2022; Pérez-Montero & Contini, 2009; Vincenzo et al., 2016). First of all, its importance relies on the use of estimators of the oxygen abundance based on the N emission lines, as an independent constraint on log(N/O) is needed to avoid effects of enhancing the metallicity through the high log(N/O) ratios (see, e.g., the difference between Oliveira et al. 2022 and Oliveira et al. 2024a). Second, an estimation of N/O complements not only the information, but also the degree of the chemical enrichment (e.g. Pérez-Montero et al., 2013, 2016; Pilyugin et al., 2004; Vincenzo et al., 2016). Third, it remains mostly unaffected by gas dynamics that can alter the chemical composition as traced by 12+log(O/H) (e.g. Amorín et al., 2012; Amorín et al., 2010; Edmunds, 1990; Köppen & Hensler, 2005; Pérez-Díaz et al., 2024a; Sánchez Almeida et al., 2015).

In addition, based on this study of the use of optical emission lines for estimating chemical abundances, we can also add another advantage to the use of log(N/O). It can be properly estimated without a bias when a particular ionizing source is assumed. Regardless of the ionizing source assumed for the gas-phase ISM, the log(N/O) abundances in our sample of LINERs are in the range [−1.20, −0.27]. They cluster around the value of ~ -0.79 (slightly suprasolar).

3.7 CONCLUSIONS

We analyzed a sample of 105 optically selected LINERs from SDSS-IV MaNGA. In particular, we studied the chemical abundances using photoionization models in their nuclear region that accounted for different scenarios that represent the uncertainty in the source of ionization: AGN models with different shapes, pAGB models with different effective temperatures, and inefficient-accretion AGN models in which the accretion disk was truncated (ADAF). To assess whether one or multiple scenarios might be feasible, we also used the WHAN diagram to distinguish between galaxies with intermediate equivalent widths of Hα, which are expected to be weak AGNs (wAGNs), and galaxies with low equivalent widths, which are though to be retired galaxies (RGs) and are thus powered by hot, old stellar populations.

Our results showed that oxygen abundances (12+log(O/H)) in the nuclear region of LINERs, with independent subtypes (wAGN or RG) and the SED, are spread over a wide range of values: $8.08 \leq$ 12+log(O/H) ≤ 8.82 in the pAGB scenario, and $8.30 \leq$ 12+log(O/H) $\leq$ 8.84for the AGN scenario. The corresponding median value is 12+log(O/H) = 8.69 (solar) for the AGN scenario, and it drops to 12+log(O/H) = 8.53 (slightly subsolar) in the pAGB scenario. The nitrogen-to-oxygen abundance ratios (log(N/O)) are mainly suprasolar, within the range $-1.20 \leq$ log(N/O) ≤ -0.38 (when AGNs are considered) or $-1.07 \leq$ log(N/O) ≤ -0.27. The median value reported in the pAGB scenario is slightly higher (log(N/O) = −0.69) than in the AGN scenario (log(N/O) = −0.79), and in both cases, it is slightly suprasolar. Overall, LINERs are mainly characterized by suprasolar log(N/O) ratios and sub- or close to solar 12+log(O/H) ratios. When we analyzed the behavior of these nuclear estimations with host galaxy physical properties such as stellar mass, we found no correlation, and we report a scatter in the MNOR diagram and not in the MZR diagram.

The assumptions on the nature of the ionizing source are critical for the 12+log(O/H), since pAGB models introduce much more scatter in the MZR relation and in their comparison with the extrapolation from metallicity gradients. This is highlighted in the behavior of the log(N/O) versus 12+log(O/H). When LINERs are considered to be powered by AGNs, little correlation is found between the two quantities, but the data fit the scatter of the reported relation in the literature. In contrast, when LINERs are considered to be powered by pAGB stars, then a negative correlation is found between the two quantities, as previously reported in the literature. We discussed several scenarios to explain this anticorrelation, although more specific studies of this result must be performed in order to obtain more robust conclusions.

Although we cannot rule out the possibility that emission in LINERs might be explained by pAGB stars, our study revealed that several problems arise from this assumption. First of all, in order to reproduce the emission detected in the nuclear region, a large number of pAGB stars is required, and it is hard to explain both the number and the simultaneous coexistence of those stars. Second, the results for the chemical enrichment (as seen from the log(N/O) vs. 12+log(O/H) diagram) indicate a complex scenario in which extreme events are needed to explain the observed relation. In contrast, when LINERs are assumed to be powered by AGNs, the chemical enrichment scenario does not depart from the reported trends in the literature in general, although some indications of an anticorrelation were found that might be explained with the scatter caused by the delay in the N production as well as other gas dynamical effects on 12+log(O/H), but these are less extreme than in the pAGB scenario.

4

THE SHAPE OF RADIAL METALLICITY GRADIENTS IN LINER GALAXY DISKS

Chapter based on the article: B. Pérez-Díaz, E. Pérez-Montero, I. A. Zinchenko, J. M. Vílchez, B. Tapia-Contreras, P. B. Tissera "Chemical enrichment in LINERs from MaNGA: II. Do AGN alter the shape of radial metallicity gradients in galaxy disks?", submitted to Astonomy & Astrophysics.

4.1 ABSTRACT

Chemical abundance radial gradients provide key information on how the processes that affect chemical enrichment of the gas-phase ISM act at different galaxy scales. Whereas in the last decades there has been an increase in the number of galaxies studied with integral field spectroscopy, there is still not a clear picture on a subsequent characterization of the chemical abundance radial gradients in galaxies hosting Active Galactic Nuclei (AGNs). This lack of analysis is even more accentuated in the case of low-ionization nuclear emission-line regions (LINERs). For the first time, we analyze the chemical abundance radial gradients in a sample of LINER-like galaxies, whose nuclear emission has been previously[1] (Paper I) discussed. We use a sample of 97 galaxies from the Mapping Nearby Galaxies at Apache Point Observatory (MaNGA), whose nuclear regions show LINER-like emission. We use the open-source code HII-CHI-Mistry to estimate the chemical abundance ratios 12+log(O/H) and log(N/O) in the HII regions across the disks in our sample, as well as in the nuclear parts where the LINER-like activity dominates. To fit the radial profiles we use a piecewise methodology which uses a non-fixed number of breaks to find the best fit for the data. We obtain that majority of our sample of galaxies exhibits departures from the single linear gradient both in 12+log(O/H) and log(N/O) (as expected from the inside-out scenario). We investigate whether these departures are driven by galaxy properties (stellar mass, neutral gas mass, stellar velocity dispersion), finding not correlation at all. We also report that in most cases there is no correlation between the shape of the 12+log(O/H) and log(N/O) radial profiles. We propose a model in which AGN feedback, acting at different scales depending on the galaxy and its evolutionary stage, might be responsible for these departures.

4.2 INTRODUCTION

The metal content of the gas-phase ISM is a witness of the evolutionary processes that shape host galaxies. As the production of metals from stars that eventually eject them, incorporating them to the ISM, and as galaxy mass assembly is related to star formation, the analysis of the metal content of the gas-phase in galaxies allows us to shed light on their evolution.

Studies analyzing the mean characteristic metallicity of the gas-phase ISM in galaxies have been performed over many decades (Hägele et al., 2008; Lequeux et al., 1979; M. Peimbert, 1967; Pilyugin & Grebel, 2016; Thuan et al., 1995; Vilchez et al., 1988), using spectroscopic information from different regimes such as ultraviolet (Feltre et al., 2016; Pérez-Montero & Amorín, 2017; Pérez-Montero et al., 2023b), optical (Belfiore et al., 2015; Curti et al., 2017; Curti et al., 2020; Pérez-Montero & Díaz, 2003) and infrared (Fernández-Ontiveros et al., 2021; Pérez-Díaz et al., 2022). By means of the determination of physical properties of the gas-phase ISM, such as temperature and density (direct

---

[1] See also Chapter 3.

method; Osterbrock & Ferland, 2006), photoionization models (Pérez-Montero, 2014; Thomas et al., 2018) or strong line calibrations based on bright emission lines (see Table 1 from Maiolino & Mannucci, 2019). Although most studies of the metal content of the gas-phase ISM are focused on star-forming galaxies (SFGs), its study has also recently extended to Active Galactic Nuclei (AGN; e.g. Carvalho et al., 2020; Dors et al., 2019; Pérez-Díaz et al., 2021; Pérez-Montero et al., 2019a).

Oxygen, whose relative abundance is usually expressed as 12+log(O/H), is generally used as the main tracer of the metal content (see Maiolino & Mannucci, 2019, for a review) as a consequence of its bright emission lines easily detected in almost all spectral ranges (ultraviolet, optical and infrared) and because it is the most abundant element in mass in the gas-phase ISM (M. Peimbert et al., 2007). However, oxygen expressed in relative terms to the hydrogen content of the gas-phase ISM is susceptible of changes in the gas composition due to inflows (e.g. Pérez-Díaz et al., 2024a), outflows (e.g. Villar Martín, M. et al., 2024) or depletion into dust (e.g. Calura et al., 2008). On the other hand, information on other chemical species can be provided to have a better understanding on the ISM chemical enrichment history. For instance, the nitrogen-to-oxygen ratio (log(N/O)), involves an α-element (O), mainly produced by massive stars, with nitrogen, which has an extra channel of production by means of CNO cycles inside stars of intermediate mass (e.g. Henry et al., 2000). Thus, under the requirement of O already present in the ISM from which stars were born, the simultaneous study of O/H and N/O allows us to quantify the several effects leading to a dilution of metallicity in the gas-phase of galaxies.

All these observational studies of metallicity in the gas-phase of galaxies can be complemented with theoretical works based on chemical evolution models (Köppen & Edmunds, 1999; Pagel & Patchett, 1975; Sharda et al., 2021; Spitoni et al., 2019), simulations of individual/interacting galaxies (Montuori et al., 2010; Perez et al., 2011; Rupke et al., 2010) or cosmological simulations (Kobayashi et al., 2007; Lia et al., 2002; Mosconi et al., 2001), in which the many astrophysical processes that enrich the ISM (supernovae feedback, outflow enrichment, pAGB stars, etc) are incorporated in te sub-grid modeling, and later on, compared to the observational results to constrain and predict the different ways in which galaxies evolve. In this context, the predicted timescales of the different processes that enrich the ISM, later affecting the overall content of gas, stars and dust, are not only relevant for the galaxy as a whole, but also at smaller scales (Sharda et al., 2021, 2024; Tissera et al., 2022). Therefore, the study of both O/H and N/O in the gas-phase ISM across different regions in the galaxy (including radial metallicity gradients) is also crucial in understanding the chemical evolution of galaxies.

Radial metallicity gradients have largely benefit in the last decades from to the advent of large surveys acquired with integral field spectroscopy (IFS) such as CALIFA (Sánchez et al., 2013), MaNGA (Bundy et al., 2015) or SAMI (Poetrodjojo et al., 2018) for low-redshift galaxies ($z < 0.2$). Several studies (e.g. Rich et al., 2012; Sánchez et al., 2014; Sánchez-Menguiano et al., 2016; Vila-Costas & Edmunds, 1992; Zinchenko et al., 2019) found evidence that most galaxies present a negative oxygen abundance gradient from the inner to the outer most parts of galaxies with discs. The analysis of the radial metallicity gradient by means of log(N/O) reveals a similar trend (e.g. Pérez-Montero et al., 2016; Pilyugin et al., 2004; Zinchenko et al., 2021; Zurita et al., 2021b). These results, also supported by the analysis of stellar populations within the disc (e.g. Muñoz-Mateos et al., 2007; V. A. Taylor et al., 2005) as well as the star formation histories (SFHs; Sánchez-Blázquez et al., 2009), reinforces the scenario in which gas accretion moves from outer to inner parts in the galaxy, reaching higher density and triggering star formation in the innermost parts, leading to its faster enrichment (Matteucci & Francois, 1989). This is the so-called inside-out growth of galaxies.

However, the above scenario is challenged by other set of observations. First of all, some high-redshift galaxies also exhibit positive or flattened radial gradients (Carton et al., 2018; Cresci et al., 2010), attributed in many cases to the infall of metal-poor gas (e.g. Bresolin et al., 2012). Bars are thought to be an efficient mechanism in gas migration within galaxies (Athanassoula, 1992; Friedli et al., 1994), but no consensus is found if either bars affect radial metallicity gradients flattening them (Vila-Costas & Edmunds, 1992; Zaritsky et al., 1994) or remain unchanged (Sánchez et al., 2014; Zinchenko et al., 2019; Zurita et al., 2021a). Likewise, contrary results are reported on whether radial gradients change with morphological type (Vila-Costas & Edmunds, 1992) or they are independent (Zaritsky et al., 1994). Many other effects add complexity to the picture: galactic fountains that causes gas being ejected from the disc due to supernovas and capture again due to the gravitational potential (Spitoni et al., 2013); interaction and merger between galaxies (Rupke et al., 2010; Sillero et al., 2017); stellar mass biasing gas accretion (Camps-Fariña et al., 2023; Spitoni et al., 2021); stellar age differentiation (Zinchenko et al., 2021); strong-metal rich galactic outflows (e.g. Tissera et al., 2022); azimuthal variations (Spitoni et al., 2019; Vogt et al., 2017); or spiral arms (Spitoni et al., 2021). Moreover, it has been reported that the idea of a single slope radial metallicity gradient might not be accurate in many cases (e.g. Sánchez-Menguiano et al., 2018; Tapia-Contreras et al., 2025). To asses the impact of some of these processes, the analysis of log(N/O) has been extensively used (e.g. Pérez-Montero et al., 2016; Zinchenko et al., 2021; Zurita et al., 2021b), finding similar results to those reported for the 12+log(O/H) radial gradient.

Another important aspect that needs to be considered in the picture of chemical enrichment within galaxies, is the effect of a possible presence of Active Galactic Nuclei (AGNs). As the realm of chemical studies of the Narrow Line Region (NLR) in AGNs is scarce, much less studies can be found on the radial metallicity gradient in galaxies with a significant fraction of AGN activity. P. Taylor and Kobayashi (2017), using cosmological simulations accounting for AGN feedback, they found that galaxies with strong AGN activity cannot recover from previous merger events and their metallicity radial profiles tend to flatten. However, it has been reported observationally that metallicity radial gradients might show a decrease in the inner parts. Indeed, do Nascimento et al. (2022) reported from the analysis of radial chemical abundance gradient in Seyfert galaxies that nuclear abundances are even lower than the expected extrapolation, supporting this scenario. Other studies, such us those analyzing 12+log(O/H) and log(N/O) abundances in the nuclear region of AGN-hosting galaxies (Oliveira et al., 2024a; Pérez-Díaz et al., 2021, 2022) support this scenario as log(N/O) mostly remains solar or suprasolar (an advanced chemical enrichment history), whereas 12+log(O/H) spread over a wide range of metallicities, from subsolar to solar, as a possible consequence of infalls of gas. More recently, Amiri et al. (2024) found not only that AGN nuclear abundances are lower than the extrapolated value, but also that there is an inverse radial metallicity gradient within the regions dominated by AGN activity.

However, the realm of low-luminosity AGNs (LLAGNs), a tag under which LINERs can be accounted for, is poorly explored. Indeed, only the galaxy UGC 4805, with IFS data from MaNGA has been analyzed (Krabbe et al., 2021), reporting that the nuclear abundances are in consonance with the extrapolation from the radial metallicity gradient. The regime of LLAGN is key in order to understand the differences in evolution between AGNs and SFGs, as the AGN emission is much weaker and, thus, its effects can be constrained to the nuclear region, producing lower deviations from the expected radial behavior. Furthermore, LLAGNs represent a predominant fraction of active galaxies in the local Universe (e.g. Ho, 2008), so a proper analysis of the radial metallicity gradients in these objects is necessary to have a clear picture on how AGNs affect the evolution of galaxies. As AGN feed and feedback is intrinsically associated to gas hydrodynamics, a simultaneous analysis of N and O radial profiles is essential to disentangle their effects.

Exploiting the capabilities of IFS data from SDSS IV - MaNGA survey (Blanton et al., 2017; Bundy et al., 2015), in Pérez-Díaz et al. (2025, hereinafter Paper I), we presented an analysis of 105 galaxies classified as LINERs. By means of HCm (Pérez-Montero, 2014), we obtained independent estimations for O/H and N/O chemical abundances in the nuclear region of these galaxies, concluding that their chemical composition is well explained under the AGN ionizing scenario. This second paper is devoted to the analysis of the radial metallicity gradients in the same sample. In section

4.3, the selection of the galaxy sample hosting LINER-like emission is explained as well as other different criteria used in this study. In section 4.4 we discuss the methodology employed to estimate chemical abundances in our sample. In section 4.5 we present the main results of this study followed up by a discussion in section 4.6. In section 4.7 we summarize our main conclusions.

4.3 SAMPLE SELECTION

4.3.1 *MaNGA data and emission line measurements*

The Mapping Nearby Galaxies at Apache Point Observatory (MaNGA; Bundy et al., 2015) is part of the Sloan Digital Sky Survey IV (SDSS IV; Blanton et al., 2017). For this work, we used data release 17 (DR17, Abdurro'uf et al. 2022). We used individual spaxels ensuring that their size was significantly smaller than that of the point spread function (PSF) in the MaNGA datacubes. Overall, the spatial resolution of these cubes has a median full width at half maximum (FWHM) of 2.54 arcsec (Law et al., 2016).

We examined the MaNGA spectra following the same procedure as in Zinchenko et al. (2016, 2021). Briefly, we used the code STARLIGHT (Asari et al., 2007; Cid Fernandes et al., 2005; Mateus et al., 2006) to fit the stellar background throughout all spaxels, adapting it for parallel datacube processing. We used simple stellar population (SSP) spectra from Bruzual and Charlot (2003) evolutionary synthesis models for stellar fitting, and we subtracted them from the observed spectrum to obtain a pure gas spectrum. After that, we fitted emission lines using our ELF3D code. Each emission line was fitted with a single-Gaussian profile. For each spectrum, we measured the fluxes of the [O II]$\lambda,\lambda3726, 3729$Å (hereinafter [O II]$\lambda3727$Å), [Ne III]$\lambda3868$Å, H_{β}, [O III]$\lambda4959$Å, [O III]$\lambda5007$Å, [N II]$\lambda6548$Å, H_{α}, [N II]$\lambda6584$Å, and [S II]$\lambda,\lambda6717, 6731$Å lines with a signal-to-noise ratio, S/N, > 3.

4.3.2 *Sample of galaxies*

Sample selection is described in more detail in Paper I. In short, we selected from the MaNGA survey (Blanton et al., 2017; Bundy et al., 2015) a sample of galaxies whose nuclear emission is dominated by LINER-like emission according to the diagnostic diagrams (Baldwin et al., 1981; Kauffmann et al., 2003; Kewley et al., 2006). After imposing that galaxies must be classified as LINERs in all diagnostic diagrams, we came up with a sample of 329 galaxies.

From that sample, we imposed the criterion that LINER-like emission comes mainly from the nuclear region (< 2 kpc), i.e., the emission line ratios from spaxels retrieving emission from the outer regions are mainly classified as HII regions according to the same diagnostic diagrams. By doing this, we ensure to have enough HII regions to properly analyze radial metallicity gradients and compare the HII regions properties with those in central spaxels. After this filter, we came up with a sample of 105 LINER-like galaxies, classified according to the WHAN diagram (Cid Fernandes et al., 2010, 2011) as weak-AGNs (wAGNs, 57) and retired galaxies (RG, 48).

In order to avoid systematic errors in the deprojection effects of the highly inclined galaxies in our sample, we imposed a minimum value for the axis ratio $b/a > 0.3$ from the r-band Sersic profile fit. This criterion excludes eight objects, leading to a final sample of 97 galaxies, divided as 55 wAGNs (56.7%) and 42 RGs (43.3%).

HII regions in each galaxy were selected from the remaining spaxels that verify the diagnostic criteria for the BPT diagrams (Baldwin et al., 1981; Kauffmann et al., 2003; Kewley et al., 2006). Particularly, we selected only those regions either classified as *SFG* (equivalently HII regions) simultaneously in the three diagrams or those regions that fall in the *composite* region (Kewley et al., 2006). As the composite region can accommodate HII regions with high log(N/O) ratios, which are expected in the central parts according to the inside-out scenario (e.g. Pérez-Montero et al., 2016; Zurita et al., 2021b), we considered them as well in our analysis.

4.3.3 *Ancillary data*

We retrieved complementary data on the physical properties of the host galaxies from the NASA-Sloan Atlas (NSA) catalog[2]. Particularly, we retrieved the stellar mass (M_*) as estimated from a K-correction fit to the elliptical Petrosian fluxes assuming an initial mass function (IMF) from Chabrier (2003) and stellar population models from Bruzual and Charlot (2003), as well as R_e radii, Sersic 50% light radius along major axis across the r-band.

Additionally, we retrieved the chemical abundances estimations for the nuclear region of our sample of LINERs as reported in Paper I. Since the authors provided the estimations based on different ionizing sources from the HII-CHI-Mistry[3] code (Pérez-Montero, 2014), we took four estimations as representative of all the considered scenarios: AGN characterized by $\alpha_{OX} = -1.6$[4]; hot old stellar populations dominated by post-asymptotic giant branch (pAGB) stars and characterized by two different effective temperatures $T_{eff} = 10^5$ K and $T_{eff} = 1.5 \cdot 10^5$ K; and advection-dominated accretion flow (ADAF) model for the AGN. Details on the considered models and how they were implemented can be found in Paper I.

4.4 METHODOLOGY

In this section we present a detailed explanation on the methodology used to estimate chemical abundances as well as other physical parameters from the nebular emission of HII regions in our sample of galaxies. We also give details on the calculation of the corresponding radial gradients estimated for those properties.

4.4.1 *HII-CHI-Mistry*

To ensure consistency with the results reached in Paper I, as well as between the estimations of chemical abundances in the nuclear region (dominated by the LINER-like emission) and the rest or regions in the disk of each galaxy in our sample, we used HII-CHI-MISTRY v5.5 (hereinafter HCM). HCM uses a grid of photoionization models (to be selected among the available ones or introduced by the user) with three free parameters, the chemical properties of the gas-phase ISM 12+log(O/H) and log(N/O) as well as the ionization parameter log(U). The code compares the emission-line fluxes predicted by the grid of models with the observed (input) emission line ratios sensitive to those parameters. Firstly, the code estimates log(N/O) which is used to constrain the grid of models in the later iterations. Secondly, the code performs an estimation of 12+log(O/H) and log(U).

In the case of HII regions, we selected as ionizing source a young stellar cluster with an age of 1 Myr, as taken from POPSTAR (Mollá et al., 2009) synthesis code for an initial mass function (IMF) that follows the trend reported by Chabrier (2003). The density of the gas is assumed to be constant with a value of 100 cm^{-3}. This grid of models was calculated using CLOUDY v17 (Ferland et al., 2017). Due to the lack of measurements of the auroral line [O III]$\lambda 4363$Å in our MaNGA sample, we used an additional constrain to the grid of models, consisting of the relation between 12+log(O/H)

---

[2] https://www.sdss4.org/dr17/manga/manga-target-selection/nsa/.

[3] The code is publicly available at http://home.iaa.csic.es/~epm/HII-CHI-mistry.html.

[4] We note that very recently, Pérez-Montero et al. (2025) obtain that LINERs are characterized by slightly higher slopes ($\alpha_{OX} \approx -1.4$). As demonstrated in Paper I, results under both assumptions are compatible.

and log(U) reported by Pérez-Montero (2014). The estimation of log(N/O) remains completely independent, thus no fixed relation with 12+log(O/H) was assumed in this work.

We used as input for HCm the emission line ratios [O II]λ3727Å, [Ne III]λ3868Å, [O III]λ5007Å, [N II]λ6584Å and [S II]λ6717Å+[S II]λ6731Å, referred to H_β emission. All emission line ratios have been corrected from reddening assuming Case B photoionization and an expected ratio between H_α and H_β of 2.86 for standard conditions found in HII regions, that is, an electron density $n_e \sim 100$ cm^{-3} and an electron temperature $T_e \sim 10^4$ K (Osterbrock & Ferland, 2006). We assumed the extinction curve from Howarth (1983) for $R_V = 3.1$.

4.4.2 *Radial metallicity gradients*

For each galaxy, we used the estimated chemical abundances (12+log(O/H) and log(N/O)) from HCm in the HII regions and their distance to the galaxy center in terms of R_e to characterize their radial metallicity gradient up to $4R_e$. In order to fit the observed trends, we tested three different methodologies to reproduce most of the scenarios explored in the literature:

- Single linear fit with no restrictions in the slope neither on the Intersect.
- Double linear fit accounting for a break[5] at exactly $R = R_e$, and again with no restrictions on the slopes or intersects.
- Piecewise fit allowing for several breaks at no fix positions but ensuring continuity in the estimation through all intervals (see Tapia-Contreras et al., 2025, for more details on the methodology).

To test the goodness of the fits, we used the Square Root Error (RSE), which can be applied to any fit:

$$\mathrm{RSE} = \frac{\sqrt{\sum_i^n (p_i - y_i)^2}}{n-2} \tag{4.1}$$

where p are the values predicted from the fit, y are the estimated values and n the number of points (i.e. number of HII regions). As piecewise methodology accounts for a non-fixed number of breaks, we also assessed the goodness of the fit accounting for the number of breaks obtained from the piecewise fit.

We show in Fig. 4.1 (a) the goodness of the different fit techniques for the 12+log(O/H) radial gradient. We conclude that single linear fit offers the highest RSE, with exception of those galaxies where piecewise methodology finds a fit without any break. When comparing piecewise methodology with double linear fit, we can see that the majority of the fits offer a lower RSE for the former one. A similar result is obtained when analyzing the fit for the radial gradient of log(N/O) (see Fig. 4.1 (b)). Then, we only consider thereafter for our analysis the results obtained from piecewise fit.

4.5 RESULTS

4.5.1 *Trends in the radial metallicity gradients*

We show in Appendix C.3 the radial metallicity gradient for each galaxy both for 12+log(O/H) and log(N/O). From Fig. C.5 we can conclude that our sample of LINER-like galaxies shows a variety of trends. We summarize these trends for both 12+log(O/H) and log (N/O) radial gradients in Table 4.1.

---

[5] Hereinafter we will refer to the point where the linear fit changes as break.

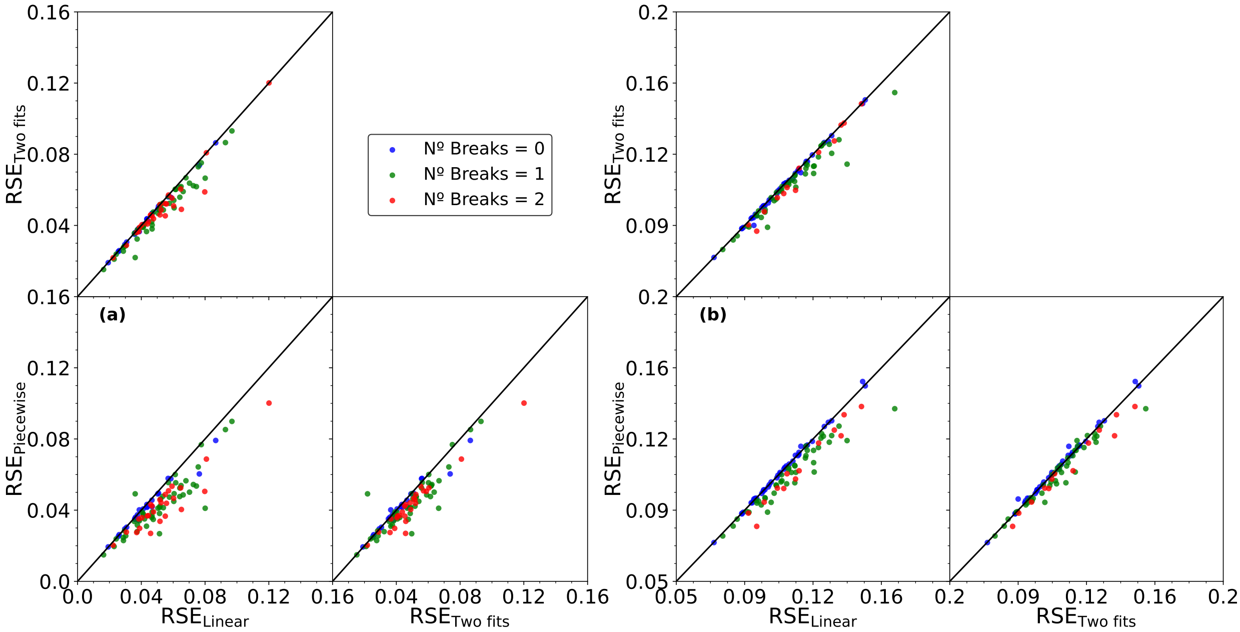

Figure 4.1: Root Square Error (RSE) for the different techniques used to fit the radial metallicity gradients of 12+log(O/H) (a) and log(N/O) (b) in our sample of LINERs. The sample is segregated according to the number of breaks used by piecewise fit for each chemical abundance ratio.

4.5.1.1 *Breaks in the fits*

Around half of our sample (49.49%) exhibits a 12+log(O/H) radial gradient with one single break, whereas the rest of galaxies are almost split between none (23.71%) or two breaks (26.80%). In the case of log(N/O) radial gradient we found a different scenario: galaxies are almost equally distributed between none or one break ($\sim 43 - 44\%$), and only a small group of galaxies (13.4%) shows two breaks. These results highlight the importance of using fit profiles more complex than a simple linear fit for radial metallicity gradients in galaxies, specially for 12+log(O/H).

Table 4.1: Statistics of the radial metallicity gradients in our sample as obtained using piecewise method. Column (1) and (2) show the number of breaks needed to fit 12+log(O/H) and log(N/O) radial gradients respectively. Column (3) shows the total number of galaxies for each group. Column (4) shows the relative number of galaxies with respect to the group. Column (5) shows the relative number of galaxies with respect to the whole sample.

N. Breaks (O/H) (1)	N. Breaks (N/O) (2)	N. Gal (3)	Perc. (%) (4)	Perc. tot. (%) (5)
0	0	9	39.13	9.28
	1	12	52.17	12.37
	2	2	8.70	2.07
1	0	18	37.50	18.56
	1	22	45.83	22.68
	2	8	16.67	8.25
2	0	14	53.84	14.43
	1	9	34.62	9.28
	2	3	11.54	3.10

When comparing between them the results from 12+log(O/H) and log(N/O) radial metallicity gradients, we observe that there is no correlation between the number of breaks in each one of them in each galaxy. Regardless of the fit obtained for 12+log(O/H), the best fit for log(N/O) radial gradient has either a none or a single break (> 80%). Moreover, for a given particular scenario of the 12+log(O/H) profile, there is a higher probability that the log(N/O) profile does not follow the same trend (> 50%). This result might be interpreted as a decoupling of 12+log(O/H) and log(N/O) radial gradients.

Table 4.2: Statistics of the breaks in the obtained radial metallicity gradients of 12+log(O/H) in terms of R_e. Column (1) shows the number of breaks. Column (2) shows the total number of galaxies. Columns (3) and (4) show the median and standard deviation distances in terms of R_e.

	12+log(O/H)			
N. Breaks (1)	N. Gal. (2)	$R_{med.}$ (3)	R_{std} (4)	Range (5)
1	48	0.87	0.49	[0.25, 2.97]
2 (Inner)	26	0.61	0.32	[0.05, 1.56]
2 (Outer)	26	1.09	0.6	[0.09, 2.93]

Table 4.3: Same as Table 4.2 but for log(N/O).

	log(N/O)			
N. Breaks (1)	N. Gal. (2)	$R_{med.}$ (3)	R_{std} (4)	Range (5)
1	43	0.83	0.53	[0.08, 2.98]
2 (Inner)	13	0.76	0.43	[0.18, 1.64]
2 (Outer)	13	1.16	0.68	[0.34, 3.17]

We also present in Tables 4.2 and 4.3 the statistics of the breaks in the obtained radial metallicity gradients both for 12+log(O/H) and log(N/O), respectively. As it can be seen, most of the breaks are found at a radial distance around R_e. More specifically, when only one break is found, it is generally located at a mean value around 0.9 ($\pm$0.5) RR_e, although in a wide range of values [0.1 R_e, 2.98 R_e].

When comparing the breaks obtained for 12+log(O/H) and log(N/O) radial gradients, we observe that, although the statistics might reflect similar values, there is not any correspondence, as observed in Fig. 4.2. This result reinforces the idea that 12+log(O/H) and log(N/O) radial gradients are essentially decoupled.

For the following analysis, we consider the part of the gradient that goes from the outer most region to the more external break as *outer* part. In the case of a galaxy presenting two breaks, we consider the region that goes between them as *middle* part. Finally, in both cases, the *inner* part is defined as the one that goes from the nuclear region to the break closer to the center. In the case of galaxies with two breaks, we consider the one closer to the center of the galaxy as *inner break*, and the other as *outer break*. No specification is made when the corresponding radial fit only presents one break.

4.5.1.2 *Slopes of the radial gradients*

We show in Fig. 4.3 the slopes of the fits in our sample of LINER-like galaxies, simultaneously for 12+log(O/H) and log(N/O). We distinguish among galaxies with no breaks (panels (a) and (d)), galaxies with one break (panels (b) and (e)) and galaxies with two breaks (panels (c) and (f)).

As it can be seen, galaxies presenting no breaks in the fit of the 12+log(O/H) radial gradient (panel (a)) show a flattened behavior, as the slope is close to $\nabla_{O/H} = 0.0$. On the contrary, galaxies with no

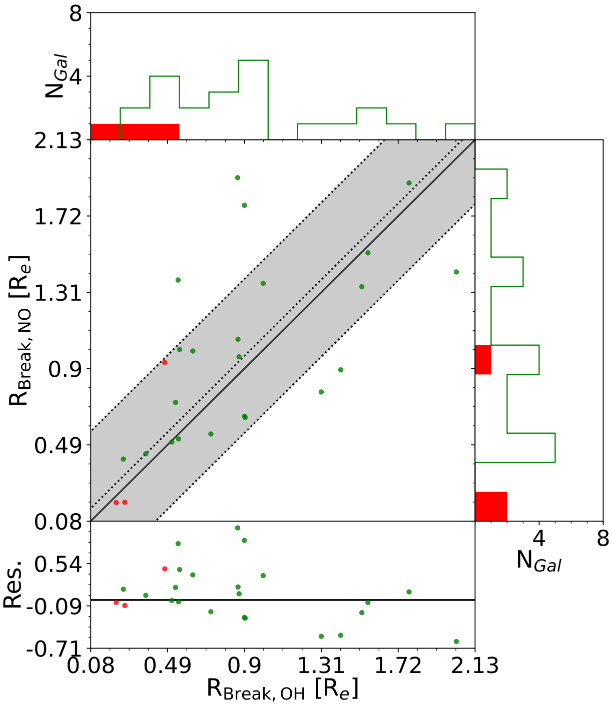

Figure 4.2: Comparison between the breaks found for the log(N/O) radial gradients (y-axis) and 12+log(O/H) radial gradients (x-axis) in our sample. Green dots correspond to LINERs showing one break in both gradients, whereas red dots correspond to LINERs showing two breaks. The solid black lines represent the one-to-one relation, the dotted lines represent the median offset, and the shaded gray area the deviation.

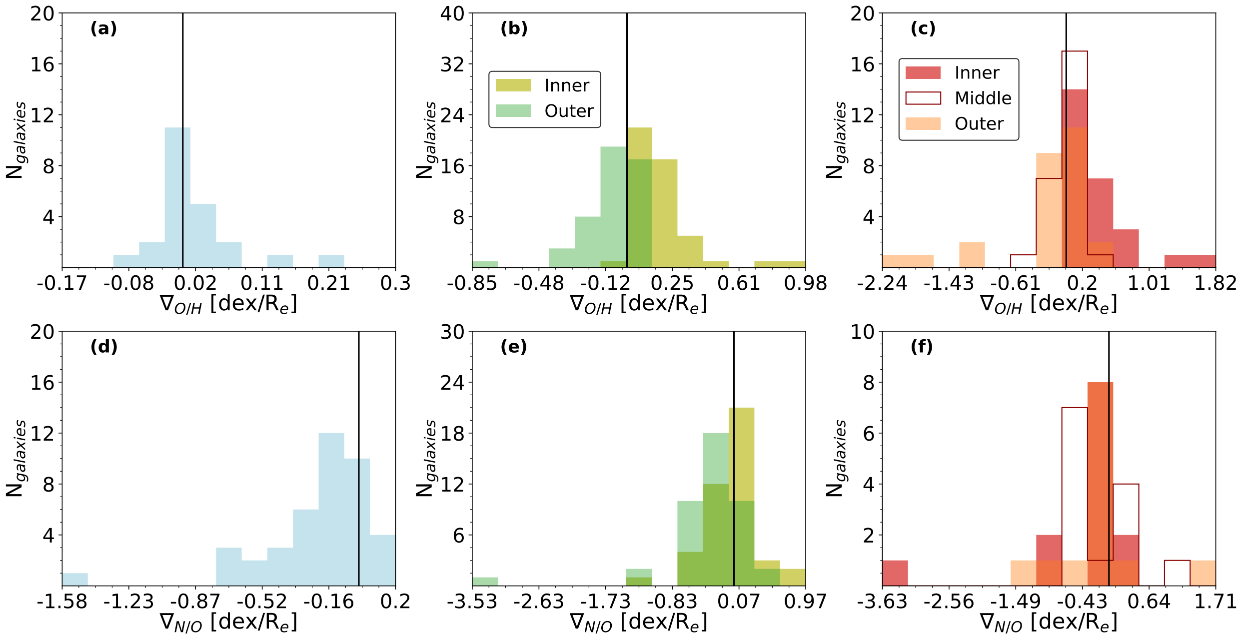

Figure 4.3: Histogram of the obtained gradient slopes in the fits for both 12+log(O/H) and log(N/O) for different categories attending to the number of obtained breaks. Slopes for 12+log(O/H): (a) galaxies with no breaks, (b) galaxies with one single break, and (c) galaxies with two breaks. Lower plots (d),(e) and (f) are similar to the above ones but for log(N/O) radial gradient. For all plots, solid black lines represent the flatten profile ($\nabla = 0$).

breaks in the log(N/O) radial fit mainly show negative gradients[6] (panel(b)), in concordance with the inside-out growth scenario. If we consider the group of galaxies with only one break (panels (b) and (d)), we observe that for both 12+log(O/H) and log(N/O) the outer slope is mainly negative or flattened, in contrast to the inner slope which is mainly positive for 12+log(O/H), with some cases (five galaxies) for log(N/O) as well.

Finally, the analysis of the slopes in galaxies with two breaks reinforces the previous results obtained for 12+log(O/H): the inner part shows positive slopes while the outer part shows negative or close to zero slopes (see panel (e)). The middle parts of the galaxies tend to show almost flattened gradients. Regarding log(N/O), apart from a galaxy that shows a strong negative slope in the inner part[7], both the inner and middle slopes are mainly negative whereas the outer parts are close to $\nabla_{N/O} = 0$.

4.5.1.3 *Intersects of the radial gradients*

Lastly, we analyzed the intersects of the metallicity radial gradients, i.e., the extrapolation of the fits to the galaxy nuclei (we considered different intersects according to the shape and breaks of their gradients). We show the results in Fig. 4.4, for which we considered as reference in each galaxy the value in the nuclear region as estimated in Paper I. These abundances were calculated assuming AGN models, which are the ones found to better reproduce most of the scaling relations in the studied sample (Paper I).

Firstly, we analyzed whether the extrapolation of the innermost radial metallicity gradients match the estimations obtained from the nuclear regions (as traced by the metallicity of the AGN). From Fig. 4.4 (a) we conclude that, on average, the extrapolations of the 12+log(O/H) fits are in agreement with the nuclear estimations (median offset of 0.02 dex), although there is a wide scatter. On the other hand, we obtained that the extrapolations of the log(N/O) fit (panel (b)) are also, on average, in agreement (median offset 0.07 dex), but with less scatter. This is a similar result as that reported in Paper I, where all ionizing scenarios were tested.

When we account for the extrapolations of the middle radial gradient (for galaxies with two breaks) or the outer gradient (for galaxies with one break), we obtained that the extrapolations from that fit lead to a clear overestimation of the nuclear abundance in both cases (panels (c) and (d)). We observe that the offset from the log(N/O) radial gradient (~ 0.27 dex/R_e) is higher that that found for the 12+log(O/H) (~ 0.14 dex/R_e). Interestingly, we observe that the extrapolations from the 12+log(O/H) middle radial gradient are systematically above the predictions for the nuclear region, whereas in the case of the log(N/O) extrapolations there is a non-negligible group of galaxies for which their middle radial fits predict lower abundances.

Finally, we analyzed the extrapolations from the outer radial fits in the case of LINERs with two breaks. The results shown in panels (e) and (f) reveal a similar picture to that observed in the extrapolations from the middle radial fit. However, in this case we also report that the deviation is much higher and that the relative number of galaxies whose radial fits predict lower abundances compared to the nuclear estimations is higher as well.

4.5.2 *Exploring the connection of galaxy properties with gradient shapes*

Several authors have discussed the role played by different galaxy properties, such as stellar mass or star formation rate, in the shape of the radial metallicity gradients observed in disk galaxies

---

[6] We notice the strong negative gradient for galaxy 8942 – 12702, which is explained by the lack of HII regions at larger radii (see Fig. C.5).

[7] Again, this outlier corresponds to galaxy 8243 – 9102, whose fit to the radial gradient can be visually inspected in Fig. C.5, the analysis of the slopes reveals that there is not enough HII regions to properly trace the inner gradient.

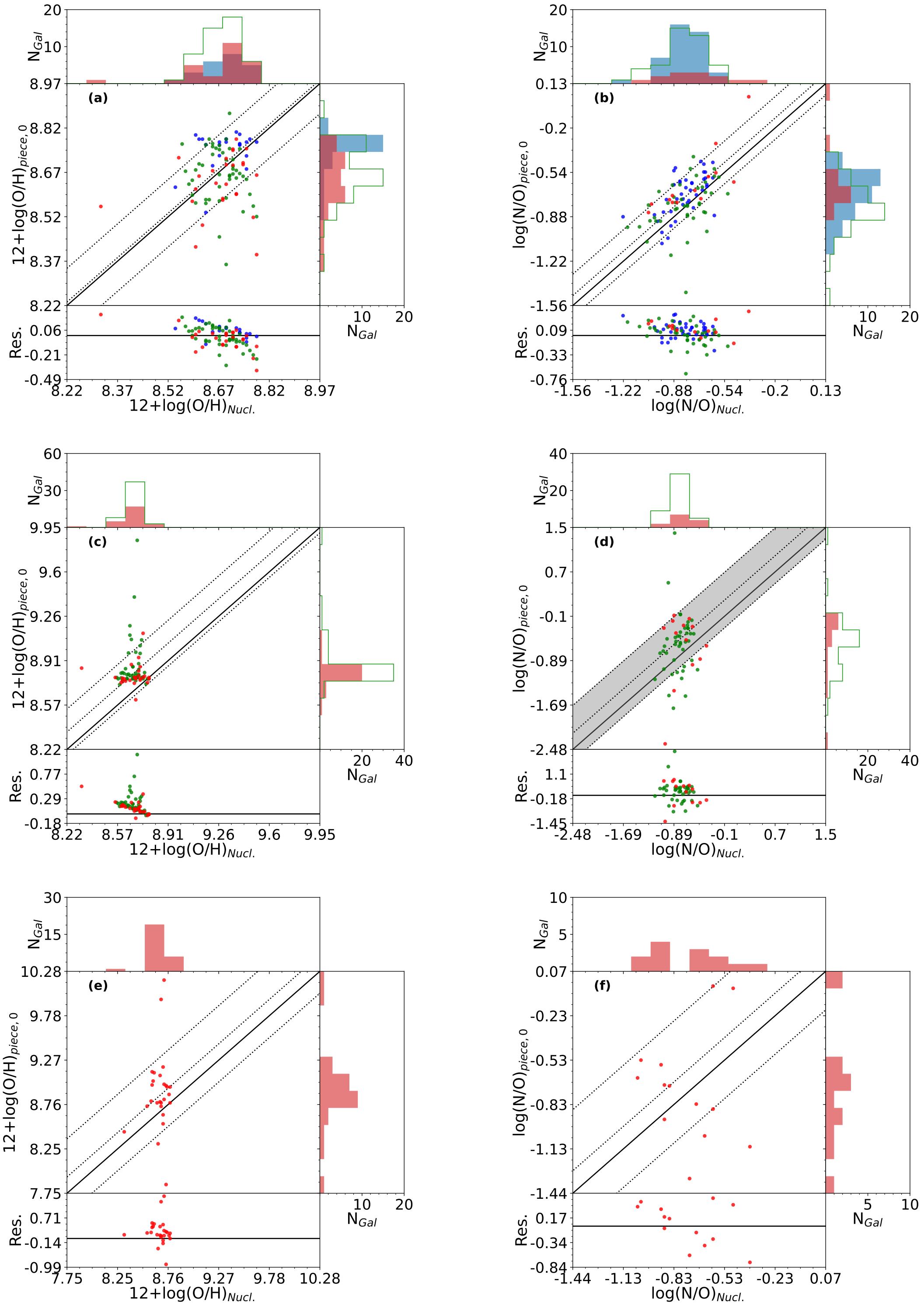

Figure 4.4: Comparison of the abundances obtained as intersects from the fits with the abundances estimated in the nuclear regions both for 12+log(O/H) (left column) and log(N/O) (right column). Plots (a) and (b) represent the extrapolation of the innermost radial fits, while plots (c) and (d) represent the extrapolation of the middle radial fits, and plots (e) and (f) the extrapolations of the outer radial fits. For all plots, Blue dots represent galaxies with no breaks in their corresponding fits, green dots galaxies with one break, and red dots galaxies with two breaks. The solid black lines represent the one-to-one relation, the dotted lines represent the median offset, and the shaded gray areas the deviation.

(e.g. Cardoso et al., 2025; Sánchez-Menguiano et al., 2018). In this section we discuss whether the variety of the metallicity radial gradient profiles found in our sample are connected to the properties of the host galaxies and/or the nature of their nuclear region. We separately explored the three characteristics of the radial profiles: the number of breaks, the slopes and the intersects.

Firstly, we analyzed whether the number of found breaks in 12+log(O/H) and log(N/O) radial fits correlate with stellar or HI mass. We found similar distributions for the whole sample and for each group of galaxies, implying that neither stellar nor HI mass are responsible for the number of breaks observed in our sample (see Fig. 4.6 and 4.7). We also explored whether the number of breaks correlate with any physical property of the nuclear part, including their derived chemical abundances, the stellar velocity dispersion (which directly correlates with the mass of the Super Massive Black Hole (SMBH) in case of AGN activity) or the equivalent width of H_α (whose strength allows us to discriminate the type of nuclear activity). In all cases, we found again that there is no correlation at all with the number of breaks (see Fig. 4.8).

We then analyzed whether the slopes of the radial fits (∇) for both 12+log(O/H) and log(N/O) correlate with stellar mass. Our results are shown in Fig. 4.5. In the case of 12+log(O/H), we obtained that: i) galaxies with no breaks tend to show flatten profiles (blue dots in panel (a)), whereas the rest of galaxies show positive slopes; ii) galaxies with one (and two breaks) tend to show negative slopes in the outer (middle) part of their profiles, being more negative when stellar mass increases (panel (c)); and, iii) the slope of outer profile in galaxies with two breaks does not correlate with stellar mass (panel (e)).

On the other hand, when analyzing log(N/O), we obtained that i) there is no correlation between stellar mass and the slope of the inner radial fit for all types of galaxies; ii) the slope of the outer fit in galaxies with one break is meanly negative and shows a strong anti-correlation with stellar mass (a similar result is obtained for the slope in the middle part of galaxies with two breaks); and, iii) similarly to 12+log(O/H), no particular trend is found for the slope of the outer profile of galaxies with two breaks.

Finally, we inspected whether intersects correlate with any of the other studied properties. In particular, we analyzed the relation between the host galaxy properties with the extrapolations of the metallicity radial fits to the nuclei ($R = 0$) (i.e. the intersects of the inner radial fits). First of all, we checked if there is a correlation with stellar mass, as it might be suggested by the so-called mass-metallicity relations (MZR and MNOR). Our results are similar to those reported in Paper I for AGN models (see Fig. 6 and 7 from that work).

We also explored whether the number of breaks introduces differences in the intersects, as shown in Fig. 4.9. Only for galaxies with no breaks in the 12+log(O/H) radial fit we obtained that they tend to solar abundances (12+log(O/H) $\sim$ 8.69), but in the rest of cases we do not see any relation between the number of breaks and the extrapolated abundances in the nuclear part.

4.5.3 *The log(N/O) vs 12+log(O/H) relation for individual HII regions*

We show in Appendix C.3 the log(N/O) vs 12+log(O/H) diagram for all the selected HII regions in each galaxy, colored by their distance to the galactic center. For the majority of our sample, we obtain that HII regions mainly follow the log(N/O) vs 12+log(O/H) relation (see Fig. C.6) within the scatter, and that the HII regions located closer to the nuclear parts exhibit higher log(N/O) ratios, concluding that there is a decreasing trend between log(N/O) and 12+log(O/H). It is worth to note that 12 galaxies ($\sim$ 13% of the sample) exhibit a decrease of 12+log(O/H) in the closer parts towards the nuclear region, while the log(N/O) remains high (solar or suprasolar). Namely, these galaxies are $10518-12705$, $11013-6104$, $12078-12703$, $7495-12704$, $8249-12704$, $8259-9102$, $8320-9102$, $8562-9102$, $8563-12705$, $8492-12702$, $8983-3703$ and $8997-12704$.

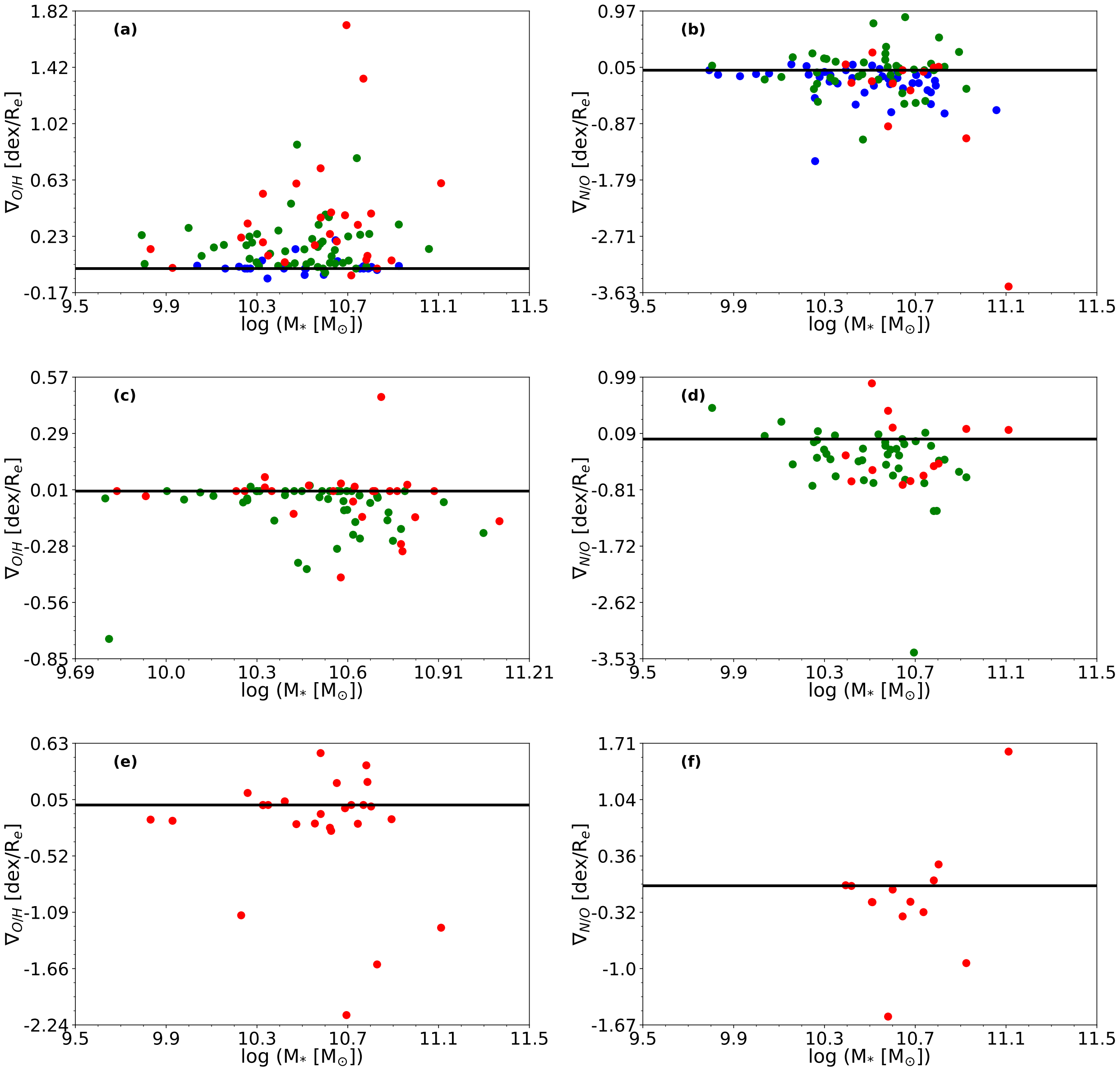

Figure 4.5: Relation between stellar mass and the slopes for the radial fits of 12+log(O/H) (left column) and log(N/O) (right column). Panels a) and b) represent the slopes of the inner radial fits, panels c) and d) the slopes of the middle radial fits, and panels e) and f) the slopes of the outer radial fits. For all plots, Blue dots represent galaxies with no breaks, green dots with one break, and red dots with two breaks. Solid black lines represent the flatten profile ($\nabla = 0$).

We show in Fig. 4.10 the results for all HII regions in our sample. First of all, looking at the ionization parameter (right column of the plot), we can check on the robustness of the methodology: the lack of measurements of the auroral line [O III]λ4363Å forces the assumption on the log(U) vs 12+log(O/H) relation to break the degeneracy. Nonetheless, it is clearly shown that this assumption introduces no dependence at all in the log(N/O) ratio by log(U).

Considering the information on the distance of the HII regions to the galactic centers, probes that the primary N production is mainly located in the outer HII regions (R ≥ 1.5 R_e), as shown in Fig. 4.10 panel (a). In addition, the HII regions in galaxies without any break in the radial fits are mainly located in the regime of secondary N production, with increasing log(N/O) with 12+log(O/H), which is consistent with previous studies (see panel (d)). Interestingly, those outer HII regions with primary N production are found in galaxies that exhibit a 12+log(O/H) gradient with one

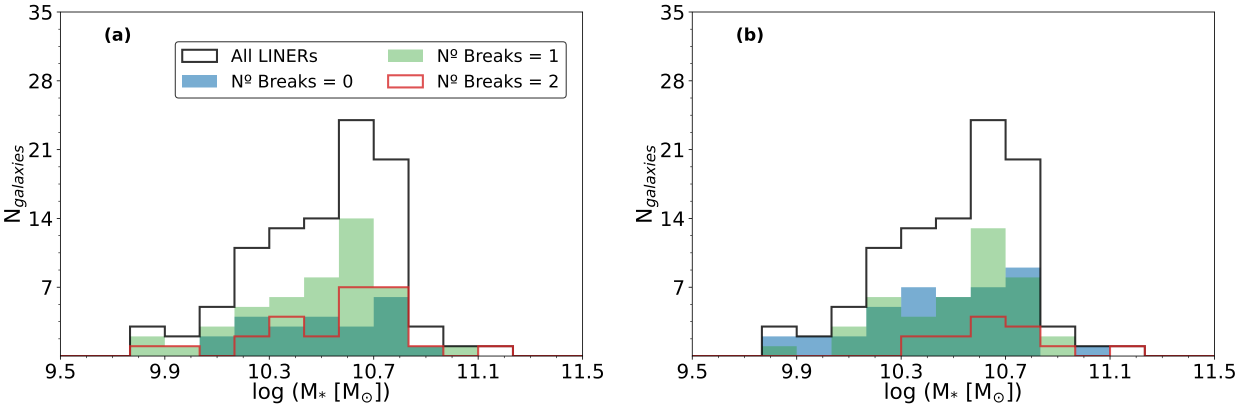

Figure 4.6: Histogram of the stellar masses for our sample of LINERs. (a) The sample is segregated according to the number of breaks shown in 12+log(O/H) radial profiles. (b) The segregation is done according to the number of breaks shown in log(N/O) radial profile.

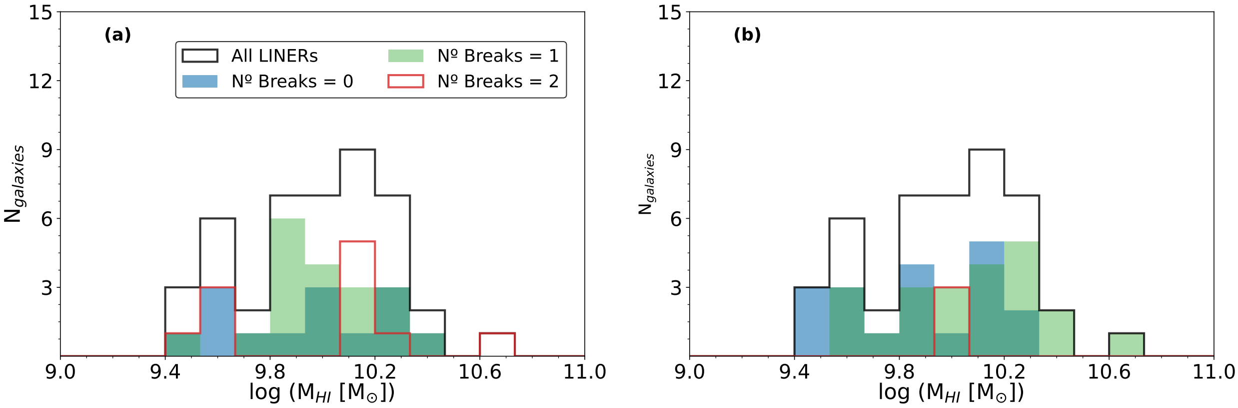

Figure 4.7: Same as Fig. 4.6 but for the HI mass.

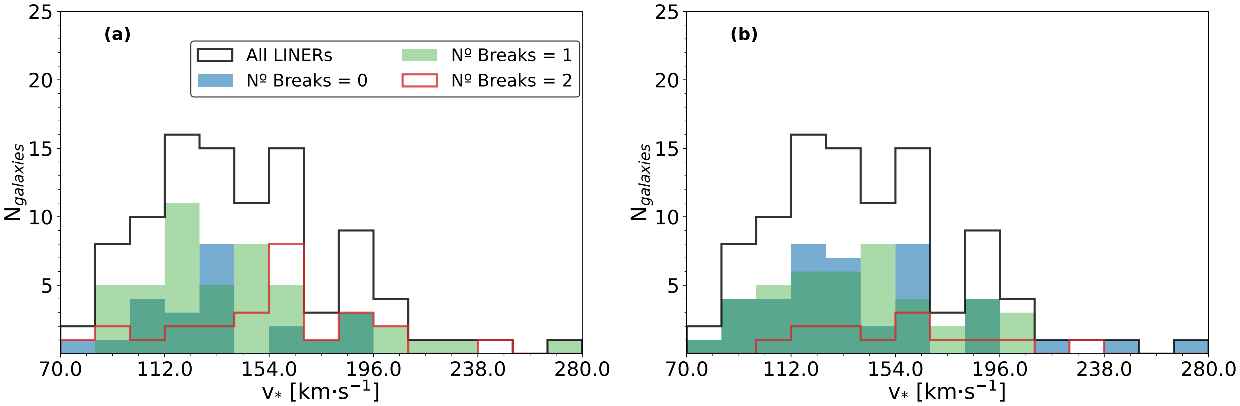

Figure 4.8: Same as Fig. 4.6 but for the stellar velocity dispersion in the nuclear regions.

break (panel (g)). Overall, the position of the large majority of HII regions is well reproduced by the scatter reported by different relations in the literature.

Finally, the analysis of the position of HII regions in the log(N/O) vs 12+log(O/H) relation based on the equivalent width of H_α (W_{H_α}) complements the picture that emerged from their distance to the galactic centers. We only found a particular trend in galaxies with no breaks in their radial fits (see panel (e)). Particularly, we obtained that HII regions with oxygen abundances close to the solar value (12+log(O/H)$_\odot$ = 8.69; Asplund et al., 2009) exhibit the highest values of W_{H_α}, as well as

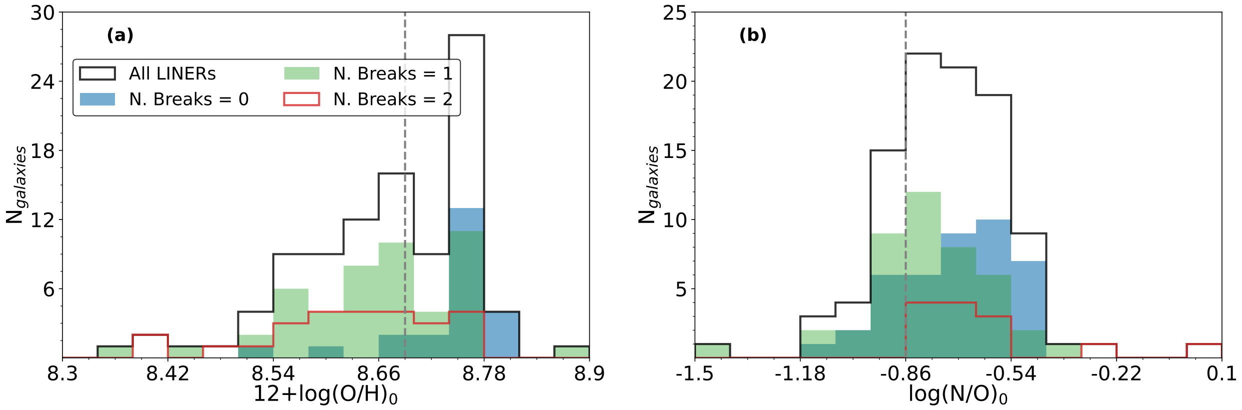

Figure 4.9: Histogram of the intersects of the inner parts of the metallicity radial fits for (a) 12+log(O/H), and (b) for log(N/O). Sample of LINERs is segregated into three groups according to the number of breaks shown in the abundance radial gradient. For both plots, gray dashed lines correspond to the solar value.

some of the closest distances to the galactic centers. This might be explained by the contamination of their spectra from AGN activity.

In summary, the majority of HII regions in our sample falls between the reported relations for log(N/O) and 12+log(O/H). Therefore, even though we observe some deviations from the reported relation, they are not introducing a departure.

4.5.4 *A representative value for the metallicity in galaxies*

A key aspect when analyzing chemical enrichment of galaxies is to define their characteristic metallicities. Several ideas have been proposed: the abundance ratios at 0.4 R_{25} (being R_{25} the isophotal radius, i.e., the radius at which the surface brightness equals 25 mag/arcsec^2; Zaritsky et al. 1994); the central (extrapolation to the nucleus) abundances (Ryder, 1995); or, the chemical abundance ratios at the effective radius (i.e. encompassing 50% of the light coming from the disk component) (e.g. Alvarez-Hurtado et al., 2022; Cresci et al., 2019; Sánchez et al., 2013; Sánchez-Menguiano et al., 2024b). This is even more critical in the case of AGNs, as their activity affects the nuclear parts and, hence, the representative value might account or not for the AGN role.

We explored three different values of the chemical abundance ratios for each galaxy: the expected value at the effective radius (R_e), the abundance ratios derived for the Narrow Line Region of the AGN (NLR) and the extrapolated abundance to the nucleus ($R = 0$). Our results are presented in Fig. 4.11, comparing them in different scaling relations such as the MZR, the mass-NO relation (MNOR) or the N/O vs O/H diagram.

We found that the metallicities of the ISM at the effective radius are the ones that best reproduce the MZR (Curti et al., 2020) (panel (a) in Fig. 4.11), whereas the MNOR (Andrews & Martini, 2013) seems to not be well reproduced in any of the considered cases. Finally, the log(N/O) vs 12+log(O/H) relation tells complementary stories depending on which chemical abundance ratio is used. If we account for chemical abundance ratios derived in the regions ionized by the AGN, we observe that there is a wide scatter, but mostly reproduced by the observing trends in literature. If we instead consider chemical abundances as extrapolated to the nuclear part from the radial fits, we observe almost an anti-correlation, which might be indicative of hydrodynamical processes affecting the oxygen abundance. Finally, the chemical abundances at the effective radius report galaxies clustering slightly above the solar oxygen abundance, but with a large spread of log(N/O) values.

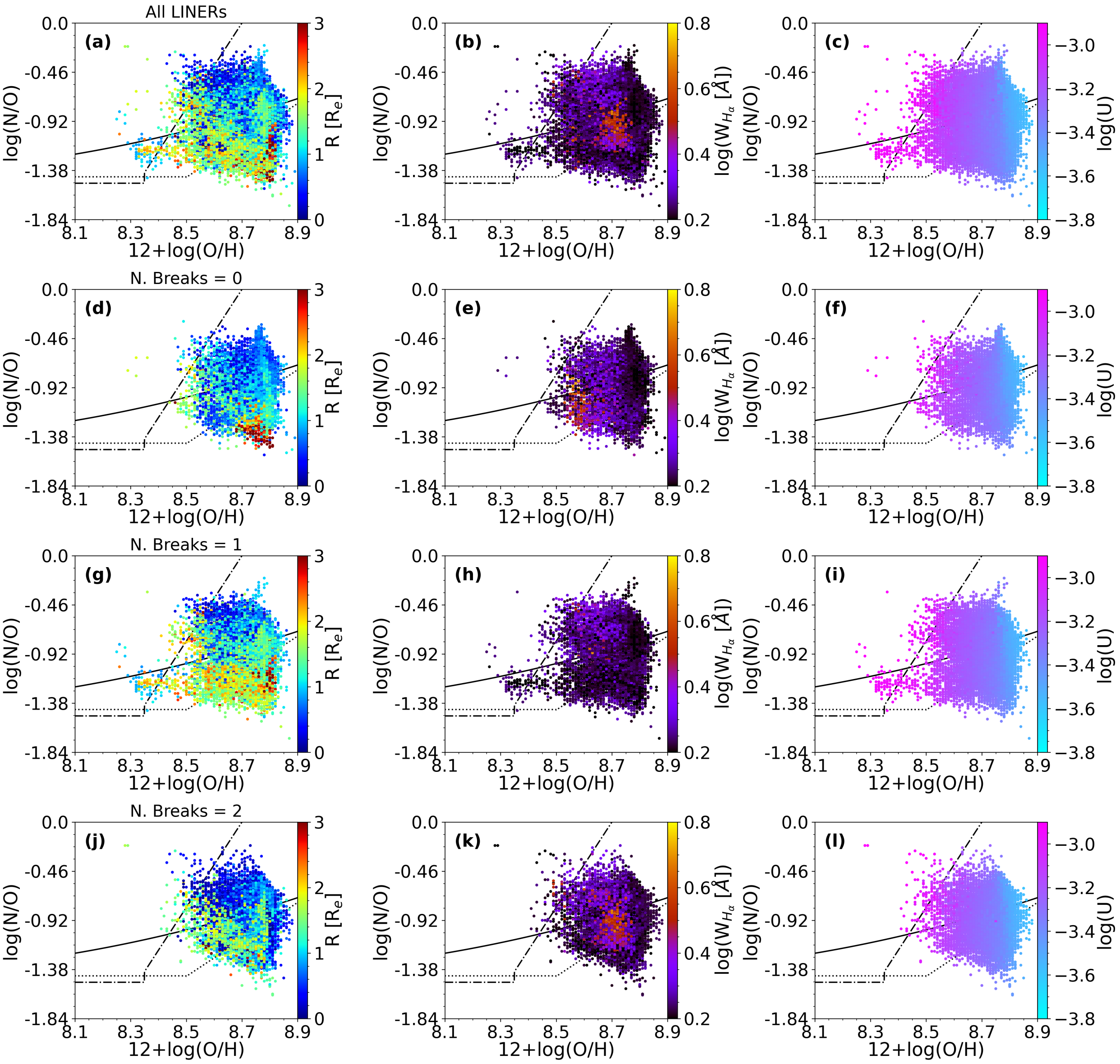

Figure 4.10: log(N/O) vs 12+log(O/H) diagram for the HII regions in our sample of LINERs. Top to bottom: first row shows diagrams for all HII regions in all LINERs; second row shows diagrams for those HII regions in LINERs with no breaks in the 12+log(O/H) radial fit; third row shows diagrams for HII regions in LINERs with one break; and forth row shows diagrams for HII regions in LINERs with two breaks. Each column shows different colorbared properties: normalized distance to the galaxy centers (left), equivalent width of H_α (middle) and ionization parameter (right). For all plots, the solid back line represents the fit provided by Coziol et al. (1999), the dotted line shows the fit by Andrews and Martini (2013), and the dash-dotted line shows the fit by (Belfiore et al., 2015).

4.6 DISCUSSION

As a general remark, we note the lack of studies analyzing metallicity radial gradients in galaxies with nuclear emission dominated by LLAGNs. Therefore, in this section we discuss our results with previous studies that are targeting different types of objects from those analyzed here.

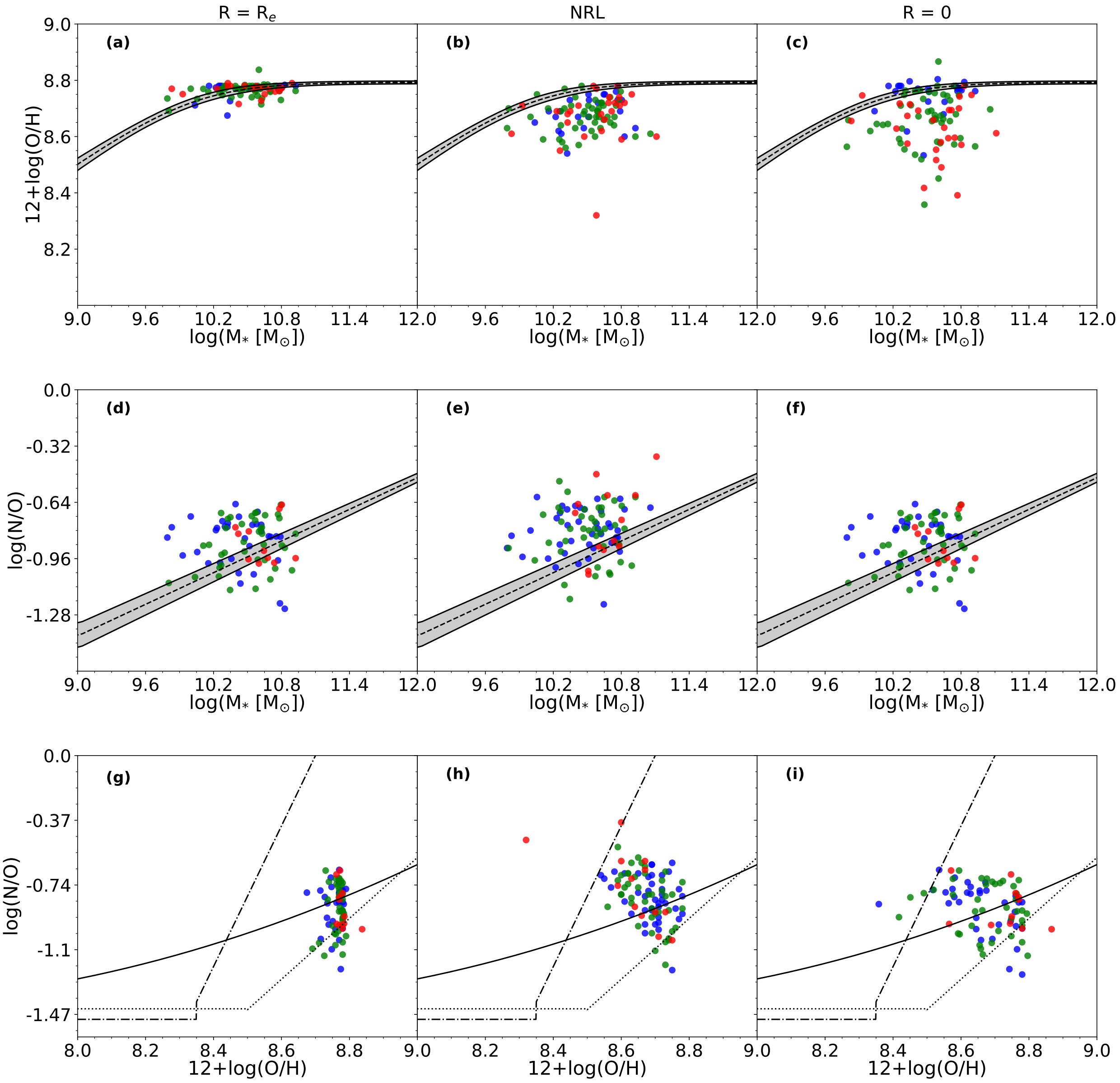

Figure 4.11: Scaling relations for the characteristics abundance ratios in our sample of LINER-like galaxies. Panels in the first row show the mass-metallicity relation (MZR), and the continuous line represents the fit obtained by Curti et al. (2020). Panels in the second row show the mass-NO relation (MNOR), with the continuous line representing the fit obtained by Andrews and Martini (2013). Panels in the third row show the log(N/O) vs 12+log(O/H relation), with the lines representing the different fits explained in Fig. 4.10. Panels in the first column show the chemical abundance ratios estimated at the effective radius. Panels in the second column show the estimations of nuclear abundances assuming AGN models with $\alpha_{OX} = -1.6$ (abundance of the Narrow Line Region, NLR). Panels in the third column show the intersects of the metallicity radial fits. For all plots, blue dots represent galaxies with no breaks in their corresponding radial fits, green dots have one break, and red dots represent galaxies with two breaks.

4.6.1 *On the shape of the O/H metallicity gradient in LINERs*

The inside-out growth scenario for galaxies, under which secular evolution of gas leads to higher gas densities in the inner parts, triggering more star formation, leads to the result of galaxies showing negative radial gradients in both the metallicity of the gas-phase ISM (as traced by 12+log(O/H)) and the metallicity of the stellar populations (Goddard et al., 2017; González Delgado et al., 2015;

Rich et al., 2012; Sánchez et al., 2014; Sánchez-Menguiano et al., 2016; Zinchenko et al., 2019). This scenario assumes that there is an equilibrium between all the dynamical effects of the gas (inflows and outflows), what permits the secular motion of the gas and guarantees the gas to have enough time for cooling and mixing. This is also supported by chemical evolution models (Matteucci & Francois, 1989).

Recent observational results from IFS surveys such as MaNGA (Bundy et al., 2015) or CALIFA (Sánchez et al., 2013) have allowed not only to increase the statistics of metallicity radial gradients at low redshift, but also to refine chemical evolution models and their predictions. The study from Belfiore et al. (2017) (MaNGA) showed that not only the negative metallicity gradient is observed in most galaxies, but that the steepness of the gradient depends on stellar mass. The study from Pérez-Montero et al. (2016) (CALIFA) also reported a similar trend, although the authors warned about the statistical significance of such trend. Indeed, both studies obtained that galaxies with moderate low stellar masses ($10^{9.5} - 10^{10.5} \mathrm{M}_{\odot}$) show steeper gradients (normalized to a characteristic size) than more massive galaxies. This result has also theoretical background from chemical evolution models. Low-stellar mass galaxies (considered as progenitors of more massive systems) have initially star formation mainly located on the central regions. As star formation occurs in the outer parts, the pollution from stars in the outskirts of galaxies helps flattening the metallicity profile, while the inner parts, already rich in primary metals, do not increase their metallicity at the same rate (for a constant value of the metal yield).

Recently, Sánchez-Menguiano et al. (2018) published a study of 102 spiral galaxies observed with MUSE. Their analysis of the metallicity radial gradients shows that only 55 galaxies exhibit the expected negative gradient, while 37 galaxies show inner drops and 26 a flat profile in the outermost parts. This implies that a significant number of galaxies deviate from the negative gradient predicted from the inside-out scenario. In the same way, Pilyugin and Tautvaišienė (2024) found that spiral galaxies can be divided into two main categories: galaxies with a single linear radial gradient (called S-galaxies) and galaxies with a flat inner gradient and a negative outer gradient (called LS-galaxies). Cosmological simulations also report results that add more complexity to the inside-out scenario: instead of a correlation between the slope of the metallicity gradient and the stellar mass, Tissera et al. (2022) obtained no correlation at all at low redshifts.

In the realm of AGN-dominated galaxies, the picture of gas-phase abundance gradients is more uncertain due to the scarcity of studies analyzing them. Amiri et al. (2024) observed that the Seyfert-host galaxy NGC 7130 exhibits an inverse metallicity gradient (i.e. metallicity of the gas-phase ISM increases with radius), and they conclude that the AGN is the responsible for the shape of the metallicity radial gradient. On the other hand, do Nascimento et al. (2022) found that the majority of metallicity radial gradients in Seyfert-like galaxies show almost flattened profiles and they report that there is a significant drop in metallicity in the parts closest to the AGN, implying that accretion of metal-poor gas is the responsible for the dilution.

Our results show that LINERs are not characterized by a single unique 12+log(O/H) radial gradient shape. Out of our sample of 97 LINER-like galaxies, we obtain that only 23 galaxies (23.7%) can be approximated with the single linear metallicity profile. For these galaxies, we obtained that the slopes ($\nabla_{O/H}$) are close to zero dex/R_e (Fig. 4.3 panel (a)) and in some rare cases they are positive. This is in agreement with the results obtained by do Nascimento et al. (2022) for Seyfert-like galaxies, as we obtain the same reported scenarios.

We also report a significant group of LINER-like galaxies that exhibit a metallicity radial gradient profile with a break. In total, 48 galaxies (49.5%) show this metallicity radial profile characterized by a positive 12+log(O/H) gradient in the inner parts (as reported in systems dominated by gas inflows), whereas the outer parts exhibits either a flattened or negative profile characteristic of the inside-out scenario (Fig. 4.3 panel (b)). This group of galaxies (which is the majority of our sample) follows the same trend reported by Amiri et al. (2024) for the Seyfert galaxy NGC 7130: the inner parts of the galaxy (dominated by AGN emission) exhibits a positive gradient, whereas the outer parts (dominated by star formation) are characterized by a mildly negative gradient.

Finally, we also report a non-negligible group of galaxies, 26 out of 97 (26.8%) that exhibit two breaks in the 12+log(O/H) metallicity radial profile. As in the previous case, the inner and middle parts are characterized by positive or almost flattened gradients, whereas the outer part is mainly characterized by a negative or flattened metallicity radial profile (Fig. 4.3 panel (c)). Only the recent work by Tapia-Contreras et al. (2025), based on cosmological simulations using the ChemodynamIc propErties of gaLaxies and the cOsmic web project (CIELO; Tissera et al., 2025), has reported a similar result for some galaxies, in which effects from galactic fountains and inflows of gas lead to these profiles.

The relation between the slope(s) of the 12+log(O/H) gradients and the stellar mass gives more insights on the processes that are shaping the metallicity radial gradient. For galaxies with no breaks, the gradient remains flat for almost all stellar mass (see Fig. 4.5 panel (a)), in contrast to the expected behavior reported by Pérez-Montero et al. (2016) and Belfiore et al. (2017). This might be explained due to the fact that these galaxies might have experienced a faster evolution, already reaching the characteristic flat profile of massive galaxies. Galaxies showing at least one break exhibit positive slopes, and reach higher values for massive galaxies, which might be explained by the fact the gravitational potential of these galaxies is more effective in favoring and capturing gas towards the inner parts, leading to a infall-dominated scenario.

The slopes in the outer parts of 12+log(O/H) radial gradients (for galaxies with at least one break) as a function of stellar mass revealed that there is a hint of anti-correlation, as reported for star-forming galaxies, although there are many galaxies with $\nabla_{O/H} \sim 0$ dex/R_e (see Fig. 4.5 panel (c)). This result reinforces the idea that the outer parts (or middle parts) behave accordingly to the inside-out scenario, although some galaxies seem to be already evolved.

Finally, the outer parts of galaxies with two breaks present a wide dispersion of values of the slope with respect to the stellar mass (Fig. 4.5 panel (e)). This can be interpreted as due to the fact that some galaxies might be experiencing galactic fountains that do not reach the very outer parts, leading to strong negative slopes, whereas others might have experienced merger events which could be stripping part of the gas or enhancing metal production due to the star-formation in the outermost parts.

4.6.2 *On the shape of the N/O metallicity radial gradient*

In the inside-out scenario, chemical evolution models predict that the log(N/O) radial gradient should be steeper than that observed for 12+log(O/H), as the time delay between nitrogen and oxygen production increases the difference between the inner and outer parts (e.g. Matteucci & Francois, 1989). Moreover, as the nitrogen production is also affected by the star-formation efficiency (e.g. Mollá et al., 2006), and the inner parts are characterized by lower star formation efficiencies (Spindler et al., 2018), this would increase even more the difference between log(N/O) and 12+log(O/H) radial profiles (Vincenzo et al., 2016).

As stated by several authors (e.g. Amorín et al., 2010; Belfiore et al., 2017; Pérez-Díaz et al., 2024a; Pérez-Montero & Contini, 2009; Vincenzo et al., 2016), measuring log(N/O) is essential to complement the picture of chemical enrichment (either for galaxies as whole or at different distances). Moreover, having a prior determination of log(N/O) is essential to use the information of nitrogen emission lines to properly measure oxygen abundances without adding biases. Indeed, several works have been published relying on estimators which are mainly tracing either the log(N/O) abundance ratio (such as O3N2; Amiri et al. 2024; do Nascimento et al. 2022; Sánchez et al. 2014; Sánchez-Menguiano et al. 2018) or the 12+log(N/H) abundance ratio (such as N2; do Nascimento et al. 2022). In contrast, our methodology allows in both the SF-dominated and

AGN-dominated regions to determine independently log(N/O) and 12+log(O/H) abundances, allowing us to simultaneously explore both radial profiles.

Pilyugin et al. (2004) published an analysis of the metallicity radial gradients (12+log(O/H) and log(N/O)) for a sample of 54 nearby spiral galaxies. Their results were in agreement with the inside-out scenario: mainly negative gradients for all the considered chemical abundance ratios, and with log(N/O) radial gradients being steeper than those reported from 12+log(O/H). A similar conclusion was reported by Pérez-Montero et al. (2016) from the analysis of metallicity radial gradients in CALIFA, obtaining that on average the slopes of the radial gradients of log(N/O) point towards steeper metallicity profiles than those obtained for 12+log(O/H). Moreover, they also analyzed the possible dependence of the slope ($\nabla_{N/O}$) with stellar mass, obtaining an slight dependence for less-massive systems but not statistically significant.

Later on, Belfiore et al. (2017) also found slightly steeper gradients in the log(N/O), but they do report an anti-correlation between the slopes and stellar mass, similar to that found in the 12+log(O/H) radial profile. They also reported higher log(N/O) ratios in the outer parts of many galaxies, concluding that pollution in the form of galactic winds from the inner to the outer parts might be responsible for this behavior. Finally, Zinchenko et al. (2021) found not only similar results to previous studies, but also found a correlation between the median slopes for the log(N/O) profile and the stellar ages (traced by the $D(4000)$ index): galaxies with older populations ($D(4000) > 1.2$) tend to have steeper gradients that the others. This result is in agreement with the general scheme for nitrogen production and the time delay between O and N production.

The previous results only cover galaxies whose nuclear activity is dominated by star-formation, and we do not have a picture on how the log(N/O) gradient behaves in galaxies with AGN activity. Our study uses a robust methodology for the independent estimation of 12+log(O/H) and log(N/O) abundances across the HII regions to the nuclear AGN-dominated region, allowing us to study log(N/O) abundance gradients for the first time in galaxies hosting LLAGNs.

Our results show that 41 LINER-like galaxies (42.3%) show a single linear profile in the log(N/O) metallicity radial gradient, with the majority of the slopes being negative or close to zero. We do report very few cases (three) with clear positive slopes (see Fig. 4.3 panel (d)). Interestingly, only nine galaxies show simultaneously a single linear profile in both their 12+log(O/H) and log(N/O) metallicity radial gradients, whereas the large majority show at least one break in the 12+log(O/H). This might imply the effect of infalls of gas that mainly affects the 12+log(O/H) (also explaining the positive slopes found in the inner parts) but do not significantly affect the log(N/O) ratio due to the non-linear relation between them.

Focusing our attention on galaxies with one break, we obtained that they represent the 44.3% of the total sample (43 galaxies). As in the case of galaxies with one break in the 12+log(O/H) radial fit. Our results also indicate that the inner parts tend to present positive slopes whereas the outer parts are biased towards negative slopes. However, contrary to the clear distinction obtained for the 12+log(O/H) radial profile, we observe a clear overlap between both distributions (see Fig. 4.3 (e)). We discuss the possible causes for these profiles together with the information from the 12+log(O/H) radial gradient:

- **One break in the log(N/O) radial profile but no breaks in the 12+log(O/H) radial profile**. Positive slopes in the inner parts might be indicative of the effects of AGN-driven outflows in the inner parts: if outflows are efficient at gas removal. This decrease in the inner parts does not only affect to 12+log(O/H), but also to log(N/O), as the gas removal would lead to a quenching on star formation and, thus, stars responsible for the production of N by means of secondary production would not be born at the same rate as in the inside-out scenario. Negative slopes can be interpreted as the effects of AGN-driven outflows with lower impact, dilution from galaxy inflows or a simultaneous combination of both.

- **One break in both log(N/O) and 12+log(O/H) radial profiles**. This is the scenario for 22 galaxies in our sample. We observe that some of them present clear negative slopes in the inner parts and less prominent or even close to flat slopes in the outer parts, which might be interpreted as the effects of those outer regions not having already undergo the secondary production N. On the other hand, there is also a group of galaxies for which we observe the contrary scenario, an almost flat profile in the inner parts, whereas there is a clear negative profile in the outer parts. This might be interpreted as the effects of quenching from AGN feed and/or feedback, simultaneously lowering the O and N abundances due to the suppression of star formation, whereas the outer part resembles the inside-out growth scenario.

Finally, we detected 13 galaxies (13.4%) that present two breaks in the log(N/O) radial profile, the majority of them found in galaxies with one break in the 12+log(O/H) profile. In most of them, a closer look to their log(N/O) profiles (see Fig. C.5) reveals that the lack of HII regions in some parts forces this profile, and that a single linear fit or imposing just one break could fit the data with similar residuals. Thus, these cases could be also likely explained by the same scenarios proposed for those galaxies with just one break in the log(N/O) profile.

Lastly, we also analyzed the possible effects of stellar mass in the slopes $\nabla_{N/O}$. For the innermost parts and for galaxies with no breaks (Fig. 4.5 (b)), we did not obtain any correlation, which is in agreement with the results from Pérez-Montero et al. (2016). In the case of the outer parts in galaxies with one break, we do not observe any significant correlation, although they are mainly negative, which again might be indicative of the standard inside-out scenario or contamination from outflows which is captured by the galaxy at the break (see for instance the effects of galactic fountains; Spitoni et al., 2013).

4.6.3 *The relation between N/O and O/H*

The log(N/O) vs 12+log(O/H) diagram is a powerful tool to discriminate the processes that might shape the chemical enrichment history of galaxies. While O has a primary production origin mainly from massive stars, N can have either a primary production origin from the same massive stars and/or a production from intermediate-mass stars ($4 - 7\ M_\odot$; Kobayashi et al., 2020a) by means of CNO cycles (secondary production; Henry et al., 2000). As a consequence, the relation between these two elements has an almost constant ratio of log(N/O) for low oxygen abundances (12+log(O/H) $\lesssim$ 8.5; Andrews & Martini, 2013; Vincenzo et al., 2016) as both species are produced in the primary process of the nucleosynthesis in massive stars. On the other hand, when there is already enough O (12+log(O/H) $\gtrsim$ 8.5) in the ISM from which stars were born, then the CNO cycles contribute to an extra enrichment of N leading to an increasing relation between log(N/O) and 12+log(O/H). However, several factors affect the expected relation between log(N/O) and 12+log(O/H) leading to a non-negligible scatter in the relation (see the discussion provided in Paper I). Hence, in the inside-out growth scenario, this is translated into a decreasing log(N/O) and 12+log(O/H) as radii increases, reaching the highest values in the regions closer to the nuclear part of the galaxies (e.g. Zinchenko et al., 2021; Zurita et al., 2021b).

However, there is no such a characterization for galaxies hosting AGNs, specially for LLAGNs. Pérez-Díaz et al. (2021) obtained that the nuclear regions of nearby LLAGNs from the Palomar Survey do not follow the expected relation between log(N/O) and 12+log(O/H), although later on Pérez-Díaz et al. (2025) analyzing LLAGNs from MaNGA obtained that the abundances in nuclear regions are consistent with the relation within the scatter if they are derived assuming that they are ionized by an AGN. (Oliveira et al., 2024a) obtained for a sample of retired galaxies from MaNGA that, if the nuclear regions are ionized by hot, old stellar populations, the trend between log(N/O) and 12+log(O/H) is inverted, i.e., log(N/O) decreases with 12+log(O/H). Moreover, still no characterization has been provided for the chemical abundance radial gradients in those galaxies.

Our results show that the majority of HII regions from the disks of our sample of LINER-like galaxies follow the expected trend between log(N/O) and 12+log(O/H), and the scatter is similar to that observed for the nuclear parts (see Paper I). In some cases, the innermost HII regions exhibit log(N/O) abundances which are characteristic of the solar and suprasolar metallicity regimes, but their 12+log(O/H) ratios are even lower than those reported for the outer parts, which can be interpreted as the effect of outflows carrying metal-rich gas (e.g. Villar Martín, M. et al., 2024) to the outer parts before nitrogen pollution from intermediate massive stars. In other cases, the inner most regions with slightly depressed O/H abundances are similar to the outermost ones, which can be interpreted as the effect of gas inflows from the outer to the inner parts (e.g. Bresolin et al., 2012), or the effects of galactic fountains (e.g. Spitoni et al., 2013; Tapia-Contreras et al., 2025).

4.6.4 *A galaxy model accounting for AGN feedback*

Among the different observational scenarios for AGNs, LLAGNs provide a useful laboratory as we can address the effects of the AGN activity in the innermost parts as they are mostly inefficient AGNs (Márquez et al., 2017). It is beyond the scope of this paper to either provide a theoretical framework or a hydrodynamical simulation that accounts for the AGNs. However, given the complementary information that we can infer from the simultaneous analysis of 12+log(O/H) and log(N/O) we can propose a general and simplified scheme that might reproduce and explain the observed trends.

The bathtub model to explain galaxy mass assembly and chemical enrichment in the whole galaxy provides feasible explanation for observed properties in large samples of galaxies such as the mass-metallicity relation (MZR), the fundamental metallicity relation (FMR) and the mass-stellar metallicity relation (e.g. Bouché et al., 2010; Lilly et al., 2013; Y.-j. Peng & Maiolino, 2014). Later on, Belfiore et al. (2019) brought together the bathtub model and the inside-out scenario (following the approach provided by Matteucci & Francois, 1989) to provide a theoretical framework to explain the metallicity gradients of the gas-phase ISM observed in galaxies. They came up with a model with four free parameters: the infall time scale and radial dependence, the star formation efficiency at the center of the galaxy and the outflow mass loading factor.

Theoretical models just by accounting for pure star formation processes are used by Belfiore et al. (2019) to reproduce the 12+log(O/H) radial gradients and trends observed by Belfiore et al. (2017). Indeed, they were able to reproduce the slight drop found in massive galaxies ($> 10^{10.5}$ $M_{\odot}$) in the innermost parts, and also positive gradients for low mass galaxies ($< 10^9$ $M_{\odot}$). However, they also warned against the degeneracy of the free parameters of their models as well as on the effects of the calibration used to estimate chemical abundances on the gas-phase ISM.

More recently, based on hydrodynamical simulations, Tapia-Contreras et al. (2025) obtained departures from the 12+log(O/H) single linear radial profile. By just accounting for the same effects (inflows, outflows and star formation efficiency), they report that some systems experience breaks depending on the dominant mechanism for gas dynamics at a different scales. They detect some inner parts with significant steeper negative slopes than in the outer parts, and they concluded this is due to an increase of the star formation activity due to past infalls of gas. On the other hand, they also report that some galaxies experience an inner drop, i.e., a change in the slope from negative (outer) to positive (inner). They conclude that they are driven by metal-rich outflows, and that they have shorter life times. They also find that galactic fountains as well as gas-inflows might introduce changes in the outer parts of the 12+log(O/H) profile.

Both approaches, the theoretical model by Belfiore et al. (2019) as well as the predictions from hydrodynamical simulations (Tapia-Contreras et al., 2025) evidence that several factors compete in the shape of metallicity radial gradients, and that the general assumption of a single, negative, profile as predicted by the inside-out scenario might not be accurate in several cases (e.g. Pilyugin & Tautvaišienė, 2024; Sánchez-Menguiano et al., 2018). However, both approaches ignore the influence of AGN activity in their evolutionary scenarios.

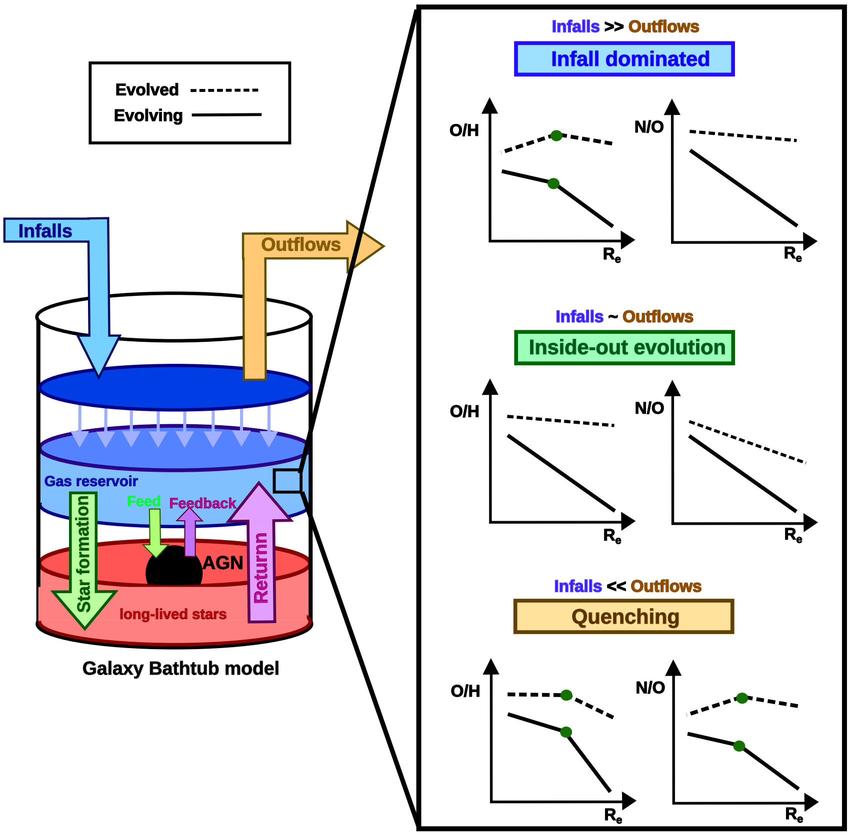

Figure 4.12: Adapted scheme from the bathtub model proposed by Lilly et al. (2013). Left part shows the scheme of galaxy flows within the galaxy. Right part shows the expected gas-phase ISM metallicity radial gradients for different scenarios. Continuous tracks of the gradients show evolving systems, whereas dashed tracks show the expected behavior for already evolved systems.

Using as starting point the bathtub model from Lilly et al. (2013), we just added an extra component representing the AGN. The expected behavior for the AGN would be similar to the effects of long-lived stars in the closed-box models: a sinking point. As the AGN feeds from gas, that gas would be captured in the closest parts such as the Narrow Line Region (NLR) and the Broad Line Region (BLR), and from there they will eventually feed the SMBH. Part of the gas captured might eventually be expelled through the AGN-driven outflows, similar to the outflows expected in the star-formation that would lead to the long-lived stars. In short, a fraction of the gas would be captured by the AGN (inflows) and part would be returned (outflows). We represent this small re-adaption on Fig. 4.12.

Therefore, considering all these factors, we propose three main scenarios, distinguishing in each of them between evolving and already evolved systems, which essentially imply low-mass or massive galaxies:

- **Inside-out**: This scenario is reached when there is equilibrium between the different hydrodynamical processes that affect the gas and allows its secular evolution.

  - For evolving systems we expect that both O/H and N/O radial profiles show clear negative slopes. We do not detect any clear example of this scenario in our sample of galaxies, indicating that most of them are already evolved systems.
  - For already evolved systems we expect a mildly negative or mostly flatten 12+log(O/H) profile for our sample, whereas the log(N/O) gradient shows a steeper profile. In this case, the HII regions in the log(N/O) vs 12+log(O/H) diagram should be located in a very tight range of oxygen abundances, with an increasing N/O as they are located closer to the nuclear part. This is the case of galaxies such as GAL 7990 − 12704, GAL 8331 − 6102 or GAL 8984 − 12705.

  In all these cases, we report that the abundances in the NLR of the AGN might not reflect the expected trend as the gas might have been captured at a different epoch (e.g. GAL 7990−12704) or there are hints of inflows that have not yet perturbed 12+log(O/H) (e.g. GAL 8331 − 6102).

- **Infall dominated**: This is the expected scenario when inflows dominate the gas dynamics in the inner parts. We also report that it could be the case in which the inflow might shape the whole radial profile as it is the case in GAL 10510 − 6103 and GAL 8141 − 6102.
  - For evolving systems we expect a drastic change in the slope of the 12+log(O/H) radial profile, presenting negative slopes in the outer parts and positive slopes in the inner parts. At the same time, the log(N/O) radial profile should reflect the expected behavior from the inside-out scenario or, some small changes in the slope due to the mixing. The position of the HII regions in the log(N/O) vs 12+log(O/H) displays an inverted "c" with the lower tail populated by middle/outer regions and the upper tail populated by inner regions. This is the case for GAL 11838-3794, GAL 11746 − 9102, GAL 8134 − 9102 or GAL 8549 − 3703.
  - For already evolved systems, we expect that the inner parts of the 12+log(O/H) radial profile shows a positive slope whereas the outer part is mainly characterized by a flat profile. The log(N/O) profile reflects again a mildly negative or almost flat profile. In this scenario, the log(N/O) vs 12+log(O/H) diagram for HII regions shows a vertical relation for the middle/outer regions, and an horizontal branch for the inner regions, with high N/O ratios and a wide range of values for 12+log(O/H). This is the case for GAL 10842 − 12704, GAL 11945 − 3704, GAL 12078 − 12703 or GAL 7495 − 12704 (among many others).

  Contrary to the inside-out scenario, there seems to be a better agreement between the trends and the abundances estimated in the NLR region of AGN. This would reinforce our proposed scenario, as the infall would feed the AGN and, thus, the metallicity in the NLR should follow the trend.

- **Quenching**: This is the expected scenario for an outflow dominated system. Due to the galactic winds driven by the AGN, extreme star formation processes or both, gas is removed from the inner parts and expelled to the halo (in less massive systems) or the outskirts of the galaxy (for massive systems), and thus, preventing the chemical enrichment of the inner parts due to the suppression of star formation. As the secondary production of nitrogen is delayed with respect to oxygen, it is expected that the effects are less notorious in the log(N/O) gradient as those stars can contaminate the remaining gas.
  - For evolving systems, this scenario predicts metallicity gradients with at least one break for both 12+log(O/H) and log(N/O). The slopes for both cases change from negative (outer parts) to positive (inner parts), as the quenching process is preventing the chemical enrichment in the inner parts, whereas the outer parts can be enriched by this material

or remain unaffected following the inside-out scenario. However, due to the time delay in nitrogen production, the profile for the log(N/O) gradient might just reflect a change in the absolute value of the slope rather than in the sign. With respect to the log(N/O) vs 12+log(O/H) diagram, HII regions from inner parts and outer parts are expected to coexist in the same range of O values, and with some differentiation in the N/O values (being higher for the inner parts). This is the case for GAL 104519 – 9102, GAL 1190 – 6103 or GAL 8258 – 12704.

- For evolved systems, we expect a similar behavior in the log(N/O) radial profile to the evolving system scenario, but 12+log(O/H) should reflect a change from an almost flat gradient (outer parts) to a positive slope (inner parts). The expected behavior in the log(N/O) vs 12+log(O/H) diagram will depend on how much nitrogen can be produced after the gas removal. If little is produced, then a clustering of HII regions in similar positions within the diagram is expected, and with independence of the distance. On the contrary, if the remaining gas (which can be more easily polluted as it is less abundant) is contaminated with nitrogen, then an anti-correlation (or flat distribution) in the log(N/O) vs 12+log(O/H) diagram is expected: inner HII regions would reflect moderate N/O ratios but low O/H abundances, and outer parts would reflect higher O/H values and moderate to low N/O values. This is the case for GAL 10839 – 12795, GAL 11013 – 6104, GAL 7964 – 9102 or GAL 8080 – 12703 (among many others).

In this case, the metallicity of the NLR of the AGN might be a footprint of the gas-phase metallicity of the ISM that was expelled, but also it can be driven away by the same AGN-driven outflows, lowering its metallicity.

Although we understand that many physical processes at micro- and macro-physical scales play a role in the evolution of metallicity radial gradients, our adapted model helps providing a physical explanation to the observed results in the case of our sample of LINER-like galaxies. The strength of the different processes and the properties of the host galaxy are important actors in determining the scenario. For instance, the quenching (or outflow dominated) scenario might lead to galactic fountains as gas might be captured and accreted again into the galaxy. We suspect this is the case for GAL 10215 – 3703 or GAL 8078 – 12703. Both galaxies exhibit in the most outer parts values of 12+log(O/H) and log(N/O) that mimic the inner parts of their galaxies (even the values derived for the NLR of the AGN).

The processes that are shaping the galactic radial gradients, specifically in the inner parts, are mainly inflows and outflows. Evidences for outflows driven by LLAGNs have been reported in the literature (Cazzoli et al., 2018, 2022; Hermosa Muñoz et al., 2022, 2024; Masegosa et al., 2011). Hot accretion flows are expected to power LLAGNs (e.g. Ho, 2008; Márquez et al., 2017), but reported evidences for such inflows have been provided in counted cases (see the case for M87; Yuan et al., 2022). On the other hand, powerful inflows and outflows can also be observed in star-forming dominated systems. For instance, Pérez-Díaz et al. (2024a) provided indirect evidence of gas inflows diluting metallicity and enhancing star formation in interacting galaxies. Powerful outflows are also expected and reported in galaxies classified as starbursts (see reviews by Veilleux et al., 2005, 2020, and references therein). Very recently, Tapia-Contreras et al. (2025) have shown that these hydrodynamical processes driven by star formation can drastically affect the shape of metallicity radial gradients finding similar results to ours. Overall, we cannot rule out that the star formation processes are also contributing to the AGN-driven hydrodynamical processes that shapes of metallicity gradients.

4.7 CONCLUSIONS

We studied the gas-phase metallicity radial gradients (12+log(O/H) and log(N/O)) in a sample of 97 LINERs from SSDS-IV MaNGA, whose central abundances were previously analyzed in Paper I. We selected galaxies whose nuclear regions are dominated by LINER-like activity, while the rest of analyzed active regions through their disks are powered by star formation (as also demonstrated by means of the diagnostic diagrams). We used HCm to estimate chemical abundances both in the nuclear and disk regions, allowing us to perform a consistent analysis while keeping track of their differences in the ionizing sources. We applied a piecewise methodology to fit those metallicity gradients allowing breaks as a consequence of changes in the slopes. Our results are summarized as follows:

1. The majority of our sample of galaxies exhibit departures from the single linear radial gradient both in 12+log(O/H) and log(N/O) (as would be expected from the inside-out scenario). Particularly, for 12+log(O/H) gradients we found that only 23 galaxies (23.7%) show the characteristic single linear fit, whereas 48 (49.5%) exhibit one break and 26 galaxies (26.8%) exhibit two. In the case of log(N/O) gradient profiles, we obtained that 41 (42.3%) galaxies are well reproduced by the single linear profile, 43 galaxies (44.3%) exhibit one break and 13 galaxies (13.4%) two breaks.

2. We obtained that for a given galaxy, the 12+log(O/H) and log(N/O) radial profiles do not follow the same trend and the positions found for the breaks are different. Moreover, for a given 12+log(O/H) radial profile, it is more likely that the log(N/O) one presents a different shape. This is in general agreement with the expected time delay between oxygen an nitrogen production.

3. We did not obtain any correlation between the general shape of the metallicity radial profiles (breaks, slopes, intersects) and stellar mass of galaxies. Only in the outer (middle) parts of galaxies exhibiting one (two) break(s) that are characterized by negative gradients we obtained a very weak anti-correlation as previously reported, although it is not statistically significant.

4. We propose an adaptation of the bathtub model (accounting for AGN feed and feedback) as a driver for the departures from the inside-out scenario. On the one hand, infalls supplying gas to the AGN and innermost parts might be the dominant mechanism for galaxies with a broken profile in the 12+log(O/H) radial profile and with an almost unaltered log(N/O) one. On the other hand, outflows removing gas from the inner parts and favoring quenching might explain the broken profiles seen simultaneously in log(N/O) and 12+log(O/H).

5. The observational effects of the imbalance between inflows and outflows in the metallicity radial gradients might depend on the evolutionary stage of the galaxy: being mild in galaxies already chemically evolved.

6. The chemical content of the gas-phase ISM surrounding the AGN (NLR) seems to be more representative of the chemical footprints of the inner parts of the galaxy, whereas the chemical content as derived from the metallicity gradient at the effective radius seems to be more representative of the galaxy as a whole when accounting for global properties such as the mass-metallicity relation.

Our studies employing a robust methodology to analyze a sample of galaxies, in which the AGN activity is not dominant at all scales, point towards that AGN feedback, together with star formation, might be drivers of the hydrodynamical processes that are shaping metallicity radial gradients in disk galaxies, although a comparative study with a consistent methodology between star-forming dominated galaxies and these LINERs (forthcoming work) might give us more insights into this scenario. Additionally, this sample can be later on explored with high-resolution spectroscopic data of the inner parts of the galaxies to provide a more precise quantification on the effects of AGNs at different scales.

5

UNVEILING CHEMICAL ENRICHMENT THROUGH INFRARED EMISSION LINES

Chapter based on the publication: B. Pérez-Díaz, E. Pérez-Montero, J. A. Fernández-Ontiveros and J. M. Vílchez (2022) *"Measuring chemical abundances in AGN from infrared nebular lines: HII-CHI-MISTRY-IR for AGN", published in Astonomy & Astrophysics, volume* 666, *A*115, *doi:*10.1051/0004-6361/202243602.

5.1 ABSTRACT

Future and on-going infrared and radio observatories such as JWST, METIS, and ALMA will increase the amount of rest-frame IR spectroscopic data for galaxies by several orders of magnitude. While studies of the chemical composition of the interstellar medium (ISM) based on optical observations have been widely spread over decades for star-forming galaxies (SFGs) and, more recently, for active galactic nuclei (AGN), similar studies need to be performed using IR data. In the case of AGN, this regime can be especially useful given that it is less affected by temperature and dust extinction, traces higher ionic species, and can also provide robust estimations of the chemical abundance ratio N/O. We present a new tool based on a Bayesian-like methodology (HII-CHI-Mistry-IR) to estimate chemical abundances from IR emission lines in AGN. We use a sample of 58 AGN with IR spectroscopic data retrieved from the literature, composed by 43 Seyferts, eight ultraluminous infrared galaxies (ULIRGs), four luminous infrared galaxies (LIRGs) and three low-ionization nuclear emission line regions (LINERs), to probe the validity of our method. The estimations of the chemical abundances based on IR lines in our sample are later compared with the corresponding abundances derived from the optical emission lines in the same objects. HII-CHI-Mistry-IR takes advantage of photoionization models, characterized by the chemical abundance ratios O/H and N/O, and the ionization parameter U, to compare their predicted emission-line fluxes with a set of observed values. Instead of matching single emission lines, the code uses some specific emission-line ratios that are sensitive to the above free parameters. We report mainly solar and also subsolar abundances for O/H in the nuclear region for our sample of AGN, whereas N/O clusters are around solar values. We find a discrepancy between the chemical abundances derived from IR and optical emission lines, the latter being higher than the former. This discrepancy, also reported by previous studies of the composition of the ISM in AGN from IR observations, is independent of the gas density or the incident radiation field to the gas, and it is likely associated with dust obscuration and/or temperature stratification within the gas nebula.

5.2 INTRODUCTION

Active galactic nuclei (AGN) are among the most luminous objects in the Universe, and can therefore be studied up to very high redshift. The interstellar medium (ISM) surrounding these nuclei is ionized by very energetic photons that are radiated from the accretion disk and jets around the supermassive black hole (SMBH). This ionization is partially reemitted in the form of strong and prominent emission lines, which can provide information on the physical and chemical properties of the region from where they originated.

Since the nebular line properties depend on the chemical composition of the ISM gas, their relative fluxes can be used to quantify the abundances of elements heavier than hydrogen and helium, known as metals (see Maiolino and Mannucci 2019 for a thorough review). While the primordial Big Bang nucleosynthesis explains the observed abundances of hydrogen or deuterium, as well as a significant fraction of helium and a small fraction of lithium (Cyburt et al., 2016), nearly all other elements are produced by stellar nucleosynthesis in the cores of stars, driven to their surfaces by convective flows and, in the late stages of their lives, are finally ejected into the ISM by stellar winds and supernovae (see review from Nomoto et al. 2013). Thus, the analysis of chemical abundances at different redshifts can provide key information on galactic evolution throughout different cosmological epochs.

The oxygen abundance (usually represented as 12+log(O/H)) is widely used as a proxy of the metal content in the ISM of galaxies, since O is the most abundant metal in mass and its presence can be easily detected through strong emission lines in the ultraviolet (UV), optical, and infrared (IR) range (Osterbrock & Ferland, 2006). Another quantity relevant for analyzing the past chemical evolution of the ISM in galaxies is the nitrogen-to-oxygen abundance ratio, represented as log(N/O). This relative abundance provides essential information on the build-up of heavy elements from stellar (Chiappini et al., 2005) to galactic (Vincenzo & Kobayashi, 2018) scales because it involves a primary metal, O, and another one, N, which may have a secondary origin. In the low-metallicity regime (i.e., 12+log(O/H) $\lesssim 8.0$), N is expected to be primarily produced by massive stars, thus N/O basically a constant shows value. However, in the high-metallicity regime, N has a significant contribution from a secondary production channel, as it is formed via the CNO cycle in intermediate-mass stars, and therefore N/O tends to increase with O/H (e.g. Pérez-Montero & Contini, 2009).This correlation between O/H and N/O has been determined in studies of chemical abundances in star-forming galaxies (SFGs) and HII regions in galaxies using optical observations from nearby and distant galaxies (e.g. Andrews & Martini, 2013; Hayden-Pawson et al., 2022; Masters et al., 2016; Pilyugin et al., 2004; Vila-Costas & Edmunds, 1993), although it has also been reported that some groups of galaxies deviate from this behavior (Amorín et al., 2010; Guseva et al., 2020; Pérez-Montero et al., 2021). Thus, the N/O determination does not only provide key information on the metal production in the ISM, but is also a necessary step in the determination of oxygen abundances when nitrogen lines are involved.

For decades, many studies have been devoted to analyzing the chemical composition of the gas-phase in SFGs using optical emission lines (e.g. Garnett & Shields, 1987; Lequeux et al., 1979; McClure & van den Bergh, 1968; Pilyugin et al., 2004; Thuan et al., 1995). Several techniques have been developed for that purpose: i) the T_e-method (also known as direct method), which measures the line ratios of specific collisional emission lines (CELs), sensitive to the electron temperature and density, to directly derive the abundances of the main ionic species (e.g. Aller, 1984; Osterbrock & Ferland, 2006); ii) by means of photoionization models to reproduce the observed CELs and then constrain chemical and physical properties of the region, using several codes such as Cloudy (Ferland et al., 2017), Mappings (Sutherland & Dopita, 2017), or Suma (Contini & Viegas, 2001); and iii) the use of empirical or semiempirical calibrations between accurate chemical abundances and the relative fluxes of strong emission lines (e.g. Curti et al., 2017; Pérez-Montero & Contini, 2009; Pilyugin & Grebel, 2016). Furthermore, new approaches take advantage of more than one of the above techniques at the same time, such as HII-CHI-Mistry (hereinafter HCm; Pérez-Montero 2014), which uses sensitive ratios to chemical abundances to search for the best fit among a grid of photoionization models.

In recent years, the analysis of chemical abundances in the gas-phase of HII regions has been extended to the narrow line region (NLR) in AGN (e.g. Contini & Viegas, 2001; Dors et al., 2015; Flury & Moran, 2020; Pérez-Díaz et al., 2021; Pérez-Montero et al., 2019a; Storchi-Bergmann et al., 1998; Thomas et al., 2019). This region of the ISM, located between $\sim 10^2$ pc and a few kpc (Bennert et al., 2006b, 2006c), is characterized by an electron density, n_e, typically in the $10^2 - 10^4$ cm^{-3} range, and an electron temperature of $T_e \sim 10^4$ K (Netzer, 2015; Vaona et al., 2012). Although these physical conditions may not depart significantly from to those of the ISM in HII regions (Osterbrock

& Ferland, 2006), the source and the shape of the ionizing continuum are completely different in both cases: the accretion disk in AGN, which produces a power-law-like continuum extending to high energies; and a thermal-like continuum from massive O- and B-type stars in HII regions. This difference has profound effects on the emission-line spectrum, as some highly ionized species are not found in HII regions, while their contribution is not negligible in AGN due to the harder radiation fields involved (Flury & Moran, 2020; Kewley et al., 2019). Thus, the techniques developed for the metal content study in SFGs must take these differences into account when applied to the AGN case (e.g. Carvalho et al., 2020; Dors et al., 2015; Flury & Moran, 2020; Pérez-Díaz et al., 2021; Pérez-Montero et al., 2019a).

Chemical abundances can also be derived using emission lines in the UV range. This is the case for galaxies at redshift $z \gtrsim 1-2$, where UV lines can be measured by optical telescopes, allowing the determination of chemical abundances in SFGs (e.g. Berg et al., 2016; Dors et al., 2014; Erb et al., 2010; Pérez-Montero & Amorín, 2017) and in AGN (Dors et al., 2019). In these cases, besides the oxygen abundance 12+log(O/H), it is also important to constrain the carbon-to-oxygen ratio log(C/O), since C emits strong UV emission lines that are easily detected and, as N, it is also a metal with both primary and secondary origins.

Nevertheless, the determination of chemical abundances using optical and, above all, UV emission lines, can be seriously affected by reddening. In particular, deeply dust-embedded regions may go unnoticed by optical and UV tracers, which therefore will not be able to probe their content of heavy elements. In addition, the optical and UV CELs present a non-negligible dependence on some physical properties of the ISM, such as the electron temperature (T_e) or the electron density (n_e), which are difficult to take into consideration, either in empirical calibrations or in models. These problems do not arise when chemical abundances are derived from IR emission lines. The relative insensitivity of IR lines to interstellar reddening allows us to peer through the dusty regions in galaxies (Fernández-Ontiveros et al., 2021; Nagao et al., 2011; Pereira-Santaella et al., 2017). In addition, the negligible dependence of the IR line emissivity on T_e (see Fig. 1 in Fernández-Ontiveros et al., 2021) avoids the large uncertainties in the temperature determination that affects the abundances based on optical lines. For instance, Dors et al. (2013) suggest that extinction effects and temperature fluctuations might be an explanation for the discrepancy between optical and infrared estimations of the neon abundances. Temperature fluctuations have also been reported in previous works, for example, Croxall et al. (2013) analyzing a sample of HII regions in NGC628 used fine-structure IR and also optical emission lines. An example of the effect of dust obscuration can be found in Fernández-Ontiveros et al. (2021), where they estimate twice the metallicity of NGC 3198 from IR emission lines when comparing with their optical estimations.

In recent decades, several IR spectroscopic telescopes, such as the *Infrared Space Observatory* (*ISO*, covering the $2.4-197$ μm range, Kessler et al. 1996), the *Spitzer Space Observatory* ($5-39$ μm, Werner et al. 2004), the *Herschel Space Observatory* ($51-671$ μm, Pilbratt et al. 2010) and the *Stratospheric Observatory for Infrared Astronomy* (*SOFIA*, covering the $50-205$ μm range, Fischer et al. 2018), have provided essential information of these emission lines for a considerable amount of sources. Moreover, upcoming missions such as the *James Webb Space Telescope* (*JWST*, which will cover the $4.9-28.9$ μm range with the Mid-InfraRed Instrument MIRI, G. H. Rieke et al. 2015; Wright et al. 2015) and the Mid-infrared ELT Imager and Spectograph (METIS, covering the N-band centered at 10μm, Brandl et al. 2021) will increase the amount of information from IR observations of local galaxies, significantly improving recent studies of chemical abundances based on IR emission lines (Fernández-Ontiveros et al., 2021; B. Peng et al., 2021; Spinoglio et al., 2021) and laying the foundations to extend the analyses to higher redshifts ($z > 4$) with the *Atacama Large Millimeter/submillimeter Array* (ALMA) (Wootten & Thompson, 2009).

In this work we present an IR version of the method HCm developed by (Pérez-Montero, 2014) to derive chemical abundances from optical emission lines in SFGs, and later extended to the NLR region of AGN by Pérez-Montero et al. (2019a) (hereinafter denoted as PM19). This version of HII-CHI-Mistry-IR, or HCm-IR, complements the work done by Fernández-Ontiveros et al. (2021) (hereinafter denoted as FO21) for SFGs. By taking advantage of a grid of photoionization models covering a wide range in 12+log(O/H), log(N/O), and log(U), our method computes these three parameters by fitting emission-line ratios that are sensitive to those quantities.

The work is organized as follows. In Sec. 5.3 we describe a sample of galaxies with available spectroscopic IR data used to check the method. This sample is composed of Seyferts, ULIRGs, LIRGs and LINERs, which show Ne^{4+} emission lines characteristic of AGN activity (Genzel et al., 1998; Pérez-Torres et al., 2021). In Sec. 5.4 we describe the methodology underlying HCm-IR, including the emission-line ratios used to estimate chemical abundances and the differences with those proposed by FO21 when applied to the AGN case. In Sec. 5.5 we present the main results from HCm-IR for our sample of galaxies, also comparing them with estimations from optical observations. In Sec. 5.6 we present a full discussion on these results and we summarize in Sec. 5.7 the main conclusions from this work.

5.3 SAMPLE

To probe the validity of the diagnostics detailed in Sec. 5.4, we compiled a sample of 58 AGN with spectroscopic observations in the mid- and far-IR ranges from *Spitzer*/IRS (Houck et al., 2004; Werner et al., 2004) and *Herschel*/PACS (Pilbratt et al., 2010; Poglitsch et al., 2010), respectively. Most of the galaxies (48) were drawn from the IR spectroscopic atlas in Fernández-Ontiveros et al. (2016), corresponding to the objects with a detection of a hydrogen recombination line in the IR range, namely Brackett-α at 4.05μm (Brα), Pfund-α at 7.46μm (Pfα), or Humphreys-α at 12.4μm (Huα). The sample was completed with nine galaxies with available additional *SOFIA*/FIFI-LS observations (Fischer et al., 2018; Temi et al., 2014) of the [N III] $\lambda 57\mu$m and/or the [OIII]$\lambda,\lambda 52, 88\mu$m lines from Spinoglio et al. (2021). Thus, the sample selection maximizes the number of AGN galaxies with detections of these lines, which allows us to obtain N/O abundance ratios that are independently derived from the oxygen abundance.

The Brα and Pfα line fluxes were collected from the literature, while new measurements of the Huα line for 11 galaxies are presented in this work (see Tab. A.10). The latter were obtained from the calibrated and extracted *Spitzer*/IRS high-resolution spectra ($R = 600$) in the CASSIS database (Lebouteiller et al., 2015). The line flux was measured by direct integration of the spectrum at the rest-frame wavelength of the line, subtracting the continuum level derived from a linear polynomial fit to the adjacent continuum on both sides of the line. The final sample thus consists of 17 Seyfert 1 nuclei (Sy1), 14 Seyfert nuclei with hidden broad lines in the polarized spectrum (Sy1h), 12 Seyfert 2 nuclei (Sy2), three LINERs, four LIRGs and eight ULIRGs.

We present in Fig. 5.1 a classification of our sample of AGN based on the so-called *BPT-IR*[1] diagram (Fernández-Ontiveros et al., 2016). In contrast with the optical diagnostic diagrams (Baldwin et al., 1981; Kauffmann et al., 2003; Kewley et al., 2006), the axes on the BPT-IR diagram represent ratios of the different ionized states for the same element, in other words, they do not show any dependence on the chemical abundances. Although pure AGN models (blue) do not cover the region where ULIRGs, LIRGs, and LINERs fall, a significant amount of our Seyfert sample are in agreement with AGN-dominated models. We also represent the same models from Fernández-Ontiveros et al. (2016) for dwarf galaxies and SFGs, and we find that they do not cover the region where our sample of AGN is located, implying that part of our sample shows both star-formation and AGN activity. Nevertheless, the detection of Ne^{4+} IR lines in these galaxies supports the idea that AGN activity

---

[1] As analogous to the optical diagnostic diagrams, also called Baldwin, Phillips & Terlevich (BPT) diagrams.

dominates our sample (Armus et al., 2007; Genzel et al., 1998; Izotov et al., 2012; Pérez-Torres et al., 2021).

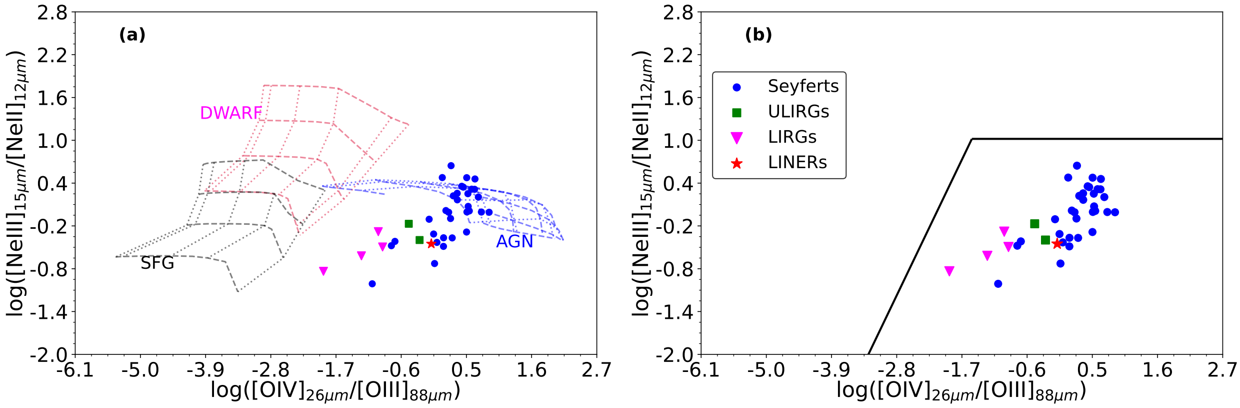

Figure 5.1: BPT or diagnostic diagram in the IR range, proposed to distinguish between spectral types (Fernández-Ontiveros et al., 2016). (a) Models computed with Cloudy v17 (Ferland et al., 2017) are presented as lines: black for SFG models computed from the library STARBUST99 (González Delgado & Leitherer, 1999) with 12+log(O/H) = 8.69 and log(N/O) = −0.86; magenta for dwarf models computed from a starburst of $\sim 10^6$ yr with 12+log(O/H) = 8.0 and log(N/O) = −0.86; and blue for AGN models computed from the same SED used in this work ($\alpha_{OX} = -0.8$ and $\alpha_{UV} = -1.0$, see Sec. 5.4) with 12+log(O/H) = 8.69 and log(N/O)= −1.0. For all models, dotted lines trace models with the same electron density (ranging $10 - 10^7$ cm^{-3}), while dashed lines represent fixed values of the ionization parameter U. (b) The diagram now shows the separation line proposed in this thesis, based on Eq. (2.4).

5.4 PHOTOIONIZATION MODELS AND ABUNDANCE ESTIMATIONS

Chemical abundances (O/H and N/O) and the ionization parameter (U) were derived using an updated version of the Python code HII-CHI-Mistry-IR[2] (FO21) from IR emission lines, adapting it to work for AGN by using the same models used for the optical version of the code, and described in PM19. We denote the optical version as HCm, while its infrared version presented here will be denoted as HCm-IR. We follow the methodology used by FO21, taking into account some differences that arise when considering AGN instead of SFG models.

5.4.1 *Grids of AGN photoionization models*

HCm-IR estimates chemical abundances (O/H and N/O) and U using a Bayesian-like calculation, by comparing certain observed IR emission-line flux ratios with the corresponding values as predicted by large grids of photoionization models. The models were computed using Cloudy v17 (Ferland et al., 2017) and they are the same as those employed by PM19. In these models, the gas phase is characterized by an electron density of $n_e = 500$ cm^{-3}. All models assume a standard dust-to-gas mass ratio and the gas-phase abundances were scaled in each model to O following the solar photospheric proportions reported by Asplund et al. (2009), with the exception of N, which is considered as a free parameter in the grids for an independent estimation of the N/O ratio. The source of ionization is an AGN spectral energy distribution (SED) composed by a Big Blue Bump peaking at 1 Ryd and a power law for X-ray nonthermal emission characterized by $\alpha_X = -1.0$. The continuum between UV and X-ray ranges is represented by a power law with an index of $\alpha_{OX} = -0.8$ or $\alpha_{OX} = -1.2$. The filling factor was set to 0.1 while two stopping criteria were considered: a fraction

---

[2] All versions of the HII-CHI-Mistry code are publicly available at: http://www.iaa.csic.es/~epm/HII-CHI-mistry.html.

Table 5.1: Computed critical densities [cm^{-3}] for fine structure IR lines from PyNeb (Luridiana et al., 2015) for different electron temperatures.

Emission line	$T_e = 5 \cdot 10^3$ K	$T_e = 1 \cdot 10^4$ K	$T_e = 1.5 \cdot 10^4$ K	$T_e = 2 \cdot 10^4$ K	$T_e = 2.5 \cdot 10^4$ K	$T_e = 3 \cdot 10^4$ K
[S iv]$\lambda10.5\mu$m	$4.0 \cdot 10^4$	$5.6 \cdot 10^4$	$6.9 \cdot 10^4$	$7.9 \cdot 10^4$	$8.8 \cdot 10^4$	$9.6 \cdot 10^4$
[Ne ii]$\lambda12.8\mu$m	$4.6 \cdot 10^5$	$6.3 \cdot 10^5$	$7.4 \cdot 10^5$	$8.4 \cdot 10^5$	$9.2 \cdot 10^5$	$1.0 \cdot 10^6$
[Ne v]$\lambda14.3\mu$m	$1.8 \cdot 10^4$	$3.2 \cdot 10^4$	$4.7 \cdot 10^4$	$6.3 \cdot 10^4$	$7.8 \cdot 10^4$	$9.3 \cdot 10^4$
[Ne iii]$\lambda15.6\mu$m	$1.5 \cdot 10^5$	$2.1 \cdot 10^5$	$2.5 \cdot 10^5$	$2.8 \cdot 10^5$	$3.0 \cdot 10^5$	$2.9 \cdot 10^5$
[S iii]$\lambda18\mu$m	$8,173$	$1.2 \cdot 10^4$	$1.5 \cdot 10^4$	$1.7 \cdot 10^4$	$1.8 \cdot 10^4$	$2.0 \cdot 10^4$
[Ne v]$\lambda24\mu$m	3579	5952	8426	$1.1 \cdot 10^4$	$1.3 \cdot 10^4$	$1.6 \cdot 10^4$
[O iv]$\lambda26\mu$m	8387	9905	$1.2 \cdot 10^4$	$1.3 \cdot 10^4$	$1.4 \cdot 10^4$	$1.5 \cdot 10^4$
[S iii]$\lambda33\mu$m	980	1417	1801	2140	2425	2686
[O iii]$\lambda52\mu$m	2753	3530	3879	4082	4233	4418
[N iii]$\lambda57\mu$m	1180	1519	1723	1859	1938	1971
[O iii]$\lambda88\mu$m	388	501	569	620	662	704
[N ii]$\lambda122\mu$m	198	238	256	267	276	283
[N ii]$\lambda205\mu$m	30	38	44	47	51	54

of free electrons of 2% or 98%. Thus, a total of four grids of photoionization models (i.e., assuming two different values for α_{OX} and two different stopping criteria) can be considered and selected by the user in an iterative process while running HCm-IR. Hereafter, we discuss the grid of models corresponding to $\alpha_{OX} = -0.8$ and a stopping criteria of 2% of free electrons. The effects of using different grids will be discussed in Sec. 5.4.5.

The grids cover a range from 12+log(O/H) = 6.9 to 9.1 in steps of 0.1 dex, a range from log(N/O) = −2.0 to 0.0 in steps of 0.125 dex, and a range from $\log(U) = -4.0to - 0.5$ in steps of 0.25 dex. The behavior of some of the emission-line ratios used by the code shows a bivaluation in the [−4.0, −2.5] and [−2.5, −0.5] ranges. This behavior for some optical emission-line ratios was also discussed in PM19 and reported by Pérez-Díaz et al. (2021). For this reason, the grids are constrained to certain U ranges by considering two branches: the low-ionization branch, which covers the [−4.0, −2.5) range, and the high-ionization branch, covering [−2.5, −0.5].

The code takes as input the following IR emission lines: H i$\lambda4.05\mu$m, H i$\lambda7.46\mu$m, [S iv]$\lambda10.5\mu$m, H i$\lambda12.4\mu$m, [Ne ii]$\lambda12.8\mu$m, [Ne v]$\lambda14.3\mu$m, [Ne iii]$\lambda15.6\mu$m, [S iii]$\lambda18\mu$m, [Ne v]$\lambda24\mu$m, [O iv]$\lambda26\mu$m, [S iii]$\lambda33\mu$m, [O iii]$\lambda52\mu$m, [N ii]$\lambda57\mu$m, [O iii]$\lambda88\mu$m, [N ii]$\lambda122\mu$m, and [N ii]$\lambda205\mu$m, which can be introduced in arbitrary units and are not necessarily reddening-corrected. Since our AGN models consider a higher electron density than SFG models used by FO21 (AGN models assume $n_e = 500$ cm^{-3} while SFG models assumed $n_e = 100$ cm^{-3}), special attention must be paid to the critical density of the emission lines, which are much lower than those that characterize optical emission lines (e.g. Osterbrock & Ferland, 2006). Considering different electron temperatures T_e characteristic of the ionic species in our models, we summarized in see Tab. 5.1 the critical densities for all emission lines used as inputs with PyNeb (Luridiana et al. 2015). Therefore, from the set of lines used by HCm-IR for SFG models (FO21), we omitted three of them due to their relatively low critical densities when compared to the electron density adopted for the models [N ii]$\lambda205\mu$m, [N ii]$\lambda122\mu$m, and [O iii]$\lambda88\mu$m. The code only takes into account [O iii]$\lambda88\mu$m when [O iii]$\lambda52\mu$m is missing, although we warn that observed emission lines may deviate from predictions due to contributions of diffuse ionized gas (DIG), leading to uncertainties in the estimated chemical abundances.

In addition, we omitted the emission line [S iii]$\lambda33\mu$m, which is an input for the SFG version of the code. Despite being stronger than [S iii]$\lambda18\mu$m, the introduction of this emission line in the calculations of the code leads to wrong estimations of both O/H and U (see Sec. 5.4.4 for more details). Also, in contrast with the input used for SFGs, we consider [Ne v] emission lines, which are preferentially detected in infrared observations of galaxies hosting AGN (Armus et al., 2007; Genzel et al., 1998; Izotov et al., 2012; Pérez-Torres et al., 2021), and the [O IV] emission line, characteristic of AGN activity (LaMassa et al., 2010; Meléndez et al., 2008; Rigby et al., 2009) since it can only be marginally produced in extremely highly ionized ($\log(U) \gtrsim -1.5$) star-forming regions.

Instead of matching single emission lines to predicted observations, HCm-IR uses particular emission-line ratios (listed below) to match observations and predictions. Then, the abundances O/H, N/O, and U are calculated following a χ^2 methodology, being the mean of all input values of the models weighted by the quadratic sum of the differences between observations and predictions, which is the same methodology described in PM19. After the first iteration, N/O is fixed and the grid of models is constrained. Then, O/H and U values are calculated in later iterations considering the already constrained model grids. When errors on the emission-line fluxes are provided, the code also takes them into account in the final uncertainty of the estimations with a Monte Carlo simulation by perturbing the nominal input emission-line fluxes in the range delimited by their corresponding error.

5.4.2 *N/O estimation*

To estimate N/O, HCm-IR considers two emission-line ratios. The first one is N3O3, proposed by several authors (e.g. Fernández-Ontiveros et al., 2021; Nagao et al., 2011; B. Peng et al., 2021; Pereira-Santaella et al., 2017), which is an infrared analog of the estimator N2O2 usually used in the optical range due to its effectiveness for both AGN and SFGs (Pérez-Montero et al., 2019a) to derive the same abundance ratio (e.g. Pérez-Montero & Contini, 2009). The N3O3 tracer is defined as:

$$\log\,(\mathrm{N3O3}) = \log\left(\frac{\mathrm{I}\left([\mathrm{N\,III}]_{57\mu m}\right)}{\mathrm{I}\left([\mathrm{O\,III}]_{52\mu m}\right)}\right) \tag{5.1}$$

Our definition of N3O3 only takes into account [O III]$\lambda 52\mu$m because the other [O III] IR emission line presents a critical density close to the electron density of our models, in contrast to the same estimator defined for star-forming regions as described by FO21, which also takes into account [O III]$\lambda 88\mu$m. When [O III]$\lambda 52\mu$m is not provided, the code calculates N3O3 using [OIII]$\lambda 88\mu$m. This modification is only taken into account when the code is applied for AGN, but not in the case of SFGs since the grid of models for those cases is calculated for $n_e \sim 100$ cm^{-3} (FO21). As for its optical analog, this estimator has little dependence on U as shown in Fig. 5.2 (a). Moreover, our grid of AGN models and the grid of SFGs show that this parameter is almost independent of the spectral type, meaning there is little distinction between AGN and SFG models.

The second emission-line ratio used by the code to derive N/O is N3S34, which takes advantage on the primary origin of sulfur (as in the case of oxygen), is defined as:

$$\log\,(\mathrm{N3S34}) = \log\left(\frac{\mathrm{I}\left([\mathrm{N\,III}]_{57\mu m}\right)}{\mathrm{I}\left([\mathrm{S\,III}]_{18\mu m}\right) + \mathrm{I}\left([\mathrm{S\,IV}]_{10\mu m}\right)}\right) \tag{5.2}$$

This ratio also correlates with N/O, presenting little dependence on O/H, as shown in Fig. 5.2 (b). Moreover, this tracer also presents a tight correlation with N/O when SFG models are considered. Thus, we have also added this estimator in the calculations of HCm-IR for SFGs, with the particular difference that emission line [S III]$\lambda 33\mu$m is also considered for SFGs.

Considering the behavior of the AGN models in both Figs. 5.2 (a) and (b), we obtain the following linear calibrations using data from the photoionization models:

$$\log\,(\mathrm{N/O}) = (0.9839 \pm 0.0016)\log\,(\mathrm{N3O3}) + (-0.1389 \pm 0.0015) \tag{5.3}$$

$$\log(\text{N/O}) = (0.727 \pm 0.007)\log(\text{N3S34}) + (0.326 \pm 0.013) \quad (5.4)$$

which can be used as alternative to the code to directly estimate N/O.

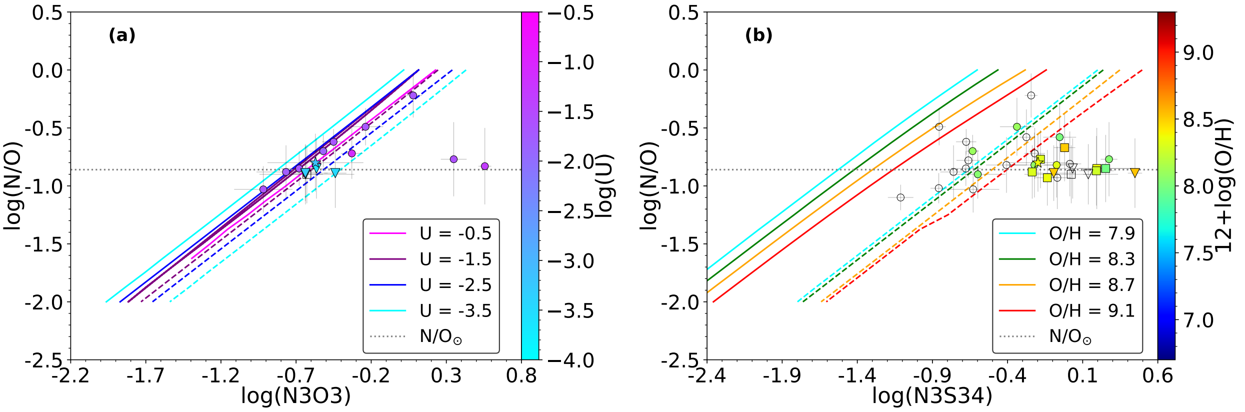

Figure 5.2: Relations between different IR emission-line ratios with N/O . (a) Relation with N3O3 in our sample. The colorbar shows estimations of $\log(U)$. AGN models for a fixed value of 12+log(O/H) = 8.6 are presented as continuous lines, while dashed lines correspond to SFG models for the same fixed value. (b) Relation with the N3S34 estimator in our sample. The colorbar shows estimations of 12+log(O/H). AGN models for a fixed value of $\log(U) = -2.0$ are presented as continuous lines, while dashed lines correspond to SFG models for the same fixed value. For both plots, blank points indicate that no estimation can be provided of the colored quantity. The following spectral types are represented: Seyferts 2 as circles; ULIRGs as squares; LIRGs as triangles; and LINERs as stars.

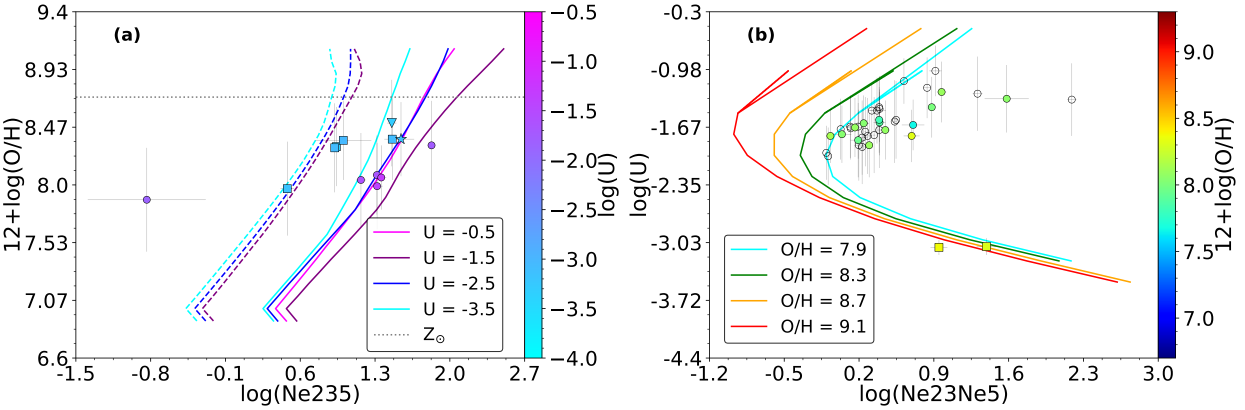

Figure 5.3: Relations of different ratios involving Ne IR emission-lines with O/H and $\log(U)$. (a) Relation between the Ne235 estimator, using H I 4μm, and 12+log(O/H) in our sample. The colorbar shows estimations of $\log(U)$. (b) Relation between estimator Ne23Ne5 and $\log(U)$ in our sample. The colorbar shows estimations of 12+log(O/H). For both plots, blank points indicate that no estimation can be provided of the colored quantity. AGN models for a fixed value of log(N/O) = −1.0 are presented as continuous lines, while dashed lines correspond to SFG models for the same fixed value. The following spectral types are represented: Seyferts 2 as circles; ULIRGs as squares; LIRGs as triangles; and LINERs as stars.

5.4.3 *O/H and U estimations*

Once N/O has been determined in a first iteration, as this involves emission-line ratios with little dependence on other input parameters, the code estimates in a second iteration both O/H and U from a subgrid of models compatible with the previous estimation of N/O. Therefore, this

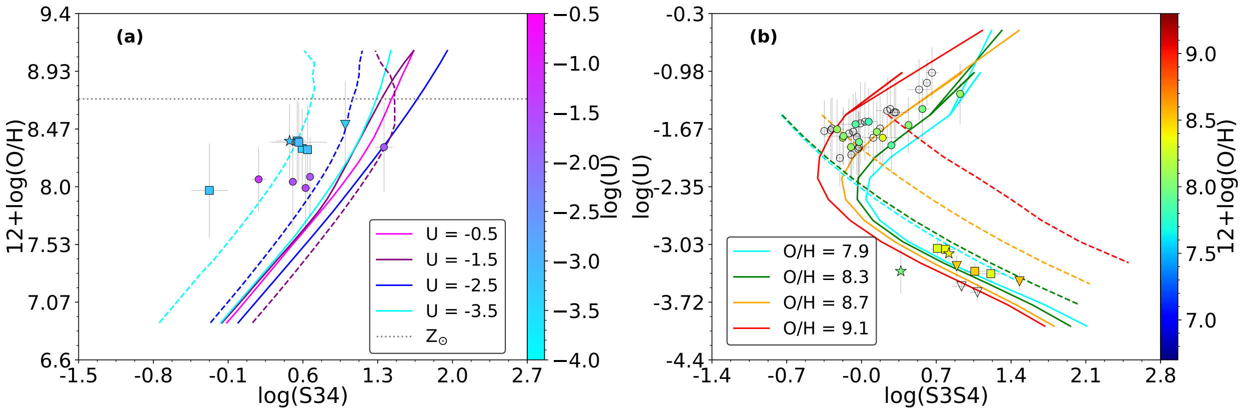

Figure 5.4: Same as for Fig. 5.3, but for S34 and S3S4.

guarantees that no previous assumption between O/H and N/O is introduced. In case N/O cannot be constrained due to the lack of key emission lines, a relation between O/H and N/O is assumed by the code. By default, this relation is the one obtained by Pérez-Montero (2014) for star-forming regions using chemical abundances based on optical emission-lines. However, this relation can be modified by any user of the code adopting alternative laws within the corresponding libraries.

To estimate O/H and U, the code uses multiple emission-line ratios that are sensitive to the above quantities. One of them is based on neon lines and comes from a modification of the estimator Ne23 proposed by Kewley et al. (2019) and FO21 to account for [Ne v] lines that are more prominent in AGN than in SFGs. Then, accordingly, the estimator Ne235 for O/H can be defined as:

$$\log\left(\mathrm{Ne235}\right) = \log\left(\frac{\mathrm{I}\left([\mathrm{Ne\,II}]_{12\mu m}\right) + \mathrm{I}\left([\mathrm{Ne\,III}]_{15\mu m}\right) + \mathrm{I}\left([\mathrm{Ne\,V}]_{14\mu m}\right) + \mathrm{I}\left([\mathrm{Ne\,V}]_{24\mu m}\right)}{\mathrm{I}\left(\mathrm{H\,I}_{i}\right)}\right) \tag{5.5}$$

with $\mathrm{H\,I}_i$ being one of the hydrogen lines that the code can take as input. In cases where more than one of the hydrogen lines are introduced as input, HCm-IR calculates Ne235 for each hydrogen line, taking all considered ratios in the resulting weighted-distribution. In addition, these same neon lines are used to estimate $\log(U)$ from the ratio Ne23Ne5, defined as:

$$\log\left(\mathrm{Ne23Ne5}\right) = \log\left(\frac{\mathrm{I}\left([\mathrm{Ne\,II}]_{12\mu m}\right) + \mathrm{I}\left([\mathrm{Ne\,III}]_{15\mu m}\right)}{\mathrm{I}\left([\mathrm{Ne\,V}]_{14\mu m}\right) + \mathrm{I}\left([\mathrm{Ne\,V}]_{24\mu m}\right)}\right) \tag{5.6}$$

which is a modification of the estimator Ne2Ne3 proposed by several authors (Fernández-Ontiveros et al., 2021; Kewley et al., 2019; Thornley et al., 2000; Yeh & Matzner, 2012) to account for the high-ionic species of Ne, which are found in AGN. Fig. 5.3 (a) shows the behavior of Ne235 with 12+log(O/H). There is little dependence on U and there is clear separation between SFG and AGN models, which is explained by the little capacity of SFG models to produce [Nev]. Fig. 5.3 (b) shows the relation between Ne23Ne5 and $\log(U)$. The behavior of the models, well reproduced by the estimations in our sample, clearly shows the bi-valuation that forces the code to distinguish between low- and high-ionization AGN. For low-ionization AGN models, little dependence is found on O/H, while it has a more significant impact on the upper branch (i.e., high-ionization AGN models). The lack of SFG models in this figure justifies the omission of [Nev] lines in SFG estimators.

Another set of IR emission lines that HCm-IR uses to estimate O/H and U are the sulfur lines. To calculate both quantities, the code uses the estimators S34 (FO21) and S3S4 (Fernández-Ontiveros et al., 2021; Yeh & Matzner, 2012) respectively, defined as:

$$\log\left(\text{S34}\right) = \log\left(\frac{\text{I}\left([\text{S}\,\textsc{iii}]_{18\mu m}\right) + \text{I}\left([\text{S}\,\textsc{iv}]_{10\mu m}\right)}{\text{I}\left(\text{H}\,\textsc{i}_i\right)}\right) \tag{5.7}$$

$$\log\left(\text{S3S4}\right) = \log\left(\frac{\text{I}\left([\text{S}\,\textsc{iii}]_{18\mu m}\right)}{\text{I}\left([\text{S}\,\textsc{iv}]_{10\mu m}\right)}\right) \tag{5.8}$$

Our definitions of these two estimators differ from those used in FO21 since we omit [S III]$\lambda 33\mu$m in our calculations. Fig. 5.4 (a) shows that S34 correlates with 12+log(O/H) and has also little dependence on U, although in this case there is no clear separation between SFG and AGN models. Fig. 5.4 (b) reinforces our preliminary statement about the need to distinguish between low- and high-ionization AGN due the bi-valuation of log(U) with S3S4. We also observed that for low-ionization parameters (log(U) < -2.5), the behavior of AGN and SFG models is similar, although they cover different regions of the diagram.

In the same fashion that we proceed with the sulfur lines, the code takes into account estimators based on IR oxygen lines. We define O34 and O3O4 to estimate 12+log(O/H) and log(U) respectively as:

$$\log\left(\text{O34}\right) = \log\left(\frac{\text{I}\left([\text{O}\,\textsc{iii}]_{52\mu m}\right) + \text{I}\left([\text{O}\,\textsc{iv}]_{26\mu m}\right)}{\text{I}\left(\text{H}\,\textsc{i}_i\right)}\right) \tag{5.9}$$

$$\log\left(\text{O3O4}\right) = \log\left(\frac{\text{I}\left([\text{O}\,\textsc{iii}]_{52\mu m}\right)}{\text{I}\left([\text{O}\,\textsc{iv}]_{26\mu m}\right)}\right) \tag{5.10}$$

Here again we have omitted the use of [O III]$\lambda 88\mu$m due to its very low critical density. However, if [O III]$\lambda 52\mu$m is not provided, the code calculates both estimators O34 and O3O4 with [O III]$\lambda 88\mu$m. Fig. 5.5 (a) shows that O34 has a strong dependence on U. However, O3O4 does not show any dependence on O/H (see Fig. 5.5 (b)), so it can be used to constrain U and estimate 12+log(O/H) with O34. In addition, Fig. 5.5 (b) shows that this estimator might be employed in SFG models, but few models are able to produce [O IV]$\lambda 26\mu$m. Nevertheless, these ratios have also been implemented in the SFG version of the code (FO21) as they can further constrain SFG models to account for the presence of [O IV]$\lambda 26\mu$m, only found for a very reduced small number of models characterized by hard radiation fields (log(U) > -1.5). Analogous results are obtained if the [OIII]$\lambda 88\mu$m emission line is considered.

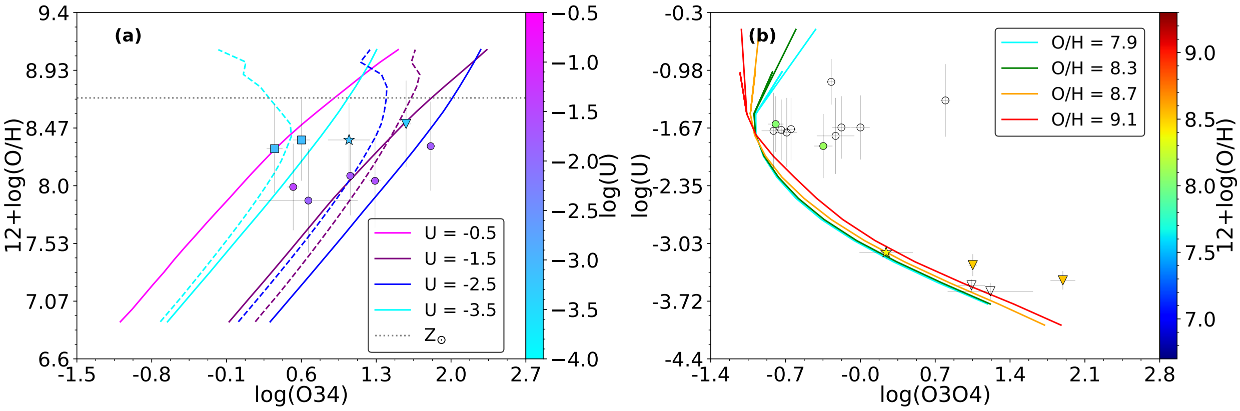

Figure 5.5: Same as for Fig. 5.3, but for O34 and O3O4.

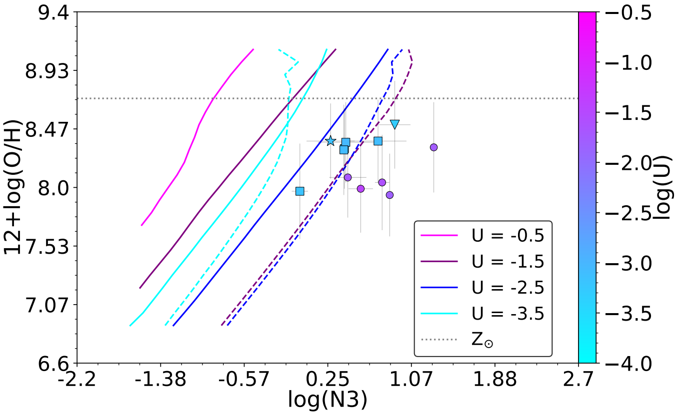

Figure 5.6: Same as for Fig. 5.3 (a), but for N3.

Although FO21 considered IR N lines to estimate both O/H and U in SFGs, both estimators (N23 and N2N3, FO21; Kewley et al. 2019; Nagao et al. 2011) imply the use of [N II], whose critical density is below the electron density of our models. Therefore, we define the estimator N3 based only on the [N III]$\lambda 57\mu$m line as:

$$\log\,(\mathrm{N3}) = \log\left(\frac{\mathrm{I}\left([\mathrm{N\,III}]_{57\mu m}\right)}{\mathrm{I}\,(\mathrm{H\,I}_i)}\right) \tag{5.11}$$

which can be used since N/O has already been constrained in a first iteration. However, as in the case of O34, Fig. 5.6 shows that this estimator also depends on U, although for a fixed value of log(U), N3 shows a tight correlation with 12+log(O/H).

It is important to notice that we cannot consider the estimator O3N2, defined by FO21 as the ratio between [O III] and [N II] IR lines, due to the very low critical densities of these lines. Therefore, there is no possible estimation of 12+log(O/H) if none of the three IR H lines (H I$\lambda 4.05\mu$m, H I$\lambda 7.46\mu$m, or H I$\lambda 12.4\mu$m) are provided.

Although we have defined estimators based on the most common observed IR emission lines from *Spitzer*, *Herschel* or ISO, additional estimators and modifications will be introduced to the code to account for more spectral lines as new and better resolved spectroscopic data is released from the upcoming IR missions such as JWST. For instance, emission line [Ne VI]$\lambda 7.7\mu$m, which is now unresolved due to low resolution in the near-IR, or fainter emission lines such as [Ar II]$\lambda 7\mu$m or [Ar III]$\lambda 9\mu$m, will be accessible from JWST. Nevertheless, with the current available IR data, it is not possible to check the validity of their use, so this will be discussed when new data is released.

5.4.4 *Subsets of emission lines*

Although HCM-IR, as described in the previous section, can take as input a set of IR emission lines in order to estimate chemical abundances and ionization, through the appropriate emission-line ratios (Eq. (5.1)-(5.11)), the code can also reach to a solution with a small subset of the input emission lines. Nevertheless, the capability of the code to find an accurate solution will depend on the available emission lines used as an input. For instance, if no measurement of [N III]$\lambda 57\mu$m is provided, then the code will be unable to calculate N/O since both estimators (N3O3 and N3S34) involve this emission line. In the case of estimating 12+log(O/H), it is necessary to provide one of the three IR hydrogen recombination lines.

In this section we explore the results from HCM-IR when different sets of emission lines are introduced as inputs. To compare the estimations from the code with reliable results, we use

Table 5.2: Median offsets and RMSEs of the residuals between theoretical abundances and log(U) values (AGN model inputs), and estimations from HCm-IR using different sets of emission lines.

Set of lines	Δ_{OH}	RMSE$_{OH}$	Δ_{NO}	RMSE$_{NO}$	Δ_{U}	RMSE$_{U}$
All lines	−0.01	0.24	0.04	0.13	−0.05	0.24
H iλ4.05μm, H iλ7.46μm, H iλ12.4μm, [Ne ii]λ12.8μm, [Ne v]λ14.3μm, [Ne iii]λ15.6μm, [Ne v]λ24μm	−0.01	0.17	–	–	−0.16	0.36
H iλ4.05μm, H iλ7.46μm, H iλ12.4μm, [O iv]λ26μm, [O iii]λ52μm, [N iii]λ57μm	0.07	0.29	0.03	0.08	−0.10	0.40
H iλ4.05μm, H iλ7.46μm, H iλ12.4μm, [S iv]λ10μm, [S iii]λ18μm, [N iii]λ57μm	−0.03	0.21	0.02	0.30	−0.07	0.27
[Ne ii]λ12.8μm, [Ne v]λ14.3μm, [Ne iii]λ15.6μm, [Ne v]λ24μm, [S iv]λ10μm, [S iii]λ18μm, [N iii]λ57μm	–	–	0.02	0.31	−0.05	0.20
H iλ4.05μm, H iλ7.46μm, Hiλ12.4μm, [S iv]λ10μm, [Ne v]λ14μm, [Ne v]λ24μm, [O iv]λ26μm, [N iii]λ57μm	0.24	0.41	−0.44	0.56	−0.09	0.53
All lines + [S iii]λ33μm	0.14	0.48	0.06	0.15	−0.12	0.58

as input the emission lines from the models whose chemical abundances and U are known, by randomly perturbing at 10% the flux of the lines, simulating observational uncertainties.

In Tab. 5.2 we present the statistics of the residuals between the input values used in the models and the corresponding predictions from HCm-IR. When all the possible emission lines of a set are used as input, we obtain low median offsets for 12+log(O/H), log(N/O), and log(U). Since we introduce a 10% uncertainty in the emission-line fluxes, considering the error propagation in the involved line ratios, the values of the root mean square error (RMSE) for each quantity are compatible with the uncertainty carried in the estimation. Moreover, considering the steps σ of the grid (0.1 dex for O/H, 0.125 dex for N/O, and 0.25 dex for log(U), the RMSEs are below 3σ in all cases.

If only highly ionized emission lines ([S iv], [O iv], and [Ne v]) are introduced as inputs, systematic offsets appear for all three quantities. Although low-ionized emission lines are key for estimating U, we obtain a significant offset even for N/O estimation (ΔN/O ~ -0.44 dex), since the code is assuming a relation between N/O and O/H, as there is no independent estimation of both quantities. Overall, we conclude that the best estimations for O/H and U are obtained when neon or sulfur lines are used, similar to what is obtained for SFGs (FO21). Analyzing N/O, best estimations involved oxygen emission line [O iii]λ52μm (i.e., estimator N3O3), since using only sulfur lines leads to higher dispersion (RMSE $\sim$ 0.3 dex).

Tab. 5.2 also shows the reason why emission line [S iii]λ33μm was omitted from the calculations: the offsets and RMSE for O/H and U increase even if we consider the whole set of emission lines, leading to wrong estimations. Moreover, Fig. 5.7 clearly shows that while predictions of N/O fit well with inputs for models, the second iteration of the code to estimate O/H and U shows an almost constant behavior: values of the O/H cluster around 8.2, while values of the U cluster around −1.7 for high-ionization AGN and −3.1 for low-ionization AGN. Thus, this emission line was omitted in the code.

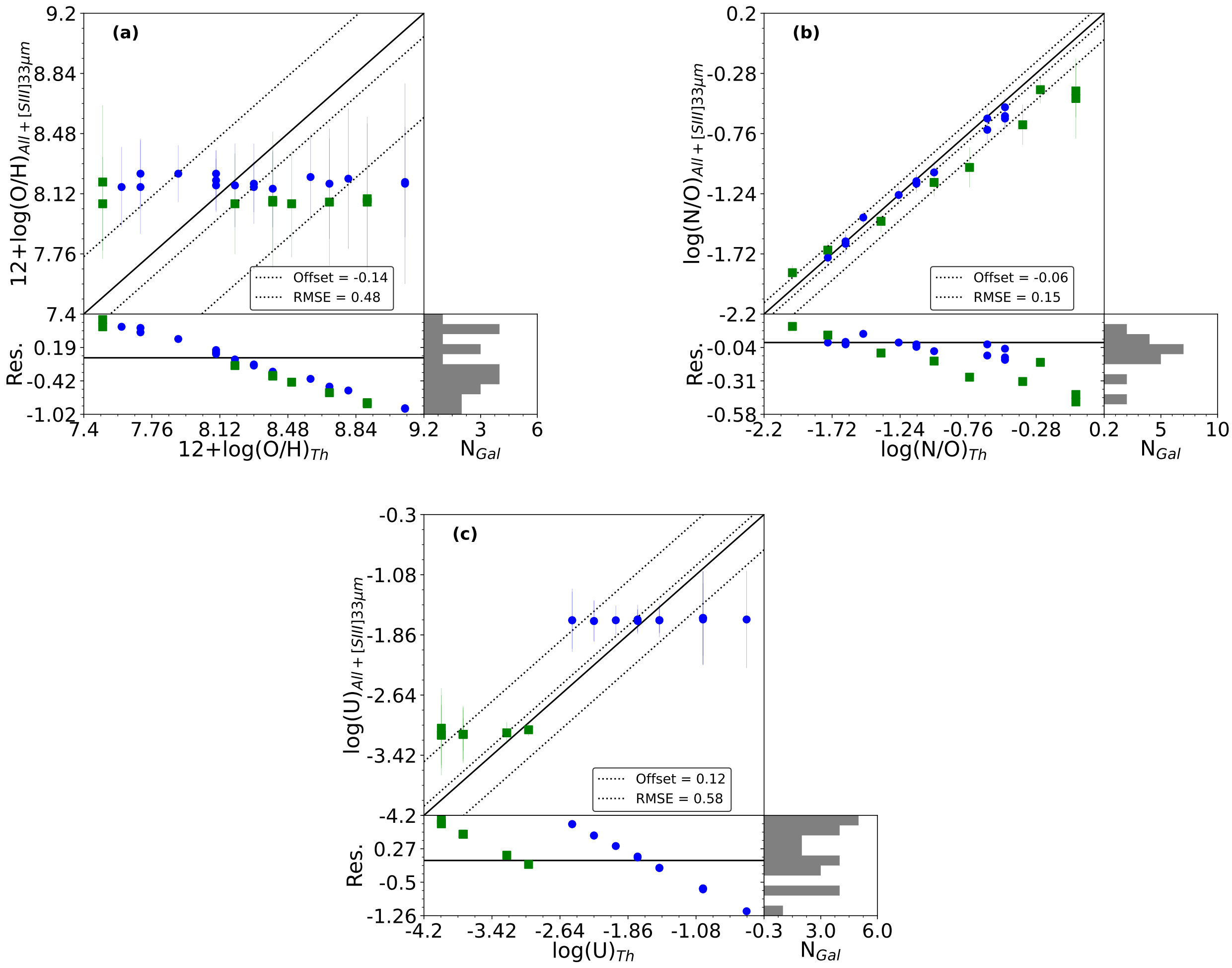

Figure 5.7: Comparison between the chemical abundances and U values introduced as inputs for the models (x-axis) with the estimations from HCm-IR when all lines plus $[\mathrm{S\,III}]\lambda 33\mu\mathrm{m}$ are used (y-axis). For all plots we present Seyferts as blue circles and LINERs as green squares. The offsets are given using the median value (dashed line) and RMSE (dot-dashed lines). Bottom plots show the residuals from the offset and their distribution in a histogram (bottom-right plot).

5.4.5 *Selection of the grid*

Although we used the grid of AGN models computed from an SED characterized by $\alpha_{OX} = -0.8$ and selecting an stopping criteria of 2% fraction of free electrons, HCm-IR provides more default grids where α_{OX} can change from -0.8 to -1.2 and the fraction of free electrons from 2% to 98%. Moreover, we included in the last update a new feature for users to introduce any grid of models. In this section, we explore the effects of changing the default grid of models to estimate chemical abundances from IR emission lines.

From Figs. 5.8 (a), (c), and (e), we conclude that no significant change is introduced in the chemical abundances or ionization parameters derived when the grid of models is computed assuming an SED characterized by $\alpha_{OX} = -1.2$; the offsets are below 0.05 dex and the RMSE is always below the step considered in the grid for the given quantity. On the other hand, the effects of selecting a different stopping criteria are more notorious in the determination of the ionization parameter; high-ionization ($U > -2.5$) AGN present a higher scatter, with values clustering around $\log(U) \sim -1.8$. This effect is mainly caused due to changes in the emission lines of highly ionizing species such as Ne^{4+} or O^{3+}. In the case of O/H, there seems to be a slight overestimation when models

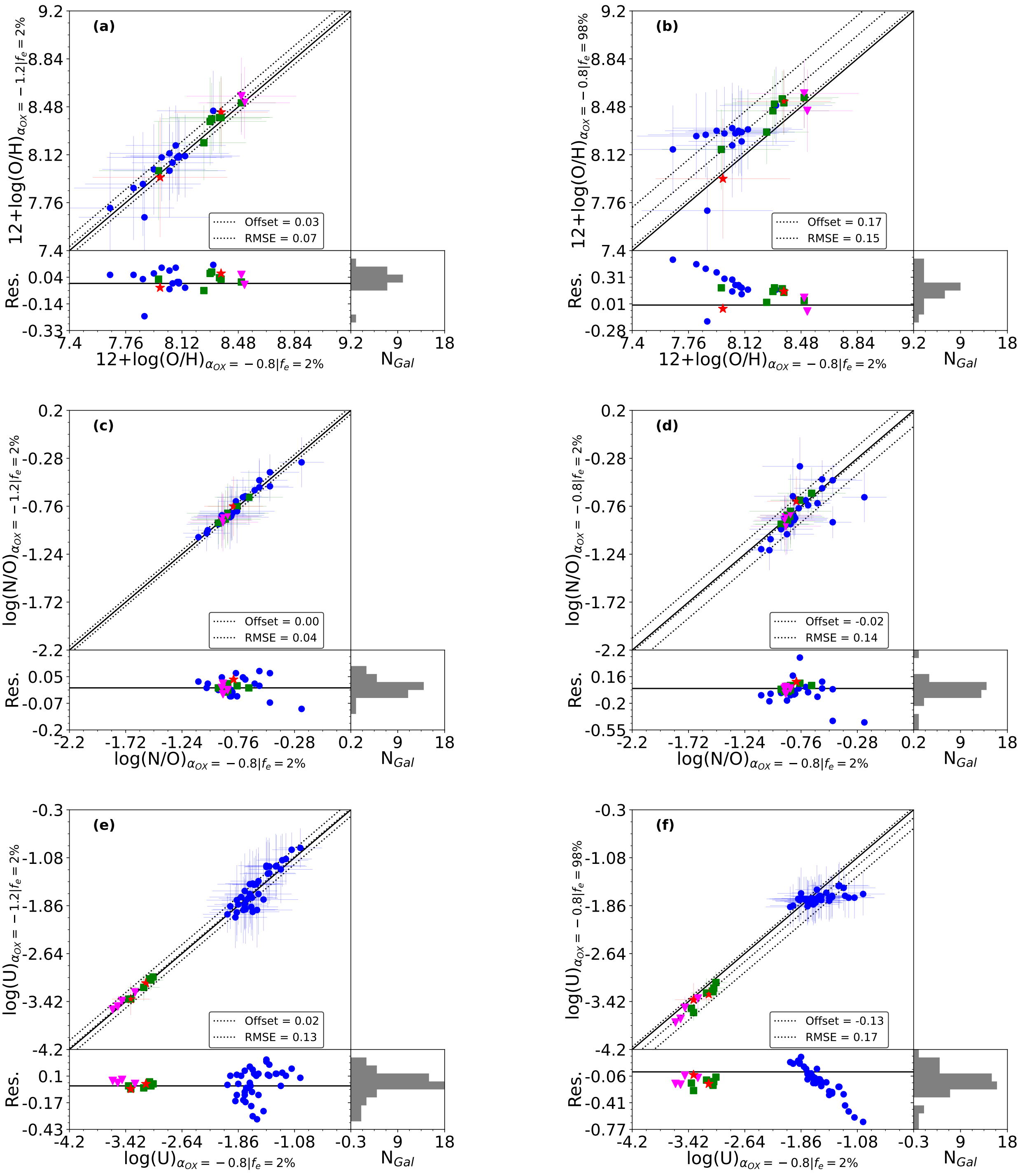

Figure 5.8: Comparison between the chemical abundances and U values introduced, obtained from the grid characterized by $\alpha_{OX} = -0.8$ and a 2% fraction of free electrons (x-axis) with models with $\alpha_{OX} = -1.2$ ((a), (c), and (e)) and models with 98% as stopping criteria ((b), (d), and (f)). For all plots we present Seyferts as blue circles, ULIRGs as green squares, LIRGs as magenta triangles, and LINERs as red stars. The offsets are given using the median value (dashed line) and RMSE (dot-dashed lines). Bottom plots show the residuals from the offset and their distribution in a histogram (bottom-right plot).

with stopping criteria of 98% free electrons are considered. N/O does not show any significant change.

Table 5.3: Statistics of the chemical abundances and $\log(U)$ values derived from HCm-IR for our sample of galaxies.

		12+log(O/H)			log(N/O))			log(U)		
Sample	N°_{tot}	N°	Med.	Sd. Dv.	N°	Med.	Sd. Dv.	N°	Med.	Sd. Dv.
All galaxies	58	26	8.05	0.24	35	−0.83	0.17	52	−1.73	0.80
Seyferts	43	15	7.99	0.16	22	−0.81	0.20	39	−1.67	0.33
ULIRGs	8	7	8.32	0.20	8	−0.86	0.07	7	−3.08	0.15
LIRGs	4	2	8.495	0.005	4	−0.885	0.019	4	−3.58	0.14
LINERs	3	2	8.17	0.18	1	−0.80	–	2	−3.24	0.10

5.5 RESULTS

We present in this section the chemical abundances and ionization parameters estimated for our sample of AGN using HCm-IR. Due to the lack of alternatives to estimate these parameters from IR observations of AGN, we use optical spectroscopic information of the same sample in order to compare results from both sets of information.

5.5.1 *Infrared estimations*

We summarize in Tab. 5.3 the statistics of the estimations of the chemical abundances and $\log(U)$ values obtained with HCm-IR from the IR emission lines in our sample distinguishing between different types of galaxies. Tab. A.11 shows these results in detail for each galaxy in our sample.

As expected from our preliminary distinction of AGN, we have two main subgroups based on U results consistent with our prior distinction; Seyferts belong to the high-ionization AGN category, as they usually present $\log(U) > -2.5$ (Ho et al., 1993; Villar-Martín et al., 2008; Zhuang et al., 2019), while LINERs fall in the category of low-ionization AGN with $\log(U) < -2.5$ (Binette, 1985; Ferland & Netzer, 1983; Halpern & Steiner, 1983; Kewley et al., 2006). In the case of ULIRGs and LIRGs, the study by Pereira-Santaella et al. (2017) showed that low ($\log(U) < -2.5$) ionization parameters are needed to reproduce observations from photoionization models, and thus we assume they fall in the category of low-ionization AGN.

Although we have relatively low statistics, the three spectral types considered as low-ionization AGN differ in their median ionization; ULIRGs show the highest value ($\log(U) \sim -3$), followed by LINERs ($\log(U) \sim -3.25$) and then by LIRGs ($\log(U) \sim -3.6$). Despite these differences being higher than their dispersions, they are still close to the step for U used in the grid (0.25 dex) of models, and thus they must be revisited in a larger sample of galaxies.

Analyzing chemical abundances, we obtained median subsolar values for all types of galaxies, Seyferts being, on average, metal-poorer than the other three spectral types. However, since the estimation of 12+log(O/H) is only available in the few galaxies with detected hydrogen recombination lines, this result must be revisited in larger samples of galaxies. N/O shows a similar median value for all types of galaxies, clustering around the solar value of $\log(N/O)_{\odot} = -0.86$ (Asplund et al., 2009).

We also present in Fig. 5.9 the well-known N/O-O/H diagram obtained from our IR estimations. It should be noted that our statistics for this plot are small because we need galaxies with estimations of both log(N/O) and 12+log(O/H). We find almost a flattened behavior around $\log(N/O)_{\odot}$, although there are some galaxies with higher ratios.

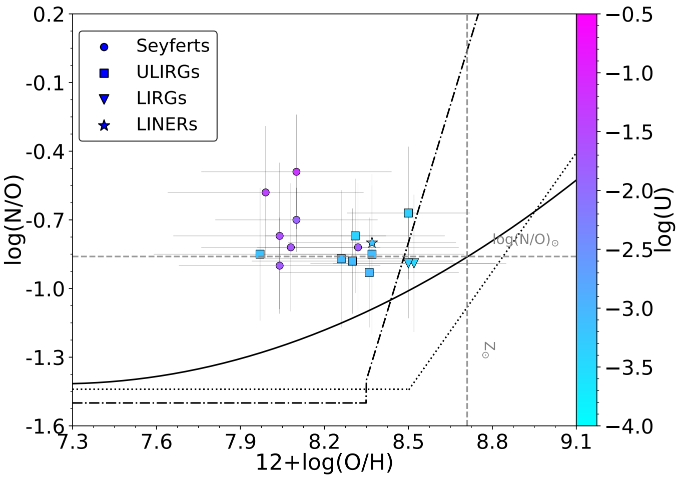

Figure 5.9: N/O vs O/H from IR estimations. The values for log(U) are given by the colorbar. Lines show reported relations in the literature: black solid (Coziol et al., 1999), dotted (Andrews & Martini, 2013) and dash-dotted (Belfiore et al., 2015).

5.5.2 *Optical estimations*

We compiled, from the literature, optical emission-line fluxes for our sample of AGN, and corrected all emission-line ratios for reddening (see Tab. A.12) relative to the Balmer line H_β, following Howarth's extinction curve (Howarth, 1983), assuming $R_V = 3.1$ and a theoretical ratio between H_α and H_β of 3.1, characteristic of the Recombination Case B for the physical conditions of the NLR in AGN. Although we have additional information from IR observations, which are necessary in order to account for some ionic species whose emission lines cannot be retrieved from optical emission lines, such as O^{3+}, and this can in turn lead to underestimations in the oxygen abundance (Dors et al., 2015; Flury & Moran, 2020; Maiolino & Mannucci, 2019), we cannot apply the direct method since only two galaxies in our sample (namely Mrk 478 and NGC 4151) present measurements of auroral line [O III]λ4363Å, which are key for determining the electron temperature T_e of the ISM. Thus, we estimated chemical abundances from optical emission lines for our sample of AGN using the optical version of HCM for AGN (PM19). The code takes as input the following reddening-corrected optical emission lines: [O II]λ3727Å, [Ne III]λ3868Å, [O III]λ4363Å, [O III]λ5007Å, [N II]λ6584Å, and [S II]λ, λ6717, 6731Å; all of them are relative to the Balmer line H_β.

To check our optical estimations, we also considered the calibration proposed by Flury and Moran (2020) based on [O III]λ5007Å and [N II]λ6584Å, given by:

$$\begin{aligned} 12 + \log\,(\mathrm{O/H})_{FM+20} =& 7.863 + 1.170u + 0.027v - 0.406uv - 0.369u^2 + 0.208v^2 + 0.354u^2v \\ & - 0.333uv^2 - 0.100u^3 + 0.323v^3 \end{aligned} \tag{5.12}$$

where $u = \log\,(\mathrm{I}\,(\,[\mathrm{N\,II}]\lambda 6584\text{Å}/\mathrm{H}_\alpha\,))$ and $v = \log\,(\mathrm{I}\,(\,[\mathrm{O\,III}]\lambda 5007\text{Å}/\mathrm{H}_\beta\,))$. This calibration is valid for the range 7.5 ≤ 12+log(O/H) ≤ 9.0.

We also considered the calibration based on the N line [N II]λ6584Å given by Carvalho et al. (2020):

$$Z/Z_\odot = a^{N2} + b$$

where $N2 = \log\left(I\left(\left([\mathrm{N\,II}]\lambda 6584\text{Å}/\mathrm{H}_\beta\right)\right)\right)$, $a = 4.01 \pm 0.08$, and $b = -0.07 \pm 0.01$. In terms of the oxygen abundance, the calibration is given by[3]:

$$12 + \log\left(\mathrm{O/H}\right)_{Ca+20} = 8.69 + \log\left(4.01^{N2} - 0.07\right) \tag{5.13}$$

which was defined in the range 8.17 ≤ 12+log(O/H) ≤ 9.0.

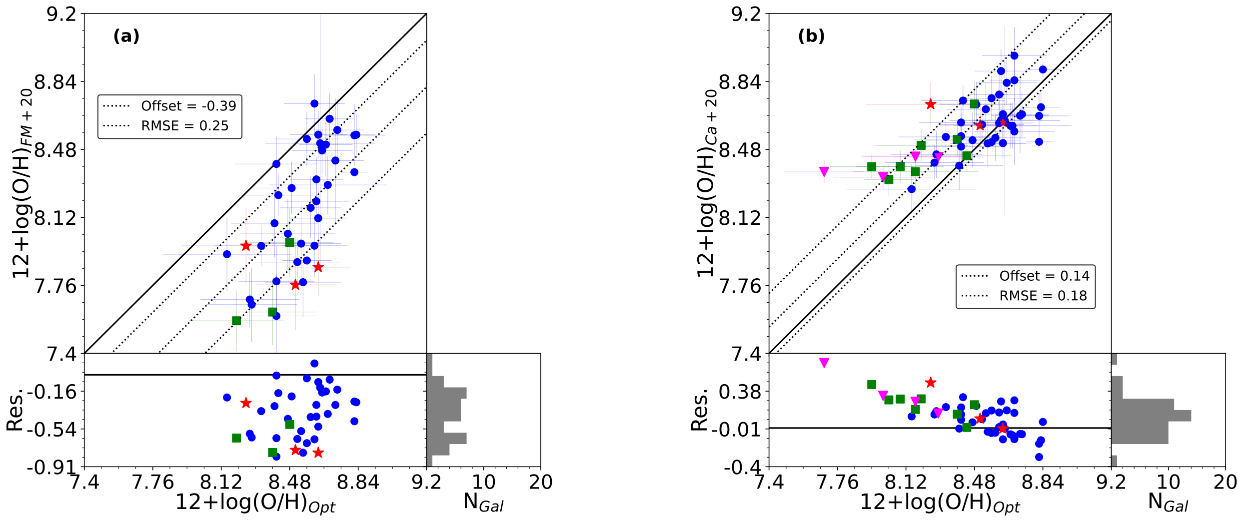

Figure 5.10: Chemical abundances derived from optical emission lines in our sample of AGN. (a) Comparison between the chemical abundances derived with the calibration from Flury and Moran (2020) (y-axis), denoted as FM20, and HCm (x-axis). (b) Comparison between the chemical abundances derived from the calibration from Carvalho et al. (2020) (y-axis), denoted as Ca+20, with HCm (x-axis). For all plots we present Seyferts as blue circles, ULIRGs as green squares, LIRGs as magenta triangles, and LINERs as red stars. The offsets are given using the median value (dashed line) and RMSE (dot-dashed lines). Bottom plots show the residuals from the offset and their distribution in a histogram (bottom-right plot).

We compared the resulting abundances in our sample of AGN (see Tab. A.13) from the calibrations described above with those from HCm in Fig. 5.10. The calibration proposed by Flury and Moran (2020) tends to underestimate HCm abundances, with a median offset of −0.39 dex. On the other hand, the calibration proposed by Carvalho et al. (2020) better fits our results, with a median offset of 0.14 dex. As shown in bottom plot of Fig. 5.10 (b), the discrepancy is higher for ULIRGs, LIRGs, and LINERs than for Seyferts. This could be explained by the fact that Carvalho et al. (2020) obtained their calibration from a sample of Seyferts 2 from the Sloan Digital Sky Survey (SDSS), in other words it was obtained using only high-ionization AGN, covering a different range of the ionization parameter to the values reported for low-ionization AGN (e.g. Kewley et al., 2006). Another possible source of error is that the calibration is based only on a nitrogen line, so it assumes a relation between 12+log(O/H) and log(N/O), although it has been reported that both quantities might not be related in low-ionization AGN (Pérez-Díaz et al., 2021).

We present in Tab. 5.4 the statistics of the chemical abundances derived from the optical version of the code. Again, we find that 12+log(O/H) presents subsolar median values for all types of galaxies. The median N/O values present more variation between different types but, considering the standard deviations, they are still compatible with them, and with the solar value obtained from IR estimations.

We also present in Fig. 5.11 the N/O-O/H diagram. We can see two different trends based on the two main categories considered throughout this study. For low-luminosity AGN (ULIRGs,

---

[3] We assume here the solar abundances from Asplund et al. (2009)

Table 5.4: Same as for Tab. 5.3, but for optical results.

		12+log(O/H)			log(N/O))			log(U)		
Sample	N°_{tot}	N°	Med.	Sd. Dv.	N°	Med.	Sd. Dv.	N°	Med.	Sd. Dv.
All galaxies	58	58	8.49	0.30	51	−0.84	0.24	58	−1.88	0.81
Seyferts	43	43	8.57	0.30	36	−0.84	0.25	43	−1.81	0.23
ULIRGs	8	8	8.19	0.19	8	−0.79	0.18	8	−3.51	0.25
LIRGs	4	4	8.09	0.23	4	−0.65	0.15	4	−3.59	0.19
LINERs	3	3	8.51	0.16	3	−0.94	0.18	3	−3.73	0.18

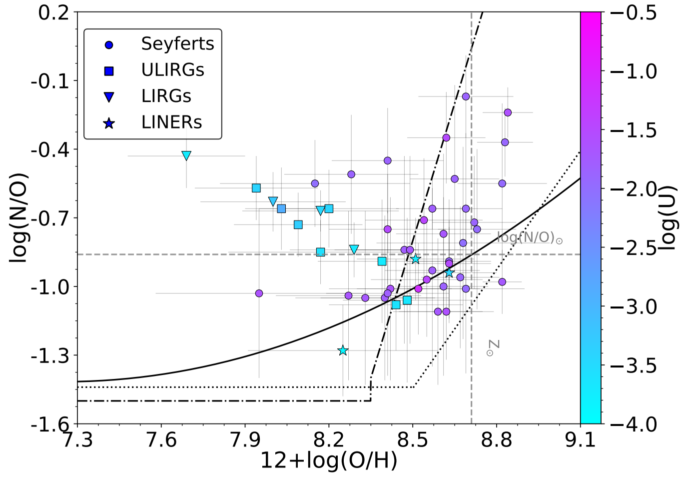

Figure 5.11: N/O vs O/H as derived from optical estimations. The log(U) values are given by the colorbar. Lines show reported relations in the literature: black solid (Coziol et al., 1999), dotted (Andrews & Martini, 2013) and dash-dotted (Belfiore et al., 2015).

LIRGs, and LINERs) there seems to be an anticorrelation between N/O and O/H (although the corresponding Pearson coefficient correlation is low r~ -0.75). In the case of high-ionization AGN, both quantities do not seem to be correlated, which was also found by Pérez-Díaz et al. (2021), although with a smaller sample of galaxies. As AGN activity is a rare phenomenon among dwarf galaxies ($<$ 1.8%, Latimer et al. 2021), and these have been challenging targets for previous IR spectroscopic facilities, our N/O versus O/H diagram cannot reproduce the metal-poor regime with sufficient statistics.

5.5.3 *Optical vs. infrared estimations*

Comparing the results listed in Tab. 5.3 and Tab. 5.4, we can see that Seyferts present lower median oxygen abundances from IR estimations than from their optical counterpart, the average offset for high-ionization AGN being higher than 0.5 dex. Although lower, we also found an average offset of 0.3 dex between optical and IR estimations for LINERs. While ULIRGs present similar oxygen abundances from both methods, in the case of LIRGs, we obtain lower abundances from optical observations. However, this result must be revisited using larger samples of galaxies, given our low statistic for LIRGs.

From Fig. 5.12 (a) we can see that 12+log(O/H) values from IR emission lines are systematically lower than the abundances derived using optical lines, which agrees with our previous statement for Seyferts. In the case of N/O, we obtained IR values clustering around the solar abundance, while optical estimations present a wider range of values, as shown in Fig. 5.12 (b). Finally, in Fig. 5.12 (c) we compare the resulting log(U) values, obtaining slightly higher values from IR estimations

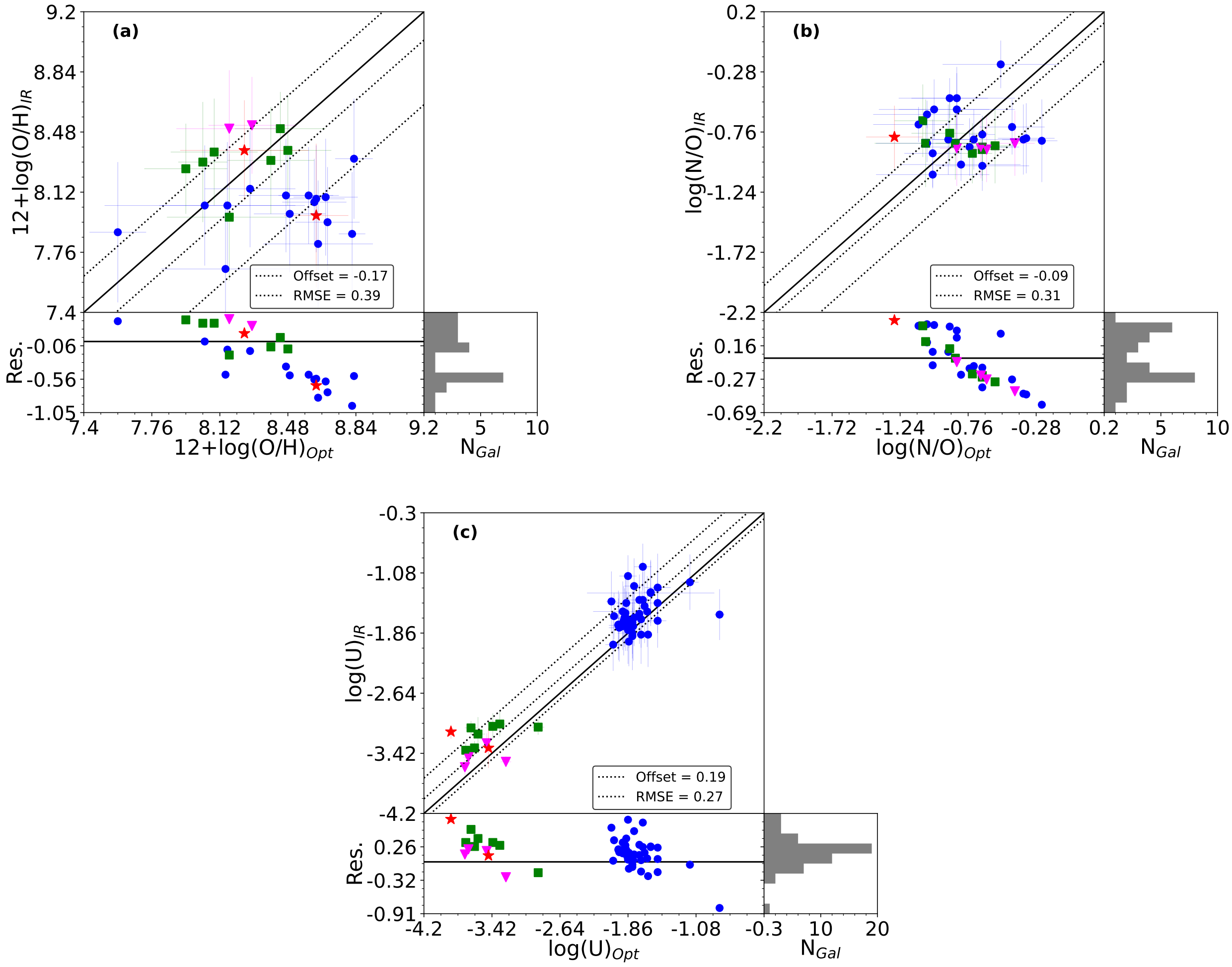

Figure 5.12: Comparison between the chemical abundances and log(U) values obtained from optical emission lines using HCm (x-axis) and the corresponding estimations from IR lines using HCm-IR (y-axis). For all plots we present Seyferts as blue circles, ULIRGs as green squares, LIRGs as magenta triangles, and LINERs as red stars. The offsets are given using the median value (dashed line) and RMSE (dot-dashed lines). Bottom plots show the residuals from the offset and their distribution in a histogram (bottom-right plot).

overall. However, since the step of the grids is 0.25 dex in log(U), and both the median offset and RMSE are close to this value, we can conclude that little difference is found.

5.5.4 *Dependency of the discrepancies*

As pointed out in the previous section, there is a significant difference between optical and infrared estimations of chemical abundances. Hereinafter, we define the discrepancy for a given quantity X as $\Delta X = X_{opt} - X_{ir}$.

We present in Fig. 5.13 the discrepancy as a function of the two chemical abundance ratios (O/H and N/O) for IR (left column) and optical estimations (right column). Fig. 5.13 (a) and (c) shows that little correlation is found between the discrepancies and their corresponding abundances from IR emission lines. This is not the case in the optical range as previously discussed: Δ log(O/H) increases with the oxygen abundance (see Fig. 5.13 (b)). A similar result is also found for Δ log(N/O) (see Fig. 5.13 (d)).

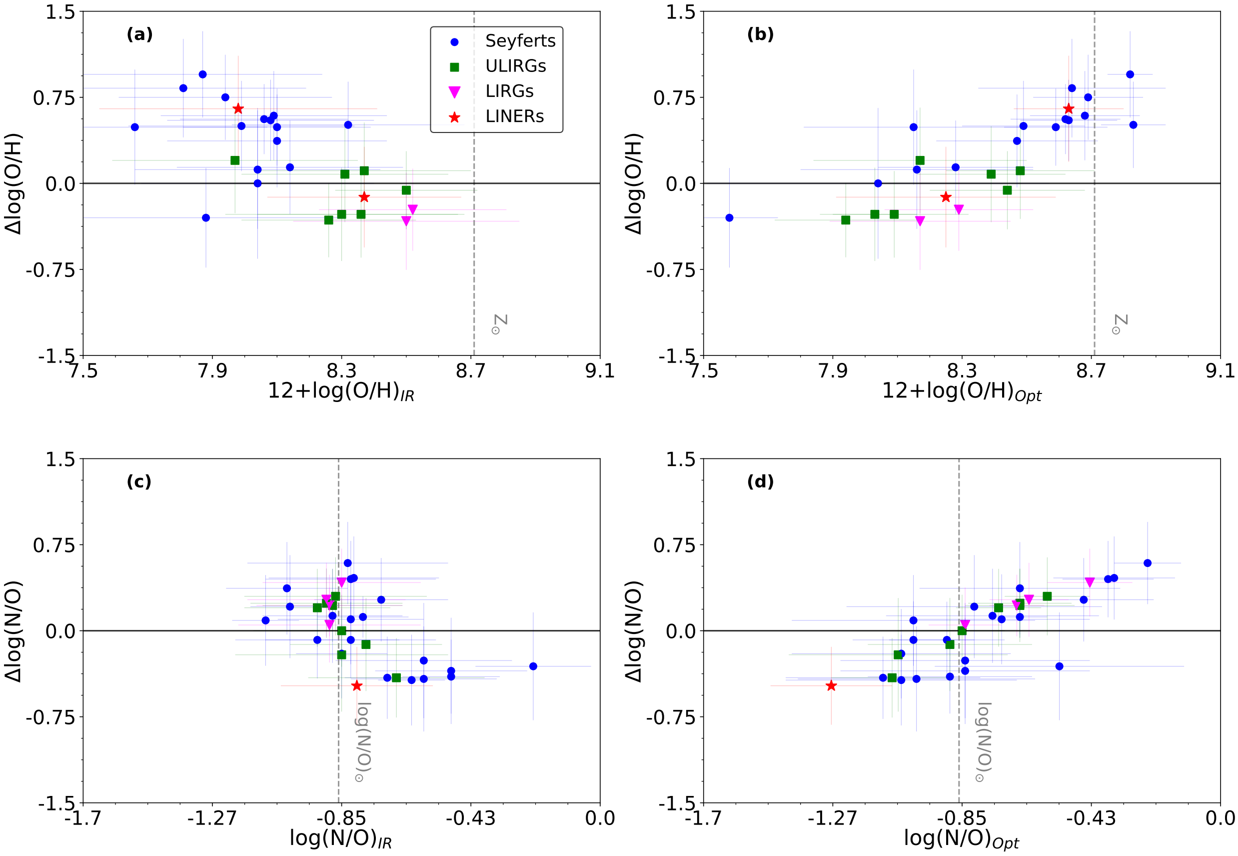

Figure 5.13: Discrepancies between the chemical abundance ratios ($\Delta X = X_{opt} - X_{IR}$) as a function of their ratios: (a) 12+log(O/H) and (c) log(N/O) both derived from IR emission lines with HCm-IR, and (b) 12+log(O/H) and (d) log(N/O) derived from optical emission lines with HCm. For all plots we present Seyferts as blue circles, ULIRGs as green squares, LIRGs as magenta triangles, and LINERs as red stars.

We replicate the same study of the discrepancies as a function of the ionization parameter U. Fig. 5.14 shows that U (either derived from optical emission lines or IR emission lines) does not drive the discrepancies found for both O/H and N/O.

In Sec. 5.4.1 we explained the importance of electron density for IR emission lines, since for wavelengths in far-IR (above 80 μm) the corresponding critical densities n_c of the lines are closer to the expected $n_e \sim 500$ cm^{-3} for the NLR of AGN (Alloin et al., 2006; Netzer, 2015; Vaona et al., 2012). This is not the case for optical emission lines whose critical densities are in the range $[10^{3.5}, 10^{6}]$ cm^{-3}. We estimated electron densities from both optical and IR emission lines, using PyNeb (Luridiana et al., 2015) and assuming an electron temperature $T_e \sim 2 \cdot 10^4$ K, which is the average electron temperature of the different ionic species in the models. We used the sulfur doublet [S II]$\lambda\lambda 6717, 6731$Å for our optical determination and the sulfur lines [S III]$\lambda 18\mu$m and [S III]$\lambda 33\mu$m to estimate n_e from IR lines.

As shown in Fig. 5.15, neither Δlog(O/H) nor Δlog(N/O) correlate with electron density. This result was also found by (Spinoglio et al., 2021), although they only analyzed nitrogen-to-oxygen abundances in a sample of AGN from SOFIA due to the spectral coverage. Our results extend this behavior to the oxygen abundances.

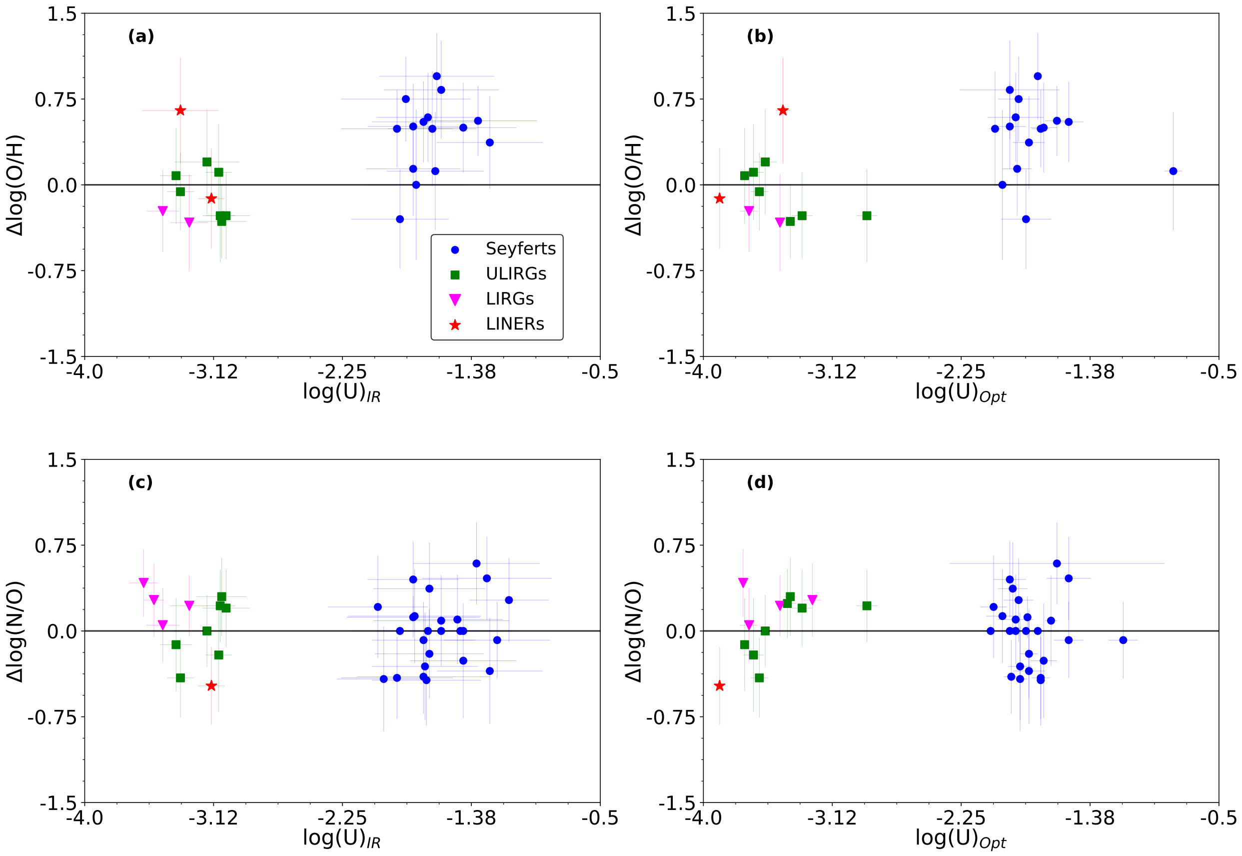

Figure 5.14: Discrepancies between the chemical abundance ratios ($\Delta X = X_{opt} - X_{IR}$) as a function of the ionization parameter: (a) and (c) estimated from IR lines, (b) and (d) estimated from optical lines.

5.6 DISCUSSION

5.6.1 *Abundances from IR lines*

IR emission lines are key for analyzing chemical abundances in both dusty-embedded regions and from the cold component ($\sim$ 1000 K) of the ionized gas, which is barely accessible for optical observations. However, in general, we warn the reader about the reduced statistics in our sample of galaxies with a reliable derivation of O/H (below 50% of our sample), due to the lack of measurements of hydrogen lines. On the other hand, slightly better statistics are found in N/O ($\sim$ 60%), but again the measurement of [N III]$\lambda 57 \mu$m is critical for that estimation. Overall, the estimation of U is almost assured when running the code ($\sim$ 90%). Nevertheless, these results must be corroborated in larger samples of AGN.

Our estimations of chemical abundances in the NLR of AGN show that the infrared emission is tracing a region characterized by subsolar oxygen abundances (12+log(O/H) $<$ 8.69). Since the measurement of at least one hydrogen line is necessary to provide an estimation of O/H, these subsolar values might be explained by an intrinsic bias: galaxies with measurements of hydrogen emission lines may be characterized by low metallicities. Moreover, as estimations of oxygen abundances require the measurement of faint emission lines as hydrogen recombination lines, these measurements are always obtained with higher uncertainties (see Tab. 5.2). Unfortunately, the lack of alternative methodologies to directly estimate IR oxygen abundances does not allow us to test this hypothesis.

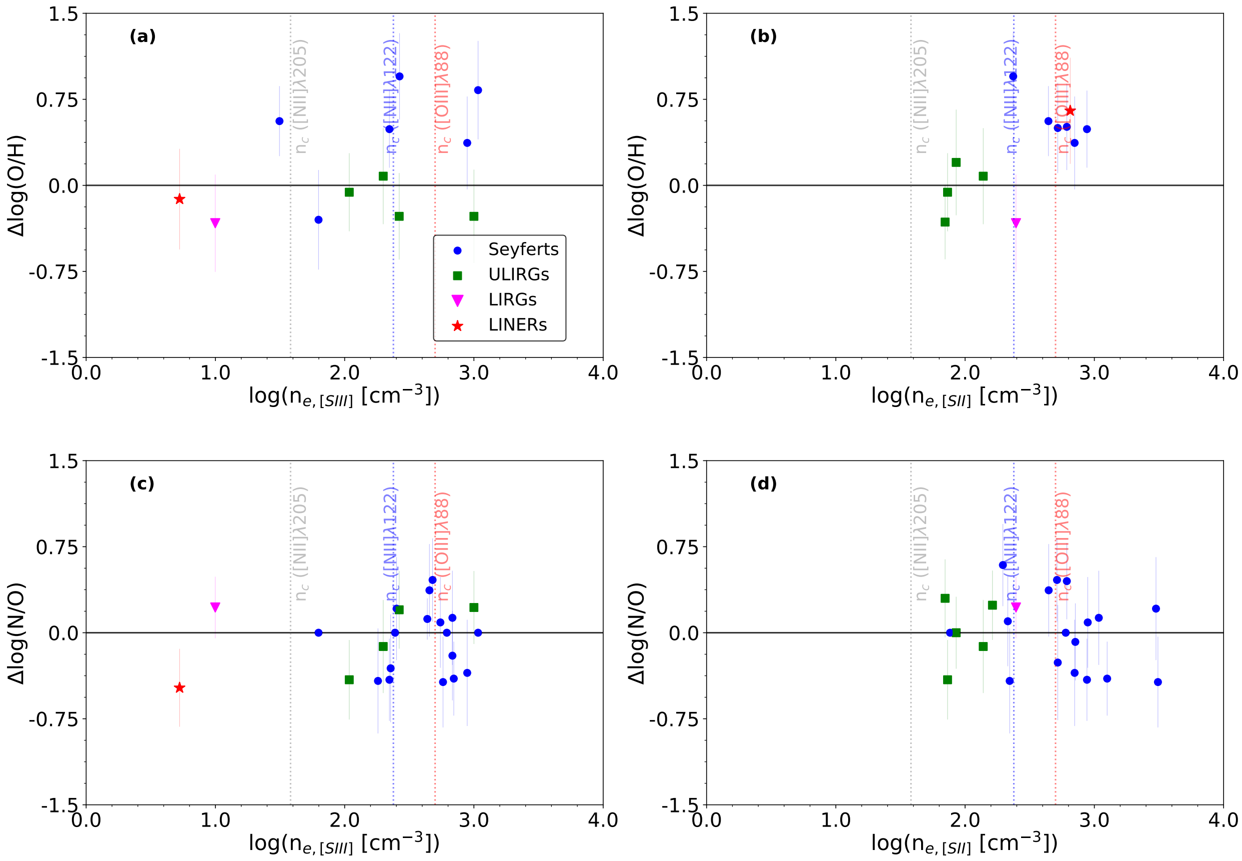

Figure 5.15: Discrepancies between the chemical abundance ratios ($\Delta X = X_{opt} - X_{IR}$) as a function of the electron density: (a) and (c) present electron densities derived from [S III] lines, (b) and (d) present densities derived from [S II] lines.

The N/O ratio seems to be constant for this sample, clustering around the solar value $\log(\mathrm{N/O})_\odot = -1.06$. In fact, N/O abundances are well constrained in the range $[-1.1, -0.4]$, which is the same range reported by Spinoglio et al. (2021) for their sample of AGN.

The lack of an apparent correlation between N/O and O/H (see Fig. 5.9), contrary to other assumed relations in the same metallicity regime, evidences that using nitrogen emission lines to estimate oxygen abundances must rely on an independent measurement of N/O, which can also be done by HCm-IR. The assumption of different relations between N/O and O/H could thus produce non-negligible deviations in the estimated O/H value as derived using N lines. For instance, contrary to our results, Chartab et al. (2022) reported oxygen abundances above the solar value by assuming a N/O-O/H relation and a fixed ionization parameter *U*. This discrepancy, also observed by Fernández-Ontiveros et al. (2021) for SFGs (showing little offset between IR and optical estimations), might be explained by the different assumption of an N/O-O/H relation for IR estimations.

5.6.2 *Discrepancies between IR and optical estimations*

While the estimations of the ionization parameter *U* derived from IR emission-lines are consistent with those derived from optical lines for low-ionization AGN, although with slightly more scatter for high-ionization objects (see Fig. 5.12 (c)), we report an offset between the estimated chemical abundances from IR and from optical lines. From Fig. 5.12 (a) we find that the Δlog(O/H) discrepancy is higher for the more metallic AGN (see also Fig. 5.13 (d)); using IR emission lines values above solar oxygen abundances cannot be reached, although there are galaxies in our sample whose optical estimations point toward oversolar abundances. This result is found for Seyferts, but also for ULIRGs and LINERs, which contrasts with the results from Chartab et al. (2022), pointing to chemical abundances estimated from IR lines in a sample of ULIRGs higher than those obtained from optical lines.

Regarding nitrogen-to-oxygen abundance ratios, these follow the same trend: their estimations from optical emission lines are higher than those from IR observations (see Fig. 5.12 (b)). This result was also found for both SFGs (B. Peng et al., 2021) and AGN (Spinoglio et al., 2021), although they only use the N3O3 estimator to derive N/O (see Eq. (5.1)), while we use both N3O3 and N3S34 (see Eq. (5.2)). Furthermore, we obtained N/O abundances clustering around $N/O_{\odot}$, in agreement with the results by Spinoglio et al. (2021).

These discrepancies between N/O and O/H from optical and IR observations also translate into the N/O-O/H diagram (see Fig. 5.9 and 5.11). While there is a trend of decreasing N/O for increasing O/H for low-ionization AGN, this is not found when IR estimations are considered. In the case of Seyferts, the range of values for O/H and N/O is more limited from IR estimations than from optical estimations. Thus, we warn the reader about using any N/O-O/H relation to estimate oxygen abundances from IR nitrogen lines, especially if this relation was obtained from optical observations.

As evidenced by Fig. 5.15, these discrepancies cannot be explained by a difference in the electron density in the observed region. On the contrary, as proposed by B. Peng et al. (2021), such a difference could ultimately indicate a large contribution from the diffuse ionized gas (DIG) to the estimated chemical abundances.

Another proposed scenario, based on the results for N/O (B. Peng et al., 2021; Spinoglio et al., 2021), is related to the ionization structure of the gas : IR lines trace high-ionization gas (O^{++}, N^{++}, S^{++}, S^{3+}), while optical lines trace low-ionization gas (O^{+}, N^{+}, S^{+}). If the ionization structure plays a role in these discrepancies found for both O/H and N/O, a trend must appear when these variations are analyzed as a function of U. As shown by Fig. 5.14, the ionization parameter, either obtained from optical lines ((a) and (c)) or from IR lines ((b) and (d)), shows no correlation with the discrepancies in both O/H and N/O. Thus, the different ionization structure cannot explain the differences obtained between IR and optical estimations of chemical abundances.

In any case, since we are analyzing the NLR in AGN, which is not obscured by the dusty torus, it seems unlikely that dusty-embedded regions of the AGN contribute to these discrepancies, although dust content within the NLR might be underestimated. However, an alternative possible explanation for these discrepancies could arise from the contribution of colder parts in the NLR, whose emission is detected in the IR range. According to our results, these zones could then be characterized by solar values of N/O and subsolar oxygen abundances, which could be consistent with our result that the differences arise above all in the most metallic galaxies.

In the case of AGN, another possible explanation could rely on the spectral resolution of the IR observations. Due to the emission of the broad line region (BLR), hydrogen recombination lines might present an additional contribution to their fluxes from these broad components, which cannot be spectrally resolved with the current IR data. However, this is not the case for the N/O abundance ratios, whose values are estimated independently of the hydrogen recombination lines, and thus an additional contribution to the chemical discrepancies may be present.

5.6.3 *The importance of N/O*

Overall, we emphasize that determining nitrogen-to-oxygen abundance is fundamental in order to understand the chemical composition and evolution of the ISM. First of all, as shown in Fig. 5.2, this ratio does not show a high discrepancy between SFG and AGN models, implying that no bias is introduced if a galaxy is wrongly classified. Although the difference arises for N3S34, N3O3 has proved to be a robust N/O estimator for both AGN and SFGs.

Secondly, the estimations of N/O involved close IR emission lines, such as [O III]$\lambda 52\mu$m, [N III]$\lambda 57\mu$m, or [O III]$\lambda 88\mu$m, which are more likely to be accessible in the same observational set. Thanks to the ongoing mission SOFIA, some of these emission lines are detected for galaxies in the local Universe, and current and future ground-based submillimeter telescopes (e.g. ALMA) will retrieve these lines for the rest-frame IR spectrum of high-redshift galaxies, allowing a redshift-dependent study of N/O.

Thirdly, this chemical abundance ratio is necessary in order to provide an unbiased estimation of oxygen abundances from nitrogen emission lines. As pointed out by several authors (e.g. Fernández-Ontiveros et al., 2021; Pérez-Díaz et al., 2021; Pérez-Montero & Contini, 2009; Spinoglio et al., 2021), assuming an arbitrary law for N/O-O/H, which is not always followed, can lead to uncertainties in the oxygen content of the gas-phase, and this can be avoided when data allows an independent previous determination of N/O.

Finally, since N/O involves the abundance of a metal with primary origin (O) and the abundance of another metal with a possible secondary origin (N), its determination also provides key information on the chemical evolution of the metals in the ISM.

5.7 CONCLUSIONS

We have presented HII-CHI-Mistry-IR for AGN, an updated version of the code proposed for SFGs. Thanks to this new method, chemical abundances in the NLR of AGN can be estimated from IR nebular emission lines, which are less affected by extinction and show little dependence on physical conditions of the ISM as the electron density or temperature. This new tool allows, whenever possible, an independent estimation of N/O, O/H, and U.

The analysis of a sample of AGN with available IR emission-line fluxes compiled from the literature shows that their oxygen abundances tend to be solar and subsolar ($12+\log(O/H) \leq 8.69$), while nitrogen-to-oxygen abundance ratios cluster around solar values ($\log(N/O) \sim -0.86$). Since both O/H and N/O are calculated independently, these new estimations show that a relation between N/O-O/H is not found for our sample of AGN.

We also estimated chemical abundances from optical observations of the same sample of AGN. In general, higher oxygen abundances are obtained from these estimations than from IR observations. An analogous result is also found for nitrogen-to-oxygen ratios. We explored if these discrepancies between optical and IR observations arise from the contribution of diffuse ionized gas, but we concluded that they are not related to electron density. We also find that these discrepancies do not correlate with the ionizing field. As these differences are found for most metallic AGN, IR emission could trace zones of the AGN characterized by subsolar oxygen abundances and solar nitrogen-to-oxygen ratios.

In the coming years, thanks to JWST and METIS for the local Universe, and ALMA, APEX, and CSO for high-redshift galaxies, the amount of galaxies (including AGN), whose IR spectral information will be retrieved with high precision, will notably increase, leading to a higher volume of AGN with IR hydrogen recombination lines measured and with many other fine-structure IR lines. With this upcoming data, further constraints can be established for the IR N/O-O/H relation, and for the systematic offset between IR and optical estimations.

6

NITROGEN AND SULFUR AS KEY WITNESSES OF THE CHEMICAL ENRICHMENT TALE

Chapter based on the publication: B. Pérez-Díaz, E. Pérez-Montero, J. A. Fernández-Ontiveros, J. M. Vílchez, A. Hernán-Caballero and R. Amorín (2024) *"Chemical abundances and deviations from the solar S/O ratio in the gas-phase interstellar medium of galaxies based on infrared emission lines", published in Astonomy & Astrophysics, volume* 685, *A168, doi:*10.1051/0004-6361/202348318.

6.1 ABSTRACT

The infrared (IR) range is extremely useful in the context of chemical abundance studies of the gas-phase interstellar medium (ISM) due to the large variety of ionic species traced in this regime, the negligible effects from dust attenuation or temperature stratification, and the amount of data that has been and will be released in the coming years. Taking advantage of available IR emission lines, we analyzed the chemical content of the gas-phase ISM in a sample of 131 star-forming galaxies (SFGs) and 73 active galactic nuclei (AGNs). In particular, we derived the chemical content via their total oxygen abundance in combination with nitrogen and sulfur abundances, and with the ionization parameter. We used a new version of the code HII-CHI-Mistry-IR v3.1, which allowed us to estimate log(N/O), 12+log(O/H), log(U) and, for the first time, 12+log(S/H) from IR emission lines, which can be applied to both SFGs and AGNs. We tested whether the estimates from this new version, which only considers sulfur lines for the derivation of sulfur abundances, are compatible with previous studies. While most of the SFGs and AGNs show solar log(N/O) abundances, we find a large spread in the log(S/O) relative abundances. Specifically, we find extremely low log(S/O) values (1/10 solar) in some SFGs and AGNs with solar-like oxygen abundances. This result warns against the use of optical and IR sulfur emission lines to estimate oxygen abundances when no prior estimation of log(S/O) is provided.

6.2 INTRODUCTION

Emission lines measured in the gas phase of the interstellar medium (ISM) in galaxies are key to inferring their physical and chemical properties. Among these emission lines, collisionally excited lines (CELs) have been widely used for this purpose in several spectral ranges, such as in the optical (e.g. Contini & Viegas, 2001; Curti et al., 2017; Garnett & Shields, 1987; Lequeux et al., 1979; Pérez-Montero, 2014), the ultraviolet (UV; e.g. Dors et al., 2014; Erb et al., 2010; Pérez-Montero & Amorín, 2017), and the infrared (IR; e.g. Fernández-Ontiveros et al., 2021; Nagao et al., 2011; B. Peng et al., 2021; Pereira-Santaella et al., 2017; Pérez-Díaz et al., 2022). As the primordial ISM metal content after the Big Bang nucleosynthesis is well constrained (Cyburt et al., 2016), any subsequent deviation from these initial chemical conditions must be attributed to stellar nucleosynthesis, whose products are ejected into the ISM in the late stages of stellar evolution. Therefore, the analysis of the metal content of the ISM is fundamental to understanding the impact of dissipative baryonic processes in galaxy evolution.

Over the decades, several techniques based on CELs have been developed and improved to infer the metal content of the ISM in star-forming galaxies (SFGs; see Maiolino & Mannucci, 2019, for a review on the topic). Moreover, in recent years, similar techniques have also started to be applied to the study of the chemical content of the ISM in the narrow line region (NLR) of active galactic nuclei

(AGNs), accounting for the corresponding differences in the sources ionizing the surrounding gas (e.g. Contini & Viegas, 2001; Dors et al., 2015; Pérez-Díaz et al., 2021; Pérez-Montero et al., 2019a).

Most of the studies devoted to the analysis of chemical abundances in the gas-phase ISM using CELs are focused on the oxygen content [12+log(O/H)], for several reasons: i) O is the most abundant metal by mass in the gas-phase ISM ($\sim$ 55%; M. Peimbert et al., 2007), and is therefore a good proxy for the total metallicity (Z); and, ii) its abundance can be derived more easily than other elements due to the presence of strong CELs in the optical, IR, and UV spectral ranges. Additionally, some authors have also analyzed the nitrogen-to-oxygen abundance ratio (log(N/O); e.g. Amorín et al., 2010; Andrews & Martini, 2013; Fernández-Ontiveros et al., 2021; B. Peng et al., 2021; Pérez-Díaz et al., 2022; Pérez-Montero & Contini, 2009; Vila-Costas & Edmunds, 1993). Nitrogen can be produced by massive stars via a primary channel – leading to an almost constant N/O ratio – but also through a secondary channel in the high-metallicity regime, due to CNO cycles in intermediate-mass stars that eject it into the ISM after a certain time delay (e.g. Henry et al., 2000). Thus, the study of N/O using nitrogen emission lines can provide complementary information on the evolution of the chemical content of the ISM. While studies of N/O from both optical and IR emission lines can be performed, in the UV other secondary elements – such as carbon – are studied instead, due to the presence of strong emission lines in this range, although it is also possible to study this by using optical recombination lines (e.g. Méndez-Delgado et al., 2022; Toribio San Cipriano et al., 2017), with the disadvantage that these emission lines are much fainter than CELs (Esteban et al., 2009).

So far, very few works have studied in a statistically significant sample of galaxies the sulfur (S) content in the gas-phase ISM. Instead, the assumption of an universal S/O ratio has been used to propose that sulfur emission lines are tracers of the total oxygen metallicity. For instance, Vilchez and Esteban (1996) were pioneers in defining the sulfur abundance parameter, S23:

$$\mathrm{S23} = \frac{\mathrm{I}\left([\mathrm{S\,II}]\,\lambda\lambda 6717, 6731\right) + \mathrm{I}\left([\mathrm{S\,III}]\,\lambda\lambda 9069, 9532\right)}{\mathrm{I}\left(\mathrm{H}_{\beta}\right)} \tag{6.1}$$

Later on, (Díaz & Pérez-Montero, 2000) provided the first calibration to directly estimate the oxygen content from S23, improving the determination of the chemical content of the gas-phase ISM, counteracting the ambiguity of the equivalent oxygen parameter, R23 (Pagel et al., 1979). As was shown by these authors, and after further improvements to the calibration of this estimator (Pérez-Montero & Díaz, 2005), two advantages arise from using sulfur emission lines instead of oxygen (i.e. R23): i) S23 is mainly single-valued in most of the metal abundance range; and, ii) sulfur lines are less affected by extinction than oxygen emission lines, although [S III] lines at 9069Å and 9531Å can suffer from telluric absorptions (e.g. Noll et al., 2012).

However, the use of S23 to estimate 12+log(O/H) directly implies that the ratio between S and O (log(S/O)) remains constant. Indeed, while S and O are both produced in the nucleosynthesis of massive stars, their yields are expected to also behave similarly, supporting the previous idea of a constant S/O ratio. Unfortunately, this assumption has not been firmly established, and only a few works have analyzed the sulfur content in the ISM (e.g. Berg et al., 2020; Díaz & Zamora, 2022; Díaz et al., 2007; Dors et al., 2023; Kehrig et al., 2006; Pérez-Montero et al., 2006) as compared to the large number of studies on the oxygen content. Therefore, further observational constrains are required to validate the assumption of an universal solar S/O ratio. For instance, while Berg et al. (2020) show that most HII regions in their sample are consistent with a S/O solar ratio, Díaz and Zamora (2022) find strong deviations from that, especially in the low-metallicity regime (12+log(O/H) < 8.1). In this regard, it is important to note that at low metallicities a higher ionization degree of the gas-phase ISM is expected, so higher ionic species (such as S^{+3}) contribute more to the total budget of the sulfur content, and thus the uncertainty due to the application of the ionization correction factor (ICF) to optical lines is higher. Moreover, Dors et al. (2023) also find a few sources among their AGN sample, with S/O ratios in some galaxies far from the solar value. Several attempts have been also made to directly calibrate the S23 parameter with the total sulfur abundance (Díaz & Zamora, 2022; Pérez-Montero et al., 2006). However, the collisional nature of the lines involved in this parameter, which make them very dependent on the electron temperature, and thus on the overall metal content of the gas, implies an additional dependence on the assumed S/O ratio.

Nevertheless, the above-mentioned studies focus on the use of optical emission lines, leading to an inconclusive response as to whether these deviations originate intrinsically in the production of S and O, or due to a variety of of effects with diverse origins such as dust attenuation, contamination from diffuse ionized gas (DIG), or the effects from the assumed ICFs, which severely affect the total sulfur abundances derived from the optical emission lines, as these do not cover the higher ionized S stages, such as S^{3+}. In this regard, the study of IR emission lines opens a new avenue through which to determine sulfur abundances, both in SFGs and AGNs, with key advantages over optical tracers. First of all, due to the atomic transitions involved in the ionic radiative process, the IR emission lines are much less affected by the electron temperature, T_e, avoiding problems due to stratification or temperature fluctuations (e.g. Jin et al., 2023; Méndez-Delgado et al., 2023; M. Peimbert, 1967; Stasińska, 2005). Secondly, the IR range allows the detection of highly ionized species such as S^{+3}, which are important for a more accurate determination of total elemental abundances, especially in AGNs. Thirdly, IR emission lines are almost unaffected by dust obscuration. Fourthly, ancillary data from observatories such as the Infrared Space Observatory (ISO; covering the $2.4 - 197\mu$m range; Kessler et al. 1996), the *Spitzer* Space Observatory ($5 - 39\mu$m; Werner et al. 2004), the *Herschel* Space Observatory ($51 - 671\mu$m, Pilbratt et al. 2010), and the Stratospheric Observatory for Infrared Astronomy (SOFIA; covering the $50 - 205\mu$m range; Fischer et al. 2018), as well as brand-new missions such as the James Webb Space Telescope (JWST, which is covering the $4.9 - 28.9\mu$m range with the Mid-InfraRed Instrument MIRI, G. H. Rieke et al. 2015; Wright et al. 2015), and upcoming facilities such as the Mid-infrared Extremely large Telescope Imager and Spectrograph (METIS, covering the N-band centered at 10μm, Brandl et al. 2021).

In this work, we compiled a sample of SFGs and AGNs with IR spectroscopic observations to derive their chemical abundances from the IR emission lines, following the methodology used in Fernández-Ontiveros et al. (2021) for SFGs and in Pérez-Díaz et al. (2022) for AGNs, which includes an independent estimation of log(N/O), 12+log(O/H) and 12+log(S/H). The paper is organized as follows. Section 6.3 provides information on the sample selection as well as on the methodology followed through this work. The main results of this study are shown in Section 6.4 and discussed in Section 6.5. Finally, we summarize our conclusion in Section 6.6.

6.3 SAMPLE AND METHODOLOGY

For this work, we compiled one of the largest sample of galaxies with IR spectroscopic observations, combining catalogs from *Spitzer*, *Herschel*, *AKARI* and *SOFIA*. In particular, we compiled the following catalogs: the dwarf galaxy sample from Cormier et al. (2015) observed with *Spitzer* and *Herschel*; the Infrared Database of Extragalactic Observables from *Spitzer*[1] (IDEOS; Hernán-Caballero et al., 2016; Spoon et al., 2022) from the *Spitzer* archive; the AGN and HII samples from Fernández-Ontiveros et al. (2016) and Spinoglio et al. (2022) combining *Spitzer*, *Herschel*, and *SOFIA* data; and the (U)LIRG catalog from Imanishi et al. (2010) observed with *AKARI*.

---

[1] http://ideos.astro.cornell.edu/.

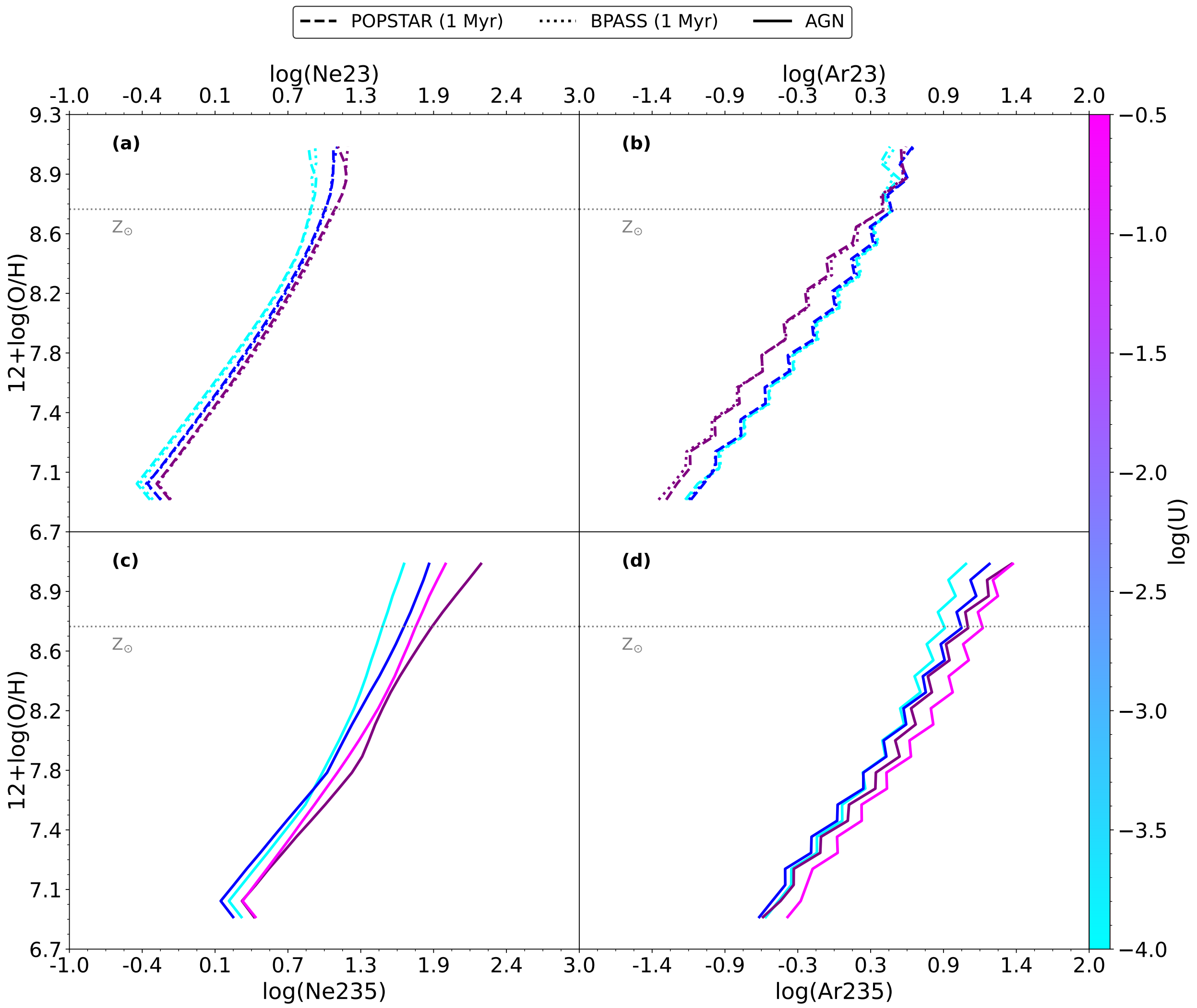

Figure 6.1: Performance of estimators based on neon ((a) and (c)) and argon ((b) and (d)) emission lines. Panels (a) and (b) show the behavior of estimators Ne23 and Ar23 for SFG models, with plus symbols presenting values from our SFG sample. Panels (c) and (d) show the behavior of estimators Ne235 and Ar235 for AGNs. SF models presented by Fernández-Ontiveros et al. (2021) are shown as dashed lines, while AGN models presented by Pérez-Díaz et al. (2022) are shown as continuous lines.

6.3.1 *Sample of star-forming galaxies*

Our sample of SFGs is composed of objects from two main sources. The data of the first subsample were directly taken from Fernández-Ontiveros et al. (2021), where they compiled a sample of 65 galaxies (30 dwarf galaxies, 22 HII regions, and 13 (U)LIRGs) with IR spectroscopic observations showing star-formation dominated emission ([Ne v]/[Ne ii] < 0.15). Additionally, we compiled another sample of galaxies from the IDEOS catalog (Hernán-Caballero et al., 2016; Spoon et al., 2022). As is described in Pérez-Díaz et al. (2024a), the sample consists of 66 ultra-luminous infrared galaxies (ULIRGs) showing star-forming dominated activity from both their [Ne v]/[Ne ii] ratio (< 0.15) and from the equivalent width of the PAH feature at 6.2μm ($W_{PAH\ 6.2\mu m} > 0.06\mu$m). While for this last sample we compiled IR emission lines from [S iv]$\lambda 10\mu$m to [S iii]$\lambda 33\mu$m from IDEOS (Spoon et al., 2022) and measurements of H i$\lambda 4.05\mu$m from *AKARI*/IRC observations ($2.5 - 5\mu$m; Imanishi et al., 2010), only the first sample from Fernández-Ontiveros et al. (2021) presents measurements from far-IR emission lines such as [O III]$\lambda52\mu$m, [N III]$\lambda57\mu$m, and [O III]$\lambda88\mu$m, which are key to estimating N/O.

6.3.2 *Sample of active galactic nuclei*

We compiled our AGN sample from Pérez-Díaz et al. (2022), who analyzed 58 AGNs with available IR spectroscopic observations, including 17 Seyfert 1 nuclei (Sy1), 14 Seyfert nuclei with hidden broad lines in the polarized spectrum (Sy1h), 12 Seyfert 2 nuclei (Sy2), 12 (U)LIRGs, and three low-ionization nuclear emission-line regions (LINERs). Additionally, we included 15 quasars from the IDEOS catalog (up to redshift ~ 0.74), for which we also added measurements, when possible, of the hydrogen recombination line, the H I Brackett α line, from their *AKARI*/IRC observations ($2.5-5\mu$m; Imanishi et al., 2010). We measured fluxes in the H I$\lambda4.05\mu$m line by fitting the rest-frame $[3.8-4.3\mu m]$ range with a model that assumes a second-order polynomial for the continuum and a Gaussian profile for the line, with the line width corresponding to the instrumental resolution of the *AKARI* or *Spitzer*/IRS spectrum at that wavelength.[2] Both samples show strong AGN emission, as is shown by their [Ne V]/[Ne II] ($\gg 0.15$) ratio.

6.3.3 *HII-CHI-MISTRY-IR*

To derive chemical abundances from the IR emission lines in our sample, we used the code HII-CHI-MISTRY-IR (hereinafter, HCM-IR) v3.1, originally developed by Pérez-Montero (2014) for optical emission lines and later extended to IR emission lines by Fernández-Ontiveros et al. (2021) for SFGs and Pérez-Díaz et al. (2022) for AGNs. This code basically performs a Bayesian-like comparison between a set of observed emission-line flux ratios sensitive to quantities such as the total oxygen abundance, the nitrogen-to-oxygen ratio, or the ionization parameter, with the predictions from large grids of photoionization models to provide the most probable values of these quantities and their corresponding uncertainties.

Version 3.1 of the code for the IR[3] presents two new features in relation to previous versions:

- The code now accepts as input the argon emission lines ([Ar II]$\lambda7\mu$m, [Ar III]$\lambda9\mu$m, [Ar V]$\lambda8\mu$m, and [Ar V]$\lambda13\mu$m), which are used to construct estimators of metallicity and excitation, analogous to those based on neon emission lines already used in previous versions; that is, Ne23 and Ne2Ne3 for SFGs (Fernández-Ontiveros et al., 2021):

$$\log\left(\mathrm{Ne23}\right) = \log\left(\frac{\mathrm{I}\left([\mathrm{Ne\,II}]_{12\mu m}\right) + \mathrm{I}\left([\mathrm{Ne\,III}]_{15\mu m}\right)}{\mathrm{I}\left(\mathrm{H\,I}_i\right)}\right) \tag{6.2}$$

$$\log\left(\mathrm{Ne2Ne3}\right) = \log\left(\frac{\mathrm{I}\left([\mathrm{Ne\,II}]_{12\mu m}\right)}{\mathrm{I}\left([\mathrm{Ne\,III}]_{15\mu m}\right)}\right) \tag{6.3}$$

  and Ne235 and Ne23Ne5 for AGNs (Pérez-Díaz et al., 2022):

$$\log\left(\mathrm{Ne235}\right) = \log\left(\frac{\mathrm{I}\left([\mathrm{Ne\,II}]_{12\mu m}\right) + \mathrm{I}\left([\mathrm{Ne\,III}]_{15\mu m}\right) + \mathrm{I}\left([\mathrm{Ne\,V}]_{14\mu m}\right) + \mathrm{I}\left([\mathrm{Ne\,V}]_{24\mu m}\right)}{\mathrm{I}\left(\mathrm{H\,I}_i\right)}\right) \tag{6.4}$$

---

[2] The spectral resolution of *AKARI* is $R \sim 100$ (D. Kim et al., 2015). For *Spitzer*/IRS, it is $\Delta\lambda = 0.06 and 0.12\mu m$ for the SL2 ($5.15-7.5\mu$m)and SL1 ($7.5-14\mu$m) modules, respectively (Spoon et al., 2022).

[3] The code is publicly available at http://home.iaa.csic.es/~epm/HII-CHI-mistry.html.

$$\log\left(\mathrm{Ne23Ne5}\right) = \log\left(\frac{\mathrm{I}\left([\mathrm{Ne\,II}]_{12\mu m}\right) + \mathrm{I}\left([\mathrm{Ne\,III}]_{15\mu m}\right)}{\mathrm{I}\left([\mathrm{Ne\,V}]_{14\mu m}\right) + \mathrm{I}\left([\mathrm{Ne\,V}]_{24\mu m}\right)}\right) \tag{6.5}$$

Following this approach, the new observables based on these IR argon lines can be defined as

$$\log\left(\mathrm{Ar23}\right) = \log\left(\frac{\mathrm{I}\left([\mathrm{Ar\,II}]_{7\mu m}\right) + \mathrm{I}\left([\mathrm{Ar\,III}]_{9\mu m}\right)}{\mathrm{I}\left(\mathrm{H\,I}_i\right)}\right) \tag{6.6}$$

$$\log\left(\mathrm{Ar2Ar3}\right) = \log\left(\frac{\mathrm{I}\left([\mathrm{Ar\,II}]_{7\mu m}\right)}{\mathrm{I}\left([\mathrm{Ar\,III}]_{9\mu m}\right)}\right) \tag{6.7}$$

$$\log\left(\mathrm{Ar235}\right) = \log\left(\frac{\mathrm{I}\left([\mathrm{Ar\,II}]_{7\mu m}\right) + \mathrm{I}\left([\mathrm{Ar\,III}]_{9\mu m}\right) + \mathrm{I}\left([\mathrm{Ar\,V}]_{8\mu m}\right) + \mathrm{I}\left([\mathrm{Ar\,V}]_{13\mu m}\right)}{\mathrm{I}\left(\mathrm{H\,I}_i\right)}\right) \tag{6.8}$$

$$\log\left(\mathrm{Ar23Ar5}\right) = \log\left(\frac{\mathrm{I}\left([\mathrm{Ar\,II}]_{7\mu m}\right) + \mathrm{I}\left([\mathrm{Ar\,III}]_{9\mu m}\right)}{\mathrm{I}\left([\mathrm{Ar\,V}]_{8\mu m}\right) + \mathrm{I}\left([\mathrm{Ar\,V}]_{13\mu m}\right)}\right) \tag{6.9}$$

with $\mathrm{H\,I}_i$ being one of the hydrogen lines that the code can take as input. The performance of these estimators is shown in Fig. 6.1 in comparison with their neon analogues. Argon emission lines offer a great opportunity for chemical abundance studies with JWST data, since they are located in a narrow IR window [7μm, 13μm], argon is a non-depleted element whose nucleosynthesis leads to a yield similar to that for oxygen, and they include transitions from highly ionized species, which helps to disentangle the power of the ionizing source.

- After the iteration[4] performed by the code to constrain N/O, and parallel to the second iteration performed to estimate 12+log(O/H) and the ionization parameter log(U), the code now performs a new iteration to estimate 12+log(S/H). This is done using the estimators S34 and S3S4 (Fernández-Ontiveros et al., 2021; Pérez-Díaz et al., 2022), based on sulfur lines, without assuming the results from the oxygen or the ionization estimations. In this way, the estimators based on sulfur emission lines (S34 and S3S4) are no longer used for the estimation of 12+log(O/H) and log(U) and, consequently, sulfur and oxygen abundances are derived independently from each other's estimations.

$$\log\left(\mathrm{S34}\right) = \log\left(\frac{\mathrm{I}\left([\mathrm{S\,III}]_{18\mu m}\right) + \mathrm{I}\left([\mathrm{S\,III}]_{33\mu m}\right) + \mathrm{I}\left([\mathrm{S\,IV}]_{10\mu m}\right)}{\mathrm{I}\left(\mathrm{H\,I}_i\right)}\right) \tag{6.10}$$

$$\log\left(\mathrm{S3S4}\right) = \log\left(\frac{\mathrm{I}\left([\mathrm{S\,III}]_{18\mu m}\right) + \mathrm{I}\left([\mathrm{S\,III}]_{33\mu m}\right)}{\mathrm{I}\left([\mathrm{S\,IV}]_{10\mu m}\right)}\right) \tag{6.11}$$

Following the prescription by Pérez-Díaz et al. (2022), the emission line [S III]$\lambda 33\mu$m is only used for SFGs. The performance of these estimators is shown in Fig. 6.2. It is relevant to emphasize the importance of IR emission lines in estimating sulfur abundances. As is shown in Fig. 6.3, S/O has little dependence on the behavior of the estimators, as the intensity of IR emission lines mainly depends on the ionic abundance. However, this is no longer the case for optical lines, as they also depend on temperature, which translates into a dependence on

---

[4] The code originally performs two consecutive iterations: during the first iteration, the grid of models in which N/O, O/H and U are free parameters is constrained by the estimation of N/O. During the second iteration, O/H and U are estimated from the constrained grid of models. With this new feature, the code performs, in parallel to the estimation of O/H and U, the estimation of S/H, i.e. the code estimates S/H from the grid constrained only by N/O.

the metallicity. Hence, estimators for sulfur based on optical emission lines (e.g. S23 Eq. (6.1)) are much more affected by the S/O assumed for the models.

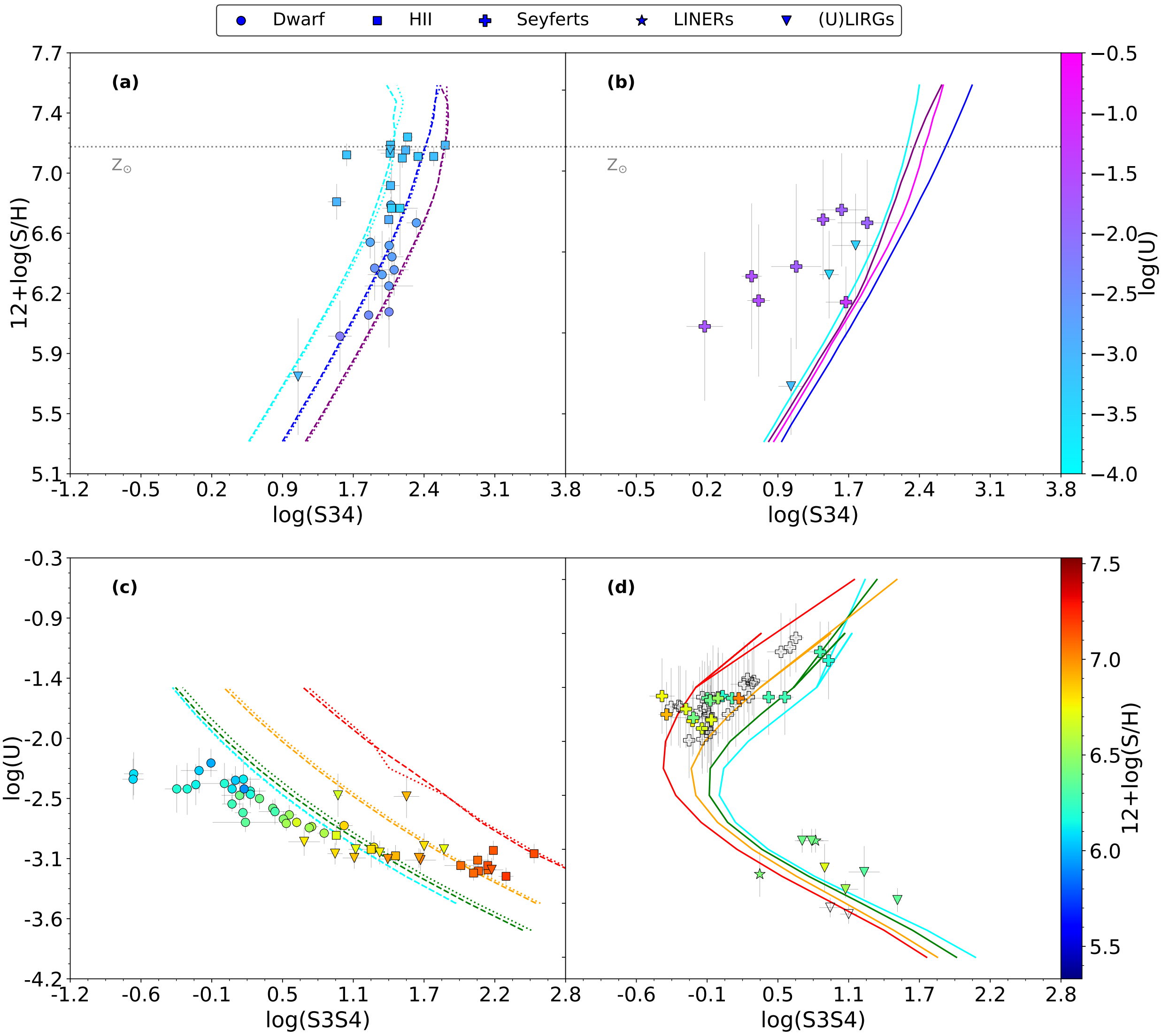

Figure 6.2: Performance of estimators based on sulfur emission lines. Panels (a) and (c) show the performance of S34 for 12+log(S/H) and S3S4 for log(U), respectively, in the case of SFGs. Panels (b) and (d) show the performance of the same estimators for AGNs. Models are shown following the same notation as in Fig. 6.1.

As is shown in Fig. 6.4, these new improvements in the code do not significantly change the results obtained with previous versions, but we do obtain more information, as now 12+log(S/H) is independently estimated. We notice that some AGNs seem to present slightly higher abundances when sulfur emission lines are no longer used in the oxygen estimation, which implies that S lines favor lower abundances (see Sec. 6.4).

6.4 RESULTS

In this section, we present an analysis of the chemical abundances obtained after applying HCm-IR to the selected samples presented in Sec. 6.3. The statistics of these results are shown in Tab. 6.1.

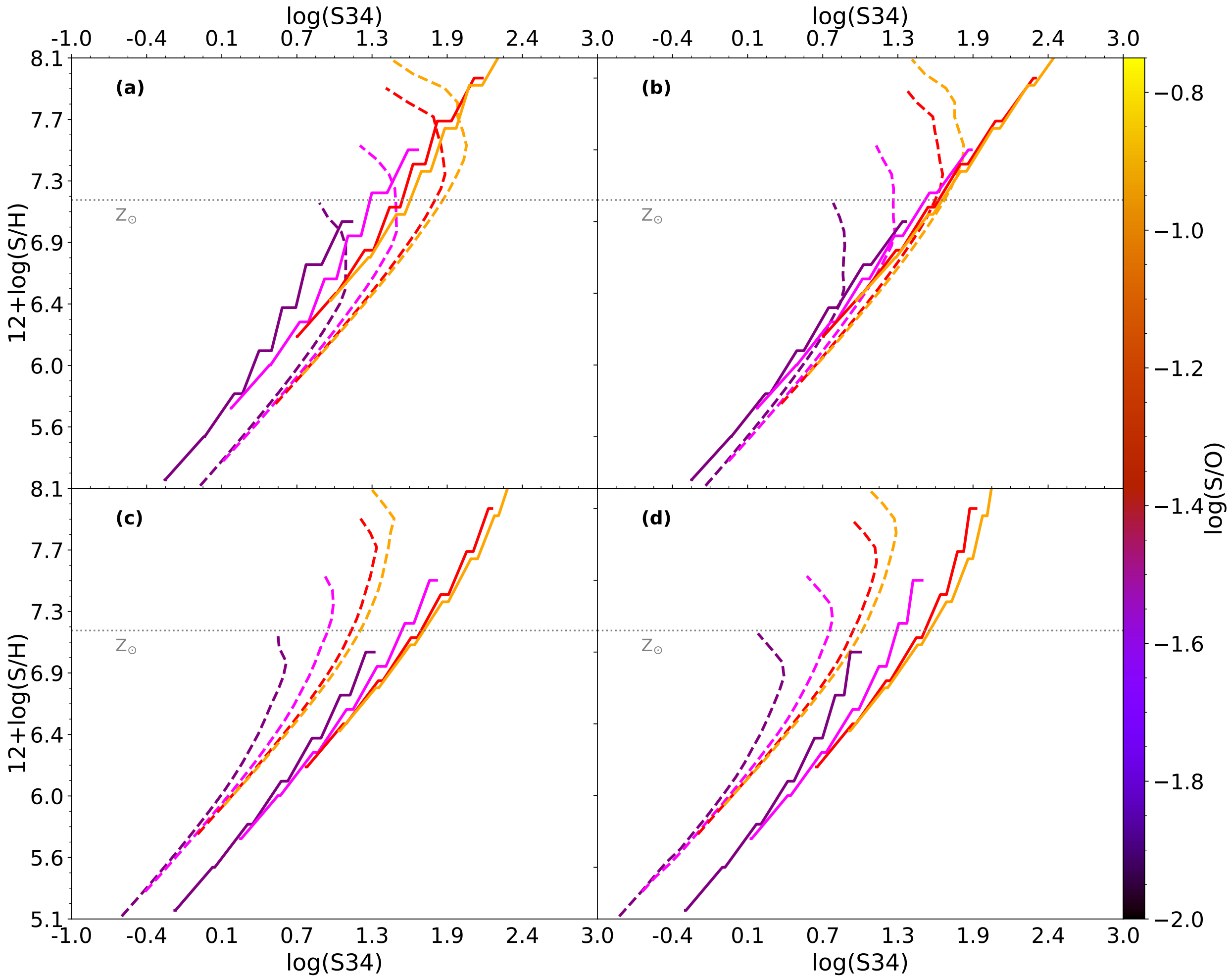

Figure 6.3: Performance of estimator S34 based on sulfur emission lines for models with S/O that is not fixed. Panel (a) shows models for a fixed value of the ionization parameter $\log(U) = -1.5$, panel (b) shows models for $\log(U) = -2.0$, panel (c) models with $\log(U) = -3.0$, and panel (d) those with $\log(U) = -3.5$. Models are shown following the same notation as in Fig. 6.1.

6.4.1 *Nitrogen-to-oxygen abundance ratios*

HCm-IR performs a first independent iteration to estimate log(N/O). Since both the IR observables (i.e. N3O3 ≡ $[\text{N III}]\lambda 57\mu\text{m}/[\text{O III}]\lambda 52\mu\text{m}$) and the procedure followed to determine N/O remain unchanged in this version, no significant difference is found in the log(N/O) distribution derived for the SFG and AGN samples when compared to studies based on previous versions of the code. In the case of SFGs, the median value of $\log(\text{N/O}) \sim -0.9$ is close to the solar ratio, in agreement with Fernández-Ontiveros et al. (2021). Regarding AGNs, the distribution is almost identical to that reported by Pérez-Díaz et al. (2022). Moreover, as IDEOS measurements do not cover the far-IR emission lines, essential to estimating log(N/O) (Fernández-Ontiveros et al., 2021; B. Peng et al., 2021; Pérez-Díaz et al., 2022), the number of N/O measurements has not increased with respect to previous works.

Fig. 6.5 shows that the distribution of the IR-based log(N/O) versus the 12+log(O/H) values obtained for our sample deviates from the abundances obtained for local SFGs using optical lines (Andrews & Martini, 2013; Pérez-Montero, 2014; Pérez-Montero & Contini, 2009). Our IR-based abundances cluster around the solar N/O ratio and do not show a trend with O/H. While this result seems to contradict previous studies (e.g. Spinoglio et al., 2022), we must bear in mind the

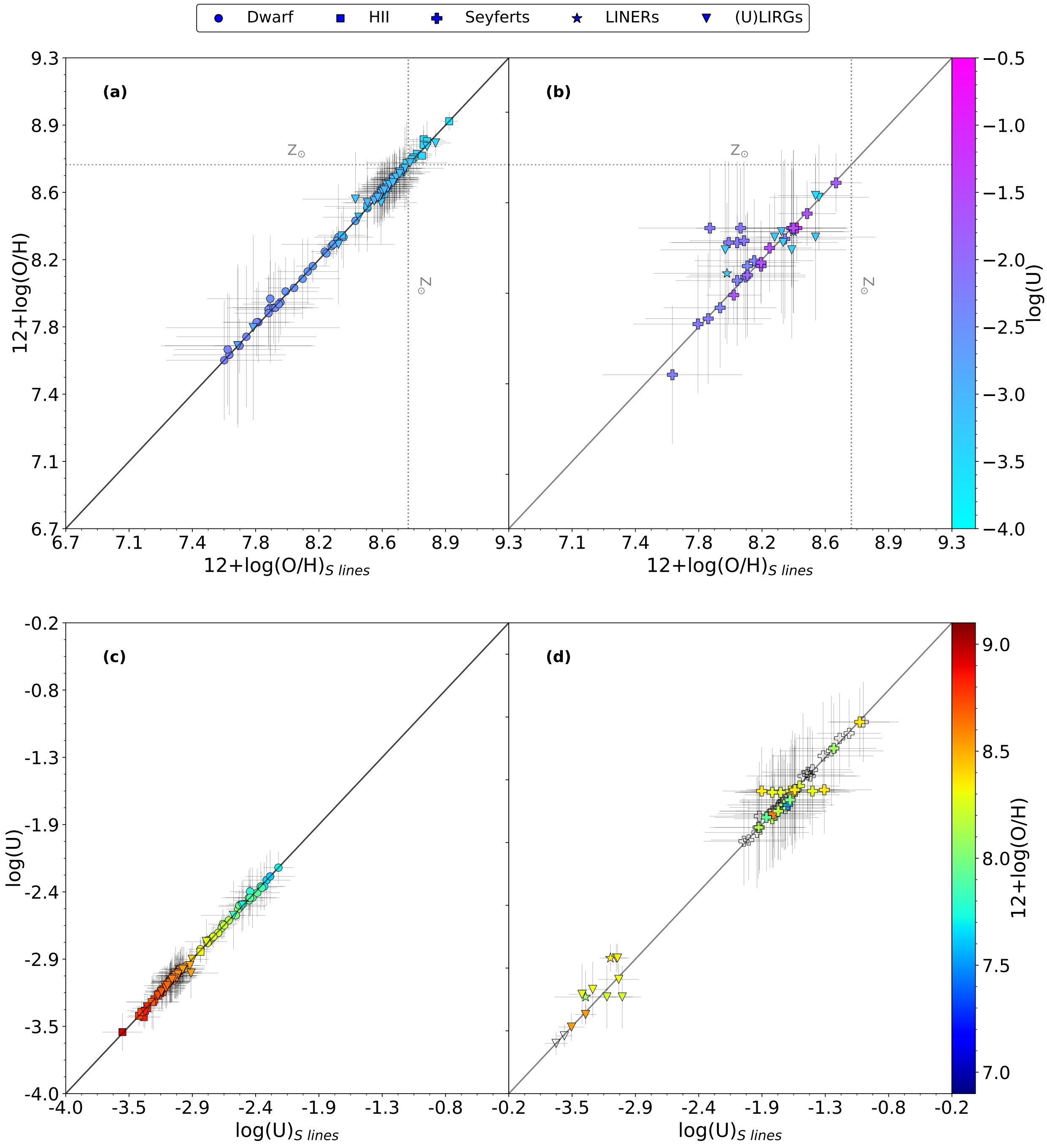

Figure 6.4: Comparison between the outputs from HCm v3.01 (x-axis) and HCm v3.1 (y-axis). Panels (a) and (b) show a comparison of SFGs and AGNs, respectively, with 12+log(O/H). Panels (c) and (d) show a comparison of SFGs and AGNs, respectively, with $\log(U)$.

low number of AGNs with N/O estimations. It is also important to note that while SFGs present values of N/O that spread from sub-solar to over-solar ratios, AGNs present either solar or slightly over-solar N/O ratios.

This result is also reported for the abundances of SFGs as derived from their IR lines (Fernández-Ontiveros et al., 2021) and for AGNs (Pérez-Díaz et al., 2022), in both cases with calculations based on HCm-IR. Since 12+log(O/H) is now obtained without considering the IR sulfur lines, in contrast to previous studies, we conclude that these behaviors on the N/O-O/H diagram persist even when the information is solely obtained from O, Ne, and Ar emission lines.

Table 6.1: Statistics of the chemical abundances and log(U) values derived from HCm-IR for our sample of galaxies.

		12+log(O/H)			12+log(S/H)			log(N/O)			log(U)		
Sample	N°_{tot}	N°	Med.	Sd. Dv.	N°	Med.	Sd. Dv.	N°	Med.	Sd. Dv.	N°	Med.	Sd. Dv.
All SFGs	131	128	8.57	0.30	59	6.68	0.38	22	−0.93	0.20	71	−2.97	0.34
Dwarfs	30	30	7.99	0.23	30	6.28	0.23	5	−1.14	0.19	30	−2.51	0.19
HII regions	22	21	8.69	0.14	14	7.09	0.17	7	−0.93	0.12	21	−3.20	0.16
(U)LIRGs	79	77	8.59	0.18	15	6.80	0.31	10	−0.86	0.09	20	−3.04	0.23
All AGNs	73	36	8.28	0.21	36	6.41	0.38	35	−0.83	0.16	65	−1.68	0.68
Seyferts	58	25	8.25	0.22	25	6.57	0.37	22	−0.79	0.19	52	−1.60	0.21
LINERs	3	2	8.22	0.12	2	6.42	0.03	1	−0.83	0.00	2	−3.08	0.15
(U)LIRGs	12	9	8.31	0.11	9	6.36	0.36	12	−0.88	0.07	11	−3.23	0.22

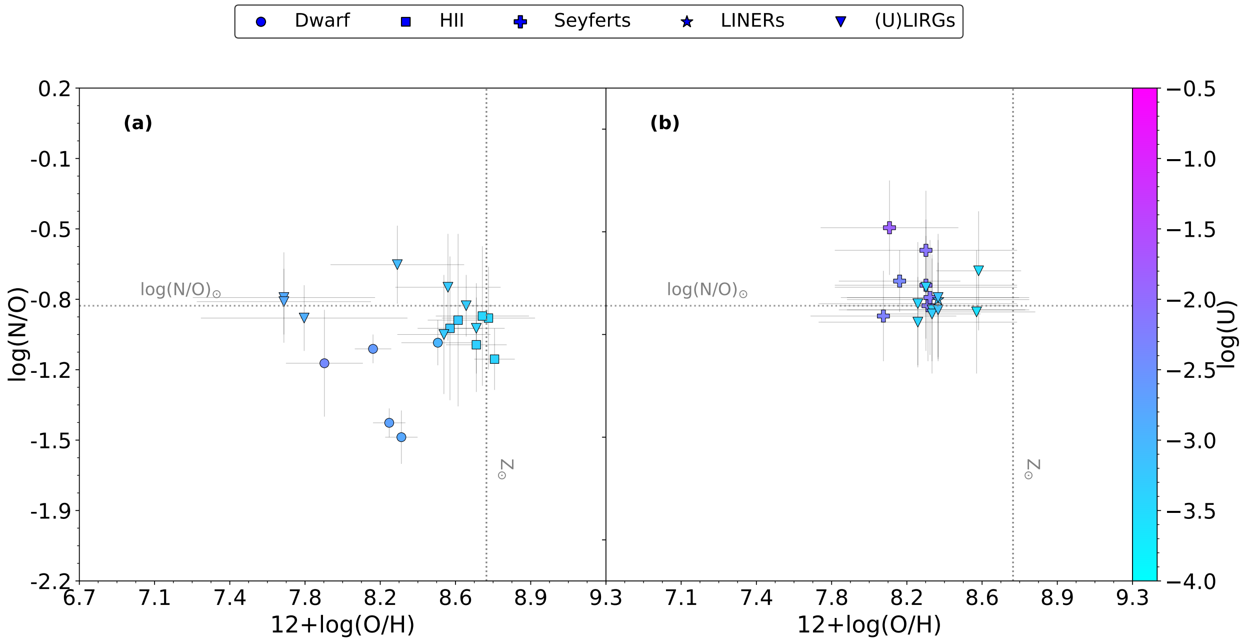

Figure 6.5: N/O vs O/H as derived from infrared emission lines for SFGs (a) and AGNs (b). The log(U) values are given by the color bar.

6.4.2 *Sulfur and oxygen abundances*

The analysis of the total oxygen abundance in our sample of SFGs is in overall agreement with Fernández-Ontiveros et al. (2021). We find the lowest 12+log(O/H) average values in dwarf galaxies (12+log(O/H)∼ 8.0), with sub-solar abundances for (U)LIRGs (12+log(O/H)∼ 8.5) and the highest values for HII regions (12+log(O/H)∼ 8.7). Nevertheless, our larger (ULIRG) sample presents a slightly higher median oxygen abundance when compared to the smaller sample of 12 objects in Fernández-Ontiveros et al. (2021). The agreement with previous determinations implies that the independent estimation of S in the last version of HCm-IR does not significantly change the abundances of O and N, as in the Bayesian-like procedure sulfur estimators are weighted among many others, reducing any possible bias. Regarding the derived average sulfur content, 12+log(S/H), in our sample of SFGs, we obtained a similar behavior to that of oxygen, the lowest value being found in dwarfs (12+log(S/H)∼ 6.3), followed by (U)LIRGs (12+log(S/H)∼ 6.8) and HII regions (12+log(S/H)∼ 7.1).

The 12+log(O/H) values obtained for AGNs are also consistent with previous studies (Pérez-Díaz et al., 2022), as there is not a significant increase in the oxygen content for high-ionization (Seyfert) AGNs. This is supported by the larger statistics after including the AGNs from IDEOS. Hence, we can conclude that, in terms of chemical content, the samples from IDEOS and from Pérez-Díaz et al. (2022) are both similar. Overall, the whole AGN sample presents similar median values for both 12+log(O/H)$\sim$ 8.25 and 12+log(S/H)$\sim$ 6.5 for all considered subtypes (Seyferts, LINERs, and (U)LIRGs).

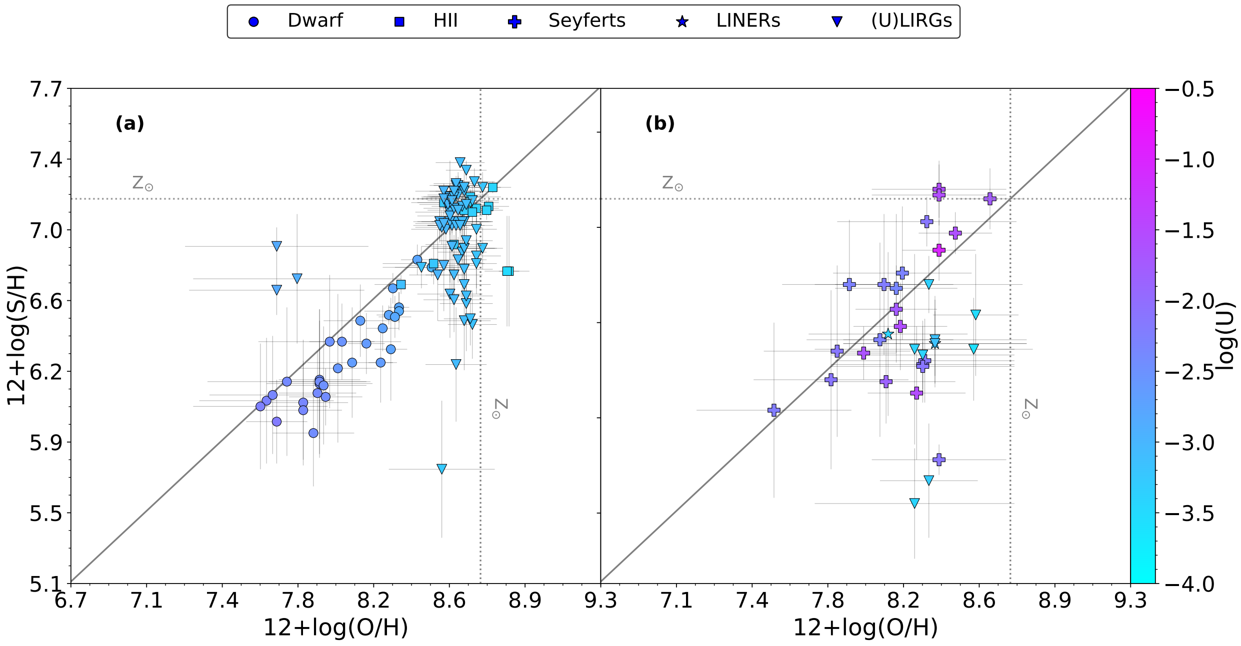

Figure 6.6: S/H vs O/H as derived from infrared emission lines for SFGs (a) and AGNs (b). The log(U) values are given by the color bar. The solid line represents the solar proportion. We notice in panel (a) that (U)LIRGs with high S/H values near the lowest values for O/H are the same galaxies that are experiencing the deep-diving phase reported by Pérez-Díaz et al. (2024a).

Finally, we also explored the relation between the ionization parameter, log(U), and the derived chemical abundances. Theoretically, if massive stars are the sources of ionization, an anti-correlation between metallicity and ionization is expected as a consequence of: i) stars becoming cooler as a result of wind and enhanced line blanketing (Massey et al., 2005); and, ii) an increase in the stellar atmosphere content leading to higher photon scattering, which later translates into a more efficient conversion of the luminosity energy into the mechanical energy in winds (Dopita et al., 2006). As is presented in Fig. 6.7, we did obtain an anti-correlation for SFGs that is stronger for oxygen (the Pearson coefficient correlation is r$\sim$ -0.98) than for sulfur (the Pearson coefficient correlation is r$\sim$ -0.8). When analyzing AGNs, we do not obtain any relation between metallicity and the ionization parameter, in agreement with previous studies (e.g. Pérez-Díaz et al., 2021, 2022; Pérez-Montero et al., 2019a). Moreover, the lack of correlation between U and O/H (and S/H) is obtained in galaxies characterized by high ionization parameters (log(U) > -2.5 such as Seyferts) but also in AGN-dominated (U)LIRGs with low ionization parameters (log(U) < -2.5), as is shown in Fig. 6.6.

6.4.3 *Sulfur-to-oxygen abundance ratios*

The median log(S/O) values obtained for our samples of SFGs (-1.89) and AGNs (-1.87) are lower than the solar ratio, log$(S/O)_\odot = -1.57$ (Asplund et al., 2009). From Fig. 6.6 we conclude that, although the median values deviate by a factor of 0.3 dex from the solar ratio, higher offsets are found in many of the (U)LIRGs (in our sample, dominated by either star-forming or AGN activity), as their sulfur abundances are significantly lower than the expected values of their corresponding oxygen estimations.

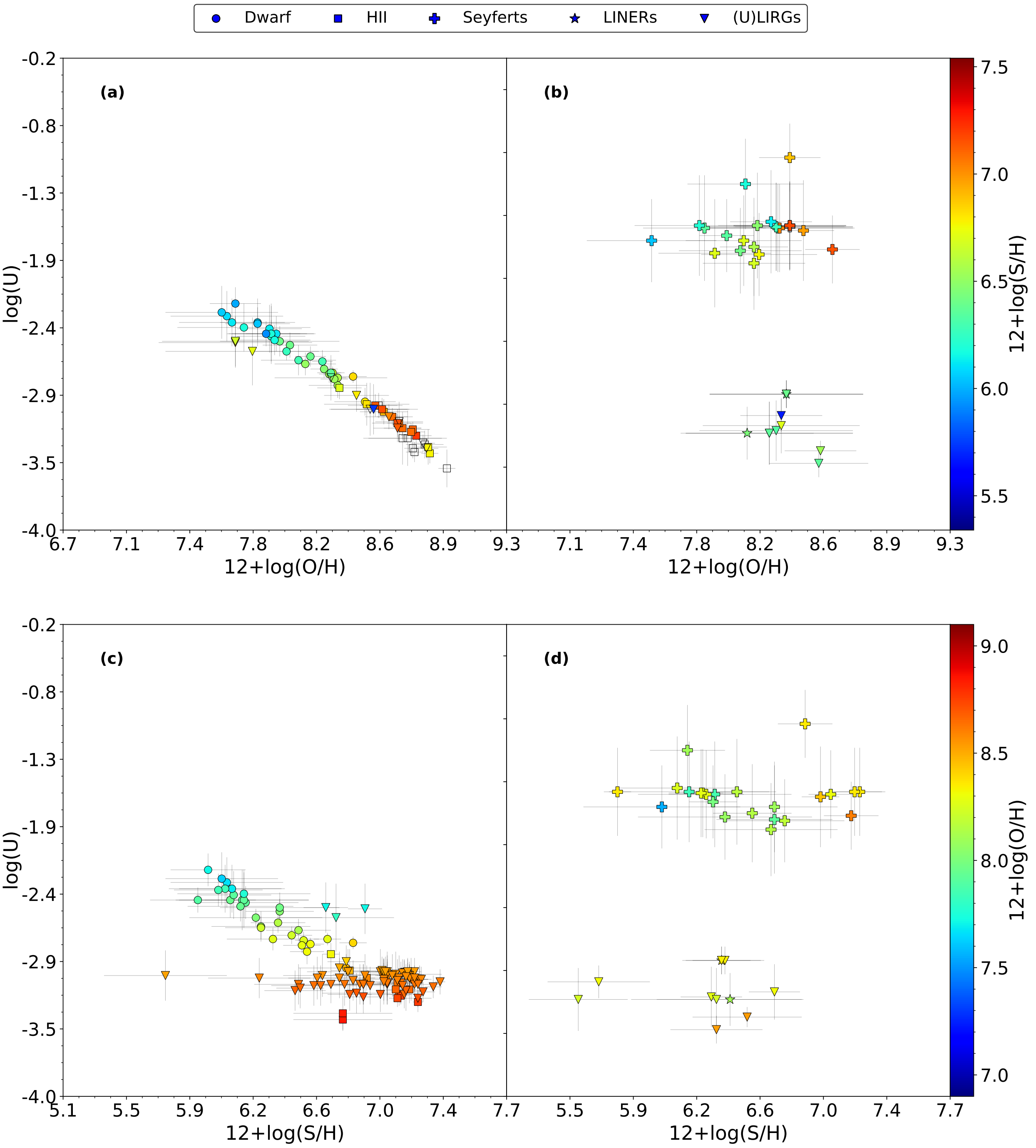

Figure 6.7: Variation in the ionization parameter, log(U), as a function of the chemical abundance ratios, 12+log(O/H) (panels (a) and (b)) and 12+log(S/H) (panels (c) and (d)). Panels (a) and (c) show results from SFGs, while panels (b) and (d) present AGNs.

First of all, we explored the possibility that these deviations in the log(S/O) chemical abundance ratio could be caused by uncertainties in the measurement of the [S IV]$\lambda 10\mu$m emission line. Among these, the flux of this line could be affected as a consequence of the presence of a silicate feature detected in the $10 - 12.58\mu$m range (Spoon et al., 2022). From Fig. 6.8 we can conclude that the

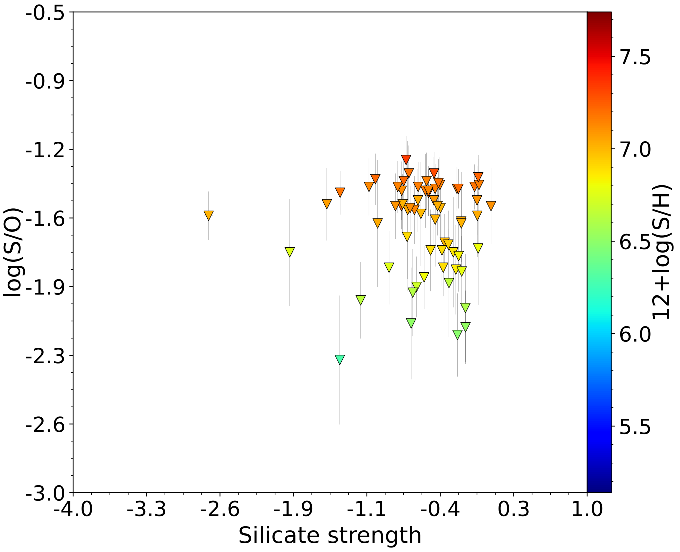

Figure 6.8: S/O vs the silicate strength in the $10 - 12.58\mu$m range as measured in IDEOS (Spoon et al., 2022). The color bar shows the values for the 12+log(S/H) chemical abundance.

silicate strength does not play any role in the estimated values of log(S/O). However, we must bear in mind that in galaxies dominated by AGN activity the silicate strength provides information on the extinction that is affecting the continuum emission, whereas the line emission can come from more extended parts.

To further explore the above-reported deviations in the chemical abundance ratio, log(S/O), of our sample, we studied its behavior as a function of the oxygen abundance. As is shown in Fig. 6.9, the deviations in log(S/O) are found in either the low-metallicity regime (12+log(O/H) < 8.0), as is the case for SFGs, or in the high-metallicity regime (12+log(O/H) > 8.4), for both SFGs and AGNs. In the two metallicity regimes, (U)LIRGs are the galaxies driving these high deviations.

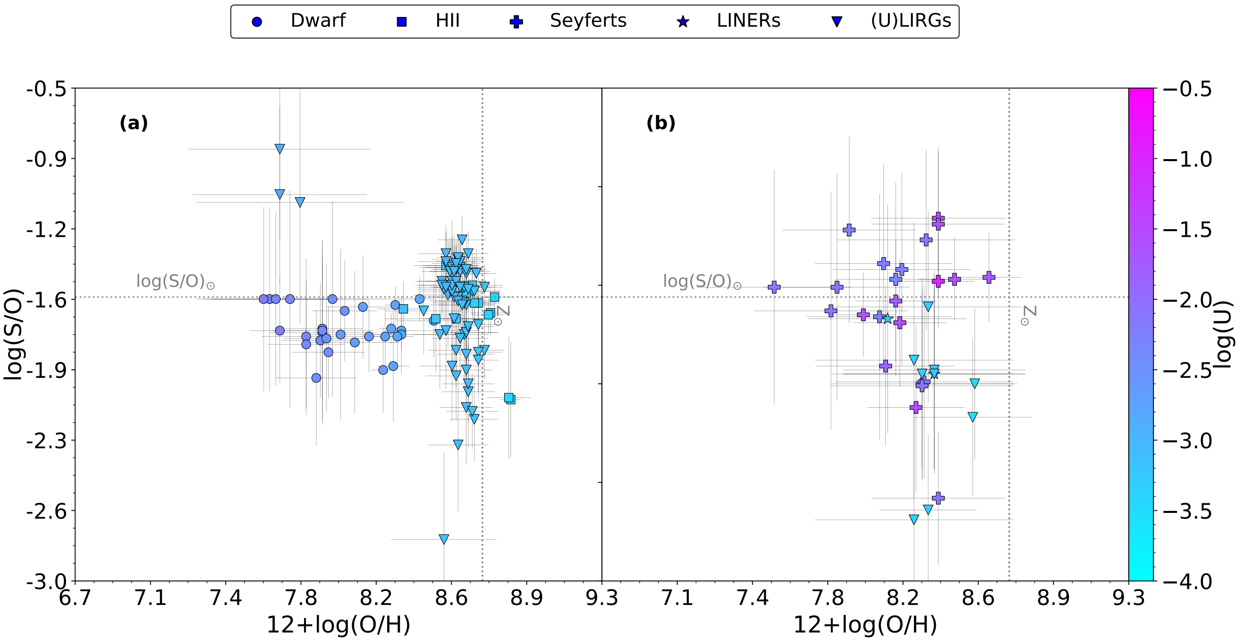

Figure 6.9: S/O vs O/H as derived from the infrared emission lines for SFGs (a) and AGNs (b). The log(U) values are given by the color bar. Again, the (U)LIRGs that show the highest S/O ratios are the same galaxies that are undergoing the deep-diving phase reported by Pérez-Díaz et al. (2024a).

In the specific case of SFGs, we explored if these deviations correlate with other physical quantities such as the stellar mass (M_*) or the star formation rate (SFR), as galaxy mass assembly is known to play an important role in the chemical enrichment of galaxies (Curti et al., 2017; Maiolino & Mannucci, 2019), materialised in the well-known mass-metallicity relation (MZR; Andrews & Martini, 2013; Lequeux et al., 1979; Tremonti et al., 2004). Although this relation is regulated by many processes such as the galactic environment (Y.-j. Peng & Maiolino, 2014), secular evolution (Somerville & Davé, 2015), star formation, and AGN feedback (Blanc et al., 2019; Thomas et al., 2019) or stellar age (Duarte Puertas et al., 2022), we only analysed those quantities that are explicitly involved in this connection between chemical enrichment and galaxy mass assembly: M_*(Lequeux et al., 1979; Tremonti et al., 2004) and SFR (SFR; Curti et al., 2017; Mannucci et al., 2010).

Figure 6.10 shows that deviations from the solar ratio $\log(\mathrm{S/O})_\odot \sim -1.57$ are observed mostly in those galaxies with high M_* ($> 10^{11}$ $\mathrm{M}_\odot$) and a high SFR (> 90 $\mathrm{M}_\odot \cdot$,yr^{-1}).

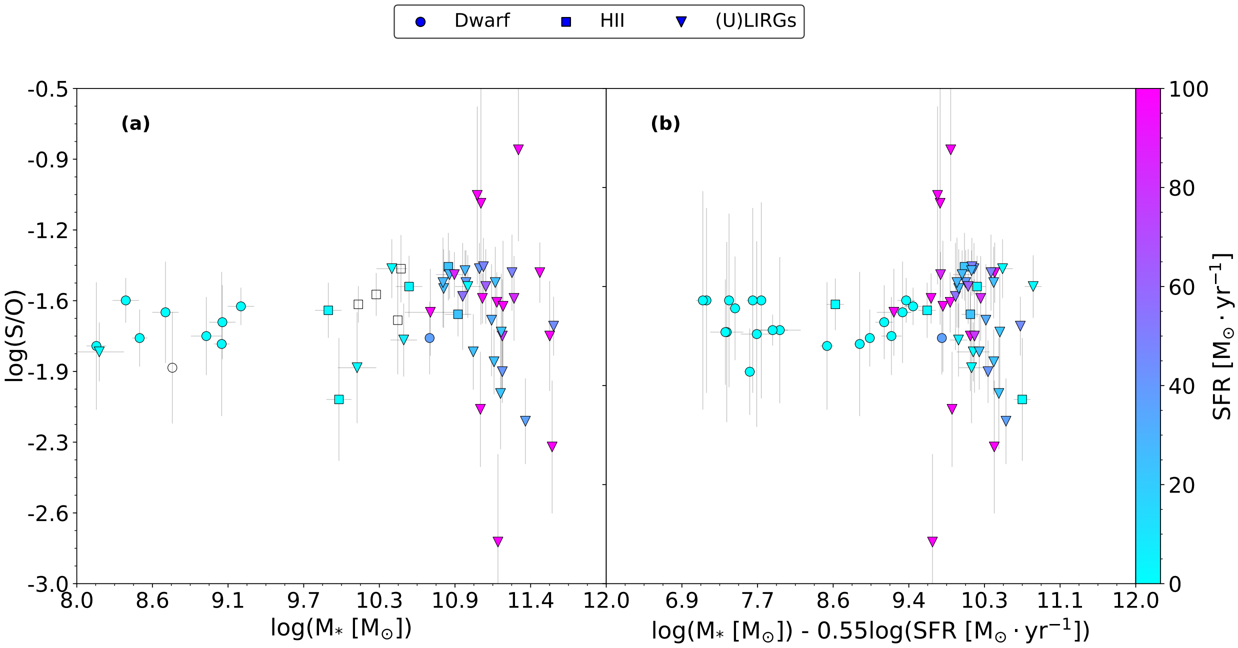

Figure 6.10: (a) S/O vs M_*. (b) S/O vs M_* corrected from SFR, as proposed by Curti et al. (2017). The SFR values are given by the color bar.

6.5 DISCUSSION

6.5.1 *Information from sulfur emission lines*

Unlike previous analyses of chemical abundances of the gas phase using IR lines, which assume a constant and universal S/O ratio, our work avoids S emission lines – namely [S IV] $\lambda 10\mu$m, [S III]$\lambda 18\mu$m, and [S III]$\lambda 33\mu$m – in estimating 12+log(O/H). Instead, the sulfur lines are used in this work to estimate 12+log(S/H) independently. Given the quantity and variety of other emission lines observed in the IR range (Ne, Ar, and O), sulfur emission lines do not play a critical role in the estimation of the oxygen abundance, as is evidenced by the high consistency between our results and previous studies using all of the lines (see Fig. 6.4).

While IR emission lines are extremely useful due to the fact that they are much less affected by temperature or dust extinction, their dependence on density should be taken into account. Far-IR emission lines present low critical densities (e.g. Pérez-Díaz et al., 2022), which implies that their fluxes can be affected even for the average conditions of the ISM in both SFGs ($n_e \sim 100$ cm^{-3}) and

AGNs ($n_e \sim 500$ cm^{-3}). This is not the case for IR sulfur emission lines, as their critical densities (n_c([S IV]$_{10\mu m}$)$\sim 5.6 \cdot 10^4$ cm^{-3}, n_c([S III]$_{18\mu m}$)$\sim 1.2 \cdot 10^4$ cm^{-3}, and n_c([S III]$_{33\mu m}$)~ 1417 cm^{-3}; Pérez-Díaz et al. 2022) are well above such conditions of the ISM.

Furthermore, as the derivation of chemical abundances based on the IR range also involves intermediate and highly ionized species (S^{2+}, S^{3+}), the influence from DIG (Domgorgen and Mathis 1994; Galarza et al. 1999; Haffner et al. 2009; Reynolds 1985; Zurita et al. 2000), whose contribution is only relevant for low-excitation lines, is expected to be negligible in the abundance calculation. In addition, the detection of high-excitation IR lines is also extremely important in the case of AGNs, especially in high-luminosity AGNs such as Seyferts or quasars, since highly ionized species are needed to correctly trace the chemical content of the gas-phase ISM, and these ions produce emission lines that are easily detected in the IR range.

6.5.2 *Deviations from the S/O solar ratio*

Our analysis of the chemical abundance ratio log(S/O) in the selected sample, calculated from the independent estimation of sulfur and oxygen abundances, reveals that many galaxies present values close to the solar ratio. As a matter of fact, about 70% of our sample of SFGs are within 0.2 dex of the solar ratio. However, this value drops to 44% when AGNs are considered. Focusing on the galaxies whose S/O ratio clearly deviates from the solar proportion (>0.3 dex), we find that 53% of the AGNs and 17% of the SFGs present such large deviations.

Regarding the different subtypes of galaxies, (U)LIRGs exhibit the greatest deviations (see Fig. 6.6). Specifically, we find that (U)LIRGs with an oxygen content close to the solar value (12+log(O/H)$_\odot \sim 8.69$) show a spread in S/O ratios of more than an order of magnitude (from -1.2 to -2.3), suggesting a strong variation in the sulfur content of galaxies with similar stellar masses, $M_* \sim 10^{11}$ M$_\odot$, and oxygen abundances, 12+log(O/H)~ 8.6 (see Fig. 6.10).

Among the (U)LIRGs that deviate from the solar log(S/O) ratio are those with very low abundances (12+log(O/H) < 8.2) compared to other galaxies of the same type. These (U)LIRGs possibly undergo a large excursion or deep dive beneath the MZR due to massive infalls of metal-poor gas (Pérez-Díaz et al., 2024a). According to our results, sulfur abundances are higher in these objects, leading to over-solar log(S/O) > -1.2 ratios. This behavior is similar to that reported by several authors using optical lines for different SFG samples (Diaz et al., 1991; Díaz & Zamora, 2022; Pilyugin et al., 2006).

Diverse mechanisms able to drive the observed log(S/O) deviation in SFGs have been proposed, including: i) changes in the initial mass function enhancing the formation of stars with masses between 12 M$_\odot$ and 20 M$_\odot$, which are the major producers of S via burning of O and Si (Díaz & Zamora, 2022); and, ii) metal enrichment from Type Ia supernovae increasing the sulfur yield (Iwamoto et al., 1999). The first scenario could be favored in the extreme star formation conditions that characterize deep-diving (U)LIRGs, as larger SFRs help to increase the number of stars with M > 10 M$_\odot$. Moreover, if (U)LIRGs have experienced a change in their IMF, which has not been reported yet, then this effect could be amplified. On the other hand, the second mechanism proposed could be important in galaxies with strong outflows; for instance, Pérez-Díaz et al. (2024a) discuss how strong feedback from the extreme episode of star formation is required for (U)LIRGs to end their deep-diving phase.

However, as is shown in Fig. 6.10, these deviations found in massive galaxies are not always associated with an increase in S, as we also observed extremely low log(S/O) abundances in similar conditions. Moreover, these scenarios do not explain why there is such a strong variation in the sulfur content of galaxies with similar oxygen abundances and stellar properties such as mass or the SFR. Another possible mechanism that could explain these lower abundances of S/H might be related to the formation of ice and dust grains that capture S in the most dense cores of molecular clouds (Hily-Blant et al., 2022). Indeed, recent studies show that sulfur abundances in these cold, dense clouds are much lower than those reported in the ionized ISM (e.g. Fuente et al., 2023), and these cold regions can be traced by IR emission lines, while they remain unobserved from optical spectroscopy. Nevertheless, we cannot explore this scenario with the current IR data.

Active galactic nuclei show an analogous behavior, with S/O abundances spread over a wide range for galaxies characterised by similar oxygen abundances. This was also reported by Dors et al. (2023) using optical emission lines; however, the information from S^{3+} – which plays an important role in deriving the total S abundance in the case of strong AGNs such as Seyferts – was missing. As in the case of SFGs, it is unclear whether the proposed scenarios of chemical enrichment from both stellar nucleosynthesis and feedback might explain the observed deviations. Nevertheless, we report the absence of AGNs with clear over-solar log(S/O) ratios, unlike deep-diving (U)LIRGs, implying either that galaxies classified as AGNs in our sample cannot meet the conditions to present such values, or that there is an observational bias towards objects with solar to sub-solar log(S/O) ratios.

In the near future, analysis of spatially resolved spectroscopic observations in the IR range for both SFGs and AGNs will shed light to better disentangle if the mechanisms proposed to explain the observed S/O variation are the same in both types of objects.

6.5.3 *The role of electron density*

The emissivities of the IR emission lines are significantly less dependent on temperature when compared with the optical transitions (e.g. Fernández-Ontiveros et al., 2021). However, the former are more affected by the electron density (n_e) due to the lower critical densities (n_c) of the IR transitions – that is, the density at which collisional de-excitations equal radiative transitions. For instance, [O III]$\lambda 88\mu$m has $n_c = 501$ cm^{-3}, whereas [O III]$\lambda 5007$Å has $6.9 \cdot 10^5$ cm^{-3}. As is shown in Pérez-Díaz et al. (2022), most of the IR emission lines used in this work have n_c well above the expected densities in SFGs (~ 100 cm^{-3}) and AGNs (~ 500 cm^{-3}), and therefore effects from the density conditions of the ISM are not critical for chemical abundance estimations. Additionally, HCm-IR (Fernández-Ontiveros et al., 2021; Pérez-Díaz et al., 2022) takes into account this information in the calculations and uses only those IR transitions whose n_c are above the expected densities for the ionized ISM in each case. Nevertheless, to test the robustness of the S/O relative abundances obtained, we investigate in this section a possible dependency on the gas density.

For this purpose, we evaluated two ratios that are extremely sensitive to n_e: [S III]$\lambda 33\mu$m/[S III]$\lambda 18\mu$m and [Ne V]$\lambda 24\mu$m/[Ne V]$\lambda 14\mu$m. The former is used to trace densities in SFGs, because it is the only available set of emission lines from the same ionic species in the mid-IR. The latter is used to measure densities in AGNs, as this ratio involves a highly ionized ion, thus avoiding possible contamination from star formation activity. In Fig. 6.11 we present the log(S/O) values as a function of these two emission-line ratios.

The lack of correlation between log(S/O) and n_e is shown in Fig. 6.11, suggesting that density variations are not causing the deviations from the solar ratio. A few SFGs (five) and AGNs (three) present densities that are compatible within the errors with the critical density regime ($n_e > n_c$), although the density uncertainties in all cases are compatible with lower values. Analysing the statistics for each sample, we find that SFGs and AGNs present median values of $n_e \sim 200$ cm^{-3} and ~ 1000 cm^{-3}, respectively, adopting an electron temperature of $T_e = 10^4$ K. Nevertheless, we note that, given the uncertainties in the emission-line ratios involved, these results are still compatible with the typical ISM densities in each case.

On the other hand, there are some considerations that may impact the determination of electron densities. For instance, it has been probed that planetary nebulae present density inhomogeneities across the gas-phase ISM (e.g. Flower, 1969; Harrington, 1969; Péquignot et al., 1978; Rubin, 1989;

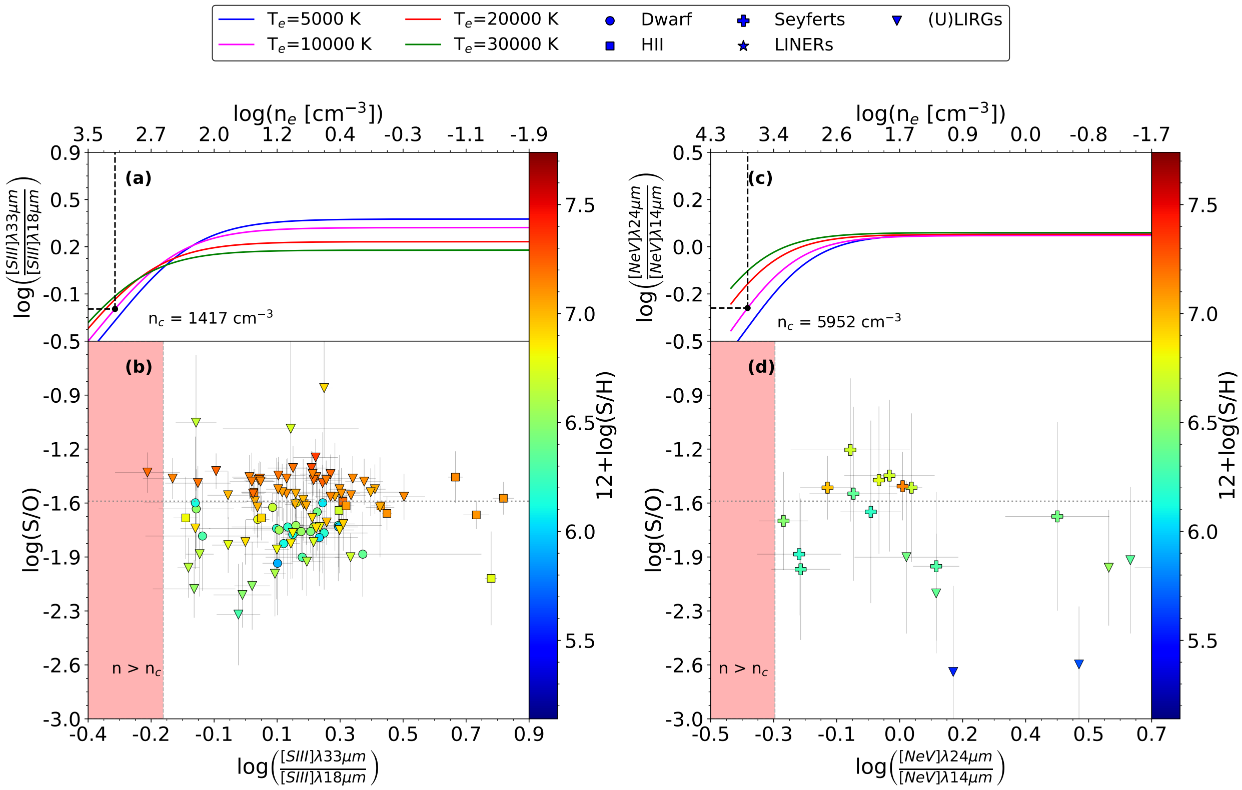

Figure 6.11: Dependence of S/O on electron density. Panels (a) and (c) show the theoretical behavior of the emission-line ratios, [S iii]$\lambda 33\mu$m/[S iii]$\lambda 18\mu$m and [Ne v]$\lambda 24\mu$m/[Ne v]$\lambda 14\mu$m, respectively, as a function of density for different values of the electron temperature, as computed by Pyneb (Luridiana et al., 2015). Panel (b) shows the behavior of log(S/O) as a function of [S iii]$\lambda 33\mu$m/[S iii]$\lambda 18\mu$m for SFGs. Panel (d) shows the behavior of log(S/O) as a function of [Ne v]$\lambda 24\mu$m/[Ne v]$\lambda 14\mu$m for AGNs. The color bar shows the values of 12+log(S/H) for both samples. Critical densities were computed assuming T_e = 10000 K and are those associated with the emission line with the lowest value.

Seaton & Osterbrock, 1957). Additionally, the action of shocks in the ISM might also induce variations in the density distribution (e.g. Aldrovandi & Contini, 1985; Contini & Aldrovandi, 1983; Dopita, 1976; Dopita et al., 1977; Dopita, 1977). While these effects can play an important role in the determination of the electron temperature, T_e, for a direct estimation of chemical abundances using CELs, HCm-IR does not make any prior estimation of T_e. Pérez-Montero et al. (2019a) show that a variation in the electron density by a factor of four has a negligible effect on the chemical abundances derived using HCm. In the case of IR estimators, such as S34, Ne23, or Ne235, only remarkable differences (higher than 0.3 dex) are found when the densities are changed from 100 cm^{-3} for SFGs and 500 cm^{-3} for AGNs to 10^4 cm^{-3} in both cases, according to photoionization models computed with Cloudy v17 (Ferland et al., 2017). This value is well above the critical density for most of the IR emission lines considered, and there are no galaxies in this regime in our sample of SFGs and AGNs, as is shown in Fig. 6.11. Therefore, we conclude that the density conditions have no significant impact on the chemical abundances of 12+log(S/H) and 12+log(O/H) estimated in this work.

Finally, we note that a few SFGs and AGNs show values above the expected ratio in the low-density regime (i.e. $n_e \rightarrow 0$). Nevertheless, the deviations from the log(S/O) solar ratio are also found in the density regime between 100 cm^{-3} and 1000 cm^{-3}, supporting the idea that these differences are not driven by variations in the gas density, but are instead intrinsic to the chemical composition of the ISM.

6.6 CONCLUSIONS

In this work we performed, for the first time, a systematic analysis of the chemical abundances estimated from IR emission lines in a sample of galaxies including both SFGs and AGNs, providing an independent estimation of the oxygen, nitrogen, and sulfur abundances for the widest sample of galaxies with IR spectroscopic observations, combining *Spitzer*, *Herschel*, *AKARI*, and *SOFIA* data. When comparing our results with previous studies of chemical abundances from IR emission lines, we find an agreement in the estimated oxygen and nitrogen abundances.

While most of the galaxies in the sample are characterized by a solar log(S/O) ratio, we report that galaxies with low to solar oxygen abundances present large deviations in log(S/O). In the first case, galaxies present higher sulfur abundances, which is consistent with studies based on optical emission lines. Among them, (U)LIRGs are characterized by high stellar masses and high SFRs, and some are reported to be experiencing an infall of metal-poor gas, strengthening the hypothesis that the large S/O ratios may be driven by stellar nucleosynthesis. In the case of galaxies with solar-like abundances, we find that (U)LIRGs present S/O ratios that span a very wide range, whereas their stellar properties remain similar, implying a possible additional sulfur production channel or a more complex picture with respect to stellar nucleosynthesis. We also tested whether these deviations from the S/O solar ratio are driven by the density conditions of the ISM, and we conclude that density is not a driver of such deviations.

Our results for AGNs are similar to those observed in SFGs, although in this case we report more galaxies deviating from the log(S/O) solar ratio. We find that the (U)LIRGs dominated by AGN activity and some Seyferts present extremely low log(S/O) ratios, while they show almost solar oxygen abundances. Unlike the SFGs, we do not find any AGN with sub-solar abundances and high log(S/O) ratios, although this could be due to the low number of low-metallicity AGNs in our sample. Reviewing these results, while the use of IR sulfur emission lines to constrain the overall metallicity of the gas-phase ISM is not required when transitions from other ionic species are detected (such as neon, argon, and oxygen), using only sulfur lines can lead to an underestimation of 12+log(O/H) in the solar (and over-solar) regime, and an overestimation for galaxies that are actually characterized by a depressed oxygen content.

A DEEP-DIVE BENEATH THE MASS-METALLICITY RELATION 7

Chapter based on the publication: B. Pérez-Díaz, E. Pérez-Montero, J. A. Fernández-Ontiveros, J. M. Vílchez and R. Amorín (2024) *"A departure from the mass-metallicity relation in merging galaxies due to an infall of metal-poor gas", published in Nature Astronomy, volume* 8, *p.* 368-376, *doi:*10.1038/s41550-023-02171-x.

7.1 ABSTRACT

Heavy element accumulation and stellar mass assembly are fundamental processes in the formation and evolution of galaxies. However, the key elements that govern them, such as gas accretion and outflows, are not fully understood. This is especially true for luminous and massive galaxies, which usually suffer strong feedback as massive outflows and large-scale gas accretion triggered by galaxy interactions. Using a sample of 77 luminous infrared (IR) galaxies, we derive chemical abundances using new diagnostics based on nebular IR lines, which peer through their dusty medium and allow us to include the obscured metals. In contrast to optically based studies, our analysis reveals that most luminous IR galaxies remain close to the mass-metallicity relation. Four galaxies with extreme star-formation rates ($> 60\ M_{\odot}\cdot yr^{-1}$) in their late merger stages show heavily depressed metallicities ($12+\log(O/H) \sim 7.7 - 8.1$) along with solar-like N/O ratios, indicative of gas mixing processes and suggesting the action of massive infall of metal-poor gas in a short phase, eventually followed by rapid enrichment. These results challenge the classical gas equilibrium scenario applied to main-sequence galaxies, suggesting that chemical enrichment and stellar-mass growth in luminous IR galaxies take place via mergers, likely driving these galaxies out of chemical equilibrium.

7.2 INTRODUCTION

The chemical composition of the gas-phase interstellar medium (ISM) is a witness of the evolution of galaxies (Maiolino & Mannucci, 2019), as heavy elements (or metals) are produced in stars by stellar nucleosynthesis and eventually ejected into the ISM at the end of their lives (Nomoto et al., 2013). As stellar mass assembly also traces the evolution and formation of galaxies, a natural connection between them arises, materialized in the so-called Mass-Metallicity Relation (MZR; Andrews & Martini, 2013; Tremonti et al., 2004) as well as in the Fundamental Metallicity Relation (FMR; Curti et al. 2020, although its universality is still under debate Baker et al. 2023), which are regulated by a wide variety of processes: galaxy environment (e.g. Y.-j. Peng & Maiolino, 2014), secular evolution (e.g. Somerville & Davé, 2015), feedback from star-formation (e.g. Blanc et al., 2019) and Active Galactic Nuclei (AGN; e.g. Thomas et al., 2019), and stellar age (e.g. Duarte Puertas et al., 2022).

These scaling relations are explained by means of self-regulated equilibrium between gas accretion, outflows and star formation (Maiolino & Mannucci, 2019). However, half of the stellar mass in galaxies that we observe nowadays was formed in a relatively short period of time (~ 3.5 Gyr) during the cosmic noon (Förster Schreiber & Wuyts, 2020), i.e., in an extreme scenario where these equilibrium conditions may not apply. Luminous and Ultra-Luminous Infrared Galaxies (LIRGs and ULIRGs, respectively) are key to understanding the complex picture of galaxy evolution, since they allow us to explore nearby galaxies with extreme star formation rates, similar to those found at the cosmic noon (Armus et al., 2009). LIRGs have infrared luminosities $L_{IR} > 10^{11}\ L_{\odot}$ by definition, dominate the star-formation activity at $z \sim 1$ and contribute significantly to the cosmic infrared background (Stierwalt et al., 2013). In addition, ULIRGs with $L_{IR} > 10^{12}$ $L_{\odot}$ are commonly found in merger systems at $z \gtrsim 2$ and may represent an evolutionary stage in the formation of AGN-hosting galaxies (Evans et al., 2005). While the scaling relation between the bulge and central supermassive black holes (SMBHs) in quiescent galaxies suggest a link between accretion rates onto SMBH and the intensity of the episodes of nuclear star formation (Magnelli et al., 2009), the study of (U)LIRGs and their extreme conditions are critical to shed light on the co-evolution of SMBHs and their host galaxies.

Despite the increasing number of studies on the gas-phase ISM metal content in galaxies, the chemical characterization of (U)LIRGs lacks consensus. On the observational side, optical estimations of the oxygen abundance (e.g. Grønnow et al., 2015; Rupke et al., 2008) suggest that chemical abundances are lower than expected for these galaxies. However, this approach presents serious challenges: i) optical emission lines are significantly affected by dust attenuation, which is particularly important in (U)LIRGs (Lo Faro et al., 2017), and therefore miss the heavy elements located in dust-embedded regions within galaxies; ii) due to the hard ionizing radiation field associated with strong starbursts, the cooling process of many metals (such as sulfur, neon or oxygen) may be dominated by highly-ionized species (S^{3+}, Ne^{2+}, and even O^{3+} in some extreme scenarios), whose emission lines are detected in the IR range; and, iii) due to the temperature dependence of optical emission lines, cold regions might remain unobserved. To avoid these problems, studies of the metallicity of ULIRGs from IR emission lines are needed, but such studies are rather scarce and show discrepancies. A study of local ULIRGs using far-IR emission lines was performed on a sample of 20 local galaxies (Pereira-Santaella et al., 2017), concluding that 12+log(O/H) ranges from 8.5 to 8.9 [0.65 $Z_{\odot}$, 1.65 $Z_{\odot}$], with many of them found 0.3 dex lower than expected by their position in the MZR. More recently, another study of five ULIRGs using again far-IR emission lines showed that, contrary to the previous study, these ULIRGs followed the MZR (Chartab et al., 2022) derived for SFGs (Tremonti et al., 2004) in the Sloan Digital Sky Survey (SDSS). However, as these studies were performed using ratios of far-IR emission lines (including [O III]$\lambda 52\mu$m, [N III]$\lambda 57\mu$m, [O III]$\lambda 88\mu$m) that are better tracers of the nitrogen-to-oxygen abundance ratio log(N/O) (Fernández-Ontiveros et al., 2021), the estimation of 12+log(O/H) relies on the local calibration of the O/H–N/O relation (Pérez-Montero et al., 2019a), that might not apply to the case of (U)LIRGs since independent estimations of both quantities lead to sub-solar abundances (Fernández-Ontiveros et al., 2021). On the theoretical side, due to the high dust content (Herrero-Illana et al., 2019) of ULIRGs, chemical evolution models predict high metal content in the ISM of these galaxies (Calura et al., 2008). On the other hand, simulations of ULIRGs, as interacting systems, have shown that the chemical content in the gas-phase ISM, mainly traced by the oxygen abundance [12+log(O/H)], experiences a drop during the merger process (Montuori et al., 2010; Rupke et al., 2010; Sparre et al., 2022). However, resolution in simulations also play an important role in understanding whether the physical explanation for metallicity dilution during merger processes is gas infall (Bustamante et al., 2018) or enhanced fragmentation (Teyssier et al., 2010), or a mixture of these. Overall, the lack of a systematic and consistent study of the chemical content in the gas-phase ISM of ULIRGs does not help in solving this problem since an independent determination of the O/H and N/O abundances based on IR emission lines is required to peer through the dusty medium of these galaxies.

7.3 SAMPLE AND METHODOLOGY

Here we provide more detailed information in the selection of the sample of Ultra-Luminous Infrared Galaxies (ULIRGs) and Star-forming Galaxies (SFGs) with IR spectroscopic data. We also described the methodology employed to estimate the chemical content of the gas-phase interstellar medium (ISM) in our sample (Sec. 7.3.1) and their chemical abundance determinations (Sec. 7.3.2). In addition, we give some details about the retrieval of other properties derived in the sample, such as the stellar mass (M_*), the star-formation rate (SFR), or the merger stage (Sec. 7.3.3). Finally, we present in detail some evolutionary models that reproduce the behaviour of our sample of galaxies (Sec. 7.3.4). Throughout this study, we assume as reference system the Solar chemical abundances: $12+\log(\mathrm{O/H})_\odot = 8.71$ and $12+\log(\mathrm{N/H})_\odot = 7.85$ (Lodders, 2021).

7.3.1 *The sample of Ultra-luminous Infrared Galaxies and Star-forming Galaxies*

7.3.1.1 *Selection*

We build our sample of galaxies with IR spectroscopic data from two different catalogs. The first one was retrieved from the IDEOS (Hernán-Caballero et al., 2016; Spoon et al., 2022) IR database, which includes the measurements of 77 fitted mid-IR observables in the range $5.4 - 36\mu$m for all galaxies observed with *Spizer* (a total of 3335 galaxies Spoon et al., 2022). From this initial sample, we omit duplicate observations of one single object and entries corresponding to galaxies presented in the first catalog, where the higher resolution spectroscopic observation was taken. After verifying that star formation dominates the ionization budget in our final sample of galaxies (see next subsection), we perform a cross-match with an *AKARI* sample of ULIRGs (Inami et al., 2018) to provide measurements of at least one hydrogen recombination line, particularly H I (5-4). In all, a total sample of 66 ULIRGs was retrieved.

The second catalog (Fernández-Ontiveros et al., 2021) consists of a sample of dwarf galaxies, SFGs, and ULIRGs that present mid- to far-IR range spectroscopic observations from the InfraRed Spectrograph (IRS, Houck et al. 2004) on board *Spitzer* and from the Photodetector Array Camera and Spectrometer (PACS, Poglitsch et al. 2010) on board *Herschel* (Fernández-Ontiveros et al., 2021; Fernández-Ontiveros et al., 2016). We compiled measurements for a sample of 66 galaxies showing detections of [O III]$\lambda 52\mu$m and [N III]$\lambda 57\mu$m far-IR lines, needed for the nitrogen-to-oxygen estimation (Fernández-Ontiveros et al., 2021; B. Peng et al., 2021; Pérez-Díaz et al., 2022), from the IFU spectroscopy instrument FIFI-LS (Fischer et al., 2018) on board the *SOFIA* airborne observatory. Additionally, we obtained measurements of hydrogen recombination lines H I (7-6) and (5-4) from the *Spitzer* calibrated spectra available in the CASSIS (Lebouteiller et al., 2015) database and from observations via *AKARI*/IRC (Imanishi et al., 2010), respectively.

7.3.1.2 *Classification*

For the first sample of galaxies, the ratio between [Ne V]$\lambda 14\mu$m and [Ne II]$\lambda 12\mu$m ensures (Fernández-Ontiveros et al., 2021; Pereira-Santaella et al., 2017) an AGN contamination lower than 10%. For the second sample, we use two criteria (Armus et al., 2007) both based on the relative emission of high ionic species ([Ne V]$\lambda 14\mu$m and [O IV]$\lambda 26\mu$m) to low ionic species (Ne II]$\lambda 12\mu$m) and on the strength of the polycyclic aromatic hydrocarbon (PAH) at 6.2μm as measured from their Drude profile (see Spoon et al. 2022, IDEOS presentation work, for further details), since AGN activity is expected to enhance higher ionic species (Pérez-Díaz et al., 2021, 2022) and the equivalent width (W) of PAHs has been proposed (Armus et al., 2007; Hernán-Caballero et al., 2020; Puget & Leger, 1989) as a tracer of the star-formation activity. Particularly, we select those galaxies characterized by $W_{\mathrm{PAH}6.2\mu m} > 0.06\mu$m, [Ne V]$\lambda 14\mu$m/[Ne II]$\lambda 12\mu$m < 0.15 and [O IV]$\lambda 26\mu$m/[Ne II]$\lambda 12\mu$m < 0.4.

In Fig. 7.1 we present both criteria for the sample of galaxies retrieved from IDEOS. To ensure the robustness in the classification and avoid AGN contamination in first order, we only select galaxies which belong to the SF-dominated region (yellow shaded region) in both diagrams. When compared our classification to that presented in IDEOS (Spoon et al., 2022), we found that the whole sample selected (66 galaxies) also show silicate strength and an equivalent width for the PAH at 11.3μm compatible with star-forming dominated activity (Sturm et al., 2002; Tommasin

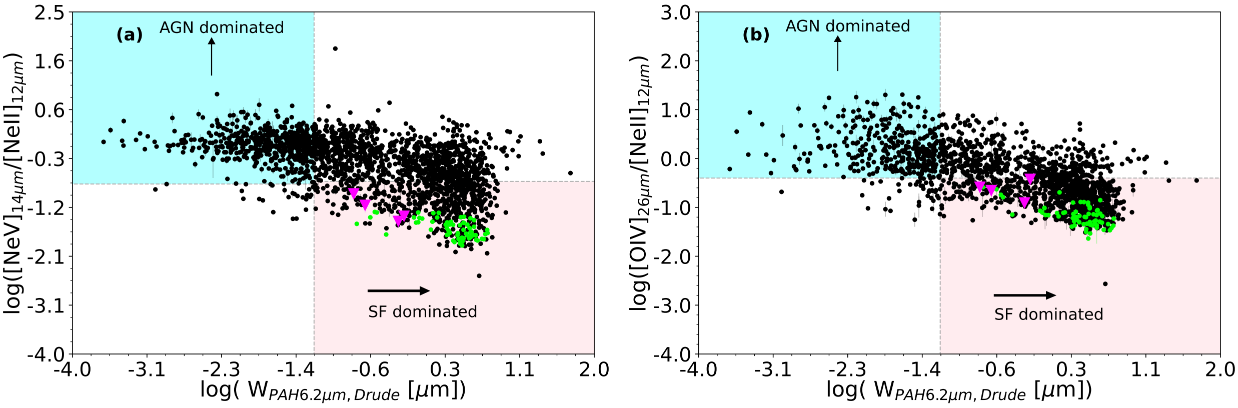

Figure 7.1: Diagnostic diagrams for the AGN contamination (Armus et al., 2007) based on IR emission lines and the PAH 6.2μm as measured from their Drude profile (see IDEOS Spoon et al., 2022 presentation work for further details). The whole sample of galaxies from IDEOS is presented in these plots, while the sample of (U)LIRGs retrieved is highlighted in green, and *deep-diving* (U)LIRGs are highlighted as magenta triangles. (a) Diagnostic diagram using [Ne v]$\lambda 14\mu$m as a high-ionized specie. (b) Diagnostic diagram using [O iv]$\lambda 26\mu$m instead. Error bars show the uncertainties associated with the corresponding quantities.

et al., 2010) (i.e. $W_{\mathrm{PAH}11.3\mu m} > 0.2\mu$m). Thus, our sample of SF dominated (U)LIRGs is consistent when applying five different criteria.

7.3.2 *Chemical abundance estimations*

The estimation of chemical abundances, the oxygen content [12+log(O/H)] and the nitrogen-to-oxygen ratio [log(N/O)], as well as the ionization parameter [log(U)] was performed using HII-CHI-Mistry-IR (Fernández-Ontiveros et al., 2021; Pérez-Díaz et al., 2022) (or HCm-IR). In brief, HCm-IR is a python code that performs a Bayesian-like calculation of the above mentioned quantities by comparing a set of emission lines with the predictions calculated from a grid of photoionization models (Pérez-Montero, 2014). By default, the code provides four different grids of models, varying the Spectral Energy Distribution (SED) used as ionization source. For our study, since our sample is dominated by star-formation, we use the POPSTAR grid, which was computed assuming a SED of simple stellar population models from POPSTAR (Mollá et al., 2009), assuming a constant density of 100 cm^{-3}, a filling factor of 0.1 and plane-parallel geometry. While previous studies of the code have shown that these assumptions do not introduced large uncertainties in the derived abundances, some differences can be found in the ionization parameter ($\sim$ 0.2 dex; Pérez-Díaz et al., 2021, 2022; Pérez-Montero, 2014; Pérez-Montero & Amorín, 2017; Pérez-Montero et al., 2019a, 2023a) and these assumptions might play a critical role when 3D instead of 1D phototionization models and optical emission lines are considered (Jin et al., 2022). Nevertheless, the emission line ratios affected by these considerations are precisely those ratios that might be affected for DIG, as they are mainly originated from boundary regions within the nebula (Jin et al., 2022). Since IR is mainly tracing medium and high ionized species, we expect that considerations on geometry as revealed by 3D models do not play a major role in this work. The grid covers a range in 12+log(O/H) from 6.9 to 9.1 in bins of 0.1 dex, in log(N/O) from −2.0 to 0.0 in bins of 0.125 dex and in log(U) from −4.0 to 1.5 in bins of 0.25 dex.

The lines accepted by the code in the input include H i$\lambda 4.05\mu$m, [Ar ii]$\lambda 6.99\mu$m, H i$\lambda 7.46\mu$m, [Ar iii]$\lambda 8.99\mu$m, H i$\lambda 12.4\mu$m, [Ne ii]$\lambda 12.8\mu$m, [Ne v]$\lambda 14.3\mu$m, [Ne iii]$\lambda 15.6\mu$m, [Ne v]$\lambda 24\mu$m, [O iv]$\lambda 26\mu$m, [O iii]$\lambda 52\mu$m, [N iii]$\lambda 57\mu$m, [O iii]$\lambda 88\mu$m. As compared to previous versions of the code employed for other samples of SFGs (Fernández-Ontiveros et al., 2021) or AGNs (Pérez-Díaz et al., 2022), we introduce two modifications (version 3.1). The first modification is that the input now accepts argon emission lines, which behave in the same way as neon emission lines. Secondly, the code no longer uses sulfur emission lines to derive the oxygen abundance ratio as they are used instead to estimate the sulfur content independently from the oxygen estimation. Some authors (Díaz & Zamora, 2022; Pérez-Montero et al., 2006) have pointed that sulfur-to-oxygen ratios might deviate from the Solar ratio in the low- and high-metal regime, implying that the use of sulfur emission lines to estimate the oxygen content might introduce a bias. The code finds solutions for 12+log(O/H), log(N/O) and log(U) as the average of the χ^2-weighted distribution of all models, χ^2 being the quadratic differences between the observed and the predicted emission-line ratios sensitive to the above chemical ratios built upon the emission lines cited above. Instead of solely taking into account the model with the minimum deviation from the observations (minimum χ^2), the code performs a weighted sum (with the weights $1/\chi^2$) for all considered models, which helps in providing a continuous solution although the models covered a discrete space in the estimated parameter. The code performs an independent estimation of log(N/O) and 12+log(O/H), although if N/O cannot be constrained due to the lack of key emission lines, a relation (Pérez-Montero et al., 2013) between O/H and N/O is assumed by the code. By default, this relation is the one obtained for star-forming regions using chemical abundances based on optical emission-lines (Pérez-Montero, 2014; Pérez-Montero & Contini, 2009). In this work, as N/O can be estimated independently from far-IR emission lines, this relation is not used.

7.3.3 *Ancillary data*

To perform our study, we have retrieved almost all properties that are key in understanding the chemical evolution of the galaxies, i.e. the stellar mass, the star-formation rate or the merger state. In this section, we describe how these values were obtained from the literature and the methodologies followed in the mentioned works to estimate them.

7.3.3.1 *Stellar mass and star formation rates*

For 30 galaxies, we retrieved their stellar masses and star formation rates from the Great Observatories All-sky LIRG Survey (GOALS; Armus et al., 2009; Howell et al., 2010). Particularly, the SFR was estimated from the *IRAS* L_{IR} and from *GALEX* FUV, which provides an estimation of the unobscured and obscured SFR respectively (Howell et al., 2010). The stellar mass was estimated from photometry using IRAC 3.6μm and Two Micron All Sky Survey (2MASS) K-band photometry.

For 21 galaxies, we retrieve their stellar masses and SFRs from the *GALSPEC* Data Release 8 (Brinchmann et al., 2004; Kauffmann et al., 2003; Tremonti et al., 2004). Particularly, these quantities were retrieved following a Bayesian technique to match two stellar absorption indices, the $D_n(4000)$ break (Balogh et al., 1999) and the Hδ_A Balmer absorption-line index (Worthey & Ottaviani, 1997), from a library of different star formation histories from Monte Carlo realizations (Kauffmann et al., 2003).

For ten galaxies, we retrieved their stellar masses (Parkash et al., 2018) derived from *WISE* bands W1 and W2 following the GAMA-derived stellar mass-to-light ratio relation (Cluver et al., 2014). Their SFRs were obtained from *WISE* bands W1 and W3 to estimate the Balmer-decrement-corrected Hα luminosity (Brown et al., 2017; Cluver et al., 2017; Parkash et al., 2018).

For seven galaxies, we retrieved their stellar masses from the S^{4}G (Muñoz-Mateos et al., 2013, 2015; Querejeta et al., 2015; Sheth et al., 2010) sample, which were estimated from the 2MASS photometry (Bell et al., 2003). For these seven galaxies, we could not retrieve their SFRs. For another four galaxies, we obtained their stellar masses from the catalog published for a subsample of galaxies from the CASSIS database whose stellar masses and SFRs were obtained after applying the photometric SED fitting code CIGALE (Boquien et al., 2019; Ciesla et al., 2015) to their UV and near-IR observations (Vika et al., 2017).

7.3.3.2 *Merger stage*

The GOALS sample also offers (Stierwalt et al., 2013) an estimation of the merger stage based on observations via IRAC 3.6μm images. By visual inspection, the authors provide a classification in the following categories: *nonmergers* when there is no sign of merger activity or its neighborhood lacks massive galaxies; *pre-mergers*, if the images reveal a pair of galaxies prior to the first encounter; *early-stage mergers*, pair of galaxies after the first encounter; *mid-stage mergers*, if they show amorphous disks, tidal tails and/or other signs of merger activity; and *late-stage mergers*, if they show a common envelope.

7.3.4 *Inflow models*

7.3.4.1 *Simulations of merging galaxies*

According to simulations of merging massive galaxies, a decrease in the metal content of galaxies happens shortly after the first pericentre passage (Rupke et al., 2010). When star-formation and metal enrichment from supernovae are included (Montuori et al., 2010), the dilution is reported to be correlated to the star formation enhancement, and as the merger advances, the dilution is reduced and chemical enrichment becomes dominant. From this last model, the variations in metallicity as well as SFR are considered relative to the initial conditions on the galaxies (see Figure 4 from Montuori et al., 2010). In this work, we considered the trends followed by galaxies in interaction with different initial conditions: $\mathrm{Z}_{ini} = 0.8\ \mathrm{Z}_\odot$, $\mathrm{Z}_{ini} = 0.4\ \mathrm{Z}_\odot$ and $\mathrm{Z}_{ini} = 0.2\ \mathrm{Z}_\odot$.

7.3.4.2 *Inflow model within galaxy evolution*

Another model that we consider to reproduce the drop of metallicity in some of the ULIRGs is based on basic equations of chemical evolution. For a standard galaxy, with original stellar mass $\mathrm{M}_{*,0}$, SFR, metallicity Z and with α being the fraction in mass of long-lived stars and p the yield of metals (mainly oxygen), we can describe the evolution of gas mass (G), mass of long-lived stars (S) and mass of metals ($\mathcal{Z}$) following the equations (Köppen & Edmunds, 1999):

$$\dot{G} = -\alpha \mathrm{SFR} \tag{7.1}$$

$$\dot{S} = \alpha \mathrm{SFR} \tag{7.2}$$

$$\dot{\mathcal{Z}} = -Z\alpha \mathrm{SFR} + p\alpha \mathrm{SFR} \tag{7.3}$$

If a flow A of gas (in either direction) is introduced in the above equations, following the prescriptions (Köppen & Edmunds, 1999), then Equation (7.1) is modified as:

$$\dot{G} = A - \alpha \mathrm{SFR} \tag{7.4}$$

Thus, we can express Equation (7.3) in terms of the metal content (Z) as:

$$G\dot{Z} = p\alpha \mathrm{SFR} - AZ \tag{7.5}$$

For our model, we considered that both A and SFR present constant values for most of the evolving time of the galaxy, although to reproduce the massive inflow, we consider that they experience a peak (parameterized as a gaussian distribution), separated by 200 Myr (i.e. the inflow A occurs before the peak in SFR), which is similar to the characteristic dynamical time of the galaxy disk (Elmegreen & Burkert, 2010), and within the range observed in simulations ($\lesssim$ 500 Myr Di Matteo et al. 2007, 2008; Renaud et al. 2014), and we consider that the duration of the infall phase is bigger than the peak of star formation rate (which corresponds to 100 $M_{\odot} \cdot yr^{-1}$, while the peak of infall rate is $\sim$ 200 $M_{\odot} \cdot yr^{-1}$). After 1 Gyr of the process, we assume that the effects of outflows are significantly higher, changing the sign of A (from positive to negative). We show in Fig. 7.2 how these parameters evolve over time. The value of α is computed from the Initial Mass Function (Kroupa, 2001) ($\alpha \sim 0.22$), and considering long-lived stars those whose masses range from 0.01 $M_{\odot}$ to 3 $M_{\odot}$. Finally, we assume a conservative yield $p = 0.003$ (Pilyugin et al., 2007). As initial conditions, we assume a galaxy with stellar mass 10^{11} $M_{\odot}$, mass gas according to the observed ratio (Parkash et al., 2018), and metallicity $Z = 0.84$ $Z_{\odot}$ according to the obtained plateau in this study for massive galaxies.

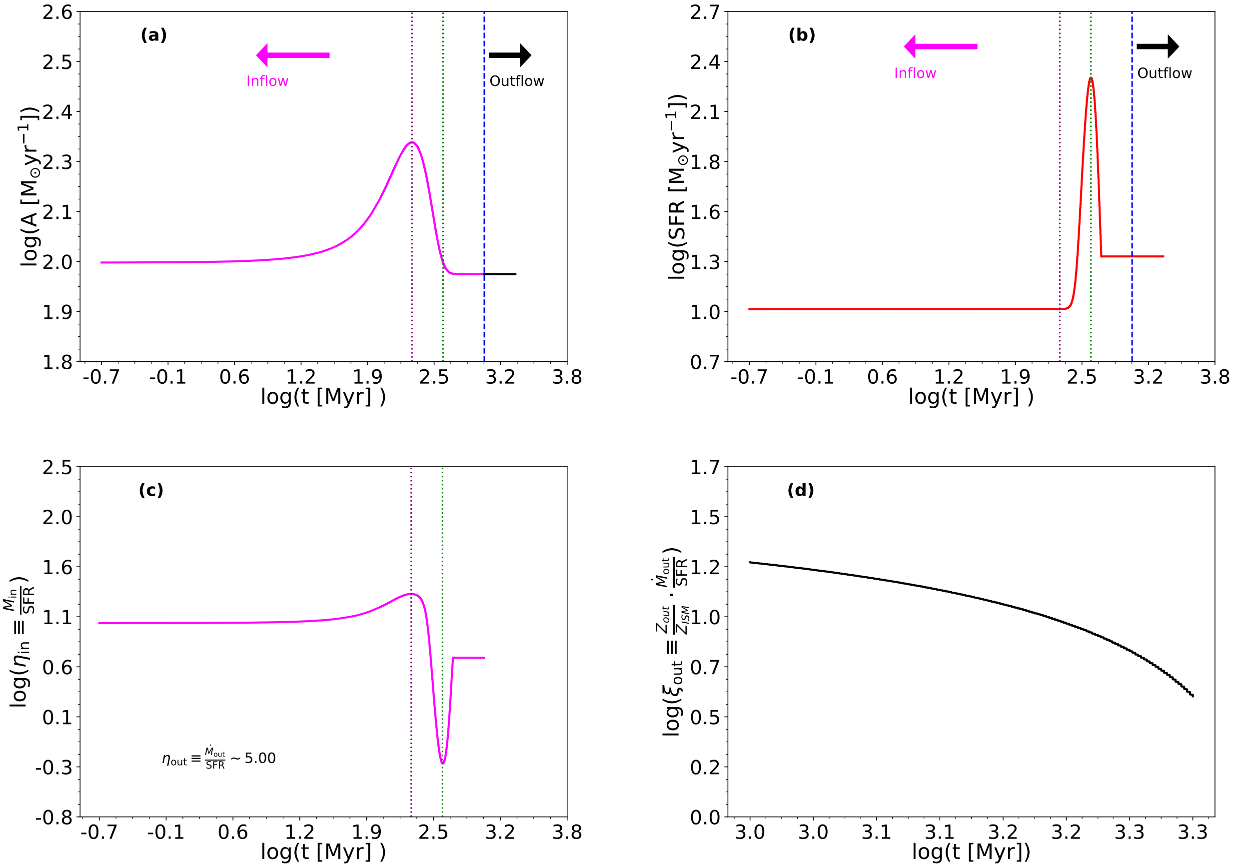

Figure 7.2: Evolution of the different quantities involved in our inflow model from Section 4.2. The blue vertical dashed line separates the inflow and outflow regimes. The magenta vertical dotted line represents the maximum of the inflow rate (A), while the green dotted line represents the maximum of the star formation rate (SFR). (a) Inflow (or outflow) rate (A) as a function of time. (b) Star formation rate (SFR) as a function of time. (c) Mass loading factor for the inflow (η_{in}) as a function of time. Since both outflow rate and star formation rate are mostly constant in the outflow-dominated regime, the mass loading factor for the outflow (η_{out}) is essentially constant ($\sim$ 5). (d) Evolution of the outflow metal loading factor (ξ_{out}) as a function of time for the outflow-dominated regime.

Overall, according to this model, the process lasts for 2 Gyr: during which secular evolution is considered only in the first 200 Myr (i.e. both A and SFR show low and constant values). From 300 Myr to 900 Myr, the infall of gas dilutes the metallicity and increases the stellar mass. Finally, after 1 Gyr, the combination of stars polluting the ISM with metals and outflows contribute to enrich the metal content, while stellar mass shows little increase as the peak of star formation has already occurred. The infall process involves a total gas mass of $2.6 \cdot 10^{9}\ M_{\odot}$, which is equivalent to 3% of the stellar mass of a $10^{11}\ M_{\odot}$ galaxy and 15% of its gas reservoirs ($\sim 1.6 \cdot 10^{10}\ M_{\odot}$ assuming the relation between gas mass-stellar mass reported for galaxies by Parkash et al. 2018).

7.4 RESULTS AND DISCUSSION

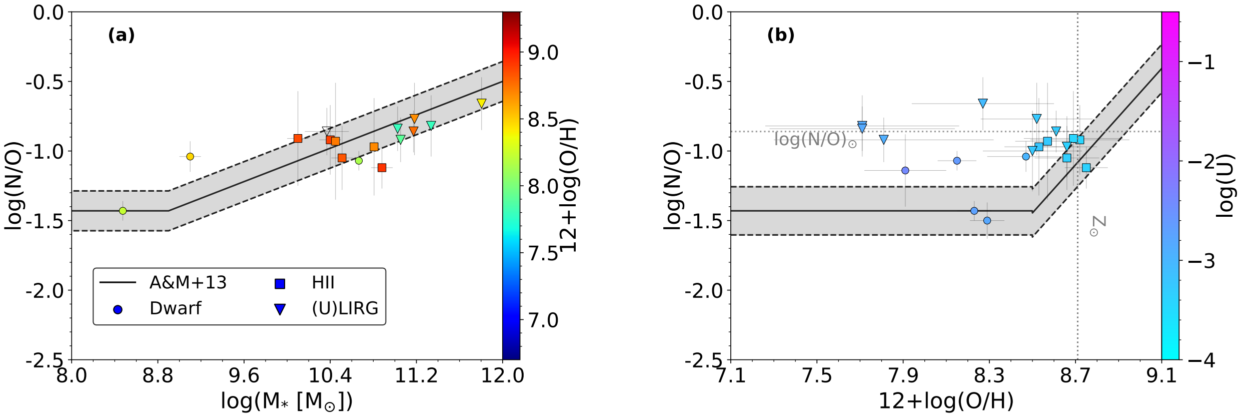

Figure 7.3: Scaling relations for log(N/O). (a) Relation between stellar mass and nitrogen-to-oxygen ratio for our sample of galaxies. The local relation found for SFGs (Andrews & Martini, 2013) (with a 10% uncertainty) is shown as "A&M+13". (b) Relation between the oxygen abundance and nitrogen-to-oxygen abundance ratio for our sample of galaxies. Error bars show the uncertainties associated with the corresponding quantities. "A&M+13" (Andrews & Martini, 2013) stands for the local relation reported for SFGs, represented with 10% of uncertainty.

In this study, we determine the chemical abundances of the ISM in a sample of 77 (U)LIRGs dominated by star-formation activity, and we use a sample of 55 HII extragalactic regions and star-forming dwarf galaxies as a control sample. Thus, a total sample of 132 galaxies with IR observations is analysed. We use spectroscopic observations of nebular emission lines in the near-, mid- and far-IR ranges acquired with *Spitzer*/IRS, *Herschel*/PACS, and *AKARI* for measurements of the Brα emission. To estimate 12+log(O/H), log(N/O) and the ionization parameter log(U) we use HII-CHI-Mistry-IR (Fernández-Ontiveros et al., 2021; Pérez-Díaz et al., 2022), a code that employs a bayesian-like comparison between the results predicted by large grids of photoionization models with specific observed emission-line ratios. This code allows us to independently estimate these three quantities without assuming any underlying relation between any of them. However if the set of emission lines used as input is reduced (e.g. when no previous estimation of N/O can be provided), the code assumes certain relations that can be changed by the user to find an estimation of the chemical content. For our sample, we use IR emission lines from H I$\lambda 4.05\mu$m to [O III]$\lambda 88\mu$m as input for the code (see Sec. 7.3.2 for more details). Despite that some degree of depletion of the gaseous abundance (e.g. iron, oxygen) on dust is expected, the methodology of this work to derive abundance is robust since it makes extensive use of lines from non depletion (e.g. neon) or at most mildly (e.g. sulfur) affected elements. Overall, we find that most galaxies in our sample have a nearly solar metallicity 12+log(O/H)$\sim$ 8.6 (0.85 $Z_{\odot}$), which is consistent with previous studies from IR (Pereira-Santaella et al., 2017) emission lines. We find a median N/O value for our sample of ~ -1.0, which is consistent with the expected values for their stellar masses (see Figure 7.3 (a)). Moreover, Fig. 7.3 (b) shows that some galaxies, especially (U)LIRGs, deviate from the local behavior in the N/O-O/H diagram, reinforcing our statement that these two chemical abundances must be estimated independently to ensure a robust analysis of the gas-phase ISM chemical content.

Considering the physical size of the *Spitzer*/IRS (Houck et al., 2004) slit ($\sim 4 - 11''$) and the median distance in our sample ($\sim$ 40 Mpc), we are analyzing the central region of (U)LIRGs ($r \lesssim 1.1 kpc$), which is not affected by shocks as those are reported in the external parts of galaxies (Monreal-Ibero et al., 2006; Rich et al., 2015). As we are using ionic species whose ionizing potentials are as low as 21.5 eV (Ne^{+}) and 23.3 eV (S^{++}), no significant contribution from Diffuse Ionized Gas (DIG) is expected to be contaminating our estimations, since its major contribution affects species with even lower ionization potentials (Blanc et al., 2009) such as S^{+} (10.4 eV) and N^{+} (14.5 eV).

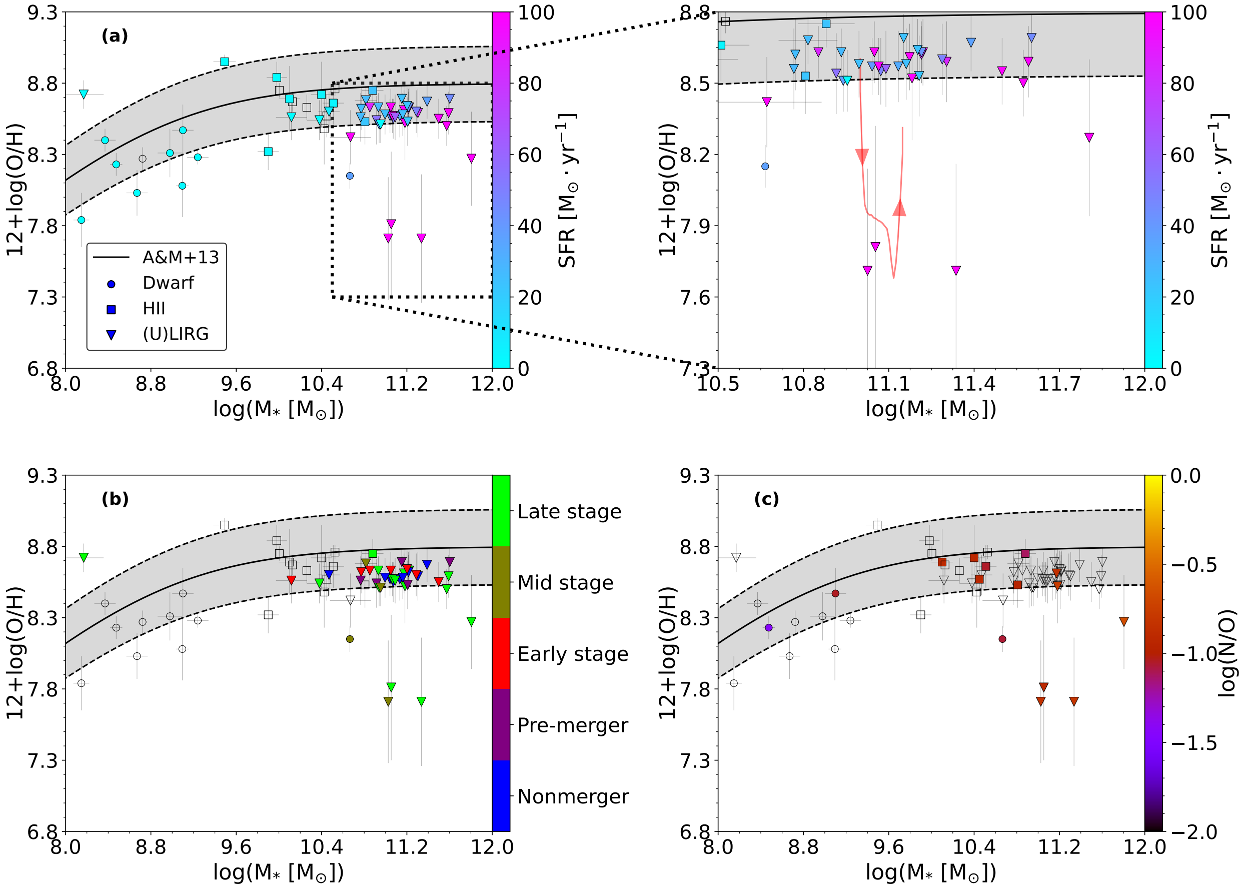

Figure 7.4: Mass-metallicity relation for our sample of SFGs. The colorbar shows different properties for their host galaxies: (a), the star-formation rate (SFR) as retrieved from the literature; (b), the merger stage as estimated from IRAC 3.6μm images; (c) the N/O chemical ratio. For all plots, blank points are associated with galaxies with no estimations of the colored properties. For plot (a) we show on the right a zoom with tracks (red line) of an inflow model within the standard evolution of a galaxy (Köppen & Edmunds, 1999) (see Sec. 7.3.4.2 for more details on this model). Error bars show the uncertainties associated with the corresponding quantities. "A&M+13" (Andrews & Martini, 2013) stands for the local relation reported for SFGs, represented with 10% of uncertainty.

We present in Figure 7.4 the MZR for 77 galaxies, including 41 (U)LIRGs, using the oxygen abundances estimated in this work. We compare our results with the MZR previously reported for SFGs ("A&M+13" track, Andrews & Martini, 2013). We find that the large majority of our sample follows the same trend as the rest of SFGs. However, the most massive ULIRGs ($\log(M_{*}[M_{\odot}]) > 10.5$) tend to lie towards the low side of the MZR, indicating that they have slightly lower metallicity as compared to the expected value for their stellar mass, confirming what has been also reported in previous studies (Pereira-Santaella et al., 2017), although the deviations that we find are smaller than the values found by other studies (Rupke et al., 2008). Interestingly, four galaxies namely Haro11, IRAS12112+0305, IRAS20551-4250 and IRAS23128-5919 strongly deviate from the MZR showing metallicities lower by a factor of $\gtrsim 2$ than expected for these *deep-diving* (U)LIRGs stellar masses according to the MZR. While Haro11 is not a ULIRG galaxy, this star-forming galaxy is reported to be a well known merger dominated galaxy that shared many of properties (Östlin et al., 2015; Östlin et al., 2021) observed in (U)LIRGs. Notably, IRAS12112+0305 was previously reported to have a super-solar abundance ($\sim 2\mathrm{Z}_\odot$; Chartab et al., 2022), while IRAS20551-4250 and IRAS23128-5919 were reported to have abundances close to the values expected from the MZR considering their masses (Herrera-Camus et al., 2018). These high estimations of O/H are driven by the nearly solar N/O values obtained here. However, our O/H estimation – independent of N/O– is significantly lower, thus suggesting a more complex mixing process of the gas affecting their chemical composition. These deviations from the local relation between N/O–O/H found in SFGs have been also reported for other types of galaxies such as *Green Pea* Galaxies (Amorín et al., 2010).

We show in Figure 7.4 that these *deep-diving* (U)LIRGs have the highest SFR values in our sample ($> 100\ \mathrm{M}_\odot{\cdot}\mathrm{yr}^{-1}$) and they are in the final stages of their mergers. Additionally, we find that the N/O ratios for these four galaxies are similar to the Solar ratio, which suggests that they have reached a relatively mature stage of their chemical enrichment history (e.g. Amorín et al., 2010). As galaxy interactions trigger large-scale gas accretion (Howell et al., 2010; Joseph & Wright, 1985; Kennicutt & Evans, 2012), these results imply that during the merging process of (U)LIRGs, metal-poor gas is accreted towards the central region of the galaxies, which dilutes the metal abundances relative to hydrogen, fuels star formation, but keeps the N/O ratio unaffected because it is independent of the effects of a massive infall of hydrogen. Additionally, intermediate-mass stars of these galaxies do not have enough time to boost the nitrogen production from CNO cycles (e.g. Vincenzo & Kobayashi, 2018). As also shown in Figure 7.5 (a), these *deep-diving* (U)LIRGs also deviate from the FMR relation, implying that these (U)LIRGs are likely out of the self-regulated equilibrium between gas accretion and star formation.

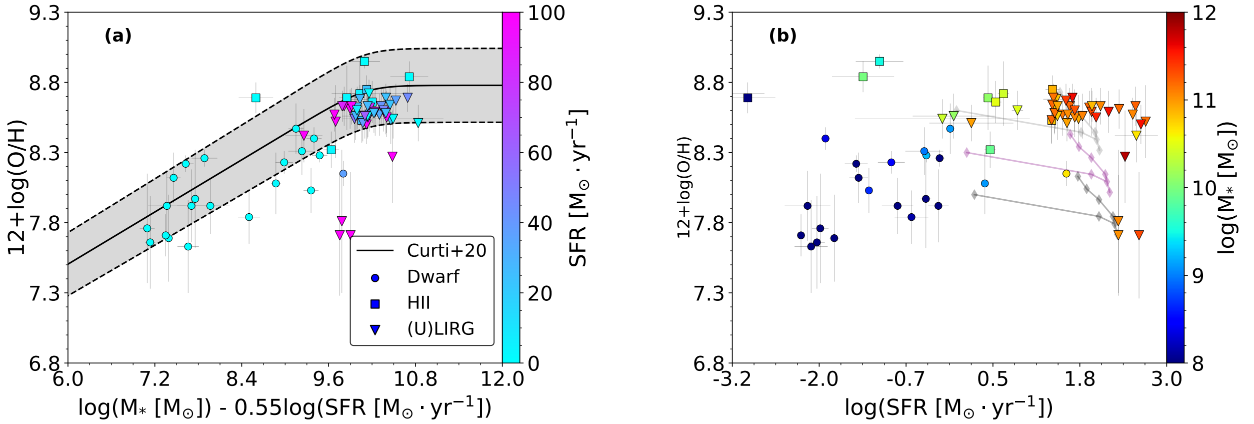

Figure 7.5: Relations between SFR, stellar mass and metallicity. (a) shows the FMR relation for log(M_* [M$_\odot$]) - αlog(SFR [M$_\odot$·yr^{-1}]) assuming $\alpha = 0.55$ (Curti et al., 2020). (b) shows the relation between O/H and SFR for our sample of galaxies, while semi-transparent lines represent tracks obtained in simulations of mergers of galaxies with the same stellar mass (Montuori et al., 2010), considering different initial conditions. Error bars show the uncertainties associated with the corresponding quantities.

To strengthen the case for massive infall of gas in these *deep-diving* (U)LIRGs, we discuss two models that reproduce the behaviour of these inflows. In Figure 7.4 (a), we present a basic infall model (Köppen & Edmunds, 1999), in which the analyzed galaxy (or common envelope of two galaxies) experiences a drop of metallicity over a period of time between 100 to 1000 Myr. These timescales further support our scenario and explain why only four galaxies (*deep-diving* (U)LIRGs) in our sample were captured in the process, as these timescales are really short for a ~12 Gyr old-like galaxy. Once the merger process is completed and stars begin to pollute the ISM again, the resulting galaxy increases its metallicity. According to this model, enriched gas removal from outflows is necessary for the merger to recover the metallicity expected from the MZR for a galaxy of that stellar mass. While mass loading factors measured in ULIRG outflows typically show moderate values (Arribas et al., 2014; Cazzoli et al., 2016; Pereira-Santaella et al., 2018), a high metal-loading factor in massive galaxies can still be expected if the outflowing gas is enriched and the gas-phase ISM metallicity drops significantly due to metal-poor gas accretion (Sanders et al., 2021). Assuming that the outflow is characterized by solar metallicity, then the metal loading factor needed in the model ranges in $\sim 2-10$, which is consistent with the reported values for local SFGs (Sanders et al., 2021). In Figure 7.5 (b) we present tracks that correspond to different stages in a merger process between two galaxies of similar masses, as inferred from simulations (Montuori et al., 2010) in the SFR-O/H relation which is known to play an important role in the MZR. While these trends are dependent on the initial conditions of the involved galaxies, they all point towards a drop in metallicity which corresponds to a period of time of $600-850$ Myr during the merger process (Montuori et al., 2010), consistent with the times derived for our infall model. While preliminary analysis of chemical abundances with spatially-resolved optical data (Rich et al., 2012) supports the gas flow scenario driven by the merger, further studies using spatially-resolved IR data following the methodology here described will provide more information on the scenario that *deep-diving* (U)LIRGs are undergoing.

Taking into account the whole sample, there are 17 galaxies with high SFRs ($> 60\mathrm{M}_{\odot}\mathrm{yr}^{-1}$), implying that *deep-diving* galaxies represent about 24% of this high SFR subsample. However, regarding the number of galaxies that currently are in later stages of the merger phase, we find 35 galaxies, meaning that *deep-diving* (U)LIRGs represent about 11% of this subsample, consistent with the ratio between the time scale for our model and the life time of the galaxy. Taking into account the characteristics of *deep-diving* galaxies (high SFR and late merger stages), only 11 galaxies share similar properties. These results suggest that, while the merger interaction is likely triggering this scenario, we should bear in mind that some galaxies might have already experienced the *deep-diving* phase (i.e. late merger stage but low SFR) while others might have not experienced a massive inflow of metal-poor gas.

7.5 CONCLUSIONS

In summary, our study reveals that (U)LIRGs exhibit *loops* in the MZR due to the rapid infall of massive clouds of metal-poor gas that promote violent star formation in these galaxies (e.g. Armus et al., 2009). This scenario explains several observed properties of (U)LIRGs, including the discrepancy among different chemical models in reproducing the dust content of these galaxies (e.g. Calura et al., 2008; Herrero-Illana et al., 2019), the required fuel to sustain their high star formation rates (e.g. Bustamante et al., 2018), and the anomalous low metal content of mid- and late-merger stage galaxies despite their high N/O ratios indicative of an advanced chemical stage. Both simulations and simple inflow models can reproduce this scenario, and once the infall phase is complete, the role of outflows (e.g. Arribas et al., 2014; Cazzoli et al., 2016; Pereira-Santaella et al., 2018) is crucial for the galaxy to regain its initial metal content. Under these conditions, the build up of heavy elements and the stellar mass growth are not self-regulated (e.g. Sharda et al., 2021) by the gas equilibrium prescription applied to main-sequence galaxies. Overall, due to the short timescales during which the infall phase can be captured, only a few galaxies in our sample demonstrate clear evidence of this scenario.

8

CONCLUDING REMARKS

8.1 SUMMARY

The research carried out throughout this thesis has demonstrated that a proper understanding and modeling of the physical and chemical properties of the ISM are invaluable tools to constrain chemical evolution of galaxies. Our aim in this work was to provide plasma diagnostics from infrared emission lines, demonstrating the limitations of optical studies and developing techniques that can provide robust and self-consistent estimations of chemical abundances for heterogeneous samples of galaxies. In this section, we briefly review the main conclusions from this research, starting from specific ones (Sec. 8.1.1) and concluding with the general remarks that summarize this thesis as a whole (Sec. 8.1.2)

8.1.1 *Conclusions*

- In Chapter 3 we have analyzed a sample of galaxies hosting LINER activity from MaNGA, focusing our study on the nuclear regions dominated by the LINER-like emission. First of all, we have obtained that classical optical diagnostics, despite their usefulness in large samples of galaxies, cannot entirely rule out some feasible combinations of chemical and physical conditions of the ionized gas for different ionizing sources. Therefore, we have tested three different scenarios: standard AGN activity, inefficient AGN activity and pAGB emission. The analysis of the chemical composition of the gas-phase ISM reveals that the nitrogen-to-oxygen [log(N/O)] abundance ratio can be estimated with very little uncertainty, as the different tested ionizing scenarios lead to similar estimations. On the contrary, the derivation of oxygen abundance [12+log(O/H)] is extremely affected by the assumed ionizing source. Overall, nuclear regions of LINER-like galaxies are characterized by solar and supra-solar N/O ratios and by a wide range (from sub- to suprasolar) of O/H abundances. We have also concluded that the AGN nature is the the most adequate for these objects.
- In Chapter 4 we have combined the analysis of a sample of LINER-like galaxies from MaNGA with the analysis, for the first time, of their gas-phase metallicity radial gradients. We have obtained that the great majority of our sample of galaxies show departures from the single linear radial gradient for both O/H and N/O chemical abundance ratios, which do not necessarily follow the same trend, and that the metallicity radial gradient shape is not correlated with the stellar mass. We have proposed a model in which AGN-driven feed (inflows) and feedback (outflows) together with star formation, might be responsible for the hydrodynamical processes that shape gas-phase metallicity gradients in galaxies hosting AGN activity.
- In Chapter 5 we have presented an updated version of the HII-CHI-Mistry code, which allows us to estimate chemical abundances from infrared emission lines in both SFGs and AGNs. We have demonstrated the potential of this tool to provide, whenever possible, independent estimations for N/O, O/H and ionization parameters [log(U)]. Our test sample reveal that AGNs are mainly characterized by solar and subsolar metallicities, with log(N/O) ratios clustering around solar values. The analysis of their optical counterparts have revealed a discrepancy between optical and infrared estimations that does not correlate with electron

density, the ionization parameter or the estimation itself, implying that they might be associated to cold regions traced only by infrared emission lines that might be characterized by subsolar metallicities.

- In Chapter 6 we have performed, for the first time, an independent estimation of oxygen, sulfur and nitrogen abundances based on infrared emission lines in an heterogeneous sample of SF- and AGN-dominated galaxies. While oxygen and nitrogen estimations are consistent with previous determinations, we have obtained that sulfur-to-oxygen [log(S/O)] abundance ratios are mainly solar in the case of SFGs, there are large deviations mainly found in (Ultra)-Luminous Infrared Galaxies [(U)LIRGs] and Seyfert galaxies. In the first case, we have obtained that neither density nor stellar mass are responsible for these deviations, implying that it might be associated to complexity on how sulfur is produced by stellar nucleosynthesis. In the case of AGNs, although we have found a similar result, we have not detected any galaxy with suprasolar S/O ratios (contrary to the case of SFGs).

- In Chapter 7 we have analyzed chemical abundances in a sample of (U)LIRGs whose main active mechanism is star formation. By means of infrared emission lines, which peer through the dusty environments that characterize these objects, we have obtained that (U)LIRGs remain close to the mass-metallicity relation, in contrast with previous studies based on optical estimations. As HII-CHI-Mistry-IR allows us to perform an independent estimation of N/O and O/H, we obtain that a small group of these galaxies exhibit heavily depressed oxygen abundances (O/H$\sim 7.7 - -8.1$), whereas N/O ratios are mainly solar, indicative of gas mixing processes and suggesting that massive infalls of metal-poor gas are fueling the intense star formation in these objects. We have also detected that systems are mainly in interaction, implying that the merger processes might be the driver of such inflows. We have also shown that this scenario, according to a simple chemical evolution model, happens in relatively short-time scales, explaining the low number of galaxies in this particular phase. Overall, we have demonstrated that chemical enrichment and stellar mass growth in (U)LIRGs occurred out-of-equilibrium.

8.1.2 *General remarks*

- As we have obtained throughout this research, it is important to analyze the chemical enrichment in galaxies hosting AGN. If all galaxies have undergone or are undergoing the AGN phase at some points of their evolution, then the analysis of the chemical conditions of the gas-phase ISM can provide us clues with the initial conditions under which the AGN might start. If not all galaxies undergo the AGN phase, then the chemical footprints of their ISM can reveal which mechanisms have not taken place yet. In both cases, it is necessary a robust and consistent methodology to simultaneously analyze AGN-hosting and star-forming galaxies. As the direct method is only feasible in very specific conditions, a tool such as HII-CHI-Mistry, which is consistent with the direct method and has been tested in both AGNs and SFGs, has been demonstrated to be useful for increasing the statistics of galaxy evolution studies. For example, we have shown in Chapter 4 that AGN activity might affect the chemical abundance distribution across the galaxy disks, and, hence, the chemical content of the Narrow Line Region seems to be more representative of the chemical footprints within the innermost parts of galaxy disks.

- Photoionization models are essential in the estimation of chemical abundances. For objects from which auroral lines can be retrieved from optical observations, the ionization correction factors (ICFs) are mainly calibrated by means of photoionization models. For objects whose ionizing source is unknown, photoionization models can be used to constrain the physical and chemical properties, and provide predictions that can be revised in follow-up observations. However, as these detailed analyses are not feasible in large samples of galaxies, the use of already computed grids of models is helpful to provide a first approximation to the conditions of the ISM in large samples of galaxies. From them, we can select from that initial study the interesting outliers, and then perform more detailed and specific studies for those objects that deviate from the general trends.

- Chemical evolution studies targeting abundances in the gas-phase ISM should be performed simultaneously analyzing the oxygen and nitrogen content, but without any prior assumption between them. As we have shown in all of our works, an independent estimation of N/O is key in assessing whether the resulting oxygen abundances are the result of the intrinsic stellar nucleosynthesis enrichment or rather they reflect changes due to the hydrodynamical processes that affect the distribution of metals. For example, in Chapter 7 we demonstrated the infall scenario as nitrogen abundances were in concordance to what was expected for their stellar masses. Moreover, in Chapter 3 we also demonstrated that the estimation of log(N/O) can be done without the need of having a prior knowledge on the ionizing source. Essentially, the same recipes for estimating log(N/O) can be blindly applied to large samples of galaxies, providing a good approximation on how chemically mature they are.
- The previous three remarks highlighted from our study naturally converge to the use of infrared emission lines in chemical evolution studies. First of all, infrared emission lines have been proven to provide the best diagnostics for the AGN activity in galaxies, as highly-excited emission lines can be retrieved in the infrared regime (see Chapters 2 and 5). Second, the infrared regime is not affected by dust extinction and the observed lines show little to no dependence on electron temperature, allowing us to study dusty-embedded and cool regions, which are associated to the star forming activity that contributes to galaxy evolution (see Chapter 7). Third, the infrared regime is very rich in emission lines from non-depleted elements such as neon and argon, allowing for robust determination of the metal content of the gas-phase ISM without the need of quantifying the dust depletion effect. Fourth, the nitrogen-to-oxygen abundance ratio is estimated in the infrared from emission lines from ions whose fraction dominate across most of the gaseous nebulae size, allowing a robust estimation.

8.2 FUTURE LINES OF RESEARCH

Throughout this research we have made use of archival data from past missions, showing the potential of our methodology and allowing us to obtain remarkable results such as the detection of *deep-diving* (U)LIRGs. However, with the launch on JWST, and the future planned missions such as METIS at the ELT, there is a bright future for infrared spectroscopic studies. As both, quantity and quality of the data increase, we might be able to deepen our knowledge in some of the still-standing issues that this thesis highlights:

- **Diagnostic diagrams built upon metallicity estimations**: The use of diagnostics diagrams is a key part in the analysis and modeling of galaxy spectra. Whereas IR diagrams provide unbiased constraints on the dominant source of ionization, optical diagnostic diagrams assumed average conditions of the metallicity for the observed ISM. The use of optical diagnostic diagrams is in most cases the only available option for high-redshift galaxies (such as those observed in JWST deep surveys) or for the search of AGN activity within dwarf galaxies. As we have highlighted in this thesis, the nitrogen-to-oxygen content can be estimated without much bias, and upon that estimation, empirical constraints can be provided. Thus, providing a classification of the regions in diagnostic diagrams (BPT and WHAN) based on the estimated values of N/O can significantly improve galaxy spectra classification.

- **Interplay between AGN and SF activity**: Chemical evolution studies mainly target one of the two group of galaxies, but in both cases, it is assumed that one dominates over the other. Indeed, we still lack refinery in how to create photoionization models that actually simultaneously mimic the conditions for galaxies where star formation and AGN activity are both relevant. Besides very simple approaches (as the one offer in this work by means of pure linear combinations), the realm of photoionization models accounting simultaneously for both scenarios is little explored. By means of infrared IFS data (such as that from JWST), we can trace up to which extent highly-excited emission lines are traced, providing a quantification to the extent of AGN activity, and allowing us to refine composite models of AGN and SF in those regions.

- **Infrared radial metallicity gradients**: Infrared IFS data is not only helpful to disentangle AGN and SF activity, but also to revisit radial metallicity gradients in galaxies whose central regions are dominated by AGN activity. First of all, by means of infrared emission lines, we can have a better understanding on whether regions located close to the nuclear parts are HII regions or part of the so-called extended narrow line region. Second, dusty and cold regions (which are expected to be also characterized by high-metallicities) are traceable through IR emission lines whereas they remain unseen in most of the optical IFS studies. Third, infrared estimations of chemical abundances can be easily performed even in SF-dominated regions characterized by extremely high metallicities, relying on non-depleted elements that might provide a better understanding on whether radial metallicity gradients present breaks or not.

- **Dust attenuation effects in the infrared regime**: Throughout this work we have assumed that dust attenuation effects are negligible when analyzing IR spectroscopic data. Whereas this statement is true in absolute terms, recent studies have shown that IR emission lines might suffer different effects due to the impact of silicate features (e.g. Gordon et al., 2023), being the silicate feature at 10 μm the most important. Our preliminary study in Chapter 6 shows that this silicate feature, affecting [S IV] emission line, is not a driver of the deviations from the S/O solar ratio. Nevertheless, a proper characterization of the dust attenuation curve in the IR regime is beyond the scope of this work. The spectral coverage and performance of the JWST would substantially help in determining whether the dust content might responsible for some of the discrepancies observed in this work, such as the optical-infrared abundance discrepancy or the deviations from the S/O solar ratio.

- **Occurrence of the deep-diving phase**: As we have reviewed in Chapter 7, the *deep-diving* phase usually lasts for ~ 600 Myr, allowing us to explain the statistics observed in our sample of (U)LIRGs. However, there are still some caveats. First of all, we have only observed the *deep-diving* phase in massive $> 10^{10.5}$ $M_{\odot}$ galaxies, but this scenario can also be applied to other less massive systems. Second, we have pointed to a merger-driven scenario as galaxies are in their late merger stages, allowing us to explain why hydrodynamics within the galaxy has been perturbed, but other non-interacting systems display similar behaviors (e.g. Green Pea galaxies, Amorín et al. 2010). Third, at redshifts $\sim 1-4$, most of the star formation occurs in dusty embedded environments (e.g. Förster Schreiber & Wuyts, 2020), therefore rest-frame IR diagnostics are essential to determine whether star formation at Cosmic Noon happens more frequently in infall dominated scenarios that drive galaxies out of equilibrium or not.

- **Lower and upper ends of the mass-metallicity relation**: The characterization of relations such as MZR, FMR and MNOR obtain from low-redshift galaxies (offering the largest statistics for galaxy evolution studies) are not fully established at all mass ranges. In the upper end, depending on the methodology used for the estimation of chemical abundances, the turn-off point and plateau for the relations (in the MZR and FMR cases) might change. Moreover, given the properties of AGN-host galaxies (see Chapters 3 and 5), the analysis of statistically significant samples of these galaxies might help in understanding what happens in massive galaxies. Regarding the lower end, local analogs (Green Peas, Blueberry galaxies, ...) of high-redshift galaxies (for which the fraction of these less massive systems is expected to significantly increase) have been extensively used to understand what happens in this regime (e.g. Amorín et al., 2010; Yang et al., 2017a, 2017b), but there is still no consensus on whether there is a change or not in these relations for low-mass galaxies, specially when analyzing the possible evolution at higher redshifts (e.g. Chemerynska et al., 2024; Curti et al., 2024). As shown by Amorín et al. (2010), the picture of chemical enrichment in these systems must be study not only by means of the oxygen content of the gas-phase ISM, but also through nitrogen.

- **Enrichment of the ISM at different cosmic epochs**: The Early Data Release from the Dark Energy Spectroscopic Instrument (DESI EDR; DESI Collaboration et al., 2024) has already demonstrated its potential for the analysis of chemical abundances in galaxies at redshifts > 0.2 (e.g. Zinchenko et al., 2024). With the new data releases such as DR1 (DESI Collaboration et al., 2025) and future ones, our understanding of chemical enrichment across different epochs will be benefited by the significant increase in the statistics. Together with studies from JWST (e.g. Nakajima et al., 2023), although limited to a significantly lower number of galaxies, the possible cosmic evolution of local relations such as the MZR or the N/O vs O/H relations can be analyzed offering us the opportunity to test its validity and refined our chemical evolution models.

- **Influence of the environmental context**: Several studies have pointed out that galaxy environment might introduce changes in how galaxies chemically evolve (e.g. Peluso et al., 2023; Rowntree et al., 2025). Therefore, studies of chemical enrichment in clusters of galaxies (e.g. Petropoulou et al., 2011, 2012), for which a flexible tool such as HII-CHI-Mistry is essential to account for the great variety of ionizing scenarios in the different cluster members, might provide more insights on how to quantify the environmental influence in galaxy evolution. The new instrument for the 3.5m telescope at Calar Alto Observatory, the Tetra-ARm Super-Ifu Spectrograph (TARSIS), and the CATARSIS legacy survey of galaxy clusters will provide an excellent laboratory to perform studies of chemical enrichment in clusters.

Part III

APPENDIX

A

DATA TABLES

A.1 ATOMIC COEFFICIENTS FOR THE CALCULATION OF IONIC ABUNDANCES

In this section we provide some useful values of the atomic coefficients needed for the calculation of ionic abundances. Due to the high dependence on both electron density (n_e) and temperature (T_e), we encourage the reader to compute them from software managing atomic databases (e.g. PYNEB) or by means of useful relations as those presented in Pérez-Montero (2017).

Table A.1: Atomic coefficients (D) for the determination of oxygen ionic abundances. Computed from PYNEB (Luridiana et al., 2015).

O^0	$D\left(n_e, T_e, \lambda_1 = 6300Å, \lambda_H = 4681Å\right)$			
	$T_e = 7.5 \cdot 10^3$ K	$T_e = 1 \cdot 10^4$ K	$T_e = 1.5 \cdot 10^4$ K	$T_e = 2.5 \cdot 10^4$ K
$n_e = 100$ cm^{-3}	1568.55	5273.20	19876.64	44171.85
$n_e = 500$ cm^{-3}	1566.41	5268.46	19864.61	44144.63
$n_e = 1000$ cm^{-3}	1565.84	5266.86	19857.58	44123.94
$n_e = 5000$ cm^{-3}	1563.30	5256.11	19795.92	43959.99

O^+	$D\left(n_e, T_e, \lambda_1 = 3726Å, \lambda_H = 4681Å\right)$			
	$T_e = 7.5 \cdot 10^3$ K	$T_e = 1 \cdot 10^4$ K	$T_e = 1.5 \cdot 10^4$ K	$T_e = 2.5 \cdot 10^4$ K
$n_e = 100$ cm^{-3}	2880.53	11692.56	51083.95	113048.95
$n_e = 500$ cm^{-3}	3138.43	12668.14	54645.35	119494.48
$n_e = 1000$ cm^{-3}	3203.42	12977.77	55885.22	121547.90
$n_e = 5000$ cm^{-3}	2472.92	10362.40	45501.41	98633.71

O^{++}	$D\left(n_e, T_e, \lambda_1 = 5007Å, \lambda_H = 4681Å\right)$			
	$T_e = 7.5 \cdot 10^3$ K	$T_e = 1 \cdot 10^4$ K	$T_e = 1.5 \cdot 10^4$ K	$T_e = 2.5 \cdot 10^4$ K
$n_e = 100$ cm^{-3}	9242.02	28316.39	93818.97	180348.98
$n_e = 500$ cm^{-3}	9345.91	28563.10	94394.41	181202.44
$n_e = 1000$ cm^{-3}	9399.14	28692.47	94703.16	181905.70
$n_e = 5000$ cm^{-3}	9439.96	28790.71	94883.18	181905.68

O^{++}	$D\left(n_e, T_e, \lambda_1 = 52\mu m, \lambda_H = 4.05\mu m\right)$			
	$T_e = 7.5 \cdot 10^3$ K	$T_e = 1 \cdot 10^4$ K	$T_e = 1.5 \cdot 10^4$ K	$T_e = 2.5 \cdot 10^4$ K
$n_e = 100$ cm^{-3}	69780.17	91259.85	138045.26	188594.52
$n_e = 500$ cm^{-3}	66337.93	87781.26	133594.91	182456.61
$n_e = 1000$ cm^{-3}	55845.42	75096.92	116319.14	160436.65
$n_e = 5000$ cm^{-3}	22569.09	31521.02	51231.89	72921.66

O^{3+}	$D\left(n_e, T_e, \lambda_1 = 25.9\mu m, \lambda_H = 4.05\mu m\right)$			
	$T_e = 7.5 \cdot 10^3$ K	$T_e = 1 \cdot 10^4$ K	$T_e = 1.5 \cdot 10^4$ K	$T_e = 2.5 \cdot 10^4$ K
$n_e = 100$ cm^{-3}	552569.99	742670.68	1082297.43	1393188.25
$n_e = 500$ cm^{-3}	497095.28	671723.30	989912.70	1285604.58
$n_e = 1000$ cm^{-3}	439591.83	597650.66	891842.39	1169737.74
$n_e = 5000$ cm^{-3}	228488.48	317473.50	497290.52	679244.92

Table A.2: Same as Tab. A.1 but for the sulfur coefficients.

S^{+}	$D\left(n_e, T_e, \lambda_1 = 6717\text{Å}, \lambda_H = 4681\text{Å}\right)$			
	$T_e = 7.5 \cdot 10^3$ K	$T_e = 1 \cdot 10^4$ K	$T_e = 1.5 \cdot 10^4$ K	$T_e = 2.5 \cdot 10^4$ K
$n_e = 100$ cm^{-3}	101337.30	229730.72	548978.96	883746.94
$n_e = 500$ cm^{-3}	84594.18	193808.44	468644.53	760579.41
$n_e = 1000$ cm^{-3}	71575.77	164762.00	400527.37	653003.68
$n_e = 5000$ cm^{-3}	36686.10	84135.15	202337.85	329104.5

S^{+}	$D\left(n_e, T_e, \lambda_1 = 6731\text{Å}, \lambda_H = 4681\text{Å}\right)$			
	$T_e = 7.5 \cdot 10^3$ K	$T_e = 1 \cdot 10^4$ K	$T_e = 1.5 \cdot 10^4$ K	$T_e = 2.5 \cdot 10^4$ K
$n_e = 100$ cm^{-3}	75319.47	170030.11	406899.55	656253.68
$n_e = 500$ cm^{-3}	79871.35	178403.96	419656.88	669332.45
$n_e = 1000$ cm^{-3}	80967.76	180290.70	420733.77	667271.08
$n_e = 5000$ cm^{-3}	63572.26	142566.14	331884.60	526148.00

S^{++}	$D\left(n_e, T_e, \lambda_1 = 9530\text{Å}, \lambda_H = 4681\text{Å}\right)$			
	$T_e = 7.5 \cdot 10^3$ K	$T_e = 1 \cdot 10^4$ K	$T_e = 1.5 \cdot 10^4$ K	$T_e = 2.5 \cdot 10^4$ K
$n_e = 100$ cm^{-3}	85528.38	162057.11	334637.06	506669.19
$n_e = 500$ cm^{-3}	86792.78	163706.48	336556.87	508511.13
$n_e = 1000$ cm^{-3}	87732.41	164967.60	338099.82	510049.70
$n_e = 5000$ cm^{-3}	89769.80	167654.45	341152.09	512875.35

S^{++}	$D\left(n_e, T_e, \lambda_1 = 18.7\mu\text{m}, \lambda_H = 4.05\mu\text{m}\right)$			
	$T_e = 7.5 \cdot 10^3$ K	$T_e = 1 \cdot 10^4$ K	$T_e = 1.5 \cdot 10^4$ K	$T_e = 2.5 \cdot 10^4$ K
$n_e = 100$ cm^{-3}	995720.51	1257137.17	1817908.77	2371164.47
$n_e = 500$ cm^{-3}	1147529.45	1425327.20	1987904.15	2533776.93
$n_e = 1000$ cm^{-3}	1172965.38	1467063.98	2042739.75	2592727.26
$n_e = 5000$ cm^{-3}	822188.76	1088426.80	1613956.66	2124496.78

S^{3+}	$D\left(n_e, T_e, \lambda_1 = 10.5\mu\text{m}, \lambda_H = 4.05\mu\text{m}\right)$			
	$T_e = 7.5 \cdot 10^3$ K	$T_e = 1 \cdot 10^4$ K	$T_e = 1.5 \cdot 10^4$ K	$T_e = 2.5 \cdot 10^4$ K
$n_e = 100$ cm^{-3}	3549916.13	4586248.17	6520410.25	8336150.61
$n_e = 500$ cm^{-3}	3503383.68	4530404.33	6446960.27	8248540.66
$n_e = 1000$ cm^{-3}	3424556.80	4438094.66	6332978.16	8117769.79
$n_e = 5000$ cm^{-3}	2873826.95	3781538.59	5512211.05	7167803.23

Table A.3: Same as Tab. A.1 but for the nitrogen coefficients.

N$^+$	$D\left(n_e, T_e, \lambda_1 = 6584\text{Å}, \lambda_H = 4681\text{Å}\right)$			
	$T_e = 7.5 \cdot 10^3$ K	$T_e = 1 \cdot 10^4$ K	$T_e = 1.5 \cdot 10^4$ K	$T_e = 2.5 \cdot 10^4$ K
$n_e = 100$ cm^{-3}	20698.14	48170.14	120489.85	200833.25
$n_e = 500$ cm^{-3}	20922.54	48620.96	121716.60	202964.00
$n_e = 1000$ cm^{-3}	20880.79	48561.94	121731.07	203147.72
$n_e = 5000$ cm^{-3}	19900.46	46558.96	117445.30	196780.13

N$^+$	$D\left(n_e, T_e, \lambda_1 = 122\mu\text{m}, \lambda_H = 4.05\mu\text{m}\right)$			
	$T_e = 7.5 \cdot 10^3$ K	$T_e = 1 \cdot 10^4$ K	$T_e = 1.5 \cdot 10^4$ K	$T_e = 2.5 \cdot 10^4$ K
$n_e = 100$ cm^{-3}	21566.90	29698.24	47391.11	66514.68
$n_e = 500$ cm^{-3}	7884.22	11147.11	18381.22	26373.04
$n_e = 1000$ cm^{-3}	4351.07	6189.32	10293.55	14862.45
$n_e = 5000$ cm^{-3}	955.40	1362.10	2274.29	3295.67

N^{++}	$D\left(n_e, T_e, \lambda_1 = 57.3\mu\text{m}, \lambda_H = 4.05\mu\text{m}\right)$			
	$T_e = 7.5 \cdot 10^3$ K	$T_e = 1 \cdot 10^4$ K	$T_e = 1.5 \cdot 10^4$ K	$T_e = 2.5 \cdot 10^4$ K
$n_e = 100$ cm^{-3}	134626.81	178071.91	267839.75	361379.35
$n_e = 500$ cm^{-3}	79745.61	108654.97	169700.74	234563.44
$n_e = 1000$ cm^{-3}	52802.61	73016.15	116329.22	162964.39
$n_e = 5000$ cm^{-3}	14387.59	20285.34	33242.92	47515.11

Table A.4: Same as Tab. A.1 but for the neon coefficients.

Ne^{+}	$D\,(n_e, T_e, \lambda_1 = 12.8\mu\mathrm{m}, \lambda_H = 4.05\mu\mathrm{m})$			
	$T_e = 7.5 \cdot 10^3$ K	$T_e = 1 \cdot 10^4$ K	$T_e = 1.5 \cdot 10^4$ K	$T_e = 2.5 \cdot 10^4$ K
$n_e = 100\ \mathrm{cm}^{-3}$	72866.03	94728.54	138114.71	180030.66
$n_e = 500\ \mathrm{cm}^{-3}$	73408.92	95314.00	138690.22	180578.17
$n_e = 1000\ \mathrm{cm}^{-3}$	73583.34	95496.87	138850.61	180711.69
$n_e = 5000\ \mathrm{cm}^{-3}$	73868.62	95705.88	138886.85	180564.80

Ne^{++}	$D\left(n_e, T_e, \lambda_1 = 3868\text{Å}, \lambda_H = 4861\text{Å}\right)$			
	$T_e = 7.5 \cdot 10^3$ K	$T_e = 1 \cdot 10^4$ K	$T_e = 1.5 \cdot 10^4$ K	$T_e = 2.5 \cdot 10^4$ K
$n_e = 100\ \mathrm{cm}^{-3}$	2384.95	9191.57	37702.82	80192.73
$n_e = 500\ \mathrm{cm}^{-3}$	2381.50	9183.09	37685.44	80163.72
$n_e = 1000\ \mathrm{cm}^{-3}$	2380.63	9180.96	37681.15	80155.23
$n_e = 5000\ \mathrm{cm}^{-3}$	2380.91	9181.96	37673.59	80148.15

Ne^{++}	$D\,(n_e, T_e, \lambda_1 = 15.5\mu\mathrm{m}, \lambda_H = 4.05\mu\mathrm{m})$			
	$T_e = 7.5 \cdot 10^3$ K	$T_e = 1 \cdot 10^4$ K	$T_e = 1.5 \cdot 10^4$ K	$T_e = 2.5 \cdot 10^4$ K
$n_e = 100\ \mathrm{cm}^{-3}$	151409.03	194935.44	274969.45	353513.07
$n_e = 500\ \mathrm{cm}^{-3}$	151872.49	195377.21	275215.18	353567.03
$n_e = 1000\ \mathrm{cm}^{-3}$	151420.76	194817.00	274427.46	352571.50
$n_e = 5000\ \mathrm{cm}^{-3}$	146169.66	188458.84	266369.69	342968.21

Ne^{4+}	$D\,(n_e, T_e, \lambda_1 = 14.3\mu\mathrm{m}, \lambda_H = 4.05\mu\mathrm{m})$			
	$T_e = 7.5 \cdot 10^3$ K	$T_e = 1 \cdot 10^4$ K	$T_e = 1.5 \cdot 10^4$ K	$T_e = 2.5 \cdot 10^4$ K
$n_e = 100\ \mathrm{cm}^{-3}$	1729475.12	1984098.45	2345912.43	2568549.49
$n_e = 500\ \mathrm{cm}^{-3}$	1714200.25	1971666.92	2336331.56	2562103.93
$n_e = 1000\ \mathrm{cm}^{-3}$	1678384.41	1940627.39	2312105.87	2544079.15
$n_e = 5000\ \mathrm{cm}^{-3}$	1364618.59	1647584.32	2067376.84	2348886.96

Ne^{4+}	$D\,(n_e, T_e, \lambda_1 = 24.3\mu\mathrm{m}, \lambda_H = 4.05\mu\mathrm{m})$			
	$T_e = 7.5 \cdot 10^3$ K	$T_e = 1 \cdot 10^4$ K	$T_e = 1.5 \cdot 10^4$ K	$T_e = 2.5 \cdot 10^4$ K
$n_e = 100\ \mathrm{cm}^{-3}$	1940573.15	2239681.45	2678162.10	2975859.09
$n_e = 500\ \mathrm{cm}^{-3}$	1708798.61	2019681.30	2484689.18	2808095.14
$n_e = 1000\ \mathrm{cm}^{-3}$	1473792.13	1786179.27	2268073.76	2614051.03
$n_e = 5000\ \mathrm{cm}^{-3}$	656597.05	879401.36	1288761.31	1640733.11

A.2 DATABASE FOR CHAPTERS 3 AND 4

We present in this appendix the full dataset used for the work presented in Chapters 3 and 4. Tab. A.5 contains all ancillary data for our sample of galaxies. Tab. A.6 lists all optical spectroscopic properties of the nuclear regions of our sample of LINER-like galaxies. Tab. A.7 - A.9 list all the estimations of chemical abundances and ionization parameters for the nuclear regions of our sample. All tables are available in electronic form at the CDS[1].

Table A.5: List of galaxies and host galaxy properties in our sample of LINER-like galaxies. MaNGA ID (1) is assigned following the convention "[PLATE]-[IFUDESIGN]". Redshift (2) is directly taken from the data reduction processed files. Classifications based on the BPT diagrams (3) and WHAN diagrams (4) are obtained using non-corrected from reddening emission line fluxes. The R_{50} petrossian isophote (5) and the stellar (6) and H I (7) masses are taken from the NASA-Sloan Atlas (NSA) catalog. The complete version of this table is available at the CDS.

MaNGA ID (1)	z (2)	Class. BPT (3)	Class. WHAN (4)	R_{50} [arcsec] (5)	$\log M_*$ [$M_\odot$] (6)	$\log M_{HI}$ [$M_\odot$] (7)
10215 – 3703	0.0320	LIN	RG	3.2158	10.1102	–
10498 – 6104	0.0507	LIN	RG	3.0719	10.2670	–
10504 – 3703	0.0230	LIN	RG	3.6443	10.0380	–
10510 – 6103	0.0195	LIN	wAGN	12.2742	10.6460	–

Table A.6: Optical spectroscopic information for our sample of LINER-like galaxies. Column (1): MaNGA ID. Column (2): equivalent width of Hα. Column (3): extinction coefficient based on Howarth (1983) extinction law. Columns (4)-(10): optical emission line ratios [O II]$\lambda\lambda$3727, 3729Å, [Ne III]λ3868Å, [O III]λ4959Å, [O III]λ5007Å, [N II]λ6548Å, [N II]λ6584Å, and [S II]$\lambda\lambda$6717, 6731Å corrected from reddening and referred to Hβ. The complete version of this table is available at the CDS.

MaNGA ID (1)	W_{H_α} [Å] (2)	$c\left(H_\beta\right)$ (3)	[O II]$\lambda\lambda$3727, 3729Å (4)	...	[S II]λ6717Å (9)	[S II]λ6731Å (10)
10215 – 3703	2.74	0.1197 ± 0.0871	3.146 ± 0.283	...	1.407 ± 0.144	0.865 ± 0.100
10498 – 6104	2.5	0.4298 ± 0.1100	2.844 ± 0.357	...	1.028 ± 0.133	0.761 ± 0.108
10504 – 3703	2.18	–	2.858 ± 0.327	...	0.985 ± 0.154	0.943 ± 0.153
10510 – 6103	3.87	1.4050 ± 0.1157	14.617 ± 1.595	...	1.458 ± 0.183	1.529 ± 0.193

Table A.7: Estimated oxygen abundances in the nuclear region of our sample of LINER-like galaxies based on different grids of photoionization models. Column (1): MaNGA ID. Columns (2)-(12): oxygen abundances for each grid considered. The complete version of this table is available at the CDS.

MaNGA ID (1)	12+log(O/H)$_{AGN\ \alpha_{OX}=-0.8}$ (2)	12+log(O/H)$_{AGN\ \alpha_{OX}=-1.0}$ (3)	...	12+log(O/H)$_{pAGB\ T_{eff}=150kK}$ (12)
10215 – 3703	8.73 ± 0.12	8.56 ± 0.10	...	8.32 ± 0.08
10498 – 6104	8.72 ± 0.24	8.66 ± 0.22	...	8.24 ± 0.09
10504 – 3703	8.71 ± 0.21	8.64 ± 0.20	...	8.28 ± 0.08
10510 – 6103	8.73 ± 0.06	8.70 ± 0.06	...	8.82 ± 0.05

---

[1] https://cdsarc.cds.unistra.fr/viz-bin/cat/J/A+A/694/A18.

Table A.8: Estimated nitrogen-to-oxygen abundance ratios in the nuclear region of our sample of LINER-like galaxies based on different grids of photoionization models. Column (1): MaNGA ID. Columns (2)-(12): nitrogen-to-oxygen abundance ratios for each grid considered. The complete version of this table is available at the CDS.

MaNGA ID (1)	$\log(\mathrm{N/O})_{AGN\ \alpha_{OX}=-0.8}$ (2)	$\log(\mathrm{N/O})_{AGN\ \alpha_{OX}=-1.0}$ (3)	... ...	$\log(\mathrm{N/O})_{pAGB\ T_{eff}=150kK}$ (12)
10215 – 3703	-0.80 ± 0.15	-0.74 ± 0.13	...	-0.63 ± 0.11
10498 – 6104	-0.67 ± 0.11	-0.67 ± 0.12	...	-0.55 ± 0.10
10504 – 3703	-0.68 ± 0.14	-0.64 ± 0.10	...	-0.57 ± 0.10
10510 – 6103	-1.20 ± 0.13	-1.14 ± 0.09	...	-1.06 ± 0.11

Table A.9: Estimated ionization parameters in the nuclear region of our sample of LINER-like galaxies based on different grids of photoionization models. Column (1): MaNGA ID. Columns (2)-(12): ionization parameters for each grid considered. The complete version of this table is available at the CDS.

MaNGA ID (1)	$\log(U)_{AGN\ \alpha_{OX}=-0.8}$ (2)	$\log(U)_{AGN\ \alpha_{OX}=-1.0}$ (3)	... ...	$\log(U)_{pAGB\ T_{eff}=150kK}$ (12)
10215 – 3703	-3.59 ± 0.08	-3.71 ± 0.04	...	-3.66 ± 0.08
10498 – 6104	-3.46 ± 0.08	-3.53 ± 0.07	...	-3.50 ± 0.07
10504 – 3703	-3.45 ± 0.11	-3.53 ± 0.12	...	-3.52 ± 0.08
10510 – 6103	-3.74 ± 0.05	-3.78 ± 0.04	...	-3.81 ± 0.04

A.3 DATABASE FOR CHAPTER 5

We present in this appendix the full dataset of mid- to far-IR spectroscopy of our sample of 58AGN (Tab. A.10) and optical spectroscopic information retrieved from the literature (Tab. A.12). Tab. A.11 and A.13 show our estimations (infrared and optical respectively) of chemical abundances and ionization parameters for our sample. All tables are available in electronic form at the CDS[2].

Table A.10: List of IR fluxes for our sample of AGN. Column (1): name of the galaxy. Columns (2) and (3): coordinates. Column (4): redshift. Column (5): spectral type. Columns (6)-(21): IR emission line fluxes and their errors in 10^{-14} erg/s/cm^2. Column (22): references for hydrogen recombination line fluxes. References: ALO00 (Alonso-Herrero et al., 2000), ARM07 (Armus et al., 2007), B-S09 (Bernard-Salas et al., 2009), BEL03 (Bellamy et al., 2003), BEL04 (Bellamy & Tadhunter, 2004), BEN04 (Bendo & Joseph, 2004), BRA08 (Brauher et al., 2008), DAN05 (Dannerbauer et al., 2005), FO16 (Fernández-Ontiveros et al., 2016), GOL95 (Goldader et al., 1995), HC18 (Herrera-Camus et al., 2018), IMA04 (Imanishi & Wada, 2004), IMA10 (Imanishi et al., 2010), INA13 (Inami et al., 2013), INA18 (Inami et al., 2018), LAM17 (Lamperti et al., 2017), LAN96 (Lancon et al., 1996), LUT02 (Lutz et al., 2002), MAR10 (Martins et al., 2010), MUE11 (Müller-Sánchez et al., 2011), MUR01 (Murphy et al., 2001), PEN21 (B. Peng et al., 2021), PIQ12 (Piqueras López et al., 2012), PS17 (Pereira-Santaella et al., 2017), REU02 (Reunanen et al., 2002), REU03 (Reunanen et al., 2003), RIF06 (Riffel et al., 2006), SEV01 (Severgnini et al., 2001), SMA12 (Smajić et al., 2012), SPI21 (Spinoglio et al., 2021), VEI97 (Veilleux et al., 1997), VEI09 (Veilleux et al., 2009), YAN21 (Yano et al., 2021), TW (This work). The complete version of this table is available at the CDS.

Name (1)	... (...)	Type (5)	... (...)	[S IV]$\lambda 10.5\mu$m (8)	... (...)	[N II]$\lambda 122\mu$m (20)	[N II]$\lambda 205\mu$m (21)	Ref. (22)
IRAS00198 − 7926	...	S2	...	8.1 ± 0.4	...	–	–	FO16,TW
NGC185	...	S2	...	–	...	–	–	FO16,TW
MCG−01 − 24 − 012	...	S2	...	2.33 ± 0.39	...	–	–	FO16,TW
NGC4593	...	S1.0	...	3.9 ± 0.6	...	2.1 ± 0.3	–	FO16,TW
NGC5506	...	S1h	...	73.5 ± 1.6	...	14.1 ± 1.2	–	FO16,TW
IRAS08572 + 3915	...	ULIRG	...	–	...	0.74 ± 0.15	–	ARM07,VEI09, HC18,YAN21
Arp299A	...	LIRG	...	5.52 ± 1.11	...	10.05 ± 0.78	–	ALO00,INA13, PEN21,SPI21
NGC6240	...	LIN	...	2.6 ± 0.27	...	23.15 ± 2.22	18.46 ± 0.39	INA18,FO16

Table A.11: Chemical abundances estimated from HCm-IR, using the grid of AGN models for $\alpha_{OX} = 0.8$ and the stopping criteria of 2% of free electrons- Column (1): name of the galaxy. Columns (2)-(4): chemical abundances and ionization parameters with their corresponding uncertainties. The complete version of this table is available at the CDS.

Name (1)	12+log(O/H) (2)	log(N/O) (3)	log(U) (4)
IRAS00198 − 7926	8.16 ± 0.34	–	-1.82 ± 0.32
NGC185	–	–	–
MCG−01 − 24 − 012	7.87 ± 0.37	–	-1.59 ± 0.39
NGC4593	7.85 ± 0.39	-0.9 ± 0.27	-1.73 ± 0.35
NGC5506	7.94 ± 0.33	-0.71 ± 0.14	-1.77 ± 0.39
IRAS08572 + 3915	7.97 ± 0.38	-0.83 ± 0.3	-3.17 ± 0.22
Arp299A	–	-0.88 ± 0.27	-3.53 ± 0.07
NGC6240	8.34 ± 0.31	-0.8 ± 0.31	-3.14 ± 0.1

---

[2] https://cdsarc.cds.unistra.fr/viz-bin/cat/J/A+A/666/A115.

Table A.12: List of optical fluxes for our sample of AGN. Column (1): name of the galaxy. Columns (2) and (3): coordinates. Column (4): redshift. Column (5): spectral type. Columns (6)-(11): optical emission line fluxes and their errors relative to H_β emission and reddening-corrected. Column (12): sum of emission lines [S II]λ6717Å and [S II]λ6731Å relative to H_β emission and reddening-corrected. Column (13): Flux of hydrogen line H_β and its error in 10^{-14} erg/s/cm^2 and reddening-corrected. Column (13): References for optical emission lines. References: BOK75 (Boksenberg et al., 1975), BUC06 (Buchanan et al., 2006), BUT09 (Buttiglione et al., 2009), CON12 (Contini, 2012), COS77 (Costero & Osterbrock, 1977), DUC97 (Duc et al., 1997), DUR88 (Durret & Bergeron, 1988), ERK97 (Erkens et al., 1997), GAR06 (García-Marín et al., 2006), GOO83 (Goodrich & Osterbrock, 1983), GU06 (Gu et al., 2006), HO93 (Ho et al., 1993), HO97 (Ho et al., 1997), KIM95 (D. .-. Kim et al., 1995), KIM98 (D. .-. Kim et al., 1998), KOS78 (Koski, 1978), KOS17 (Koss et al., 2017), KRA94 (Kraemer et al., 1994), LUM01 (Lumsden et al., 2001), MAL86 (Malkan, 1986), MAL17 (Malkan et al., 2017), MOR88 (Morris & Ward, 1988), MOO96 (Moorwood et al., 1996), MOU06 (Moustakas & Kennicutt, 2006), OLI94 (Oliva et al., 1994), OST75 (Osterbrock & Miller, 1975), OST76 (Osterbrock & Koski, 1976), OST93 (Osterbrock & Martel, 1993), PAS79 (Pastoriza, 1979), PHI78 (Phillips, 1978), PHI83 (Phillips et al., 1983), RUP08 (Rupke et al., 2008), SHA07 (Shang et al., 2007), SHU80 (Shuder, 1980), SIM98 (Simpson & Meadows, 1998), STO97 (Storchi-Bergmann et al., 1997), VAC97 (Vaceli et al., 1997), VEI99 (Veilleux et al., 1999), WES85 (Westin, 1985), WIL79 (Wilson & Penston, 1979), WIN92 (Winkler, 1992), WU98 (Wu et al., 1998). The complete version of this table is available at the CDS.

Name (1)	...	Type (5)	[O II]λ3727Å (6)	...	[S II]λ3727Å (11)	$F(H_\beta)$ (12)	Ref. (13)
IRAS00198 − 7926	...	S2	–	...	0.96 ± 0.30	4.42 ± 1.83	LUM01
NGC185	...	S2	–	...	4.5 ± 1.0	0.09 ± 0.24	HO97
MCG−01 − 24 − 012	...	S2	4.56 ± 0.08	...	1.86 ± 0.03	1.04 ± 0.21	KOS17
NGC4593	...	S1.0	0.10 ± 0.03	...	0.023 ± 0.007	367 ± 57	MOR88,MAL17
NGC5506	...	S1h	8.0 ± 2.2	...	1.92 ± 0.42	139 ± 23	MAL17,SHU80, DUR88
IRAS08572 + 3915	...	ULIRG	2.707 ± 0.49	...	1.22 ± 0.18	1.11 ± 0.47	RUP08
Arp299A	...	LIRG	–	...	0.69 ± 0.10	21.2 ± 2.1	GAR06
NGC6240	...	LIN	45.9 ± 12.5	...	3.43 ± 1.06	89.99 ± 15.55	MAL17,CON12

Table A.13: Chemical abundances estimated from optical emission lines. Column (1): name of the galaxy. Columns (2)-(4): chemical abundances and ionization parameters with their corresponding uncertainties derived from HCm using the grid of AGN models for $\alpha_{OX} = 0.8$ and the stopping criteria of 2% of free electrons. Column (5): oxygen abundances and their uncertainties derived with the calibration proposed by Flury and Moran (2020) (Eq. (5.12)). Column (6): oxygen abundances and their uncertainties derived with the calibration proposed by Carvalho et al. (2020) (Eq. (5.13)). The complete version of this table is available at the CDS.

Name (1)	12+log(O/H) (2)	log(N/O) (3)	$\log(U)$ (4)	$12+\log(\mathrm{O/H})_{FM+20}$ (5)	$12+\log(\mathrm{O/H})_{Ca+20}$ (6)
IRAS00198 − 7926	8.28 ± 0.24	−0.51 ± 0.26	−1.87 ± 0.10	7.65 ± 0.20	8.45 ± 0.13
NGC185	8.55 ± 0.2	−0.97 ± 0.25	−1.47 ± 0.1	7.78 ± 0.18	8.51 ± 0.12
MCG−01 − 24 − 012	8.82 ± 0.07	−0.98 ± 0.14	−1.73 ± 0.01	8.36 ± 0.01	8.52 ± 0.1
NGC4593	8.04 ± 0.53	–	−1.97 ± 0.06	–	–
NGC5506	8.59 ± 0.16	−1.11 ± 0.32	−1.71 ± 0.06	8.17 ± 0.16	8.54 ± 0.12
IRAS08572 + 3915	8.17 ± 0.33	−0.85 ± 0.14	−3.58 ± 0.08	-	8.36 ± 0.09
Arp299A	8.00 ± 0.26	−0.63 ± 0.13	−3.26 ± 0.06	–	8.33 ± 0.06
NGC6240	8.25 ± 0.34	−1.28 ± 0.20	−3.89 ± 0.02	7.96 ± 0.20	8.72 ± 0.11

A.4 DATABASE FOR CHAPTERS 6 AND 7

We present in this appendix the full dataset of mid- to far-IR spectroscopy of our samples of SFGs (Tab. A.14) and AGNs (Tab. A.16) analyzed in Chapter 6. Database for Chapter 7 are tables for SFGs. Tab. A.15 and Tab. A.17 show our estimations from IR emission lines (for SFGs and AGNs, respectively) of chemical abundances and ionisation parameters for our sample. All tables are available in electronic form at the CDS[3].

Table A.14: List of IR fluxes and stellar properties for our sample of SFGs. Column (1): Name of galaxy. Columns (2) and (3): Coordinates. Column (4): Redshift. Column (5): Spectral type. Columns (6)-(19): IR emission line fluxes and their errors in 10^{-14} erg/s/cm^2. Column (20): Stellar masses. Column (21): SFRs. Column (22): References for IR line fluxes. Column (23): References for stellar properties. References IR fluxes. ARM07 (Armus et al., 2007), B-S09 (Bernard-Salas et al., 2009), BRE19 (De Breuck et al., 2019), COR15 (Cormier et al., 2015), DAN05 (Dannerbauer et al., 2005), FAR07 (Farrah et al., 2007), FER15 (Ferkinhoff et al., 2015), FO16 (Fernández-Ontiveros et al., 2016), FO21 (Fernández-Ontiveros et al., 2021), G+A09 (Goulding & Alexander, 2009), HC18 (Herrera-Camus et al., 2018), IMA10 (Imanishi et al., 2010), INA13 (Inami et al., 2013), LAM18 (Lamarche et al., 2018), NOV19 (Novak et al., 2019), PS17 (Pereira-Santaella et al., 2017), RIG18 (Rigopoulou et al., 2018), TAD19 (Tadaki et al., 2019), UZG16 (Uzgil et al., 2016), VEI09 (Veilleux et al., 2009). Stellar properties. GalDR8 Galspec Data Release 8. HOW10 (Howell et al., 2010), PAR18 (Parkash et al., 2018), SHE10 (Sheth et al., 2010), VIK17 (Vika et al., 2017). The complete version of this table is available at the CDS.

Name (1)	...	Type (5)	Br$_\alpha$ (6)	...	log (M$_*$ [M$_\odot$]) (20)	SFR [M$_\odot \cdot$ yr^{-1}] (21)	Ref. (22)	Ref. ste. (23)
Haro11	...	Dwarf	–	...	10.67	37.02	COR15	HOW10
IRAS00397 – 1312	...	ULIRG	–	...	10.7 ± 0.2	369.5	VEI09,PS17	VIK17
NGC253	...	HII	–	...	10.4 ± 0.1	4.7 ± 0.9	B-S09	PAR18
HS0052 + 2536	...	Dwarf	–	...	9.09 ± 0.06	2.5 ± 0.3	COR15	VIK17
UM311	...	Dwarf	–	...	6.69 ± 0.07	0.040 ± 0.012	COR15	GalDR8
NGC625	...	Dwarf	–	...	8.67 ± 0.1	0.0562 ± 0.007	COR15	PAR18

Table A.15: Chemical abundances estimated from HCm-IR, using the grid of POPSTAR for our sample of SFGs. Column (1): Name of galaxy. Columns (2)-(5): Chemical abundances and ionisation parameters with their corresponding uncertainties. The complete version of this table is available at the CDS.

Name (1)	12+log(O/H) (2)	12+log(S/H) (3)	log(N/O) (4)	log(U) (5)
Haro11	8.15 ± 0.09	6.39 ± 0.16	-1.07 ± 0.07	-2.62 ± 0.08
IRAS00397 – 1312	8.42 ± 0.19	6.79 ± 0.11	–	-2.93 ± 0.13
NGC253	8.72 ± 0.23	–	-0.92 ± 0.25	-3.27 ± 0.22
HS0052 + 2536	8.08 ± 0.22	6.29 ± 0.29	–	-2.65 ± 0.12
UM311	8.12 ± 0.18	6.51 ± 0.19	–	-2.68 ± 0.09
NGC625	8.03 ± 0.16	6.4 ± 0.2	–	-2.53 ± 0.1

---

[3] https://cdsarc.cds.unistra.fr/viz-bin/cat/J/A+A/685/A168.

Table A.16: List of IR fluxes for our sample of AGNs. Column (1): Name of galaxy. Columns (2) and (3): Coordinates. Column (4): Redshift. Column (5): Spectral type. Columns (6)-(23): IR emission line fluxes and their errors in 10^{-14} erg/s/cm^2. Column (24): References for IR line fluxes. References: ALO00 (Alonso-Herrero et al., 2000), ARM07 (Armus et al., 2007), B-S09 (Bernard-Salas et al., 2009), BEL03 (Bellamy et al., 2003), BEL04 (Bellamy & Tadhunter, 2004), BEN04 (Bendo & Joseph, 2004), BRA08 (Brauher et al., 2008), DAN05 (Dannerbauer et al., 2005), FO16 (Fernández-Ontiveros et al., 2016), GOL95 (Goldader et al., 1995), HC16 (Hernán-Caballero et al., 2016), HC18 (Herrera-Camus et al., 2018), IMA04 (Imanishi & Wada, 2004), IMA10 (Imanishi et al., 2010), INA13 (Inami et al., 2013), INA18 (Inami et al., 2018), KIM15 (D. Kim et al., 2015), LAM17 (Lamperti et al., 2017), LAN96 (Lancon et al., 1996), LUT02 (Lutz et al., 2002), MAR10 (Martins et al., 2010), MUE11 (Müller-Sánchez et al., 2011), MUR01 (Murphy et al., 2001), PD22 (Pérez-Díaz et al., 2022), PEN21 (B. Peng et al., 2021), PIQ12 (Piqueras López et al., 2012), PS17 (Pereira-Santaella et al., 2017), REU02 (Reunanen et al., 2002), REU03 (Reunanen et al., 2003), RIF06 (Riffel et al., 2006), SEV01 (Severgnini et al., 2001), SMA12 (Smajić et al., 2012), SPI21 (Spinoglio et al., 2022), SPO22 (Spoon et al., 2022), VEI97 (Veilleux et al., 1997), VEI09 (Veilleux et al., 2009), YAN21 (Yano et al., 2021). The complete version of this table is available at the CDS.

Name (1)	...	Type (5)	...	[O III]$\lambda 88\mu$m (21)	[N II]$\lambda 122\mu$m (22)	[N II]$\lambda 205\mu$ m (23)	Ref. (24)
IRAS00198 − 7926	...	S2	...	12.51 ± 4.5	–	–	FO16,PD22
NGC185	...	S2	...	–	–	–	FO16,PD22
MCG−01 − 24 − 012	...	S2	...	–	–	–	FO16,PD22
NGC4593	...	S1.0	...	4.09 ± 0.48	2.11 ± 0.25	–	FO16,PD22
NGC5506	...	S1h	...	102.26 ± 3.31	14.14 ± 1.15	–	FO16,PD22
Mrk1383	...	S1.0	...	–	–	–	FO16,PD22

Table A.17: Chemical abundances estimated from HCm-IR, using the grid of AGN models for $\alpha_{OX} = 0.8$ and the stopping criteria of 2% of free electrons for our sample of AGNs. Column (1): Name of galaxy. Columns (2)-(5): Chemical abundances and ionisation parameters with their corresponding uncertainties. The complete version of this table is available at the CDS.

Name (1)	12+log(O/H) (2)	12+log(S/H) (3)	log(N/O) (4)	log(U) (5)
IRAS00198 − 7926	8.18 ± 0.34	6.76 ± 0.35	–	-1.81 ± 0.33
NGC185	–	–	–	–
MCG−01 − 24 − 012	7.86 ± 0.36	6.35 ± 0.45	–	-1.6 ± 0.42
NGC4593	8.07 ± 0.36	6.41 ± 0.51	-0.91 ± 0.22	-1.78 ± 0.34
NGC5506	8.15 ± 0.3	6.68 ± 0.39	-0.74 ± 0.15	-1.88 ± 0.37
Mrk1383	7.83 ± 0.38	6.2 ± 0.47	–	-1.58 ± 0.4

B

IR OBSERVATORIES: ARCHIVAL DATA AND ONGOING MISSIONS

B.1 CHRONOLOGICAL LIST

Although IR observations of extragalactic sources were performed (see G. H. Rieke & Lebofsky, 1979, for a review of the pre-IRAS legacy) decades before, the launch of the space mission *Infrared Astronomical Satellite* (IRAS) in 1983 made a clear revolution in our understanding of the Universe. Using just four bands at 12μm, 25μm, 60μm and 100μm, IRAS provided an unbiased scan of almost the entire sky through IR emission (Neugebauer et al., 1984). The invaluable legacy from IRAS motivates the subsequent missions that were, are and will be performed to retrieve IR information. As our interest focus on emission lines, we present a review those missions with instruments capable of performing spectroscopic observations.

B.1.1 *Infrared Space Observatory*

The *Infrared Space Observatory* (ISO) launched in 1995, was the first space mission after IRAS targeting the IR regime from 2.5μm to 240μm (Kessler et al., 1996). Equipped with a 60 cm Ritchey-Chrétien telescope, ISO incorporated two key instruments to perform spectroscopic IR analysis: the short- and long-wavelength spectrometers (SWS and LWS, respectively; Clegg et al., 1996; de Graauw et al., 1996; Kessler et al., 1996). The SWS covered the $2.38 - 45.2\mu$m regime, with a resolution ranging from 1000 to 2000 and the possibility of enhanced the resolution by a factor ~20 if Fabry-Perot filters were inserting (de Graauw et al., 1996; Schaeidt et al., 1996). The LWS covered the $43 - 196.9\mu$m regime, with two different resolution modes: medium ($\sim 150 - 200$) and high ($\sim 6800 - 9700$) (Clegg et al., 1996; B. M. Swinyard et al., 1996).

Although a great advantage as for the first time IR spectroscopic information from a space observatory was retrieved, numerous problems raised from the uncertainties in the calibration, which were specially notorious with the LWS instrument (Decin et al., 2000; Sloan et al., 2003; B. Swinyard et al., 2000). As ISO-legacy, Sloan et al. (2003) provided an atlas of SWS spectra treated uniformly with the same pipeline and calibration[1].

B.1.2 *Spitzer Space Telescope*

The *Spitzer Space Telescope* was launched in 2003, containing a 85 cm telescope (Werner et al., 2004). The instrument incorporated to perform spectroscopic operations was the Infrared Spectrograph (IRS), covering the range of $5.3 - 38\mu$m with both low ($\sim 64 - 128$) and high (~ 600) resolutions (Houck et al., 2004; Werner et al., 2004) . The low-resolution mode was composed by two modules: the short-low module, with a slit size of 3.7×57 arcsecs, covering the $5.2 - 14.5\mu$m and the long-low module, with a slit size of 10.5×16.8 arsecs, covering the $14 - 38\mu$m. The high-resolution mode was also composed by two modules: the short-high module, with a slit size of 4.7×11.3 arcsec, covering the range $9.9 - 19.6\mu$m and the long-high, with a slit size of 11.1×22.3 arscec, covering the $18.7 - 37.2\mu$m range.

---

[1] This database is accessible through https://irsa.ipac.caltech.edu/data/SWS/overview.html.

Spitzer/IRS archival data is available from two archives, the Spitzer Heritage Archive[2] (HSA) and the Combined Atlas of Sources with Spitzer IRS Spectra[3] (CASSIS). Additionally, Spoon et al. (2022) published a database with all observables measured from the available high-quality spectra from CASSIS, the Infrared Database of Extragalactic Observables from Spitzer[4] (IDEOS; Hernán-Caballero et al., 2016; Spoon et al., 2022).

B.1.3 *AKARI*

The infrared astronomical mission *AKARI* was launched in 2006, and it contains a 68.5 cm Ritchey-Chrétien telescope together with two imaging instruments, the Far-Infrared Surveyor (FIS) and the Infrared Camera (IRC) (Murakami et al., 2007). The IRC instrument operated in the $1.8 - 26.5\mu$m and allowed low-resolution ($\sim 20 - 120$) near- to mid-IR spectroscopy replacing the imaging filters with transmission-type dispersers (Ohyama et al., 2007).

All archival data from *AKARI* is available from the Data Archive and Transmission System[5] (DARTS), although there are additional datasets with spectroscopic information available in the literature, such as the catalogs from Imanishi et al. (2010), Inami et al. (2018) or Lai et al. (2020).

B.1.4 *Herschel Space Observatory*

The *Herschel Space Observatory* was launched in 2009, containing a 3.5 m Cassegrain telescope and three different instruments that provide spectroscopic and/or photometric observations (Pilbratt et al., 2010). The Heterodyne Instrument for Far Infrared (HIFI) was a heterodyne spectrometer pixel-size field-of-view that provide a wavelength coverage in two ranges [157μm, 212μm] and [240μm, 625μm], with a resolving power of $\sim 10^6$ (de Graauw et al., 2010). The Spectral and Photometric Imaging REceiver (SPIRE) provided a three band imaging photometer and an imaging Fourier-transform spectrometer covering the range $194 - 671\mu$m with high ($\sim 370 - 1300$) and low ($\sim 20 - 60$) resolution (Griffin et al., 2010). The Photodetector Array Camera and Spectrometer (PACS) provided also a three band photometer and a spectrometer fed by an integral field unit that captures the emission in the range $55 - 210\mu$m with high ($\sim 1000 - 4000$) resolution (Poglitsch et al., 2010).

Archival data from *Herschel* is available from both the Infrared Science Archive[6] (IRSA) and directly from the Herschel Science Archive[7] (HSA).

B.1.5 *Stratospheric Observatory for Infrared Astronomy*

The *Statrospheric Observatory for Infrared Astronomy* (SOFIA) an IR mission consisting of a 2.7 m telescope onboard a Boeing 747Sp aircraft that operates between 11.23 km and 13.72 km of altitude (Young et al., 2012). Given the flexibility of the mission, several instruments have been incorporated to the telescope allowing spectroscopic observations. The First Light Infrared Test Experiment CAMera (FLITECAM) operated in the $1.0 - 5.5\mu$m regime, allowing spectroscopic observations with a selection of three grisms providing a medium (~ 1500) resolution (McLean et al., 2006). The Faint Object infraRed CAmera for the SOFIA Telescope (FORCAST) provided an spectrograph based on a suite of grisms that covers the range $5 - 40\mu$m with moderate (~ 200) resolution (Herter et al.,

---

[2] This database is accessible through https://irsa.ipac.caltech.edu/applications/Spitzer/SHA.
[3] This database is accessible through https://cassis.sirtf.com/.
[4] More information on the data processing and products can be found at http://ideos.astro.cornell.edu/.
[5] Several databases can be found at https://darts.isas.jaxa.jp/missions/akari.
[6] The Herschel Data Search might be access through https://irsa.ipac.caltech.edu/applications/Herschel/.
[7] HSA catalogs are available at https://archives.esac.esa.int/hsa/whsa/.

2018). The German REceiver for Astronomy at Terahertz Frequencies (GREAT) was a heterodyne instrument covering the $63.2 - 611\mu$m range with extremely high ($> 10^7$) resolution (Heyminck et al., 2012; Risacher et al., 2018). The Echelon-cross-echelle Spectrograph (EXES) covered the range $5 - 28\mu$m with moderately-low (~ 300), medium (~ 1000) and high (up to 10^5) resolution modes (Richter et al., 2018). Finally, the Field-Imaging Far-Infrared Line Spectrometer (FIFI-LS) was a legacy instrument from PACS at *Herschel*, since its design its identical and covered the range $51 - 203\mu$m with a medium ($\sim 500 - 2000$) resolution (Fischer et al., 2018).

Given the number of science cases and projects carried out while SOFIA was operating, it is advisable to search for the archival data at IRSA[8].

B.1.6 *James Webb Space Telescope*

The *James Webb Space Telescope* (JWST) was launched in 2021, and it is the only dedicated IR observatory not ground-based operating at the moment of this thesis. It contains a 6.5 m telescope, composed of 18 hexagonal beryllium primary mirror segment assemblies, and four instruments each of them with at least one observing mode allowing IR spectroscopy. The Near Infrared Camera (NIRCam) allows for high (~ 1600) resolution wide-field slitless spectroscopy in the range of $2.5 - 5.0\mu$m (M. J. Rieke et al., 2023). The Near Infrared Imager and Slitless Spectrograph (NIRISS) allows either single-object slitless spectroscopy between 0.6μm and 2.8μm at low (~ 70) resolution or wide-field slitless spectroscopy between $0.8 - 2.2\mu$m at medium (~ 150) resolution (Doyon et al., 2023). The Near Infrared Spectrograph (NIRSpec) provides low (100), medium (1000) and high (3000) resolution in the range $[0.6\mu\text{m}, 5.3\mu\text{m}]$ under three different spectroscopic modes: multi-object, fixed slit and integral field unit spectroscopy (Böker et al., 2023). Finally, the Mid-Infrared Instrument (MIRI) provides integral field unit spectroscopy at two resolutions: low (~ 100) between $5\mu m$ and $12\mu m$ and medium ($\sim 1300 - 3300$) between $5\mu m$ and $28\mu m$ in four channels (Wright et al., 2023).

JWST is an ongoing mission, but publicly available data (including raw and processed files) can be either retrieved from the Mikulski Archive for Space Telescopes[9] (MAST) or the JWST Science Archive[10].

B.1.7 *Ground-based observations*

Space observatories provide the best capabilities for large spectroscopic surveys, as the background noise is significantly reduced. However, there is also archival and ongoing data from ground-based observatories.

For example, the NASA *Infrared Telescope Facility* (IRTF) is still operating as observatory located at Mauna Kea, Hawai'i, equipped with a 3.2m telescope and three instruments allowing IR spectroscopy. The instrument SpeX is a low-to-medium ($\sim 50 - 2500$) cryogenic spectrograph operating in the range $0.8 - 5.5\mu$m. The Texas Echelon Cross Echelle Spectrograph (TEXES) operates in the range $5 - 25\mu$m at medium-high ($\sim 15,000$) and high (~100,000) resolutions (Lacy et al., 2002). Finally, the iSHELL is a high ($\sim 75,000$) resolution spectrograph operating in $[1.1\mu\text{m}, 5.3\mu\text{m}]$ range (Rayner et al., 2016). Archival data is available for the observing nights since the second semester 2000[11].

---

[8] An overview on the data available from SOFIA is found in https://irsa.ipac.caltech.edu/Missions/sofia.html.

[9] Data and observing proposals available through https://mast.stsci.edu/search/.

[10] https://jwst.esac.esa.int/archive/.

[11] Prior to 2016 (second semester), data is available at https://irtfdata.ifa.hawaii.edu/browse/, whereas after that it is located at https://irsa.ipac.caltech.edu/applications/irtf/.

Table B.1: Summary of the IR spectroscopic instruments for different observatories.

Observatory	Instrument	Mode	Range	Resolution
ISO	SWS	Medium-mode	$2.38 - 45.2\mu m$	$\sim 1000 - 2000$
		High-mode		$\sim 2 \cdot 10^4 - 4 \cdot 10^4$
	LWS	Medium-mode	$43 - 196.9\mu m$	$\sim 150 - 2000$
		High-mode		$\sim 6800 - 9700$
Spitzer	IRS	Short-low	$5.2 - 14.5\mu m$	$\sim 64 - 128$
		Long-low	$14 - 38\mu m$	
		Short-high	$9.9 - 19.6\mu m$	~ 600
		Long-high	$18.7 - 37.2\mu m$	
AKARI	IRC	Dispersers	$1.8 - 26.5\mu m$	$\sim 20 - 120$
Herschel	HIFI	Heterodyne	$157 - 212\mu m$	$\sim 10^6$
			$240 - 625\mu m$	
	SPIRE	FTS	$194 - 671\mu m$	$\sim 20 - 60$
				$\sim 370 - 1300$
	PACS	Spectrometer	$55 - 210\mu m$	$\sim 1000 - 4000$
SOFIA	FLITECAM	Grisms	$1.0 - 5.5\mu m$	~ 1500
	FORCAST	Grisms	$5 - 40\mu m$	~ 200
	GREAT	Heterodyne	$63.2 - 611\mu m$	$\gtrsim 10^7$
	EXES	Low-mode	$5 - 28\mu m$	~ 300
		Medium-mode		~ 1000
		High-mode		$\lesssim 10^5$
	FIFI-LS	Spectrometer	$51 - 203\mu m$	$\sim 500 - 2000$
JWST	NIRCam	WF-Slitless	$2.5 - 5.0\mu m$	~ 1600
	NIRISS	SO-slitless	$0.6 - 2.8\mu m$	~ 70
		WF-slitless	$0.8 - 2.2\mu m$	~ 150
	NIRSpec	MOS	$0.6 - 5.3\mu m$	~ 100
		Fixed slit		~ 1000
		IFU		~ 3000
	MIRI	Low-mode	$5 - 12\mu m$	~ 100
		Medium-mode	$5 - 28\mu m$	$\sim 1300 - 3300$
IRTF	SpeX	-	$0.8 - 5.5\mu m$	$\sim 50 - 2500$
	TEXES	Medium-mode	$5 - 25\mu m$	$\sim 1.5 \cdot 10^4$
		High-mode		$\sim 10^5$
	iSHELL	-	$1.1 - 5.3\mu m$	$\sim 7.5 \cdot 10^4$

It is also important to note that radio observatories such as the Atacama Large Millimeter Array (ALMA) can also be used for far-IR spectroscopic observations for high-redshift ($z \gtrsim 3$) galaxies (e.g. Mordini et al., 2021). Indeed, over the recent years several studies have been published on the detection and analysis of far-IR lines from galaxies up to $z \sim 12$ (see Harikane et al., 2020; Sugahara et al., 2021; Wong et al., 2022; Zavala et al., 2024, among many others).

B.2 SUMMARY TABLE OF IR SPECTROSCOPIC INSTRUMENTS

We offer in Tab. B.1 a summary of all IR spectroscopic instruments and their main properties.

C

SUPPLEMENTARY FIGURES

C.1 SUPPLEMENTARY FIGURES FOR CHAPTER 2

C.1.1 *Comparison of the chemical abundance estimations from the direct method and HII-CHI-Mistry*

From the sample of SFGs from SDSS DR9 GALSPEC (Ahn et al., 2012) (see Sec. 2.5.1), we select a subsample of 806 galaxies that present reliable measurements of the [O III]λ4363Å auroral line (i.e. their relative error is less than 20%). For that sample, chemical abundances [12+log(O/H) and log(N/O)] are estimated by three different ways from the reddening-corrected emission lines:

- The T$_e$-method: We estimate electron densities (n_e) from the sulfur [S II]λ,λ6717, 6731Å doublet using PYNEB (Luridiana et al., 2015) and assuming an electron temperature of $T_e = 10^4$ K. We then compute from PYNEB the T([O III]) from the ratio between [O III]λ5007Å and [O III]λ4363Å, assuming the electron density derived from the sulfur doublet. The other temperatures, T([O II]) and T([N II]) are obtained from T([O III]) assuming the model-based relations reported by Pérez-Montero (2014). Ionic abundances are estimated then from the brightest emission lines for each ion, assuming the electron density estimated from the sulfur doublet and the corresponding temperature for each ion. The final abundances are estimated as:

$$\frac{O}{H} \approx \frac{O^+}{H^+} + \frac{O^{++}}{H^+} \tag{C.1}$$

$$\frac{N}{O} \approx \frac{N^+}{O^+}\mathrm{ICF}_{Am+21}\left(\frac{O^{++}}{O^+ + O^{++}}\right) \tag{C.2}$$

  using the ICF from Amayo et al. (2021).

- HCm including the [O III]λ4363Å auroral line as input. In this case, together with the auroral line, the input lines are [O II]λ3727Å, [Ne III]λ3868Å, [O III]λ5007Å, [N II]λ6584Å, [S II]λ6717Å and [S II]λ6731Å. We select the POPSTAR grid of models, which offers the best performance for estimating chemical abundances in SFGs.

- HCm without [O III]λ4363Å auroral line. The input set only contains [O II]λ3727Å, [Ne III]λ3868Å, [O III]λ5007Å, [N II]λ6584Å, and [S II]λ6717Å+[S II]λ6731Å. We again select the POPSTAR grid of models, which offers the best performance for estimating chemical abundances in SFGs.

We show a comparison of the results from these three methods in Fig. C.1 (for N/O) and C.2 (for O/H). Regarding N/O, it can be seen that in general there is an good agreement between the estimations of the T$_e$-method and those from HCm. We also note that, outside the range [−1.35, −0.85] (which encompasses most of our sample) there are few galaxies that clearly show a discrepancy, specially at low N/O ratios. Regarding O/H, we obtain that there is also a good agreement between the estimations from the T$_e$-method and those from HCm when oxygen auroral lines are included (see Fig. C.2 (a)). When the auroral line is not introduced, we observe a significant increase in the scatter when compared to the direct method (see Fig. C.2 (b)).

Overall, we can conclude that there is a good agreement between the optical estimations of chemical abundances (both O/H and N/O) from the T$_e$-method and HCm. We note that discrepancies arises when the auroral line is not included in the code, but the effect in N/O is mostly negligible.

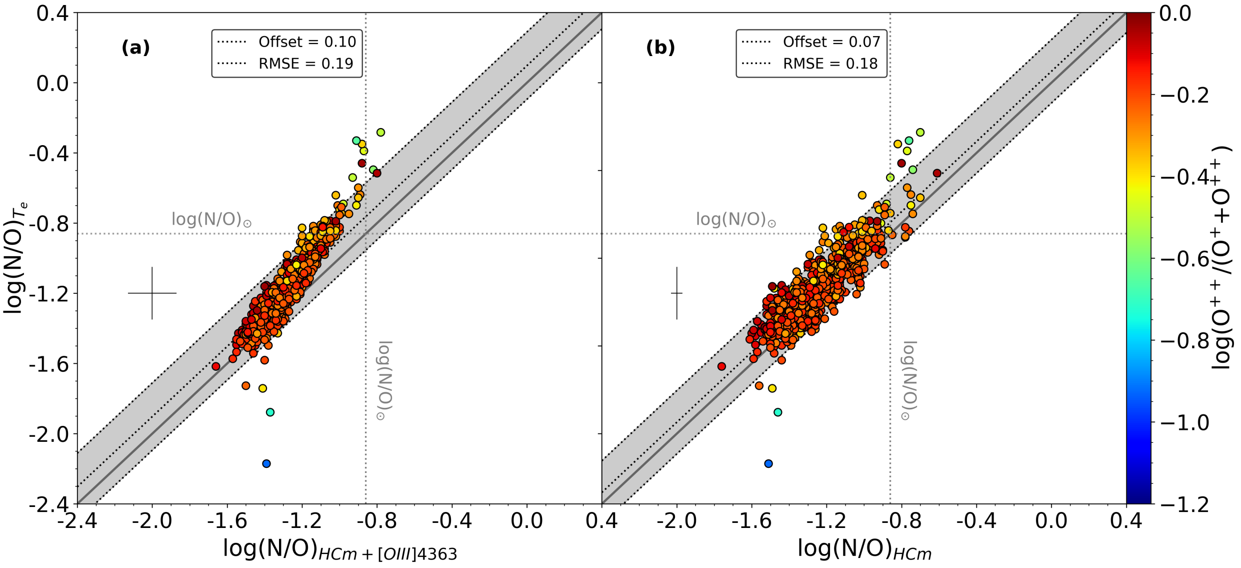

Figure C.1: Comparison between the chemical abundance ratios log(N/O) estimated from the T_e-method (y-axis) and from HCm (x-axis). (a) Auroral line [O III]λ4363Å is included in the input set of lines for HCm. (b) Input set of lines for HCm does not include oxygen auroral line. The offsets are given using the median value (dashed line) and RMSE (dot-dashed lines).

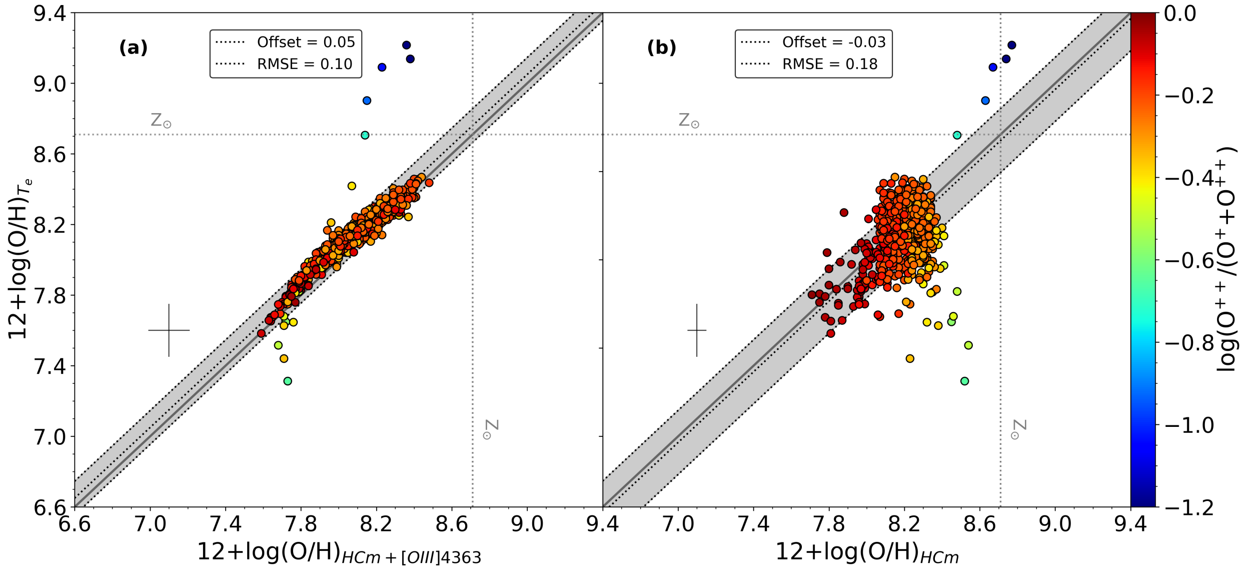

Figure C.2: Same as Fig. C.1 but for 12+log(O/H).

C.2 SUPPLEMENTARY FIGURES FOR CHAPTER 3

C.2.1 *Comparison of estimations of chemical abundances from different grids of photoionization models*

We show in Fig. C.3 the comparison among the oxygen abundances estimated in the nuclear region of our sample of LINER-like galaxies based on different grids of photoionization models. Despite there is a little discrepancy when AGN models with $\alpha_{OX} = -1.2$ are considered, we can conclude that changes in the slope (α_{OX}) of the AGN SED do not induce changes in the estimation of 12+log(O/H). In the same way, very little change is found when switching from pAGB models characterized by $T_{eff} = 1 \cdot 10^5$ K to $T_{eff} = 1.5 \cdot 10^5$ K. When comparing AGN models and pAGB models, we observed that from 12+log(O/H) = 8.1 to 12+log(O/H) = 8.7 (solar value), pAGB models predict systematically lower chemical abundances than AGN models. Fig. C.3 also highlights the problem of assuming pAGB models with low effective temperatures ($T_{eff} = 5 \cdot 10^4$ K).

On the contrary, Fig. C.4 shows the excellent agreement among the estimations of log(N/O). Omitting pAGB models characterized by $T_{eff} = 5 \cdot 10^4$ K, which have been already probed to be inappropriate for this analysis, there is correlation one-to-one correlation for all photoionization models considered. We also noticed that there is a small offset between AGN models and ADAF or pAGB models, although the correlation one-to-one still holds.

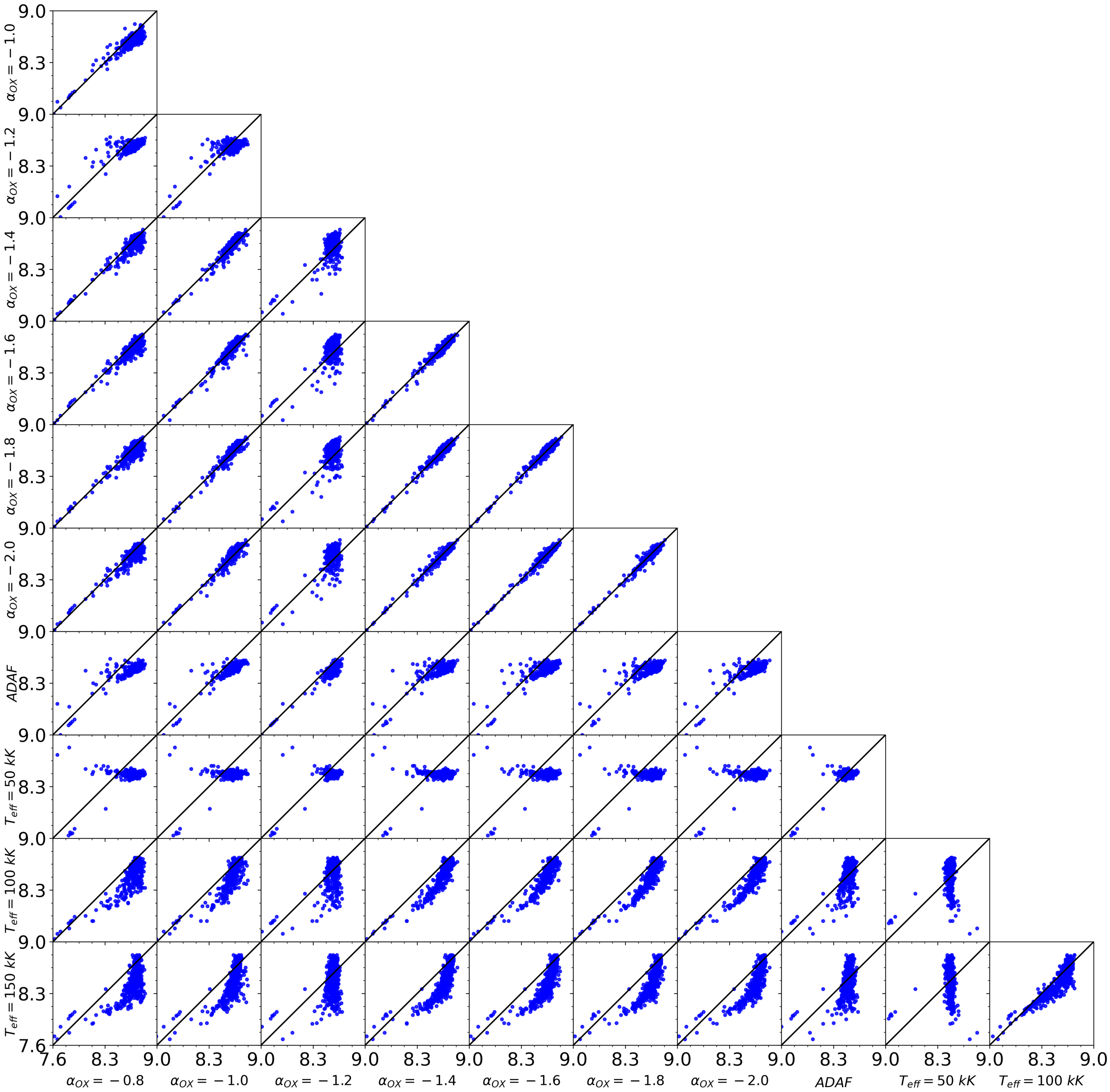

Figure C.3: Comparative plot of oxygen abundances in the nuclear regions of our sample of LINERs for each grid of photoionization models considered in this work.

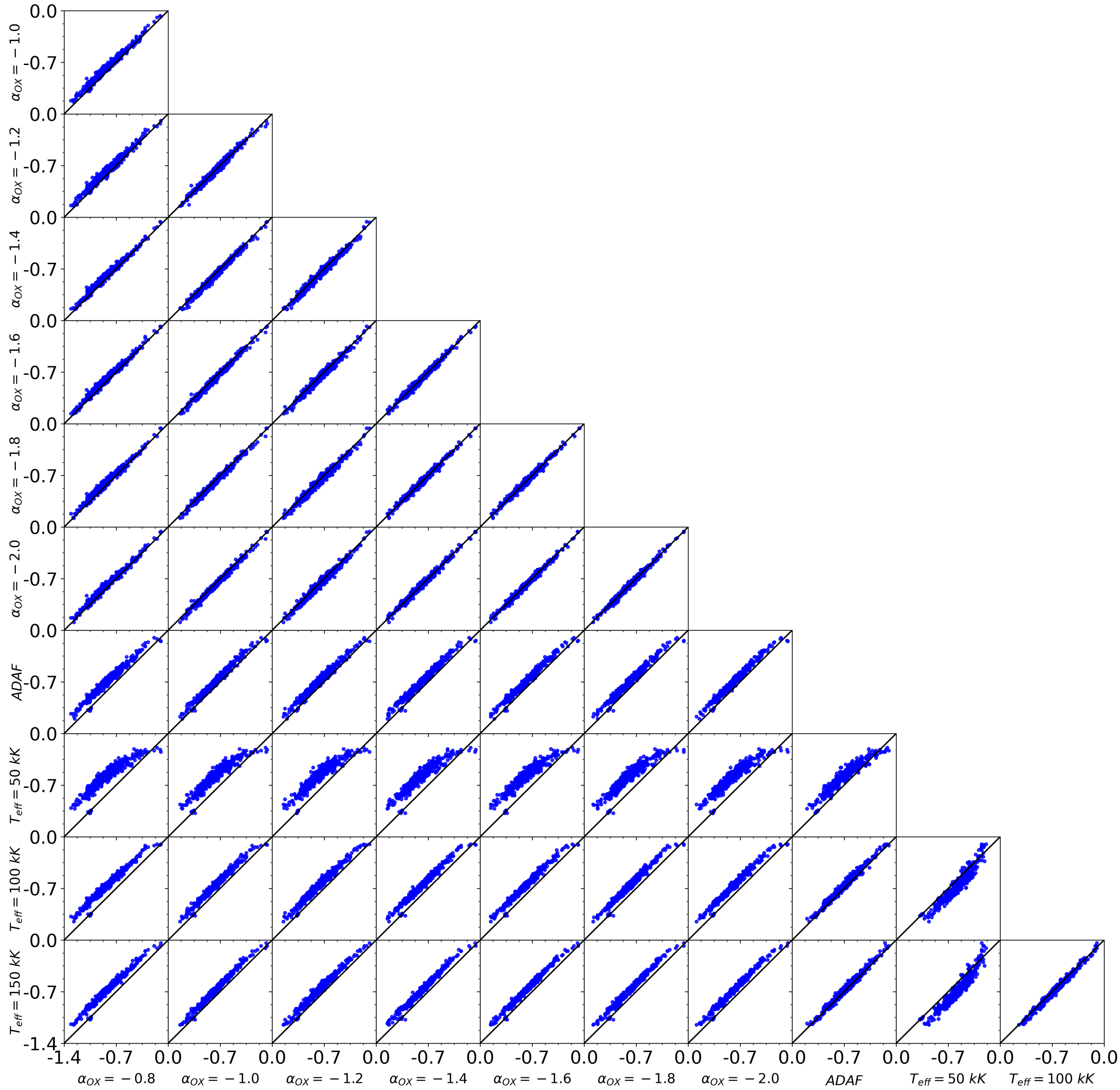

Figure C.4: Same as Fig. C.3 but for the nitrogen-to-oxygen abundance ratio.

C.3 SUPPLEMENTARY FIGURES FOR CHAPTER 4

C.3.1 *Radial metallicity gradients*

We present in this section the abundance radial gradients, as traced by 12+log(O/H) and log(N/O), for our sample of LINER-like galaxies. We only display those regions classified as HII regions according to the diagnostic diagrams (Baldwin et al., 1981; Kauffmann et al., 2003; Kewley et al., 2006), and we normalized their distances to the galaxy center by R_e. For the nuclear estimations, we show the values discussed in Paper I.

The results are showed in Fig. C.5, where we show all HII regions considered (gray dots) and the median value (blue) at a given distance considering 15 different intervals in distance and ensuring that each segment contains at least 10 HII regions. We also represent the fit (solid black line) obtained from the piecewise algorithm.

C.3.2 *Relation between log(N/O) and 12+log(O/H)*

We present in this section the log(N/O) vs 12+log(O/H) diagram (Fig. C.6) for the HII regions selected in each galaxy in our sample. We also present the estimations of the chemical abundances of the nuclear region that comprehends the LINER-like emission.

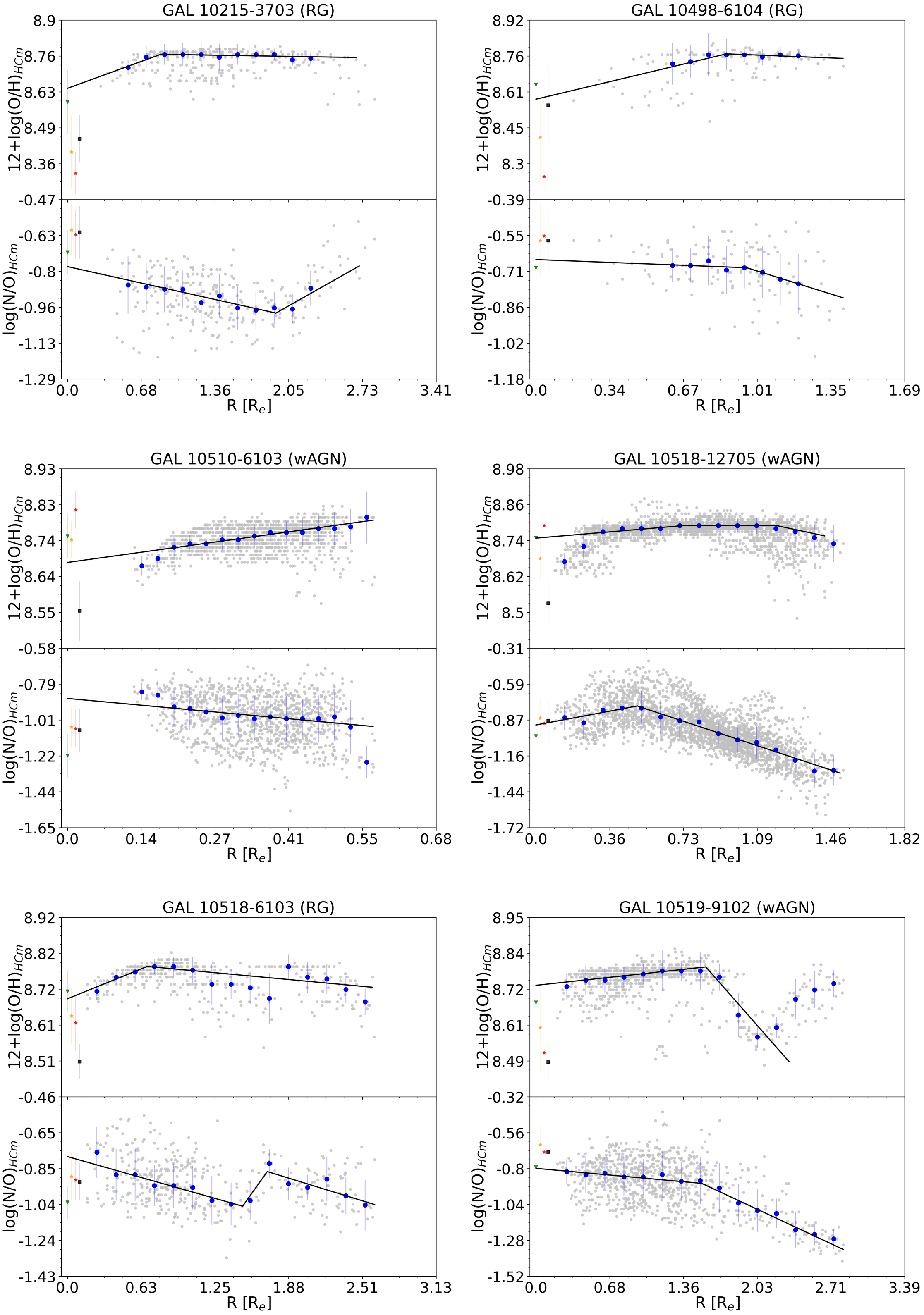

Figure C.5: Radial metallicity gradients, 12+log(O/H) and log(N/O), in our sample of LINER-like galaxies. Nuclear estimations of the corresponding chemical abundance ratio are represented as follows: green triangles are the estimations from AGN models with $\alpha_{OX} = -1.6$; orange and red stars are the estimations from pAGB models with $T_{eff} = 10^5$ K and $T_{eff} = 1.5 \cdot 10^5$ K respectively; and black squares are the estimations from ADAF models.

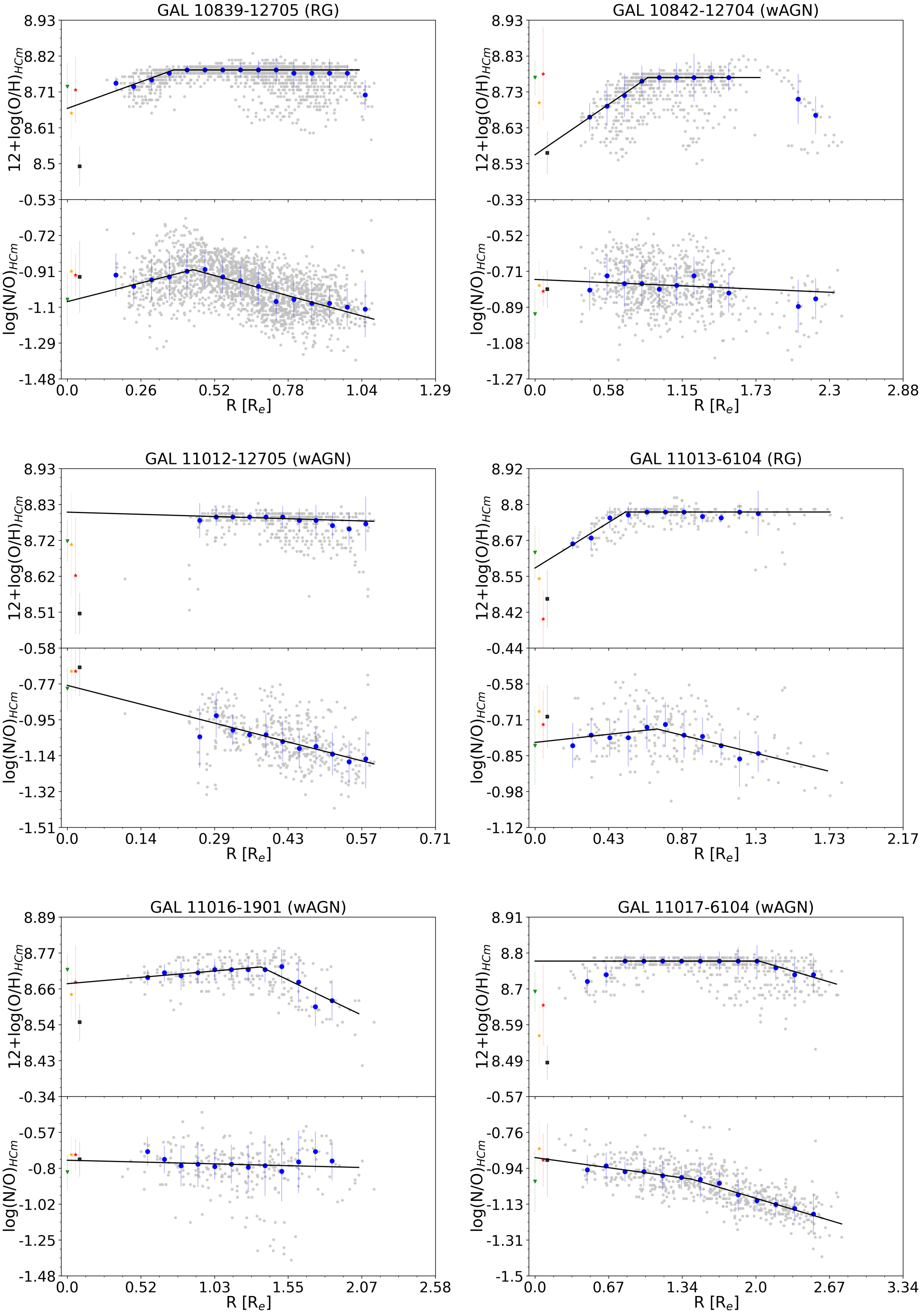

Figure C.5: continued.

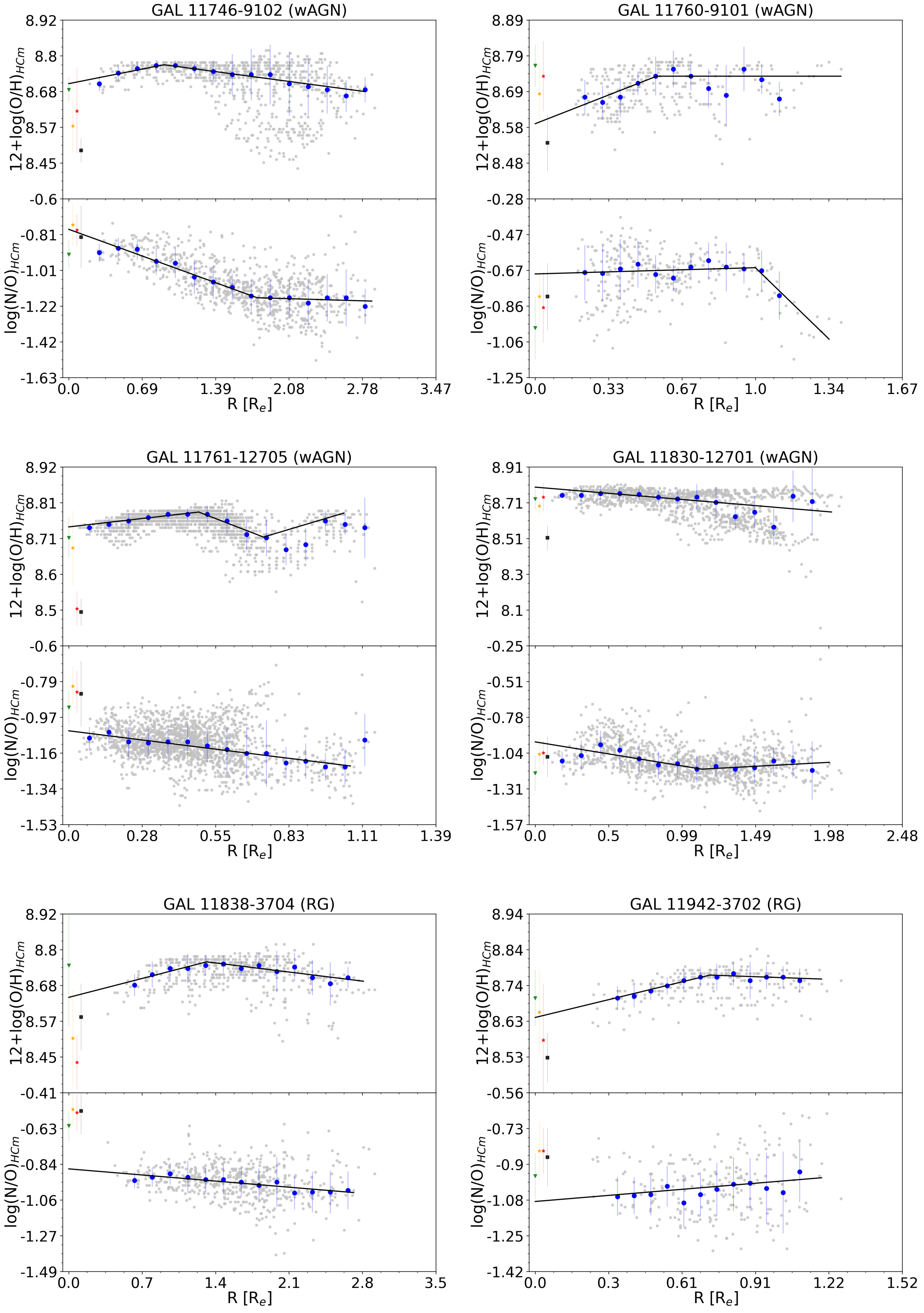

Figure C.5: continued.

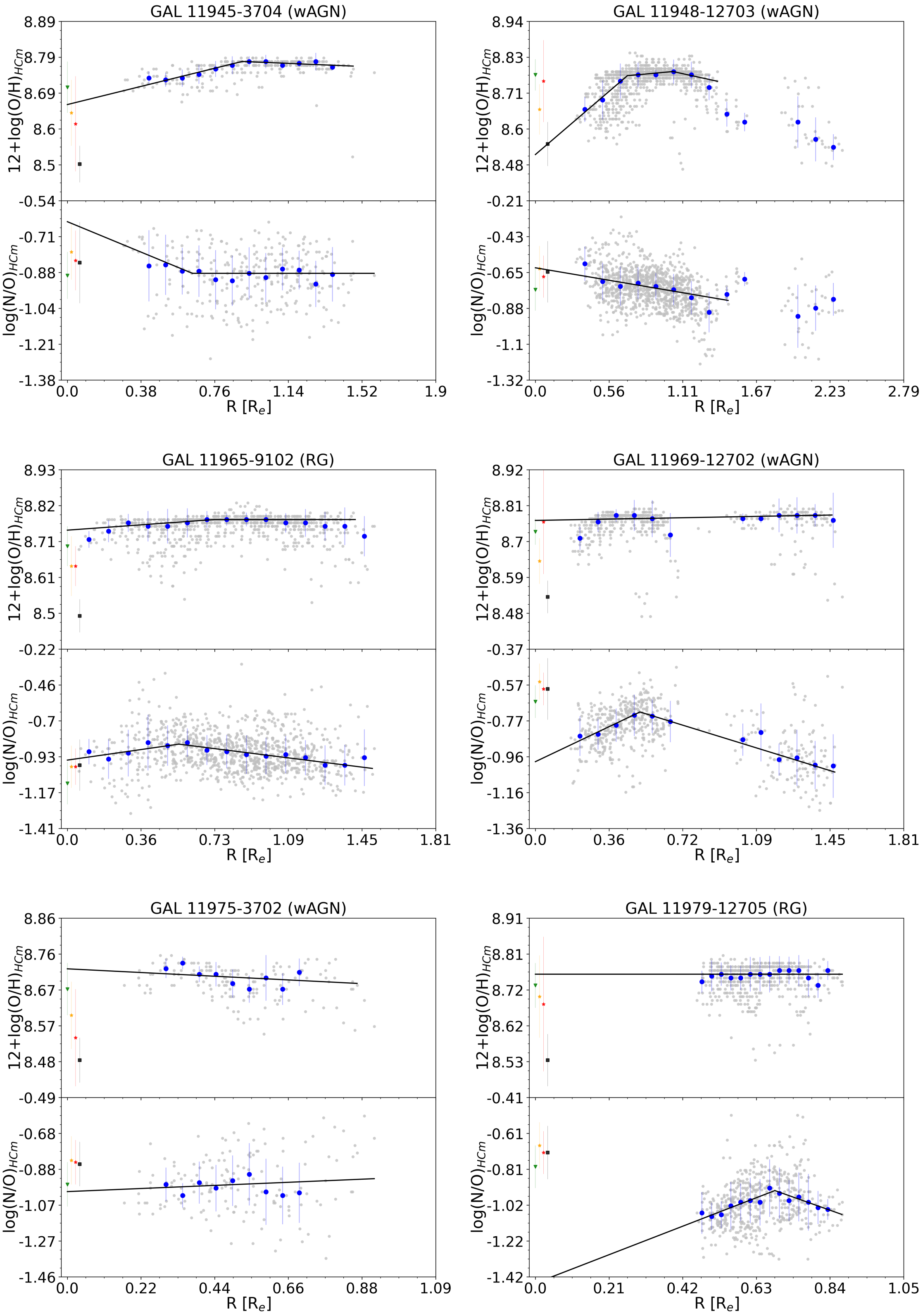

Figure C.5: continued.

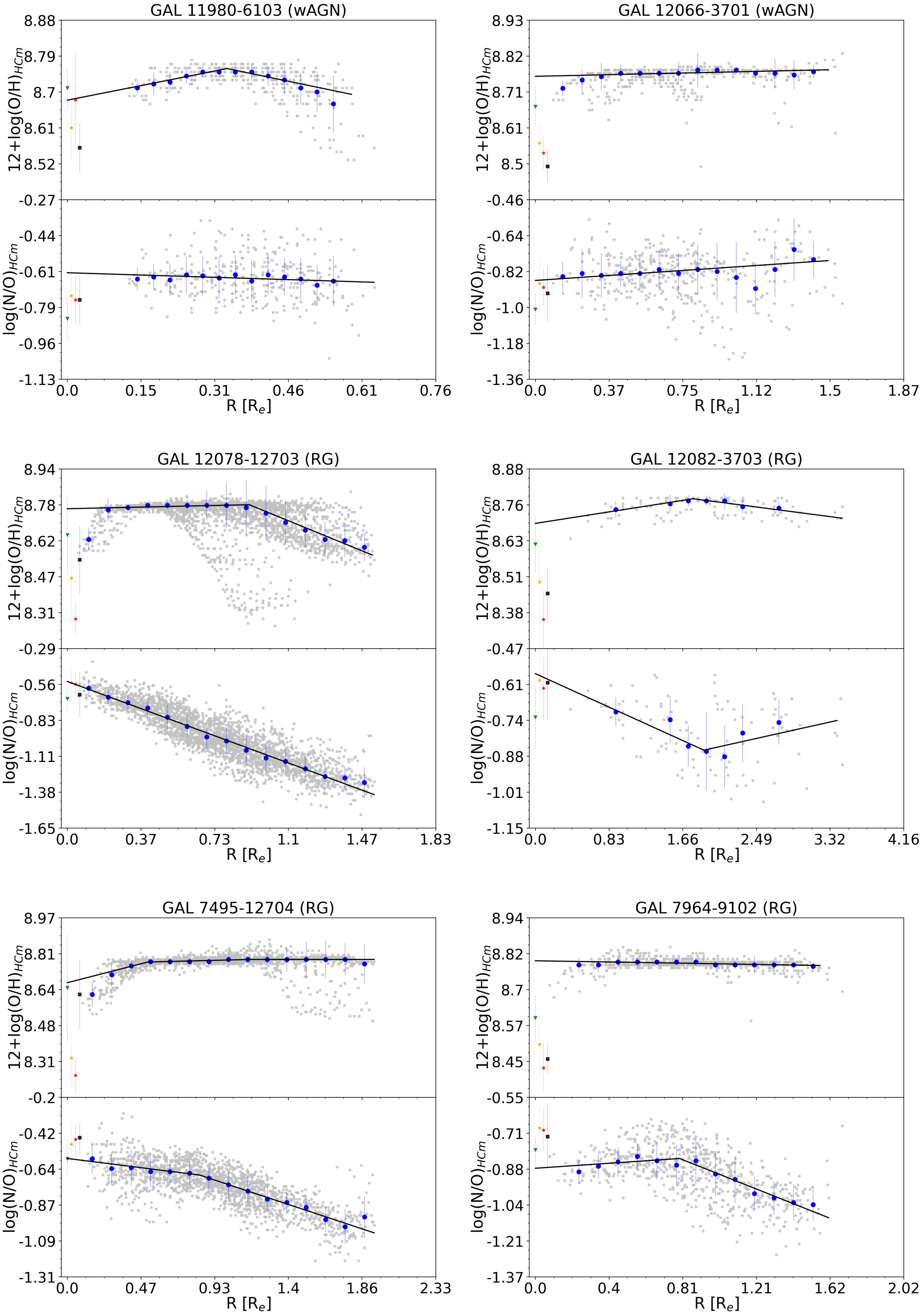

Figure C.5: continued.

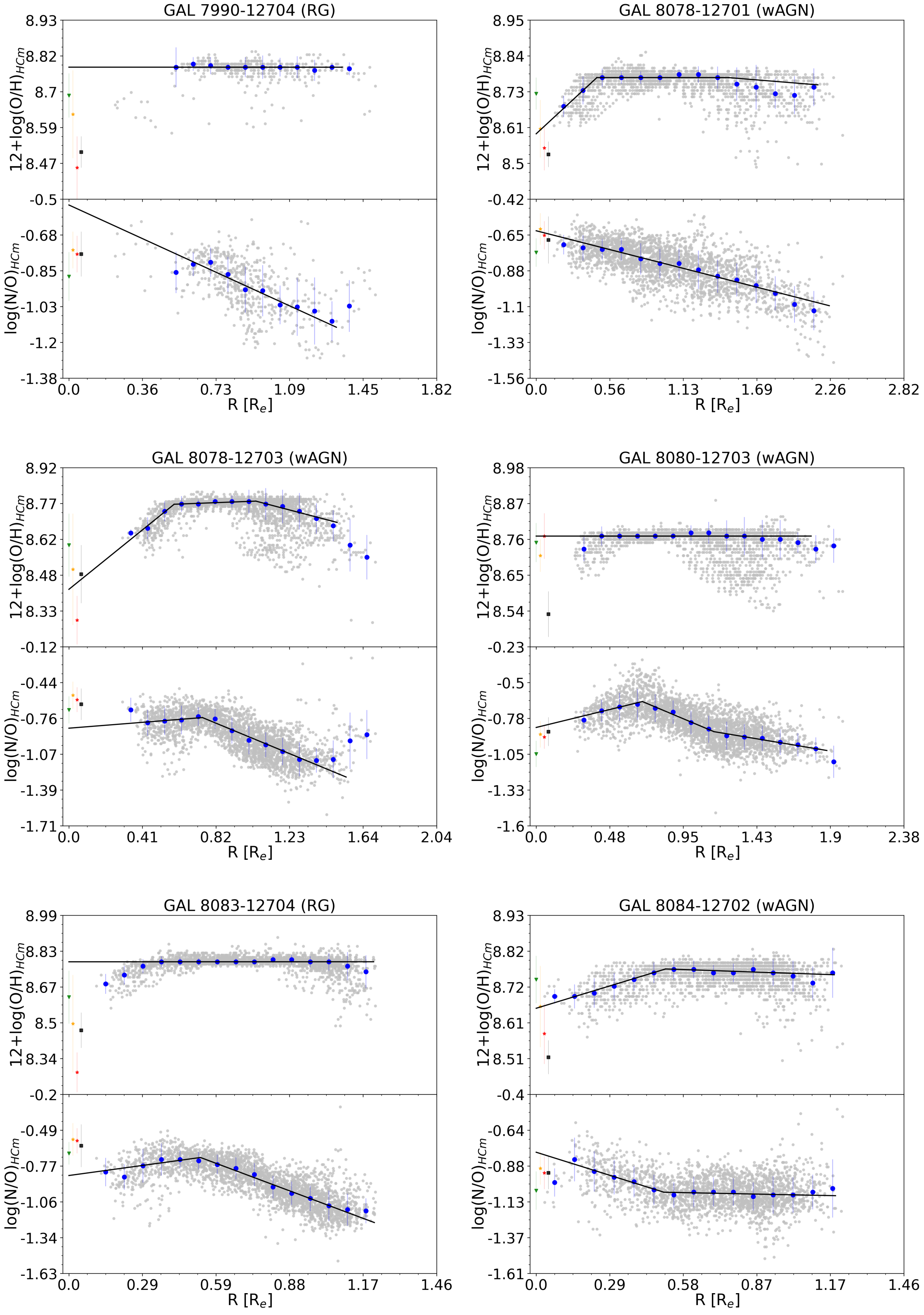

Figure C.5: continued.

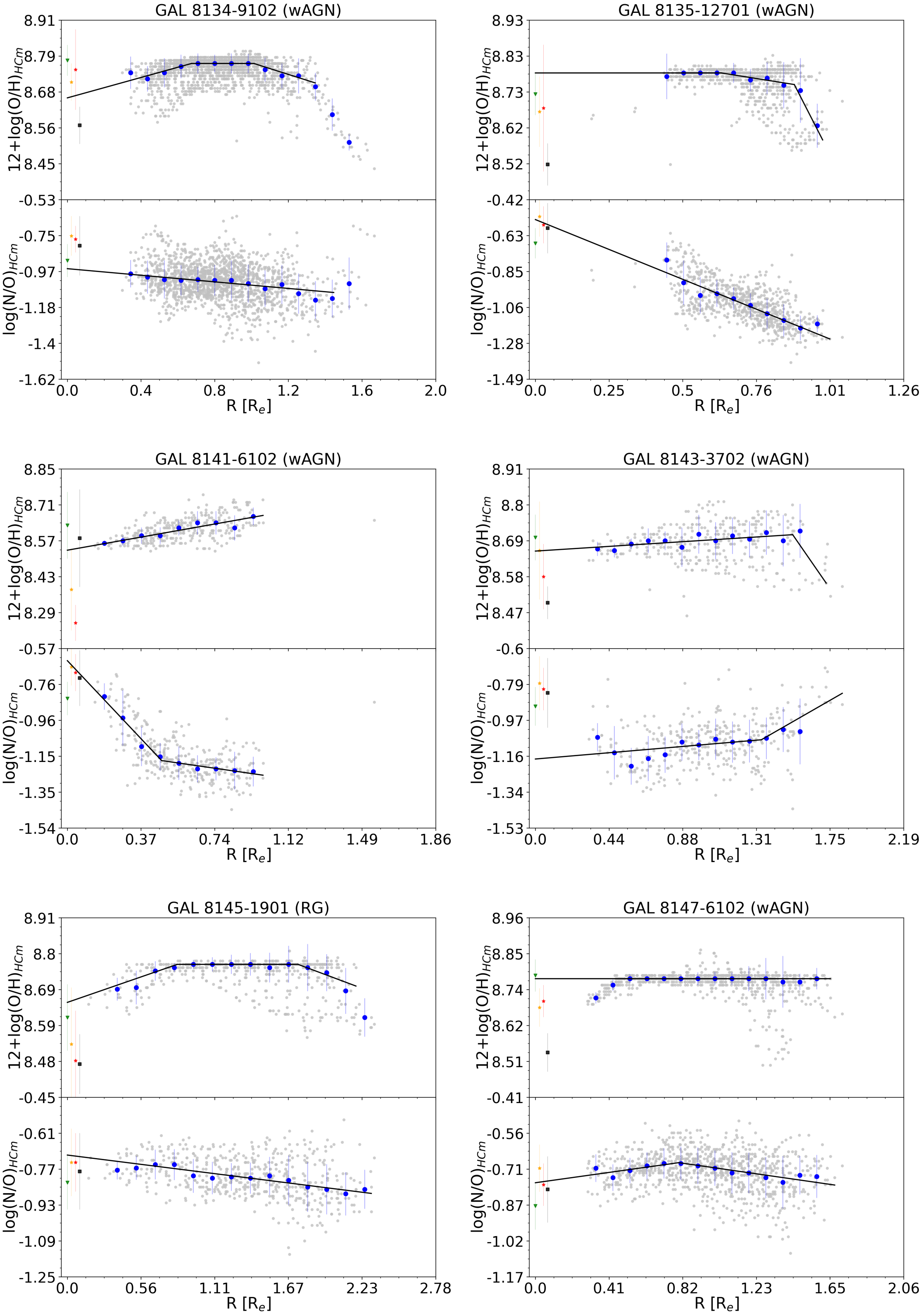

Figure C.5: continued.

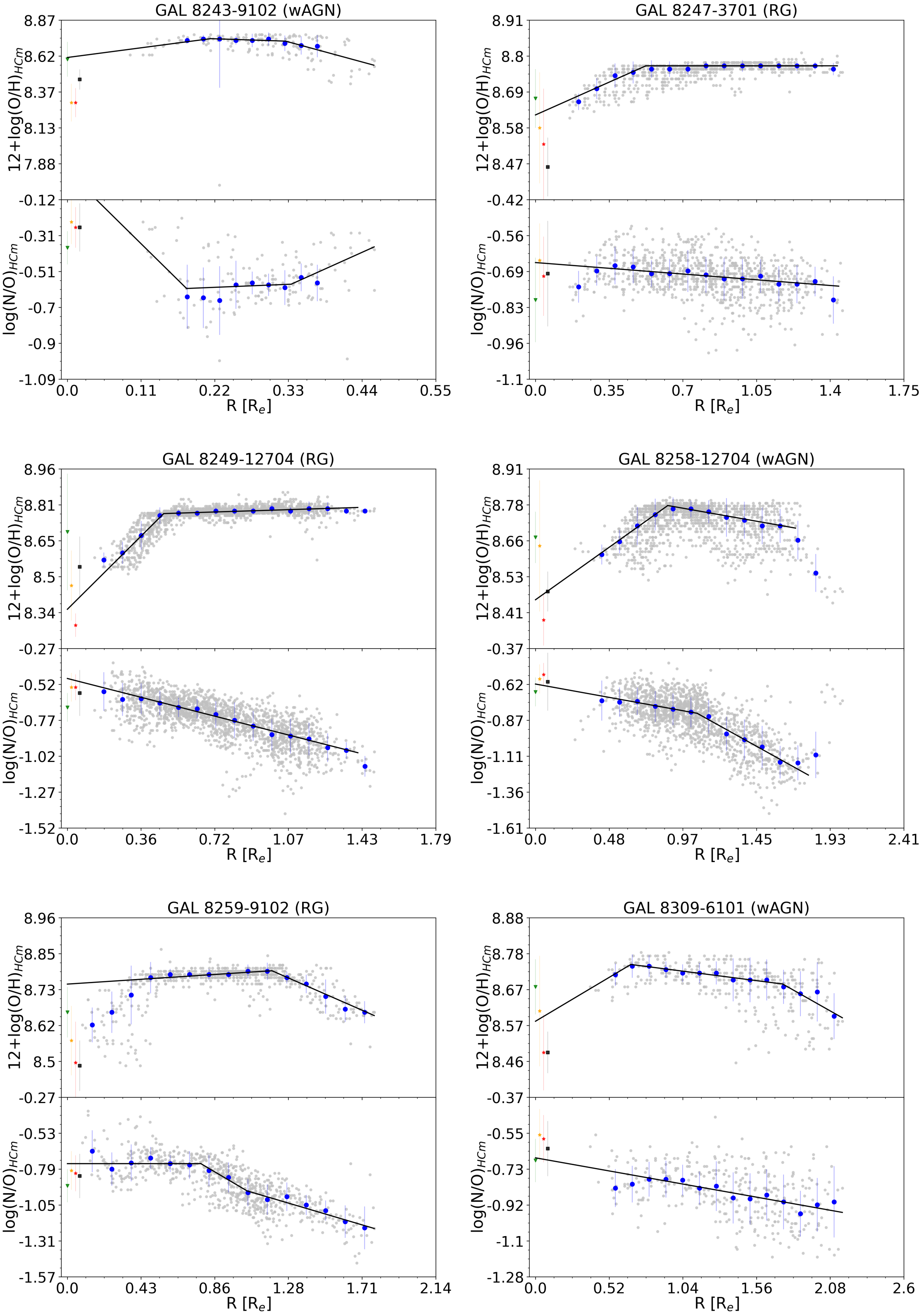

Figure C.5: continued.

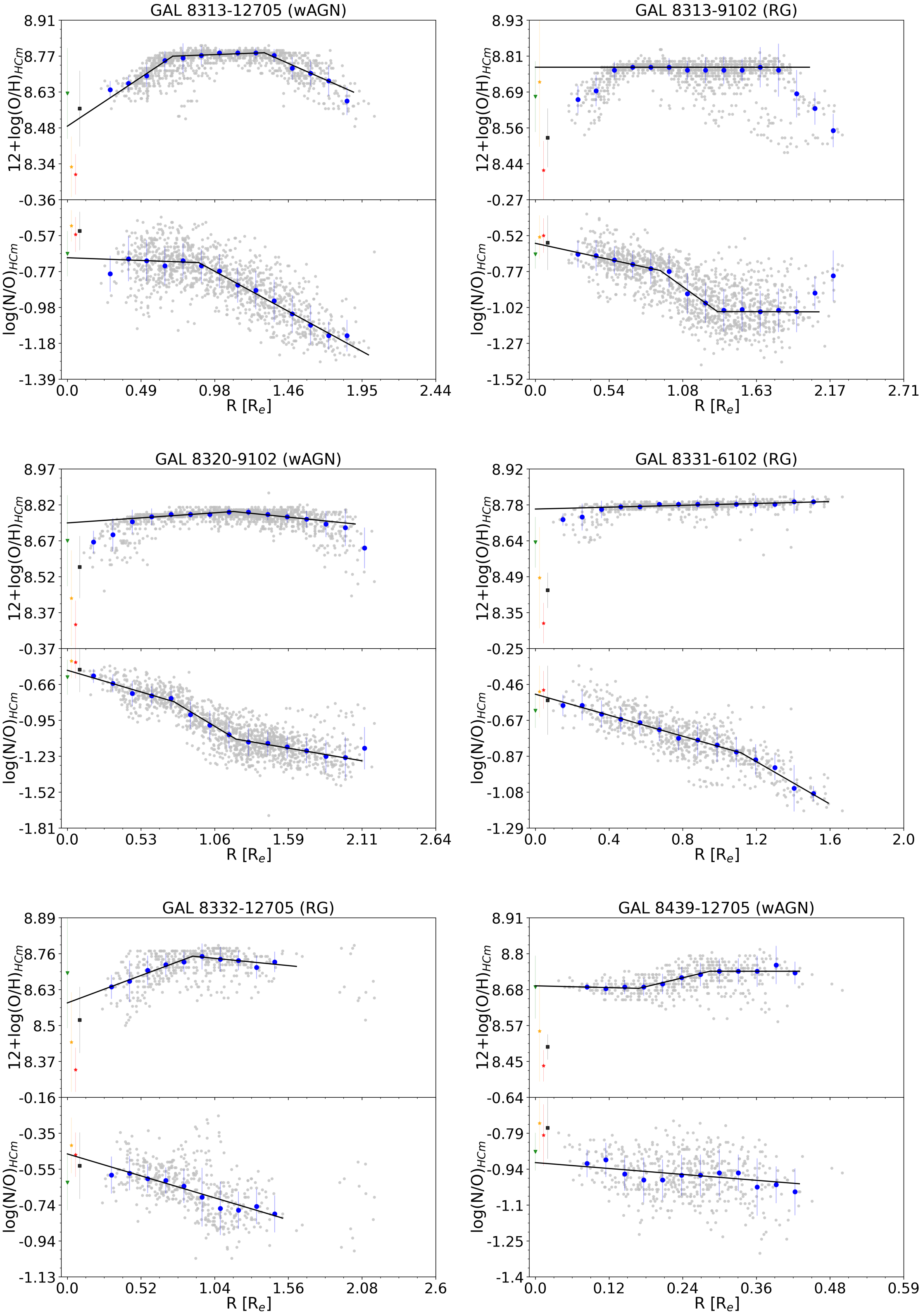

Figure C.5: continued.

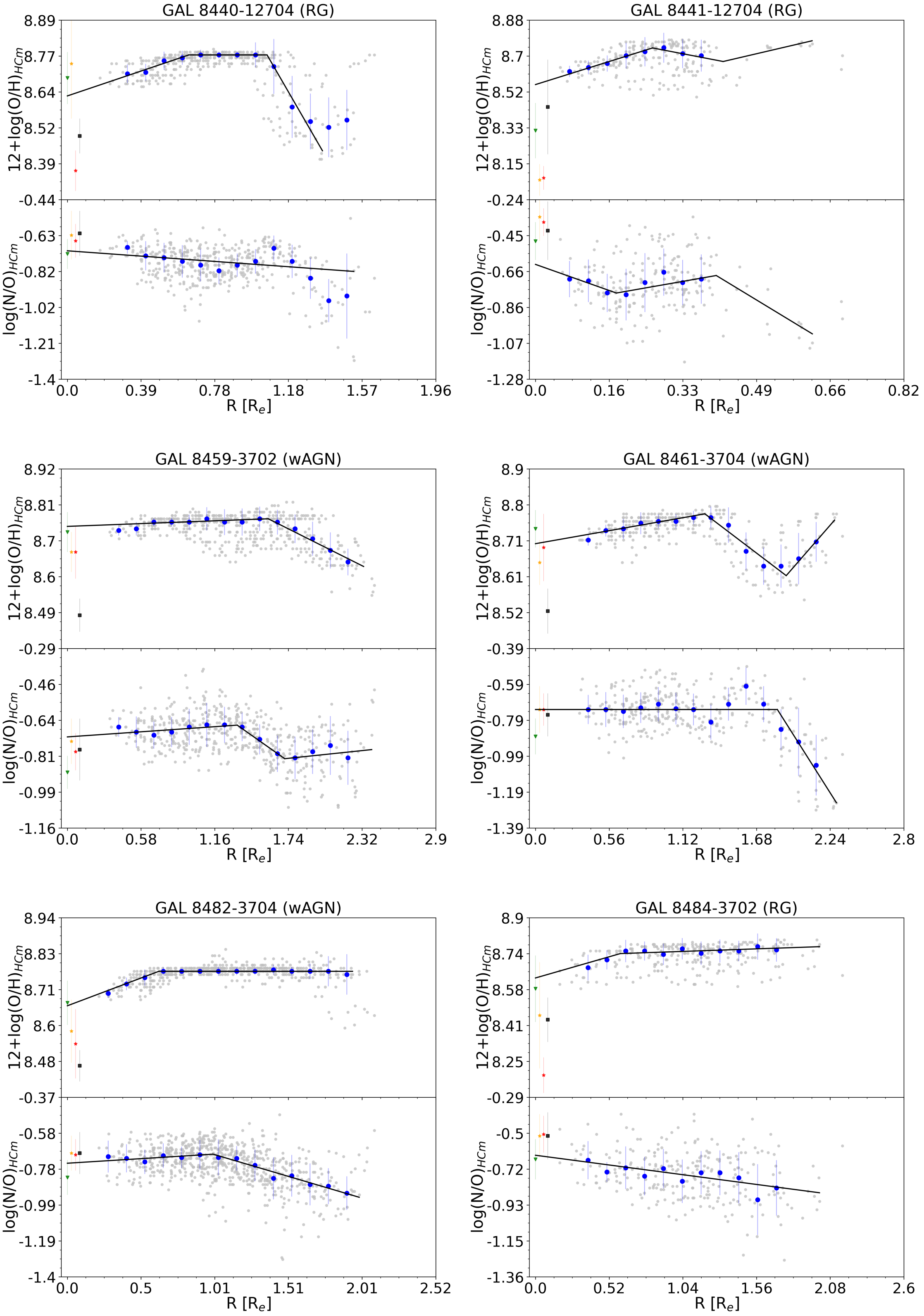

Figure C.5: continued.

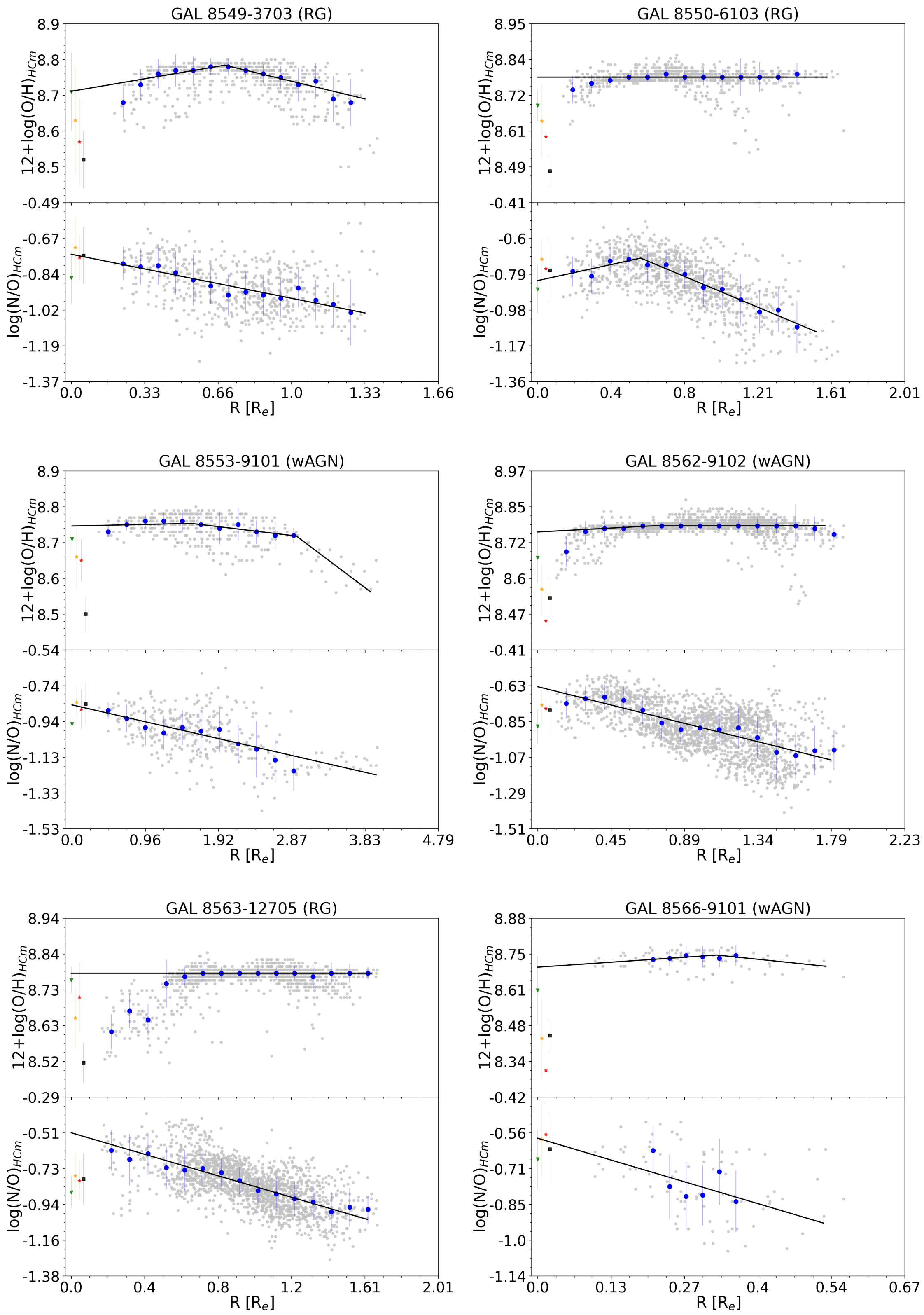

Figure C.5: continued.

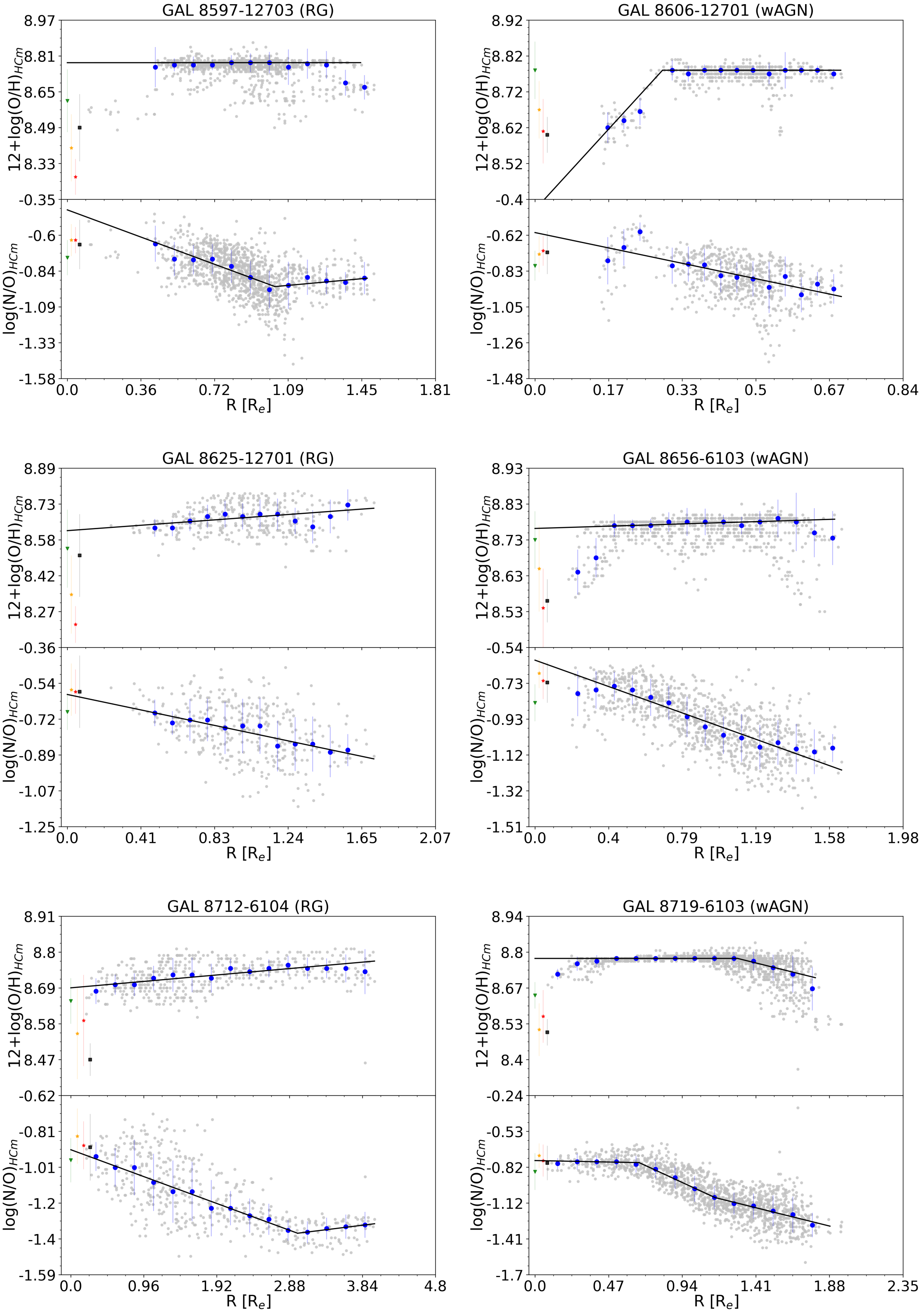

Figure C.5: continued.

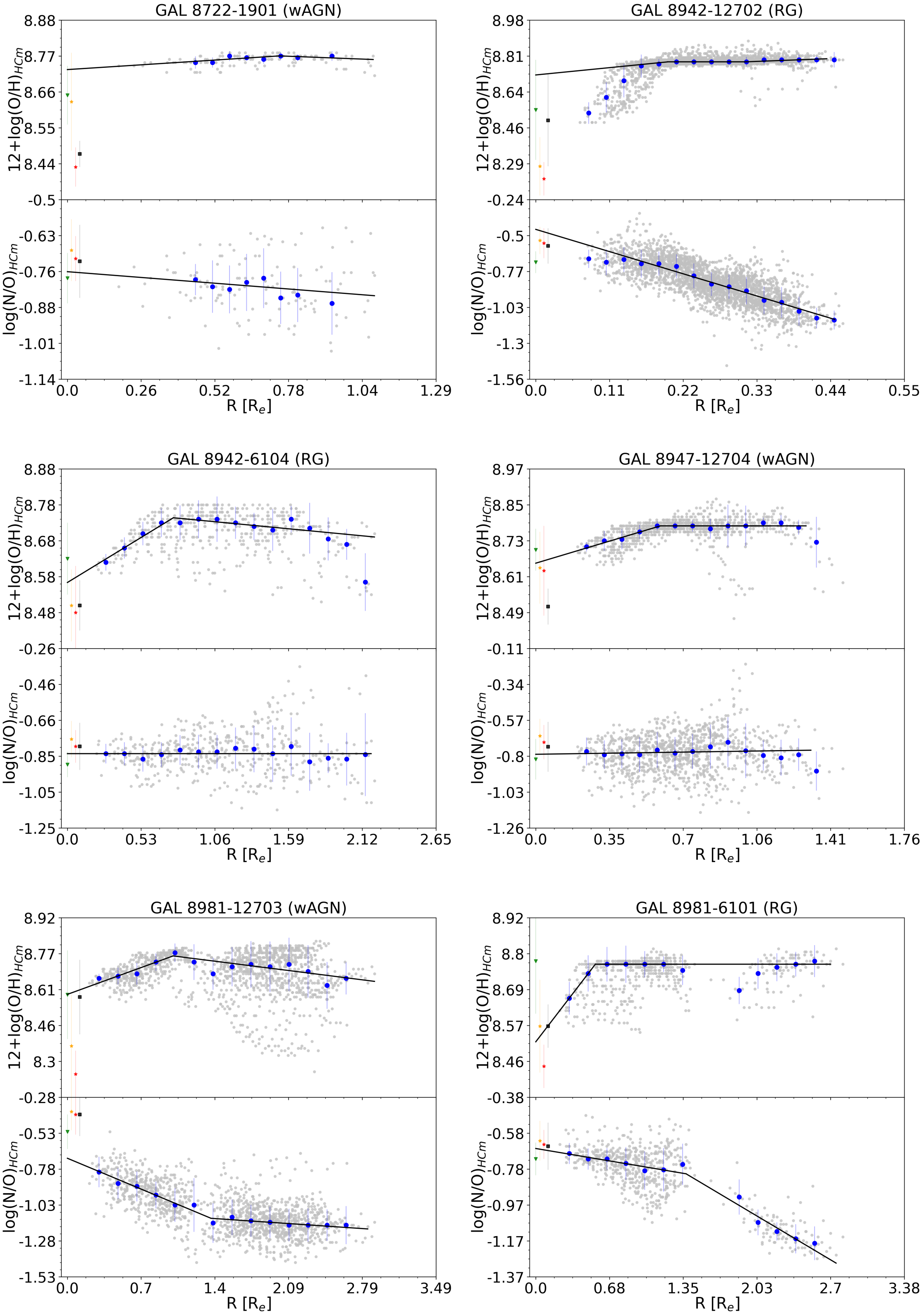

Figure C.5: continued.

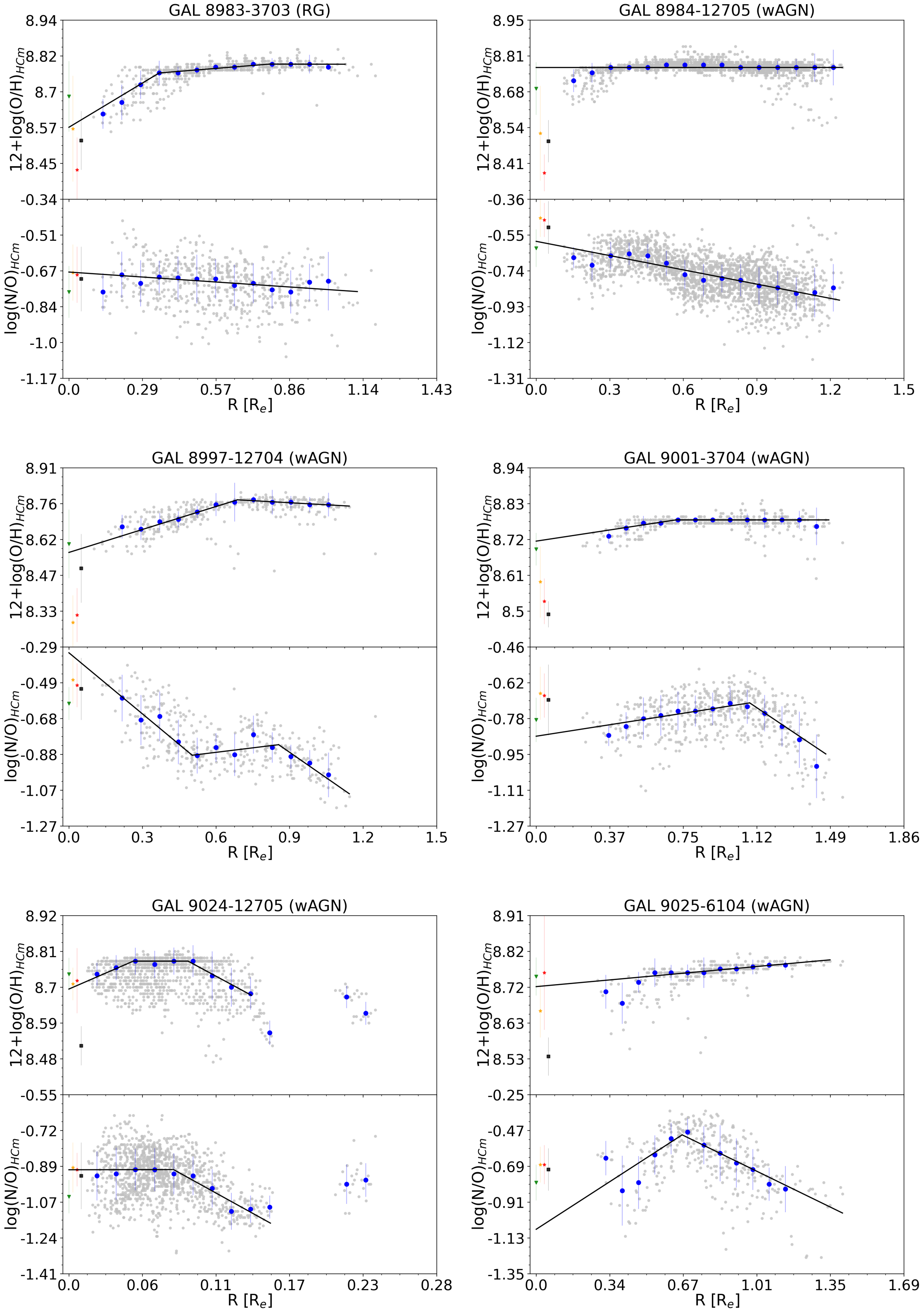

Figure C.5: continued.

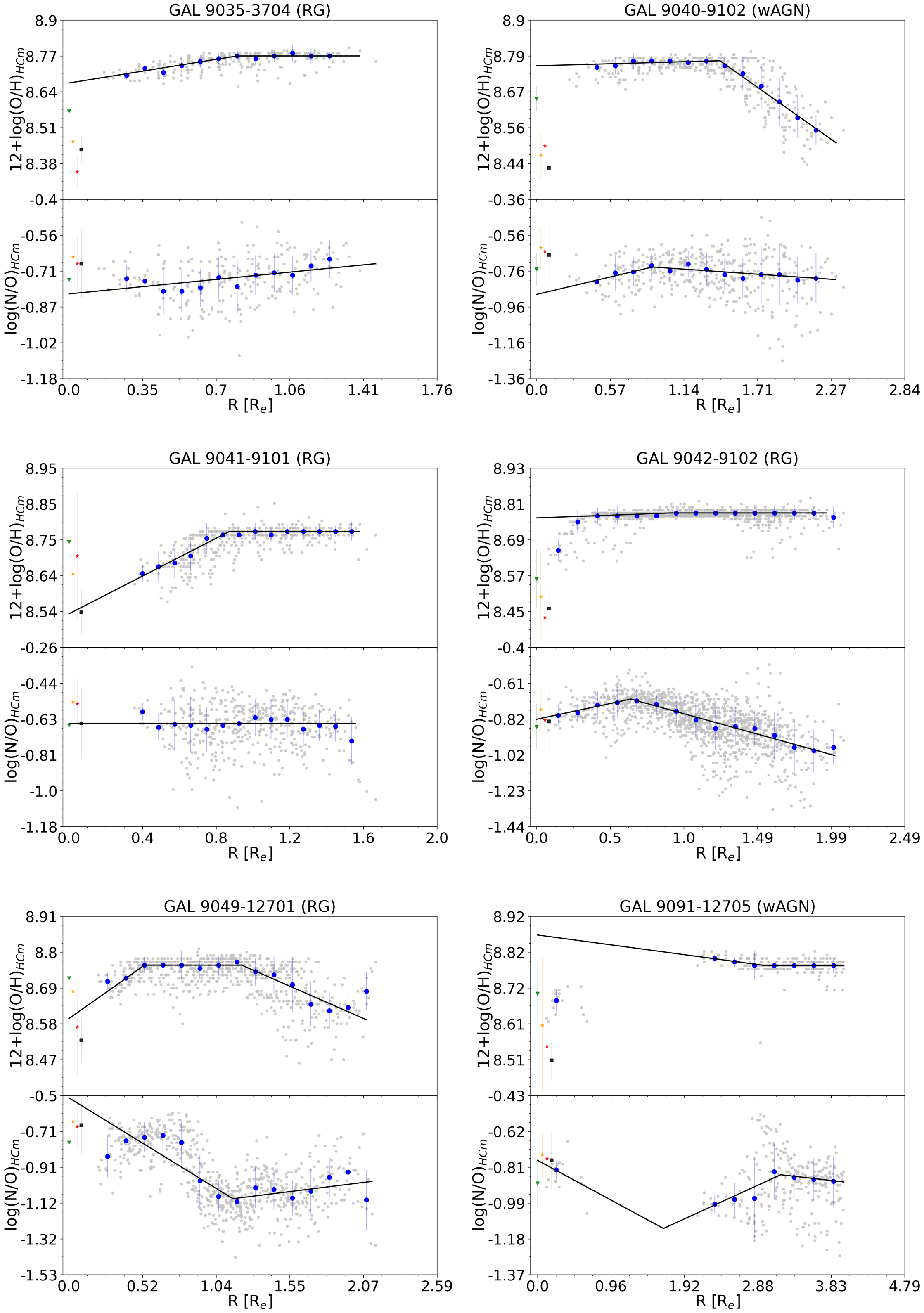

Figure C.5: continued.

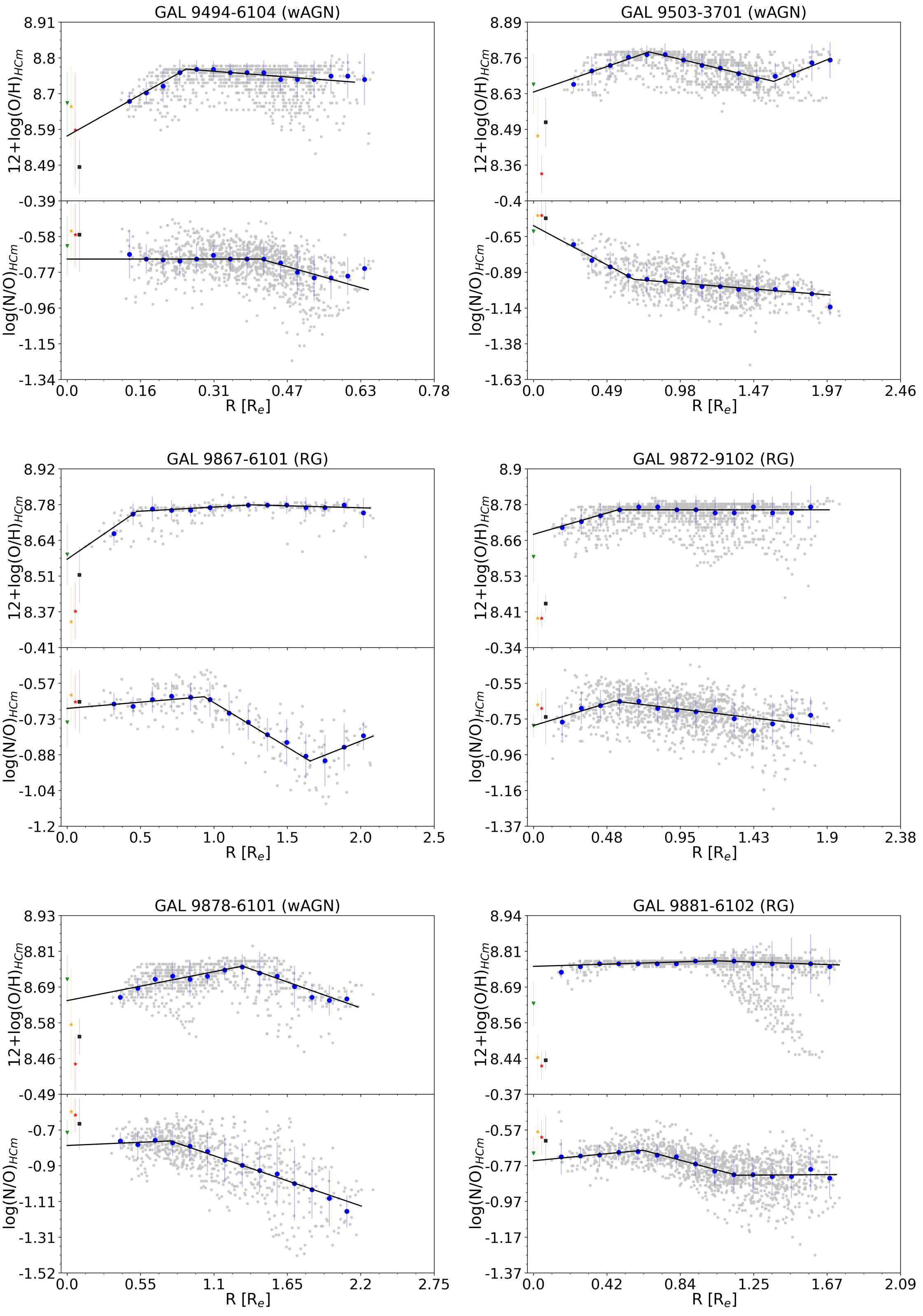

Figure C.5: continued.

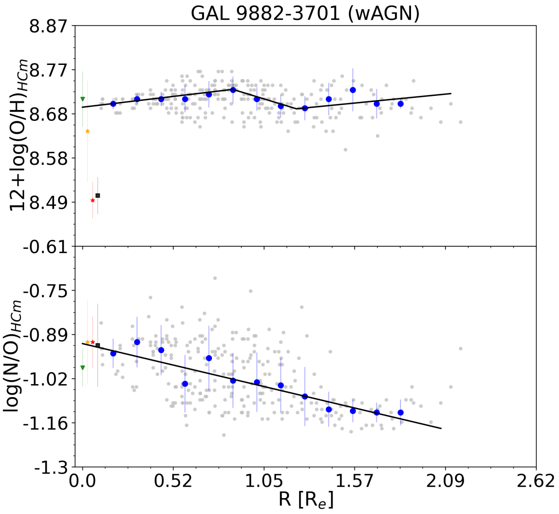

Figure C.5: continued.

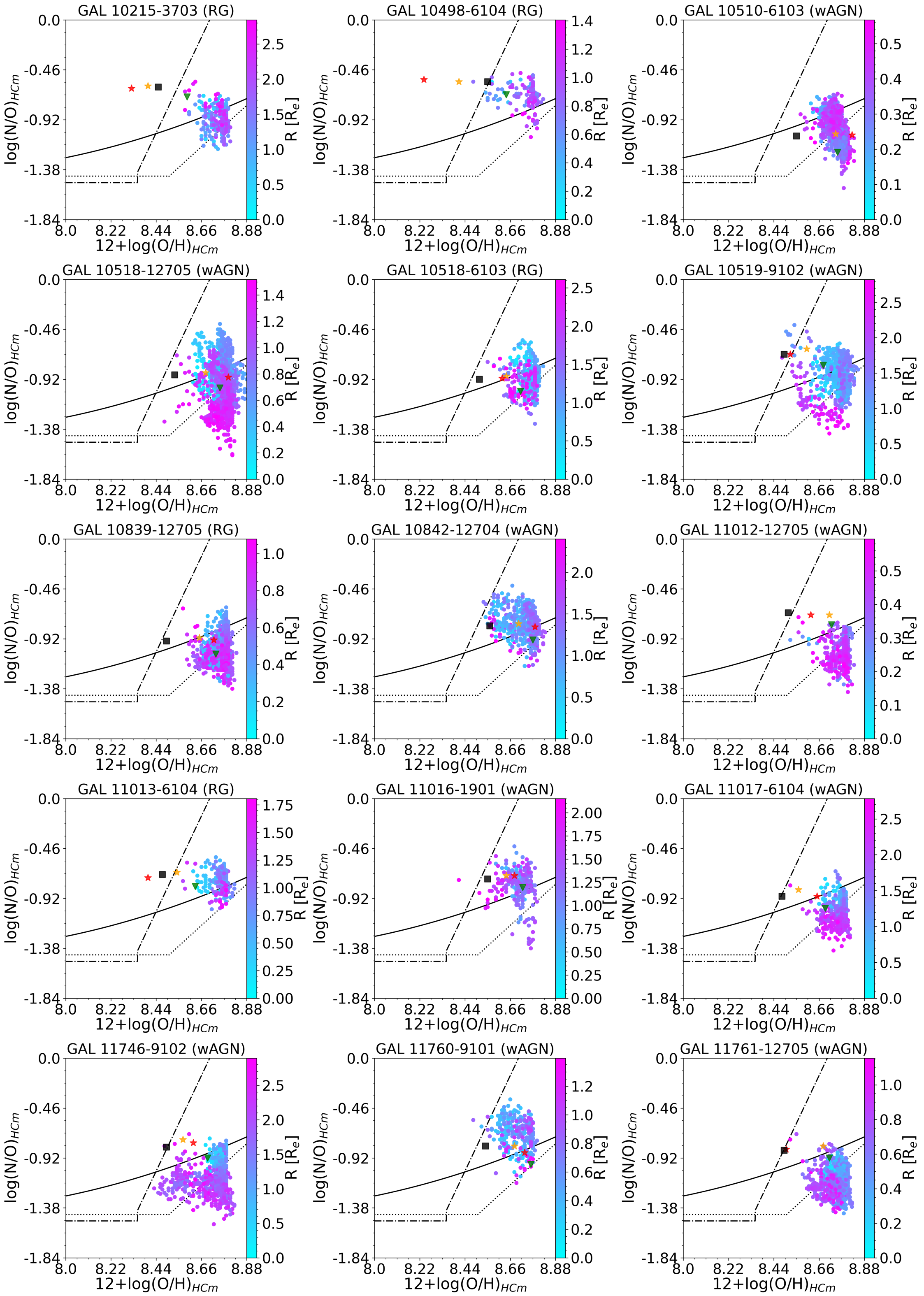

Figure C.6: N/O vs O/H diagram for the HII regions in our sample of LINERs. The colorbar shows the distance to the galactic center in terms of R$_e$. Nuclear estimations of the corresponding chemical abundance ratio are represented as follows: green triangles are the estimations from AGN models with $\alpha_{OX} = -1.6$; orange and red stars are the estimations from pAGB models with $T_{eff} = 10^5$ K and $T_{eff} = 1.5 \cdot 10^5$ K respectively; and black squares are the estimations from ADAF models. The solid back line represents the fit provided by Coziol et al. (1999), the dotted line shows the fit by Andrews and Martini (2013), and the dash-dotted line shows the fit by Belfiore et al. (2015).

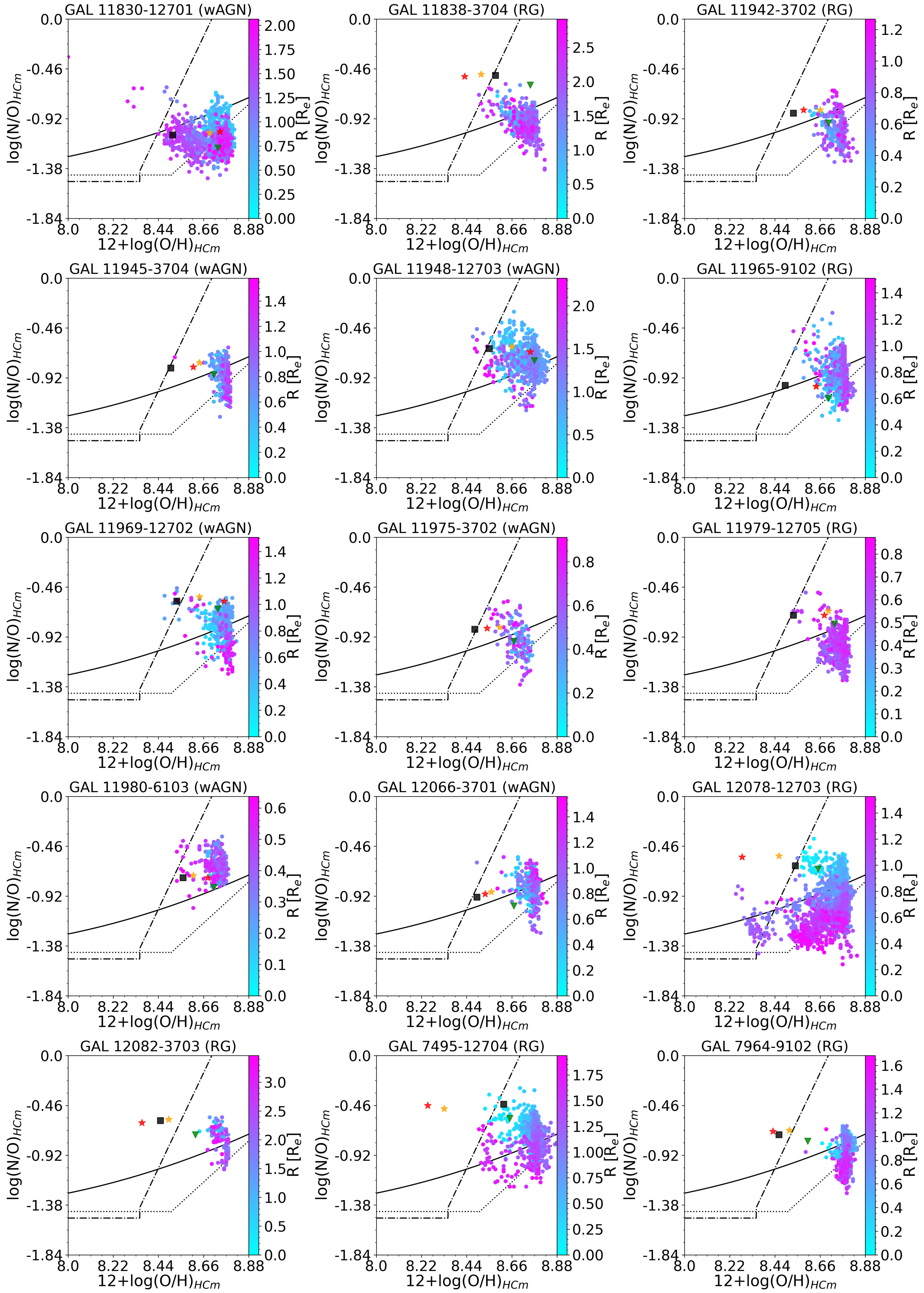

Figure C.6: continued.

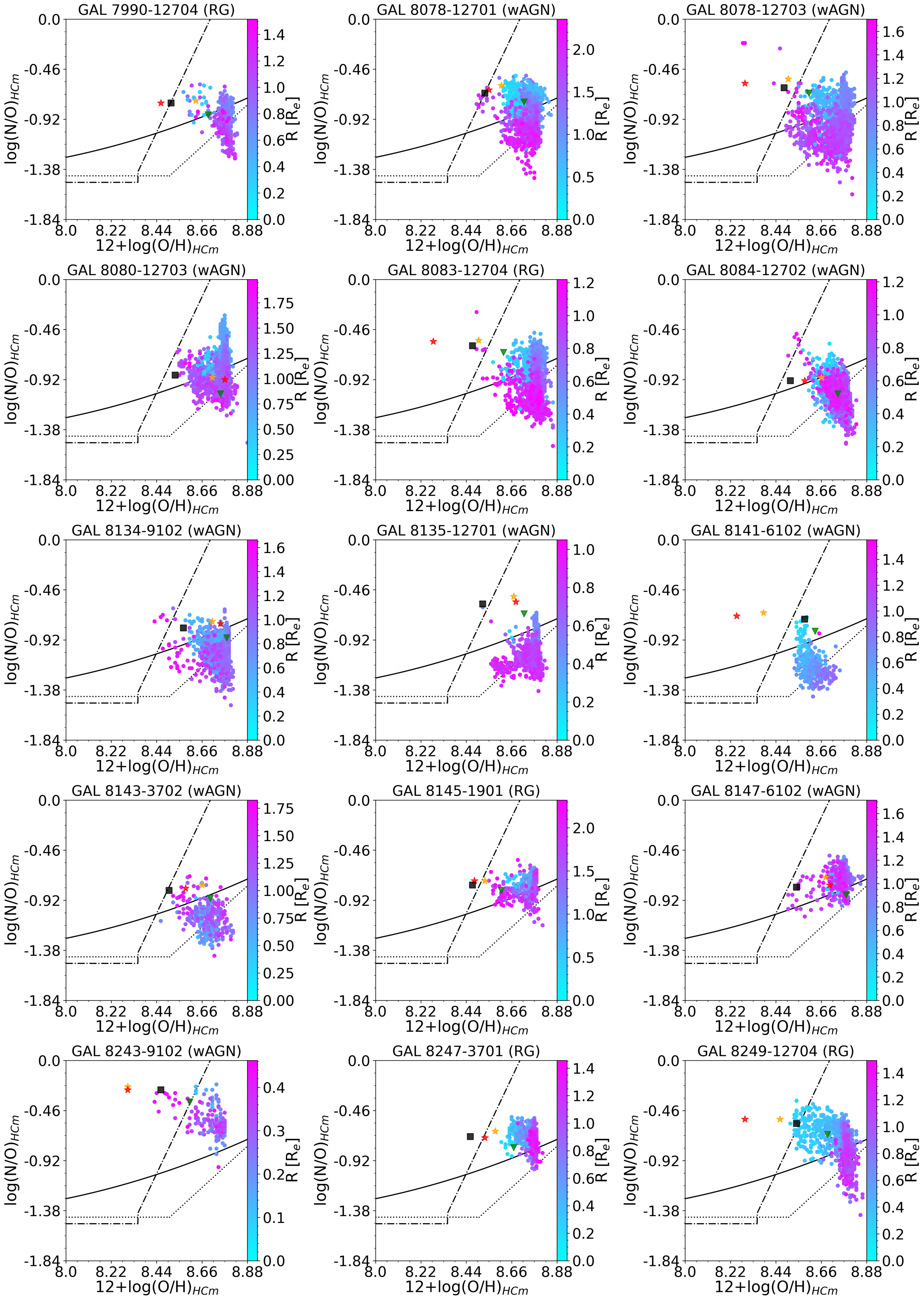

Figure C.6: continued.

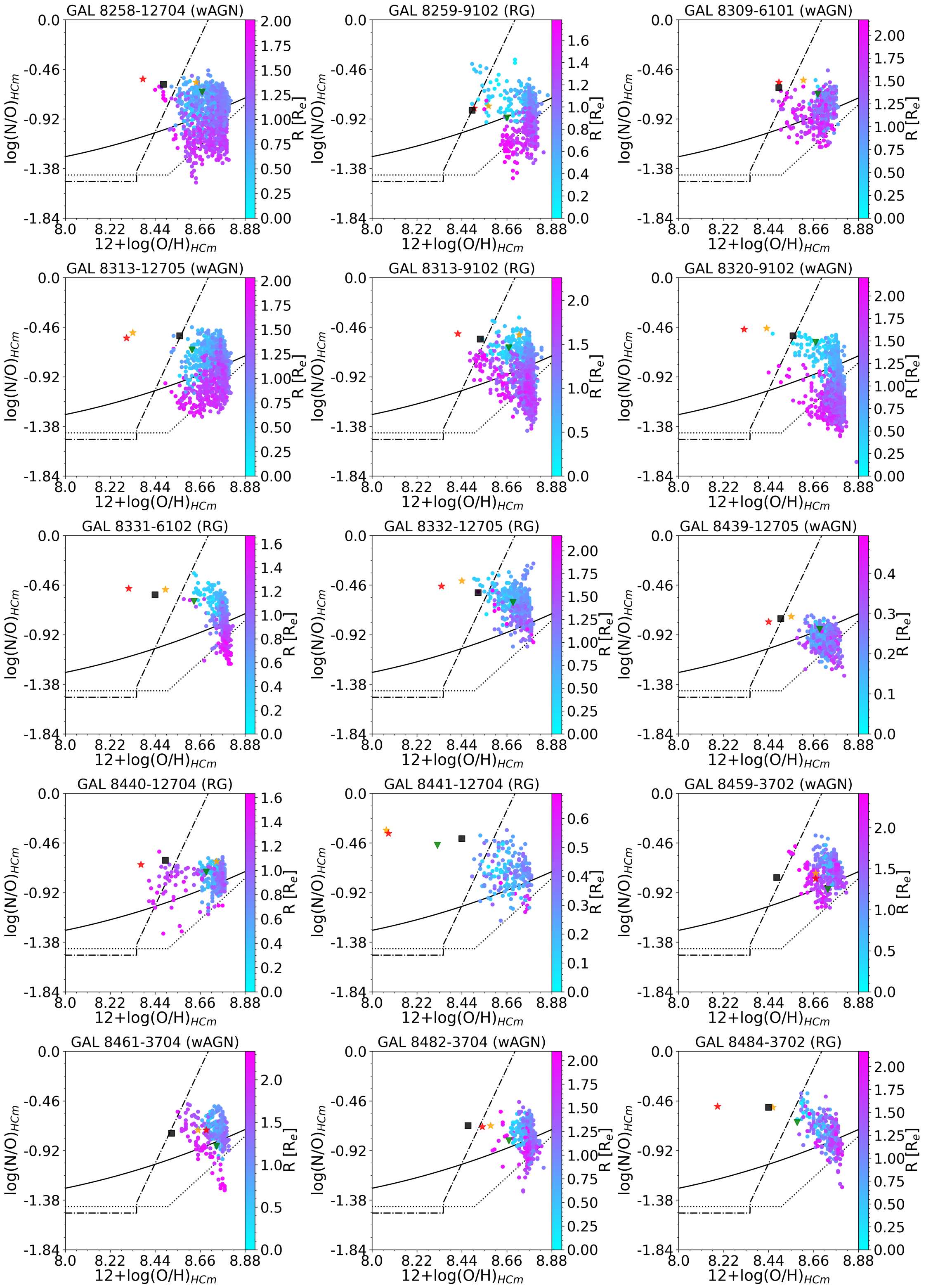

Figure C.6: continued.

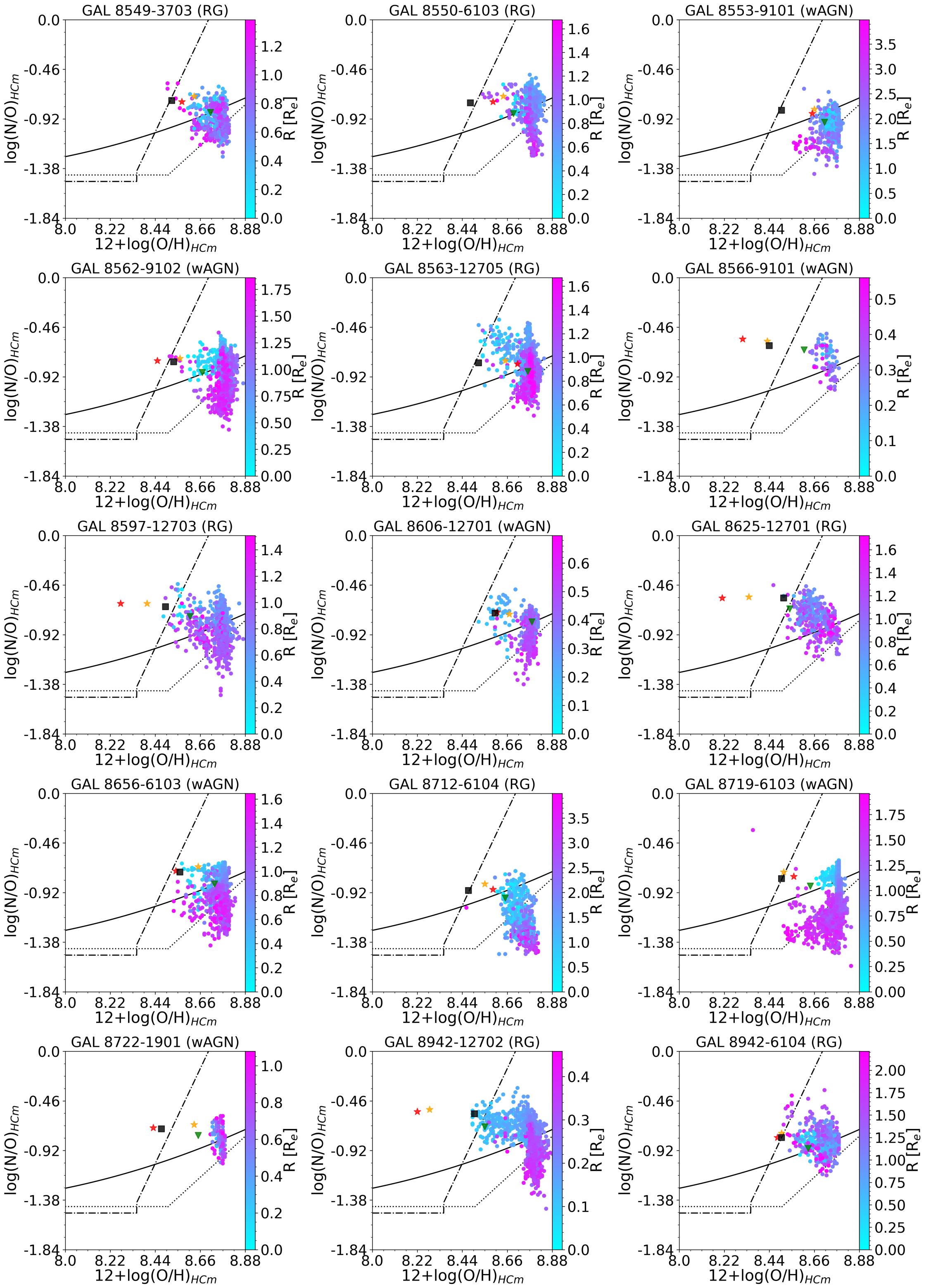

Figure C.6: continued.

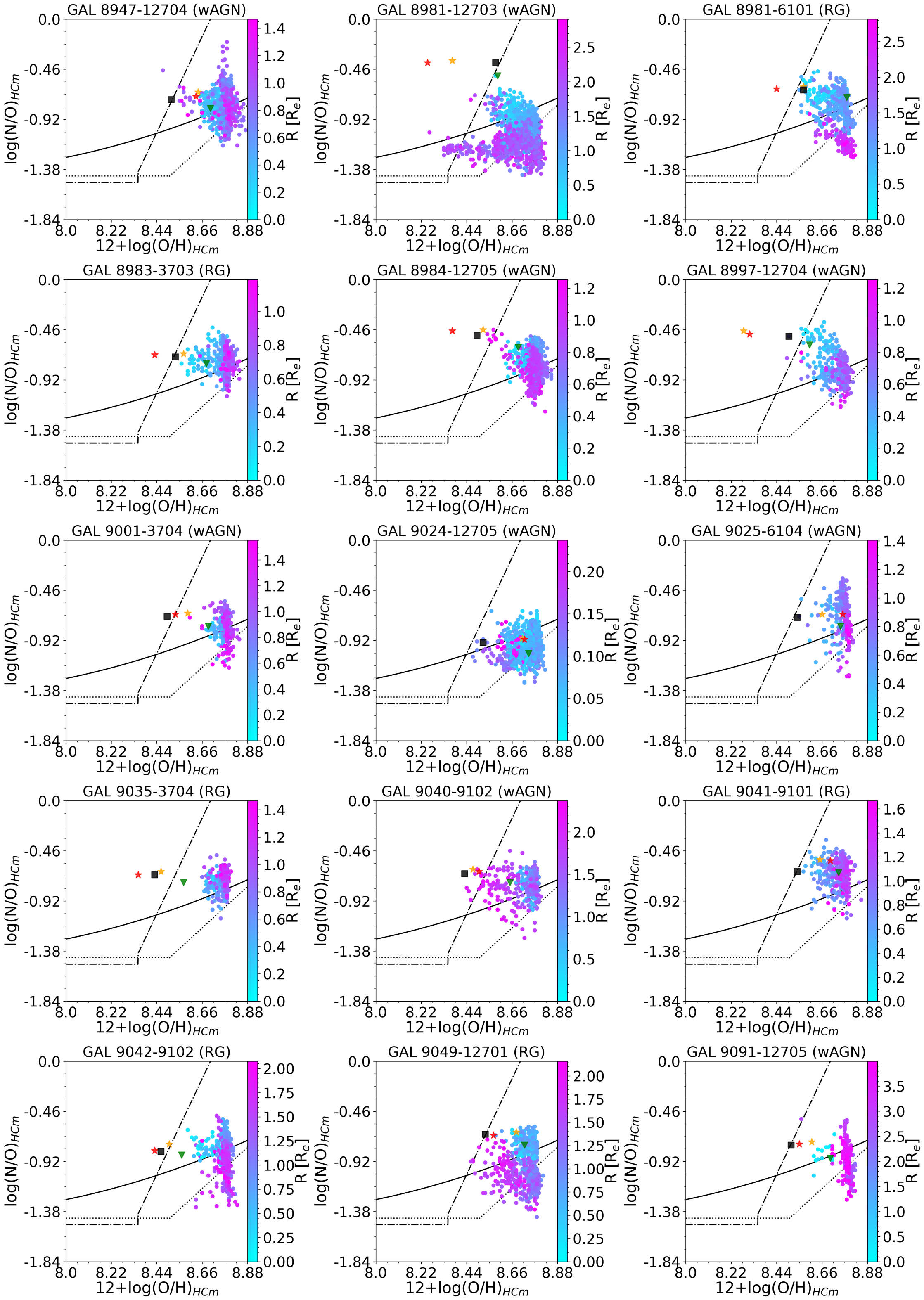

Figure C.6: continued.

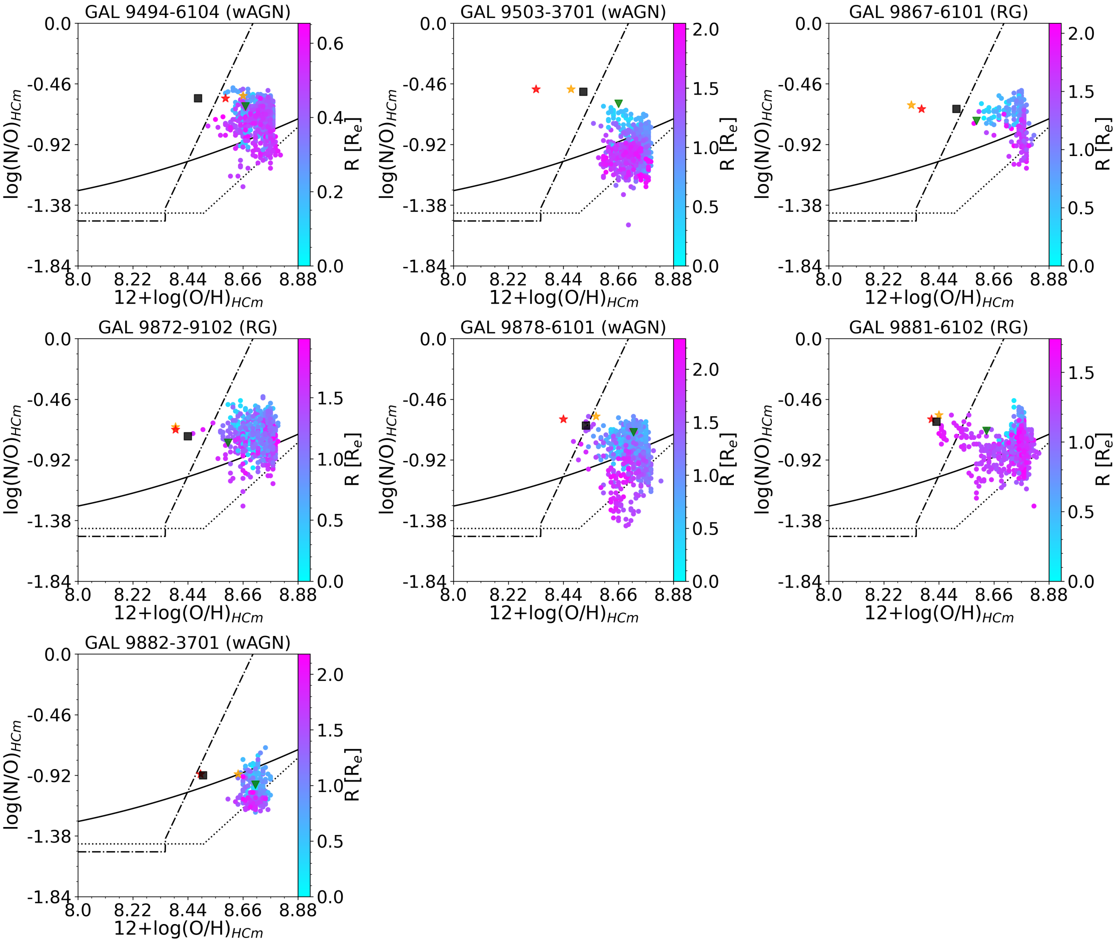

Figure C.6: continued.

BIBLIOGRAPHY

Aalto, S. (2007). Molecular gas properties in interacting and merging galaxies. *New A Rev.*, *51*(1-2), 52–57. https://doi.org/10.1016/j.newar.2006.11.010

Abdurro'uf, Accetta, K., Aerts, C., Silva Aguirre, V., Ahumada, R., Ajgaonkar, N., Filiz Ak, N., ... Zhu, K. (2022). The Seventeenth Data Release of the Sloan Digital Sky Surveys: Complete Release of MaNGA, MaStar, and APOGEE-2 Data. *ApJS*, *259*(2), Article 35, 35. https://doi.org/10.3847/1538-4365/ac4414

Adil, S. A., Akarsu, Ö., Malekjani, M., Ó Colgáin, E., Pourojaghi, S., Sen, A. A., & Sheikh-Jabbari, M. M. (2024). S_8 increases with effective redshift in ΛCDM cosmology. *MNRAS*, *528*(1), L20–L26. https://doi.org/10.1093/mnrasl/slad165

Affleck, I., & Dine, M. (1985). A new mechanism for baryogenesis. *Nuclear Physics B*, *2*, 361–380. https://doi.org/10.1016/0550-3213(85)90021-5

Ahn, C. P., Alexandroff, R., Allende Prieto, C., Anderson, S. F., Anderton, T., Andrews, B. H., Aubourg, É., ... Steinmetz, M. (2012). The Ninth Data Release of the Sloan Digital Sky Survey: First Spectroscopic Data from the SDSS-III Baryon Oscillation Spectroscopic Survey. *ApJS*, *203*(2), Article 21, 21. https://doi.org/10.1088/0067-0049/203/2/21

Aldrovandi, S. M. V., & Contini, M. (1985). Composite models for the narrow emission line region of active galactic nuclei. III. The ejected filament. *A&A*, *149*, 109–117.

Algera, H. S. B., Inami, H., Oesch, P. A., Sommovigo, L., Bouwens, R. J., Topping, M. W., Schouws, S., ... van der Werf, P. P. (2023). The ALMA REBELS survey: the dust-obscured cosmic star formation rate density at redshift 7. *MNRAS*, *518*(4), 6142–6157. https://doi.org/10.1093/mnras/stac3195

Ali, A., Sabin, L., Snaid, S., & Basurah, H. M. (2012). Interacting planetary nebulae. I. Classification and orientation. *A&A*, *541*, Article A98, A98. https://doi.org/10.1051/0004-6361/201118389

Allen, M. G., Groves, B. A., Dopita, M. A., Sutherland, R. S., & Kewley, L. J. (2008). The MAPPINGS III Library of Fast Radiative Shock Models. *ApJS*, *178*(1), 20–55. https://doi.org/10.1086/589652

Aller, L. H. (1984). *Physics of thermal gaseous nebulae*. https://doi.org/10.1007/978-94-010-9639-3

Alloin, D., Collin-Souffrin, S., Joly, M., & Vigroux, L. (1979). Nitrogen and oxygen abundances in galaxies. *A&A*, *78*, 200–216.

Alloin, D., Johnson, R., & Lira, P. (2006). *Physics of Active Galactic Nuclei at all Scales* (Vol. 693). Springer.

Alonso-Herrero, A., Rieke, G. H., Rieke, M. J., & Scoville, N. Z. (2000). Extreme Star Formation in the Interacting Galaxy Arp 299 (IC 694+NGC 3690). *ApJ*, *532*(2), 845–866. https://doi.org/10.1086/308622

Alvarez-Hurtado, P., Barrera-Ballesteros, J. K., Sánchez, S. F., Colombo, D., López-Sánchez, A. R., & Aquino-Ortíz, E. (2022). Which Galaxy Property is the Best Gauge of the Oxygen Abundance? *ApJ*, *929*(1), Article 47, 47. https://doi.org/10.3847/1538-4357/ac58fb

Amayo, A., Delgado-Inglada, G., & Stasińska, G. (2021). Ionization correction factors and dust depletion patterns in giant H II regions. *MNRAS*, *505*(2), 2361–2376. https://doi.org/10.1093/mnras/stab1467

Amiri, A., Knapen, J. H., Comerón, S., Marconi, A., & Lehmer, B. D. (2024). Gas-Phase metallicity for the Seyfert galaxy NGC 7130. *arXiv e-prints*, Article arXiv:2407.12158, arXiv:2407.12158. https://doi.org/10.48550/arXiv.2407.12158

Amorín, R., Pérez-Montero, E., Vílchez, J. M., & Papaderos, P. (2012). The Star Formation History and Metal Content of the Green Peas. New Detailed GTC-OSIRIS Spectrophotometry of Three Galaxies. *ApJ*, *749*(2), Article 185, 185. https://doi.org/10.1088/0004-637X/749/2/185

Amorín, R., Pérez-Montero, E., & Vílchez, J. M. (2010). On the Oxygen and Nitrogen Chemical Abundances and the Evolution of the "Green Pea" Galaxies. *ApJ*, *715*(2), L128–L132. https://doi.org/10.1088/2041-8205/715/2/L128

Anders, E., & Grevesse, N. (1989). Abundances of the elements: Meteoritic and solar. *Geochim. Cosmochim. Acta*, *53*(1), 197–214. https://doi.org/10.1016/0016-7037(89)90286-X

Andrews, B. H., & Martini, P. (2013). The Mass-Metallicity Relation with the Direct Method on Stacked Spectra of SDSS Galaxies. *ApJ*, *765*(2), Article 140, 140. https://doi.org/10.1088/0004-637X/765/2/140

Annibali, F., Bressan, A., Rampazzo, R., Zeilinger, W. W., Vega, O., & Panuzzo, P. (2010). Nearby early-type galaxies with ionized gas. IV. Origin and powering mechanism of the ionized gas. *A&A*, *519*, Article A40, A40. https://doi.org/10.1051/0004-6361/200913774

Antonucci, R. (2012). A panchromatic review of thermal and nonthermal active galactic nuclei. *Astronomical and Astrophysical Transactions*, *27*(4), 557–602. https://doi.org/10.48550/arXiv.1210.2716

Antonucci, R. (1993). Unified models for active galactic nuclei and quasars. *ARA&A*, *31*, 473–521. https://doi.org/10.1146/annurev.aa.31.090193.002353

Arcones, A., & Thielemann, F.-K. (2023). Origin of the elements. *A&A Rev.*, *31*(1), Article 1, 1. https://doi.org/10.1007/s00159-022-00146-x

Arellano-Córdova, K. Z., Berg, D. A., Mingozzi, M., James, B. L., Rogers, N. S. J., Skillman, E. D., Cullen, F., ... Wofford, A. (2024). CLASSY. IX. The Chemical Evolution of the Ne, S, Cl, and Ar Elements. *ApJ*, *968*(2), Article 98, 98. https://doi.org/10.3847/1538-4357/ad34cf

Armus, L., Charmandaris, V., Bernard-Salas, J., Spoon, H. W. W., Marshall, J. A., Higdon, S. J. U., Desai, V., ... Herter, T. L. (2007). Observations of Ultraluminous Infrared Galaxies with the Infrared Spectrograph on the Spitzer Space Telescope. II. The IRAS Bright Galaxy Sample. *ApJ*, *656*(1), 148–167. https://doi.org/10.1086/510107

Armus, L., Mazzarella, J. M., Evans, A. S., Surace, J. A., Sanders, D. B., Iwasawa, K., Frayer, D. T., ... Xu, K. (2009). GOALS: The Great Observatories All-Sky LIRG Survey. *PASP*, *121*(880), 559. https://doi.org/10.1086/600092

Arribas, S., Colina, L., Bellocchi, E., Maiolino, R., & Villar-Martín, M. (2014). Ionized gas outflows and global kinematics of low-z luminous star-forming galaxies. *A&A*, *568*, Article A14, A14. https://doi.org/10.1051/0004-6361/201323324

Arroyo-Polonio, A., Iglesias-Páramo, J., Kehrig, C., Vílchez, J. M., Amorín, R., Breda, I., Pérez-Montero, E., ... Hayes, M. (2023). A MUSE/VLT spatially resolved study of the emission structure of Green Pea galaxies. *A&A*, *677*, Article A114, A114. https://doi.org/10.1051/0004-6361/202346192

Asari, N. V., Cid Fernandes, R., Stasińska, G., Torres-Papaqui, J. P., Mateus, A., Sodré, L., Schoenell, W., & Gomes, J. M. (2007). The history of star-forming galaxies in the Sloan Digital Sky Survey. *MNRAS*, *381*(1), 263–279. https://doi.org/10.1111/j.1365-2966.2007.12255.x

Asplund, M., Grevesse, N., Sauval, A. J., & Scott, P. (2009). The Chemical Composition of the Sun. *ARA&A*, *47*(1), 481–522. https://doi.org/10.1146/annurev.astro.46.060407.145222

Athanassoula, E. (1992). The existence and shapes of dust lanes in galactic bars. *MNRAS*, *259*, 345–364. https://doi.org/10.1093/mnras/259.2.345

Baker, W. M., Maiolino, R., Belfiore, F., Curti, M., Bluck, A. F. L., Lin, L., Ellison, S. L., ... Pan, H.-A. (2023). The metallicity's fundamental dependence on both local and global galactic quantities. *MNRAS*, *519*(1), 1149–1170. https://doi.org/10.1093/mnras/stac3594

Baldwin, J. A., Phillips, M. M., & Terlevich, R. (1981). Classification parameters for the emission-line spectra of extragalactic objects. *PASP*, *93*, 5–19. https://doi.org/10.1086/130766

Balogh, M. L., Morris, S. L., Yee, H. K. C., Carlberg, R. G., & Ellingson, E. (1999). Differential Galaxy Evolution in Cluster and Field Galaxies at z~0.3. *ApJ*, *527*(1), 54–79. https://doi.org/10.1086/308056

Barquín-González, L., Mateos, S., Carrera, F. J., Ordovás-Pascual, I., Alonso-Herrero, A., Caccianiga, A., Cardiel, N., ... Severgnini, P. (2024). Extinction and AGN over host galaxy contrast effects on the optical spectroscopic classification of AGN. *A&A*, *687*, Article A159, A159. https://doi.org/10.1051/0004-6361/202348948

Belfiore, F., Maiolino, R., Bundy, K., Thomas, D., Maraston, C., Wilkinson, D., Sánchez, S. F., ... Simmons, A. (2015). P-MaNGA Galaxies: emission-lines properties - gas ionization and chemical abundances from prototype observations. *MNRAS*, *449*(1), 867–900. https://doi.org/10.1093/mnras/stv296

Belfiore, F., Vincenzo, F., Maiolino, R., & Matteucci, F. (2019). From 'bathtub' galaxy evolution models to metallicity gradients. *MNRAS*, *487*(1), 456–474. https://doi.org/10.1093/mnras/stz1165

Belfiore, F., Maiolino, R., Tremonti, C., Sánchez, S. F., Bundy, K., Bershady, M., Westfall, K., ... Brinkmann, J. (2017). SDSS IV MaNGA - metallicity and nitrogen abundance gradients in local galaxies. *MNRAS*, *469*(1), 151–170. https://doi.org/10.1093/mnras/stx789

Bell, E. F., McIntosh, D. H., Katz, N., & Weinberg, M. D. (2003). The Optical and Near-Infrared Properties of Galaxies. I. Luminosity and Stellar Mass Functions. *ApJS*, *149*(2), 289–312. https://doi.org/10.1086/378847

Bellamy, M. J., & Tadhunter, C. N. (2004). A giant molecular cloud falling through the heart of Cygnus A: clues to the triggering of the activity. *MNRAS*, *353*(1), 105–112. https://doi.org/10.1111/j.1365-2966.2004.08050.x

Bellamy, M. J., Tadhunter, C. N., Morganti, R., Wills, K. A., Holt, J., Taylor, M. D., & Watson, C. A. (2003). Near-infrared spectroscopy of PKS 1549-79: a protoquasar revealed? *MNRAS*, *344*(4), L80–L84. https://doi.org/10.1046/j.1365-8711.2003.07078.x

Bendo, G. J., & Joseph, R. D. (2004). Nuclear Stellar Populations in the Infrared Space Observatory Atlas of Bright Spiral Galaxies. *AJ*, *127*(6), 3338–3360. https://doi.org/10.1086/420712

Bennert, N., Jungwiert, B., Komossa, S., Haas, M., & Chini, R. (2006a). Size and properties of the narrow-line region in Seyfert-2 galaxies from spatially-resolved optical spectroscopy. *A&A*, *456*(3), 953–966. https://doi.org/10.1051/0004-6361:20065319

Bennert, N., Jungwiert, B., Komossa, S., Haas, M., & Chini, R. (2006b). Size and properties of the narrow-line region in Seyfert-2 galaxies from spatially-resolved optical spectroscopy. *A&A*, *456*(3), 953–966. https://doi.org/10.1051/0004-6361:20065319

Bennert, N., Jungwiert, B., Komossa, S., Haas, M., & Chini, R. (2006c). Size and properties of the narrow-line region in Seyfert-1 galaxies from spatially-resolved optical spectroscopy. *A&A*, *459*(1), 55–69. https://doi.org/10.1051/0004-6361:20065477

Berg, D. A., Pogge, R. W., Skillman, E. D., Croxall, K. V., Moustakas, J., Rogers, N. S. J., & Sun, J. (2020). CHAOS IV: Gas-phase Abundance Trends from the First Four CHAOS Galaxies. *ApJ*, *893*(2), Article 96, 96. https://doi.org/10.3847/1538-4357/ab7eab

Berg, D. A., Skillman, E. D., Henry, R. B. C., Erb, D. K., & Carigi, L. (2016). Carbon and Oxygen Abundances in Low Metallicity Dwarf Galaxies. *ApJ*, *827*(2), Article 126, 126. https://doi.org/10.3847/0004-637X/827/2/126

Bergvall, N., Marquart, T., Way, M. J., Blomqvist, A., Holst, E., Östlin, G., & Zackrisson, E. (2016). Local starburst galaxies and their descendants. Statistics from the Sloan Digital Sky Survey. *A&A*, *587*, Article A72, A72. https://doi.org/10.1051/0004-6361/201525692

Berkhuijsen, E. M., & Müller, P. (2008). Densities and filling factors of the diffuse ionized gas in the Solar neighbourhood. *A&A*, *490*(1), 179–187. https://doi.org/10.1051/0004-6361:200809675

Bernard-Salas, J., Spoon, H. W. W., Charmandaris, V., Lebouteiller, V., Farrah, D., Devost, D., Brandl, B. R., ... Houck, J. R. (2009). A Spitzer High-resolution Mid-Infrared Spectral Atlas of Starburst Galaxies. *ApJS*, *184*(2), 230–247. https://doi.org/10.1088/0067-0049/184/2/230

Béthermin, M., Fudamoto, Y., Ginolfi, M., Loiacono, F., Khusanova, Y., Capak, P. L., Cassata, P., ... Zucca, E. (2020). The ALPINE-ALMA [CII] survey: Data processing, catalogs, and statistical source properties. *A&A*, *643*, Article A2, A2. https://doi.org/10.1051/0004-6361/202037649

Bica, E., Ortolani, S., Barbuy, B., & Oliveira, R. A. P. (2024). A census of new globular clusters in the Galactic bulge. *A&A*, *687*, Article A201, A201. https://doi.org/10.1051/0004-6361/202346377

Binette, L. (1985). Photoionization models for liners : gas distribution abundances. *A&A*, *143*, 334–346.

Binette, L., Magris, C. G., Stasińska, G., & Bruzual, A. G. (1994). Photoionization in elliptical galaxies by old stars. *A&A*, *292*, 13–19.

Blagrave, K. P. M., Martin, P. G., Rubin, R. H., Dufour, R. J., Baldwin, J. A., Hester, J. J., & Walter, D. K. (2007). Deviations from He I Case B Recombination Theory and Extinction Corrections in the Orion Nebula. *ApJ*, *655*(1), 299–315. https://doi.org/10.1086/510151

Blanc, G. A., Heiderman, A., Gebhardt, K., Evans, N. J., II, & Adams, J. (2009). The Spatially Resolved Star Formation Law From Integral Field Spectroscopy: VIRUS-P Observations of NGC 5194. *ApJ*, *704*(1), 842–862. https://doi.org/10.1088/0004-637X/704/1/842

Blanc, G. A., Kewley, L., Vogt, F. P. A., & Dopita, M. A. (2015). IZI: Inferring the Gas Phase Metallicity (Z) and Ionization Parameter (q) of Ionized Nebulae Using Bayesian Statistics. *ApJ*, *798*(2), Article 99, 99. https://doi.org/10.1088/0004-637X/798/2/99

Blanc, G. A., Lu, Y., Benson, A., Katsianis, A., & Barraza, M. (2019). A Characteristic Mass Scale in the Mass-Metallicity Relation of Galaxies. *ApJ*, *877*(1), Article 6, 6. https://doi.org/10.3847/1538-4357/ab16ec

Blanton, M. R., Bershady, M. A., Abolfathi, B., Albareti, F. D., Allende Prieto, C., Almeida, A., Alonso-García, J., ... Zou, H. (2017). Sloan Digital Sky Survey IV: Mapping the Milky Way, Nearby Galaxies, and the Distant Universe. *AJ*, *154*(1), Article 28, 28. https://doi.org/10.3847/1538-3881/aa7567

Blanton, M. R., Lin, H., Lupton, R. H., Maley, F. M., Young, N., Zehavi, I., & Loveday, J. (2003). An Efficient Targeting Strategy for Multiobject Spectrograph Surveys: the Sloan Digital Sky Survey "Tiling" Algorithm. *AJ*, *125*(4), 2276–2286. https://doi.org/10.1086/344761

Blasi, P. (2013). The origin of galactic cosmic rays. *A&A Rev.*, *21*, Article 70, 70. https://doi.org/10.1007/s00159-013-0070-7

Böker, T., Beck, T. L., Birkmann, S. M., Giardino, G., Keyes, C., Kumari, N., Muzerolle, J., ... Willott, C. J. (2023). In-orbit Performance of the Near-infrared Spectrograph NIRSpec on the James Webb Space Telescope. *PASP*, *135*(1045), Article 038001, 038001. https://doi.org/10.1088/1538-3873/acb846

Boksenberg, A., Shortridge, K., Allen, D. A., Fosbury, R. A. E., Penston, M. V., & Savage, A. (1975). New observation of the optical spectrum of the Seyfert galaxy NGC 4151. *MNRAS*, *173*, 381–396. https://doi.org/10.1093/mnras/173.2.381

Boquien, M., Burgarella, D., Roehlly, Y., Buat, V., Ciesla, L., Corre, D., Inoue, A. K., & Salas, H. (2019). CIGALE: a python Code Investigating GALaxy Emission. *A&A*, *622*, Article A103, A103. https://doi.org/10.1051/0004-6361/201834156

Bouché, N., Dekel, A., Genzel, R., Genel, S., Cresci, G., Förster Schreiber, N. M., Shapiro, K. L., ... Tacconi, L. (2010). The Impact of Cold Gas Accretion Above a Mass Floor on Galaxy Scaling Relations. *ApJ*, *718*(2), 1001–1018. https://doi.org/10.1088/0004-637X/718/2/1001

Bouwens, R. J., Illingworth, G., Ellis, R. S., Oesch, P., & Stefanon, M. (2022). z 2-9 Galaxies Magnified by the Hubble Frontier Field Clusters. II. Luminosity Functions and Constraints on a Faint-end Turnover. *ApJ*, *940*(1), Article 55, 55. https://doi.org/10.3847/1538-4357/ac86d1

Bower, R. G., Benson, A. J., Malbon, R., Helly, J. C., Frenk, C. S., Baugh, C. M., Cole, S., & Lacey, C. G. (2006). Breaking the hierarchy of galaxy formation. *MNRAS*, *370*(2), 645–655. https://doi.org/10.1111/j.1365-2966.2006.10519.x

Brandl, B., Bettonvil, F., van Boekel, R., Glauser, A., Quanz, S., Absil, O., Amorim, A., ... METIS Consortium. (2021). METIS: The Mid-infrared ELT Imager and Spectrograph. *The Messenger*, *182*, 22–26. https://doi.org/10.18727/0722-6691/5218

Brauher, J. R., Dale, D. A., & Helou, G. (2008). A Compendium of Far-Infrared Line and Continuum Emission for 227 Galaxies Observed by the Infrared Space Observatory. *ApJS*, *178*(2), 280–301. https://doi.org/10.1086/590249

Bresolin, F., Gieren, W., Kudritzki, R.-P., Pietrzyński, G., Urbaneja, M. A., & Carraro, G. (2009). Extragalactic Chemical Abundances: Do H II Regions and Young Stars Tell the Same Story? The Case of the Spiral Galaxy NGC 300. *ApJ*, *700*(1), 309–330. https://doi.org/10.1088/0004-637X/700/1/309

Bresolin, F., Kennicutt, R. C., & Ryan-Weber, E. (2012). Gas Metallicities in the Extended Disks of NGC 1512 and NGC 3621. Chemical Signatures of Metal Mixing or Enriched Gas Accretion? *ApJ*, *750*(2), Article 122, 122. https://doi.org/10.1088/0004-637X/750/2/122

Brinchmann, J., Charlot, S., White, S. D. M., Tremonti, C., Kauffmann, G., Heckman, T., & Brinkmann, J. (2004). The physical properties of star-forming galaxies in the low-redshift Universe. *MNRAS*, *351*(4), 1151–1179. https://doi.org/10.1111/j.1365-2966.2004.07881.x

Brown, M. J. I., Moustakas, J., Kennicutt, R. C., Bonne, N. J., Intema, H. T., de Gasperin, F., Boquien, M., ... Peek, J. E. G. (2017). Calibration of Ultraviolet, Mid-infrared, and Radio Star Formation Rate Indicators. *ApJ*, *847*(2), Article 136, 136. https://doi.org/10.3847/1538-4357/aa8ad2

Bruzual, G., & Charlot, S. (2003). Stellar population synthesis at the resolution of 2003. *MNRAS*, *344*(4), 1000–1028. https://doi.org/10.1046/j.1365-8711.2003.06897.x

Bruzual A., G. (1983). Spectral evolution of galaxies. I. Early-type systems. *ApJ*, *273*, 105–127. https://doi.org/10.1086/161352

Buchanan, C. L., McGregor, P. J., Bicknell, G. V., & Dopita, M. A. (2006). Radio-Excess IRAS Galaxies. IV. Optical Spectroscopy. *AJ*, *132*(1), 27–49. https://doi.org/10.1086/504409

Bullock, J. S., & Boylan-Kolchin, M. (2017). Small-Scale Challenges to the ΛCDM Paradigm. *ARA&A*, *55*(1), 343–387. https://doi.org/10.1146/annurev-astro-091916-055313

Bundy, K., Bershady, M. A., Law, D. R., Yan, R., Drory, N., MacDonald, N., Wake, D. A., ... Zhang, K. (2015). Overview of the SDSS-IV MaNGA Survey: Mapping nearby Galaxies at Apache Point Observatory. *ApJ*, *798*(1), Article 7, 7. https://doi.org/10.1088/0004-637X/798/1/7

Busso, M., Gallino, R., Lambert, D. L., Travaglio, C., & Smith, V. V. (2001). Nucleosynthesis and Mixing on the Asymptotic Giant Branch. III. Predicted and Observed s-Process Abundances. *ApJ*, *557*(2), 802–821. https://doi.org/10.1086/322258

Bustamante, S., Sparre, M., Springel, V., & Grand, R. J. J. (2018). Merger-induced metallicity dilution in cosmological galaxy formation simulations. *MNRAS*, *479*(3), 3381–3392. https://doi.org/10.1093/mnras/sty1692

Buttiglione, S., Capetti, A., Celotti, A., Axon, D. J., Chiaberge, M., Macchetto, F. D., & Sparks, W. B. (2009). An optical spectroscopic survey of the 3CR sample of radio galaxies with $z < 0.3$. I. Presentation of the data. *A&A*, *495*(3), 1033–1060. https://doi.org/10.1051/0004-6361:200811102

Byrne, L., Christensen, C., Tsekitsidis, M., Brooks, A., & Quinn, T. (2019). Implementing Dust Shielding as a Criteria for Star Formation. *ApJ*, *871*(2), Article 213, 213. https://doi.org/10.3847/1538-4357/aaf9aa

Calabrò, A., Amorín, R., Fontana, A., Pérez-Montero, E., Lemaux, B. C., Ribeiro, B., Bardelli, S., ... Zucca, E. (2017). Characterization of star-forming dwarf galaxies at 0.1 $\lesssim z \lesssim$ 0.9 in VUDS: probing the low-mass end of the mass-metallicity relation. *A&A*, *601*, Article A95, A95. https://doi.org/10.1051/0004-6361/201629762

Calura, F., Pipino, A., & Matteucci, F. (2008). The cycle of interstellar dust in galaxies of different morphological types. *A&A*, *479*(3), 669–685. https://doi.org/10.1051/0004-6361:20078090

Calzetti, D., Armus, L., Bohlin, R. C., Kinney, A. L., Koornneef, J., & Storchi-Bergmann, T. (2000). The Dust Content and Opacity of Actively Star-forming Galaxies. *ApJ*, *533*(2), 682–695. https://doi.org/10.1086/308692

Cameron, A. J., Katz, H., Rey, M. P., & Saxena, A. (2023). Nitrogen enhancements 440 Myr after the big bang: supersolar N/O, a tidal disruption event, or a dense stellar cluster in GN-z11? *MNRAS*, *523*(3), 3516–3525. https://doi.org/10.1093/mnras/stad1579

Camps-Fariña, A., Sánchez-Blázquez, P., Roca-Fàbrega, S., & Sánchez, S. F. (2023). Measuring the physical imprints of gas flows in galaxies. I. Accretion rate histories. *A&A*, *678*, Article A65, A65. https://doi.org/10.1051/0004-6361/202346479

Cao, X. (2009). An accretion disc-corona model for X-ray spectra of active galactic nuclei. *MNRAS*, *394*(1), 207–213. https://doi.org/10.1111/j.1365-2966.2008.14347.x

Capelo, P. R., Feruglio, C., Hickox, R. C., & Tombesi, F. (2023). Black Hole-Galaxy Co-evolution and the Role of Feedback. In *Handbook of x-ray and gamma-ray astrophysics* (p. 126). https://doi.org/10.1007/978-981-16-4544-0_115-1

Cappellari, M. (2017). Improving the full spectrum fitting method: accurate convolution with Gauss-Hermite functions. *MNRAS*, *466*(1), 798–811. https://doi.org/10.1093/mnras/stw3020

Cardelli, J. A., Clayton, G. C., & Mathis, J. S. (1989). The Relationship between Infrared, Optical, and Ultraviolet Extinction. *ApJ*, *345*, 245. https://doi.org/10.1086/167900

Cardoso, A. F. S., Cavichia, O., Mollá, M., & Sánchez-Menguiano, L. (2025). Analysis of the Internal Radial Gradient of Chemical Abundances in Spiral Galaxies from CALIFA. *ApJ*, *980*(1), Article 45, 45. https://doi.org/10.3847/1538-4357/ad9eab

Carton, D., Brinchmann, J., Contini, T., Epinat, B., Finley, H., Richard, J., Patrício, V., ... Wisotzki, L. (2018). First gas-phase metallicity gradients of 0.1 $\lesssim z \lesssim$ 0.8 galaxies with MUSE. *MNRAS*, *478*(4), 4293–4316. https://doi.org/10.1093/mnras/sty1343

Carvalho, S. P., Dors, O. L., Cardaci, M. V., Hägele, G. F., Krabbe, A. C., Pérez-Montero, E., Monteiro, A. F., ... Freitas-Lemes, P. (2020). Chemical abundances of Seyfert 2 AGNs - II. N2 metallicity calibration based on SDSS. *MNRAS*, *492*(4), 5675–5683. https://doi.org/10.1093/mnras/staa193

Castellano, M., Napolitano, L., Fontana, A., Roberts-Borsani, G., Treu, T., Vanzella, E., Zavala, J. A., ... Yoon, I. (2024). JWST NIRSpec Spectroscopy of the Remarkable Bright Galaxy GHZ2/GLASS-z12 at Redshift 12.34. *ApJ*, *972*(2), Article 143, 143. https://doi.org/10.3847/1538-4357/ad5f88

Cazzoli, S., Arribas, S., Maiolino, R., & Colina, L. (2016). Neutral gas outflows in nearby [U]LIRGs via optical NaD feature. *A&A*, *590*, Article A125, A125. https://doi.org/10.1051/0004-6361/201526788

Cazzoli, S., Hermosa Muñoz, L., Márquez, I., Masegosa, J., Castillo-Morales, Á., Gil de Paz, A., Hernández-García, L., ... Ramos Almeida, C. (2022). Unexplored outflows in nearby low luminosity AGNs. The case of NGC 1052. *A&A*, *664*, Article A135, A135. https://doi.org/10.1051/0004-6361/202142695

Cazzoli, S., Márquez, I., Masegosa, J., del Olmo, A., Pović, M., González-Martín, O., Balmaverde, B., ... García-Burillo, S. (2018). Optical spectroscopy of local type-1 AGN LINERs. *MNRAS*, *480*(1), 1106–1162. https://doi.org/10.1093/mnras/sty1811

Chabrier, G. (2003). The Galactic Disk Mass Function: Reconciliation of the Hubble Space Telescope and Nearby Determinations. *ApJ*, *586*(2), L133–L136. https://doi.org/10.1086/374879

Chartab, N., Cooray, A., Ma, J., Nayyeri, H., Zilliot, P., Lopez, J., Fadda, D., … Wardlow, J. (2022). Gas Phase Metallicities of Local Ultra-Luminous Infrared Galaxies Follow Normal Star-Forming Galaxies. *arXiv e-prints*, Article arXiv:2201.07478, arXiv:2201.07478.

Chastenet, J., Sandstrom, K., Leroy, A. K., Bot, C., Chiang, I.-D., Chown, R., Gordon, K. D., … Williams, T. G. (2025). The Resolved Behavior of Dust Mass, Polycyclic Aromatic Hydrocarbon Fraction, and Radiation Field in ~800 Nearby Galaxies. *ApJS*, *276*(1), Article 2, 2. https://doi.org/10.3847/1538-4365/ad8a5c

Chatzikos, M., Bianchi, S., Camilloni, F., Chakraborty, P., Gunasekera, C. M., Guzmán, F., Milby, J. S., … Ferland, G. J. (2023). The 2023 Release of Cloudy. *Rev. Mexicana Astron. Astrofis.*, *59*, 327–343. https://doi.org/10.22201/ia.01851101p.2023.59.02.12

Chemerynska, I., Atek, H., Dayal, P., Furtak, L. J., Feldmann, R., Greene, J. E., Maseda, M. V., … Whitaker, K. E. (2024). The Extreme Low-mass End of the Mass–Metallicity Relation at z ~ 7. *ApJ*, *976*(1), Article L15, L15. https://doi.org/10.3847/2041-8213/ad8dc910.1134/S1063772908080040

Chen, Y., Jones, T., Sanders, R., Fadda, D., Sutter, J., Minchin, R., Huntzinger, E., … Roberts-Borsani, G. (2023). Accurate oxygen abundance of interstellar gas in Mrk 71 from optical and infrared spectra. *Nature Astronomy*, *7*, 771–778. https://doi.org/10.1038/s41550-023-01953-7

Chen, Y., Jones, T., Sanders, R., Fadda, D., Sutter, J., Minchin, R., Huntzinger, E., … Roberts-Borsani, G. (2024). Reply to: Effects of density and temperature variations on the metallicity of Mrk71. *Nature Astronomy*, *8*, 278–279. https://doi.org/10.1038/s41550-024-02199-7

Chiappini, C., Matteucci, F., & Ballero, S. K. (2005). The origin of nitrogen. Implications of recent measurements of N/O in Galactic metal-poor halo stars. *A&A*, *437*(2), 429–436. https://doi.org/10.1051/0004-6361:20042292

Chiappini, C., Matteucci, F., & Romano, D. (2001). Abundance Gradients and the Formation of the Milky Way. *ApJ*, *554*(2), 1044–1058. https://doi.org/10.1086/321427

Chiosi, C. (1980). Chemical evolution of the galactic disk: the inflow problem. *A&A*, *83*, 206–216.

Chung, A., van Gorkom, J. H., Kenney, J. D. P., Crowl, H., & Vollmer, B. (2009). VLA Imaging of Virgo Spirals in Atomic Gas (VIVA). I. The Atlas and the H I Properties. *AJ*, *138*(6), 1741–1816. https://doi.org/10.1088/0004-6256/138/6/1741

Cid Fernandes, R., Mateus, A., Sodré, L., Stasińska, G., & Gomes, J. M. (2005). Semi-empirical analysis of Sloan Digital Sky Survey galaxies - I. Spectral synthesis method. *MNRAS*, *358*, 363–378. https://doi.org/10.1111/j.1365-2966.2005.08752.x

Cid Fernandes, R., Stasińska, G., Mateus, A., & Vale Asari, N. (2011). A comprehensive classification of galaxies in the Sloan Digital Sky Survey: how to tell true from fake AGN? *MNRAS*, *413*(3), 1687–1699. https://doi.org/10.1111/j.1365-2966.2011.18244.x

Cid Fernandes, R., Stasińska, G., Schlickmann, M. S., Mateus, A., Vale Asari, N., Schoenell, W., & Sodré, L. (2010). Alternative diagnostic diagrams and the 'forgotten' population of weak line galaxies in the SDSS. *MNRAS*, *403*(2), 1036–1053. https://doi.org/10.1111/j.1365-2966.2009.16185.x

Ciesla, L., Charmandaris, V., Georgakakis, A., Bernhard, E., Mitchell, P. D., Buat, V., Elbaz, D., … Xilouris, M. (2015). Constraining the properties of AGN host galaxies with spectral energy distribution modelling. *A&A*, *576*, Article A10, A10. https://doi.org/10.1051/0004-6361/201425252

Clegg, P. E., Ade, P. A. R., Armand, C., Baluteau, J. .-., Barlow, M. J., Buckley, M. A., Berges, J. .-., … White, G. J. (1996). The ISO Long-Wavelength Spectrometer. *A&A*, *315*, L38–L42.

Cluver, M. E., Jarrett, T. H., Dale, D. A., Smith, J. .-. T., August, T., & Brown, M. J. I. (2017). Calibrating Star Formation in WISE Using Total Infrared Luminosity. *ApJ*, *850*(1), Article 68, 68. https://doi.org/10.3847/1538-4357/aa92c7

Cluver, M. E., Jarrett, T. H., Hopkins, A. M., Driver, S. P., Liske, J., Gunawardhana, M. L. P., Taylor, E. N., ... Wilkins, S. M. (2014). Galaxy and Mass Assembly (GAMA): Mid-infrared Properties and Empirical Relations from WISE. *ApJ*, *782*(2), Article 90, 90. https://doi.org/10.1088/0004-637X/782/2/90

Cole, S., Lacey, C. G., Baugh, C. M., & Frenk, C. S. (2000). Hierarchical galaxy formation. *MNRAS*, *319*(1), 168–204. https://doi.org/10.1046/j.1365-8711.2000.03879.x

Colina, L., Crespo Gómez, A., Álvarez-Márquez, J., Bik, A., Walter, F., Boogaard, L., Labiano, A., ... Vandenbussche, B. (2023). Uncovering the stellar structure of the dusty star-forming galaxy GN20 at z = 4.055 with MIRI/JWST. *A&A*, *673*, Article L6, L6. https://doi.org/10.1051/0004-6361/202346535

Compiègne, M., Verstraete, L., Jones, A., Bernard, J. .-., Boulanger, F., Flagey, N., Le Bourlot, J., ... Ysard, N. (2011). The global dust SED: tracing the nature and evolution of dust with DustEM. *A&A*, *525*, Article A103, A103. https://doi.org/10.1051/0004-6361/201015292

Conroy, C. (2013). Modeling the Panchromatic Spectral Energy Distributions of Galaxies. *ARA&A*, *51*(1), 393–455. https://doi.org/10.1146/annurev-astro-082812-141017

Contini, M. (2012). Metallicity in the merger Seyfert galaxy NGC 6240. *MNRAS*, *426*(1), 719–731. https://doi.org/10.1111/j.1365-2966.2012.21764.x

Contini, M., & Aldrovandi, S. M. V. (1983). Composite models for the narrow emission line region of active galactic nuclei. I. The infalling filament. *A&A*, *127*, 15–24.

Contini, M., & Viegas, S. M. (2001). A Grid of Composite Models for the Simulation of Starburst Galaxy and H II Region Spectra. *ApJS*, *137*(1), 75–115. https://doi.org/10.1086/322527

Cooke, R. J., Noterdaeme, P., Johnson, J. W., Pettini, M., Welsh, L., Peroux, C., Murphy, M. T., & Weinberg, D. H. (2022). Primordial Helium-3 Redux: The Helium Isotope Ratio of the Orion Nebula. *ApJ*, *932*(1), Article 60, 60. https://doi.org/10.3847/1538-4357/ac6503

Cormier, D., Madden, S. C., Lebouteiller, V., Abel, N., Hony, S., Galliano, F., Rémy-Ruyer, A., ... Spinoglio, L. (2015). The Herschel Dwarf Galaxy Survey. I. Properties of the low-metallicity ISM from PACS spectroscopy. *A&A*, *578*, Article A53, A53. https://doi.org/10.1051/0004-6361/201425207

Corradi, R. L. M., García-Rojas, J., Jones, D., & Rodríguez-Gil, P. (2015). Binarity and the Abundance Discrepancy Problem in Planetary Nebulae. *ApJ*, *803*(2), Article 99, 99. https://doi.org/10.1088/0004-637X/803/2/99

Costero, R., & Osterbrock, D. E. (1977). The Optical Spectra of Narrow-Line Radio Galaxies. *ApJ*, *211*, 675–683. https://doi.org/10.1086/154977

Cox, D. P. (2005). The Three-Phase Interstellar Medium Revisited. *ARA&A*, *43*(1), 337–385. https://doi.org/10.1146/annurev.astro.43.072103.150615

Cox, J. P., & Salpeter, E. E. (1964). Equilibrium Models for Helium-Burning Stars. III. Semi-Degenerate Stars of Small Mass. *ApJ*, *140*, 485. https://doi.org/10.1086/147943

Coziol, R., Reyes, R. E. C., Considère, S., Davoust, E., & Contini, T. (1999). The abundance of nitrogen in starburst nucleus galaxies. *A&A*, *345*, 733–746. https://doi.org/10.48550/arXiv.astro-ph/9903279

Cresci, G., Mannucci, F., & Curti, M. (2019). Fundamental metallicity relation in CALIFA, SDSS-IV MaNGA, and high-z galaxies. *A&A*, *627*, Article A42, A42. https://doi.org/10.1051/0004-6361/201834637

Cresci, G., Mannucci, F., Maiolino, R., Marconi, A., Gnerucci, A., & Magrini, L. (2010). Gas accretion as the origin of chemical abundance gradients in distant galaxies. *Nature*, *467*(7317), 811–813. https://doi.org/10.1038/nature09451

Crovisier, J., & Dickey, J. M. (1983). The spatial power spectrum of galactic neutral hydrogen from observations of the 21-cm emission line. *A&A*, *122*, 282–296.

Croxall, K. V., Pogge, R. W., Berg, D. A., Skillman, E. D., & Moustakas, J. (2016). CHAOS III: Gas-phase Abundances in NGC 5457. *ApJ*, *830*(1), Article 4, 4. https://doi.org/10.3847/0004-637X/830/1/4

Croxall, K. V., Smith, J. D., Brandl, B. R., Groves, B. A., Kennicutt, R. C., Kreckel, K., Johnson, B. D., ... Schinnerer, E. (2013). Toward a Removal of Temperature Dependencies from Abundance Determinations: NGC 628. *ApJ*, *777*(2), Article 96, 96. https://doi.org/10.1088/0004-637X/777/2/96

Curti, M., Cresci, G., Mannucci, F., Marconi, A., Maiolino, R., & Esposito, S. (2017). New fully empirical calibrations of strong-line metallicity indicators in star-forming galaxies. *MNRAS*, *465*(2), 1384–1400. https://doi.org/10.1093/mnras/stw2766

Curti, M., Maiolino, R., Curtis-Lake, E., Chevallard, J., Carniani, S., D'Eugenio, F., Looser, T. J., ... Sun, F. (2024). JADES: Insights into the low-mass end of the mass-metallicity-SFR relation at $3 < z < 10$ from deep JWST/NIRSpec spectroscopy. *A&A*, *684*, Article A75, A75. https://doi.org/10.1051/0004-6361/202346698

Curti, M., Mannucci, F., Cresci, G., & Maiolino, R. (2020). The mass-metallicity and the fundamental metallicity relation revisited on a fully T_e-based abundance scale for galaxies. *MNRAS*, *491*(1), 944–964. https://doi.org/10.1093/mnras/stz2910

Curtis, S., Ebinger, K., Fröhlich, C., Hempel, M., Perego, A., Liebendörfer, M., & Thielemann, F.-K. (2019). PUSHing Core-collapse Supernovae to Explosions in Spherical Symmetry. III. Nucleosynthesis Yields. *ApJ*, *870*(1), Article 2, 2. https://doi.org/10.3847/1538-4357/aae7d2

Cyburt, R. H., Fields, B. D., Olive, K. A., & Yeh, T.-H. (2016). Big bang nucleosynthesis: Present status. *Reviews of Modern Physics*, *88*(1), Article 015004, 015004. https://doi.org/10.1103/RevModPhys.88.015004

Dalgarno, A. (2006). Interstellar Chemistry Special Feature: The galactic cosmic ray ionization rate. *Proceedings of the National Academy of Science*, *103*(33), 12269–12273. https://doi.org/10.1073/pnas.0602117103

Dannerbauer, H., Rigopoulou, D., Lutz, D., Genzel, R., Sturm, E., & Moorwood, A. F. M. (2005). Follow-up near-infrared spectroscopy of ultraluminous infrared galaxies observed by ISO. *A&A*, *441*(3), 999–1010. https://doi.org/10.1051/0004-6361:20052812

Davies, R. L., Groves, B., Kewley, L. J., Dopita, M. A., Hampton, E. J., Shastri, P., Scharwächter, J., ... Srivastava, S. (2016). Dissecting galaxies: spatial and spectral separation of emission excited by star formation and AGN activity. *MNRAS*, *462*(2), 1616–1629. https://doi.org/10.1093/mnras/stw1754

Davis, M., Efstathiou, G., Frenk, C. S., & White, S. D. M. (1985). The evolution of large-scale structure in a universe dominated by cold dark matter. *ApJ*, *292*, 371–394. https://doi.org/10.1086/163168

Dayal, P., Ferrara, A., & Dunlop, J. S. (2013). The physics of the fundamental metallicity relation. *MNRAS*, *430*(4), 2891–2895. https://doi.org/10.1093/mnras/stt083

De Breuck, C., Weiß, A., Béthermin, M., Cunningham, D., Apostolovski, Y., Aravena, M., Archipley, M., ... Vishwas, A. (2019). A dense, solar metallicity ISM in the $z = 4.2$ dusty star-forming galaxy SPT 0418-47. *A&A*, *631*, Article A167, A167. https://doi.org/10.1051/0004-6361/201936169

de Graauw, T., Haser, L. N., Beintema, D. A., Roelfsema, P. R., van Agthoven, H., Barl, L., Bauer, O. H., ... Young, E. (1996). Observing with the ISO Short-Wavelength Spectrometer. *A&A*, *315*, L49–L54.

de Graauw, T., Helmich, F. P., Phillips, T. G., Stutzki, J., Caux, E., Whyborn, N. D., Dieleman, P., … Zwart, F. (2010). The Herschel-Heterodyne Instrument for the Far-Infrared (HIFI). *A&A*, *518*, Article L6, L6. https://doi.org/10.1051/0004-6361/201014698

de Nicola, S., Marconi, A., & Longo, G. (2019). The fundamental relation between supermassive black holes and their host galaxies. *MNRAS*, *490*(1), 600–612. https://doi.org/10.1093/mnras/stz2472

deBoer, R. J., Görres, J., Wiescher, M., Azuma, R. E., Best, A., Brune, C. R., Fields, C. E., … Uberseder, E. (2017). The ^{12}C(α ,γ)^{16}O reaction and its implications for stellar helium burning. *Reviews of Modern Physics*, *89*(3), Article 035007, 035007. https://doi.org/10.1103/RevModPhys.89.035007

Decin, L., Waelkens, C., Eriksson, K., Gustafsson, B., Plez, B., Sauval, A. J., Van Assche, W., & Vandenbussche, B. (2000). ISO-SWS calibration and the accurate modelling of cool-star atmospheres. I. Method. *A&A*, *364*, 137–156. https://doi.org/10.48550/arXiv.astro-ph/0008316

Dell'Agli, F., Tosi, S., Kamath, D., Stanghellini, L., Bianchi, S., Ventura, P., Marini, E., & García-Hernández, D. A. (2023). Dust from evolved stars: a pilot analysis of the AGB to PN transition. *MNRAS*, *526*(4), 5386–5392. https://doi.org/10.1093/mnras/stad3080

Dere, K. P., Del Zanna, G., Young, P. R., Landi, E., & Sutherland, R. S. (2019). CHIANTI—An Atomic Database for Emission Lines. XV. Version 9, Improvements for the X-Ray Satellite Lines. *ApJS*, *241*(2), Article 22, 22. https://doi.org/10.3847/1538-4365/ab05cf

DESI Collaboration, Abdul-Karim, M., Adame, A. G., Aguado, D., Aguilar, J., Ahlen, S., Alam, S., … Peterson, P. (2025). Data Release 1 of the Dark Energy Spectroscopic Instrument. *arXiv e-prints*, Article arXiv:2503.14745, arXiv:2503.14745. https://doi.org/10.48550/arXiv.2503.14745

DESI Collaboration, Adame, A. G., Aguilar, J., Ahlen, S., Alam, S., Aldering, G., Alexander, D. M., … Pothier, S. (2024). The Early Data Release of the Dark Energy Spectroscopic Instrument. *AJ*, *168*(2), Article 58, 58. https://doi.org/10.3847/1538-3881/ad3217

Di Matteo, P., Bournaud, F., Martig, M., Combes, F., Melchior, A. .-., & Semelin, B. (2008). On the frequency, intensity, and duration of starburst episodes triggered by galaxy interactions and mergers. *A&A*, *492*(1), 31–49. https://doi.org/10.1051/0004-6361:200809480

Di Matteo, P., Combes, F., Melchior, A. .-., & Semelin, B. (2007). Star formation efficiency in galaxy interactions and mergers: a statistical study. *A&A*, *468*(1), 61–81. https://doi.org/10.1051/0004-6361:20066959

Diaz, Á. I., Terlevich, E., Vilchez, J. M., Pagel, B. E. J., & Edmunds, M. G. (1991). Abundance analysis of Giant HII regions in M51. *MNRAS*, *253*, 245. https://doi.org/10.1093/mnras/253.2.245

Díaz, Á. I., & Pérez-Montero, E. (2000). An empirical calibration of nebular abundances based on the sulphur emission lines. *MNRAS*, *312*(1), 130–138. https://doi.org/10.1046/j.1365-8711.2000.03117.x

Díaz, Á. I., Terlevich, E., Castellanos, M., & Hägele, G. F. (2007). The metal abundance of circumnuclear star-forming regions in early-type spirals. Spectrophotometric observations. *MNRAS*, *382*(1), 251–269. https://doi.org/10.1111/j.1365-2966.2007.12351.x

Díaz, Á. I., & Zamora, S. (2022). On the use of sulphur as a tracer for abundances in galaxies. *MNRAS*, *511*(3), 4377–4392. https://doi.org/10.1093/mnras/stac387

Dickey, J. M., & Lockman, F. J. (1990). H I in the galaxy. *ARA&A*, *28*, 215–261. https://doi.org/10.1146/annurev.aa.28.090190.001243

Dimitriadis, G., Chiotellis, A., & Vink, J. (2014). Early X-ray emission from Type Ia supernovae originating from symbiotic progenitors or recurrent novae. *MNRAS*, *443*(2), 1370–1380. https://doi.org/10.1093/mnras/stu1249 do Nascimento, J. C., Dors, O. L., Storchi-Bergmann, T., Mallmann, N. D., Riffel, R., Ilha, G. S., Riffel, R. A., ... Armah, M. (2022). Gas-phase metallicity determinations in nearby AGNs with SDSS-IV MaNGA: evidence of metal-poor accretion. *MNRAS*, *513*(1), 807–821. https://doi.org/10.1093/mnras/stac771

Docenko, D., & Sunyaev, R. A. (2008). Optical and near-infrared recombination lines of oxygen ions from Cassiopeia A knots. *A&A*, *484*(3), 755–771. https://doi.org/10.1051/0004-6361:200809579

Doherty, C. L., Gil-Pons, P., Siess, L., & Lattanzio, J. C. (2017). Super-AGB Stars and their Role as Electron Capture Supernova Progenitors. *PASA*, *34*, Article e056, e056. https://doi.org/10.1017/pasa.2017.52

Domgorgen, H., & Mathis, J. S. (1994). The Ionization of the Diffuse Ionized Gas. *ApJ*, *428*, 647. https://doi.org/10.1086/174275

Dopita, M. A. (1976). Optical emission from shock waves. I. Abundances in N49. *ApJ*, *209*, 395–401. https://doi.org/10.1086/154732

Dopita, M. A., Mathewson, D. S., & Ford, V. L. (1977). Optical emission from shock waves. III. Abundances in supernova remnants. *ApJ*, *214*, 179–188. https://doi.org/10.1086/155242

Dopita, M. A. (1977). Optical Emission from Shock Waves. II. Diagnostic Diagrams. *ApJS*, *33*, 437. https://doi.org/10.1086/190435

Dopita, M. A., Fischera, J., Sutherland, R. S., Kewley, L. J., Leitherer, C., Tuffs, R. J., Popescu, C. C., ... Groves, B. A. (2006). Modeling the Pan-Spectral Energy Distribution of Starburst Galaxies. III. Emission Line Diagnostics of Ensembles of Evolving H II Regions. *ApJS*, *167*(2), 177–200. https://doi.org/10.1086/508261

Dopita, M. A., & Sutherland, R. S. (1995). Spectral Signatures of Fast Shocks. II. Optical Diagnostic Diagrams. *ApJ*, *455*, 468. https://doi.org/10.1086/176596

Dors, O. L., Cardaci, M. V., Hägele, G. F., Rodrigues, I., Grebel, E. K., Pilyugin, L. S., Freitas-Lemes, P., & Krabbe, A. C. (2015). On the central abundances of active galactic nuclei and star-forming galaxies. *MNRAS*, *453*(4), 4102–4111. https://doi.org/10.1093/mnras/stv1916

Dors, O. L., Maiolino, R., Cardaci, M. V., Hägele, G. F., Krabbe, A. C., Pérez-Montero, E., & Armah, M. (2020). Chemical abundances of Seyfert 2 AGNs - III. Reducing the oxygen abundance discrepancy. *MNRAS*, *496*(3), 3209–3221. https://doi.org/10.1093/mnras/staa1781

Dors, O. L., Monteiro, A. F., Cardaci, M. V., Hägele, G. F., & Krabbe, A. C. (2019). Semi-empirical metallicity calibrations based on ultraviolet emission lines of type-2 AGNs. *MNRAS*, *486*(4), 5853–5866. https://doi.org/10.1093/mnras/stz1242

Dors, O. L., Valerdi, M., Freitas-Lemes, P., Krabbe, A. C., Riffel, R. A., Amôres, E. B., Riffel, R., ... Oliveira, C. B. (2022). Chemical abundances in Seyfert galaxies - IX. Helium abundance estimates. *MNRAS*, *514*(4), 5506–5527. https://doi.org/10.1093/mnras/stac1722

Dors, O. L. (2021). Chemical abundances in Seyfert galaxies - VI. Empirical abundance calibration. *MNRAS*, *507*(1), 466–474. https://doi.org/10.1093/mnras/stab2166

Dors, O. L., Cardaci, M. V., Hägele, G. F., & Krabbe, Â. C. (2014). Metallicity evolution of AGNs from UV emission lines based on a new index. *MNRAS*, *443*(2), 1291–1300. https://doi.org/10.1093/mnras/stu1218

Dors, O. L., Hägele, G. F., Cardaci, M. V., Pérez-Montero, E., Krabbe, Â. C., Vílchez, J. M., Sales, D. A., ... Riffel, R. A. (2013). Optical and mid-infrared neon abundance determinations in star-forming regions. *MNRAS*, *432*(3), 2512–2528. https://doi.org/10.1093/mnras/stt610

Dors, O. L., Valerdi, M., Riffel, R. A., Riffel, R., Cardaci, M. V., Hägele, G. F., Armah, M., ... Storchi-Bergmann, T. (2023). Chemical abundances in Seyfert galaxies - X. Sulphur abundance estimates. *MNRAS*, *521*(2), 1969–1987. https://doi.org/10.1093/mnras/stad635

Doyon, R., Willott, C. J., Hutchings, J. B., Sivaramakrishnan, A., Albert, L., Lafrenière, D., Rowlands, N., ... Sawicki, M. (2023). The Near Infrared Imager and Slitless Spectrograph for the James

Webb Space Telescope. I. Instrument Overview and In-flight Performance. *PASP*, *135*(1051), Article 098001, 098001. https://doi.org/10.1088/1538-3873/acd41b

Draine, B. T. (2003). Interstellar Dust Grains. *ARA&A*, *41*, 241–289. https://doi.org/10.1146/annurev.astro.41.011802.094840

Duarte Puertas, S., Vilchez, J. M., Iglesias-Páramo, J., Mollá, M., Pérez-Montero, E., Kehrig, C., Pilyugin, L. S., & Zinchenko, I. A. (2022). Mass-metallicity and star formation rate in galaxies: A complex relation tuned to stellar age. *A&A*, *666*, Article A186, A186. https://doi.org/10.1051/0004-6361/202141571

Dubois, Y., Peirani, S., Pichon, C., Devriendt, J., Gavazzi, R., Welker, C., & Volonteri, M. (2016). The HORIZON-AGN simulation: morphological diversity of galaxies promoted by AGN feedback. *MNRAS*, *463*(4), 3948–3964. https://doi.org/10.1093/mnras/stw2265

Duc, P. .-., Mirabel, I. F., & Maza, J. (1997). Southern ultraluminous infrared galaxies: an optical and infrared database. *A&AS*, *124*, 533–557. https://doi.org/10.1051/aas:1997205

Durret, F., & Bergeron, J. (1988). Long slit spectroscopy of emission line galaxies. I. The sample. *A&AS*, *75*, 273–297.

Dutta, R. (2019). Cold neutral hydrogen gas in galaxies. *Journal of Astrophysics and Astronomy*, *40*(5), Article 41, 41. https://doi.org/10.1007/s12036-019-9610-5

Eckert, D., Gaspari, M., Gastaldello, F., Le Brun, A. M. C., & O'Sullivan, E. (2021). Feedback from Active Galactic Nuclei in Galaxy Groups. *Universe*, *7*(5), Article 142, 142. https://doi.org/10.3390/universe7050142

Edmunds, M. G. (1990). General Constraints on the Effect of Gas Flows in the Chemical Evolution of Galaxies. *MNRAS*, *246*, 678.

Edmunds, M. G., & Pagel, B. E. J. (1978). Nitrogen synthesis and the "age" of galaxies. *MNRAS*, *185*, 77P–80. https://doi.org/10.1093/mnras/185.1.77P

Efstathiou, G. (2025). Challenges to the Λ CDM cosmology. *Philosophical Transactions of the Royal Society of London Series A*, *383*(2290), Article 20240022, 20240022. https://doi.org/10.1098/rsta.2024.0022

Eldridge, J. J., Stanway, E. R., Xiao, L., McClelland, L. A. S., Taylor, G., Ng, M., Greis, S. M. L., & Bray, J. C. (2017). Binary Population and Spectral Synthesis Version 2.1: Construction, Observational Verification, and New Results. *PASA*, *34*, Article e058, e058. https://doi.org/10.1017/pasa.2017.51

Elliott, E., Mountain, M., Postman, M., Koekemoer, A., Ubeda, L., & Livio, M. (2013). Space Telescopes in the Ultraviolet, Optical, and Infrared (UV/O/IR). In T. D. Oswalt & I. S. McLean (Eds.), *Planets, stars and stellar systems. volume 1: Telescopes and instrumentation* (p. 361). https://doi.org/10.1007/978-94-007-5621-2_9

Elmegreen, B. G. (1997). Intercloud Structure in a Turbulent Fractal Interstellar Medium. *ApJ*, *477*(1), 196–203. https://doi.org/10.1086/303705

Elmegreen, B. G., & Burkert, A. (2010). Accretion-Driven Turbulence and the Transition to Global Instability in Young Galaxy Disks. *ApJ*, *712*(1), 294–302. https://doi.org/10.1088/0004-637X/712/1/294

Erb, D. K., Pettini, M., Shapley, A. E., Steidel, C. C., Law, D. R., & Reddy, N. A. (2010). Physical Conditions in a Young, Unreddened, Low-metallicity Galaxy at High Redshift. *ApJ*, *719*(2), 1168–1190. https://doi.org/10.1088/0004-637X/719/2/1168

Erkens, U., Appenzeller, I., & Wagner, S. (1997). The nature of the FHIL winds from AGN. *A&A*, *323*, 707–716.

Esteban, C., Bresolin, F., Peimbert, M., García-Rojas, J., Peimbert, A., & Mesa-Delgado, A. (2009). Keck HIRES Spectroscopy of Extragalactic H II Regions: C and O Abundances from Recombination Lines. *ApJ*, *700*(1), 654–678. https://doi.org/10.1088/0004-637X/700/1/654

Evans, A. S., Mazzarella, J. M., Surace, J. A., Frayer, D. T., Iwasawa, K., & Sanders, D. B. (2005). Molecular Gas and Nuclear Activity in Radio Galaxies Detected by IRAS. *ApJS*, *159*(2), 197–213. https://doi.org/10.1086/431345

Faisst, A. L., Yang, L., Brinch, M., Casey, C. M., Chartab, N., Dessauges-Zavadsky, M., Drakos, N. E., ... Zavala, J. A. (2025). COSMOS-Web: The Role of Galaxy Interactions and Disk Instabilities in Producing Starbursts at z < 4. *ApJ*, *980*(2), Article 204, 204. https://doi.org/10.3847/1538-4357/ada566

Falgarone, E., Phillips, T. G., & Walker, C. K. (1991). The Edges of Molecular Clouds: Fractal Boundaries and Density Structure. *ApJ*, *378*, 186. https://doi.org/10.1086/170419

Falgarone, E., & Puget, J. L. (1985). A model of clumped molecular clouds. I - Hydrostatic structure of dense cores. *A&A*, *142*(1), 157–170.

Fang, X., Storey, P. J., & Liu, X. .-. (2011). New effective recombination coefficients for nebular N ii lines. *A&A*, *530*, Article A18, A18. https://doi.org/10.1051/0004-6361/201116511

Farrah, D., Bernard-Salas, J., Spoon, H. W. W., Soifer, B. T., Armus, L., Brandl, B., Charmandaris, V., ... Houck, J. (2007). High-Resolution Mid-Infrared Spectroscopy of Ultraluminous Infrared Galaxies. *ApJ*, *667*(1), 149–169. https://doi.org/10.1086/520834

Feltre, A., Charlot, S., & Gutkin, J. (2016). Nuclear activity versus star formation: emission-line diagnostics at ultraviolet and optical wavelengths. *MNRAS*, *456*(3), 3354–3374. https://doi.org/10.1093/mnras/stv2794

Ferkinhoff, C., Brisbin, D., Nikola, T., Stacey, G. J., Sheth, K., Hailey-Dunsheath, S., & Falgarone, E. (2015). Band-9 ALMA Observations of the [N II] 122 μm Line and FIR Continuum in Two High-z galaxies. *ApJ*, *806*(2), Article 260, 260. https://doi.org/10.1088/0004-637X/806/2/260

Ferland, G. J., Chatzikos, M., Guzmán, F., Lykins, M. L., van Hoof, P. A. M., Williams, R. J. R., Abel, N. P., ... Stancil, P. C. (2017). The 2017 Release Cloudy. *Rev. Mexicana Astron. Astrofis.*, *53*, 385–438.

Ferland, G. J., & Mushotzky, R. F. (1984). Osmic rays and the emission-line regions of active galactic nuclei. *ApJ*, *286*, 42–52. https://doi.org/10.1086/162574

Ferland, G. J., & Netzer, H. (1983). Are there any shock-heated galaxies ? *ApJ*, *264*, 105–113. https://doi.org/10.1086/160577

Fernández, V., Terlevich, E., Díaz, A. I., Terlevich, R., & Rosales-Ortega, F. F. (2018). Primordial helium abundance determination using sulphur as metallicity tracer. *MNRAS*, *478*(4), 5301–5319. https://doi.org/10.1093/mnras/sty1206

Fernández-Ontiveros, J. A., Pérez-Montero, E., Vílchez, J. M., Amorín, R., & Spinoglio, L. (2021). Measuring chemical abundances with infrared nebular lines: HII-CHI-MISTRY-IR. *A&A*, *652*, Article A23, A23. https://doi.org/10.1051/0004-6361/202039716

Fernández-Ontiveros, J. A., Spinoglio, L., Pereira-Santaella, M., Malkan, M. A., Andreani, P., & Dasyra, K. M. (2016). Far-infrared Line Spectra of Active Galaxies from the Herschel/PACS Spectrometer: The Complete Database. *ApJS*, *226*(2), Article 19, 19. https://doi.org/10.3847/0067-0049/226/2/19

Ferrière, K. M. (2001). The interstellar environment of our galaxy. *Reviews of Modern Physics*, *73*(4), 1031–1066. https://doi.org/10.1103/RevModPhys.73.1031

Fields, B. D. (2011). The Primordial Lithium Problem. *Annual Review of Nuclear and Particle Science*, *61*(1), 47–68. https://doi.org/10.1146/annurev-nucl-102010-130445

Fields, B. D. (2023). Big bang nucleosynthesis: Nuclear physics in the early universe. In I. Tanihata, H. Toki, & T. Kajino (Eds.), *Handbook of nuclear physics* (pp. 3379–3405). Springer Nature Singapore. https://doi.org/10.1007/978-981-19-6345-2_111

Fischer, C., Beckmann, S., Bryant, A., Colditz, S., Fumi, F., Geis, N., Hamidouche, M., ... Vacca, W. (2018). FIFI-LS: The Field-Imaging Far-Infrared Line Spectrometer on SOFIA. *Journal of*

Astronomical Instrumentation, *7*(4), Article 1840003-556, 1840003–556. https://doi.org/10.1142/S2251171718400032

Florido, E., Zurita, A., & Pérez-Montero, E. (2022). New calibrations for estimating the N/O ratio in H II regions. *MNRAS*, *513*(2), 2006–2018. https://doi.org/10.1093/mnras/stac919

Flower, D. R. (1969). The ionization structure of planetary nebulae-VIII. Models of the nebulae NGC 7662 and IC 418. *MNRAS*, *146*, 243. https://doi.org/10.1093/mnras/146.3.243

Flury, S. R., & Moran, E. C. (2020). Chemical abundances in active galaxies. *MNRAS*, *496*(2), 2191–2203. https://doi.org/10.1093/mnras/staa1563

Förster Schreiber, N. M., & Wuyts, S. (2020). Star-Forming Galaxies at Cosmic Noon. *ARA&A*, *58*, 661–725. https://doi.org/10.1146/annurev-astro-032620-021910

Friedli, D., Benz, W., & Kennicutt, R. (1994). On the Influence of Bars and Star Formation on Galactic Abundance Gradients. *ApJ*, *430*, L105. https://doi.org/10.1086/187449

Frisch, P. C., Redfield, S., & Slavin, J. D. (2011). The Interstellar Medium Surrounding the Sun. *ARA&A*, *49*(1), 237–279. https://doi.org/10.1146/annurev-astro-081710-102613

Fuente, A., Rivière-Marichalar, P., Beitia-Antero, L., Caselli, P., Wakelam, V., Esplugues, G., Rodríguez-Baras, M., ... Marcelino, N. (2023). Gas phase Elemental abundances in Molecular cloudS (GEMS). VII. Sulfur elemental abundance. *A&A*, *670*, Article A114, A114. https://doi.org/10.1051/0004-6361/202244843

Gabici, S. (2022). Low-energy cosmic rays: regulators of the dense interstellar medium. *A&A Rev.*, *30*(1), Article 4, 4. https://doi.org/10.1007/s00159-022-00141-2

Galametz, M., Hony, S., Albrecht, M., Galliano, F., Cormier, D., Lebouteiller, V., Lee, M. Y., ... Onishi, T. (2016). The dust properties and physical conditions of the interstellar medium in the LMC massive star-forming complex N11. *MNRAS*, *456*(2), 1767–1790. https://doi.org/10.1093/mnras/stv2773

Galarza, V. C., Walterbos, R. A. M., & Braun, R. (1999). Spectrophotometry of H II Regions, Diffuse Ionized Gas, and Supernova Remnants in M31: The Transition from Photoionization to Shock Ionization. *AJ*, *118*(6), 2775–2796. https://doi.org/10.1086/301113

Galliano, F., Hony, S., Bernard, J. .-., Bot, C., Madden, S. C., Roman-Duval, J., Galametz, M., ... Skibba, R. (2011). Non-standard grain properties, dark gas reservoir, and extended submillimeter excess, probed by Herschel in the Large Magellanic Cloud. *A&A*, *536*, Article A88, A88. https://doi.org/10.1051/0004-6361/201117952

Galliano, F., Galametz, M., & Jones, A. P. (2018). The Interstellar Dust Properties of Nearby Galaxies. *ARA&A*, *56*, 673–713. https://doi.org/10.1146/annurev-astro-081817-051900

Gal-Yam, A. (2017). Observational and Physical Classification of Supernovae. In A. W. Alsabti & P. Murdin (Eds.), *Handbook of supernovae* (p. 195). https://doi.org/10.1007/978-3-319-21846-5_35

García-Marín, M., Colina, L., Arribas, S., Alonso-Herrero, A., & Mediavilla, E. (2006). Integral Field Spectroscopy of the Luminous Infrared Galaxy Arp 299 (IC 694 + NGC 3690). *ApJ*, *650*(2), 850–871. https://doi.org/10.1086/507411

García-Rojas, J., Esteban, C., Peimbert, A., Rodríguez, M., Peimbert, M., & Ruiz, M. T. (2007). The chemical composition of the Galactic H II regions M8 and M17. A revision based on deep VLT echelle spectrophotometry. *Rev. Mexicana Astron. Astrofis.*, *43*, 3–31. https://doi.org/10.48550/arXiv.astro-ph/0610065

García-Rojas, J., Peña, M., & Peimbert, A. (2009). Faint recombination lines in Galactic PNe with a [WC] nucleus. *A&A*, *496*(1), 139–152. https://doi.org/10.1051/0004-6361:200811185

García-Rojas, J., & Esteban, C. (2007). On the Abundance Discrepancy Problem in H II Regions. *ApJ*, *670*(1), 457–470. https://doi.org/10.1086/521871

Garn, T., & Best, P. N. (2010). Predicting dust extinction from the stellar mass of a galaxy. *MNRAS*, *409*(1), 421–432. https://doi.org/10.1111/j.1365-2966.2010.17321.x

Garnett, D. R., & Shields, G. A. (1987). The Composition Gradient across M81. *ApJ*, *317*, 82. https://doi.org/10.1086/165257

Garrison-Kimmel, S., Rocha, M., Boylan-Kolchin, M., Bullock, J. S., & Lally, J. (2013). Can feedback solve the too-big-to-fail problem? *MNRAS*, *433*(4), 3539–3546. https://doi.org/10.1093/mnras/stt984

Gaskell, C. M., & Ferland, G. J. (1984). Theoretical hydrogen-line ratios for the narrow-line regions of active galactic nuclei. *PASP*, *96*, 393–397. https://doi.org/10.1086/131352

Gaskell, C. M. (2009). What broad emission lines tell us about how active galactic nuclei work. *New A Rev.*, *53*(7-10), 140–148. https://doi.org/10.1016/j.newar.2009.09.006

Genzel, R., Lutz, D., Sturm, E., Egami, E., Kunze, D., Moorwood, A. F. M., Rigopoulou, D., ... Thatte, N. (1998). What Powers Ultraluminous IRAS Galaxies? *ApJ*, *498*(2), 579–605. https://doi.org/10.1086/305576

Gitti, M., Brighenti, F., & McNamara, B. R. (2012). Evidence for AGN Feedback in Galaxy Clusters and Groups. *Advances in Astronomy*, *2012*, Article 950641, 950641. https://doi.org/10.1155/2012/950641

Glover, S. C. O., & Clark, P. C. (2012). Is molecular gas necessary for star formation? *MNRAS*, *421*(1), 9–19. https://doi.org/10.1111/j.1365-2966.2011.19648.x

Goddard, D., Thomas, D., Maraston, C., Westfall, K., Etherington, J., Riffel, R., Mallmann, N. D., ... Schneider, D. P. (2017). SDSS-IV MaNGA: Spatially resolved star formation histories in galaxies as a function of galaxy mass and type. *MNRAS*, *466*(4), 4731–4758. https://doi.org/10.1093/mnras/stw3371

Goldader, J. D., Joseph, R. D., Doyon, R., & Sanders, D. B. (1995). Spectroscopy of Luminous Infrared Galaxies at 2 Microns. I. The Ultraluminous Galaxies (L IR 2pt>-11.5pt-3pt approximately 10 12 L_{sun}). *ApJ*, *444*, 97. https://doi.org/10.1086/175585

Goldberg, L., Muller, E. A., & Aller, L. H. (1960). The Abundances of the Elements in the Solar Atmosphere. *ApJS*, *5*, 1. https://doi.org/10.1086/190053

González Delgado, R. M., García-Benito, R., Pérez, E., Cid Fernandes, R., de Amorim, A. L., Cortijo-Ferrero, C., Lacerda, E. A. D., ... Zibetti, S. (2015). The CALIFA survey across the Hubble sequence. Spatially resolved stellar population properties in galaxies. *A&A*, *581*, Article A103, A103. https://doi.org/10.1051/0004-6361/201525938

González Delgado, R. M., & Leitherer, C. (1999). Synthetic Spectra of H Balmer and HE I Absorption Lines. I. Stellar Library. *ApJS*, *125*(2), 479–488. https://doi.org/10.1086/313284

Goodrich, R. W., & Osterbrock, D. E. (1983). MRK 744 and MRK 1066 : two Seyfert galaxies with strong absorption-line spectra. *ApJ*, *269*, 416–422. https://doi.org/10.1086/161052

Gordon, K. D., Clayton, G. C., Decleir, M., Fitzpatrick, E. L., Massa, D., Misselt, K. A., & Tollerud, E. J. (2023). One Relation for All Wavelengths: The Far-ultraviolet to Mid-infrared Milky Way Spectroscopic R(V)-dependent Dust Extinction Relationship. *ApJ*, *950*(2), Article 86, 86. https://doi.org/10.3847/1538-4357/accb59

Gordon, K. D., Clayton, G. C., Misselt, K. A., Landolt, A. U., & Wolff, M. J. (2003). A Quantitative Comparison of the Small Magellanic Cloud, Large Magellanic Cloud, and Milky Way Ultraviolet to Near-Infrared Extinction Curves. *ApJ*, *594*(1), 279–293. https://doi.org/10.1086/376774

Gordon, K. D., Misselt, K. A., Bouwman, J., Clayton, G. C., Decleir, M., Hines, D. C., Pendleton, Y., ... Whittet, D. C. B. (2021). Milky Way Mid-Infrared Spitzer Spectroscopic Extinction Curves: Continuum and Silicate Features. *ApJ*, *916*(1), Article 33, 33. https://doi.org/10.3847/1538-4357/ac00b7

Goulding, A. D., & Alexander, D. M. (2009). Towards a complete census of AGN in nearby Galaxies: a large population of optically unidentified AGN. *MNRAS*, *398*(3), 1165–1193. https://doi.org/10.1111/j.1365-2966.2009.15194.x

Gredel, R., Lepp, S., Dalgarno, A., & Herbst, E. (1989). Cosmic-Ray–induced Photodissociation and Photoionization Rates of Interstellar Molecules. *ApJ*, *347*, 289. https://doi.org/10.1086/168117

Grevesse, N., & Sauval, A. J. (1998). Standard Solar Composition. *Space Sci. Rev.*, *85*, 161–174. https://doi.org/10.1023/A:1005161325181

Griffin, M. J., Abergel, A., Abreu, A., Ade, P. A. R., André, P., Augueres, J. .-., Babbedge, T., ... Zonca, E. (2010). The Herschel-SPIRE instrument and its in-flight performance. *A&A*, *518*, Article L3, L3. https://doi.org/10.1051/0004-6361/201014519

Grimes, J. P., Heckman, T., Strickland, D., & Ptak, A. (2005). A Chandra X-Ray Investigation of the Violent Interstellar Medium: From Dwarf Starbursts to Ultraluminous Infrared Galaxies. *ApJ*, *628*(1), 187–204. https://doi.org/10.1086/430692

Grisoni, V., Matteucci, F., & Romano, D. (2021). Nitrogen evolution in the halo, thick disc, thin disc, and bulge of the Galaxy. *MNRAS*, *508*(1), 719–727. https://doi.org/10.1093/mnras/stab2579

Grønnow, A. E., Finlator, K., & Christensen, L. (2015). Merging galaxies produce outliers from the fundamental metallicity relation. *MNRAS*, *451*(4), 4005–4017. https://doi.org/10.1093/mnras/stv1232

Gu, Q., Melnick, J., Cid Fernandes, R., Kunth, D., Terlevich, E., & Terlevich, R. (2006). Emission-line properties of Seyfert 2 nuclei. *MNRAS*, *366*(2), 480–490. https://doi.org/10.1111/j.1365-2966.2005.09872.x

Guarneri, F., Pasquini, L., D'Odorico, V., Cristiani, S., Cupani, G., Di Marcantonio, P., González Hernández, J. I., ... Trost, A. (2024). Fundamental physics with ESPRESSO: a new determination of the D/H ratio towards PKS1937-101. *MNRAS*, *529*(2), 839–854. https://doi.org/10.1093/mnras/stae452

Gunasekera, C. M., van Hoof, P. A. M., Chatzikos, M., & Ferland, G. J. (2023). The 23.01 Release of Cloudy. *Research Notes of the American Astronomical Society*, *7*(11), Article 246, 246. https://doi.org/10.3847/2515-5172/ad0e75

Guseva, N. G., Izotov, Y. I., Schaerer, D., Vílchez, J. M., Amorín, R., Pérez-Montero, E., Iglesias-Páramo, J., ... Ramambason, L. (2020). Properties of five z ∼ 0.3-0.4 confirmed LyC leakers: VLT/XShooter observations. *MNRAS*, *497*(4), 4293–4310. https://doi.org/10.1093/mnras/staa2197

Gustavino, C. (2014). BBN, Neutrinos and Nuclear Astrophysics. *Proceedings of the 52th International Winter Meeting on Nuclear Physics (Bormio2014). 27 - 31 January*, Article 50, 50. https://doi.org/10.22323/1.212.0050

Ha, T., Li, Y., Kounkel, M., Xu, S., Li, H., & Zheng, Y. (2022). Turbulence in Milky Way Star-forming Regions Traced by Young Stars and Gas. *ApJ*, *934*(1), Article 7, 7. https://doi.org/10.3847/1538-4357/ac76bf

Haffner, L. M., Dettmar, R. .-., Beckman, J. E., Wood, K., Slavin, J. D., Giammanco, C., Madsen, G. J., ... Reynolds, R. J. (2009). The warm ionized medium in spiral galaxies. *Reviews of Modern Physics*, *81*(3), 969–997. https://doi.org/10.1103/RevModPhys.81.969

Hägele, G. F., Díaz, Á. I., Terlevich, E., Terlevich, R., Pérez-Montero, E., & Cardaci, M. V. (2008). Precision abundance analysis of bright HII galaxies. *MNRAS*, *383*(1), 209–229. https://doi.org/10.1111/j.1365-2966.2007.12527.x

Hall, P. D., & Jeffery, C. S. (2018). The positive binding energy envelopes of low-mass helium stars. *MNRAS*, *475*(3), 3889–3895. https://doi.org/10.1093/mnras/sty055

Halpern, J. P., & Steiner, J. E. (1983). Low ionization active galactic nuclei : X-ray or shock heated ? *ApJ*, *269*, L37–L41. https://doi.org/10.1086/184051

Hamilton, D. (1985). The spectral evolution of galaxies. I. an observational approach. *ApJ*, *297*, 371–389. https://doi.org/10.1086/163537

Harikane, Y., Ouchi, M., Inoue, A. K., Matsuoka, Y., Tamura, Y., Bakx, T., Fujimoto, S., ... Vallini, L. (2020). Large Population of ALMA Galaxies at $z > 6$ with Very High [O III] 88 μm to [C II] 158 μm Flux Ratios: Evidence of Extremely High Ionization Parameter or PDR Deficit? *ApJ*, *896*(2), Article 93, 93. https://doi.org/10.3847/1538-4357/ab94bd

Harries, J., Carli, B., Rizzi, R., Serio, C., Mlynczak, M., Palchetti, L., Maestri, T., ... Masiello, G. (2008). The Far-infrared Earth. *Reviews of Geophysics*, *46*(4), Article RG4004, RG4004. https://doi.org/10.1029/2007RG000233

Harrington, J. P. (1969). Ionization Stratification and Chemical Abundances in the Planetary Nebula NGC 7662. *ApJ*, *156*, 903. https://doi.org/10.1086/150023

Hayden-Pawson, C., Curti, M., Maiolino, R., Cirasuolo, M., Belfiore, F., Cappellari, M., Concas, A., ... Vincenzo, F. (2022). The KLEVER survey: nitrogen abundances at z 2 and probing the existence of a fundamental nitrogen relation. *MNRAS*, *512*(2), 2867–2889. https://doi.org/10.1093/mnras/stac584

Heap, S. R., Lanz, T., & Hubeny, I. (2006). Fundamental Properties of O-Type Stars. *ApJ*, *638*(1), 409–432. https://doi.org/10.1086/498635

Heckman, T. M., & Best, P. N. (2014). The Coevolution of Galaxies and Supermassive Black Holes: Insights from Surveys of the Contemporary Universe. *ARA&A*, *52*, 589–660. https://doi.org/10.1146/annurev-astro-081913-035722

Hennebelle, P., & Grudić, M. Y. (2024). The Physical Origin of the Stellar Initial Mass Function. *ARA&A*, *62*(1), 63–111. https://doi.org/10.1146/annurev-astro-052622-031748

Henry, R. B. C., Edmunds, M. G., & Köppen, J. (2000). On the Cosmic Origins of Carbon and Nitrogen. *ApJ*, *541*(2), 660–674. https://doi.org/10.1086/309471

Hermosa Muñoz, L., Cazzoli, S., Márquez, I., Masegosa, J., Chamorro-Cazorla, M., Gil de Paz, A., Castillo-Morales, Á., ... Cardiel, N. (2024). The MEGARA view of outflows in LINERs. *A&A*, *683*, Article A43, A43. https://doi.org/10.1051/0004-6361/202347675

Hermosa Muñoz, L., Márquez, I., Cazzoli, S., Masegosa, J., & Agís-González, B. (2022). A search for ionised gas outflows in an Hα imaging atlas of nearby LINERs. *A&A*, *660*, Article A133, A133. https://doi.org/10.1051/0004-6361/202142629

Hernán-Caballero, A., Spoon, H. W. W., Alonso-Herrero, A., Hatziminaoglou, E., Magdis, G. E., Pérez-González, P. G., Pereira-Santaella, M., ... Rigopoulou, D. (2020). Extinction in the 11.2 µm PAH band and the low $L_{11.2}/L_{IR}$ in ULIRGs. *MNRAS*, *497*(4), 4614–4625. https://doi.org/10.1093/mnras/staa2282

Hernán-Caballero, A., Spoon, H. W. W., Lebouteiller, V., Rupke, D. S. N., & Barry, D. P. (2016). The infrared database of extragalactic observables from Spitzer - I. The redshift catalogue. *MNRAS*, *455*(2), 1796–1806. https://doi.org/10.1093/mnras/stv2464

Hernandez, S., Smith, L. J., Jones, L. H., Togi, A., Meléndez, M. B., Abril-Melgarejo, V., Adamo, A., ... Ramos Almeida, C. (2025). JWST/MIRI Detection of [Ne v] and [Ne VI] in M83: Evidence for the Long Sought-after Active Galactic Nucleus? *ApJ*, *983*(2), Article 154, 154. https://doi.org/10.3847/1538-4357/adba5d

Herpich, F., Stasińska, G., Mateus, A., Vale Asari, N., & Cid Fernandes, R. (2018). Why do many early-type galaxies lack emission lines? I. Fossil clues. *MNRAS*, *481*(2), 1774–1785. https://doi.org/10.1093/mnras/sty2391

Herrera-Camus, R., Sturm, E., Graciá-Carpio, J., Lutz, D., Contursi, A., Veilleux, S., Fischer, J., ... Verma, A. (2018). SHINING, A Survey of Far-infrared Lines in Nearby Galaxies. I. Survey Description, Observational Trends, and Line Diagnostics. *ApJ*, *861*(2), Article 94, 94. https://doi.org/10.3847/1538-4357/aac0f6

Herrero-Illana, R., Privon, G. C., Evans, A. S., Díaz-Santos, T., Pérez-Torres, M. Á., U, V., Alberdi, A., ... Surace, J. (2019). Molecular gas and dust properties of galaxies from the Great Observatories

All-sky LIRG Survey. *A&A*, *628*, Article A71, A71. https://doi.org/10.1051/0004-6361/201834088

Herter, T. L., Adams, J. D., Gull, G. E., Schoenwald, J., Keller, L. D., Pirger, B. E., Henderson, C. P., ... Ennico, K. (2018). FORCAST: A Mid-Infrared Camera for SOFIA. *Journal of Astronomical Instrumentation*, *7*(4), Article 1840005-451, 1840005–451. https://doi.org/10.1142/S2251171718400056

Heyminck, S., Graf, U. U., Güsten, R., Stutzki, J., Hübers, H. W., & Hartogh, P. (2012). GREAT: the SOFIA high-frequency heterodyne instrument. *A&A*, *542*, Article L1, L1. https://doi.org/10.1051/0004-6361/201218811

Hily-Blant, P., Pineau des Forêts, G., Faure, A., & Lique, F. (2022). Sulfur gas-phase abundance in dense cores. *A&A*, *658*, Article A168, A168. https://doi.org/10.1051/0004-6361/201936498

Hirschi, R., Meynet, G., & Maeder, A. (2005). Stellar evolution with rotation. XIII. Predicted GRB rates at various Z. *A&A*, *443*(2), 581–591. https://doi.org/10.1051/0004-6361:20053329

Ho, L. C. (2008). Nuclear activity in nearby galaxies. *ARA&A*, *46*, 475–539. https://doi.org/10.1146/annurev.astro.45.051806.110546

Ho, L. C. (2009). Radiatively Inefficient Accretion in Nearby Galaxies. *ApJ*, *699*(1), 626–637. https://doi.org/10.1088/0004-637X/699/1/626

Ho, L. C., Filippenko, A. V., & Sargent, W. L. W. (1993). A Reevaluation of the Excitation Mechanism of LINERs. *ApJ*, *417*, 63. https://doi.org/10.1086/173291

Ho, L. C., Filippenko, A. V., & Sargent, W. L. W. (1997). A Search for “Dwarf” Seyfert Nuclei. III. Spectroscopic Parameters and Properties of the Host Galaxies. *ApJS*, *112*(2), 315–390. https://doi.org/10.1086/313041

Hocuk, S., Szűcs, L., Caselli, P., Cazaux, S., Spaans, M., & Esplugues, G. B. (2017). Parameterizing the interstellar dust temperature. *A&A*, *604*, Article A58, A58. https://doi.org/10.1051/0004-6361/201629944

Hony, S., Kemper, F., Woods, P. M., van Loon, J. T., Gorjian, V., Madden, S. C., Zijlstra, A. A., ... Tielens, A. G. G. M. (2011). The Spitzer discovery of a galaxy with infrared emission solely due to AGN activity. *A&A*, *531*, Article A137, A137. https://doi.org/10.1051/0004-6361/201116845

Houck, J. R., Roellig, T. L., van Cleve, J., Forrest, W. J., Herter, T., Lawrence, C. R., Matthews, K., ... Teplitz, H. I. (2004). The Infrared Spectrograph (IRS) on the Spitzer Space Telescope. *ApJS*, *154*(1), 18–24. https://doi.org/10.1086/423134

Howarth, I. D. (1983). LMC and galactic extinction. *Monthly Notices of the Royal Astronomical Society*, *203*(2), 301–304. https://doi.org/10.1093/mnras/203.2.301

Howell, J. H., Armus, L., Mazzarella, J. M., Evans, A. S., Surace, J. A., Sanders, D. B., Petric, A., ... Xu, K. (2010). The Great Observatories All-sky LIRG Survey: Comparison of Ultraviolet and Far-infrared Properties. *ApJ*, *715*(1), 572–588. https://doi.org/10.1088/0004-637X/715/1/572

Hubber, D. A., Ercolano, B., & Dale, J. (2016). Observing gas and dust in simulations of star formation with Monte Carlo radiation transport on Voronoi meshes. *MNRAS*, *456*(1), 756–766. https://doi.org/10.1093/mnras/stv2676

Iglesias-Páramo, J., Buat, V., Hernández-Fernández, J., Xu, C. K., Burgarella, D., Takeuchi, T. T., Boselli, A., ... Yi, S. K. (2007). UV to IR SEDs of UV-Selected Galaxies in the ELAIS Fields: Evolution of Dust Attenuation and Star Formation Activity from z = 0.7 to 0.2. *ApJ*, *670*(1), 279–294. https://doi.org/10.1086/521867

Iliadis, C. (2007). *Nuclear Physics of Stars*.

Ilić, D., Shapovalova, A. I., Popović, L. Č., Chavushyan, V., Burenkov, A. N., Kollatschny, W., Kovačević, A., ... Rafanelli, P. (2017). Long-Term Monitoring of the Broad-Line Region Properties in a Selected Sample of AGN. *Frontiers in Astronomy and Space Sciences*, *4*, Article 12, 12. https://doi.org/10.3389/fspas.2017.00012

Imanishi, M., Nakagawa, T., Shirahata, M., Ohyama, Y., & Onaka, T. (2010). AKARI IRC Infrared 2.5-5 μm Spectroscopy of a Large Sample of Luminous Infrared Galaxies. *ApJ*, *721*(2), 1233–1261. https://doi.org/10.1088/0004-637X/721/2/1233

Imanishi, M., & Wada, K. (2004). Comparison of Nuclear Starburst Luminosities between Seyfert 1 and 2 Galaxies Based on Near-Infrared Spectroscopy. *ApJ*, *617*(1), 214–231. https://doi.org/10.1086/425245

Inami, H., Armus, L., Charmandaris, V., Groves, B., Kewley, L., Petric, A., Stierwalt, S., ... Veilleux, S. (2013). Mid-infrared Atomic Fine-structure Emission-line Spectra of Luminous Infrared Galaxies: Spitzer/IRS Spectra of the GOALS Sample. *ApJ*, *777*(2), Article 156, 156. https://doi.org/10.1088/0004-637X/777/2/156

Inami, H., Armus, L., Matsuhara, H., Charmandaris, V., Díaz-Santos, T., Surace, J., Stierwalt, S., ... Mazzarella, J. (2018). The AKARI 2.5-5 micron spectra of luminous infrared galaxies in the local Universe. *A&A*, *617*, Article A130, A130. https://doi.org/10.1051/0004-6361/201833053

Isobe, Y., Ouchi, M., Tominaga, N., Watanabe, K., Nakajima, K., Umeda, H., Yajima, H., ... Zhang, Y. (2023). JWST Identification of Extremely Low C/N Galaxies with [N/O] $\gtrsim$ 0.5 at z 6-10 Evidencing the Early CNO-cycle Enrichment and a Connection with Globular Cluster Formation. *ApJ*, *959*(2), Article 100, 100. https://doi.org/10.3847/1538-4357/ad09be

Iwamoto, K., Brachwitz, F., Nomoto, K., Kishimoto, N., Umeda, H., Hix, W. R., & Thielemann, F.-K. (1999). Nucleosynthesis in Chandrasekhar Mass Models for Type IA Supernovae and Constraints on Progenitor Systems and Burning-Front Propagation. *ApJS*, *125*(2), 439–462. https://doi.org/10.1086/313278

Izotov, Y. I., Stasińska, G., & Guseva, N. G. (2013). Primordial ^{4}He abundance: a determination based on the largest sample of H II regions with a methodology tested on model H II regions. *A&A*, *558*, Article A57, A57. https://doi.org/10.1051/0004-6361/201220782

Izotov, Y. I., Thuan, T. X., & Guseva, N. G. (2021). Large binocular telescope observations of new six compact star-forming galaxies with [Ne V] λ3426 Å emission. *MNRAS*, *508*(2), 2556–2574. https://doi.org/10.1093/mnras/stab2798

Izotov, Y. I., Thuan, T. X., & Privon, G. (2012). The detection of [Ne V] emission in five blue compact dwarf galaxies. *MNRAS*, *427*(2), 1229–1237. https://doi.org/10.1111/j.1365-2966.2012.22051.x

Jaskot, A. E., & Oey, M. S. (2013). The Origin and Optical Depth of Ionizing Radiation in the "Green Pea" Galaxies. *ApJ*, *766*(2), Article 91, 91. https://doi.org/10.1088/0004-637X/766/2/91

Jiang, T., Malhotra, S., Rhoads, J. E., & Yang, H. (2019). Direct T $_e$ Metallicity Calibration of R23 in Strong Line Emitters. *ApJ*, *872*(2), Article 145, 145. https://doi.org/10.3847/1538-4357/aaee8a

Jin, Y., Kewley, L. J., & Sutherland, R. (2022). Messenger Monte Carlo MAPPINGS V (M^3)-A Self-consistent, Three-dimensional Photoionization Code. *ApJ*, *927*(1), Article 37, 37. https://doi.org/10.3847/1538-4357/ac48f3

Jin, Y., Sutherland, R., Kewley, L. J., & Nicholls, D. C. (2023). Spatially Resolved Temperature and Density Structures of Nearby H II Regions. *ApJ*, *958*(2), Article 179, 179. https://doi.org/10.3847/1538-4357/acffb5

Jones, S., Hirschi, R., Nomoto, K., Fischer, T., Timmes, F. X., Herwig, F., Paxton, B., ... Bertolli, M. G. (2013). Advanced Burning Stages and Fate of 8-10 M $_\odot$ Stars. *ApJ*, *772*(2), Article 150, 150. https://doi.org/10.1088/0004-637X/772/2/150

Jones, T., Martin, C., & Cooper, M. C. (2015). Temperature-based Metallicity Measurements at z=0.8: Direct Calibration of Strong-line Diagnostics at Intermediate Redshift. *ApJ*, *813*(2), Article 126, 126. https://doi.org/10.1088/0004-637X/813/2/126

Joseph, R. D., & Wright, G. S. (1985). Recent star formation in interacting galaxies - II. Super starbursts in merging galaxies. *MNRAS*, *214*, 87–95. https://doi.org/10.1093/mnras/214.2.87

Kalberla, P. M. W., & Haud, U. (2019). Turbulent power distribution in the local interstellar medium. *A&A*, *627*, Article A112, A112. https://doi.org/10.1051/0004-6361/201834533

Karakas, A. I., & Lugaro, M. (2016). Stellar Yields from Metal-rich Asymptotic Giant Branch Models. *ApJ*, *825*(1), Article 26, 26. https://doi.org/10.3847/0004-637X/825/1/26

Kauffmann, G., Heckman, T. M., Tremonti, C., Brinchmann, J., Charlot, S., White, S. D. M., Ridgway, S. E., ... Schneider, D. P. (2003). The host galaxies of active galactic nuclei. *MNRAS*, *346*(4), 1055–1077. https://doi.org/10.1111/j.1365-2966.2003.07154.x

Kehrig, C., Vílchez, J. M., Guerrero, M. A., Iglesias-Páramo, J., Hunt, L. K., Duarte-Puertas, S., & Ramos-Larios, G. (2018). The extended He II λ4686 emission in the extremely metal-poor galaxy SBS 0335 - 052E seen with MUSE. *MNRAS*, *480*(1), 1081–1095. https://doi.org/10.1093/mnras/sty1920

Kehrig, C., Vílchez, J. M., Pérez-Montero, E., Iglesias-Páramo, J., Brinchmann, J., Kunth, D., Durret, F., & Bayo, F. M. (2015). The Extended He II λ4686-emitting Region in IZw 18 Unveiled: Clues for Peculiar Ionizing Sources. *ApJ*, *801*(2), Article L28, L28. https://doi.org/10.1088/2041-8205/801/2/L28

Kehrig, C., Vílchez, J. M., Sánchez, S. F., Telles, E., Pérez-Montero, E., & Martín-Gordón, D. (2008). The interplay between ionized gas and massive stars in the HII galaxy IIZw70: integral field spectroscopy with PMAS. *A&A*, *477*(3), 813–822. https://doi.org/10.1051/0004-6361:20077987

Kehrig, C., Vílchez, J. M., Telles, E., Cuisinier, F., & Pérez-Montero, E. (2006). A spectroscopic study of the near-IR [SIII] lines in a sample of HII galaxies: chemical abundances. *A&A*, *457*(2), 477–484. https://doi.org/10.1051/0004-6361:20054488

Kennicutt, R. C., & Evans, N. J. (2012). Star Formation in the Milky Way and Nearby Galaxies. *ARA&A*, *50*, 531–608. https://doi.org/10.1146/annurev-astro-081811-125610

Kessler, M. F., Steinz, J. A., Anderegg, M. E., Clavel, J., Drechsel, G., Estaria, P., Faelker, J., ... Ximenez de Ferran, S. (1996). The Infrared Space Observatory (ISO) mission. *A&A*, *500*, 493–497.

Kewley, L. J., Dopita, M. A., Sutherland, R. S., Heisler, C. A., & Trevena, J. (2001). Theoretical Modeling of Starburst Galaxies. *ApJ*, *556*(1), 121–140. https://doi.org/10.1086/321545

Kewley, L. J., & Ellison, S. L. (2008). Metallicity Calibrations and the Mass-Metallicity Relation for Star-forming Galaxies. *ApJ*, *681*(2), 1183–1204. https://doi.org/10.1086/587500

Kewley, L. J., Groves, B., Kauffmann, G., & Heckman, T. (2006). The host galaxies and classification of active galactic nuclei. *MNRAS*, *372*(3), 961–976. https://doi.org/10.1111/j.1365-2966.2006.10859.x

Kewley, L. J., Nicholls, D. C., & Sutherland, R. S. (2019). Understanding Galaxy Evolution Through Emission Lines. *ARA&A*, *57*, 511–570. https://doi.org/10.1146/annurev-astro-081817-051832

Kim, D. .-., Sanders, D. B., Veilleux, S., Mazzarella, J. M., & Soifer, B. T. (1995). Optical Spectroscopy of Luminous Infrared Galaxies. I. Nuclear Data. *ApJS*, *98*, 129. https://doi.org/10.1086/192157

Kim, D. .-., Veilleux, S., & Sanders, D. B. (1998). The IRAS 1 Jy Sample of Ultraluminous Infrared Galaxies. II. Optical Spectroscopy. *ApJ*, *508*(2), 627–647. https://doi.org/10.1086/306409

Kim, D., Im, M., Kim, J. H., Jun, H. D., Woo, J.-H., Lee, H. M., Lee, M. G., ... Lee, S.-K. (2015). The AKARI 2.5-5.0 μm Spectral Atlas of Type-1 Active Galactic Nuclei: Black Hole Mass Estimator, Line Ratio, and Hot Dust Temperature. *ApJS*, *216*(1), Article 17, 17. https://doi.org/10.1088/0067-0049/216/1/17

Kisielius, R., Storey, P. J., Davey, A. R., & Neale, L. T. (1998). Recombination coefficients for Ne Ii lines at nebular temperatures and densities. *A&AS*, *133*, 257–269. https://doi.org/10.1051/aas:1998319

Kobayashi, C., Karakas, A. I., & Lugaro, M. (2020a). The Origin of Elements from Carbon to Uranium. *ApJ*, *900*(2), Article 179, 179. https://doi.org/10.3847/1538-4357/abae65

Kobayashi, C., Leung, S.-C., & Nomoto, K. (2020b). New Type Ia Supernova Yields and the Manganese and Nickel Problems in the Milky Way and Dwarf Spheroidal Galaxies. *ApJ*, *895*(2), Article 138, 138. https://doi.org/10.3847/1538-4357/ab8e44

Kobayashi, C., Springel, V., & White, S. D. M. (2007). Simulations of Cosmic Chemical Enrichment. *MNRAS*, *376*(4), 1465–1479. https://doi.org/10.1111/j.1365-2966.2007.11555.x

Kobayashi, C., Tsujimoto, T., & Nomoto, K. (2000). The History of the Cosmic Supernova Rate Derived from the Evolution of the Host Galaxies. *ApJ*, *539*(1), 26–38. https://doi.org/10.1086/309195

Kobulnicky, H. A., Kennicutt, J., Robert C., & Pizagno, J. L. (1999). On Measuring Nebular Chemical Abundances in Distant Galaxies Using Global Emission-Line Spectra. *ApJ*, *514*(2), 544–557. https://doi.org/10.1086/306987

Kobulnicky, H. A., & Skillman, E. D. (1996). Elemental Abundance Variations and Chemical Enrichment from Massive Stars in Starbursts. I. NGC 4214. *ApJ*, *471*, 211. https://doi.org/10.1086/177964

Kobulnicky, H. A., Skillman, E. D., Roy, J.-R., Walsh, J. R., & Rosa, M. R. (1997). Hubble Space Telescope Faint Object Spectroscope Spectroscopy of Localized Chemical Enrichment from Massive Stars in NGC 5253. *ApJ*, *477*(2), 679–692. https://doi.org/10.1086/303742

Köppen, J., & Edmunds, M. G. (1999). Gas flows and the chemical evolution of galaxies - III. Graphical analysis and secondary elements. *MNRAS*, *306*(2), 317–326. https://doi.org/10.1046/j.1365-8711.1999.02584.x

Köppen, J., & Hensler, G. (2005). Effects of episodic gas infall on the chemical abundances in galaxies. *A&A*, *434*(2), 531–541. https://doi.org/10.1051/0004-6361:20042266

Kormendy, J., & Ho, L. C. (2013). Coevolution (Or Not) of Supermassive Black Holes and Host Galaxies. *ARA&A*, *51*(1), 511–653. https://doi.org/10.1146/annurev-astro-082708-101811

Koski, A. T. (1978). Spectrophotometry of Seyfert 2 galaxies and narrow-line radio galaxies. *ApJ*, *223*, 56–73. https://doi.org/10.1086/156235

Koss, M., Trakhtenbrot, B., Ricci, C., Lamperti, I., Oh, K., Berney, S., Schawinski, K., ... Winter, L. (2017). BAT AGN Spectroscopic Survey. I. Spectral Measurements, Derived Quantities, and AGN Demographics. *ApJ*, *850*(1), Article 74, 74. https://doi.org/10.3847/1538-4357/aa8ec9

Koutsoumpou, E., Fernández-Ontiveros, J. A., Dasyra, K. M., & Spinoglio, L. (2025). Cosmic-ray ionization of low-excitation lines in active galactic nuclei and starburst galaxies. *A&A*, *693*, Article A215, A215. https://doi.org/10.1051/0004-6361/202452232

Krabbe, A. C., Oliveira, C. B., Zinchenko, I. A., Hernández-Jiménez, J. A., Dors, O. L., Hägele, G. F., Cardaci, M. V., & Telles, N. R. (2021). Chemical abundance of the LINER galaxy UGC 4805 with SDSS-IV MaNGA. *MNRAS*, *505*(2), 2087–2102. https://doi.org/10.1093/mnras/stab1346

Kraemer, S. B., Wu, C.-C., Crenshaw, D. M., & Harrington, J. P. (1994). IUE Spectra and Photoionization Models of the Seyfert 2 Galaxies NGC 7674 and I ZW 92. *ApJ*, *435*, 171. https://doi.org/10.1086/174803

Kroupa, P. (2001). On the variation of the initial mass function. *MNRAS*, *322*(2), 231–246. https://doi.org/10.1046/j.1365-8711.2001.04022.x

Kulkarni, S. R., & Fich, M. (1985). The fraction of high velocity dispersion HI in the Galaxy. *ApJ*, *289*, 792–802. https://doi.org/10.1086/162943

Kumari, N., James, B. L., Irwin, M. J., Amorín, R., & Pérez-Montero, E. (2018). O/H-N/O: the curious case of NGC 4670. *MNRAS*, *476*(3), 3793–3815. https://doi.org/10.1093/mnras/sty402

Lacy, J. H., Richter, M. J., Greathouse, T. K., Jaffe, D. T., & Zhu, Q. (2002). TEXES: A Sensitive High-Resolution Grating Spectrograph for the Mid-Infrared. *PASP*, *114*(792), 153–168. https://doi.org/10.1086/338730

Lai, T. S. .-., Smith, J. D. T., Baba, S., Spoon, H. W. W., & Imanishi, M. (2020). All the PAHs: An AKARI-Spitzer Cross-archival Spectroscopic Survey of Aromatic Emission in Galaxies. *ApJ*, *905*(1), Article 55, 55. https://doi.org/10.3847/1538-4357/abc002

Lamarche, C., Verma, A., Vishwas, A., Stacey, G. J., Brisbin, D., Ferkinhoff, C., Nikola, T., … Tecza, M. (2018). Resolving Star Formation on Subkiloparsec Scales in the High-redshift Galaxy SDP.11 Using Gravitational Lensing. *ApJ*, *867*(2), Article 140, 140. https://doi.org/10.3847/1538-4357/aae394

Lamareille, F., Mouhcine, M., Contini, T., Lewis, I., & Maddox, S. (2004). The luminosity-metallicity relation in the local Universe from the 2dF Galaxy Redshift Survey. *MNRAS*, *350*(2), 396–406. https://doi.org/10.1111/j.1365-2966.2004.07697.x

LaMassa, S. M., Heckman, T. M., Ptak, A., Martins, L., Wild, V., & Sonnentrucker, P. (2010). Indicators of Intrinsic Active Galactic Nucleus Luminosity: A Multi-wavelength Approach. *ApJ*, *720*(1), 786–810. https://doi.org/10.1088/0004-637X/720/1/786

Lamperti, I., Koss, M., Trakhtenbrot, B., Schawinski, K., Ricci, C., Oh, K., Landt, H., … Veilleux, S. (2017). BAT AGN Spectroscopic Survey - IV: Near-Infrared Coronal Lines, Hidden Broad Lines, and Correlation with Hard X-ray Emission. *MNRAS*, *467*(1), 540–572. https://doi.org/10.1093/mnras/stx055

Lancon, A., Rocca-Volmerange, B., & Thuan, T. X. (1996). H+K spectroscopy of luminous infrared galaxies. *A&AS*, *115*, 253.

Lara-López, M. A., Bongiovanni, A., Cepa, J., Pérez García, A. M., Sánchez-Portal, M., Castañeda, H. O., Fernández Lorenzo, M., & Pović, M. (2010). Study of star-forming galaxies in SDSS up to redshift 0.4. II. Evolution from the fundamental parameters: mass, metallicity and star formation rate. *A&A*, *519*, Article A31, A31. https://doi.org/10.1051/0004-6361/200913886

Lara-López, M. A., Cepa, J., Bongiovanni, A., Pérez García, A. M., Castañeda, H., Fernández Lorenzo, M., Pović, M., & Sánchez-Portal, M. (2009). Study of star-forming galaxies in SDSS up to redshift 0.4. I. Metallicity evolution. *A&A*, *505*(2), 529–539. https://doi.org/10.1051/0004-6361/200912214

Larsen, T. I., Sommer-Larsen, J., & Pagel, B. E. J. (2001). The chemical evolution of gas-rich dwarf galaxies. *MNRAS*, *323*(3), 555–576. https://doi.org/10.1046/j.1365-8711.2001.04142.x

Larson, R. B. (2005). Thermal physics, cloud geometry and the stellar initial mass function. *MNRAS*, *359*(1), 211–222. https://doi.org/10.1111/j.1365-2966.2005.08881.x

Latimer, L. J., Reines, A. E., Bogdan, A., & Kraft, R. (2021). The AGN Fraction in Dwarf Galaxies from eROSITA: First Results and Future Prospects. *ApJ*, *922*(2), Article L40, L40. https://doi.org/10.3847/2041-8213/ac3af6

Law, D. R., Cherinka, B., Yan, R., Andrews, B. H., Bershady, M. A., Bizyaev, D., Blanc, G. A., … Zhang, K. (2016). The Data Reduction Pipeline for the SDSS-IV MaNGA IFU Galaxy Survey. *AJ*, *152*(4), Article 83, 83. https://doi.org/10.3847/0004-6256/152/4/83

Lebouteiller, V., Barry, D. J., Goes, C., Sloan, G. C., Spoon, H. W. W., Weedman, D. W., Bernard-Salas, J., & Houck, J. R. (2015). CASSIS: The Cornell Atlas of Spitzer/Infrared Spectrograph Sources. II. High-resolution Observations. *ApJS*, *218*(2), Article 21, 21. https://doi.org/10.1088/0067-0049/218/2/21

Leitherer, C., Tremonti, C. A., Heckman, T. M., & Calzetti, D. (2011). An Ultraviolet Spectroscopic Atlas of Local Starbursts and Star-forming Galaxies: The Legacy of FOS and GHRS. *AJ*, *141*(2), Article 37, 37. https://doi.org/10.1088/0004-6256/141/2/37

Lequeux, J., Peimbert, M., Rayo, J. F., Serrano, A., & Torres-Peimbert, S. (1979). Reprint of 1979A&A....80..155L. Chemical composition and evolution of irregular and blue compact galaxies. *A&A*, *500*, 145–156.

Lequeux, J. (2005). *The Interstellar Medium*. https://doi.org/10.1007/b137959

Leroy, A. K., Bolatto, A., Gordon, K., Sandstrom, K., Gratier, P., Rosolowsky, E., Engelbracht, C. W., ... Kawamura, A. (2011). The CO-to-H_2 Conversion Factor from Infrared Dust Emission across the Local Group. *ApJ*, *737*(1), Article 12, 12. https://doi.org/10.1088/0004-637X/737/1/12

Leung, S.-C., & Nomoto, K. (2019). Final evolution of super-AGB stars and supernovae triggered by electron capture. *PASA*, *36*, Article e006, e006. https://doi.org/10.1017/pasa.2018.49

Li, J., Kreckel, K., Sarbadhicary, S., Egorov, O. V., Groves, B., Long, K. S., Congiu, E., ... Williams, T. G. (2024). Discovery of 2200 new supernova remnants in 19 nearby star-forming galaxies with MUSE spectroscopy. *A&A*, *690*, Article A161, A161. https://doi.org/10.1051/0004-6361/202450730

Lia, C., Portinari, L., & Carraro, G. (2002). Star formation and chemical evolution in smoothed particle hydrodynamics simulations: a statistical approach. *MNRAS*, *330*(4), 821–836. https://doi.org/10.1046/j.1365-8711.2002.05118.x

Lian, J., Thomas, D., Maraston, C., Goddard, D., Parikh, T., Fernández-Trincado, J. G., Roman-Lopes, A., ... Yan, R. (2018). SDSS-IV MaNGA: modelling the metallicity gradients of gas and stars - radially dependent metal outflow versus IMF. *MNRAS*, *476*(3), 3883–3901. https://doi.org/10.1093/mnras/sty425

Lilly, S. J., Carollo, C. M., Pipino, A., Renzini, A., & Peng, Y. (2013). Gas Regulation of Galaxies: The Evolution of the Cosmic Specific Star Formation Rate, the Metallicity-Mass-Star-formation Rate Relation, and the Stellar Content of Halos. *ApJ*, *772*(2), Article 119, 119. https://doi.org/10.1088/0004-637X/772/2/119

Limongi, M., & Chieffi, A. (2018). Presupernova Evolution and Explosive Nucleosynthesis of Rotating Massive Stars in the Metallicity Range $-3 \leq [\mathrm{Fe/H}] \leq 0$. *ApJS*, *237*(1), Article 13, 13. https://doi.org/10.3847/1538-4365/aacb24

Llerena, M., Amorín, R., Cullen, F., Pentericci, L., Calabrò, A., McLure, R., Carnall, A., ... Zamorani, G. (2022). The VANDELS survey: Global properties of CIII]λ1908 Å emitting star-forming galaxies at $z \sim 3$. *A&A*, *659*, Article A16, A16. https://doi.org/10.1051/0004-6361/202141651

Lo Faro, B., Buat, V., Roehlly, Y., Alvarez-Marquez, J., Burgarella, D., Silva, L., & Efstathiou, A. (2017). Characterizing the UV-to-NIR shape of the dust attenuation curve of IR luminous galaxies up to $z \sim 2$. *MNRAS*, *472*(2), 1372–1391. https://doi.org/10.1093/mnras/stx1901

Lodders, K. (2021). Relative Atomic Solar System Abundances, Mass Fractions, and Atomic Masses of the Elements and Their Isotopes, Composition of the Solar Photosphere, and Compositions of the Major Chondritic Meteorite Groups. *Space Sci. Rev.*, *217*(3), Article 44, 44. https://doi.org/10.1007/s11214-021-00825-8

López-Sánchez, Á. R., & Esteban, C. (2010). Massive star formation in Wolf-Rayet galaxies. IV. Colours, chemical-composition analysis and metallicity-luminosity relations. *A&A*, *517*, Article A85, A85. https://doi.org/10.1051/0004-6361/201014156

Lumsden, S. L., Heisler, C. A., Bailey, J. A., Hough, J. H., & Young, S. (2001). Spectropolarimetry of a complete infrared-selected sample of Seyfert 2 galaxies. *MNRAS*, *327*(2), 459–474. https://doi.org/10.1046/j.1365-8711.2001.04741.x

Luridiana, V., Morisset, C., & Shaw, R. A. (2015). PyNeb: a new tool for analyzing emission lines. I. Code description and validation of results. *A&A*, *573*, Article A42, A42. https://doi.org/10.1051/0004-6361/201323152

Lutz, D., Maiolino, R., Moorwood, A. F. M., Netzer, H., Wagner, S. J., Sturm, E., & Genzel, R. (2002). Infrared spectroscopy around 4 mu m of Seyfert 2 galaxies: Obscured broad line regions and coronal lines. *A&A*, *396*, 439–448. https://doi.org/10.1051/0004-6361:20021389

Madden, S. C., Cormier, D., Hony, S., Lebouteiller, V., Abel, N., Galametz, M., De Looze, I., ... Ramambason, L. (2020). Tracing the total molecular gas in galaxies: [CII] and the CO-dark gas. *A&A*, *643*, Article A141, A141. https://doi.org/10.1051/0004-6361/202038860

Maeder, A., Przybilla, N., Nieva, M.-F., Georgy, C., Meynet, G., Ekström, S., & Eggenberger, P. (2014). Evolution of surface CNO abundances in massive stars. *A&A*, *565*, Article A39, A39. https://doi.org/10.1051/0004-6361/201220602

Magnelli, B., Elbaz, D., Chary, R. R., Dickinson, M., Le Borgne, D., Frayer, D. T., & Willmer, C. N. A. (2009). The $0.4 < z < 1.3$ star formation history of the Universe as viewed in the far-infrared. *A&A*, *496*(1), 57–75. https://doi.org/10.1051/0004-6361:200811443

Maiolino, R., & Mannucci, F. (2019). De re metallica: the cosmic chemical evolution of galaxies. *A&A Rev.*, *27*(1), Article 3, 3. https://doi.org/10.1007/s00159-018-0112-2

Makki, T. R., El Eid, M. F., & Mathews, G. J. (2019). A critical analysis of the Big Bang Nucleosynthesis. *Modern Physics Letters A*, *34*(24), Article 1950194, 1950194. https://doi.org/10.1142/S0217732319501943

Malkan, M. A. (1986). Near-Ultraviolet Spectroscopy of Seyfert Nuclei: Reddening and Bowen Fluorescence. *ApJ*, *310*, 679. https://doi.org/10.1086/164718

Malkan, M. A., Jensen, L. D., Rodriguez, D. R., Spinoglio, L., & Rush, B. (2017). Emission Line Properties of Seyfert Galaxies in the 12 μm Sample. *ApJ*, *846*(2), Article 102, 102. https://doi.org/10.3847/1538-4357/aa8302

Mandal, A. K., Rakshit, S., Stalin, C. S., Petrov, R. G., Mathew, B., & Sagar, R. (2021). Estimation of the size and structure of the broad line region using Bayesian approach. *MNRAS*, *502*(2), 2140–2157. https://doi.org/10.1093/mnras/stab012

Mannucci, F., Cresci, G., Maiolino, R., Marconi, A., & Gnerucci, A. (2010). A fundamental relation between mass, star formation rate and metallicity in local and high-redshift galaxies. *MNRAS*, *408*(4), 2115–2127. https://doi.org/10.1111/j.1365-2966.2010.17291.x

Mannucci, F., Cresci, G., Maiolino, R., Marconi, A., Pastorini, G., Pozzetti, L., Gnerucci, A., ... Salvati, M. (2009). LSD: Lyman-break galaxies Stellar populations and Dynamics - I. Mass, metallicity and gas at z ~3.1. *MNRAS*, *398*(4), 1915–1931. https://doi.org/10.1111/j.1365-2966.2009.15185.x

Marchand, P., Masson, J., Chabrier, G., Hennebelle, P., Commerçon, B., & Vaytet, N. (2016). Chemical solver to compute molecule and grain abundances and non-ideal MHD resistivities in prestellar core-collapse calculations. *A&A*, *592*, Article A18, A18. https://doi.org/10.1051/0004-6361/201526780

Marconi, A., Amiri, A., Feltre, A., Belfiore, F., Cresci, G., Curti, M., Mannucci, F., ... Venturi, G. (2024). HOMERUN: A new approach to photoionization modeling: I. Reproducing observed emission lines with percent accuracy and obtaining accurate physical properties of the ionized gas. *A&A*, *689*, Article A78, A78. https://doi.org/10.1051/0004-6361/202449240

Márquez, I., Masegosa, J., González-Martin, O., Hernández-Garcia, L., Pović, M., Netzer, H., Cazzoli, S., & del Olmo, A. (2017). The AGN nature of LINER nuclear sources. *Frontiers in Astronomy and Space Sciences*, *4*, Article 34, 34. https://doi.org/10.3389/fspas.2017.00034

Martínez-Paredes, M., Bruzual, G., Morisset, C., Kim, M., Meléndez, M., & Binette, L. (2023). On the origin of optical and IR emission lines in star-forming galaxies. *MNRAS*, *525*(2), 2916–2934. https://doi.org/10.1093/mnras/stad2447

Martins, L. P., Rodríguez-Ardila, A., de Souza, R., & Gruenwald, R. (2010). Nuclear and extended spectra of NGC 1068 - I. Hints from near-infrared spectroscopy. *MNRAS*, *406*(4), 2168–2184. https://doi.org/10.1111/j.1365-2966.2010.17042.x

Martizzi, D., Vogelsberger, M., Artale, M. C., Haider, M., Torrey, P., Marinacci, F., Nelson, D., ... Springel, V. (2019). Baryons in the Cosmic Web of IllustrisTNG - I: gas in knots, filaments, sheets, and voids. *MNRAS*, *486*(3), 3766–3787. https://doi.org/10.1093/mnras/stz1106

Masegosa, J., Márquez, I., Ramirez, A., & González-Martín, O. (2011). The nature of nuclear H_α emission in LINERs. *A&A*, *527*, Article A23, A23. https://doi.org/10.1051/0004-6361/201015047

Massey, P., Puls, J., Pauldrach, A. W. A., Bresolin, F., Kudritzki, R. P., & Simon, T. (2005). The Physical Properties and Effective Temperature Scale of O-Type Stars as a Function of Metallicity. II. Analysis of 20 More Magellanic Cloud Stars and Results from the Complete Sample. *ApJ*, *627*(1), 477–519. https://doi.org/10.1086/430417

Masters, D., Faisst, A., & Capak, P. (2016). A Tight Relation between N/O Ratio and Galaxy Stellar Mass Can Explain the Evolution of Strong Emission Line Ratios with Redshift. *ApJ*, *828*(1), Article 18, 18. https://doi.org/10.3847/0004-637X/828/1/18

Mateus, A., Sodré, L., Cid Fernandes, R., Stasińska, G., Schoenell, W., & Gomes, J. M. (2006). Semi-empirical analysis of Sloan Digital Sky Survey galaxies - II. The bimodality of the galaxy population revisited. *MNRAS*, *370*, 721–737. https://doi.org/10.1111/j.1365-2966.2006.10565.x

Mathis, J. S., Rumpl, W., & Nordsieck, K. H. (1977). The size distribution of interstellar grains. *ApJ*, *217*, 425–433. https://doi.org/10.1086/155591

Matteucci, F., & Francois, P. (1989). Galactic chemical evolution : abundance gradients of individual elements. *MNRAS*, *239*, 885–904. https://doi.org/10.1093/mnras/239.3.885

Matteucci, F. (2012). *Chemical Evolution of Galaxies*. https://doi.org/10.1007/978-3-642-22491-1

Matteucci, F. (2021). Modelling the chemical evolution of the Milky Way. *A&A Rev.*, *29*(1), Article 5, 5. https://doi.org/10.1007/s00159-021-00133-8

McClure, R. D., & van den Bergh, S. (1968). UB V Observations of Field Galaxies. *AJ*, *73*, 1008. https://doi.org/10.1086/110760

McClymont, W., Tacchella, S., Smith, A., Kannan, R., Maiolino, R., Belfiore, F., Hernquist, L., ... Vogelsberger, M. (2024). The nature of diffuse ionized gas in star-forming galaxies. *MNRAS*, *532*(2), 2016–2031. https://doi.org/10.1093/mnras/stae1587

McLean, I. S., Smith, E. C., Aliado, T., Brims, G., Kress, E., Magnone, K., Milburn, J., ... Shuping, R. Y. (2006, June). FLITECAM: a 1-5 micron camera and spectrometer for SOFIA. In I. S. McLean & M. Iye (Eds.), *Ground-based and airborne instrumentation for astronomy* (62695B, Vol. 6269). https://doi.org/10.1117/12.672173

Meléndez, M., Kraemer, S. B., Armentrout, B. K., Deo, R. P., Crenshaw, D. M., Schmitt, H. R., Mushotzky, R. F., ... Winter, L. (2008). New Indicators for AGN Power: The Correlation between [O IV] 25.89 μm and Hard X-Ray Luminosity for Nearby Seyfert Galaxies. *ApJ*, *682*(1), 94–103. https://doi.org/10.1086/588807

Méndez-Delgado, J. E., Amayo, A., Arellano-Córdova, K. Z., Esteban, C., García-Rojas, J., Carigi, L., & Delgado-Inglada, G. (2022). Gradients of chemical abundances in the Milky Way from H II regions: distances derived from Gaia EDR3 parallaxes and temperature inhomogeneities. *MNRAS*, *510*(3), 4436–4455. https://doi.org/10.1093/mnras/stab3782

Méndez-Delgado, J. E., Esteban, C., García-Rojas, J., Kreckel, K., & Peimbert, M. (2023). Temperature inhomogeneities cause the abundance discrepancy in H II regions. *Nature*, *618*(7964), 249–251. https://doi.org/10.1038/s41586-023-05956-2

Meynet, G., Chomienne, V., Ekström, S., Georgy, C., Granada, A., Groh, J., Maeder, A., ... Massey, P. (2015). Impact of mass-loss on the evolution and pre-supernova properties of red supergiants. *A&A*, *575*, Article A60, A60. https://doi.org/10.1051/0004-6361/201424671

Meynet, G., & Maeder, A. (2002). The origin of primary nitrogen in galaxies. *A&A*, *381*, L25–L28. https://doi.org/10.1051/0004-6361:20011554

Michałowski, M. J., Gall, C., Hjorth, J., Frayer, D. T., Tsai, A. .-., Rowlands, K., Takeuchi, T. T., ... Bartczak, P. (2024). The Fate of the Interstellar Medium in Early-type Galaxies. III. The Mechanism of Interstellar Medium Removal and the Quenching of Star Formation. *ApJ*, *964*(2), Article 129, 129. https://doi.org/10.3847/1538-4357/ad1b52

Mihos, J. C., Keating, K. M., Holley-Bockelmann, K., Pisano, D. J., & Kassim, N. E. (2012). The H I Environment of the M101 Group. *ApJ*, *761*(2), Article 186, 186. https://doi.org/10.1088/0004-637X/761/2/186

Mineo, S., Gilfanov, M., & Sunyaev, R. (2012). X-ray emission from star-forming galaxies - II. Hot interstellarmedium. *MNRAS*, *426*(3), 1870–1883. https://doi.org/10.1111/j.1365-2966.2012.21831.x

Mingozzi, M., Belfiore, F., Cresci, G., Bundy, K., Bershady, M., Bizyaev, D., Blanc, G., ... Zhang, K. (2020). SDSS IV MaNGA: Metallicity and ionisation parameter in local star-forming galaxies from Bayesian fitting to photoionisation models. *A&A*, *636*, Article A42, A42. https://doi.org/10.1051/0004-6361/201937203

Mingozzi, M., Garcia Del Valle-Espinosa, M., James, B. L., Rickards Vaught, R. J., Hayes, M., Amorín, R. O., Leitherer, C., ... Xu, X. (2025). Exploring the mysterious high-ionization source powering [Ne V] in high-z analog SBS0335-052 E with JWST/MIRI. *arXiv e-prints*, Article arXiv:2502.07662, arXiv:2502.07662. https://doi.org/10.48550/arXiv.2502.07662

Mingozzi, M., James, B. L., Berg, D. A., Arellano-Córdova, K. Z., Plat, A., Scarlata, C., Aloisi, A., ... Xu, X. (2024). CLASSY. VIII. Exploring the Source of Ionization with UV Interstellar Medium Diagnostics in Local High-z Analogs. *ApJ*, *962*(1), Article 95, 95. https://doi.org/10.3847/1538-4357/ad1033

Mitchell, P. D., Lacey, C. G., Lagos, C. D. P., Frenk, C. S., Bower, R. G., Cole, S., Helly, J. C., ... Theuns, T. (2018). Comparing galaxy formation in semi-analytic models and hydrodynamical simulations. *MNRAS*, *474*(1), 492–521. https://doi.org/10.1093/mnras/stx2770

Mocák, M., Müller, E., Weiss, A., & Kifonidis, K. (2008). The core helium flash revisited. I. One and two-dimensional hydrodynamic simulations. *A&A*, *490*(1), 265–277. https://doi.org/10.1051/0004-6361:200810169

Mollá, M., García-Vargas, M. L., & Bressan, A. (2009). PopStar I: evolutionary synthesis model description. *MNRAS*, *398*(1), 451–470. https://doi.org/10.1111/j.1365-2966.2009.15160.x

Mollá, M., Vílchez, J. M., Gavilán, M., & Díaz, A. I. (2006). The nitrogen-to-oxygen evolution in galaxies: the role of the star formation rate. *MNRAS*, *372*(3), 1069–1080. https://doi.org/10.1111/j.1365-2966.2006.10892.x

Monreal-Ibero, A., Arribas, S., & Colina, L. (2006). LINER-like Extended Nebulae in ULIRGs: Shocks Generated by Merger-Induced Flows. *ApJ*, *637*(1), 138–146. https://doi.org/10.1086/498257

Montoro-Molina, B., Guerrero, M. A., Pérez-Díaz, B., Toalá, J. A., Cazzoli, S., Miller Bertolami, M. M., & Morisset, C. (2022). Chemistry and physical properties of the born-again planetary nebula HuBi 1. *MNRAS*, *512*(3), 4003–4020. https://doi.org/10.1093/mnras/stac336

Montuori, M., Di Matteo, P., Lehnert, M. D., Combes, F., & Semelin, B. (2010). The dilution peak, metallicity evolution, and dating of galaxy interactions and mergers. *A&A*, *518*, Article A56, A56. https://doi.org/10.1051/0004-6361/201014304

Moorwood, A. F. M., van der Werf, P. P., Kotilainen, J. K., Marconi, A., & Oliva, E. (1996). Starburst superwind and LINER activity in NGC4945. *A&A*, *308*, L1.

Mor, R., Netzer, H., & Elitzur, M. (2009). Dusty Structure Around Type-I Active Galactic Nuclei: Clumpy Torus Narrow-line Region and Near-nucleus Hot Dust. *ApJ*, *705*(1), 298–313. https://doi.org/10.1088/0004-637X/705/1/298

Moraes, M., & Diaz, M. (2009). HR Del Remnant Anatomy Using Two-Dimensional Spectral Data and Three-Dimensional Photoionization Shell Models. *AJ*, *138*(6), 1541–1556. https://doi.org/10.1088/0004-6256/138/6/1541

Mordini, S., Spinoglio, L., & Fernández-Ontiveros, J. A. (2021). Calibration of mid- to far-infrared spectral lines in galaxies. *A&A*, *653*, Article A36, A36. https://doi.org/10.1051/0004-6361/202140696

Morganti, R. (2017). The many routes to AGN feedback. *Frontiers in Astronomy and Space Sciences*, *4*, Article 42, 42. https://doi.org/10.3389/fspas.2017.00042

Morisset, C., & Stasinska, G. (2008). An atlas of synthetic line profiles of Planetary Nebulae. *Rev. Mexicana Astron. Astrofis.*, *44*, 171–180. https://doi.org/10.48550/arXiv.0801.4906

Morisset, C., Stasińska, G., & Peña, M. (2005). Modelling of aspherical nebulae - I. A quick pseudo-3D photoionization code. *MNRAS*, *360*(2), 499–508. https://doi.org/10.1111/j.1365-2966.2005.09049.x

Morisset, C. (2006, January). Cloudy_3D, a new pseudo-3D photoionization code. In M. J. Barlow & R. H. Méndez (Eds.), *Planetary nebulae in our galaxy and beyond* (pp. 467–468, Vol. 234). https://doi.org/10.1017/S1743921306003772

Morisset, C., Luridiana, V., García-Rojas, J., Gómez-Llanos, V., Bautista, M., & Mendoza, C. (2020). Atomic Data Assessment with PyNeb. *Atoms*, *8*(4), Article 66, 66. https://doi.org/10.3390/atoms8040066

Morris, S. L., & Ward, M. J. (1988). Spectrophotometry of active galaxies - I. The observations. *MNRAS*, *230*, 639–669. https://doi.org/10.1093/mnras/230.4.639

Mosconi, M. B., Tissera, P. B., Lambas, D. G., & Cora, S. A. (2001). Chemical evolution using smooth particle hydrodynamical cosmological simulations - I. Implementation, tests and first results. *MNRAS*, *325*(1), 34–48. https://doi.org/10.1046/j.1365-8711.2001.04198.x

Mosquera, A. M., Kochanek, C. S., Chen, B., Dai, X., Blackburne, J. A., & Chartas, G. (2013). The Structure of the X-Ray and Optical Emitting Regions of the Lensed Quasar Q 2237+0305. *ApJ*, *769*(1), Article 53, 53. https://doi.org/10.1088/0004-637X/769/1/53

Moustakas, J., & Kennicutt, J., Robert C. (2006). An Integrated Spectrophotometric Survey of Nearby Star-forming Galaxies. *ApJS*, *164*(1), 81–98. https://doi.org/10.1086/500971

Müller-Sánchez, F., Prieto, M. A., Hicks, E. K. S., Vives-Arias, H., Davies, R. I., Malkan, M., Tacconi, L. J., & Genzel, R. (2011). Outflows from Active Galactic Nuclei: Kinematics of the Narrow-line and Coronal-line Regions in Seyfert Galaxies. *ApJ*, *739*(2), Article 69, 69. https://doi.org/10.1088/0004-637X/739/2/69

Muñoz-Mateos, J. C., Gil de Paz, A., Boissier, S., Zamorano, J., Jarrett, T., Gallego, J., & Madore, B. F. (2007). Specific Star Formation Rate Profiles in Nearby Spiral Galaxies: Quantifying the Inside-Out Formation of Disks. *ApJ*, *658*(2), 1006–1026. https://doi.org/10.1086/511812

Muñoz-Mateos, J. C., Sheth, K., Gil de Paz, A., Meidt, S., Athanassoula, E., Bosma, A., Comerón, S., … Zaritsky, D. (2013). The Impact of Bars on Disk Breaks as Probed by S^4G Imaging. *ApJ*, *771*(1), Article 59, 59. https://doi.org/10.1088/0004-637X/771/1/59

Muñoz-Mateos, J. C., Sheth, K., Regan, M., Kim, T., Laine, J., Erroz-Ferrer, S., Gil de Paz, A., … Courtois, H. (2015). The Spitzer Survey of Stellar Structure in Galaxies (S^4G): Stellar Masses, Sizes, and Radial Profiles for 2352 Nearby Galaxies. *ApJS*, *219*(1), Article 3, 3. https://doi.org/10.1088/0067-0049/219/1/3

Murakami, H., Baba, H., Barthel, P., Clements, D. L., Cohen, M., Doi, Y., Enya, K., … Yasuda, A. (2007). The Infrared Astronomical Mission AKARI*. *PASJ*, *59*, S369–S376. https://doi.org/10.1093/pasj/59.sp2.S369

Murphy, J., T. W., Soifer, B. T., Matthews, K., Armus, L., & Kiger, J. R. (2001). K-Band Spectroscopy of Ultraluminous Infrared Galaxies: The 2 JY Sample. *AJ*, *121*(1), 97–127. https://doi.org/10.1086/318031

Nadler, E. O., Benson, A., Driskell, T., Du, X., & Gluscevic, V. (2023). Growing the first galaxies' merger trees. *MNRAS*, *521*(3), 3201–3220. https://doi.org/10.1093/mnras/stad666

Nadolny, J., Michałowski, M. J., Parente, M., Hjorth, J., Gall, C., Leśniewska, A., Solar, M., … Ryzhov, O. (2024). The fate of the interstellar medium in early-type galaxies: IV. The impact of stellar feedback, mergers, and black holes on the cold interstellar medium in simulated galaxies. *A&A*, *689*, Article A210, A210. https://doi.org/10.1051/0004-6361/202449839

Nagao, T., Maiolino, R., Marconi, A., & Matsuhara, H. (2011). Metallicity diagnostics with infrared fine-structure lines. *A&A*, *526*, Article A149, A149. https://doi.org/10.1051/0004-6361/201015471

Nakajima, K., Ouchi, M., Isobe, Y., Harikane, Y., Zhang, Y., Ono, Y., Umeda, H., & Oguri, M. (2023). JWST Census for the Mass-Metallicity Star Formation Relations at z = 4-10 with Self-consistent Flux Calibration and Proper Metallicity Calibrators. *The Astrophysical Journal Suplement Series*, *269*(2), Article 33, 33. https://doi.org/10.3847/1538-4365/acd556

Nashimoto, M., Tanaka, M., Chiba, M., Hayashi, K., Komiyama, Y., & Okamoto, T. (2022). The Missing Satellite Problem outside of the Local Group. II. Statistical Properties of Satellites of Milky Way-like Galaxies. *ApJ*, *936*(1), Article 38, 38. https://doi.org/10.3847/1538-4357/ac83a4

Nemmen, R. S., Storchi-Bergmann, T., & Eracleous, M. (2014). Spectral models for low-luminosity active galactic nuclei in LINERs: the role of advection-dominated accretion and jets. *MNRAS*, *438*(4), 2804–2827. https://doi.org/10.1093/mnras/stt2388

Nesvadba, N. P. H., Cañameras, R., Kneissl, R., Koenig, S., Yang, C., Le Floc'h, E., Omont, A., & Scott, D. (2019). Planck's Dusty GEMS. VII. Atomic carbon and molecular gas in dusty starburst galaxies at z = 2 to 4. *A&A*, *624*, Article A23, A23. https://doi.org/10.1051/0004-6361/201833777

Netzer, H. (2015). Revisiting the Unified Model of Active Galactic Nuclei. *ARA&A*, *53*, 365–408. https://doi.org/10.1146/annurev-astro-082214-122302

Neugebauer, G., Habing, H. J., van Duinen, R., Aumann, H. H., Baud, B., Beichman, C. A., Beintema, D. A., ... Young, E. (1984). The Infrared Astronomical Satellite (IRAS) mission. *ApJ*, *278*, L1–L6. https://doi.org/10.1086/184209

Nicholls, D. C., Dopita, M. A., & Sutherland, R. S. (2012). Resolving the Electron Temperature Discrepancies in H II Regions and Planetary Nebulae: κ-distributed Electrons. *ApJ*, *752*(2), Article 148, 148. https://doi.org/10.1088/0004-637X/752/2/148

Nieva, M.-F., & Przybilla, N. (2014). Fundamental properties of nearby single early B-type stars. *A&A*, *566*, Article A7, A7. https://doi.org/10.1051/0004-6361/201423373

Nobels, F. S. J., Schaye, J., Schaller, M., Bahé, Y. M., & Chaikin, E. (2022). The interplay between AGN feedback and precipitation of the intracluster medium in simulations of galaxy groups and clusters. *MNRAS*, *515*(4), 4838–4859. https://doi.org/10.1093/mnras/stac2061

Noll, S., Kausch, W., Barden, M., Jones, A. M., Szyszka, C., Kimeswenger, S., & Vinther, J. (2012). An atmospheric radiation model for Cerro Paranal. I. The optical spectral range. *A&A*, *543*, Article A92, A92. https://doi.org/10.1051/0004-6361/201219040

Nomoto, K., Kobayashi, C., & Tominaga, N. (2013). Nucleosynthesis in Stars and the Chemical Enrichment of Galaxies. *ARA&A*, *51*(1), 457–509. https://doi.org/10.1146/annurev-astro-082812-140956

Novak, M., Bañados, E., Decarli, R., Walter, F., Venemans, B., Neeleman, M., Farina, E. P., ... Wang, F. (2019). An ALMA Multiline Survey of the Interstellar Medium of the Redshift 7.5 Quasar Host Galaxy J1342+0928. *ApJ*, *881*(1), Article 63, 63. https://doi.org/10.3847/1538-4357/ab2beb

Nymark, T. K., Fransson, C., & Kozma, C. (2006). X-ray emission from radiative shocks in type II supernovae. *A&A*, *449*(1), 171–192. https://doi.org/10.1051/0004-6361:20054169

Ogiya, G., & Burkert, A. (2015). Re-examining the too-big-to-fail problem for dark matter haloes with central density cores. *MNRAS*, *446*(3), 2363–2369. https://doi.org/10.1093/mnras/stu2283

Ohyama, Y., Onaka, T., Matsuhara, H., Wada, T., Kim, W., Fujishiro, N., Uemizu, K., ... Ikeda, Y. (2007). Near-Infrared and Mid-Infrared Spectroscopy with the Infrared Camera (IRC) for AKARI. *PASJ*, *59*, S411. https://doi.org/10.1093/pasj/59.sp2.S411

Oliva, E., Salvati, M., Moorwood, A. F. M., & Marconi, A. (1994). Size and physical conditions of the coronal line region in a nearby Seyfert 2: the Circinus galaxy. *A&A*, *288*, 457–465.

Oliveira, C. B., Krabbe, A. C., Dors, O. L., Zinchenko, I. A., Hernandez-Jimenez, J. A., Cardaci, M. V., Hägele, G. F., & Ilha, G. S. (2024a). Chemical abundances of LINER galaxies - nitrogen abundance estimations. *MNRAS*, *531*(1), 199–212. https://doi.org/10.1093/mnras/stae1172

Oliveira, C. B., Krabbe, A. C., Hernandez-Jimenez, J. A., Dors, O. L., Zinchenko, I. A., Hägele, G. F., Cardaci, M. V., & Monteiro, A. F. (2022). Chemical abundance of LINER galaxies - metallicity calibrations based on SDSS-IV MaNGA. *MNRAS*, *515*(4), 6093–6108. https://doi.org/10.1093/mnras/stac2118

Oliveira, C. B., Dors, O., Zinchenko, I., Cardaci, M., Hägele, G., Morais, I., Santos, P., & Almeida, G. (2024b). Semi-empirical calibration of the oxygen abundance for LINER galaxies based on SDSS-IV MaNGA - The case for strong and weak AGN. *PASA*, *41*, Article e099, e099. https://doi.org/10.1017/pasa.2024.110

Osterbrock, D. E., & Koski, A. T. (1976). NGC 4151 and Markarian 6 - two intermediate-type Seyfert galaxies. *MNRAS*, *176*, 61P–66P. https://doi.org/10.1093/mnras/176.1.61P

Osterbrock, D. E., & Ferland, G. J. (2006). *Astrophysics of gaseous nebulae and active galactic nuclei*.

Osterbrock, D. E., & Martel, A. (1993). Spectroscopic Study of the CfA Sample of Seyfert Galaxies. *ApJ*, *414*, 552. https://doi.org/10.1086/173102

Osterbrock, D. E., & Miller, J. S. (1975). The Optical Emission-Line Spectrum of Cygnus a. *ApJ*, *197*, 535–544. https://doi.org/10.1086/153541

Östlin, G., Marquart, T., Cumming, R. J., Fathi, K., Bergvall, N., Adamo, A., Amram, P., & Hayes, M. (2015). Kinematics of Haro 11: The miniature Antennae. *A&A*, *583*, Article A55, A55. https://doi.org/10.1051/0004-6361/201323233

Östlin, G., Rivera-Thorsen, T. E., Menacho, V., Hayes, M., Runnholm, A., Micheva, G., Oey, M. S., ... Smith, L. (2021). The Source of Leaking Ionizing Photons from Haro11: Clues from HST/COS Spectroscopy of Knots A, B, and C. *ApJ*, *912*(2), Article 155, 155. https://doi.org/10.3847/1538-4357/abf1e8

Owen, R. A., & Warwick, R. S. (2009). X-ray emission from the extended discs of spiral galaxies. *MNRAS*, *394*(4), 1741–1757. https://doi.org/10.1111/j.1365-2966.2009.14464.x

Padovani, P., Alexander, D. M., Assef, R. J., De Marco, B., Giommi, P., Hickox, R. C., Richards, G. T., ... Salvato, M. (2017). Active galactic nuclei: what's in a name? *A&A Rev.*, *25*(1), Article 2, 2. https://doi.org/10.1007/s00159-017-0102-9

Page, M. J., Stevens, J. A., Ivison, R. J., & Carrera, F. J. (2004). The Evolutionary Sequence of Active Galactic Nuclei and Galaxy Formation Revealed. *ApJ*, *611*(2), L85–L88. https://doi.org/10.1086/423892

Pagel, B. E. J., & Edmunds, M. G. (1981). Abundances in stellar populations and the interstellar medium in galaxies. *ARA&A*, *19*, 77–113. https://doi.org/10.1146/annurev.aa.19.090181.000453

Pagel, B. E. J., Edmunds, M. G., Blackwell, D. E., Chun, M. S., & Smith, G. (1979). On the composition of H II regions in southern galaxies - I. NGC 300 and 1365. *MNRAS*, *189*, 95–113. https://doi.org/10.1093/mnras/189.1.95

Pagel, B. E. J., & Patchett, B. E. (1975). Metal abundances in nearby stars and the chemical history of the solar neighbourhood. *MNRAS*, *172*, 13–40. https://doi.org/10.1093/mnras/172.1.13

Pannella, M., Carilli, C. L., Daddi, E., McCracken, H. J., Owen, F. N., Renzini, A., Strazzullo, V., ... Willott, C. J. (2009). Star Formation and Dust Obscuration at $z \approx 2$: Galaxies at the Dawn of Downsizing. *ApJ*, *698*(2), L116–L120. https://doi.org/10.1088/0004-637X/698/2/L116

Parkash, V., Brown, M. J. I., Jarrett, T. H., & Bonne, N. J. (2018). Relationships between HI Gas Mass, Stellar Mass, and the Star Formation Rate of HICAT+WISE (H I-WISE) Galaxies. *ApJ*, *864*(1), Article 40, 40. https://doi.org/10.3847/1538-4357/aad3b9

Pastoriza, M. G. (1979). Photographic photometry and the optical spectrum of the Seyfert galaxy IC 4329 A. *ApJ*, *234*, 837–841. https://doi.org/10.1086/157564

Peimbert, A., & Peimbert, M. (2010). On the O/H, Mg/H, Si/H, and Fe/H Gas and Dust Abundance Ratios in Galactic and Extragalactic H II Regions. *ApJ*, *724*(1), 791–798. https://doi.org/10.1088/0004-637X/724/1/791

Peimbert, M., & Costero, R. (1969). Chemical Abundances in Galactic HII Regions. *Boletin de los Observatorios Tonantzintla y Tacubaya*, *5*, 3–22.

Peimbert, M., Torres-Peimbert, S., & Rayo, J. F. (1978). Abundance gradients in the Galaxy derived from H II regions. *ApJ*, *220*, 516–524. https://doi.org/10.1086/155933

Peimbert, M. (1967). Temperature Determinations of H II Regions. *ApJ*, *150*, 825. https://doi.org/10.1086/149385

Peimbert, M., Luridiana, V., & Peimbert, A. (2007). Revised Primordial Helium Abundance Based on New Atomic Data. *ApJ*, *666*(2), 636–646. https://doi.org/10.1086/520571

Peimbert, M., Peimbert, A., & Delgado-Inglada, G. (2017). Nebular Spectroscopy: A Guide on Hii Regions and Planetary Nebulae. *PASP*, *129*(978), 082001. https://doi.org/10.1088/1538-3873/aa72c3

Peimbert, M., Peimbert, A., Ruiz, M. T., & Esteban, C. (2004). Physical Conditions of the Planetary Nebula NGC 5315 Derived from VLT Echelle Observations and the t^2 Problem. *ApJS*, *150*(2), 431–454. https://doi.org/10.1086/381090

Peluso, G., Radovich, M., Moretti, A., Mingozzi, M., Vulcani, B., Poggianti, B. M., Marasco, A., & Gullieuszik, M. (2023). Gas-phase Metallicity of Local Active Galactic Nuclei in the GASP and MaNGA Surveys: The Role of Ram Pressure Stripping. *ApJ*, *958*(2), Article 147, 147. https://doi.org/10.3847/1538-4357/acf833

Peng, B., Lamarche, C., Stacey, G. J., Nikola, T., Vishwas, A., Ferkinhoff, C., Rooney, C., ... Higdon, S. J. U. (2021). Far-Infrared Line Diagnostics: Improving N/O Abundance Estimates for Dusty Galaxies. *ApJ*, *908*(2), Article 166, 166. https://doi.org/10.3847/1538-4357/abd4e2

Peng, Y.-j., & Maiolino, R. (2014). The dependence of the galaxy mass-metallicity relation on environment and the implied metallicity of the IGM. *MNRAS*, *438*(1), 262–270. https://doi.org/10.1093/mnras/stt2175

Pequignot, D., Petitjean, P., & Boisson, C. (1991). Total and effective radiative recombination coefficients. *A&A*, *251*, 680–688.

Péquignot, D., Aldrovandi, S. M. V., & Stasińska, G. (1978). Charge transfer reactions: a consistent model of the planetary nebula NGC 7027. *A&A*, *63*, 313–324.

Pereira, D. S., Ferraz, J., Lobo, F. S. N., & Mimoso, J. P. (2023). Baryogenesis: A symmetry breaking in the primordial universe revisited. *Symmetry*, *16*(1), 13. https://doi.org/10.3390/sym16010013

Pereira-Santaella, M., Colina, L., García-Burillo, S., Combes, F., Emonts, B., Aalto, S., Alonso-Herrero, A., ... van der Werf, P. (2018). Spatially resolved cold molecular outflows in ULIRGs. *A&A*, *616*, Article A171, A171. https://doi.org/10.1051/0004-6361/201833089

Pereira-Santaella, M., Rigopoulou, D., Farrah, D., Lebouteiller, V., & Li, J. (2017). Far-infrared metallicity diagnostics: application to local ultraluminous infrared galaxies. *MNRAS*, *470*(1), 1218–1232. https://doi.org/10.1093/mnras/stx1284

Perez, J., Michel-Dansac, L., & Tissera, P. B. (2011). Chemical evolution during gas-rich galaxy interactions. *MNRAS*, *417*(1), 580–590. https://doi.org/10.1111/j.1365-2966.2011.19300.x

Pérez-Díaz, B., Masegosa, J., Márquez, I., & Pérez-Montero, E. (2021). Chemical abundances in the nuclear region of nearby galaxies from the Palomar Survey. *MNRAS*, *505*(3), 4289–4309. https://doi.org/10.1093/mnras/stab1522

Pérez-Díaz, B., Pérez-Montero, E., Fernández-Ontiveros, J. A., & Vílchez, J. M. (2022). Measuring chemical abundances in AGN from infrared nebular lines: HII-CHI-MISTRY-IR for AGN. *A&A*, *666*, Article A115, A115. https://doi.org/10.1051/0004-6361/202243602

Pérez-Díaz, B., Pérez-Montero, E., Fernández-Ontiveros, J. A., Vílchez, J. M., & Amorín, R. (2024a). A departure from the mass-metallicity relation in merging galaxies due to an infall of metal-poor gas. *Nature Astronomy*, *8*, 368–376. https://doi.org/10.1038/s41550-023-02171-x

Pérez-Díaz, B., Pérez-Montero, E., Fernández-Ontiveros, J. A., Vílchez, J. M., Hernán-Caballero, A., & Amorín, R. (2024b). Chemical abundances and deviations from the solar S/O ratio in the gas-phase interstellar medium of galaxies based on infrared emission lines. *A&A*, *685*, Article A168, A168. https://doi.org/10.1051/0004-6361/202348318

Pérez-Díaz, B., Pérez-Montero, E., Zinchenko, I. A., & Vílchez, J. M. (2025). Chemical enrichment in LINERs from MaNGA: I. Tracing the nuclear abundances of oxygen and nitrogen in LINERs with varied ionizing sources. *A&A*, *694*, Article A18, A18. https://doi.org/10.1051/0004-6361/202452862

Pérez-Montero, E. (2014). Deriving model-based T_e-consistent chemical abundances in ionized gaseous nebulae. *MNRAS*, *441*(3), 2663–2675. https://doi.org/10.1093/mnras/stu753

Pérez-Montero, E. (2017). Ionized Gaseous Nebulae Abundance Determination from the Direct Method. *PASP*, *129*(974), 043001. https://doi.org/10.1088/1538-3873/aa5abb

Pérez-Montero, E., & Amorín, R. (2017). Using photo-ionisation models to derive carbon and oxygen gas-phase abundances in the rest UV. *MNRAS*, *467*(2), 1287–1293. https://doi.org/10.1093/mnras/stx186

Pérez-Montero, E., Amorín, R., Pérez-Díaz, B., Vílchez, J. M., & García-Benito, R. (2023a). Assessing model-based carbon and oxygen abundance derivation from ultraviolet emission lines in AGNs. *MNRAS*, *521*(1), 1556–1569. https://doi.org/10.1093/mnras/stad621

Pérez-Montero, E., Amorín, R., Sánchez Almeida, J., Vílchez, J. M., García-Benito, R., & Kehrig, C. (2021). Extreme emission-line galaxies in SDSS - I. Empirical and model-based calibrations of chemical abundances. *MNRAS*, *504*(1), 1237–1252. https://doi.org/10.1093/mnras/stab862

Pérez-Montero, E., & Contini, T. (2009). The impact of the nitrogen-to-oxygen ratio on ionized nebula diagnostics based on [NII] emission lines. *MNRAS*, *398*(2), 949–960. https://doi.org/10.1111/j.1365-2966.2009.15145.x

Pérez-Montero, E., Contini, T., Lamareille, F., Maier, C., Carollo, C. M., Kneib, J. .-., Le Fèvre, O., ... Zucca, E. (2013). The cosmic evolution of oxygen and nitrogen abundances in star-forming galaxies over the past 10 Gyr. *A&A*, *549*, Article A25, A25. https://doi.org/10.1051/0004-6361/201220070

Pérez-Montero, E., & Díaz, Á. I. (2007). The nature of the Wolf-Rayet galaxy Mrk 209 from photoionization models. *MNRAS*, *377*(3), 1195–1205. https://doi.org/10.1111/j.1365-2966.2007.11670.x

Pérez-Montero, E., & Díaz, A. I. (2003). Line temperatures and elemental abundances in H II galaxies. *MNRAS*, *346*(1), 105–118. https://doi.org/10.1046/j.1365-2966.2003.07064.x

Pérez-Montero, E., & Díaz, A. I. (2005). A comparative analysis of empirical calibrators for nebular metallicity. *MNRAS*, *361*(3), 1063–1076. https://doi.org/10.1111/j.1365-2966.2005.09263.x

Pérez-Montero, E., Díaz, A. I., Vílchez, J. M., & Kehrig, C. (2006). An empirical calibration of sulphur abundance in ionised gaseous nebulae. *A&A*, *449*(1), 193–201. https://doi.org/10.1051/0004-6361:20054216

Pérez-Montero, E., Dors, O. L., Vílchez, J. M., García-Benito, R., Cardaci, M. V., & Hägele, G. F. (2019a). A bayesian-like approach to derive chemical abundances in type-2 active galactic nuclei based on photoionization models. *MNRAS*, *489*(2), 2652–2668. https://doi.org/10.1093/mnras/stz2278

Pérez-Montero, E., Fernández-Ontiveros, J. A., Pérez-Díaz, B., Vílchez, J. M., & Amorín, R. (2025). Exploring the hardness of the ionizing radiation with the infrared softness diagram: II. Bimodal distributions in both the ionizing continuum slope and the excitation in active galactic nuclei. *A&A*, *696*, Article A229, A229. https://doi.org/10.1051/0004-6361/202453276

Pérez-Montero, E., Fernández-Ontiveros, J. A., Pérez-Díaz, B., Vílchez, J. M., Kumari, N., & Amorín, R. (2024). Exploring the hardness of the ionising radiation with the infrared softness diagram. I. Similar effective temperature scales for starbursts and (ultra)luminous infrared galaxies. *A&A*, *684*, Article A40, A40. https://doi.org/10.1051/0004-6361/202348089

Pérez-Montero, E., García-Benito, R., Hägele, G. F., & Díaz, Á. I. (2010). Disentangling the metallicity and star formation history of HII galaxies through tailor-made models. *MNRAS*, *404*(4), 2037–2055. https://doi.org/10.1111/j.1365-2966.2010.16421.x

Pérez-Montero, E., García-Benito, R., & Vílchez, J. M. (2019b). Revisiting the hardening of the stellar ionizing radiation in galaxy discs. *MNRAS*, *483*(3), 3322–3335. https://doi.org/10.1093/mnras/sty3330

Pérez-Montero, E., García-Benito, R., Vílchez, J. M., Sánchez, S. F., Kehrig, C., Husemann, B., Duarte Puertas, S., ... CALIFA Collaboration. (2016). The dependence of oxygen and nitrogen abundances on stellar mass from the CALIFA survey. *A&A*, *595*, Article A62, A62. https://doi.org/10.1051/0004-6361/201628601

Pérez-Montero, E., Kehrig, C., Vílchez, J. M., García-Benito, R., Duarte Puertas, S., & Iglesias-Páramo, J. (2020). Photon leaking or very hard ionizing radiation? Unveiling the nature of He II-emitters using the softness diagram. *A&A*, *643*, Article A80, A80. https://doi.org/10.1051/0004-6361/202038509

Pérez-Montero, E., & Vílchez, J. M. (2009). On the hardening of the ionizing radiation in HII regions across galactic discs through softness parameters. *MNRAS*, *400*(4), 1721–1725. https://doi.org/10.1111/j.1365-2966.2009.15590.x

Pérez-Montero, E., Vílchez, J. M., Cedrés, B., Hägele, G. F., Mollá, M., Kehrig, C., Díaz, A. I., ... Martín-Gordón, D. (2011). Integral field spectroscopy of nitrogen overabundant blue compact dwarf galaxies. *A&A*, *532*, Article A141, A141. https://doi.org/10.1051/0004-6361/201116582

Pérez-Montero, E., Zinchenko, I. A., Vílchez, J. M., Zurita, A., Florido, E., & Pérez-Díaz, B. (2023b). The softness diagram for MaNGA star-forming regions: diffuse ionized gas contamination or local HOLMES predominance? *A&A*, *669*, Article A88, A88. https://doi.org/10.1051/0004-6361/202244591

Pérez-Torres, M., Mattila, S., Alonso-Herrero, A., Aalto, S., & Efstathiou, A. (2021). Star formation and nuclear activity in luminous infrared galaxies: an infrared through radio review. *A&A Rev.*, *29*(1), Article 2, 2. https://doi.org/10.1007/s00159-020-00128-x

Peterson, B. M. (2006). The Broad-Line Region in Active Galactic Nuclei. In D. Alloin (Ed.), *Physics of active galactic nuclei at all scales* (p. 77, Vol. 693). https://doi.org/10.1007/3-540-34621-X_3

Peterson, B. M., Denney, K. D., De Rosa, G., Grier, C. J., Pogge, R. W., Bentz, M. C., Kochanek, C. S., ... Ciroi, S. (2013). The Size of the Narrow-line-emitting Region in the Seyfert 1 Galaxy NGC 5548 from Emission-line Variability. *ApJ*, *779*(2), Article 109, 109. https://doi.org/10.1088/0004-637X/779/2/109

Petropoulou, V., Vílchez, J., & Iglesias-Páramo, J. (2012). Environmental Effects on the Metal Enrichment of Low-mass Galaxies in Nearby Clusters. *ApJ*, *749*(2), Article 133, 133. https://doi.org/10.1088/0004-637X/749/2/133

Petropoulou, V., Vílchez, J., Iglesias-Páramo, J., Papaderos, P., Magrini, L., Cedrés, B., & Reverte, D. (2011). Spatially Resolved Spectroscopy and Chemical History of Star-forming Galaxies in the Hercules Cluster: The Effects of the Environment. *ApJ*, *734*(1), Article 32, 32. https://doi.org/10.1088/0004-637X/734/1/32

Phillips, M. M. (1978). Permitted fe II Emission in Seyfert 1 Galaxies and QSOs I. Observations. *ApJS*, *38*, 187. https://doi.org/10.1086/190553

Phillips, M. M., Charles, P. A., & Baldwin, J. A. (1983). Nearby galaxies with Seyfert-like nuclei. *ApJ*, *266*, 485–501. https://doi.org/10.1086/160797

Pilbratt, G. L., Riedinger, J. R., Passvogel, T., Crone, G., Doyle, D., Gageur, U., Heras, A. M., ... Schmidt, M. (2010). Herschel Space Observatory. An ESA facility for far-infrared and submillimetre astronomy. *A&A*, *518*, Article L1, L1. https://doi.org/10.1051/0004-6361/201014759

Pilyugin, L. S., & Grebel, E. K. (2016). New calibrations for abundance determinations in H II regions. *MNRAS*, *457*(4), 3678–3692. https://doi.org/10.1093/mnras/stw238

Pilyugin, L. S., & Tautvaišienė, G. (2024). Two sequences of spiral galaxies with different shapes of the metallicity gradients. *A&A*, *682*, Article A41, A41. https://doi.org/10.1051/0004-6361/202347032

Pilyugin, L. S., Vílchez, J. M., & Contini, T. (2004). Oxygen and nitrogen abundances in nearby galaxies. Correlations between oxygen abundance and macroscopic properties. *A&A*, *425*, 849–869. https://doi.org/10.1051/0004-6361:20034522

Pilyugin, L. S., Thuan, T. X., & Vílchez, J. M. (2006). Oxygen abundances in the most oxygen-rich spiral galaxies. *MNRAS*, *367*(3), 1139–1146. https://doi.org/10.1111/j.1365-2966.2006.10033.x

Pilyugin, L. S., Thuan, T. X., & Vílchez, J. M. (2007). On the maximum value of the cosmic abundance of oxygen and the oxygen yield. *MNRAS*, *376*(1), 353–360. https://doi.org/10.1111/j.1365-2966.2007.11444.x

Piqueras López, J., Colina, L., Arribas, S., Alonso-Herrero, A., & Bedregal, A. G. (2012). VLT-SINFONI integral field spectroscopy of low-z luminous and ultraluminous infrared galaxies. I. Atlas of the 2D gas structure. *A&A*, *546*, Article A64, A64. https://doi.org/10.1051/0004-6361/201219372

Planck Collaboration, Aghanim, N., Akrami, Y., Ashdown, M., Aumont, J., Baccigalupi, C., Ballardini, M., ... Zonca, A. (2020). Planck 2018 results. VI. Cosmological parameters. *A&A*, *641*, Article A6, A6. https://doi.org/10.1051/0004-6361/201833910

Poetrodjojo, H., Groves, B., Kewley, L. J., Medling, A. M., Sweet, S. M., van de Sande, J., Sanchez, S. F., ... Scott, N. (2018). The SAMI Galaxy Survey: Spatially resolved metallicity and ionization mapping. *MNRAS*, *479*(4), 5235–5265. https://doi.org/10.1093/mnras/sty1782

Poggianti, B. M., & Barbaro, G. (1997). Indicators of star formation: 4000 Å break and Balmer lines. *A&A*, *325*, 1025–1030. https://doi.org/10.48550/arXiv.astro-ph/9703067

Poglitsch, A., Waelkens, C., Geis, N., Feuchtgruber, H., Vandenbussche, B., Rodriguez, L., Krause, O., ... Wiezorrek, E. (2010). The Photodetector Array Camera and Spectrometer (PACS) on the Herschel Space Observatory. *A&A*, *518*, Article L2, L2. https://doi.org/10.1051/0004-6361/201014535

Pović, M., Márquez, I., Netzer, H., Masegosa, J., Nordon, R., Pérez, E., & Schoenell, W. (2016). Star formation and AGN activity in the most luminous LINERs in the local universe. *MNRAS*, *462*(3), 2878–2903. https://doi.org/10.1093/mnras/stw1842

Priestley, F. D., De Looze, I., & Barlow, M. J. (2022). The impact of metallicity-dependent dust destruction on the dust-to-metals ratio in galaxies. *MNRAS*, *509*(1), L6–L10. https://doi.org/10.1093/mnrasl/slab114

Przybilla, N., Firnstein, M., Nieva, M. F., Meynet, G., & Maeder, A. (2010). Mixing of CNO-cycled matter in massive stars. *A&A*, *517*, Article A38, A38. https://doi.org/10.1051/0004-6361/201014164

Przybilla, N., Nieva, M.-F., & Butler, K. (2008). A Cosmic Abundance Standard: Chemical Homogeneity of the Solar Neighborhood and the ISM Dust-Phase Composition. *ApJ*, *688*(2), L103. https://doi.org/10.1086/595618

Puget, J. L., & Leger, A. (1989). A new component of the interstellar matter: small grains and large aromatic molecules. *ARA&A*, *27*, 161–198. https://doi.org/10.1146/annurev.aa.27.090189.001113

Querejeta, M., Meidt, S. E., Schinnerer, E., Cisternas, M., Muñoz-Mateos, J. C., Sheth, K., Knapen, J., ... Comerón, S. (2015). The Spitzer Survey of Stellar Structure in Galaxies (S^4G): Precise

Stellar Mass Distributions from Automated Dust Correction at 3.6 μm. *ApJS*, *219*(1), Article 5, 5. https://doi.org/10.1088/0067-0049/219/1/5

Rauch, T. (2003). A grid of synthetic ionizing spectra for very hot compact stars from NLTE model atmospheres. *A&A*, *403*, 709–714. https://doi.org/10.1051/0004-6361:20030412

Rauscher, T., Heger, A., Hoffman, R. D., & Woosley, S. E. (2002). Nucleosynthesis in Massive Stars with Improved Nuclear and Stellar Physics. *ApJ*, *576*(1), 323–348. https://doi.org/10.1086/341728

Rayner, J., Tokunaga, A., Jaffe, D., Bonnet, M., Ching, G., Connelley, M., Kokubun, D., ... Warmbier, E. (2016, August). iSHELL: a construction, assembly and testing. In C. J. Evans, L. Simard, & H. Takami (Eds.), *Ground-based and airborne instrumentation for astronomy vi* (p. 990884, Vol. 9908). https://doi.org/10.1117/12.2232064

Rayo, J. F., Peimbert, M., & Torres-Peimbert, S. (1982). Gradient in the physical conditions of M 101 and the pregalactic helium abundance. *ApJ*, *255*, 1–10. https://doi.org/10.1086/159796

Reifarth, R., Lederer, C., & Käppeler, F. (2014). Neutron reactions in astrophysics. *Journal of Physics G Nuclear Physics*, *41*(5), Article 053101, 053101. https://doi.org/10.1088/0954-3899/41/5/053101

Reis, R. C., & Miller, J. M. (2013). On the Size and Location of the X-Ray Emitting Coronae around Black Holes. *ApJ*, *769*(1), Article L7, L7. https://doi.org/10.1088/2041-8205/769/1/L7

Relaño, M., De Looze, I., Saintonge, A., Hou, K. .-., Romano, L. E. C., Nagamine, K., Hirashita, H., ... van der Giessen, S. A. (2022). Dust grain size evolution in local galaxies: a comparison between observations and simulations. *MNRAS*, *515*(4), 5306–5334. https://doi.org/10.1093/mnras/stac2108

Relaño, M., Kennicutt, R., Lisenfeld, U., Verley, S., Hermelo, I., Boquien, M., Albrecht, M., ... Staguhn, J. (2016). Dust properties in H II regions in M 33. *A&A*, *595*, Article A43, A43. https://doi.org/10.1051/0004-6361/201628139

Relaño, M., Lisenfeld, U., Hou, K. .-., De Looze, I., Vílchez, J. M., & Kennicutt, R. C. (2020). Evolution of grain size distribution in galactic discs. *A&A*, *636*, Article A18, A18. https://doi.org/10.1051/0004-6361/201937087

Renaud, F., Bournaud, F., Kraljic, K., & Duc, P. .-. (2014). Starbursts triggered by intergalactic tides andinterstellar compressive turbulence. *MNRAS*, *442*, L33–L37. https://doi.org/10.1093/mnrasl/slu050

Renzini, A., & Buzzoni, A. (1986, January). Global properties of stellar populations and the spectral evolution of galaxies. In C. Chiosi & A. Renzini (Eds.), *Spectral evolution of galaxies* (pp. 195–231, Vol. 122). https://doi.org/10.1007/978-94-009-4598-2_19

Reunanen, J., Kotilainen, J. K., & Prieto, M. A. (2002). Near-infrared spectroscopy of nearby Seyfert galaxies - I. First results. *MNRAS*, *331*(1), 154–168. https://doi.org/10.1046/j.1365-8711.2002.05181.x

Reunanen, J., Kotilainen, J. K., & Prieto, M. A. (2003). Near-infrared spectroscopy of nearby Seyfert galaxies - II. Molecular content and coronal emission. *MNRAS*, *343*(1), 192–208. https://doi.org/10.1046/j.1365-8711.2003.06771.x

Reynolds, R. J. (1985). S II lambda 6716 in the galactic emission-line background. *ApJ*, *294*, 256–262. https://doi.org/10.1086/163294

Rich, J. A., Kewley, L. J., & Dopita, M. A. (2015). Galaxy Mergers Drive Shocks: An Integral Field Study of GOALS Galaxies. *ApJS*, *221*(2), Article 28, 28. https://doi.org/10.1088/0067-0049/221/2/28

Rich, J. A., Torrey, P., Kewley, L. J., Dopita, M. A., & Rupke, D. S. N. (2012). An Integral Field Study of Abundance Gradients in nearby Luminous Infrared Galaxies. *ApJ*, *753*(1), Article 5, 5. https://doi.org/10.1088/0004-637X/753/1/5

Richardson, C. T., Simpson, C., Polimera, M. S., Kannappan, S. J., Bellovary, J. M., Greene, C., & Jenkins, S. (2022). Optical and JWST Mid-IR Emission Line Diagnostics for Simultaneous IMBH and Stellar Excitation in z 0 Dwarf Galaxies. *ApJ*, *927*(2), Article 165, 165. https://doi.org/10.3847/1538-4357/ac510c

Richter, M. J., Dewitt, C. N., McKelvey, M., Montiel, E., McMurray, R., & Case, M. E. (2018). EXES: The Echelon-cross-echelle Spectrograph for SOFIA. *Journal of Astronomical Instrumentation*, *7*(4), Article 1840013, 1840013. https://doi.org/10.1142/S2251171718400135

Rieke, G. H., & Lebofsky, M. J. (1979). Infrared emission of extragalactic sources. *ARA&A*, *17*, 477–511. https://doi.org/10.1146/annurev.aa.17.090179.002401

Rieke, G. H., Wright, G. S., Böker, T., Bouwman, J., Colina, L., Glasse, A., Gordon, K. D., ... Waelkens, C. (2015). The Mid-Infrared Instrument for the James Webb Space Telescope, I: Introduction. *PASP*, *127*(953), 584. https://doi.org/10.1086/682252

Rieke, M. J., Kelly, D. M., Misselt, K., Stansberry, J., Boyer, M., Beatty, T., Egami, E., ... Young, E. T. (2023). Performance of NIRCam on JWST in Flight. *PASP*, *135*(1044), Article 028001, 028001. https://doi.org/10.1088/1538-3873/acac53

Riemer-Sørensen, S., Kotuš, S., Webb, J. K., Ali, K., Dumont, V., Murphy, M. T., & Carswell, R. F. (2017). A precise deuterium abundance: remeasurement of the z = 3.572 absorption system towards the quasar PKS1937-101. *MNRAS*, *468*(3), 3239–3250. https://doi.org/10.1093/mnras/stx681

Riffel, R., Rodríguez-Ardila, A., & Pastoriza, M. G. (2006). A 0.8-2.4 μm spectral atlas of active galactic nuclei. *A&A*, *457*(1), 61–70. https://doi.org/10.1051/0004-6361:20065291

Rigby, J. R., Diamond-Stanic, A. M., & Aniano, G. (2009). Calibration Of [O IV] 26 μm as a Measure of Intrinsic Active Galactic Nucleus Luminosity. *ApJ*, *700*(2), 1878–1883. https://doi.org/10.1088/0004-637X/700/2/1878

Rigopoulou, D., Pereira-Santaella, M., Magdis, G. E., Cooray, A., Farrah, D., Marques-Chaves, R., Perez-Fournon, I., & Riechers, D. (2018). On the far-infrared metallicity diagnostics: applications to high-redshift galaxies. *MNRAS*, *473*(1), 20–29. https://doi.org/10.1093/mnras/stx2311

Risacher, C., Güsten, R., Stutzki, J., Hübers, H. .-., Aladro, R., Bell, A., Buchbender, C., ... Wohler, B. (2018). The upGREAT Dual Frequency Heterodyne Arrays for SOFIA. *Journal of Astronomical Instrumentation*, *7*(4), Article 1840014, 1840014. https://doi.org/10.1142/S2251171718400147

Romano, D. (2022). The evolution of CNO elements in galaxies. *A&A Rev.*, *30*(1), Article 7, 7. https://doi.org/10.1007/s00159-022-00144-z

Ross, J. E., & Aller, L. H. (1976). The Chemical Composition of the Sun. *Science*, *191*(4233), 1223–1229. https://doi.org/10.1126/science.191.4233.1223

Rowntree, A. R., Vincenzo, F., Singh, A., Park, C., Lee, J., Pichon, C., Dubois, Y., ... Kim, Y. (2025). The Role of Large-Scale Environment in Shaping the Stellar Mass-Gas Metallicity Relation Across Time. *arXiv e-prints*, Article arXiv:2503.12928, arXiv:2503.12928. https://doi.org/10.48550/arXiv.2503.12928

Rubin, R. H. (1989). The Effect of Density Variations on Elemental Abundance Ratios in Gaseous Nebulae. *ApJS*, *69*, 897. https://doi.org/10.1086/191330

Rupke, D. S. N., Kewley, L. J., & Barnes, J. E. (2010). Galaxy Mergers and the Mass-Metallicity Relation: Evidence for Nuclear Metal Dilution and Flattened Gradients from Numerical Simulations. *ApJ*, *710*(2), L156–L160. https://doi.org/10.1088/2041-8205/710/2/L156

Rupke, D. S. N., Veilleux, S., & Baker, A. J. (2008). The Oxygen Abundances of Luminous and Ultraluminous Infrared Galaxies. *ApJ*, *674*(1), 172–193. https://doi.org/10.1086/522363

Ryder, S. D. (1995). The Local Metallicity–Surface Brightness Relationship in Galactic Disks. *ApJ*, *444*, 610. https://doi.org/10.1086/175634

Ryzhov, O., Michałowski, M. J., Nadolny, J., Hjorth, J., Leśniewska, A., Solar, M., Nowaczyk, P., … Takeuchi, T. T. (2025). The Fate of the Interstellar Medium in Early-type Galaxies. V. Active Galactic Nucleus Feedback from Optical Spectral Classification. *ApJS*, *276*(2), Article 55, 55. https://doi.org/10.3847/1538-4365/ad93cd

Saikia, G., Gogoi, R., Gupta, R., & Vaidya, D. B. (2019). Modelling the mid-infrared polarization in dust around young stars. *MNRAS*, *484*(3), 3582–3589. https://doi.org/10.1093/mnras/stz231

Saintonge, A., Catinella, B., Tacconi, L. J., Kauffmann, G., Genzel, R., Cortese, L., Davé, R., … Roberts-Borsani, G. W. (2017). xCOLD GASS: The Complete IRAM 30 m Legacy Survey of Molecular Gas for Galaxy Evolution Studies. *ApJS*, *233*(2), Article 22, 22. https://doi.org/10.3847/1538-4365/aa97e0

Salpeter, E. E. (1955). The Luminosity Function and Stellar Evolution. *ApJ*, *121*, 161. https://doi.org/10.1086/145971

Sánchez, S. F., Rosales-Ortega, F. F., Iglesias-Páramo, J., Mollá, M., Barrera-Ballesteros, J., Marino, R. A., Pérez, E., … López-Sánchez, Á. R. (2014). A characteristic oxygen abundance gradient in galaxy disks unveiled with CALIFA. *A&A*, *563*, Article A49, A49. https://doi.org/10.1051/0004-6361/201322343

Sánchez, S. F., Rosales-Ortega, F. F., Jungwiert, B., Iglesias-Páramo, J., Vílchez, J. M., Marino, R. A., Walcher, C. J., … CALIFA Collaboration. (2013). Mass-metallicity relation explored with CALIFA. I. Is there a dependence on the star-formation rate? *A&A*, *554*, Article A58, A58. https://doi.org/10.1051/0004-6361/201220669

Sánchez Almeida, J., Elmegreen, B. G., Muñoz-Tuñón, C., Elmegreen, D. M., Pérez-Montero, E., Amorín, R., Filho, M. E., … Vílchez, J. M. (2015). Localized Starbursts in Dwarf Galaxies Produced by the Impact of Low-metallicity Cosmic Gas Clouds. *ApJ*, *810*(2), Article L15, L15. https://doi.org/10.1088/2041-8205/810/2/L15

Sánchez-Blázquez, P., Courty, S., Gibson, B. K., & Brook, C. B. (2009). The origin of the light distribution in spiral galaxies. *MNRAS*, *398*(2), 591–606. https://doi.org/10.1111/j.1365-2966.2009.15133.x

Sánchez-Menguiano, L., Sánchez, S. F., Pérez, I., García-Benito, R., Husemann, B., Mast, D., Mendoza, A., … CALIFA Collaboration. (2016). Shape of the oxygen abundance profiles in CALIFA face-on spiral galaxies. *A&A*, *587*, Article A70, A70. https://doi.org/10.1051/0004-6361/201527450

Sánchez-Menguiano, L., Sánchez, S. F., Pérez, I., Ruiz-Lara, T., Galbany, L., Anderson, J. P., Krühler, T., … Lyman, J. D. (2018). The shape of oxygen abundance profiles explored with MUSE: evidence for widespread deviations from single gradients. *A&A*, *609*, Article A119, A119. https://doi.org/10.1051/0004-6361/201731486

Sánchez-Menguiano, L., Sánchez, S. F., Sánchez Almeida, J., & Muñoz-Tuñón, C. (2024a). More fundamental than the fundamental metallicity relation. The effect of the stellar metallicity on the gas-phase mass-metallicity and gravitational potential-metallicity relations. *A&A*, *682*, Article L11, L11. https://doi.org/10.1051/0004-6361/202348423

Sánchez-Menguiano, L., Sánchez Almeida, J., Sánchez, S. F., & Muñoz-Tuñón, C. (2024b). Stellar mass is not the best predictor of galaxy metallicity. The gravitational potential-metallicity relation ΦZR. *A&A*, *681*, Article A121, A121. https://doi.org/10.1051/0004-6361/202346708

Sanders, R. L., Shapley, A. E., Jones, T., Reddy, N. A., Kriek, M., Siana, B., Coil, A. L., … Barro, G. (2021). The MOSDEF Survey: The Evolution of the Mass-Metallicity Relation from z = 0 to z 3.3. *ApJ*, *914*(1), Article 19, 19. https://doi.org/10.3847/1538-4357/abf4c1

Schaefer, A. L., Tremonti, C., Kauffmann, G., Andrews, B. H., Bershady, M. A., Boardman, N. F., Bundy, K., … Sánchez, S. F. (2022). SDSS-IV MaNGA: Exploring the Local Scaling Relations for N/O. *ApJ*, *930*(2), Article 160, 160. https://doi.org/10.3847/1538-4357/ac651a

Schaeidt, S. G., Morris, P. W., Salama, A., Vandenbussche, B., Beintema, D. A., Boxhoorn, D. R., Feuchtgruber, H., … Zaal, P. (1996). The photometric calibration of the ISO Short Wavelength Spectrometer. *A&A*, *315*, L55–L59.

Schaerer, D., Ginolfi, M., Béthermin, M., Fudamoto, Y., Oesch, P. A., Le Fèvre, O., Faisst, A., … Zucca, E. (2020). The ALPINE-ALMA [C II] survey. Little to no evolution in the [C II]-SFR relation over the last 13 Gyr. *A&A*, *643*, Article A3, A3. https://doi.org/10.1051/0004-6361/202037617

Schaerer, D., Marques-Chaves, R., Xiao, M., & Korber, D. (2024). Discovery of a new N-emitter in the epoch of reionization. *A&A*, *687*, Article L11, L11. https://doi.org/10.1051/0004-6361/202450721

Schaye, J., Crain, R. A., Bower, R. G., Furlong, M., Schaller, M., Theuns, T., Dalla Vecchia, C., … Trayford, J. (2015). The EAGLE project: simulating the evolution and assembly of galaxies and their environments. *MNRAS*, *446*(1), 521–554. https://doi.org/10.1093/mnras/stu2058

Schmidt, M. (1963). 3C 273 : A Star-Like Object with Large Red-Shift. *Nature*, *197*(4872), 1040. https://doi.org/10.1038/1971040a0

Schneider, N., Bontemps, S., Simon, R., Ossenkopf, V., Federrath, C., Klessen, R. S., Motte, F., … Brunt, C. (2011). The link between molecular cloud structure and turbulence. *A&A*, *529*, Article A1, A1. https://doi.org/10.1051/0004-6361/200913884

Schruba, A., Leroy, A. K., Walter, F., Bigiel, F., Brinks, E., de Blok, W. J. G., Kramer, C., … Wiesemeyer, H. (2012). Low CO Luminosities in Dwarf Galaxies. *AJ*, *143*(6), Article 138, 138. https://doi.org/10.1088/0004-6256/143/6/138

Searle, L. (1971). Evidence for Composition Gradients across the Disks of Spiral Galaxies. *ApJ*, *168*, 327. https://doi.org/10.1086/151090

Searle, L., & Sargent, W. L. W. (1972). Inferences from the Composition of Two Dwarf Blue Galaxies. *ApJ*, *173*, 25. https://doi.org/10.1086/151398

Seaton, M. J., & Osterbrock, D. E. (1957). Relative [O II] Intensities in Gaseous Nebulae. *ApJ*, *125*, 66. https://doi.org/10.1086/146282

Severgnini, P., Risaliti, G., Marconi, A., Maiolino, R., & Salvati, M. (2001). An X-ray and near-IR spectroscopic analysis of the ULIRG IRAS 05189-2524. *A&A*, *368*, 44–51. https://doi.org/10.1051/0004-6361:20000522

Shang, Z., Wills, B. J., Wills, D., & Brotherton, M. S. (2007). Spectral Properties from Lyα to Hα for an Essentially Complete Sample of Quasars. I. Data. *AJ*, *134*(1), 294–393. https://doi.org/10.1086/518505

Sharda, P., Ginzburg, O., Krumholz, M. R., Forbes, J. C., Wisnioski, E., Mingozzi, M., Zovaro, H. R. M., & Dekel, A. (2024). The interplay between feedback, accretion, transport, and winds in setting gas-phase metal distribution in galaxies. *MNRAS*, *528*(2), 2232–2256. https://doi.org/10.1093/mnras/stae088

Sharda, P., Krumholz, M. R., Wisnioski, E., Forbes, J. C., Federrath, C., & Acharyya, A. (2021). The physics of gas phase metallicity gradients in galaxies. *MNRAS*, *502*(4), 5935–5961. https://doi.org/10.1093/mnras/stab252

Shaver, P. A., McGee, R. X., Newton, L. M., Danks, A. C., & Pottasch, S. R. (1983). The galactic abundance gradient. *MNRAS*, *204*, 53–112. https://doi.org/10.1093/mnras/204.1.53

Sheth, K., Regan, M., Hinz, J. L., Gil de Paz, A., Menéndez-Delmestre, K., Muñoz-Mateos, J.-C., Seibert, M., … Aravena, M. (2010). The Spitzer Survey of Stellar Structure in Galaxies (S4G). *PASP*, *122*(898), 1397. https://doi.org/10.1086/657638

Shuder, J. M. (1980). The optical spectra of narrow-line X-ray galaxies. *ApJ*, *240*, 32–40. https://doi.org/10.1086/158204

Sillero, E., Tissera, P. B., Lambas, D. G., & Michel-Dansac, L. (2017). The evolution of the metallicity gradient and the star formation efficiency in disc galaxies. *MNRAS*, *472*(4), 4404–4413. https://doi.org/10.1093/mnras/stx2265

Simmonds, C., Tacchella, S., Hainline, K., Johnson, B. D., Puskás, D., Robertson, B., Baker, W. M., … Zhu, Y. (2024). Ionizing properties of galaxies in JADES for a stellar mass complete sample: resolving the cosmic ionizing photon budget crisis at the Epoch of Reionization. *MNRAS*, *535*(4), 2998–3019. https://doi.org/10.1093/mnras/stae2537

Simpson, C., & Meadows, V. (1998). The Nuclear Spectrum of the Radio Galaxy NGC 5128 (Centaurus A). *ApJ*, *505*(2), L99–L102. https://doi.org/10.1086/311616

Skillman, E. D., Kennicutt, R. C., & Hodge, P. W. (1989). Oxygen Abundances in Nearby Dwarf Irregular Galaxies. *ApJ*, *347*, 875. https://doi.org/10.1086/168178

Sloan, G. C., Kraemer, K. E., Price, S. D., & Shipman, R. F. (2003). A Uniform Database of 2.4-45.4 Micron Spectra from the Infrared Space Observatory Short Wavelength Spectrometer. *ApJS*, *147*(2), 379–401. https://doi.org/10.1086/375443

Smajić, S., Fischer, S., Zuther, J., & Eckart, A. (2012). Unveiling the nucleus of <ASTROBJ>NGC 7172</ASTROBJ>. *A&A*, *544*, Article A105, A105. https://doi.org/10.1051/0004-6361/201118256

Smirnova, P., Makarenko, E. I., Clarke, S. D., Glukhov, E., Walch, S., Vaezzadeh, I., & Seifried, D. (2025). How do supernova remnants cool?: II. Machine learning analysis of supernova remnant simulations. *A&A*, *693*, Article A38, A38. https://doi.org/10.1051/0004-6361/202451108

Smith, J. D. T., Draine, B. T., Dale, D. A., Moustakas, J., Kennicutt, R. C., Jr., Helou, G., Armus, L., … Walter, F. (2007). The Mid-Infrared Spectrum of Star-forming Galaxies: Global Properties of Polycyclic Aromatic Hydrocarbon Emission. *ApJ*, *656*(2), 770–791. https://doi.org/10.1086/510549

Sobral, D., Best, P. N., Matsuda, Y., Smail, I., Geach, J. E., & Cirasuolo, M. (2012). Star formation at z=1.47 from HiZELS: an H>α+[O II] double-blind study. *MNRAS*, *420*(3), 1926–1945. https://doi.org/10.1111/j.1365-2966.2011.19977.x

Somerville, R. S., & Davé, R. (2015). Physical Models of Galaxy Formation in a Cosmological Framework. *ARA&A*, *53*, 51–113. https://doi.org/10.1146/annurev-astro-082812-140951

Sparke, L. S., & Gallagher, J. S., III. (2006). *Galaxies in the Universe - 2nd Edition*. https://doi.org/10.2277/0521855934

Sparre, M., Whittingham, J., Damle, M., Hani, M. H., Richter, P., Ellison, S. L., Pfrommer, C., & Vogelsberger, M. (2022). Gas flows in galaxy mergers: supersonic turbulence in bridges, accretion from the circumgalactic medium, and metallicity dilution. *MNRAS*, *509*(2), 2720–2735. https://doi.org/10.1093/mnras/stab3171

Spindler, A., Wake, D., Belfiore, F., Bershady, M., Bundy, K., Drory, N., Masters, K., … Wild, V. (2018). SDSS-IV MaNGA: the spatial distribution of star formation and its dependence on mass, structure, and environment. *MNRAS*, *476*(1), 580–600. https://doi.org/10.1093/mnras/sty247

Spinoglio, L., Fernandez-Ontiveros, J. A., Malkan, M. A., Kumar, S., Pereira-Santaella, M., Perez-Diaz, B., Perez-Montero, E., … Fischer, C. (2021). SOFIA observations of far-IR fine-structure lines in galaxies to measure metallicity. *arXiv e-prints*, Article arXiv:2111.04434, arXiv:2111.04434.

Spinoglio, L., Fernández-Ontiveros, J. A., Malkan, M. A., Kumar, S., Pereira-Santaella, M., Pérez-Díaz, B., Pérez-Montero, E., … Fischer, C. (2022). SOFIA Observations of Far-IR Fine-structure Lines in Galaxies to Measure Metallicity. *ApJ*, *926*(1), Article 55, 55. https://doi.org/10.3847/1538-4357/ac37b7

Spitoni, E., Calura, F., Silva Aguirre, V., & Gilli, R. (2021). The G-dwarf distribution in star-forming galaxies: A tug of war between infall and outflow. *A&A*, *648*, Article L5, L5. https://doi.org/10.1051/0004-6361/202140836

Spitoni, E., Cescutti, G., Minchev, I., Matteucci, F., Silva Aguirre, V., Martig, M., Bono, G., & Chiappini, C. (2019). 2D chemical evolution model: The impact of Galactic disc asymmetries on azimuthal chemical abundance variations. *A&A*, *628*, Article A38, A38. https://doi.org/10.1051/0004-6361/201834665

Spitoni, E., Cescutti, G., Recio-Blanco, A., Minchev, I., Poggio, E., Palicio, P. A., Matteucci, F., ... Vasini, A. (2023). 2D chemical evolution models. II. Effects of multiple spiral arm patterns on O, Eu, Fe, and Ba abundance gradients. *A&A*, *680*, Article A85, A85. https://doi.org/10.1051/0004-6361/202347325

Spitoni, E., Matteucci, F., & Marcon-Uchida, M. M. (2013). Effects of the radial inflow of gas and galactic fountains on the chemical evolution of M 31. *A&A*, *551*, Article A123, A123. https://doi.org/10.1051/0004-6361/201220401

Spoon, H. W. W., Hernán-Caballero, A., Rupke, D., Waters, L. B. F. M., Lebouteiller, V., Tielens, A. G. G. M., Loredo, T., ... Viola, V. (2022). The Infrared Database of Extragalactic Observables from Spitzer. II. The Database and Diagnostic Power of Crystalline Silicate Features in Galaxy Spectra. *ApJS*, *259*(2), Article 37, 37. https://doi.org/10.3847/1538-4365/ac4989

Spoon, H. W. W., Marshall, J. A., Houck, J. R., Elitzur, M., Hao, L., Armus, L., Brandl, B. R., & Charmandaris, V. (2007). Mid-Infrared Galaxy Classification Based on Silicate Obscuration and PAH Equivalent Width. *ApJ*, *654*(1), L49–L52. https://doi.org/10.1086/511268

Springel, V., Pakmor, R., Pillepich, A., Weinberger, R., Nelson, D., Hernquist, L., Vogelsberger, M., ... Naiman, J. (2018). First results from the IllustrisTNG simulations: matter and galaxy clustering. *MNRAS*, *475*(1), 676–698. https://doi.org/10.1093/mnras/stx3304

Stasińska, G. (2005). Biases in abundance derivations for metal-rich nebulae. *A&A*, *434*(2), 507–520. https://doi.org/10.1051/0004-6361:20042216

Stasińska, G. (2006). [Ar III]/[O III] and [S III]/[O III]: well-behaved oxygen abundance indicators for HII regions and star forming galaxies. *A&A*, *454*(3), L127–L130. https://doi.org/10.1051/0004-6361:20065516

Stasińska, G., Tenorio-Tagle, G., Rodríguez, M., & Henney, W. J. (2007). Enrichment of the interstellar medium by metal-rich droplets and the abundance bias in H ii regions. *A&A*, *471*(1), 193–204. https://doi.org/10.1051/0004-6361:20065675

Stasińska, G., Vale Asari, N., Cid Fernandes, R., Gomes, J. M., Schlickmann, M., Mateus, A., Schoenell, W., ... Seagal Collaboration. (2008). Can retired galaxies mimic active galaxies? Clues from the Sloan Digital Sky Survey. *MNRAS*, *391*(1), L29–L33. https://doi.org/10.1111/j.1745-3933.2008.00550.x

Stierwalt, S., Armus, L., Surace, J. A., Inami, H., Petric, A. O., Diaz-Santos, T., Haan, S., ... Xu, K. (2013). Mid-infrared Properties of Nearby Luminous Infrared Galaxies. I. Spitzer Infrared Spectrograph Spectra for the GOALS Sample. *ApJS*, *206*(1), Article 1, 1. https://doi.org/10.1088/0067-0049/206/1/1

Storchi-Bergmann, T., Bica, E., Kinney, A. L., & Bonatto, C. (1997). The nature of the optical continuum in NGC5128 (CentaurusA). *MNRAS*, *290*(2), 231–244. https://doi.org/10.1093/mnras/290.2.231

Storchi-Bergmann, T., Schmitt, H. R., Calzetti, D., & Kinney, A. L. (1998). Chemical Abundance Calibrations for the Narrow-Line Region of Active Galaxies. *AJ*, *115*(3), 909–914. https://doi.org/10.1086/300242

Stoughton, C., Lupton, R. H., Bernardi, M., Blanton, M. R., Burles, S., Castander, F. J., Connolly, A. J., ... Zheng, W. (2002). Sloan Digital Sky Survey: Early Data Release. *AJ*, *123*(1), 485–548. https://doi.org/10.1086/324741

Strickland, D. K., Heckman, T. M., Colbert, E. J. M., Hoopes, C. G., & Weaver, K. A. (2004). A High Spatial Resolution X-Ray and Hα Study of Hot Gas in the Halos of Star-forming Disk Galaxies. I. Spatial and Spectral Properties of the Diffuse X-Ray Emission. *ApJS*, *151*(2), 193–236. https://doi.org/10.1086/382214

Strieder, F. (2010). Carbon burning in stars - Prospects for underground measurements of the ^{12}C+^{12}C fusion reactions. *Journal of Physics Conference Series*, *202*, Article 012025, 012025. https://doi.org/10.1088/1742-6596/202/1/012025

Strigari, L. E., Bullock, J. S., Kaplinghat, M., Diemand, J., Kuhlen, M., & Madau, P. (2007). Redefining the Missing Satellites Problem. *ApJ*, *669*(2), 676–683. https://doi.org/10.1086/521914

Sturm, E., Lutz, D., Verma, A., Netzer, H., Sternberg, A., Moorwood, A. F. M., Oliva, E., & Genzel, R. (2002). Mid-Infrared line diagnostics of active galaxies. A spectroscopic AGN survey with ISO-SWS. *A&A*, *393*, 821–841. https://doi.org/10.1051/0004-6361:20021043

Sugahara, Y., Inoue, A. K., Hashimoto, T., Yamanaka, S., Fujimoto, S., Tamura, Y., Matsuo, H., ... Zackrisson, E. (2021). Big Three Dragons: A [N II] 122 μm Constraint and New Dust-continuum Detection of a z = 7.15 Bright Lyman-break Galaxy with ALMA. *ApJ*, *923*(1), Article 5, 5. https://doi.org/10.3847/1538-4357/ac2a36

Sutherland, R. S., Bicknell, G. V., & Dopita, M. A. (2003a). The Numerical Simulation of Radiative Shocks. II. Thermal Instabilities in Two-dimensional Models. *ApJ*, *591*(1), 238–257. https://doi.org/10.1086/375294

Sutherland, R. S., Bisset, D. K., & Bicknell, G. V. (2003b). The Numerical Simulation of Radiative Shocks. I. The Elimination of Numerical Shock Instabilities Using a Local Oscillation Filter. *ApJS*, *147*(1), 187–195. https://doi.org/10.1086/374795

Sutherland, R. S., & Dopita, M. A. (2017). Effects of Preionization in Radiative Shocks. I. Self-consistent Models. *ApJS*, *229*(2), Article 34, 34. https://doi.org/10.3847/1538-4365/aa6541

Swinyard, B. M., Clegg, P. E., Ade, P. A. R., Armand, C., Baluteau, J. .-., Barlow, M. J., Berges, J. .-., ... White, G. J. (1996). Calibration and performance of the ISO Long-Wavelength Spectrometer. *A&A*, *315*, L43–L48.

Swinyard, B., Clegg, P., Leeks, S., Griffin, M., Lim, T., & Burgdorf, M. (2000). Space Operation and Performance of Doped Germanium Photo-Conducting Detectors in the Far Infrared: Experience from the ISO LWS. *Experimental Astronomy*, *10*, 157–176. https://doi.org/10.1023/A:1008084116564

Tadaki, K.-i., Iono, D., Hatsukade, B., Kohno, K., Lee, M. M., Matsuda, Y., Michiyama, T., ... Umehata, H. (2019). CNO Emission of an Unlensed Submillimeter Galaxy at z = 4.3. *ApJ*, *876*(1), Article 1, 1. https://doi.org/10.3847/1538-4357/ab1415

Tapia-Contreras, B., Tissera, P. B., Sillero, E., Gonzalez-Jara, J., Casanueva-Villarreal, C., Pedrosa, S., Bignone, L., ... Domínguez-Tenreiro, R. (2025). Insight into the physical processes that shape the metallicity profiles in galaxies. *arXiv e-prints*, Article arXiv:2502.02080, arXiv:2502.02080. https://doi.org/10.48550/arXiv.2502.02080

Taylor, P., & Kobayashi, C. (2017). The metallicity and elemental abundance gradients of simulated galaxies and their environmental dependence. *MNRAS*, *471*(4), 3856–3870. https://doi.org/10.1093/mnras/stx1860

Taylor, V. A., Jansen, R. A., Windhorst, R. A., Odewahn, S. C., & Hibbard, J. E. (2005). UBVR and Hubble Space Telescope Mid-Ultraviolet and Near-Infrared Surface Photometry and Radial Color Gradients of Late-Type, Irregular, and Peculiar Galaxies. *ApJ*, *630*(2), 784–803. https://doi.org/10.1086/432028

Temi, P., Marcum, P. M., Young, E., Adams, J. D., Adams, S., Andersson, B. .-., Becklin, E. E., ... Zinnecker, H. (2014). The SOFIA Observatory at the Start of Routine Science Operations: Mission Capabilities and Performance. *ApJS*, *212*(2), Article 24, 24. https://doi.org/10.1088/0067-0049/212/2/24

Teyssier, R., Chapon, D., & Bournaud, F. (2010). The Driving Mechanism of Starbursts in Galaxy Mergers. *ApJ*, *720*(2), L149–L154. https://doi.org/10.1088/2041-8205/720/2/L149

Thomas, A. D., Dopita, M. A., Kewley, L. J., Groves, B. A., Sutherland, R. S., Hopkins, A. M., & Blanc, G. A. (2018). Interrogating Seyferts with NebulaBayes: Spatially Probing the Narrow-line Region Radiation Fields and Chemical Abundances. *ApJ*, *856*(2), Article 89, 89. https://doi.org/10.3847/1538-4357/aab3db

Thomas, A. D., Kewley, L. J., Dopita, M. A., Groves, B. A., Hopkins, A. M., & Sutherland, R. S. (2019). The Mass-Metallicity Relation of Local Active Galaxies. *ApJ*, *874*(1), Article 100, 100. https://doi.org/10.3847/1538-4357/ab08a1

Thornley, M. D., Förster Schreiber, N. M., Lutz, D., Genzel, R., Spoon, H. W. W., Kunze, D., & Sternberg, A. (2000). Massive Star Formation and Evolution in Starburst Galaxies: Mid-infrared Spectroscopy with the ISO Short Wavelength Spectrometer. *ApJ*, *539*(2), 641–657. https://doi.org/10.1086/309261

Thuan, T. X., Izotov, Y. I., & Lipovetsky, V. A. (1995). Heavy Element Abundances in a New Sample of Low-Metallicity Blue Compact Galaxies. *ApJ*, *445*, 108. https://doi.org/10.1086/175676

Tissera, P. B., Bignone, L., Gonzalez-Jara, J., Muñoz-Escobar, I., Cataldi, P., Miranda, V. P., Barrientos-Acevedo, D., ... Jara-Ferreira, F. (2025). The CIELO project: The chemo-dynamical properties of galaxies and the cosmic web. *A&A*, *697*, Article A134, A134. https://doi.org/10.1051/0004-6361/202453348

Tissera, P. B., Rosas-Guevara, Y., Sillero, E., Pedrosa, S. E., Theuns, T., & Bignone, L. (2022). The evolution of the oxygen abundance gradients in star-forming galaxies in the EAGLE simulations. *MNRAS*, *511*(2), 1667–1684. https://doi.org/10.1093/mnras/stab3644

Togi, A., & Smith, J. D. T. (2016). Lighting the Dark Molecular Gas: H_2 as a Direct Tracer. *ApJ*, *830*(1), Article 18, 18. https://doi.org/10.3847/0004-637X/830/1/18

Tommasin, S., Spinoglio, L., Malkan, M. A., & Fazio, G. (2010). Spitzer-IRS High-Resolution Spectroscopy of the 12 μm Seyfert Galaxies. II. Results for the Complete Data Set. *ApJ*, *709*(2), 1257–1283. https://doi.org/10.1088/0004-637X/709/2/1257

Toribio San Cipriano, L., Domínguez-Guzmán, G., Esteban, C., García-Rojas, J., Mesa-Delgado, A., Bresolin, F., Rodríguez, M., & Simón-Díaz, S. (2017). Carbon and oxygen in H II regions of the Magellanic Clouds: abundance discrepancy and chemical evolution. *MNRAS*, *467*(3), 3759–3774. https://doi.org/10.1093/mnras/stx328

Tremonti, C. A., Heckman, T. M., Kauffmann, G., Brinchmann, J., Charlot, S., White, S. D. M., Seibert, M., ... Brinkmann, J. (2004). The Origin of the Mass-Metallicity Relation: Insights from 53,000 Star-forming Galaxies in the Sloan Digital Sky Survey. *ApJ*, *613*(2), 898–913. https://doi.org/10.1086/423264

Tsamis, Y. G., Barlow, M. J., Liu, X. .-., Danziger, I. J., & Storey, P. J. (2003). Heavy elements in Galactic and Magellanic Cloud HII regions: recombination-line versus forbidden-line abundances. *MNRAS*, *338*(3), 687–710. https://doi.org/10.1046/j.1365-8711.2003.06081.x

Ueta, T., & Otsuka, M. (2021). Proper Plasma Analysis Practice (PPAP), an Integrated Procedure of Extinction Correction and Plasma Diagnostics: A Demo with an HST/WFC3 Image Set of NGC 6720. *PASP*, *133*(1027), Article 093002, 093002. https://doi.org/10.1088/1538-3873/ac20ab

Urry, C. M., & Padovani, P. (1995). Unified Schemes for Radio-Loud Active Galactic Nuclei. *PASP*, *107*, 803. https://doi.org/10.1086/133630

Ursini, F., Dovčiak, M., Zhang, W., Matt, G., Petrucci, P. .-., & Done, C. (2020). Estimating the size of X-ray lamppost coronae in active galactic nuclei. *A&A*, *644*, Article A132, A132. https://doi.org/10.1051/0004-6361/202039158

Uzgil, B. D., Bradford, C. M., Hailey-Dunsheath, S., Maloney, P. R., & Aguirre, J. E. (2016). Constraining the ISM Properties of the Cloverleaf Quasar Host Galaxy with Herschel Spectroscopy. *ApJ*, *832*(2), Article 209, 209. https://doi.org/10.3847/0004-637X/832/2/209

Vaceli, M. S., Viegas, S. M., Gruenwald, R., & de Souza, R. E. (1997). Spectroscopy of Seyfert 2 Galaxies, Liners, and H(II) Galaxies. *AJ*, *114*, 1345. https://doi.org/10.1086/118568

Valentino, F., Magdis, G. E., Daddi, E., Liu, D., Aravena, M., Bournaud, F., Cortzen, I., ... Puglisi, A. (2020). The Properties of the Interstellar Medium of Galaxies across Time as Traced by the Neutral Atomic Carbon [C I]. *ApJ*, *890*(1), Article 24, 24. https://doi.org/10.3847/1538-4357/ab6603

Vallucci-Goy, V., Lebreuilly, U., & Hennebelle, P. (2024). Dust evolution during a protostellar collapse: Influence on the coupling between the neutral gas and magnetic field. *A&A*, *690*, Article A23, A23. https://doi.org/10.1051/0004-6361/202348268

Valluri, M., & Anupama, G. C. (1996). H(alpha) Imaging of the Hickson Compact Group 62. *AJ*, *112*, 1390. https://doi.org/10.1086/118106

van Vleck, J. H. (1947). The Absorption of Microwaves by Uncondensed Water Vapor. *Physical Review*, *71*(7), 425–433. https://doi.org/10.1103/PhysRev.71.425

van Zee, L., & Haynes, M. P. (2006). Oxygen and Nitrogen in Isolated Dwarf Irregular Galaxies. *ApJ*, *636*(1), 214–239. https://doi.org/10.1086/498017

van Zee, L., Salzer, J. J., Haynes, M. P., O'Donoghue, A. A., & Balonek, T. J. (1998). Spectroscopy of Outlying H II Regions in Spiral Galaxies: Abundances and Radial Gradients. *AJ*, *116*(6), 2805–2833. https://doi.org/10.1086/300647

Vaona, L., Ciroi, S., Di Mille, F., Cracco, V., La Mura, G., & Rafanelli, P. (2012). Spectral properties of the narrow-line region in Seyfert galaxies selected from the SDSS-DR7. *Monthly Notices of the Royal Astronomical Society*, *427*(2), 1266–1283. https://doi.org/10.1111/j.1365-2966.2012.22060.x

Veilleux, S., Rupke, D. S. N., Kim, D. .-., Genzel, R., Sturm, E., Lutz, D., Contursi, A., ... Barnes, J. E. (2009). Spitzer Quasar and Ulirg Evolution Study (QUEST). IV. Comparison of 1 Jy Ultraluminous Infrared Galaxies with Palomar-Green Quasars. *ApJS*, *182*(2), 628–666. https://doi.org/10.1088/0067-0049/182/2/628

Veilleux, S., Cecil, G., & Bland-Hawthorn, J. (2005). Galactic Winds. *ARA&A*, *43*(1), 769–826. https://doi.org/10.1146/annurev.astro.43.072103.150610

Veilleux, S., Goodrich, R. W., & Hill, G. J. (1997). Infrared Spectroscopy of Seyfert 2 Galaxies: A Look through the Obscuring Torus? II. *ApJ*, *477*(2), 631–660. https://doi.org/10.1086/303735

Veilleux, S., Kim, D. .-., & Sanders, D. B. (1999). Optical Spectroscopy of the IRAS 1 JY Sample of Ultraluminous Infrared Galaxies. *ApJ*, *522*(1), 113–138. https://doi.org/10.1086/307634

Veilleux, S., Maiolino, R., Bolatto, A. D., & Aalto, S. (2020). Cool outflows in galaxies and their implications. *A&A Rev.*, *28*(1), Article 2, 2. https://doi.org/10.1007/s00159-019-0121-9

Veilleux, S., & Osterbrock, D. E. (1987). Spectral Classification of Emission-Line Galaxies. *ApJS*, *63*, 295. https://doi.org/10.1086/191166

Venditti, A., Bromm, V., Finkelstein, S. L., Calabrò, A., Napolitano, L., Graziani, L., & Schneider, R. (2024). A Hide-and-seek Game: Looking for Population III Stars during the Epoch of Reionization through the He II λ1640 Line. *ApJ*, *973*(1), Article L12, L12. https://doi.org/10.3847/2041-8213/ad7387

Ventura, P., Stanghellini, L., Dell'Agli, F., & García-Hernández, D. A. (2017). The evolution of Galactic planetary nebula progenitors through the comparison of their nebular abundances with AGB yields. *MNRAS*, *471*(4), 4648–4661. https://doi.org/10.1093/mnras/stx1907

Verde, L., Schöneberg, N., & Gil-Marín, H. (2024). A Tale of Many H $_0$. *ARA&A*, *62*(1), 287–331. https://doi.org/10.1146/annurev-astro-052622-033813

Vika, M., Ciesla, L., Charmandaris, V., Xilouris, E. M., & Lebouteiller, V. (2017). The physical properties of Spitzer/IRS galaxies derived from their UV to 22 μm spectral energy distribution. *A&A*, *597*, Article A51, A51. https://doi.org/10.1051/0004-6361/201629031

Vila-Costas, M. B., & Edmunds, M. G. (1992). The relation between abundance gradients and the physical properties of spiral galaxies. *MNRAS*, *259*, 121–145. https://doi.org/10.1093/mnras/259.1.121

Vila-Costas, M. B., & Edmunds, M. G. (1993). The nitrogen-to-oxygen ratio in galaxies and its implications for the origin of nitrogen. *MNRAS*, *265*, 199–212. https://doi.org/10.1093/mnras/265.1.199

Vilchez, J. M., & Esteban, C. (1996). The chemical composition of HII regions in the outer Galaxy. *MNRAS*, *280*(3), 720–734. https://doi.org/10.1093/mnras/280.3.720

Vilchez, J. M., & Pagel, B. E. J. (1988). On the determination of temperatures of ionizing stars in H II regions. *MNRAS*, *231*, 257–267. https://doi.org/10.1093/mnras/231.2.257

Vilchez, J. M., Pagel, B. E. J., Diaz, A. I., Terlevich, E., & Edmunds, M. G. (1988). The chemical composition gradient across M 33. *MNRAS*, *235*, 633–653. https://doi.org/10.1093/mnras/235.3.633

Vílchez, J. M., Relaño, M., Kennicutt, R., De Looze, I., Mollá, M., & Galametz, M. (2019). Metals and dust content across the galaxies M 101 and NGC 628. *MNRAS*, *483*(4), 4968–4983. https://doi.org/10.1093/mnras/sty3455

Villar Martín, M., López Cobá, C., Cazzoli, S., Pérez Montero, E., & Cabrera Lavers, A. (2024). Agn feedback can produce metal enrichment on galaxy scales. *A&A*, *690*, A397. https://doi.org/10.1051/0004-6361/202449621

Villar-Martín, M., Humphrey, A., Martínez-Sansigre, A., Pérez-Torres, M., Binette, L., & Zhang, X. G. (2008). Emission-line activity in type 2 quasars from the Sloan Digital Sky Survey. *MNRAS*, *390*(1), 218–226. https://doi.org/10.1111/j.1365-2966.2008.13779.x

Vincenzo, F., Belfiore, F., Maiolino, R., Matteucci, F., & Ventura, P. (2016). Nitrogen and oxygen abundances in the Local Universe. *MNRAS*, *458*(4), 3466–3477. https://doi.org/10.1093/mnras/stw532

Vincenzo, F., & Kobayashi, C. (2018). Extragalactic archaeology with the C, N, and O chemical abundances. *A&A*, *610*, Article L16, L16. https://doi.org/10.1051/0004-6361/201732395

Vogt, F. P. A., Pérez, E., Dopita, M. A., Verdes-Montenegro, L., & Borthakur, S. (2017). Evidence for azimuthal variations of the oxygen-abundance gradient tracing the spiral structure of the galaxy HCG 91c. *A&A*, *601*, Article A61, A61. https://doi.org/10.1051/0004-6361/201629853

Wakelam, V., Bron, E., Cazaux, S., Dulieu, F., Gry, C., Guillard, P., Habart, E., ... Watanabe, N. (2017). H_2 formation on interstellar dust grains: The viewpoints of theory, experiments, models and observations. *Molecular Astrophysics*, *9*, 1–36. https://doi.org/10.1016/j.molap.2017.11.001

Werner, M. W., Roellig, T. L., Low, F. J., Rieke, G. H., Rieke, M., Hoffmann, W. F., Young, E., ... Cruikshank, D. P. (2004). The Spitzer Space Telescope Mission. *ApJS*, *154*(1), 1–9. https://doi.org/10.1086/422992

Westin, B. A. M. (1985). The nucleus of the Seyfert 1 galaxy NGC 7469 : physical conditions andstructure. *A&A*, *151*, 137–143.

Wilson, A. S., & Penston, M. V. (1979). IC 4329A: the nearest quasar? *ApJ*, *232*, 389–399. https://doi.org/10.1086/157298

Winkler, H. (1992). Variability studies of Seyfert galaxies - II. Spectroscopy. *MNRAS*, *257*, 677–688. https://doi.org/10.1093/mnras/257.4.677

Wolfire, M. G., McKee, C. F., Hollenbach, D., & Tielens, A. G. G. M. (2003). Neutral Atomic Phases of the Interstellar Medium in the Galaxy. *ApJ*, *587*(1), 278–311. https://doi.org/10.1086/368016

Wong, Y. H. V., Wang, P., Hashimoto, T., Takagi, T., Goto, T., Kim, S. J., Wu, C. K. .-., ... Hsiao, T. Y. .-. (2022). ALMA Detections of [O III] and [C II] Emission Lines From A1689-zD1 at z = 7.13. *ApJ*, *929*(2), Article 161, 161. https://doi.org/10.3847/1538-4357/ac5cc7

Wootten, A., & Thompson, A. R. (2009). The Atacama Large Millimeter/Submillimeter Array. *IEEE Proceedings*, *97*(8), 1463–1471. https://doi.org/10.1109/JPROC.2009.2020572

Worthey, G., & Ottaviani, D. L. (1997). Hγ and Hδ Absorption Features in Stars and Stellar Populations. *ApJS*, *111*(2), 377–386. https://doi.org/10.1086/313021

Wright, G. S., Wright, D., Goodson, G. B., Rieke, G. H., Aitink-Kroes, G., Amiaux, J., Aricha-Yanguas, A., … Zhender, A. (2015). The Mid-Infrared Instrument for the James Webb Space Telescope, II: Design and Build. *PASP*, *127*(953), 595. https://doi.org/10.1086/682253

Wright, G. S., Rieke, G. H., Glasse, A., Ressler, M., García Marín, M., Aguilar, J., Alberts, S., … Wolff, S. (2023). The Mid-infrared Instrument for JWST and Its In-flight Performance. *PASP*, *135*(1046), Article 048003, 048003. https://doi.org/10.1088/1538-3873/acbe66

Wu, H., Zou, Z. L., Xia, X. Y., & Deng, Z. G. (1998). A statistical study of the spectra of very luminous IRAS galaxies. I. Data. *A&AS*, *127*, 521–526. https://doi.org/10.1051/aas:1998374

Yamagishi, M., Kaneda, H., Ishihara, D., Oyabu, S., Onaka, T., Shimonishi, T., & Suzuki, T. (2015). Systematic Variations in CO_2/H_2O Ice Abundance Ratios in Nearby Galaxies Found with AKARI Near-infrared Spectroscopy. *ApJ*, *807*(1), Article 29, 29. https://doi.org/10.1088/0004-637X/807/1/29

Yamasawa, D., Habe, A., Kozasa, T., Nozawa, T., Hirashita, H., Umeda, H., & Nomoto, K. (2011). The Role of Dust in the Early Universe. I. Protogalaxy Evolution. *ApJ*, *735*(1), Article 44, 44. https://doi.org/10.1088/0004-637X/735/1/44

Yang, H., Malhotra, S., Gronke, M., Rhoads, J. E., Leitherer, C., Wofford, A., Jiang, T., … Wang, J. (2017a). Lyα Profile, Dust, and Prediction of Lyα Escape Fraction in Green Pea Galaxies. *ApJ*, *844*(2), Article 171, 171. https://doi.org/10.3847/1538-4357/aa7d4d

Yang, H., Malhotra, S., Rhoads, J. E., & Wang, J. (2017b). Blueberry Galaxies: The Lowest Mass Young Starbursts. *The Astrophisical Journal*, *847*(1), Article 38, 38. https://doi.org/10.3847/1538-4357/aa8809

Yano, K., Baba, S., Nakagawa, T., Malkan, M. A., Isobe, N., Shirahata, M., Doi, R., & Bhalotia, V. (2021). Anomalous Hydrogen Recombination Line Ratios in Ultraluminous Infrared Galaxies. *ApJ*, *922*(2), Article 272, 272. https://doi.org/10.3847/1538-4357/ac26be

Yates, R. M., & Kauffmann, G. (2014). Dilution in elliptical galaxies: implications for the relation between metallicity, stellar mass and star formation rate. *MNRAS*, *439*(4), 3817–3834. https://doi.org/10.1093/mnras/stu233

Yeh, S. C. C., & Matzner, C. D. (2012). Ionization Parameter as a Diagnostic of Radiation and Wind Pressures in H II Regions and Starburst Galaxies. *ApJ*, *757*(2), Article 108, 108. https://doi.org/10.1088/0004-637X/757/2/108

York, D. G., Adelman, J., Anderson, J. E., Jr., Anderson, S. F., Annis, J., Bahcall, N. A., Bakken, J. A., … SDSS Collaboration. (2000). The Sloan Digital Sky Survey: Technical Summary. *AJ*, *120*(3), 1579–1587. https://doi.org/10.1086/301513

Young, E. T., Becklin, E. E., Marcum, P. M., Roellig, T. L., De Buizer, J. M., Herter, T. L., Güsten, R., … Zinnecker, H. (2012). Early Science with SOFIA, the Stratospheric Observatory For Infrared Astronomy. *ApJ*, *749*(2), Article L17, L17. https://doi.org/10.1088/2041-8205/749/2/L17

Yuan, F., Cui, W., & Narayan, R. (2005). An Accretion-Jet Model for Black Hole Binaries: Interpreting the Spectral and Timing Features of XTE J1118+480. *ApJ*, *620*(2), 905–914. https://doi.org/10.1086/427206

Yuan, F., Wang, H., & Yang, H. (2022). The Accretion Flow in M87 is Really MAD. *ApJ*, *924*(2), Article 124, 124. https://doi.org/10.3847/1538-4357/ac4714

Yuan, F., Zdziarski, A. A., Xue, Y., & Wu, X.-B. (2007). Modeling the Hard States of XTE J1550-564 during Its 2000 Outburst. *ApJ*, *659*(1), 541–548. https://doi.org/10.1086/512078

Yuk, H., Dai, X., Jayasinghe, T., Fu, H., Mishra, H. D., Kochanek, C. S., Shappee, B. J., & Stanek, K. Z. (2022). Variability Selected Active Galactic Nuclei from ASAS-SN Survey: Constraining the Low Luminosity AGN Population. *ApJ*, *930*(2), Article 110, 110. https://doi.org/10.3847/1538-4357/ac6423

Zahid, H. J., Dima, G. I., Kewley, L. J., Erb, D. K., & Davé, R. (2012). A Census of Oxygen in Star-forming Galaxies: An Empirical Model Linking Metallicities, Star Formation Rates, and Outflows. *ApJ*, *757*(1), Article 54, 54. https://doi.org/10.1088/0004-637X/757/1/54

Zamora, S., Díaz, Á. I., Terlevich, E., & Fernández, V. (2022). Interstellar extinction correction in ionized regions using He I lines. *MNRAS*, *516*(1), 749–756. https://doi.org/10.1093/mnras/stac2201

Zaritsky, D., Kennicutt, J., Robert C., & Huchra, J. P. (1994). H II Regions and the Abundance Properties of Spiral Galaxies. *ApJ*, *420*, 87. https://doi.org/10.1086/173544

Zavala, J. A., Bakx, T., Mitsuhashi, I., Castellano, M., Calabro, A., Akins, H., Buat, V., ... Yung, L. Y. A. (2024). ALMA Detection of [O III] 88 μm at z = 12.33: Exploring the Nature and Evolution of GHZ2 as a Massive Compact Stellar System. *ApJ*, *977*(1), Article L9, L9. https://doi.org/10.3847/2041-8213/ad8f38

Zhao, Y., Liu, J., Zhang, Z.-Y., & Bisbas, T. G. (2024). Ionized Carbon in Galaxies: The [C II] 158 μm Line as a Total Molecular Gas Mass Tracer Revisited. *ApJ*, *977*(1), Article 46, 46. https://doi.org/10.3847/1538-4357/ad8c3e

Zhuang, M.-Y., Ho, L. C., & Shangguan, J. (2019). A New Method to Measure Star Formation Rates in Active Galaxies Using Mid-infrared Neon Emission Lines. *ApJ*, *873*(2), Article 103, 103. https://doi.org/10.3847/1538-4357/ab0650

Zinchenko, I. A., Just, A., Pilyugin, L. S., & Lara-Lopez, M. A. (2019). Characterizing the radial oxygen abundance distribution in disk galaxies. *A&A*, *623*, Article A7, A7. https://doi.org/10.1051/0004-6361/201834364

Zinchenko, I. A., Pilyugin, L. S., Grebel, E. K., Sánchez, S. F., & Vílchez, J. M. (2016). Oxygen abundance maps of CALIFA galaxies. *MNRAS*, *462*, 2715–2733. https://doi.org/10.1093/mnras/stw1857

Zinchenko, I. A., Sobolenko, M., Vílchez, J. M., & Kehrig, C. (2024). Characterizing chemical abundance ratios in extremely metal-poor star-forming galaxies in DESI EDR. *A&A*, *690*, Article A28, A28. https://doi.org/10.1051/0004-6361/202450232

Zinchenko, I. A., Vílchez, J. M., Pérez-Montero, E., Sukhorukov, A. V., Sobolenko, M., & Duarte Puertas, S. (2021). The dependence of the gradients of oxygen and nitrogen-to-oxygen on stellar age in MaNGA galaxies. *A&A*, *655*, Article A58, A58. https://doi.org/10.1051/0004-6361/202141522

Zoldan, A., De Lucia, G., Xie, L., Fontanot, F., & Hirschmann, M. (2017). H I-selected galaxies in hierarchical models of galaxy formation and evolution. *MNRAS*, *465*(2), 2236–2253. https://doi.org/10.1093/mnras/stw2901

Zurita, A., Florido, E., Bresolin, F., Pérez, I., & Pérez-Montero, E. (2021a). Bar effect on gas-phase abundance gradients - II. Luminosity-dependent flattening. *MNRAS*, *500*(2), 2380–2400. https://doi.org/10.1093/mnras/staa2208

Zurita, A., Florido, E., Bresolin, F., Pérez-Montero, E., & Pérez, I. (2021b). Bar effect on gas-phase abundance gradients. I. Data sample and chemical abundances. *MNRAS*, *500*(2), 2359–2379. https://doi.org/10.1093/mnras/staa2246

Zurita, A., Rozas, M., & Beckman, J. E. (2000). The origin of the ionization of the diffuse interstellar medium in spiral galaxies. I. Photometric measurements. *A&A*, *363*, 9–28.